

# Radio, X-ray, and Gravitational Wave Emission from Neutron Stars

**Christine Tsung Yi Chung**

Submitted in total fulfilment of the requirements  
of the degree of Doctor of Philosophy

August 2010

School of Physics

The University of Melbourne



# Abstract

Multi-messenger observations of neutron stars provide a rich database from which fundamental properties, such as their ellipticities, the strengths and structures of their magnetic fields, and their spin histories since birth can be inferred. This thesis consists of three projects aimed at measuring these properties using radio, X-ray, and gravitational wave emission.

Firstly, we analyse X-ray timing data from the accreting millisecond pulsar XTE J1814–338, and attempt to reproduce the data using a model of a freely precessing pulsar. Precessing pulsars have nonzero ellipticities and hence are sources of continuous gravitational waves. Precession in an accretion-powered pulsar is expected to produce characteristic variations in the pulse properties. Assuming surface intensity maps with one and two hotspots, we compute theoretically the periodic modulation of the mean flux, pulse-phase residuals and fractional amplitudes of the first and second harmonic of the pulse profiles. We then search for these signatures in 37 days of X-ray timing data from XTE J1814–338. We analyse a 12.2-d modulation observed previously and show that it is consistent with a freely precessing neutron star only if the inclination angle is  $< 0.1^\circ$ , an a priori unlikely orientation. We conclude that if the observed flux variations are due to precession, the surface intensity map must be over-simplified. Our model allows us to place an upper limit on  $\epsilon$  of  $3.0 \times 10^{-9}$  independently of the surface intensity map, and we estimate the tilt angle  $\theta$  to lie roughly between  $5^\circ$  and  $10^\circ$ . On the other hand, if the observed flux variations are not due to precession, the detected X-ray modulation serves as a firm upper limit on any underlying precession signal. We then place an upper limit on the product  $\epsilon \cos \theta$  of  $\leq 9.9 \times 10^{-10}$ . The first scenario translates into a maximum gravitational wave strain of  $\sim 10^{-27}$  from XTE J1814–338 (assuming a distance of 8 kpc), and a corresponding signal-to-noise ratio of  $\lesssim 10^{-3}$  (for a 120 day integration time) for the advanced Laser Interferometer Gravitational Wave Observatory (LIGO) ground-based detector.

Secondly, we design and implement a semi-coherent cross-correlation algorithm which will be used to search for a young neutron star in the supernova remnant SNR 1987A using data from LIGO. We introduce an astrophysical model for the gravitational wave phase which describes a neutron star's spin down in terms of its magnetic field strength  $B$  and ellipticity  $\epsilon$ , instead of its frequency derivatives. This model allows accurate tracking of the gravitational wave phase from a neutron star spinning down rapidly, an issue which has hindered previous searches for such young objects. We calculate the semi-coherent phase metric and estimate the range of search parameters achievable given our computational resources. We also present results of software verification tests. We verify that when searching over pure noise, the cross-correlation detection statistic is distributed as a zero mean, unit variance Gaussian. In the presence

of a signal, the mean and variance of the detection statistic depend on the gravitational wave strain. We also compare results obtained by searching over exact source inclination and polarization angles to those obtained by averaging over these angles. For standard LIGO sensitivity, in the frequency band between approximately 100 Hz and 300 Hz, we will be able to place limits of  $B \gtrsim 10^{13}$  G and  $\epsilon \lesssim 10^{-4}$ . Monte Carlo sensitivity estimates show that the smallest detectable gravitational wave strain at 150 Hz for a search using  $10^9$  templates is  $\approx 6 \times 10^{-25}$ .

Finally, we use radio pulsar polarimetry to investigate the magnetic geometry and orientation of pulsars. Polarimetric studies of pulsar radio emission traditionally concentrate on how the Stokes vector  $(I, Q, U, V)$  varies with pulse longitude, with special emphasis on the position angle (PA) swing of the linearly polarized component. The interpretation of the PA swing in terms of the rotating vector model is limited by the assumption of an axisymmetric magnetic field and the degeneracy of the output with respect to the orientation and magnetic geometry of the pulsar; different combinations of the latter two properties can produce similar PA swings. We introduce Stokes phase portraits as a supplementary diagnostic tool with which the orientation and magnetic geometry can be inferred more accurately. The Stokes phase portraits feature unique patterns in the  $I$ - $Q$ ,  $I$ - $U$ , and  $Q$ - $U$  planes, whose shapes depend sensitively on the magnetic geometry, inclination angle, beam and polarization patterns, and emission altitude. We construct look-up tables of Stokes phase portraits and PA swings for pure and current-modified dipole fields, filled core and hollow cone beams, and two empirical linear polarization models, including the effects of relativistic aberration. We apply Stokes tomography to observations of 26 radio pulsars, and show that for 60% of the sample, the observed emission is incompatible with a pure magnetic dipole at low emission altitudes. We model in detail two pulsars, PSR J0827+2637 and PSR J0304+1932, using a pure and current-modified dipole respectively. We also apply Stokes tomography to two millisecond radio pulsars, PSR J1939+2134 and PSR J0437–4715. The Stokes phase portraits for PSR J1939+2134 at 0.61 GHz are consistent with a current-modified dipole. However the fit is less accurate for PSR J1939+2134 at 1.414 GHz, and for PSR J0437–4715 at 1.44 GHz, indicating that these objects have a more complicated magnetic field geometry, such as a surface quadrupole, a force-free or vacuum-like field, or a polar magnetic mountain.

# Declaration

This is to certify that:

1. This thesis entitled “**Radio, X-ray and Gravitational Wave Emission from Neutron Star Mountains**” comprises only my original work, except where indicated in the Preface,
2. Due acknowledgement has been made in the text to all other material used,
3. The thesis is less than 100,000 words in length, exclusive of tables, figures, bibliography and appendices.

.....  
Christine Chung



# Preface

While most of the work presented herein is my own, there is some that is the result of collaborative work, or the result of the work of others.

- Chapter 1 is a fully referenced literature review. The writing is my own.
- Chapter 2 is based very closely on the following publication. The work is original and my own. I carried out all the numerical simulations and data analysis presented in this chapter, made all the figures, and wrote the text (edited by Dr. Andrew Melatos and Dr. Duncan Galloway). The X-ray timing data used in this chapter was provided by Dr. Duncan Galloway.

Chung, C. T. Y., Galloway, D. K., Melatos, A. Does the accreting millisecond pulsar XTE J1814-338 precess? *Monthly notices of the Royal Astronomical Society*, volume 391, page 254, 2008

- Chapter 3 is based very closely on the following publication. The work is original and my own. The cross-correlation algorithm described in Section 3.3 was invented by Dr. Sanjeev Dhurandhar, Dr. Badri Krishnan, Himan Mukhopadhyay, and Dr. John Whelan, and proper references are made in the text. The astrophysical phase model described in Section 3.5 was developed by myself in collaboration with my supervisor, Dr. Andrew Melatos. The calculation of the semi-coherent metric and the estimates of the computational cost presented in Section 3.6 was carried out by myself, following discussions with Dr. Andrew Melatos, Dr. Badri Krishnan, and Dr. John Whelan.

Chung, C. T. Y., Melatos, A., Krishnan, B., Whelan, J. T. Designing a cross-correlation search for continuous-wave gravitational radiation from a neutron star in the supernova remnant SNR 1987A *Monthly notices of the Royal Astronomical Society*, in preparation.

- Chapter 4 has not been published elsewhere. The work is original and my own. I implemented the cross-correlation algorithm as part of the LAL/LALApps software suite used by the LIGO Scientific Collaboration (LSC). The code was largely written by me but contains some functions written by Dr. Badri Krishnan. It also makes use of general-purpose LAL functions. The use of linked lists to handle data in the code was suggested by Dr. Andrew Melatos. The software verification and sensitivity estimates presented in Sections 4.2–4.3 were carried out by myself following discussions with Dr. Badri Krishnan, Dr. John Whelan, Dr. Andrew Melatos, and the LSC internal review committee (Dr. Teviet Creighton,

Dr. Eric Thrane, and Dr. Alberto Vecchio). The Octave scripts used to run Monte Carlo tests in Sections 4.2–4.3 are based on scripts provided by Dr. Carlos Peralta, a member of the LSC from 2007-2009. The calculations in Appendix 4C were carried out by myself, based closely on those in the Appendix of Dhurandhar et al. (2008).

- Chapter 5 is based very closely on the following publication. The work is original and my own. The observational data used in this chapter are courtesy of the European Pulsar Network database.

Chung, C. T. Y., Melatos, A. Stokes tomography of radio pulsar magnetospheres. I. Linear polarization *Monthly notices of the Royal Astronomical Society*, submitted.

- Chapter 6 is based very closely on the following publication. The work is original and my own. The observational data used in this chapter are courtesy of the European Pulsar Network database.

Chung, C. T. Y., Melatos, A. Stokes tomography of radio pulsar magnetospheres. II. Millisecond pulsars *Monthly notices of the Royal Astronomical Society*, in preparation.

- The conclusions in chapter 7 have not been published elsewhere. The work is original and my own. Section 7.4.2 makes use of numerical magnetic field geometries provided by Dr. Matthias Vigelius.

# Acknowledgements

“I feel a very unusual sensation –  
if it is not indigestion, I think it must be gratitude.”  
*Benjamin Disraeli*

Over the last four years, I have indeed been given much to be grateful for. Firstly, my heartfelt thanks goes to my supervisor, Dr. Andrew Melatos, for his endless patience and support. It has been a privilege working with someone whose attention to detail is surpassed only by his tireless dedication to his students’ work. I am also grateful to my co-supervisors: Dr. Duncan Galloway, for teaching me all about X-ray data reduction and for his careful proofreading, and Dr. Elisabetta Barberio, who pointed out at the beginning the importance of figuring things out for myself.

During my PhD, I had the opportunity to spend time at the AEI in Potsdam. I thank Dr. Badri Krishnan and Dr. John Whelan for their kind hospitality, and for their ongoing collaboration. I also thank the LSC review committee (Dr. Teviet Creighton, Dr. Eric Thrane, and Dr. Alberto Vecchio) and Dr. Sanjeev Dhurandhar whose valuable insight has greatly improved the work presented in this thesis.

The friends I have made in the School of Physics over the last few years are wonderful people, and I cannot thank them enough. Xiao Ming, for our morning coffees (one day they will get it just right!) and for always offering a shoulder to lean on. Alpha, Carlos, and Matthias, for not only their cherished friendship, but for also patiently answering every pulsar-related question I’ve ever thrown at them. Chun-Hsu, for the many kind words of support offered, and for reassuring me that  $1 + 1$  does always equal 2. Adrian, Ivy, Rebecca, and Swati, for always listening and encouraging.

Lastly, I thank my family for the strength they have provided me. Most of all, I am grateful to my husband Dudley who has stood by me unflinchingly through it all.



# Contents

<b>1</b>	<b>Introduction</b>	<b>1</b>
1.1	Neutron stars . . . . .	1
1.1.1	History . . . . .	1
1.1.2	Evolution and structure of neutron stars . . . . .	2
1.1.3	Neutron star structure . . . . .	5
1.2	Thesis motivation . . . . .	5
1.3	Rotation-powered pulsars . . . . .	8
1.3.1	Radio pulse profiles . . . . .	8
1.3.2	Polarization . . . . .	13
1.3.3	Timing properties . . . . .	17
1.3.4	Magnetic field strength and geometry . . . . .	19
1.4	Accretion-powered pulsars . . . . .	21
1.4.1	Timing properties . . . . .	24
1.4.2	Magnetic field strength . . . . .	30
1.5	Gravitational radiation . . . . .	31
1.5.1	Detectors . . . . .	33
1.5.2	Classification of high-frequency gravitational wave signals . . . . .	37
1.5.3	Continuous wave signals . . . . .	40
1.6	Searches for continuous gravitational waves . . . . .	48
1.6.1	Coherent searches . . . . .	49
1.6.2	Semi-coherent searches . . . . .	50
1.6.3	Current astrophysical limits from non-detection of continuous gravitational waves . . . . .	55
1.7	Thesis outline . . . . .	57
<b>2</b>	<b>Does the accreting millisecond pulsar XTE J1814–338 precess?</b>	<b>63</b>
2.1	Introduction . . . . .	63
2.2	Precession model . . . . .	66
2.2.1	Equations of motion . . . . .	66
2.2.2	Synthetic pulse profiles . . . . .	68
2.3	Biaxial star: Single hotspot . . . . .	70
2.3.1	Tilt angle, $\theta$ . . . . .	70
2.3.2	Hotspot latitude, $\alpha$ , and inclination, $\chi$ . . . . .	72
2.3.3	Initial longitude, $\phi(0)$ . . . . .	72
2.3.4	Geometry of the phase shifts . . . . .	73
2.4	Biaxial star: Two hotspots . . . . .	76
2.4.1	Tilt angle, $\theta$ . . . . .	76
2.4.2	Hotspot latitude, $\alpha$ and inclination, $\chi$ . . . . .	77
2.4.3	Initial longitude, $\phi(0)$ . . . . .	77

2.4.4	Geometry of the phase shifts . . . . .	78
2.5	Triaxial star . . . . .	78
2.6	X-ray timing analysis . . . . .	83
2.6.1	XTE J1814–338 . . . . .	84
2.6.2	Observations . . . . .	84
2.6.3	Timing analysis . . . . .	85
2.6.4	Pulse folding . . . . .	85
2.6.5	First harmonic . . . . .	87
2.6.6	Searching for precession . . . . .	88
2.7	Comparison between data and simulations . . . . .	91
2.8	Conclusion . . . . .	95
<b>3</b>	<b>Designing a cross-correlation search for continuous-wave gravitational radiation from a neutron star in SNR 1987A</b>	<b>97</b>
3.1	Introduction . . . . .	97
3.2	A young neutron star in SNR 1987A . . . . .	99
3.3	The cross-correlation algorithm . . . . .	102
3.4	Sensitivity . . . . .	105
3.4.1	Detection threshold . . . . .	105
3.4.2	Minimum ellipticity and indirect, age-based limit . . . . .	106
3.5	An astrophysical model for the gravitational wave phase . . . . .	107
3.5.1	Historical spin down . . . . .	109
3.6	Template spacing . . . . .	111
3.6.1	Semi-coherent phase metric . . . . .	113
3.6.2	Computational cost of the search . . . . .	115
3.6.3	Astrophysical upper limits . . . . .	117
3.7	Conclusion . . . . .	119
<b>4</b>	<b>Implementing the Cross-Correlation Search</b>	<b>123</b>
4.1	Software development . . . . .	123
4.1.1	Algorithm . . . . .	124
4.2	Verification . . . . .	125
4.2.1	Distribution of $\rho/\sigma_\rho$ when searching over pure noise . . . . .	125
4.2.2	Distribution of $\rho/\sigma_\rho$ as a function of signal strength . . . . .	130
4.2.3	Averaging over $\cos \iota$ and $\psi$ . . . . .	134
4.3	Sensitivity estimates . . . . .	142
4.3.1	Estimating $\rho_{\text{th}}$ . . . . .	143
4.3.2	Sensitivity without spin down . . . . .	144
4.3.3	Sensitivity with spin down . . . . .	145
4.4	Conclusion . . . . .	149
<b>5</b>	<b>Stokes tomography of radio pulsar magnetospheres. I. Linear polarization</b>	<b>153</b>
5.1	Introduction . . . . .	153
5.2	Stokes tomography . . . . .	155
5.2.1	Radiation field . . . . .	155
5.2.2	Numerical algorithm . . . . .	158

5.2.3	Relativistic aberration . . . . .	159
5.2.4	Beam pattern . . . . .	160
5.2.5	Linear polarization . . . . .	163
5.2.6	Summary of algorithm . . . . .	163
5.3	Dipole field at low emission altitudes . . . . .	165
5.3.1	Filled core emission . . . . .	166
5.3.2	Hollow cone emission . . . . .	175
5.4	Dipole field at $r = 0.1r_{\text{LC}}$ . . . . .	186
5.4.1	Filled core beam . . . . .	191
5.4.2	Hollow cone . . . . .	195
5.4.3	How common are low emission altitudes? . . . . .	195
5.5	Current-modified dipole field . . . . .	200
5.5.1	Filled core emission . . . . .	205
5.5.2	Hollow cone emission . . . . .	213
5.5.3	Emission altitude . . . . .	218
5.6	A detailed single-peaked example: PSR J0826+2637 . . . . .	230
5.6.1	Pure versus current-modified dipole . . . . .	232
5.6.2	Orientation $(\alpha, i)$ . . . . .	235
5.6.3	Beam and polarization patterns . . . . .	235
5.6.4	Emission altitude . . . . .	236
5.7	A detailed double-peaked example: PSR J0304+1932 . . . . .	238
5.7.1	Pure versus current-modified dipole . . . . .	240
5.7.2	Orientation $(\alpha, i)$ . . . . .	240
5.7.3	Beam and polarization patterns . . . . .	243
5.7.4	Emission altitude . . . . .	244
5.8	Conclusion . . . . .	247

<b>6</b>	<b>Stokes tomography of radio pulsar magnetospheres. II. Millisecond pulsars</b>	<b>253</b>
6.1	Introduction . . . . .	254
6.2	Stokes tomography . . . . .	255
6.2.1	Radiation field . . . . .	255
6.2.2	Look-up tables of Stokes phase portraits . . . . .	257
6.2.3	Interpulses . . . . .	258
6.2.4	Relativistic aberration . . . . .	260
6.3	Miniature population study . . . . .	261
6.3.1	General trends . . . . .	263
6.3.2	Magnetic geometry and orientation . . . . .	265
6.3.3	Emission altitude . . . . .	267
6.4	A detailed example of interpulse emission: PSR J1939+2134 . . . . .	271
6.4.1	Magnetic geometry . . . . .	272
6.4.2	Orientation $(\alpha, i)$ . . . . .	272
6.4.3	Beam and polarization patterns . . . . .	275
6.4.4	Emission altitude . . . . .	276
6.5	A detailed multi-peaked example: PSR J0437–4715 . . . . .	279
6.5.1	Magnetic geometry . . . . .	283
6.5.2	Orientation . . . . .	284

---

6.5.3	Beam pattern . . . . .	284
6.5.4	Decomposed phase portraits . . . . .	286
6.6	Conclusion . . . . .	287
<b>7</b>	<b>Conclusion</b>	<b>291</b>
7.1	Multimessenger studies of neutron stars . . . . .	291
7.2	X-ray light curves and precession . . . . .	291
7.3	Gravitational waves and ellipticity . . . . .	293
7.4	Radio emission, orientation, and magnetic field structure . . . . .	295
7.4.1	Vacuum dipole field . . . . .	295
7.4.2	Magnetic mountains . . . . .	297
	<b>Appendices</b>	<b>303</b>
	<b>Bibliography</b>	<b>341</b>

# List of Figures

1.1	Period-period derivative ( $P, \dot{P}$ ) diagram of a sample of 947 observed radio pulsars from the ATNF Pulsar Catalogue. . . . .	6
1.2	Emission geometry of a radio pulsar . . . . .	10
1.3	Pulse profiles of four pulsars showing a single-peaked profile (B0611+22), a double-peaked profile (B0301+19), a triple-peaked profile (B1821+05), and a quintuple-peaked profile (B1237+05). . . . .	11
1.4	Pulse profile and polarization angle swing for the millisecond pulsar PSR J2124–3358. . . . .	12
1.5	Pulse profile widths of a sample of radio pulsars, measured at 10% of the peak intensity, as a function of pulse period. . . . .	12
1.6	Examples of S-shaped PA swings and pulse profiles from eight radio pulsars. . . . .	14
1.7	Comparison of the fractional linear, absolute circular, and circular polarization of 24 MSPs and 281 slow pulsars. Histograms of the steepest slope of the PA swing for 22 MSPs and 178 slow pulsars are also shown. . . . .	16
1.8	Spin distribution of 1509 rotation-powered pulsars, separated into binary pulsars, high-energy (optical, X-ray and gamma-ray) pulsars, and AXPs. . . . .	18
1.9	Main characteristics of HMXBs and LMXBs, showing typical values for the masses of the primary and secondary stars, orbital separations, and orbital periods. . . . .	23
1.10	Spin distributions of a sample of accretion-powered pulsars in HMXBs from the galaxy, and the Small and Large Magellanic Clouds. . . . .	25
1.11	Timing data from 9 AMSP outbursts, from six AMSPs. . . . .	29
1.12	Effects of the two gravitational wave polarizations on a ring of test particles. . . . .	32
1.13	Improvements to the LIGO sensitivity curve from its first science run (S1) to its fifth (S5). . . . .	35
1.14	Expected noise floor for various Advanced LIGO narrow-band tunings. . . . .	36
1.15	Maximum expected gravitational wave strain for known LMXBs assuming spin frequency stalling due to gravitational waves for a coherent, <i>single-template</i> search over a 2 year observation. . . . .	45
1.16	Expected gravitational wave strain for known LMXBs, for a coherent, <i>multi-template</i> search over a 2 year observation. . . . .	46

1.17	Maximum expected gravitational wave strain for known LMXBs assuming the presence of r-modes, and a coherent, single-template search across a 2 year observation. . . . .	48
1.18	Probability density functions (PDFs) for $2\mathcal{F}$ for simulated continuous-wave signals injected into S1 data from the GEO and LIGO detectors. . . . .	51
1.19	Gravitational wave strain upper limits from an all-sky Power-Flux S5 search across the frequency band 50–1100 Hz, and the frequency derivative band $-5 \times 10^{-9}$ –0 Hz s <sup>-1</sup> . . . . .	58
2.1	Geometry of precession. . . . .	67
2.2	Surface intensity maps of the single and double hotspot configurations. . . . .	69
2.3	Sample simulation output for a biaxial star with a single hotspot. . . . .	71
2.4	Relative precession phase of the RMS and pulse-phase residuals, $\Delta\Gamma_{\text{phase-rms}}$ , RMS and mean flux, $\Delta\Gamma_{\text{flux-rms}}$ , and amplitude of the folded pulse-phase residuals, $B_{\text{phase}}$ , versus tilt angle $\theta$ and inclination angle $\chi$ , both measured in degrees for a biaxial pulsar with one hotspot. . . . .	74
2.5	Relative precession phase of the RMS and pulse-phase residuals, $\Delta\Gamma_{\text{phase-rms}}$ , RMS and mean flux, $\Delta\Gamma_{\text{flux-rms}}$ , and amplitude of the folded pulse-phase residuals, $B_{\text{phase}}$ , versus inclination angle $\chi$ and hotspot latitude $\alpha$ , both measured in degrees for a biaxial pulsar with one hotspot. . . . .	75
2.6	Schematic illustrating the rotation of one hotspot, from (a) the start of one precession cycle, to (b) midway through the precession cycle. . . . .	76
2.7	Relative precession phase of the RMS and pulse-phase residuals, $\Delta\Gamma_{\text{phase-rms}}$ , RMS and mean flux, $\Delta\Gamma_{\text{flux-rms}}$ , and amplitude of the folded pulse-phase residuals, $B_{\text{phase}}$ , versus inclination angle $\chi$ and tilt angle $\theta$ , both measured in degrees, for a biaxial pulsar with two hotspots. . . . .	79
2.8	Relative precession phase of the RMS and pulse-phase residuals, $\Delta\Gamma_{\text{phase-rms}}$ , RMS and mean flux, $\Delta\Gamma_{\text{flux-rms}}$ , and amplitude of the folded pulse-phase residuals, $B_{\text{phase}}$ , versus inclination angle $\chi$ and hotspot latitude $\alpha$ , both measured in degrees, for a biaxial pulsar with two hotspots. . . . .	80
2.9	Relative precession phase of the RMS and pulse-phase residuals, $\Delta\Gamma_{\text{phase-rms}}$ , RMS and mean flux, $\Delta\Gamma_{\text{flux-rms}}$ , and amplitude of the folded pulse-phase residuals, $B_{\text{phase}}$ , versus inclination angle $\chi$ and initial phase $\phi(0)$ , both measured in degrees, for a biaxial pulsar with two hotspots. . . . .	81
2.10	Schematic illustrating the rotation of two hotspots, from (a) the start of one precession cycle, to (b) midway through the precession cycle. . . . .	82
2.11	Total flux of XTE J1814–338 (in units of $10^{-9}$ erg/cm <sup>2</sup> /s) versus time (Modified Julian Date). . . . .	86

2.12	Flux time series, fractional RMS of the first harmonic component, and pulse-phase residuals of first harmonic. . . . .	89
2.13	Lomb periodogram for the mean flux, fractional RMS, and pulse-phase residuals. . . . .	90
2.14	Slow variation of the pulse characteristics <i>refolded</i> on the candidate precession period $P_p = 293$ hr. . . . .	92
2.15	Refolded simulated time series for the best match configuration ( $\theta = 3^\circ, \chi = 179.95^\circ, \phi = 210^\circ, \alpha = 45^\circ$ ). . . . .	94
3.1	Theoretical sensitivity of the cross-correlation search for SNR 1987A . . . . .	106
3.2	Gravitational wave and electromagnetic dominated regions in the $\nu, \dot{\nu}$ plane. . . . .	112
3.3	Effect of varying $B$ on the $\nu, \dot{\nu}$ plane. . . . .	113
3.4	Contour plots of $h_0$ as a function of $\epsilon$ and $B(10^{11}$ G) for SNR 1987A for birth frequencies of $\nu_b = 250$ and 1200 Hz. . . . .	118
3.5	Log-log contour plots of $h_0$ as a function of $\epsilon$ and $B$ for a range of birth frequencies, $\nu_b$ , and braking indices $n$ . . . . .	120
4.1	Flow chart summarising the algorithm used in <i>lalapps-pulsar-crosscorr</i> . . . . .	126
4.2	PDFs of $\rho$ for $T_{\text{lag}} = 0$ s and $T_{\text{lag}} = 3600$ s for $T_{\text{obs}} = 1$ hour, 5 hours, 1 day, 1 month, and 1 year. . . . .	131
4.3	Skewness and kurtosis excess of $\rho/\sigma_\rho$ as a function of total SFT duration, for $T_{\text{lag}} = 3600$ s and SFTs containing pure Gaussian noise. . . . .	132
4.4	Skewness and kurtosis excess of $\rho/\sigma_\rho$ as a function of total SFT duration, for $T_{\text{lag}} = 0$ s and SFTs containing pure Gaussian noise. . . . .	133
4.5	The mean standard deviation of the normalized detection statistic $\langle \rho/\sigma_{(0)} \rangle$ as a function of injected gravitational wave strain $h_0$ . . . . .	135
4.6	Distribution of $\rho_{\text{ave}}/\rho_{\text{exact}}$ and $\rho_{\text{random}}/\rho_{\text{exact}}$ as a function of $\rho_{\text{exact}}$ for $T_{\text{lag}} = 0$ s. . . . .	139
4.7	Distribution of $\rho_{\text{ave}}/\rho_{\text{exact}}$ and $\rho_{\text{random}}/\rho_{\text{exact}}$ as a function of injected signal frequency for $T_{\text{lag}} = 0$ s. . . . .	139
4.8	Distribution of $\rho_{\text{ave}}/\rho_{\text{exact}}$ and $\rho_{\text{random}}/\rho_{\text{exact}}$ as a function of $\rho_{\text{exact}}$ for $T_{\text{lag}} = 3600$ s. . . . .	141
4.9	Distribution of $\rho_{\text{ave}}/\rho_{\text{exact}}$ and $\rho_{\text{random}}/\rho_{\text{exact}}$ as a function of injected signal frequency for $T_{\text{lag}} = 3600$ s. . . . .	141
4.10	Distribution of $\rho_{\text{ave}}/\rho_{\text{exact}}$ and $\rho_{\text{random}}/\rho_{\text{exact}}$ as a function of $\rho_{\text{exact}}$ for $T_{\text{lag}} = 7200$ s. . . . .	142
4.11	Distribution of $\rho_{\text{ave}}/\rho_{\text{exact}}$ and $\rho_{\text{random}}/\rho_{\text{exact}}$ as a function of injected signal frequency for $T_{\text{lag}} = 7200$ s. . . . .	142
4.12	Analytic estimates for $\rho_{\text{th}}$ as a function of $N$ . . . . .	144
4.13	The mean, normalized detection statistic $\langle \rho/\sigma_\rho \rangle$ (averaged over $10^3$ trials) as a function of injected gravitational wave strain $h_0$ . . . . .	146
4.14	Confidence levels, $C$ , as a function of injected gravitational wave strain $h_0$ for a search with $10^3$ templates. . . . .	147

4.15	Confidence levels, $C$ , as a function of injected gravitational wave strain $h_0$ for a search with $10^9$ templates. . . . .	148
5.1	Orientation of the inertial axes $\mathbf{e}_x, \mathbf{e}_y, \mathbf{e}_z$ and pulsar body axes $\mathbf{e}_1, \mathbf{e}_2, \mathbf{e}_3$ at an instant where $\mathbf{e}_2$ and $\mathbf{e}_3$ lie in the $\mathbf{e}_y$ - $\mathbf{e}_z$ plane. . .	159
5.2	Theoretical pulse profiles, PA swings, and Stokes phase portraits for a pure dipole and a beam pattern symmetric about $\mathbf{e}_3$ , or tilted by $10^\circ$ with respect to $\mathbf{e}_3$ and $\mathbf{e}_1$ , as described in the text. . . . .	162
5.3	(a) Recipe to generate look-up tables of Stokes phase portraits, PA swings, and pulse profiles for a given orientation and magnetic geometry. (b) Iterative recipe to extract orientation and magnetic geometry from observational data. . . . .	164
5.4	Dipole field at a low emission altitude $r \ll r_{\text{LC}}$ . Example of a pulse profile for a filled core beam with linear polarization $L = I \cos \theta_0$ and $(\alpha, i) = (70^\circ, 20^\circ)$ . . . . .	166
5.5	Examples of the path traced by the emission point $\hat{\mathbf{x}}_0(t)$ in the body frame, overplotted on the intensity map for a filled core beam. . . . .	167
5.6	Two orientations with equal PA-swing gradients ( $ d(\text{PA})/dl $ ) at the inflection point, but different Stokes phase portraits. . . . .	170
5.7	Dipole field at a low emission altitude $r \ll r_{\text{LC}}$ . Look-up table of Stokes phase portraits in the $I$ - $Q$ plane for a filled core beam with degree of linear polarization $L = I \cos \theta_0$ , where $\theta_0$ is the emission point colatitude. . . . .	171
5.8	Dipole field at $r \ll r_{\text{LC}}$ . Layout as for Figure 5.7, but for $I$ - $U$ . . . . .	172
5.9	Dipole field at $r \ll r_{\text{LC}}$ . Layout as for Figure 5.7, but for $Q$ - $U$ . . . . .	173
5.10	Dipole field at $r \ll r_{\text{LC}}$ . Layout as for Figure 5.7, but for position angle versus pulse longitude. . . . .	174
5.11	Dipole field at $r \ll r_{\text{LC}}$ . Example of a pulse profile for a filled core beam with linear polarization $L = I \sin \theta_0$ and $(\alpha, i) = (30^\circ, 30^\circ)$ . . . . .	175
5.12	Dipole field at $r \ll r_{\text{LC}}$ . Look-up table of Stokes phase portraits in the $I$ - $Q$ plane for a filled core beam with degree of linear polarization $L = I \sin \theta_0$ , where $\theta_0$ is the emission point colatitude. . . . .	176
5.13	Dipole field at $r \ll r_{\text{LC}}$ . As for Figure 5.12, but for $I$ - $U$ . . . . .	177
5.14	Dipole field at $r \ll r_{\text{LC}}$ . As for Figure 5.12, but for $Q$ - $U$ . . . . .	178
5.15	Dipole field at $r \ll r_{\text{LC}}$ . Layout as for Figure 5.17, but for position angle versus pulse longitude. . . . .	179
5.16	Dipole field at $r \ll r_{\text{LC}}$ . Examples of pulse profiles for a hollow cone with opening angle $25^\circ$ and linear polarization $L = I \cos \theta_0$ for two different orientations $(\alpha, i)$ . . . . .	181
5.17	Dipole field at $r \ll r_{\text{LC}}$ . Look-up table of Stokes phase portraits in the $I$ - $Q$ plane for a hollow cone with opening angle $25^\circ$ with degree of linear polarization $L = I \cos \theta_0$ , where $\theta_0$ is the emission point colatitude. . . . .	182
5.18	Dipole field at $r \ll r_{\text{LC}}$ . Layout as for Figure 5.17, but for $I$ - $U$ . . . . .	183

5.19	Dipole field at $r \ll r_{\text{LC}}$ . Layout as for Figure 5.17, but for $Q-U$ .	184
5.20	Dipole field at $r \ll r_{\text{LC}}$ . Layout as for Figure 5.17, but for position angle versus pulse longitude. . . . .	185
5.21	As for Figure 5.16, but with linear polarization $L = I \sin \theta$ . . . .	186
5.22	Dipole field at $r \ll r_{\text{LC}}$ . Look-up table of Stokes phase portraits in the $I-Q$ plane for a hollow cone with opening angle $25^\circ$ with degree of linear polarization $L = I \sin \theta_0$ , where $\theta_0$ is the emission point colatitude. . . . .	187
5.23	Dipole field at $r \ll r_{\text{LC}}$ . Layout as for Figure 5.22, but for $I-U$ .	188
5.24	Dipole field at $r \ll r_{\text{LC}}$ . Layout as for Figure 5.22, but for $Q-U$ .	189
5.25	Dipole field at $r \ll r_{\text{LC}}$ . Layout as for Figure 5.22, but for position angle versus pulse longitude. . . . .	190
5.26	Dipole field at $r = 0.1r_{\text{LC}}$ . Look-up table of Stokes phase portraits in the $I-Q$ plane for a filled core beam with degree of linear polarization $L = I \cos \theta_0$ , where $\theta_0$ is the emission point colatitude. . . . .	192
5.27	Dipole field at $r = 0.1r_{\text{LC}}$ . Layout as for Figure 5.26, but for $I-U$ .	193
5.28	Dipole field at $r = 0.1r_{\text{LC}}$ . Layout as for Figure 5.26, but for $Q-U$ . . . . .	194
5.29	Dipole field at $r = 0.1r_{\text{LC}}$ . Look-up table of Stokes phase portraits in the $I-Q$ plane for a hollow cone with opening angle $25^\circ$ with degree of linear polarization $L = I \cos \theta_0$ , where $\theta_0$ is the emission point colatitude. . . . .	196
5.30	Dipole field at $r = 0.1r_{\text{LC}}$ . Layout as for Figure 5.29, but for $I-U$ .	197
5.31	Dipole field at $r = 0.1r_{\text{LC}}$ . Layout as for Figure 5.29, but for $Q-U$ . . . . .	198
5.32	Pulse profiles, Stokes phase portraits and PA swings for a selection of six superficially dipolar pulsars that closely follow the pulse-width-period relation at 610 MHz. . . . .	201
5.33	As for Figure 5.32, for six other objects selected according to the same criterion. . . . .	202
5.34	Pulse profiles, Stokes phase portraits and PA swings for a selection of six superficially dipolar pulsars that exhibit a clean, S-shaped PA swing. . . . .	203
5.35	As for Figure 5.32 for six other objects selected according to the same criterion. . . . .	204
5.36	Current-modified dipole field at $r = 0.1r_{\text{LC}}$ . Example of a pulse profile for a filled core beam with linear polarization $L = I \cos \theta_0$ and $(\alpha, i) = (70^\circ, 30^\circ)$ at $r = 0.1 r_{\text{LC}}$ . . . . .	207
5.37	Current-modified dipole field at $r = 0.1r_{\text{LC}}$ . Examples of the path traced by the emission point $\hat{\mathbf{x}}_0(t)$ in the body frame, overplotted on the intensity map for a filled core beam. . . . .	208
5.38	Current-modified dipole field at $r = 0.1r_{\text{LC}}$ . Look-up table of Stokes phase portraits in the $I-Q$ plane for a filled core beam at $r = 0.1 r_{\text{LC}}$ with degree of linear polarization $L = I \cos \theta_0$ , where $\theta_0$ is the emission point colatitude. . . . .	209
5.39	As for Figure 5.38, but for $I-U$ . . . . .	210

5.40	As for Figure 5.38, but for $Q-U$ . . . . .	211
5.41	Current-modified dipole field at $r = 0.1r_{\text{LC}}$ . Layout as for Figure 5.38, but for position angle versus pulse longitude . . . . .	212
5.42	Current-modified dipole field at $r = 0.1r_{\text{LC}}$ . Example of a pulse profile for a filled core beam with linear polarization $L = I \sin \theta_0$ and $(\alpha, i) = (30^\circ, 30^\circ)$ at $r = 0.1 r_{\text{LC}}$ . . . . .	213
5.43	Current-modified dipole field at $r = 0.1r_{\text{LC}}$ . Look-up table of Stokes phase portraits in the $I-Q$ plane for a filled core beam at $r = 0.1 r_{\text{LC}}$ and degree of linear polarization $L = I \sin \theta_0$ , where $\theta_0$ is the emission point colatitude. . . . .	214
5.44	As for Figure 5.43, but for $I-U$ . . . . .	215
5.45	As for Figure 5.43, but for $Q-U$ . . . . .	216
5.46	Current-modified dipole field at $r = 0.1r_{\text{LC}}$ . Layout as for Figure 5.43, but for position angle versus pulse longitude. . . . .	217
5.47	Current-modified dipole field at $r = 0.1r_{\text{LC}}$ . Examples of pulse profiles for a hollow cone with opening angle $25^\circ$ and degree of linear polarization $L = I \cos \theta_0$ at $r = 0.1 r_{\text{LC}}$ . . . . .	219
5.48	Current-modified dipole field at $r = 0.1r_{\text{LC}}$ . Look-up table of Stokes phase portraits in the $I-Q$ plane for a hollow cone with opening angle $25^\circ$ at $r = 0.1 r_{\text{LC}}$ and degree of linear polarization $L = I \cos \theta_0$ , where $\theta_0$ is the emission point colatitude. . . . .	220
5.49	As for Figure 5.48, but for $I-U$ . . . . .	221
5.50	As for Figure 5.48, but for $Q-U$ . . . . .	222
5.51	Current-modified dipole field at $r = 0.1r_{\text{LC}}$ . Layout as for Figure 5.48, but for position angle versus pulse longitude. . . . .	223
5.52	Current-modified dipole field at $r = 0.1r_{\text{LC}}$ . Examples of pulse profiles for a hollow cone with opening angle $25^\circ$ and degree of linear polarization $L = I \sin \theta_0$ at $r = 0.1 r_{\text{LC}}$ . . . . .	224
5.53	Current-modified dipole field at $r = 0.1r_{\text{LC}}$ . Look-up table of Stokes phase portraits in the $I-Q$ plane for a hollow cone with opening angle $25^\circ$ at $r = 0.1 r_{\text{LC}}$ and degree of linear polarization $L = I \sin \theta_0$ , where $\theta_0$ is the emission point colatitude. . . . .	225
5.54	As for Figure 5.53, but for $I-U$ . . . . .	226
5.55	As for Figure 5.53, but for $Q-U$ . . . . .	227
5.56	Current-modified dipole field at $r = 0.1r_{\text{LC}}$ . Layout as for Figure 5.53, but for position angle versus pulse longitude. . . . .	228
5.57	Stokes phase portraits, PA swings and emission point locus $\hat{\mathbf{x}}_0(t)$ in the body frame for a filled core beam with polarization $L = I \cos \theta_0$ and $(\alpha, i) = (70^\circ, 30^\circ)$ , at five altitudes. . . . .	231
5.58	Multi-frequency pulse profiles, PA swing and Stokes phase portraits for PSR J0826+2637. . . . .	233
5.59	Polarimetry of PSR J0826+2637 at 0.925 GHz. . . . .	234
5.60	Pure dipole, low-altitude model for PSR J0826+2637 at $r = 0.006r_{\text{LC}}$ , sharing the pulse profile, Stokes phase portraits and PA swing for filled core beam with polarization pattern given by (5.17) for $(\alpha, i) = (42^\circ, 68^\circ)$ . . . . .	237

5.61	Simulated pulse profiles, PA swing and Stokes phase portraits for PSR J0826+2637 at four emission altitudes. . . . .	239
5.62	Multi-frequency pulse profiles, PA swing and Stokes phase portraits for PSR J0304+1932. . . . .	241
5.63	Polarimetry of PSR J0304+1932 at 1.418 GHz. . . . .	242
5.64	Current-modified dipole field model for PSR J0304+1932. Pulse profile, Stokes phase portraits and PA swing for a hollow cone given by (5.18) with degree of linear polarization given by the data for $(\alpha, i) = (76^\circ, 46^\circ)$ at $r = 0.1r_{\text{LC}}$ . . . . .	245
5.65	Simulated pulse profiles, PA swing and Stokes phase portraits for PSR J0304+1932 at three emission altitudes. . . . .	246
6.1	Stokes tomography of a model pulsar with an interpulse but without relativistic aberration. . . . .	259
6.2	Locus $\hat{\mathbf{x}}_0(t)$ traced out by the emission point(s) $P_1$ and $P_2$ over one rotation, in the body frame of the model pulsar considered in Figure 6.1. . . . .	259
6.3	Stokes tomography for a model pulsar including relativistic aberration but without an interpulse. . . . .	262
6.4	Locus $\hat{\mathbf{x}}_0(t)$ traced out by the emission point $P_1$ across one rotation, in the body frame of the model pulsar considered in Figure 6.3. . . . .	262
6.5	Pulse profiles, Stokes phase portraits and PA swings for PSR J0437–4715 at 1.44 GHz and 4.6 GHz, PSR J1012+5307 at 0.61 GHz, and PSR J1022+1001 at 0.41 GHz, 0.61 GHz, and 1.414 GHz. . . . .	268
6.6	Pulse profiles, Stokes phase portraits and PA swings for PSR J1713+0747 at 0.41 GHz, 0.61 GHz and 1.414 GHz, PSR J1744–1134 at 0.61 GHz, PSR J1824–2452 at 0.61 GHz, and PSR J1911–1114 at 0.41 GHz. . . . .	269
6.7	Pulse profiles, Stokes phase portraits and PA swings for PSR J1911–1114 at 0.61 GHz, and PSR J1939+2134 at 0.61 GHz and 1.414 GHz (Stairs et al. 1999). The data for each pulsar occupy a row in landscape mode. From left to right, the columns show: (1) $I/I_{\text{max}}$ (solid curve) and $L/I_{\text{max}}$ (dashed curve) versus time (in s), (2) the $I$ - $Q$ phase portrait, (3) the $I$ - $U$ phase portrait, (4) the $Q$ - $U$ phase portrait, (5) the PA swing versus time (in s) (data points with $L \geq 0.1L_{\text{max}}$ and $I \geq 0.1I_{\text{max}}$ plotted only). Data are presented courtesy of the EPN online archive. . . . .	270
6.8	Polarimetry of the main pulse and the interpulse of PSR J1939+2134 at 0.61 GHz. . . . .	273
6.9	As for Figure 6.8 but at 1.414 GHz. . . . .	274
6.10	Theoretical polarization model of the main pulse and the interpulse of PSR J1939+2134 for a current-modified dipole emitting at $r = 0.4r_{\text{LC}}$ , with orientation $(\alpha, i) = (22^\circ, 80^\circ)$ , beam pattern given by (6.10), and linear polarization given by (6.11). . . . .	277

6.11	Theoretical polarization model of Pulse 1 of PSR J1939+2134 as a function of emission altitude, for a current-modified dipole with $(\alpha, i) = (22^\circ, 80^\circ)$ . . . . .	280
6.12	As for Figure 6.11 but for Pulse 2 of PSR J1939+2134. . . . .	281
6.13	Polarimetry of PSR J0437–4715 at 1.44 GHz. . . . .	282
6.14	Bottom-up, component-wise assembly of theoretical polarization models for PSR J0437–4715 for a current-modified dipole emitting at $r = 0.1r_{\text{LC}}$ with $(\alpha, i) = (32^\circ, 26^\circ)$ . . . . .	288
6.15	Theoretical polarization model of PSR J0437–4715 for a pure dipole emitting at $r = 0.1r_{\text{LC}}$ with $(\alpha, i) = (32^\circ, 26^\circ)$ , beam pattern given by (6.12), (6.13) and (6.14), and linear polarization given by (6.17). . . . .	289
7.1	Comparison of the pulse profile, PA swing, and Stokes phase portraits for a vacuum dipole field to those of a pure dipole at $r = 0.1r_{\text{LC}}$ . . . . .	298
7.2	Pulse profile, PA swing, and Stokes phase portraits for a field distorted by the formation of a magnetic mountain. . . . .	300
A1	Colloquial descriptors of phase portraits encountered in this chapter. . . . .	322
A2	Current-modified dipole. Look-up table of Stokes phase portraits in the $I$ - $Q$ plane for filled core beams with degree of linear polarization $L = I \cos \theta$ , where $\theta$ is the emission point colatitude, and $r = 0.1r_{\text{LC}}$ . . . . .	324
A3	Current-modified dipole. Layout as for Figure A2, but for $I$ - $U$ . . . . .	325
A4	Current-modified dipole. Layout as for Figure A2, but for $Q$ - $U$ . . . . .	326
A5	Current-modified dipole. Layout as for Figure A2, but for position angle versus pulse longitude. . . . .	327
A6	Current-modified dipole. Look-up table of Stokes phase portraits in the $I$ - $Q$ plane for filled core beams with degree of linear polarization $L = I \sin \theta$ , where $\theta$ is the emission point colatitude, and $r = 0.1r_{\text{LC}}$ . . . . .	328
A7	Current-modified dipole. Layout as for Figure A6, but for $I$ - $U$ . . . . .	329
A8	Current-modified dipole. Layout as for Figure A6, but for $Q$ - $U$ . . . . .	330
A9	Current-modified dipole. Layout as for Figure A6, but for position angle versus pulse longitude . . . . .	331
A10	Current-modified dipole. Look-up table of Stokes phase portraits in the $I$ - $Q$ plane for hollow cones with opening angle $25^\circ$ and degree of linear polarization $L = I \cos \theta$ , where $\theta$ is the emission point colatitude, and $r = 0.1r_{\text{LC}}$ . . . . .	332
A11	Current-modified dipole. Layout as for Figure A10, but for $I$ - $U$ . . . . .	333
A12	Current-modified dipole. Layout as for Figure A10, but for $Q$ - $U$ . . . . .	334
A13	Current-modified dipole. Layout as for Figure A10, but for position angle versus pulse longitude. . . . .	335

---

A14	Current-modified dipole. Look-up table of Stokes phase portraits in the $I$ - $Q$ plane for hollow cones with opening angle $25^\circ$ and degree of linear polarization $L = I \sin \theta$ , where $\theta$ is the emission point colatitude, and $r = 0.1r_{LC}$ . . . . .	336
A15	Current-modified dipole. Layout as for Figure A14, but for $I$ - $U$ . . . . .	337
A16	Current-modified dipole. Layout as for Figure A14, but for $Q$ - $U$ . . . . .	338
A17	Current-modified dipole. Layout as for Figure A14, but for position angle versus pulse longitude. . . . .	339



# List of Tables

1.1	Three fundamental properties of neutron stars (ellipticity, magnetic field, and angular velocity) investigated through radio, X-ray, and gravitational wave studies in this thesis, and the evolutionary stage to which each technique applies. . . . .	7
1.2	Catalogue of kHz QPO sources which display no other persistent pulsations or X-ray bursts. . . . .	27
1.3	Upper limits on gravitational wave strain and ellipticity set by recent searches for gravitational waves from neutron stars. . . .	59
2.1	Orbital parameters for XTE J1814–338. . . . .	87
2.2	Results of fitting the folded mean flux, fractional RMS, and pulse-phase residuals (folding period = 292.59 hours) with the expression $A + B \sin(2\pi\Gamma + C)$ . . . . .	91
3.1	Table of $\nu_b$ , $\epsilon$ , and $B$ which are detectable by the cross-correlation search. . . . .	119
4.1	Mean $\mu$ and standard deviation $\sigma$ of $10^5$ values of $\rho$ for a search over simulated Gaussian noise using observation times $T_{\text{obs}} = 1$ hour, 5 hours, 1 day, 1 month, and 1 year. . . . .	129
4.2	$\rho_{\text{th}}$ for each frequency band used in the Monte Carlo searches over pure noise, without spin down. . . . .	144
4.3	Table of confidence levels, $C$ , as a function of $h_0$ for injected signals at 150.05 Hz, 300.05 Hz and 600.05 Hz and $10^3$ search templates. . . . .	148
4.4	Table of confidence levels, $C$ , as a function of $h_0$ for injected signals at 150.05 Hz, 300.05 Hz and 600.05 Hz and $10^9$ search templates. . . . .	149
5.1	Catalog of Stokes phase portraits and PA swing look-up tables.	248
5.2	Summary of shapes seen in Stokes phase portraits for a pure dipole. . . . .	248
5.3	Summary of shapes seen in Stokes phase portraits for a current-modified dipole. . . . .	249
6.1	Pulse periods $P$ and observation frequencies of 16 millisecond pulsars from the EPN online database with $P < 10$ ms. . . . .	264
A1	All command line options for the cross-correlation search code, <i>lalapps_pulsar_crosscorr</i> , in LALApps. . . . .	317



# Frequently employed acronyms

**AMSP** accreting millisecond pulsar

**EOS** equation of state

**HMXB** high-mass X-ray binary

**LIGO** Laser Interferometer Gravitational Wave Observatory

**LMXB** low-mass X-ray binary

**LSC** LIGO Scientific Collaboration

**MSP** millisecond pulsar

**PA** polarization angle

**QPO** quasi-periodic oscillation

**RXTE** Rossi X-ray Timing Explorer

**S5** LIGO fifth science run



# 1 Introduction

## 1.1 Neutron stars

### 1.1.1 History

The existence of neutron stars was first proposed by Baade & Zwicky (1934), who attributed the huge energy release in supernovae to the gravitational collapse of a star. Baade & Zwicky advanced the idea that a supernova was the transition of an ordinary star into a collapsed object consisting of densely packed neutrons. In 1942, optical observations of a bright star (“Minkowski’s star”) at the centre of the Crab Nebula were made (Baade 1942; Minkowski 1942). More than twenty years later, Hewish & Okoye (1965) reported on an unusual source of high radio brightness in the same region, although at the time, they did not link the observations to a neutron star. Three years later, radio pulses were detected from the same source, making it one of the first, and most famous, pulsars to be discovered (Davies et al. 1968). The idea that pulsars are actually rapidly rotating neutron stars was then postulated by Gold (1968).<sup>1</sup> It was not until 1969, when optical pulsations were also detected from “Minkowski’s star”, that it was recognised as the optical counterpart of the Crab pulsar (Cocke et al. 1969).

To date, pulsars have been observed in radio, infra-red, optical, X-ray and  $\gamma$ -ray wavelengths. The extremely high magnetic fields and densities, as well as the rapid spin periods, found in pulsars have filled the last 40 years of timing and spectral observations with a plethora of intriguing phenomena. As well as being objects of phenomenological interest, they are excellent tests of general relativity. The famous binary pulsar system PSR 1913+16 (Hulse & Taylor 1975) provided the first indirect evidence of gravitational radiation through its orbital decay. Neutron stars are also considered to be the most promising sources of continuous gravitational waves (Wagoner 1984; Bildsten 1998; Watts et al. 2008a). Neutron star inspirals may yield the first direct

---

<sup>1</sup>Throughout this chapter, we use the term ‘neutron star’ to mean all objects of this class, and ‘pulsar’ to mean the subset of neutron stars which emit pulses.

detection of gravitational waves.

There are two broad classes of neutron stars: isolated, rotation-powered neutron stars and accretion-powered neutron stars in binary systems. They can be further classified as pulsing or non-pulsing, and as fast (with period  $\lesssim 0.1$  s) or slow (with period  $\gtrsim 0.1$  s) rotators. Accreting neutron stars are detected primarily in X-rays, and are classified according to their companion mass. High-mass X-ray binaries (HMXBs) have companions with mass  $\geq 10M_{\odot}$  and accrete via a stellar wind, whereas low-mass X-ray binaries (LMXBs) have companion masses of  $\lesssim 1M_{\odot}$  and accrete via Roche-lobe overflow (e.g. Psaltis 2006). There are also non-accreting binary radio pulsars which orbit high-mass ( $0.5 M_{\odot}$ – $1.4 M_{\odot}$ ) or low-mass ( $< 0.45M_{\odot}$ ) companions. The recycling scenario for pulsars links many of these classes to various stages of pulsar evolution and is discussed in Section 1.1.2.

## 1.1.2 Evolution and structure of neutron stars

### Core collapse

We now summarise briefly the formation and evolution of neutron stars; detailed reviews are provided in Tauris & van den Heuvel (2006); Ghosh (2007).

One mechanism that is believed to form neutron stars is a core-collapse (Type II) supernova (Colgate & White 1966). A massive ( $\geq 8M_{\odot}$ ) star undergoes several stages of nuclear burning until its core is composed of iron. When its iron core exceeds the Chandrasekhar mass ( $1.4 M_{\odot}$ ), it can no longer be supported by the electron degeneracy pressure which supports its structure. It undergoes gravitational collapse, which is halted when the density of the core becomes sufficient for the nucleons to feel their short-range repulsive strong force interactions, as well as the neutron degeneracy pressure. This abrupt halt of the inner core's collapse, and its subsequent rebound, generates a shock wave which propagates outwards, expelling the outer layers of stellar material (see e.g. Woosley & Janka 2005, for a detailed review). The extreme temperatures of the core during the core-collapse phase result in a neutrino burst which transports a large amount of kinetic and electromagnetic energy within seconds. Observations of a neutrino burst during the supernova SN 1987A confirmed the core-collapse scenario, and indicated that the gravitational energy released during the process is  $\sim 10^{53}$  erg (Hirata et al. 1987; Nakamura & Fukugita 1989). During core-collapse, neutron stars are sometimes 'kicked', obtaining velocities of up to  $1600 \text{ km s}^{-1}$  (Cordes et al. 1993; Chatterjee & Cordes 2004). If the initial mass of the star is  $\gtrsim 25M_{\odot}$ , a black hole is formed

instead of a neutron star (Heger et al. 2003).

There is still debate about whether neutron stars are born with large ( $\geq 10^8$  G) magnetic fields, or if their fields increase after birth. One model states that during core-collapse, the weak field of the progenitor is compressed, resulting in an amplified field in the neutron star (Ruderman & Sutherland 1973). Alternatively, the fields may be amplified via dynamo action during the first few seconds of a proto-neutron star's life (Thompson & Duncan 1993).

### Isolated pulsars

A young neutron star with a sufficiently high magnetic field and spin period switches on as a rotation-powered pulsar. Although the exact emission mechanism is still unknown, a common theory is that in order to switch on, the magnetic field must be strong enough to produce a potential drop of order  $10^{15}$ – $10^{16}$  V (Goldreich & Julian 1969; Sturrock 1971; Michel 1982). Electrons in the magnetosphere are accelerated along the field lines and emit curvature radiation, which in turn produces more electrons. This process leads to a pair cascade, seeding a large amount of dense charges which generate radio waves. Radio pulsars spin down gradually and their magnetic fields decay until they cross the pulsar “death line”, where the polar cap voltage is too weak to enable radio emission (Sturrock 1971; Ruderman & Sutherland 1975; Chen & Ruderman 1993b; Arons 1998).

### Binary systems

Newly-born pulsars in binaries have either a) a massive main-sequence companion in a wide orbit, or b) a low-mass companion in a narrow orbit. Eventually, they begin to accrete matter from their companions, during which they are spun up and emit X-rays. As noted in Section 1.1.1, the mass of their companion determines whether they are HMXBs or LMXBs (see Section 1.4). Once the accretion process has exhausted the material from the disk, the pulsars cease X-ray emission and begin to emit at radio frequencies.

### Recycling scenario

Until little over a decade ago, there was no direct evidence to prove how millisecond radio pulsars fit into the evolutionary model of neutron stars. The standard recycling scenario posits that accreting X-ray pulsars are the progenitors of millisecond radio pulsars (Radhakrishnan & Srinivasan 1982; Alpar et al. 1982). A pulsar in a LMXB system accretes mass from its companion star,

with the accreted material forming a disc around the pulsar. At the Alfvén radius, the boundary of the magnetosphere, the magnetic pressure balances the ram pressure from the incoming disk material. Matter flows from the disc onto the pulsar’s surface along the pulsar’s magnetic field lines, transferring mass and angular momentum to the pulsar in two ways. Firstly, a positive material torque is exerted on the pulsar by the infalling matter. Secondly, a magnetic torque, which may be positive or negative, is applied via the magnetic field lines which are frozen into the disk. The pulsar is spun up to millisecond periods, reaching equilibrium when the pulsar’s rotational speed equals the Keplerian speed of the disk at the Alfvén radius (Ghosh & Lamb 1979). Most millisecond radio pulsars remain in their binary state, with their companion becoming a white dwarf. At the end of the recycling phase, in addition to their radio emission, they can produce a relativistic electron-positron wind (Ruderman et al. 1989). Once accretion has stopped, the companion star can be eroded by the pulsar wind, leaving behind an isolated millisecond pulsar in the so-called ‘black widow’ scenario (Fruchter et al. 1988; Kulkarni & Hester 1988; Tavani 1992). In globular clusters, the companion can also be lost through a collision with a nearby star (Verbunt et al. 1987).

The recycling scenario was confirmed by the discovery of the first accreting millisecond X-ray pulsar (AMSP), SAX J1808.4-3658 (Wijnands & van der Klis 1998; Chakrabarty & Morgan 1998), which provided the missing link between the slow X-ray pulsars and millisecond radio pulsars. To date, there are thirteen known AMSPs (Wijnands 2004; Morgan et al. 2005; Galloway 2007; Krimm et al. 2007; Altamirano et al. 2009; Markwardt et al. 2009; Altamirano et al. 2010). Due to their large spin frequencies and the likelihood that accretion distorts their shape, AMSPs are considered likely sources of gravitational waves (Watts et al. 2008a).

The characteristic age of a rotation-powered pulsar is defined as  $\tau_c = P/[(n-1)\dot{P}]$ , where  $P$  is the pulsar’s spin period,  $\dot{P}$  is its period derivative,  $n = \ddot{\Omega}\Omega/\dot{\Omega}^2$  is its braking index, and  $\Omega = 2\pi/P$  is its angular frequency. This is an approximate measure of a pulsar’s true age, assuming a constant magnetic field and braking index (typically assumed to be  $n = 3$ ), and assuming that its initial spin period is much less than its current period. A sample population of radio pulsars from the ATNF Pulsar Catalogue is shown in the  $P$ - $\dot{P}$  plot in Figure 1.1. An example evolutionary track for a pulsar with  $n = 3$  and  $B = 10^{13}$  G is marked by the solid line. Young pulsars are born in the upper left region of the plot and spin down until they reach the central island. Isolated pulsars spin down further, moving rightwards in the plot until they eventually cross the

death line. Binary millisecond radio pulsars are denoted by circles in the bottom left region of the plot. Note that the relatively empty region between these objects and the central island is populated mostly by accreting pulsars undergoing recycling. The spin-up line in the plot represents the minimum period attainable via accretion assuming magnetocentrifugal balance. The dotted and dashed lines represent the range of  $P$  and  $\dot{P}$  expected with characteristic ages between  $10^4$ – $10^7$  yr and magnetic fields ranging from  $1 \times 10^{11}$  G– $5 \times 10^{13}$  G. The magnetic fields of radio pulsars are inferred from  $P$  and  $\dot{P}$ , assuming that their rotational energy is converted into magnetic dipole radiation (see Section 1.3.4).

### 1.1.3 Neutron star structure

The first model of a neutron star comprised an ideal fluid in a spherically symmetric body. Using an equation of state for an ideal, degenerate neutron gas, Oppenheimer & Volkoff (1939) placed an upper limit on the neutron star mass of  $\sim 0.7M_{\odot}$  (corresponding to a radius of 9.6 km), above which there is no equilibrium configuration, and the core collapses indefinitely. For twenty years, this limit was in apparent contradiction with the Chandrasekhar limit ( $1.44 M_{\odot}$ ), which is the maximum possible mass of a white dwarf before it collapses to form a neutron star (Chandrasekhar 1931). However, the authors neglected neutron-neutron interactions which, when included, increase this limit to  $\sim 2M_{\odot}$  (Cameron 1959).

At such extreme densities, it is unclear what properties the neutron star interior possesses (see detailed reviews by Balberg & Shapiro 2000; Lattimer & Prakash 2007). The currently accepted model is that the neutron star consists of a core and crust. The thin, outer crust contains nuclei, ions, and electrons, with a density of  $\rho \sim 10^{14}$  kg m $^{-3}$ , while the inner crust contains a dense neutron superfluid coexisting with the ionic lattice. The outer core contains superfluid neutrons, electrons, and protons, with  $\rho \sim 10^{17}$  kg m $^{-3}$ . The composition of the inner core is unknown, and could possibly be quark matter or a kaon condensate (Glendenning 2001; Alford et al. 2008).

## 1.2 Thesis motivation

Certain fundamental properties of neutron stars, such as their ellipticities, the strengths and structures of their magnetic fields, and their spin histories from birth to the present, cannot be measured directly. Whatever information

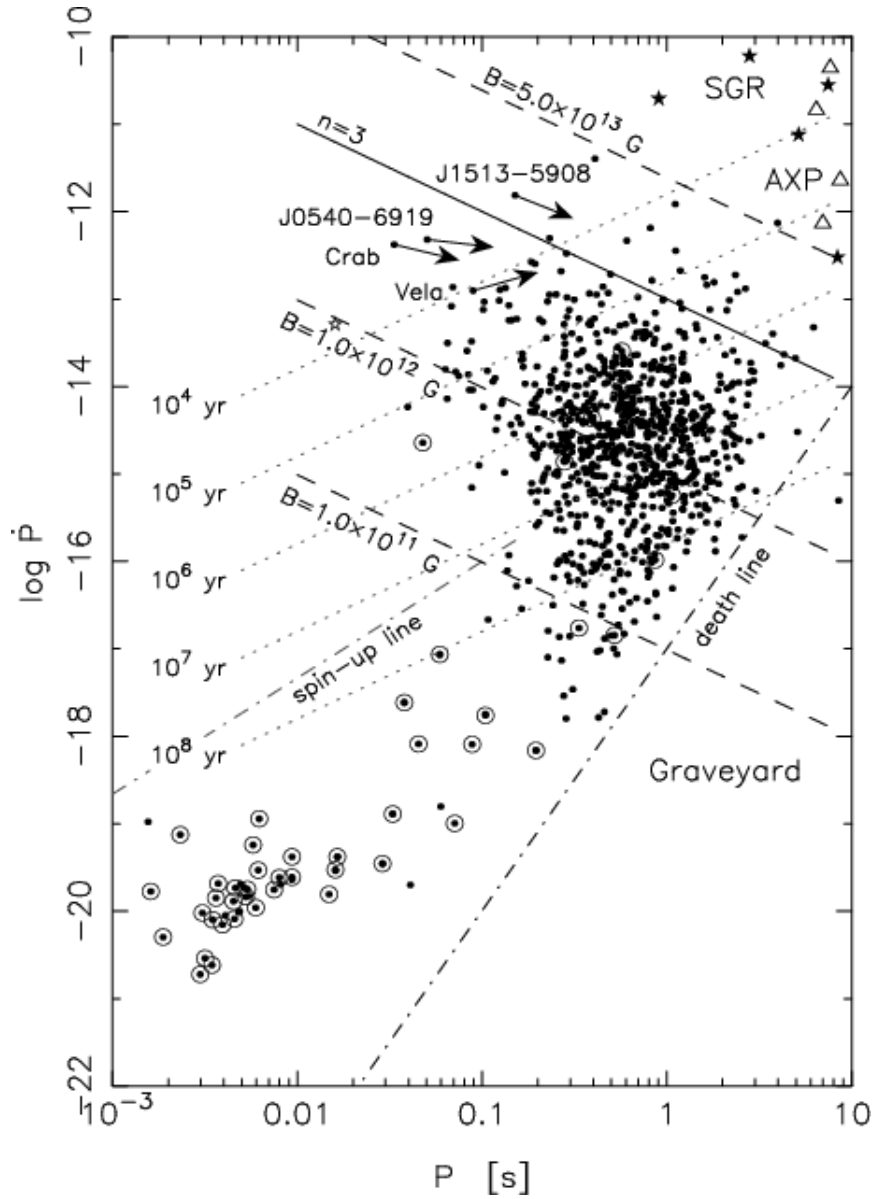


**Figure 1.1:** Period-period derivative ( $P, \dot{P}$ ) diagram of a sample of 947 observed radio pulsars from the ATNF Pulsar Catalogue. Binary pulsars are denoted by circles. The dotted and dashed lines represent constant characteristic ages and constant magnetic fields. The solid line represents the evolutionary track for a constant electromagnetic braking index of  $n = 3$ . The spin-up line represents the minimum period attainable via accretion (from Tauris & Konar 2001).

	Radio polarimetry	X-ray timing	Gravitational waves
Ellipticity, $\epsilon$		✓	✓
Magnetic field, $\mathbf{B}$ (geometry)	✓		
Magnetic field, $ \mathbf{B} $ (strength)	⊗	✓	✓
Angular velocity, $\boldsymbol{\Omega}$ (orientation)	✓	✓	
Angular velocity, $ \boldsymbol{\Omega} $ (magnitude)	⊗	✓	✓
Evolutionary stage:			
Young, non-recycled	✓		✓
Old, non-recycled	✓		
Recycled	✓	✓	

**Table 1.1:** Top panel: three fundamental properties of neutron stars (ellipticity, magnetic field, and angular velocity) investigated through radio, X-ray, and gravitational wave studies in this thesis. Bottom panel: Evolutionary stage to which each technique applies. ⊗ indicates quantities known by other means.

we have is inferred indirectly from spectral, polarization, and timing studies of their pulsed emission. To our advantage, however, multi-wavelength and multi-messenger observations allow us to study these objects from a range of perspectives, each contributing to form a complete picture. To this end, this thesis consists of three independent projects aimed at studying radio, X-ray, and gravitational wave emission from neutron stars. Firstly, we analyze X-ray data from an accreting millisecond pulsar, XTE J1814–338, whose timing properties indicate that it may have a nonzero ellipticity, causing it to freely precess. Ellipticity estimates are of great interest to current gravitational wave search efforts, as the gravitational wave strain emitted by a pulsar is directly proportional to its ellipticity. Secondly, we design a cross-correlation search for gravitational waves from the young neutron star in the supernova remnant SN 1987A using data from the Laser Interferometer Gravitational Wave Observatory (LIGO) and show how the search places limits on the birth and current magnetic field strengths, ellipticity, and birth spin frequency of this object. Finally, we introduce a new approach towards radio pulsar polarimetry, called Stokes tomography, to model the spin axis orientations (i.e. angular velocity vector,  $\boldsymbol{\Omega}$ ), magnetic field geometries, and emission altitudes of radio pulsars. In Table 1.1, we summarise how the three projects provide insight into three primary properties of neutron stars at different stages in their life cycle.

In this chapter, we summarise the aspects of neutron star physics that are

specifically relevant to our work, including current theoretical models, outstanding issues faced today, and how the work in this thesis contributes to the field. In Section 1.3, we discuss rotation-powered pulsars which emit primarily in the radio band. Accretion-powered pulsars, which emit X-rays, are discussed in Section 1.4. In Section 1.5, we explain why neutron stars are likely gravitational wave emitters and review current gravitational wave search efforts. A detailed outline of the work in the thesis is presented in Section 1.7.

## 1.3 Rotation-powered pulsars

In this section, we summarise briefly the properties of rotation-powered pulsars (RPPs), with an emphasis on the topics covered in this thesis, namely pulse and polarization profiles (Section 1.3.1), timing properties (Section 1.3.3) and magnetic field structure (Section 1.3.4). For complete reviews of pulsar physics, the reader is referred to textbooks by e.g. Lyne & Graham-Smith (2006); Ghosh (2007).

There are currently 1827 known rotation-powered pulsars at the time of writing. They are concentrated near the galactic plane.<sup>2</sup> Most RPPs are detected primarily in radio, although sources like the Crab pulsar are visible up to gamma-ray wavelengths. There are also a small number of high-energy sources classified as RPPs, known as anomalous X-ray pulsars (AXPs) and soft gamma-ray repeaters (SGRs), which are isolated and spin down similarly to normal pulsars (Mereghetti 2008). However, their unusually high luminosity and rapid spin-down rates imply that their emission is not powered by rotation but rather by tapping the energy in their extreme magnetic fields, which can be as high as  $10^{15}$  G (Thompson & Duncan 1996). AXPs and SGRs are collectively known as magnetars. In this section, we focus the discussion primarily on radio pulsars.

### 1.3.1 Radio pulse profiles

Radio pulsar emission is generally highly polarised and is frequency dependent [see e.g. Seiradakis & Wielebinski (2004) for a detailed review]. At a particular frequency,  $\sim 10$ – $100$  individual pulses are normally summed to produce an averaged characteristic pulse profile (Helfand et al. 1975). The individual components of the profile (normally Gaussian) can be traced to specific coherent emission regions in the pulsar’s magnetosphere (e.g. Rankin 1983; Lyne &

---

<sup>2</sup>A complete catalogue is available at <http://www.atnf.csiro.au/research/pulsar/psrcat/>

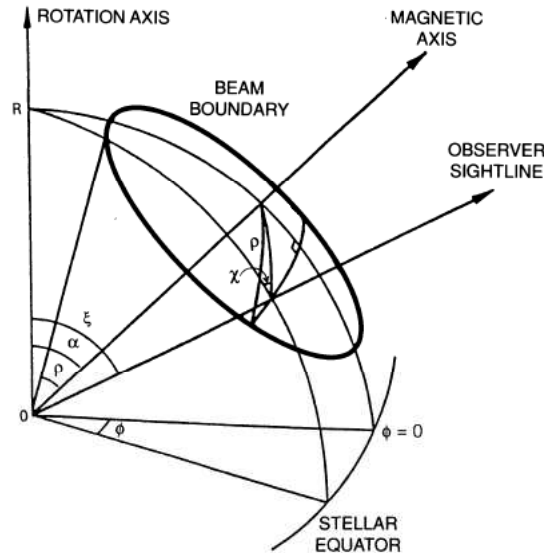
Manchester 1988; Seiradakis et al. 1995; Kijak & Gil 1998). The pulse and polarization profiles of young, slowly rotating pulsars differ somewhat from those of the older, recycled millisecond pulsars (MSPs). This is largely due to their distinct evolutionary histories: there is evidence that recycled MSP magnetic fields are distorted as a result of accretion (see Section 1.3.4).

Figure 1.2 shows the emission geometry of a radio pulsar, assuming a single conal beam centred on the magnetic axis. As the exact pulsar emission mechanism is still unknown, the pulse profiles of slow RPPs are usually modelled morphologically according to the number of components in their pulse profile. Single and double profiles can be explained by the hollow-cone model (Komesaroff 1970), in which one cone-shaped emission region is centered on each magnetic pole. A single-component profile corresponds to the line-of-sight grazing the edge of the cone, whereas a double profile corresponds to the line-of-sight cutting through the centre of the cone. Triple profiles are explained by adding a central pencil beam to the hollow cone (Radhakrishnan & Cooke 1969). There are also five-component profiles which are modelled by a central beam surrounded by inner and outer cones (Rankin 1983, 1993). Examples of such single, double, triple, and quintuple-peaked pulse profiles are shown in Figure 1.3. Alternatively, the patchy-beam model postulates a group of emission regions randomly located within the outer open magnetic field lines (Lyne & Manchester 1988). Recently, a new scheme was proposed, in which the emission originates from elongated fan beams positioned around the magnetic poles, classified as either spoke-like, wedge-like, or stream-like (Dyks et al. 2010). Rankin (1990) noted empirically that pulse widths  $W$  narrow with increasing spin period according to  $W \propto P^{-1/2}$ . Assuming a dipole magnetic field, this happens because the faster the pulsar spins, the wider the separation between tangents to the outermost open field lines at a given altitude<sup>3</sup>. The beam, which fills some fraction of these open field lines, widens accordingly (Backer 1995).

The profiles of MSPs display similar multi-component features, although the pulse profiles are generally more complex. A study of pulse profiles of 40 MSPs and 180 slow pulsars by Kramer et al. (1998) revealed an average of  $4.2 \pm 0.4$  Gaussian components for the MSPs compared with  $3.0 \pm 0.1$  components for the slow pulsars. The authors also found that MSPs have pulses which are  $\sim 4$  times wider (see Figure 1.5). As the wider MSP pulse profiles are ‘stretched’ longitudinally across a single pulse, they appear more complex because their

---

<sup>3</sup>Open field lines lose outside the speed-of-light cylinder (radius  $r_{\text{LC}} = cP/2\pi$ )



**Figure 1.2:** Emission geometry of a radio pulsar, assuming a single conal beam centred on the magnetic axis. Shown are the angle between the rotation and magnetic axes,  $\alpha$ , the angle between the rotation axis and the observer sightline,  $\zeta$ , the stellar longitude  $\phi$ , the polarization angle  $\chi$ , and the radius of the emission beam  $\rho$ . The thick circle represents the boundary of the emission beam (after Rankin 1993).

individual components are spaced out and hence are more easily identified (Kramer et al. 1998). On average, MSPs are also less luminous than slower pulsars, although the two luminosity distributions do overlap.

One example of an extremely complex, wide MSP pulse profile from PSR J2124–3358 is shown in Figure 1.4. Manchester & Han (2004) identified at least 12 components spanning almost the entire pulse period (4.931 ms), stating that the patchy-beam model is clearly a better fit for this object than the core-and-cone model. Note also the complicated polarization angle swing shown in Figure 1.4 (we discuss the polarization properties of MSPs in Section 1.3.2).

In slow RPPs, there is evidence for a radius-to-frequency mapping (RFM; Ruderman & Sutherland 1975; Cordes 1978; von Hoensbroech & Xilouris 1997a) in which the pulse width decreases with increasing observation frequency. Assuming that radio emission originates from plasma which flows along open magnetic field lines above the magnetic poles, this indicates that higher frequencies probe denser regions closer to the pulsar surface, where the field lines are narrower. However, there are a few exceptions to the RFM, in which the pulse width increases with frequency (Johnston et al. 2008a). In these cases, the outer components of the profile are thought to brighten intrinsically with frequency, relative to the central components, causing an apparent broadening

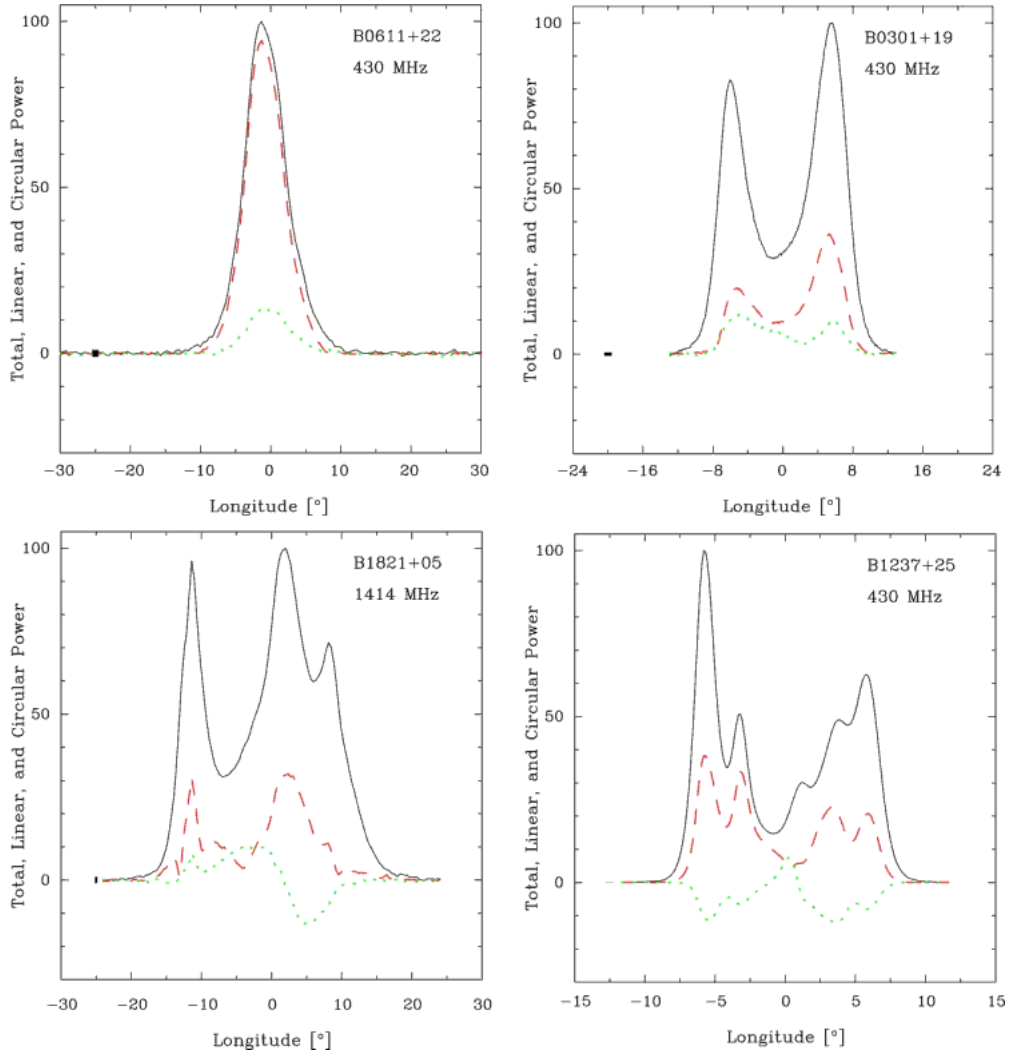


**Figure 1.3:** Pulse profiles of four pulsars showing a single-peaked profile (B0611+22; top left panel), a double-peaked profile (B0301+19; top right panel), a triple-peaked profile (B1821+05; bottom left panel), and a quintuple-peaked profile (B1237+05; bottom right panel). The black, red, and green lines show total intensity, linearly polarized intensity, and circularly polarized intensity respectively (from Hankins & Rankin 2010).

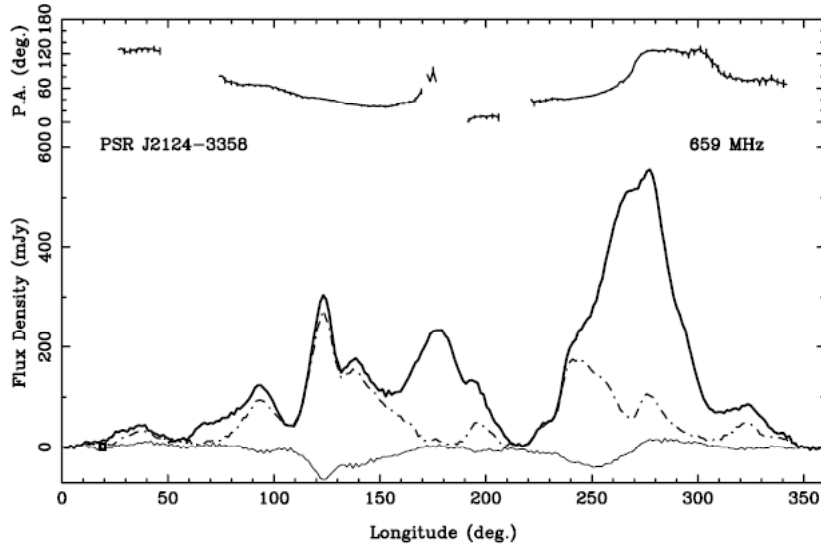


**Figure 1.4:** Pulse profile (bottom curves) and polarization angle swing (top curves) for the millisecond pulsar PSR J2124–3358, which has a spin period of 4.931 ms. The bottom curves show total intensity (thick line), linearly polarized intensity (dot-dashed line), and circularly polarized intensity (thin line). The pulse profile contains at least 12 components, and spans most of the pulse period (from Manchester & Han 2004).

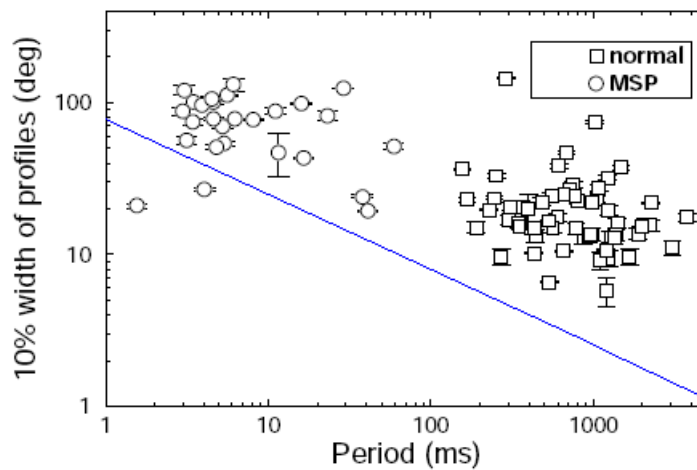


**Figure 1.5:** Pulse profile widths of a sample of radio pulsars, measured at 10% of the peak intensity, as a function of pulse period. Slowly rotating pulsars are denoted by squares, and MSPs are denoted by circles (from Kramer et al. 1998). The blue line shows the  $W \propto P^{-1/2}$  relation. Rankin (1990) showed empirically that the half-power pulse widths of pulsars of 110 sample pulsars depend only on the magnetic inclination angle and the polar cap radius, and always lie above the blue line.

of the pulse.

The RFM is satisfied poorly by MSPs. In many cases, multi-frequency observations show that the pulse widths remain fairly constant. One possible reason is that all the emission originates from a narrow range of altitudes due to the MSP's compact magnetosphere (Kramer et al. 1999, see Section 1.3.4). Interestingly, the fan-beam model of Dyks et al. (2010) contradicts the idea that higher frequencies probe lower emission altitudes in all RPPs. The authors suggest instead that high frequencies probe lower-density regions at the outskirts of the elongated beam, and that all radio frequencies originate at the same altitude.

### 1.3.2 Polarization

Radio polarimetry is another important diagnostic of the pulsar's magnetic geometry and orientation. The polarization position angle (PA), defined as the angle between the pulsar's projected rotation axis and the electric field vector at the emission point, varies in a characteristic way across a pulse. As the electric field vector is linked closely to the magnetic field geometry (it is thought to lie either parallel or perpendicular to the magnetic field tangent vector), the shape of the PA swing across one pulse period reflects the structure of the magnetic field. Traditionally, the PA swing is analysed concurrently with the pulse profile. The most commonly used model to describe pulsar polarization is the Rotating Vector Model (RVM; Radhakrishnan & Cooke 1969), which describes the PA swing as a function of the angle between the magnetic axis and the rotation axis, the observer's inclination angle, and the pulse phase. The RVM assumes a dipolar magnetic field and predicts the S-shaped PA swing which is observed in many slow pulsars (see Figure 1.6 for examples of 'well-behaved' PA swings). However, not all pulsars can be fit well using the model. It is not applicable for most MSPs, whose PA profiles are either flat or display varying amounts of distortion, indicating deviations from a dipolar field (see for example, the complex PA swing for the MSP PSR J2124–3358 in Figure 1.4) (Xilouris et al. 1998; Stairs et al. 1999; Ord et al. 2004).

A new method for analysing polarization data, Stokes tomography, is introduced in Chapters 5 and 6 of this thesis. Stokes tomography exploits the fact that, when plotted against each other over one pulse period, the Stokes parameters form patterns which are unique (or nearly so) for different combinations of magnetic and observer inclination angles, as well as for various magnetic

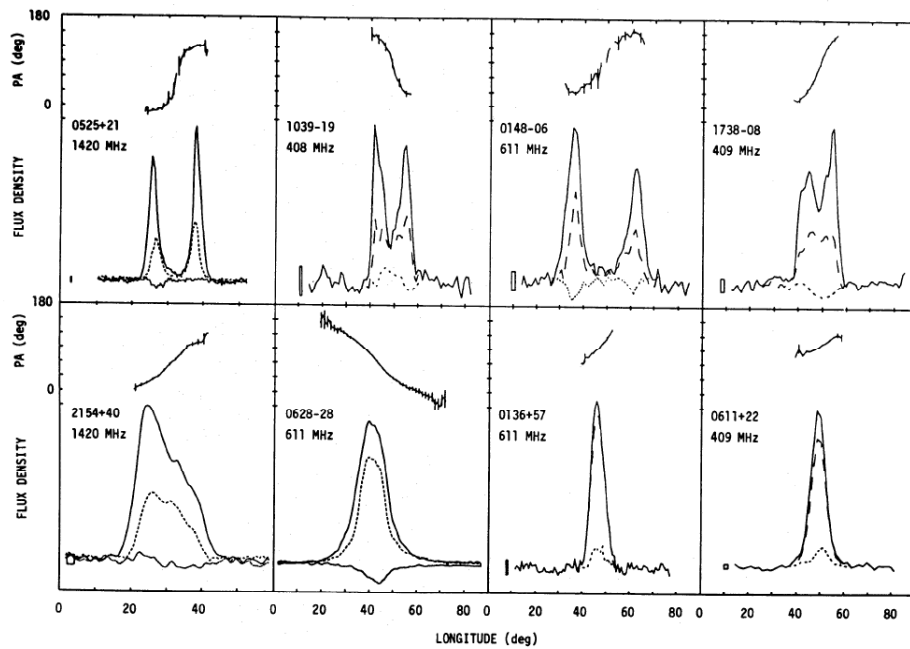


**Figure 1.6:** Examples of S-shaped PA swings and pulse profiles from eight radio pulsars. At the bottom of each panel, the solid, dashed, and dotted lines represent the total intensity, linearly polarized, and circularly polarized components of the pulse profile. The PA swing is shown at the top of each panel, with  $\pm 2\sigma$  error bars where available (from Lyne & Manchester 1988).

field configurations. This method has the advantage that it is not restricted to any particular model (e.g. axisymmetric dipole) for the pulsar's magnetic field or emission geometry.

Aside from the differences in the shape of the PA swing, MSPs also have significantly higher linear and circular polarizations than slow pulsars. Figure 1.7 shows a statistical comparison of the (a) fractional linear, (b) absolute circular ( $|V|/I$ ), and (c) circular ( $V/I$ ) polarization of 24 MSPs and 281 slow pulsars, where  $V$  is the circularly polarized component, and  $I$  is the total intensity of the emission in the canonical Stokes vector  $(I, Q, U, V)$ . A detailed explanation of the Stokes parameters is presented in chapter 5. The steepest slope of the PA swing (d) is also shown for 22 MSPs and 178 slow pulsars (Xilouris et al. 1998). In panels (b) and (c), both  $|V|$  and  $V$  are important quantities as the net circular polarization does not always provide an accurate description of the overall degree of circular polarization. For example, flips in the handedness of the polarization between pulses can lead to an integrated profile with low  $V$ , while the individual pulses may actually be highly circularly polarized (Karastergiou et al. 2003). In Figure 1.7 (c), the handedness has been calibrated by referencing the measurements of  $V$  to those of a canonical pulsar, PSR B1929+10. In panel (d), the steepest slope of the PA swing in the RVM occurs when the observer's line-of-sight is aligned with the magnetic meridian, with  $(d\psi/d\phi)_{\max} = \sin \alpha / \sin(i - \alpha)$ , where  $\phi$  is the pulse phase,  $\alpha$  is the magnetic inclination angle, and  $i$  is the observer's inclination angle. However, this relation may not apply to MSPs which have shallower PA slopes, implying that the emission originates from further out in the magnetosphere, where the field may be swept-back (Barnard & Arons 1986; Xilouris et al. 1998). Here, the slope of the PA swing is reduced as the toroidal component of the swept-back field increases.

The degree of polarization in RPPs is frequency dependent, though the amount by which it changes is different for each pulsar (Xilouris et al. 1998; Gould & Lyne 1998; Johnston et al. 2008a). Generally, the degree of linear polarization decreases with increasing frequency. This can be explained in two ways. Firstly, the polarized emission is emitted by particles with a high Lorentz factor  $\gamma$  and is beamed into a cone of opening angle  $\gamma^{-1}$  around each particle's velocity vector. The duration of the detected radiation (i.e. of each particle 'bunch') therefore scales as  $\gamma^{-1}$ ; often, it is shorter than the data sampling rate. The emission is incoherently summed in the detector, resulting in a decrease in the fractional polarization. At high frequencies, which are thought to probe lower regions of the magnetosphere, this effect is exacerbated as the field

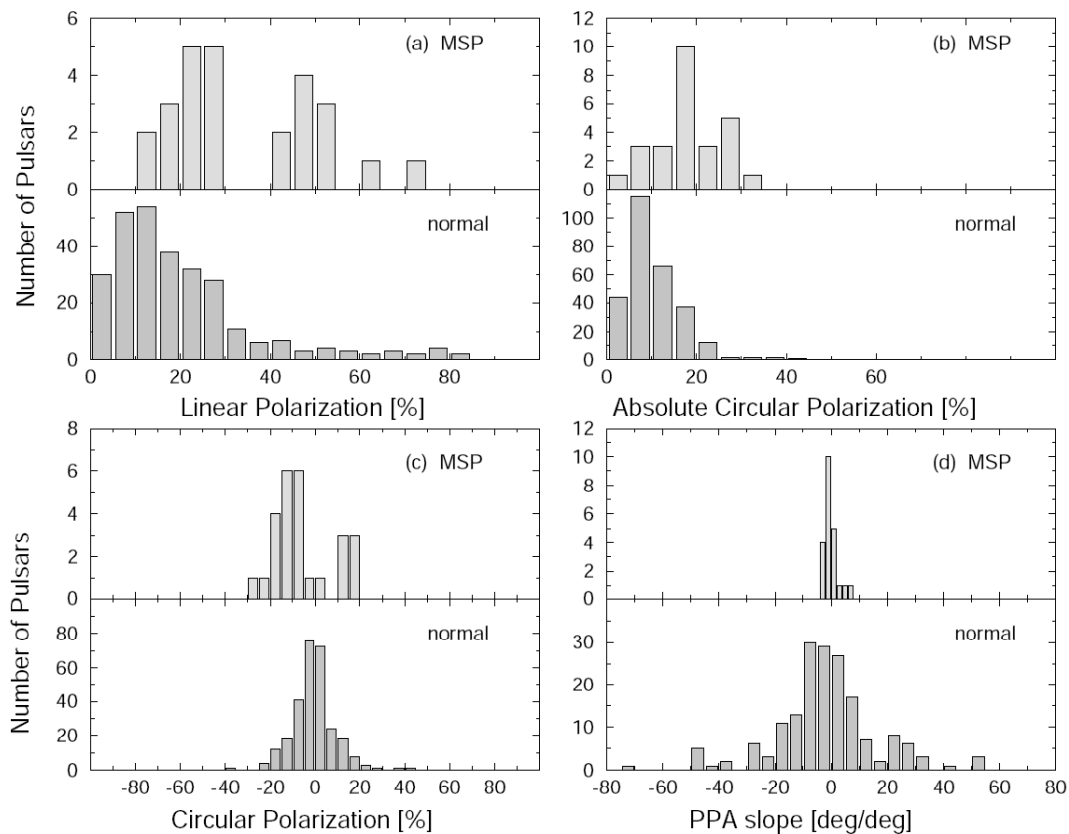


**Figure 1.7:** Comparison of the (a) fractional linear, (b) absolute circular, and (c) circular polarization of 24 MSPs (upper panels) and 281 slow pulsars (lower panel). Histograms of the steepest slope of the PA swing for 22 MSPs and 178 slow pulsars are shown in (d) (from Xilouris et al. 1998).

lines are closer together, reducing the number of independently radiating particle bunches. Alternatively, the superposition of two orthogonally polarized modes of emission with different spectral indices and intensities determines the fractional polarization. The larger the difference in intensities, the higher the linear polarization. If one mode has a much steeper spectrum, the two spectra can intersect at a high frequency, decreasing the degree of linear polarization (Karastergiou et al. 2005; Johnston et al. 2008a). Interestingly, the shape of many PA swings also changes with frequency, which is unexpected in the context of the dipole-field geometry assumed by the RVM (Johnston et al. 2008a).

Another effect which must be taken into account is that the polarization changes continuously as it propagates through the magnetosphere. This can result in the polarized emission changing significantly between when it is emitted, and when it is actually observed (Cheng & Ruderman 1979; Stinebring 1982; Barnard & Arons 1986; Melrose et al. 2006). The polarization state of the emission only becomes fixed at the polarization-limiting radius, defined as the radius beyond which the pulsar plasma is ineffective in altering the polarization. Barnard & Arons (1986) estimated this radius to be close to the light cylinder radius for  $P \lesssim 0.6$  s, and to decrease as  $P$  increases (Barnard & Arons 1986). However, its exact location is uncertain (von Hoensbroech et al. 1998).

### 1.3.3 Timing properties

Most rotation-powered pulsars are remarkably stable clocks, with precisions comparable to atomic clocks (Matsakis et al. 1997). An important property of radio pulsars is that they all spin down gradually, allowing their spin periods to be measured with a precision of 1 part in  $10^{14}$  (Ghosh 2007)<sup>4</sup>. Figure 1.8 shows the spin distribution of 1509 rotation-powered pulsars (Manchester et al. 2005). The distribution is clearly bimodal, with a dichotomy between millisecond and slowly rotating pulsars. Most isolated radio pulsars are slow rotators with periods of between 0.1–1 s. Binary pulsars populate approximately 75% of the millisecond spin period range, whereas the young, high-energy (optical, X-ray and gamma-ray) pulsars have periods of between 0.03–0.15 s. The AXPs are the slowest, with periods ranging from 5–12 s. As mentioned in Section 1.1.2, the gap in the spin distribution is bridged mostly by pulsars which are in the

---

<sup>4</sup>Accretion-powered pulsars are much less stable. Aside from the long-term timing noise described in Section 1.4.1, 5% of observed burst oscillations from LMXBs display anomalies like frequency drifts as large as  $\sim 1.3\%$  of the spin frequency  $\nu_*$  (Galloway et al. 2001), perhaps due to atmospheric motions (Spitkovsky et al. 2002).

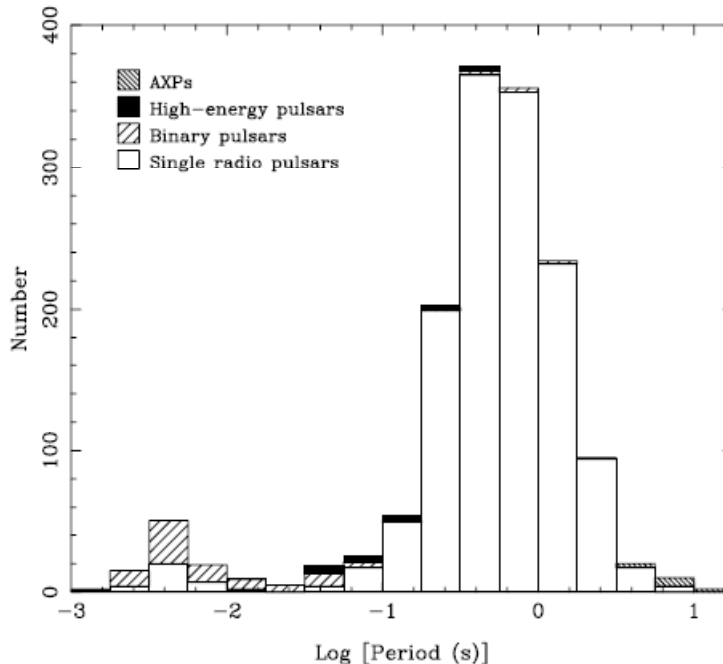


**Figure 1.8:** Spin distribution of 1509 rotation-powered pulsars, separated into binary pulsars, high-energy (optical, X-ray and gamma-ray) pulsars, and AXPs (Manchester et al. 2005).

process of being spun up by accretion.

Occasionally, at random times, some pulsars “glitch”, experiencing discontinuous decreases in their spin periods. These glitches are thought to be caused by intermittent coupling between the crust and the superfluid interior of the pulsar (Lyne & Graham-Smith 2006). Studies of recent data also provide evidence that glitches can be modelled as an avalanche process, and have a Poissonian waiting time distribution (Melatos et al. 2008). Long term ( $> 10$  yr) timing observations of RPPs conducted by Hobbs et al. (2010) show that for pulsars younger than  $10^5$  years, glitches are the dominant source of timing noise. Other sources of long-term timing noise include unmodelled planetary companions (Cordes 1993), or free precession, which we now discuss.

### Free precession

If a pulsar has a nonzero ellipticity, and if its axis of symmetry is displaced from its angular momentum vector, it will precess. In the absence of external torques, free precession occurs, modulating the times of arrivals and intensities of the observed pulse profiles at the precession frequency,  $\nu_p \approx \nu_* \epsilon \cos \theta$ , where  $\nu_*$  is the spin frequency, and  $\theta$  is the tilt angle between the pulsar’s symmetry

axis and the angular momentum vector (see Figure 2.1). As noted in Section 1.2, freely precessing pulsars are excellent sources of continuous gravitational waves.

There are arguments that free precession is not an observable effect. Damping mechanisms such as internal dissipation (Bondi & Gold 1955; Alpar & Saulis 1988) and gravitational radiation (Cutler & Jones 2001) can reduce the tilt angle over time. Additionally, recent modelling by Glampedakis et al. (2009) suggest that instabilities in the superfluid interior prevent the pulsar from precessing.

On the other hand, there are many mechanisms that could deform a pulsar for up to  $\sim 10^7$  years, including stresses in the crust (Ushomirsky et al. 2000), large internal magnetic fields (Bonazzola & Gourgoulhon 1996; Cutler 2002), and mountains on the surface (Melatos 2000; Jones & Andersson 2002; Vigelius & Melatos 2009b, see Section 1.5.3). To date, only one radio source, PSR B1828–11, shows strong evidence for free precession, with a precession period of 500 days and a tilt angle of  $\sim 3^\circ$  (Stairs et al. 2000; Akgün et al. 2006). Another tentative candidate is PSR B1642–03 (Shabanova et al. 2001). Several X-ray sources, e.g. RX J0720.4–3125 (Hohle & Haberl 2009) and XTE J1814–338 (Chung et al. 2008, Chapter 2) also display modulations consistent with free precession, although the data are not conclusive.

### 1.3.4 Magnetic field strength and geometry

The magnetic fields of slow RPPs are commonly approximated as dipoles rotating in a vacuum (Deutsch 1955). The simplest model states that the rotational energy of RPPs is converted into electromagnetic energy via magnetic dipole radiation, at a rate (Pacini 1967; Pacini & Salpeter 1968; Ostriker & Gunn 1969)

$$\dot{E} = I\Omega\dot{\Omega} = -\frac{\mu^2\Omega^4\sin^2\alpha}{3c^2}, \quad (1.1)$$

where  $\mu$  is the star's magnetic dipole moment,  $I$  is its moment of inertia,  $\Omega = 2\pi/P$  is its angular frequency,  $\alpha$  is the angle between the magnetic axis and the spin axis, and  $c$  is the speed of light. Using the canonical value of  $I = 10^{45} \text{ g cm}^2$ , and assuming  $\sin\alpha = 1$ ,  $\mu$  is determined to be

$$\mu = 3.2 \times 10^{37} (P\dot{P})^{1/2} \text{ G cm}^3. \quad (1.2)$$

Improvements to the model of a rotating dipole in vacuo, taking into account the corotating magnetosphere, were made by Melatos (1997).

In reality, of course, a pulsar does not reside in a vacuum. The magnetosphere can significantly alter the structure of the magnetic field, especially at large altitudes. The characteristic size of the magnetosphere is given by the light cylinder radius,  $R_{\text{LC}} = c/\Omega \approx 4.8 \times 10^3(P/1\text{ s})$ . Inside this radius, the magnetosphere corotates with the star, generating a charge density known as the Goldreich-Julian density  $\rho_{\text{GJ}}$  (Goldreich & Julian 1969). Electric currents flow along the magnetic field lines, inducing a purely toroidal magnetic field  $B_1 = (r/R_{\text{LC}})(J/J_{\text{GJ}})B \cos \alpha$ , where  $r$  is the radial distance from the star,  $J$  is the current density,  $J_{\text{GJ}} = \rho_{\text{GJ}}c$  is the Goldreich-Julian current density, and  $B$  is the dipole field strength (Hibschman & Arons 2001). Additionally, perturbations to the magnetic field are caused by relativistic sweep-back of field lines (Shitov 1983, 1985). At low altitudes ( $r \ll R_{\text{LC}}$ ), this effect is of order  $(r/R_{\text{LC}})^2$ , although it grows to  $(r/R_{\text{LC}})^{1/2}$  at the outer boundary of the open field line region (Dyks & Harding 2004).

Recently, a more realistic three-dimensional model of a force-free magnetosphere was constructed (Spitkovsky 2006; Kalapotharakos & Contopoulos 2009). Numerical simulations of this model involve a rotating, conducting sphere immersed in a massless, infinitely conducting fluid. The charge density of the fluid is approximately equal to the Goldreich-Julian density. The force-free field has been used to model light curves from high-energy gamma-ray pulsars, whose emission is thought to originate in the outer magnetosphere (Bai & Spitkovsky 2009a).

There is much greater uncertainty regarding the magnetic field geometry of MSPs. MSP magnetospheres are more compact than those of slower pulsars because of their smaller spin periods. It has been argued, from the lack of dramatic frequency-dependent pulse profile changes in some MSPs, that either the magnetic field does not change with radius, or the compactness of the magnetosphere results in multi-frequency emission originating from a narrow range of altitudes (Kramer et al. 1999). However, as evidenced by the shapes of their pulse profiles and PA swings, there are likely differences between the magnetic field structures of MSPs and slow pulsars. The field structure of MSPs is expected to be altered by an amount proportional to the total mass transferred during accretion (Ruderman 1991; Chen & Ruderman 1993a). This distortion can occur when e.g. magnetic field lines which are frozen-in to the accreted material are dragged along as the matter spreads equatorwards (Melatos & Phinney 2001; Payne & Melatos 2004; Vigelius & Melatos 2008). The magnetic field can remain distorted for up to  $10^8$  years before relaxing into a dipole (Vigelius & Melatos 2009b). Several models involving higher-order magnetic

multipoles have also surfaced, after a quadrupolar magnetic field was proposed by Gil (1985) to explain the observed emission from the MSP PSR B1937+214. These higher-order multipoles may be comparable to, or even dominate, the dipolar component close to the stellar surface (Shakura et al. 1991; Arons 1993; Asseo & Khechinashvili 2002). The authors suggest that these non-dipolar fields are necessary to model complex pulse profiles. For example, Asseo & Khechinashvili (2002) state that the existence of complex multipoles allows pair-production in ‘favourable regions’, distributed in such a way that the 20 isolated subbeams observed in PSR B0943+10 can be explained.

## 1.4 Accretion-powered pulsars

We now turn to discuss accretion-powered pulsars (APPs), which exist in binary systems and emit primarily in the X-ray band. The X-ray luminosities typically observed from these sources ( $\sim 10^{37}$  erg s $^{-1}$ ) are too large to be powered by their rotation alone. The emission is instead generated by the energy released by matter from the companion star falling into the pulsar’s gravitational potential well at a rate of  $\dot{M} \sim 10^{-9}M_{\odot}$  yr $^{-1}$  (Zel’dovich & Novikov 1965; Zel’Dovich & Shakura 1969; Pringle & Rees 1972; Lamb et al. 1973). As the accreted matter falls towards the surface of the pulsar, it is channeled along the magnetic field lines towards the magnetic poles (Davidson 1973; Lamb et al. 1973). “Hotspots” are produced at the poles, which radiate as the infalling material forms an accretion column. The intensity of the observed emission is proportional to  $\dot{M}$ .

Unlike rotation-powered pulsars, APPs can spin up as the accreted matter transfers angular momentum to them (Ghosh & Lamb 1979). They experience a spin-up torque  $N \approx \dot{M}\sqrt{GM_{\star}r_m}$ , where  $G$  is the gravitational constant,  $M_{\star}$  is the pulsar radius,  $r_m \sim 10^6$  m is the magnetospheric radius (Bildsten et al. 1997).

In this section, we briefly describe the two classes of APPs, and detail the key properties of APPs relevant to this thesis, namely their timing properties (Section 1.4.1), magnetic fields and ellipticities (Section 1.4.2).

### High-mass X-ray binaries

The initial masses and separations of stars play an important role in the formation of X-ray binaries. HMXBs originate from systems in which both stars are massive ( $> 12M_{\odot}$ ). The more massive primary star evolves quickly and

explodes in a supernova. If the mass ejected during the supernova is less than the combined masses of the remnant neutron star and the secondary star, or if the neutron star is kicked along a favourable direction during an asymmetric explosion, the system remains a binary. HMXBs have generally eccentric orbits, and are not close enough for the primary star to fill its Roche lobe. The neutron star captures material from its companion's stellar wind through Bondi-Hoyle accretion (Bondi & Hoyle 1944). The material from the stellar wind forms a common envelope through which angular momentum is transferred to the neutron star. The lifetimes of HMXBs are short ( $10^5$ – $10^7$  yr) (Psaltis 2006), after which time the companion (usually a type O or B star) explodes as a supernova. This leaves behind a double pulsar system comprising the original neutron star, now a recycled millisecond pulsar, and a young pulsar. There are currently ten known double pulsar systems, the most recently discovered being PSR J1906+0746 (Lorimer et al. 2006; Lorimer 2008).

### Low-mass X-ray binaries

In order to produce LMXBs, there needs to be a significant difference between the initial masses of the primary and secondary stars (Tauris & van den Heuvel 2006). The more massive primary enters its red giant phase first, while the secondary star is still on the main sequence. The primary star loses material and angular momentum to the secondary main-sequence star via Roche-lobe overflow, and via a stellar wind. A common envelope forms, which depletes the primary star's hydrogen shell ( $\geq 70\%$  of its total mass) and shrinks the binary orbit. Once the hydrogen shell is expelled, the primary star collapses and explodes in a supernova if its helium-core mass is  $\geq 2.8M_{\odot}$ . The system is now observed as an LMXB. The closeness of the resulting neutron star and the secondary star allows for accretion, again via Roche-lobe overflow, in which the secondary star is now the mass donor. Due to its lower mass, the secondary star evolves more slowly than the primary and can take  $\sim 2.2$  Gyr to enter its giant phase. The lifetimes of LMXBs are typically  $\sim 10^7$ – $10^9$  yr (Psaltis 2006).

Figure 1.9 shows the binary configuration of HMXBs and LMXBs, along with typical values for the masses of the primary and secondary stars, orbital separations, and orbital periods. Aside from those previously stated, there are several interesting differences between HMXBs and LMXBs (Psaltis 2004). Firstly, most HMXBs display persistent pulsations, whereas LMXBs are mostly transient objects which are quiescent for long periods. This occurs because the magnetic field of a neutron star, which collimates the accretion flow onto

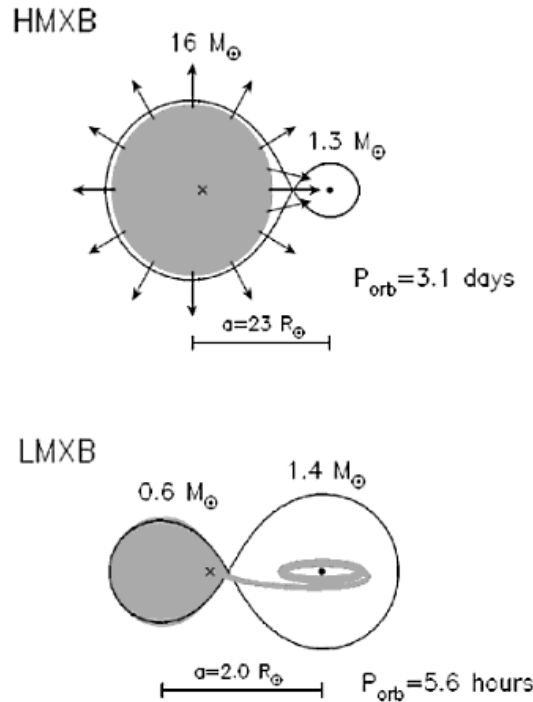


**Figure 1.9:** Main characteristics of HMXBs (top panel) and LMXBs (bottom panel), showing typical values for the masses of the primary and secondary stars, orbital separations, and orbital periods (From Tauris & van den Heuvel 2006).

hotspots, decreases with the amount of accreted mass. Secondly, HMXBs are distributed along the galactic plane (Lutovinov et al. 2007), whereas LMXBs are found near older stars around the Galactic centre and in globular clusters (Grimm et al. 2002; Revnivtsev et al. 2008).

The X-ray spectrum of APPs is generally described by a flat power law with an exponential cutoff at  $\geq 10$  keV, caused by Compton upscattering of thermal emission from the polar caps by high energy electrons in the accretion column (Mészáros 1992). Low magnetic field APPs can also be classified according to their position on an X-ray colour-colour diagram as Z sources and atoll sources. Z sources are named for the Z-shaped track which they trace in the X-ray colour-colour diagram during an outburst, whereas atoll sources trace out either a banana shape, or an island (Hasinger & van der Klis 1989). It is thought that Z sources have stronger magnetic fields ( $> 10^9$ – $10^{10}$  G) and reach higher accretion rates than atoll sources. Recently, however, observations of the transient neutron star XTE J1701–462 (Lin et al. 2009) showed that it changed from displaying characteristics of a Z source to those of an atoll source over the course of a 20-month outburst. The authors conclude that neutron

stars in LMXBs evolve from being Z sources to atoll sources as their accretion rate drops.

### 1.4.1 Timing properties

X-ray timing is crucial in understanding the physics of accretion-powered pulsars. Their time-dependent behaviour is much more complex than the mostly steady, predictable spindown of radio pulsars. In this section, we summarise only a few of the many varied phenomena observed [for detailed reviews, see (Bildsten et al. 1997; Psaltis 2004; Ghosh 2007)].

Slower pulsars with spin periods of  $\gtrsim 1$  s are typically found in HMXBs. The spin distributions of a sample of accretion-powered pulsars in HMXBs from the galaxy and the Small and Large Magellanic Clouds are shown in Figure 1.10. Slow pulsars undergo two different types of spin period evolution. The spin period of transient sources depends on their accretion rate; they spin up as the accretion rate increases. When the accretion rate drops sufficiently, the magnetospheric radius exceeds the corotation radius. Further accretion is centrifugally inhibited, causing the star to lose angular momentum and spin down. This is known as the propeller effect (Illarionov & Sunyaev 1975). Long-term data reveal that persistent, disk-fed sources undergo torque reversals between periods of spin-up and spin-down (Bildsten et al. 1997). The timescales in which the pulsars experience these transitions vary dramatically. The accreting pulsar Cen X-3 switches every 10–100 days between spinning up at an average rate of  $\sim 7 \times 10^{-12} \text{ Hz s}^{-1}$ , and spinning down at an average rate of  $\sim -3 \times 10^{-12} \text{ Hz s}^{-1}$ . Other pulsars such as GX 1+4 switch every 10–20 years.

The following discussion highlights the timing properties of rapidly rotating LMXBs, which are an essential component of this thesis. Very generally, the orbital parameters of a binary pulsar are estimated by fitting a model to the pulse times-of-arrivals (Deeter et al. 1981). Once these are accounted for, along with the spin period derivatives, any timing residuals are considered to be ‘noise’. It is these (often complex) timing residuals that contain useful information which is crucial when piecing together a complete model. AMSPs are the subset of pulsed LMXBs which rotate with millisecond periods. In chapter 2, we study timing data from AMSP XTE J1814–338 in detail. Interestingly, both the timing residuals and X-ray luminosity of this object are modulated at roughly the same period, which is a possible signature of precession. In our analysis, we attempt to replicate the data by modelling a precessing pul-

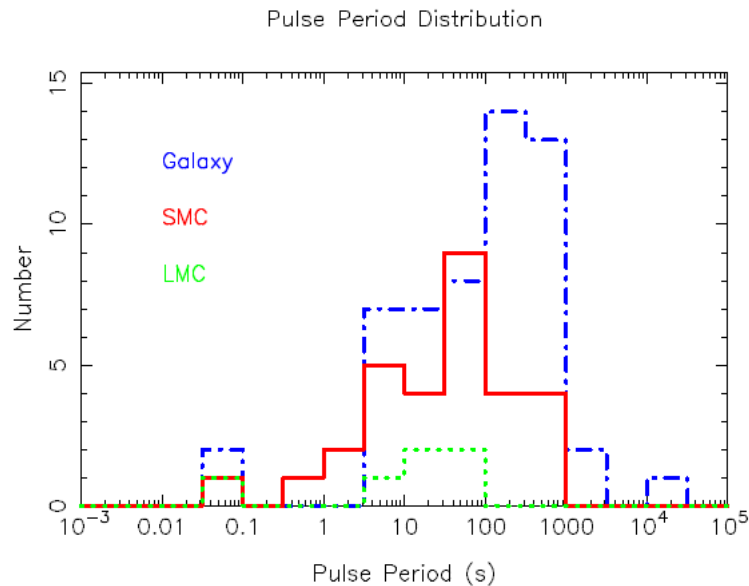


**Figure 1.10:** Spin distributions of a sample of accretion-powered pulsars in HMXBs from the galaxy (dot-dashed blue lines), and the Small (solid red lines) and Large (dotted green lines) Magellanic Clouds (Laycock et al. 2005).

sar over a range of magnetic and observer inclination angles. The modelling puts interesting limits on the star’s ellipticity and hence its gravitational wave emission.

Only 20% of the known LMXB population have measured spin periods (Galloway 2008). Most neutron stars in LMXBs have weak magnetic fields ( $\lesssim 10^8$  G) and do not appear to pulse, as the accreted material is not channeled onto hotspots (Cumming et al. 2001). One sub-class of LMXBs that do pulse are the AMSPs, which are transient: they are only observable during ‘outbursts’, phases of active accretion that last for several weeks and occur once every few months–years. At other times, any emission is too weak to be detected with existing instruments. During the outburst phase, pulsations are persistent, with average fractional amplitudes of  $\sim 5\%$  (Galloway 2008). Another sub-class of pulsed LMXBs displays intermittent pulsations. The most famous example is HETE J1900.1–2455, which was detected in outburst in 2005 and has remained in outburst ever since, with the exception of a three-week quiescent phase in 2007 (Kaaret et al. 2006; Degenaar et al. 2007). However, pulsations were only ever detected in the first two months of the outburst (Galloway 2007). The cause of the intermittency is still unknown but has been linked to the magnetic field; models include intermittent obscuration of the magnetic poles (Gögüş et al. 2007), wandering of the hotspot around

the magnetic poles (Romanova et al. 2004a; Lamb et al. 2009), and burial of the magnetic field (Cumming et al. 2001; Cumming 2008).

A unique characteristic of LMXBs is the presence of thermonuclear (Type I) X-ray bursts on the surface of the neutron star. These bursts are caused by unstable ignition of the accreted H/He, starting from a point on the surface and spreading to cover the entire star within 10–100 s (Strohmayer et al. 2003). They can occur as frequently as once every few hours, causing the observed X-ray luminosity to increase by an order of magnitude. Coherent oscillations are observed across the duration of the burst, and have been confirmed in a number of systems to be a direct measure of the neutron star spin period (Chakrabarty et al. 2003; Strohmayer et al. 2003).

Persistent pulsations and Type I X-ray bursts are the only two reliable methods of measuring the spin periods of LMXBs. Another phenomenon linked to the spin period is kHz quasi-periodic oscillations (QPOs) (van der Klis et al. 1996; Strohmayer et al. 1996). These oscillations appear as twin peaks in the power spectrum which vary in frequency with the X-ray intensity. Although the origin of QPOs is not fully understood, most models involve inhomogeneities in the inner accretion disk oscillating at one of the peak frequencies [see van der Klis (2004) for a detailed review of QPOs]. In some objects, the separation of the peaks has been observed to coincide with the exact neutron star spin frequency (e.g. XTE J1807–294 Linares et al. 2005), and half the spin frequency (e.g. SAX J1808.4–3658 Wijnands et al. 2003). There are, however, many exceptions to this rule as the QPO peak separations vary, and many peak separations are seemingly unrelated to the spin frequency. To name a few, SAX J1808.4–3658 has a spin frequency of 401 Hz and a QPO separation of  $182 \pm 8$  Hz (van Straaten et al. 2005), SAX J1750.8–2980 has a spin frequency of 601 Hz and a QPO separation of  $317 \pm 9$  Hz (Kaaret et al. 2002), and 4U 0614+09 has a spin frequency of 415 Hz and multiple QPO separations of 275–350 Hz (Strohmayer et al. 1996; Méndez & van der Klis 1999; Di Salvo et al. 2001; Migliari et al. 2003). A catalogue of known kHz QPO sources is presented in Table 1.2, following the list compiled by (Watts et al. 2008a). The catalogue lists only sources which show no other persistent pulsations or bursts. The authors assume that the spin frequency of the sources lies within the range of observed QPO peak separations.

The timing noise exhibited by LMXBs varies from source to source. It is difficult to monitor due to its transient nature, but can reveal systematic variations in the magnetic field structure, the location of the hotspots, or the motion of the pulsar. In AMSPs especially, the limited amount of data makes

Source	$\nu_*$ (Hz)
Cyg X-2	351±34
GX 340+0	343±92
4U 1735–44	316±32
GX 5–1	288±69
4U 1820–30	285±65
Sco X-1	272 ±40
GX 17+2	272±50
XTE J2123–058	272±50
GX 349+2	266±13

**Table 1.2:** Catalogue of kHz QPO sources which display no other persistent pulsations or X-ray bursts. Spin frequencies,  $\nu_*$ , are assumed to lie within the range of observed QPO peak separations (Watts et al. 2008a, and references therein).

constructing a detailed coherent, dynamic model of these objects a daunting task. Examples of timing noise in AMSPs are shown in Figure 1.11, in which timing data from nine outbursts from six different pulsars are plotted, along with their light curves. We now list the results of several recent efforts to model the data from the two most studied AMSPs, SAX J1808.4–3658 and XTE J1848–338.

The ‘nearly-aligned moving spot model’ for AMSPs states that the hotspot is located near the spin axis (Lamb et al. 2009). Changes in the accretion rate and inner disk structure push the hotspot around, causing variations in the shapes of the pulse profiles and times-of-arrival. This model also proposes that the transient nature of AMSPs is explained by assuming that the magnetic poles are nearly aligned with the spin axis. During periods of persistent accretion, the material accretes onto hotspots close to the spin axis, making pulsations difficult to detect. As the mass transfer becomes transient, small changes in the accretion flow can suddenly cause the hotspots to move away from the spin axis, allowing pulses to be observed. Numerical simulations show that complicated modes of accretion can alter the shape and position of hotspots (Romanova et al. 2004a; Kulkarni & Romanova 2005; Long et al. 2008). Patruno et al. (2009) pointed out that if indeed the motion of the hotspot accounts for the observed timing residuals in these objects, this may introduce a bias in the measured spin frequencies, implying that several AMSPs have lower spin frequency derivatives than previously estimated.

Long-term timing of the AMSP SAX J1808.4-3658 (Hartman et al. 2009a) uncovered an unusually large rate of increase in its orbital period over the last

ten years,  $(3.80 \pm 0.06) \times 10^{-12} \text{ s s}^{-1}$ . The increase suggests that the pulsar's companion is degenerate or fully convective, however it is not clear why the increase is so large, an effect which cannot be explained by accretion alone (di Salvo et al. 2008; Burderi et al. 2009). A possible scenario is that SAX J1808.4–3658 periodically turns into a black widow pulsar which ejects matter from the binary system via a particle wind during quiescent periods (di Salvo et al. 2008). The binary system spins up to conserve angular momentum. An alternative is that short-term interchange of angular momentum occurs between the pulsar and its companion due to tidal dissipation or uneven heating in the companion (Hartman et al. 2009a). Timing and spectral analysis of individual outbursts from this object also reveal short-term variations, which have been explained by screening of the antipodal hotspot by a receding accretion disk (Ibragimov & Poutanen 2009; Poutanen et al. 2009), and transitions between accretion phases (Hartman et al. 2009b).

As mentioned earlier, XTE J1814–338 displays modulations throughout its one observed outburst (see top left panel in Figure 1.11). Additionally, the Type-I X-ray burst oscillations observed from this source are phase-coherent with the persistent pulsations (Watts et al. 2008b). Several models exist to explain the modulations, including the wandering of the hotspot in response to a varying accretion rate (Papitto et al. 2007), and the pulsar undergoing free precession (Chung et al. 2008, see Chapter 2).

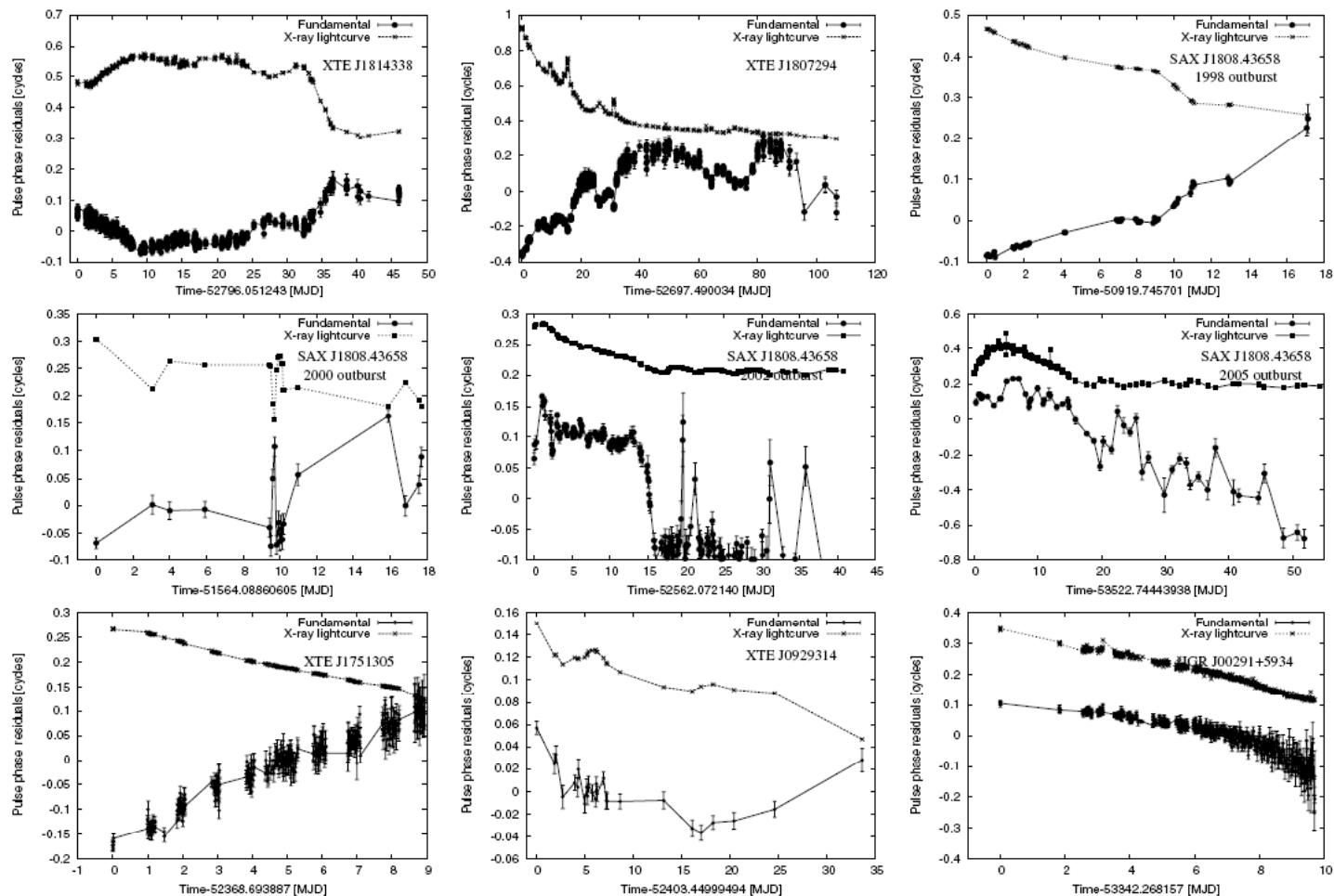


**Figure 1.11:** Timing data from 9 AMSP outbursts, from six AMSPs. The names of the pulsars are shown in the top right corner of each panel. The timing variation in each pulsar is quantified by the pulse phase residuals (bullets, in units of phase cycles), while the 2.5–16 keV light curves (in arbitrary units) are denoted by crosses (from Patruno et al. 2009).

### 1.4.2 Magnetic field strength

Unlike RPPs, in which the magnetic field strength can be determined from equation (1.2), the field strength of APPs must be inferred indirectly. In some HMXBs, the surface magnetic field can be measured by identifying the cyclotron resonance absorption line in the hard X-ray spectrum. The energy at which electron-cyclotron resonance occurs is  $E_r = \hbar e B / m_e = 11.6(B/10^{12} \text{ G})$  keV, where  $\hbar$  is Planck's constant,  $e$  is the electron charge,  $B$  is the surface field strength, and  $m_e$  is the electron mass (Truemper et al. 1978; Makishima 2003). Using this method, the inferred field strength for HMXBs lies in the range  $(1-4) \times 10^{12}$  G.

Alternatively, assuming that the magnetospheric corotation speed in HMXBs equals the Keplerian velocity of the accretion disk, one can relate the magnetic dipole moment  $\mu$  of the neutron star to its X-ray luminosity  $L$ , and spin period  $P$  to obtain (Ghosh & Lamb 1979)

$$\mu = 4.3 \times 10^{29} P^{7/6} (L/10^{37} \text{ erg s}^{-1})^{1/2} \text{ G cm}^3. \quad (1.3)$$

A comparison of the two methods shows poor agreement (Makishima et al. 1999), implying that either the neutron stars are prevented from reaching equilibrium by some process, or that they are spun up more slowly by wind accretion, or that the surface field is tangled, containing higher-order multipoles which do not contribute to  $\mu$ .

In transient LMXBs, measuring the magnetic field involves two steps, making use of observations in both quiescent and outburst phases. The X-ray luminosity during quiescence is due to either 1) low levels of residual accretion (e.g. Stella et al. 1994), 2) rotation power (e.g. Possenti et al. 2002), or 3) the release of built up thermal energy in the crust from the active accretion phase (e.g. Rutledge et al. 2001; Yakovlev & Pethick 2004). If the quiescent luminosity [ $\approx (10^{32}-10^{33}) \text{ erg s}^{-1}$ ] is due primarily to the first two processes, an upper limit on the field strength can be placed (Burderi et al. 2002). If, however, the third process dominates, the magnetic field cannot be constrained. During the outburst phase, in order to produce coherent oscillations, the magnetospheric radius must be larger than the stellar radius, so that the accreted material can be channelled onto the surface (Psaltis & Chakrabarty 1999). Hence, the outburst X-ray luminosity [ $\approx (10^{36}-10^{38}) \text{ erg s}^{-1}$ ] provides a lower limit on the field strength. Constraints on the magnetic field of the AMSP SAX J1808.4-3685 were placed using this two-step method, yielding an estimate

of  $(1\text{--}5)\times 10^8$  G (Di Salvo & Burderi 2003). This constraint was tightened to  $(0.4\text{--}1.5)\times 10^8$  G using a larger data set (Hartman et al. 2008).

Much information can also be gleaned from the long-term evolution of AMSP X-ray pulse profiles, as variations in the shapes and intensity are directly correlated to changes in the emitting hotspot(s). Poutanen et al. (2009) proposed a model in which the accreted material is channelled by the field lines onto two antipodal hotspots, assuming a pure dipole. The shapes and sizes of these spots, which can be extracted from the pulse profiles, depend intricately on the magnetic inclination, accretion rate, and magnetic moment. For example, a nearly-aligned magnetic dipole with a large inner-disk radius produces a circular hotspot, whereas a disk closer to the star produces a ring-like hotspot. If the dipole axis is tilted away from the spin axis, the hotspot becomes crescent-shaped.

A detailed spectral analysis of SAX J1808.4–3685 during its 2002 outburst was conducted using this model, providing a clear picture of what happens over the course of an outburst in this source (Ibragimov & Poutanen 2009). The authors concluded that one of the hotspots is located at a colatitude of  $\sim 4^\circ\text{--}10^\circ$ , while the antipodal hotspot is initially obscured by the inner accretion disk. As the outburst progresses, the hotspot shrinks and the disk recedes, allowing the antipodal hotspot to be visible. The estimated magnetic field strength is  $(0.8 \pm 0.5) \times 10^8$  G, in agreement with previous findings. In the precession model for XTE J1814–338 presented in Chapter 2, we assume simple, circular, antipodal hotspots for a range of magnetic inclination angles. Poutanen et al. (2009) noted that although their model works well when applied to the outbursts of SAX J1808.4–3685, it does not explain the correlation between the modulations in timing residuals and X-ray flux seen in XTE J1814–338.

## 1.5 Gravitational radiation

A major prediction of the general theory of relativity is the existence of gravitational waves, perturbations in space-time which propagate at the speed of light. In the weak-field limit, the space-time metric can be written as  $g_{\mu\nu} = \eta_{\mu\nu} + h_{\mu\nu}$ , where  $\eta_{\mu\nu}$  is the Minkowski metric, and  $|h_{\mu\nu}| \ll 1$  represents the deviation from flat space-time. At Earth, the waves are approximately planar, and travel in two polarization states (+ and  $\times$ ). The amplitudes of the polarizations are denoted by the wave strains,  $h_+$  and  $h_\times$ . Typically, the perturbation is expressed in the transverse-traceless gauge as  $h_{\mu\nu} = h_+ e_{\mu\nu}^+ + h_\times e_{\mu\nu}^\times$ , where

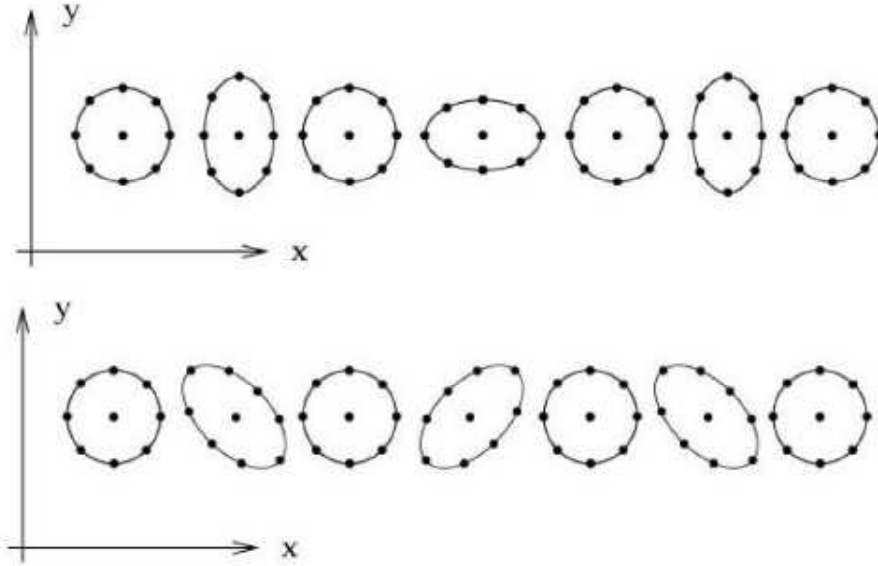


**Figure 1.12:** Effects of the two gravitational wave polarizations on a ring of test particles. Top panel: + polarization, bottom panel:  $\times$  polarization. From left to right, the gravitational wave phases are  $0, \pi/2, \pi, 3\pi/2, 2\pi, 5\pi/2, 3\pi$  (from Camenzind 2006).

$e_{xx}^+ = -e_{yy}^+ = 1$  and  $e_{xy}^\times = e_{yx}^\times = 1$  for a wave travelling in the  $z$  direction. Figure 1.12 illustrates the difference between the two polarizations by showing snapshots of their effects on a ring of test particles orthogonal to the wave vector. As the wave passes through the ring, it oscillates between a circular and elliptical shape every quarter-period. The perturbations due to the + polarization are rotated by  $45^\circ$  with respect to those of the  $\times$  polarization.

As gravitational waves are extremely weak, the only sources massive enough to produce a signal that is detectable with current technology are astrophysical phenomena. At the very lowest ( $10^{-16}$  Hz) and highest ( $10^8$  Hz) ends of the frequency spectrum, gravitational waves originate from the very early universe. Relic gravitational waves from the Big Bang, with frequencies  $\lesssim 10^{-16}$  Hz, redshift the frequencies of the photons of the cosmic microwave background (CMB), causing observed temperature fluctuations (Kamionkowski & Kosowsky 1998; Maggiore 2000). On the other hand, the spectrum of gravitational waves produced at very early times ( $\lesssim 10^{-27}$  s after the Big Bang) is expected to be redshifted so that it peaks in the GHz band (Maggiore 2000).

Between  $10^{-11}$  and  $10^{-5}$  Hz, potential sources include cosmic string cusps (Damour & Vilenkin 2001), and the formation and mergers of supermassive black holes (SMBHs) (Thorne & Braginskii 1976). Additionally, the formation

of intermediate-mass black holes in dense star clusters is expected to produce signals in the range  $10^{-8}$  Hz– $10^{-5}$  Hz (Portegies Zwart 2007), and inspiralling compact binaries are thought to produce signals between  $10^{-6}$  and  $10^{-5}$  Hz (Schneider et al. 2001). In the  $10^{-4}$ – $10^{-2}$  Hz band, the dominant source of gravitational radiation is thought to be the decaying orbits of highly eccentric SMBH binaries (Enoki & Nagashima 2007). Gravitational radiation from coalescing black holes and neutron stars, rapidly rotating neutron stars, and core-collapse events are produced in the Hz–kHz band. As we detail in Section 1.5.1, most current ground-based detectors operate in this band. The space-based LISA<sup>5</sup>, which will search for low frequency ( $10^{-4}$ – $10^{-1}$  Hz) signals, is scheduled to launch in 2015.

### 1.5.1 Detectors

Since the first gravitational wave detector was built by Weber (1960), detector technology has progressed immensely. There are three types of detectors currently in use: resonant-bar, spherical resonant-mass, and interferometric. In the former type, as a gravitational wave passes through a cylindrical bar, it resonates longitudinally, and the ends of the bar are displaced by an amount  $\propto hl$ , where  $h$  is the gravitational wave strain, and  $l$  is the length of the bar. The sensitivity of new-generation bar detectors is boosted by the use of cryogenic antennae to reduce thermal noise in the bars (Fafone 2004). The three major bar detectors in operation are AURIGA<sup>6</sup> (Italy), EXPLORER<sup>7</sup> (Switzerland), and NAUTILUS<sup>8</sup> (Italy). AURIGA's sensitivity at its resonant frequencies ( $\sim 911$  and  $\sim 929$  Hz) is  $\sim 2 \times 10^{-22}$  Hz<sup>-1/2</sup>. EXPLORER has a resonant frequency of 921 Hz, at which it has a sensitivity of  $3 \times 10^{-21}$  Hz<sup>-1/2</sup>. As of 2002, NAUTILUS is tuned to 935 Hz, with a sensitivity of  $2 \times 10^{-21}$  Hz<sup>-1/2</sup>. A search targeting the Galactic Centre, involving all three detectors and the Virgo interferometer, was undertaken recently (Acernese et al. 2008). The search was performed using nine frequency templates between 866–946 Hz, yielding upper limits on the wave strain of  $1 \times 10^{-20}$ – $2 \times 10^{-18}$  across all nine templates.

One drawback of resonant-bar detectors is that their sensitivity depends on the source location and the orientation of the bar. Spherical resonant-mass antennas avoid this problem as they have omnidirectional antenna patterns (Harry et al. 1996). Two detectors of this kind are in development: Mini-

---

<sup>5</sup><http://lisa.jpl.nasa.gov>

<sup>6</sup><http://www.auriga.lnl.infn.it>

<sup>7</sup><http://www.roma1.infn.it/rog/explorer/>

<sup>8</sup><http://www.roma1.infn.it/rog/nautilus/>

GRAIL<sup>9</sup> (Holland) and Mario Schenberg (Brazil). These detectors operate at higher frequencies; MiniGRAIL has a sensitivity of  $1.5 \times 10^{-20} \text{ Hz}^{-1/2}$  at its resonance frequency of 2943 Hz (Gottardi et al. 2007). It has recently finished its first commissioning run and has an expected sensitivity of  $2 \times 10^{-21} \text{ Hz}^{-1/2}$  at 3200 Hz (Lenzi et al. 2008; Costa et al. 2008).

The most sensitive instruments are the interferometers. There are several major ongoing collaborations worldwide involving the LIGO<sup>10</sup> (USA), Virgo<sup>11</sup> (Italy), GEO 600<sup>12</sup> (Germany), and TAMA 300<sup>13</sup> (Japan) detectors. These are ground-based interferometers which operate in the kHz regime.

The cross-correlation search for continuous gravitational waves described in Chapters 3 and 4 of this thesis is undertaken as part of the LIGO Scientific Collaboration (LSC). It analyses LIGO data. We therefore direct subsequent discussion toward the operational details of the LIGO detector. LIGO comprises a network of three Michelson interferometers: two with 4 km baselines (H1 in Hanford, Washington, and L1 in Livingston, Louisiana), and one 2 km baseline (H2, in Hanford, Washington). As of 2009, however, H2 is no longer being used. The detector operates in the 0.04–7 kHz frequency band and is able to detect changes in the interferometer arm lengths as small as  $\sim 10^{-20}$  m.

The two major sources of noise in the detector are displacement noise and sensing noise (Abbott et al. 2007c). Displacement noise causes motion of the test masses or mirrors and dominates at low frequencies ( $\lesssim 100$  Hz). The largest contribution to this noise is seismic (e.g. wind, ocean waves, and earthquakes), although thermal noise from the excitation of the test mass pendula, and thermal acoustic waves perturbing the mirror surfaces, also play a part. To a lesser degree, contributions arise from actuator noise in the electronics, and noise in the Michelson and power recycling cavity servo loops. Sensing noise dominates at higher frequencies ( $\gtrsim 100$  Hz) and affects the detection of the mirror motion. In LIGO, the sensing noise is primarily photon shot noise. In principle, photon shot noise can be reduced by increasing the laser power at the expense of increasing the thermal noise.

In 2005, during its fifth science run (S5), LIGO achieved its design sensitivity of  $2.5 \times 10^{-23} \text{ Hz}^{-1/2}$  at 150 Hz. Figure 1.13 tracks the improvements that have been made to the LIGO sensitivity curve since its first science run in 2002. The black line, which partially overlaps the S5 curve, shows the design

---

<sup>9</sup><http://www.minigrail.nl>

<sup>10</sup><http://www.ligo.caltech.edu>

<sup>11</sup><http://www.virgo.infn.it>

<sup>12</sup><http://www.geo600.uni-hannover.de>

<sup>13</sup><http://tamago.mtk.nao.ac.jp>

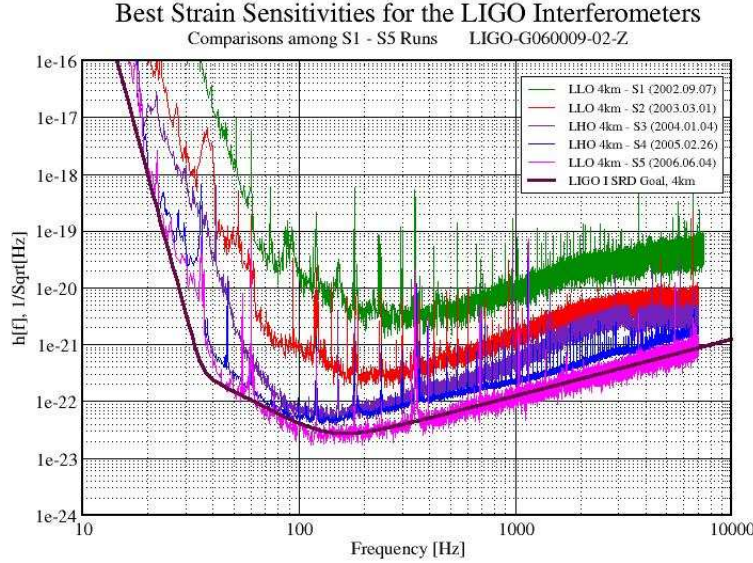


**Figure 1.13:** Improvements to the LIGO sensitivity curve from its first science run (S1, 2002, top curve) to its fifth (S5, 2006, bottom curve). The black line indicates the design sensitivity, which was reached during S5 (from <http://www.ligo.caltech.edu/advLIGO/scripts/summary.shtml>).

sensitivity. At the time of writing, the sixth science run (S6) is under way using enhanced LIGO, with a two-fold increase in sensitivity achieved already at frequencies  $\gtrsim 200$  Hz. Further improvements will be made with Advanced LIGO, scheduled to start running in 2016, which will increase broad-band sensitivity by a factor of 10. It will also offer narrow-band tuning, achieving greater sensitivity within a given  $\sim 1$  Hz band while reducing it elsewhere (Abbott et al. 2007a). This feature will be helpful when searching for pulsars with known spin frequencies, for example. Figure 1.14 illustrates the expected noise floor for various Advanced LIGO narrow-band tunings, as well as the various noise contributions from e.g. gas fluctuations, suspension, and optical coating thermal noise. Narrow-band tunings for a stochastic background, binary black hole (BH-BH) and binary neutron star (NS-NS) inspirals, and pulsars at 650, 800, and 1000 Hz are shown.

A method of gravitational-wave detection which does not involve a purpose-built detector is via pulsar timing arrays. By monitoring the long-term timing residuals of an array of ultra-stable millisecond radio pulsars, observers can identify a passing gravitational wave if the residuals are correlated. Pulsar timing arrays are sensitive to very low frequencies ( $\lesssim 10^{-8}$  Hz) and require precise timing measurements at the nanosecond level. The two major ventures

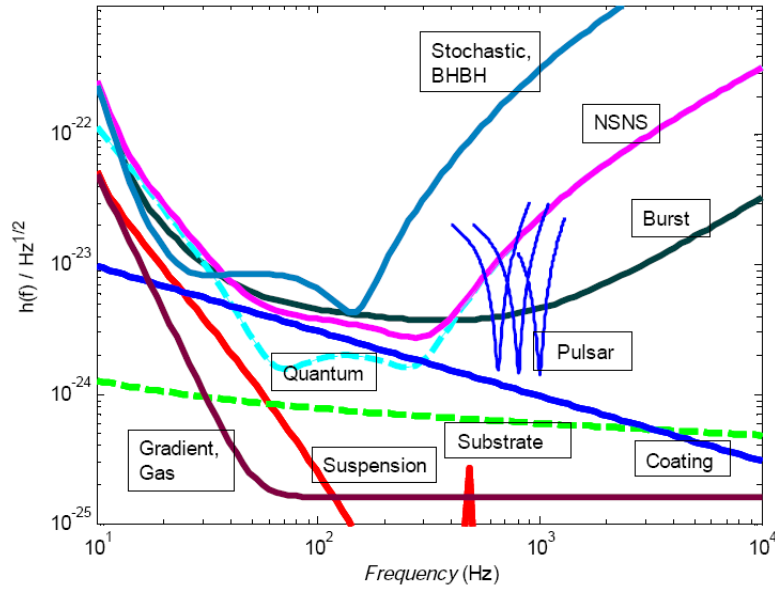


**Figure 1.14:** Expected noise floor for various Advanced LIGO narrow-band tunings. Noise curves are shown for tunings optimised for a stochastic background, a  $50 M_{\odot}$  BH-BH inspiral (teal), a  $1.4 M_{\odot}$  NS-NS inspiral (pink), bursts (dark green) and pulsars at 650, 800, and 1000 Hz (dark blue). The contributions from gravitational gradients and gas fluctuations, suspension and substrate noise, and optical coating thermal noise are shown as maroon, red, dashed-green, and blue curves respectively. The dashed cyan curve shows the contribution from quantum noise for the NS-NS curve (from Abbott et al. 2007a).

in this field are the Parkes Pulsar Timing Array (Hobbs et al. 2009) and the European Pulsar Timing Array (Janssen et al. 2008).

### 1.5.2 Classification of high-frequency gravitational wave signals

There are four main classes of gravitational wave sources which are the focus of the different working groups within the LSC. Compact binary mergers and gravitational wave bursts are transient signals, whereas the stochastic background and continuous wave signals from neutron stars are persistent. We discuss the first three classes briefly, and dedicate Section 1.5.3 to continuous wave signals, as they are the subject of Chapters 3 and 4 of this thesis.

#### Compact binary coalescence (CBC)

Compact objects such as black holes or neutron stars in binary systems emit characteristic gravitational wave signals as they pass through three phases: inspiral, merge, and ringdown (Thorne 1987). In the inspiral phase, the binary orbit shrinks as the gravitational wave signal sweeps upward in frequency and amplitude. The signal can be accurately described by post-Newtonian waveforms for systems with a total mass of up to  $\approx 20\text{--}30 M_{\odot}$  (Blanchet 2006). The dynamics of the merger phase, i.e. the transition between the inspiral and an “unstable plunge” is described analytically by the effective one-body approximation (EOB) (Buonanno & Damour 1999). The EOB models the two-body problem as the motion of a test particle in an external metric. The ringdown phase occurs after a merger in systems where the total mass exceeds  $2 M_{\odot}$ . A perturbed black hole is left behind which emits gravitational waves as it settles down into an equilibrium state (Berti et al. 2006). The inspiral, merger and ringdown phases were successfully modelled numerically by Pretorius (2005, 2007), using a spatial harmonic gauge to guarantee numerical stability, providing a test bed for different waveform models as well as various search templates.

An important class of CBC sources is the extreme mass-ratio inspirals (EMRIs), the inspiral of a compact object into a more massive black hole (Ryan 1997; Barack & Cutler 2007). The characteristic frequency of gravitational waves emitted by EMRIs depends on the central black hole mass  $M_c$ : for signals to be produced within the LIGO band,  $M_c$  must be  $\lesssim 100 M_{\odot}$ . For supermassive black holes at the centres of galaxies, with  $10^5 M_{\odot} \lesssim M_c \lesssim 10^7 M_{\odot}$ ,

the signals produced have a much smaller frequency, making them ideal candidates for LISA. Observations of EMRIs will enable precise tests of general relativity and astrophysical models of black holes.

### Bursts

Gravitational wave bursts are perhaps the most elusive signals, as they occur unexpectedly, last for a short time, and are usually poorly modelled. Yet a wide range of sources exists, and burst signals are generically stronger than many other types. For example, the core collapse of massive stars is a promising burst source, with an expected rate of  $\sim 2$  per century in the galaxy (Diehl et al. 2006). The waveforms resulting from core collapse have been predicted to last up to several hundred milliseconds, with frequencies between 50 Hz and several kHz (Zwerger & Mueller 1997; Dimmelmeier et al. 2001, 2002; Ott et al. 2004). The gravitational wave emission mechanisms which occur during core-collapse are neutrino emission, magnetohydrodynamic (MHD) instabilities, and acoustic turbulence in proto-neutron stars. Each of these mechanisms have their own “mutually exclusive” signature. Neutrino emission and MHD instabilities emit strongly for rapidly rotating cores, whereas the acoustic mechanism requires slow or no rotation to emit waves which are strong enough to be detected by advanced LIGO (Ott 2009).

Bursts are also expected from perturbed or accreting black holes (Kokkotas & Schmidt 1999), Lorentz-boosted cosmic string cusps (Damour & Vilenkin 2005), pulsar glitches (Peralta et al. 2006; Warszawski et al. 2009) and eccentric black hole binaries (Capozziello & de Laurentis 2008; Kocsis et al. 2006). Compact binary mergers which do not conform to the known waveform models used by the CBC Group in the LSC are also considered potential sources. For events such as core collapse and neutron star-neutron star or neutron star-black hole mergers, which are thought to produce gamma-ray and neutrino bursts, there are exciting opportunities for gravitational wave, electromagnetic, and neutrino detections to be made simultaneously.

Soft gamma-ray repeaters (SGRs) occasionally emit short, intense gamma-ray bursts with luminosities up to  $10^{42}$  erg  $s^{-1}$ . These bursts are thought to be caused by crustal cracking, and lead to gravitational wave emission (de Freitas Pacheco 1998; Owen 2005). A LIGO search associated with  $\sim 200$  SGR triggers placed upper limits on the model-dependent gravitational wave emission energies of between  $3 \times 10^{45}$ – $9 \times 10^{52}$  erg (Abbott et al. 2008c). A new search method has recently been proposed, which involves “stacking”

potential signals from multiple SGR bursts. The search uses a generalised X-ray light curve to model the bursts, and one of several available gravitational wave emission models, which place different weightings on individual bursts. The search may improve on the energy upper limits by almost two orders of magnitude (Kalmus et al. 2009). Another important upper limit derived from SGR searches is the quantity  $E_{\text{GW}}/E_{\text{EM}}$ , the ratio of gravitational wave to electromagnetic emission energies. Current upper limits lie in the range  $5 \times 10^1 - 6 \times 10^6$ , a factor of 3 higher than what will be achieved by the flare-stacking method (Abbott et al. 2008c; Kalmus et al. 2009).

### Stochastic background

A background of stochastic gravitational waves, analogous to the Cosmic Microwave Background, is the superposition of many incoherent cosmological and astrophysical sources. This type of signal is persistent. The cosmological component can be produced by e.g. pre-big-bang models (Gasperini & Veneziano 1993; Buonanno et al. 1997; Gasperini & Veneziano 2003), the amplification of quantum vacuum fluctuations during inflation (Grishchuk 1974; Starobinskii 1979; Grishchuk 1997), cosmological phase transitions (Kosowsky et al. 1992; Apreeda et al. 2002) and cosmic strings (Caldwell & Allen 1992; Damour & Vilenkin 2005). There is also a contribution from unresolved burst and continuous wave sources such as coalescing binary neutron stars (Regimbau & de Freitas Pacheco 2006b), early-phase inspirals of neutron star, black hole, and white dwarf binaries (Schneider et al. 2001), rotating neutron stars (Regimbau & de Freitas Pacheco 2001, 2006a), supernovae (Coward et al. 2002) and LMXBs (Cooray 2004).

The expected strength of an isotropic stochastic background signal is parameterised by  $\Omega_{\text{gw}}(\nu)$ , the gravitational wave energy density in units of the closure density, where  $\nu$  is the frequency of the gravitational wave signal. It is proportional to  $H_0^2$ , the Hubble constant squared (Abbott et al. 2007b). There are several models describing how  $\Omega_{\text{gw}}$  scales with frequency: inflationary models predict a constant  $\Omega_{\text{gw}}(\nu)$ , while some cosmological models predict a broken power-law spectrum (Maggiore 2000). A cross-correlation search using the S4 data from LIGO and ALLEGRO placed an upper limit on an isotropic background wave strain of  $1.5 \times 10^{-23} \text{ Hz}^{-1/2}$  at 915 Hz (Abbott et al. 2007b). More recently, a cross-correlation search of S5 data resulted in an upper limit of  $\Omega_{\text{gw}}(100 \text{ Hz}) < 6.9 \times 10^{-6}$ , lower than previous limits obtained from big bang nucleosynthesis and the cosmic microwave background (Abbott et al. 2009b).

If the background is dominated by an ensemble of galactic astrophysical sources, the signal can become anisotropic. In this case, the signal strength is characterised by the assumed signal strain power spectrum,  $H(\nu)$ . A separate all-sky search was conducted on S4 LIGO data, again using the cross-correlation method, and a sky map of  $H(\nu)$  upper limits was produced assuming two different power laws for  $H(\nu)$ . For a  $\nu^{-3}$  power law (corresponding to a scale-invariant primordial perturbation spectrum), the upper limit ranges from  $1.2 \times 10^{-48} (100 \text{ Hz}/\nu)^3 \text{ Hz}^{-1}$ – $1.2 \times 10^{-47} (100 \text{ Hz}/f)^3 \text{ Hz}^{-1}$ , depending on sky position. For a signal power spectrum which is constant in frequency, the upper limit ranges from  $8.5 \times 10^{-49} \text{ Hz}^{-1}$ – $6.1 \times 10^{-48} \text{ Hz}^{-1}$  (Abbott et al. 2007e). As an example comparison, the theoretical strain power spectrum resulting from all known LMXBs in the Virgo galaxy cluster is  $H(\nu) \approx 10^{-55} \text{ Hz}^{-1}$ .

### 1.5.3 Continuous wave signals

Continuous wave signals are persistent signals. The most promising sources are rapidly rotating neutron stars. If a neutron star's figure is elastically deformed in some way, i.e. the star has a non-zero mass quadrupole moment<sup>14</sup>, it will emit periodic gravitational waves at once and twice the spin frequency if it precesses, and at  $\sim 4/3$  times the spin frequency if it experiences  $r$ -mode instabilities (Bildsten 1998; Abbott et al. 2007d; Watts et al. 2008a). Deformations can be caused by magnetic mountains (Payne & Melatos 2004; Melatos & Payne 2005; Payne & Melatos 2006; Vigelius & Melatos 2008), thermocompositional mountains caused by uneven electron capture layers in the crust (Ushomirsky et al. 2000), internal magnetic fields (Cutler 2002; Haskell et al. 2008),  $r$ -mode oscillations (Andersson 1998; Owen et al. 1998; Nayyar & Owen 2006), and nonaxisymmetric, post-glitch fluid flow inside the star (van Eysden & Melatos 2008). All these mechanisms can drive free precession (Jones & Andersson 2002) of the neutron star (see Chapter 2).

A particularly compelling argument in support of accreting neutron stars as gravitational wave sources comes from the spin distribution of the known population. Although neutron stars have a theoretical breakup frequency of  $\sim 1.5$  kHz for most nuclear equations of state (Cook et al. 1994; Bildsten 1998), the fastest known accreting millisecond pulsar, IGR J00291+5934 (Eckert et al. 2004), spins at only 599 Hz. The fastest radio millisecond pulsar, PSR

---

<sup>14</sup>The maximum  $m = 2$  quadrupole moment of a neutron star,  $Q_{22}$ , is related to its ellipticity  $\epsilon$  via  $\epsilon = (8\pi/15)^{1/2} Q_{22}/I_{zz}$ , where  $I_{ab}$  is the moment of inertia tensor, and  $z$  is the rotation axis (Owen 2005).

J1748–2446ad (Hessels et al. 2006), and the fastest nonpulsating LMXB, 4U 1608–52 (Hartman et al. 2003), spin at frequencies of 716 Hz and 619 Hz respectively. A popular model explaining this discrepancy states that the accretion torque which acts to spin up the neutron star is balanced by energy loss through gravitational radiation (Wagoner 1984). The neutron star thus reaches an equilibrium state at a spin frequency which is much lower than the estimated breakup frequency. An indirect limit on the gravitational wave strain  $h_0$  can be expressed in terms of the observable X-ray flux,  $F_X$ , and  $\nu_*$ , as (Watts et al. 2008a)

$$h_0 \approx 3 \times 10^{-27} \frac{R_*^{3/4}}{M_*^{1/4}} \left( \frac{F_X}{10^{-8} \text{erg cm}^{-2} \text{s}^{-1}} \right)^{1/2} \left( \frac{1 \text{ kHz}}{\nu_*} \right)^{1/2} \quad (1.4)$$

where  $R_*$  and  $M_*$  are the typical neutron star radius and mass values (in units of 10 km and  $1.4 M_\odot$  respectively). If the star is a rigid body, the characteristic gravitational wave strain is given by (Jaranowski et al. 1998)

$$h_0 = \frac{4\pi^2 G I \epsilon \nu_*^2}{d c^4}, \quad (1.5)$$

where  $I$  is the star’s moment of inertia,  $d$  is its distance, and  $\epsilon$  is its ellipticity.

### Young neutron stars

The work in this thesis focuses on modelling and searching for gravitational waves from young ( $\lesssim 10^3$  yr), rapidly decelerating neutron stars. In particular, we target the supernova remnant SN 1987A. No confirmed pulsations have been observed from the source, however there is compelling evidence that a 23-year old neutron star resides in SN 1987A (see Chapter 3 for a detailed discussion). The violent core-collapse process which forms neutron stars is thought to leave them largely deformed, making them strong gravitational wave emitters. Many nearby astrophysical targets, such as supernova remnants, star forming regions, and globular clusters, are therefore likely candidates for a targeted search, even if they are not yet associated with any known pulsar.

Due to their high spin-down rates, however, young, nonpulsing neutron stars prove to be computationally challenging targets. Usually, two or more frequency derivatives are required to accurately track their phase across a period of several months. The only LIGO search of this kind which has been performed so far has been directed at the neutron star in the supernova remnant Cas A (Wette et al. 2008), which is 3.4 kpc away and is 327 years old (Fesen

et al. 2006). This search is in its final stages of analysis, and upper limits are expected soon. Using the astrophysical phase model introduced in Chapter 3, however, we bypass the need to search over multiple frequency derivatives, making searches for these types of objects more computationally feasible. Other potential targets in supernova remnants include Vela Jr., which has a distance of 480 pc and is thought to be 680 years old (Iyudin et al. 2007), and RX J1713.7–3946 which is 1.3 kpc away and is 1.6 kyr old (although these ages and distances are unconfirmed) (Cassam-Chenaï et al. 2004).

A dense star forming region lies at the Galactic Centre 8 kpc away, which may harbor up to 50 young star clusters (Portegies Zwart et al. 2001). Keane & Kramer (2008) estimated a galactic neutron star birth rate of between 5.7–10.8 neutron stars per century, obtained by population synthesis of radio and X-ray pulsars. However, the estimated core-collapse supernova rate in the galaxy is only  $1.9 \pm 1.1$  per century (Diehl et al. 2006). This discrepancy results from either an overestimation of the birth rates of the pulsars, some neutron stars being ‘double counted’ as they morph from one class to another, or the existence of some unknown neutron star formation process (Keane & Kramer 2008). Assuming, however, that the estimate of the galactic neutron star birth rate is accurate (ignoring the possibility that some neutron stars may be double-counted), and that the nuclear stellar disk contains  $10^{-2}$  of the total galactic mass (Launhardt et al. 2002), a back-of-the-envelope calculation yields a neutron star birth rate in the galactic centre of 0.6–2 per 1000 years. The young galactic star cluster Westerlund 1 also contains the magnetar CXO J164710.2–455216 (Muno et al. 2006). Although the exact age of the magnetar is unknown, Westerlund 1 is thought to be only  $\sim 3$ –5 Myr old (Belczynski & Taam 2008). Newly born magnetars are expected to have internal magnetic fields as large as  $\gtrsim 10^{16}$  G, making them excellent candidates for gravitational searches (Stella et al. 2005).

Globular clusters are also excellent places to search for young neutron stars. For example, 47 Tuc, which is 4.9 kpc away and has a radius of 0.56 kpc, contains 22 known millisecond pulsars (Camilo et al. 2000; Lorimer et al. 2003). Ivanova et al. (2008) extrapolated this population, estimating that  $\sim 300$  neutron stars exist in the cluster. Other nearby globular clusters include NGC 6397 (2 kpc away), NGC 6121 (2.2 kpc away), NGC 6656 (3.2 kpc away), and NGC 6752 (4.0 kpc away) (Harris 1996).

We now briefly summarise the mechanics behind the two main sources of deformation (mountains, and r-mode oscillations), and summarise the estimated gravitational wave strains for known LMXBs resulting from each process.

### Mountains

Figure 1.15 shows the maximum expected gravitational wave strains for known LMXBs assuming the presence of mountains (of whatever provenance) and a coherent 2-yr observation. The blue squares show the 10 known AMSPs. The filled triangles denote LMXBs exhibiting Type-I X-ray bursts whose frequency is confirmed from multiple burst oscillations, and the open triangles denote those whose reported frequency is tentative because only one burst has been detected. The red triangles denote LMXBs in which twin kHz QPOs have been detected. The spin frequencies for these sources is assumed to be half the peak separation (see Section 1.4.1 for a discussion of the uncertainties related to inferring the spin frequency from QPO peak separations). The signal amplitudes are calculated using the long-term averaged flux measurements for each source; we note that individual outburst flux levels are higher and lead to larger estimated signal amplitudes. Detector sensitivities are shown for initial LIGO (I-LIGO), enhanced LIGO (E-LIGO), Advanced LIGO (A-LIGO) and the Einstein Telescope (ET) (Watts et al. 2008a).

Figure 1.15 presents the most optimistic scenario; it assumes a coherent search over a 2 year observation, and the use of a single search template built from all the ‘correct’ signal parameters, i.e. sufficient to accurately track the gravitational wave phase over the entire observation time. Realistically, however, the complex timing behaviour discussed in Section 1.4.1 indicates that the gravitational wave phase wanders significantly over a time-scale of  $\sim$  months. One therefore needs to search over multiple templates; the exact number varies from source to source. Figure 1.16 shows the expected wave strains for the same mountain scenario as Figure 1.15, but for a multi-template search. The signal amplitudes are scaled by a source-dependent factor,  $11.4/F$ <sup>15</sup>. This figure is illustrative only: technically the noise curves should be multiplied by  $F$  while the signal amplitudes remain unchanged, however this would result in a different noise curve for each individual source. Even so, the effect of increasing the

<sup>15</sup>The statistical factor  $F$  is 11.4 for a coherent search with a false alarm rate of 1%, and a false dismissal rate of 10%, for a single search template (see Section 1.6.1).  $F$  increases proportional to the fourth root of the number of templates.

number of templates is clear, as only one source (Sco X-1) is now detectable by broad-band Advanced LIGO.

- **Thermocompositional mountains**

Material accreted onto the surface of a neutron star is ‘burned’ to heavy elements within days. As these heavy ashes are compressed into the surface, they replace the primordial neutron-star crust, and become neutron-rich by subsequent electron capture. A transition layer separates this region from regions where electron capture occurs slowly or not at all. The depth of this layer is temperature-dependent, so a lateral temperature gradient in the accreted crust can lead to lateral density variations. A 5% gradient at the base of the crust produces a mass quadrupole moment of  $\sim 10^{38}$  g cm<sup>2</sup> (Bildsten 1998). When the elastic response of the crust is taken into account, however, the quadrupole moment is reduced by a factor of 20–50, as the denser material tends to sink, rather than spread sideways (Ushomirsky et al. 2000).

- **Internal magnetic fields**

Large internal magnetic fields can significantly distort a neutron star (Bonazzola & Gourgoulhon 1996). If the magnetic and spin axes are misaligned, a time-dependent quadrupole moment is generated. The degree of distortion is highly dependent on the distribution of the magnetic field. For a toroidal field  $B_t \gtrsim 3.4 \times 10^{12}$  G  $(\nu_*/300 \text{ Hz})^2$ , the neutron star is distorted into a prolate shape with  $\epsilon \sim 10^{-6} (\langle B_t \rangle / 10^{15} \text{ G})$  (Cutler 2002). As the star rotates, such a large internal field also causes the tilt angle,  $\theta$ , to increase until the magnetic and angular momentum axes are orthogonal. Recently, Haskell et al. (2008) developed a formalism to compute the deformation of an ideal fluid star with an arbitrary magnetic field distribution and a barotropic equation of state.

- **Magnetic mountains**

In the magnetic mountain scenario, the accreted matter spreads equatorwards as the hydrostatic pressure at the base of the polar accretion column overcomes the magnetic tension. As the field lines are frozen into the mountain, the field becomes distorted as the matter spreads (Melatos & Phinney 2001), reducing the magnetic dipole moment by up to four orders of magnitude (Bisnovatyi-Kogan & Komberg 1974; Romani 1990; Payne & Melatos 2007). Payne & Melatos (2004, 2006) investigated

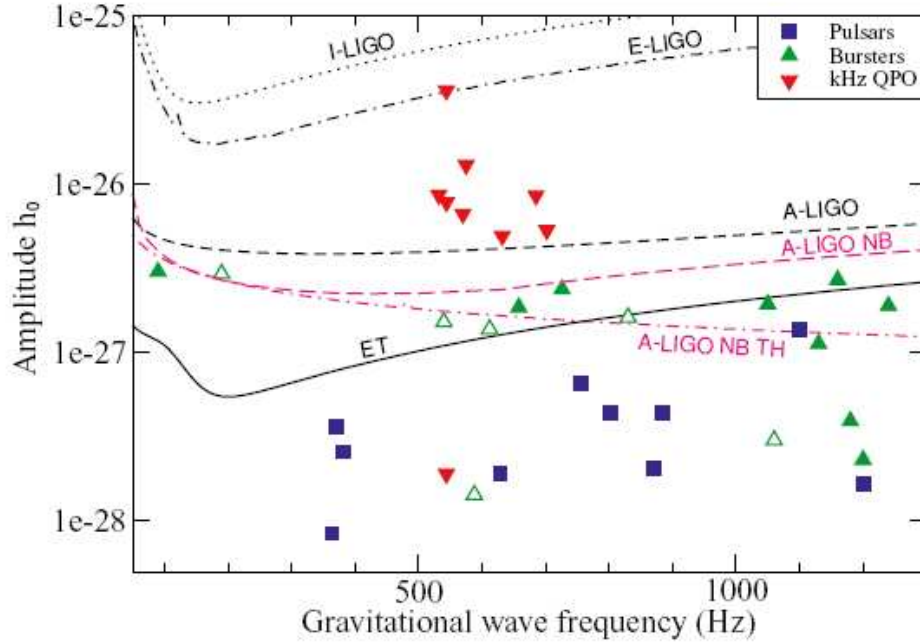


**Figure 1.15:** Maximum expected gravitational wave strain for known LMXBs assuming spin frequency stalling due to gravitational waves (Bildsten 1998) and equation (1.5) for a coherent, *single-template* search over a 2 year observation. The blue squares show the 10 known AMSPs. The filled triangles denote LMXBs exhibiting Type-I X-ray bursts whose frequency is confirmed, and the open triangles denote those whose frequency is unconfirmed. The red triangles denote LMXBs in which kHz QPOs have been detected. Detector sensitivities for initial LIGO (I-LIGO), enhanced LIGO (E-LIGO), Advanced LIGO (A-LIGO) and the Einstein Telescope (ET) are plotted as solid and broken curves (from Watts et al. 2008a).

this process numerically for the axisymmetric case, finding that magnetic mountains are magnetohydrodynamically stable. The formation of magnetic mountains can result in  $\epsilon \sim 10^{-4}$  (Vigelius & Melatos 2008; Wette et al. 2010). The surface upon which the mountain forms can also affect the ellipticity; if it grows on a hard surface,  $\epsilon$  can approach  $\sim 2 \times 10^{-4}$ , however if it grows on a fluid base, it ‘sinks’, reducing  $\epsilon$  by 25–60% (Wette et al. 2010). The inclusion of Ohmic diffusion in the model, which causes the mountain to relax resistively, reduces  $\epsilon$  over a time-scale of  $\sim 7.6 \times 10^7$  yr (Vigelius & Melatos 2009a). Conversely, upper limits on  $\epsilon$  can also be used to constrain the electrical resistivity of millisecond radio pulsars; Vigelius & Melatos (2010) place lower limits on the electric resistivity of  $\gtrsim 10^{-27} \text{ s}^{-1}$ .

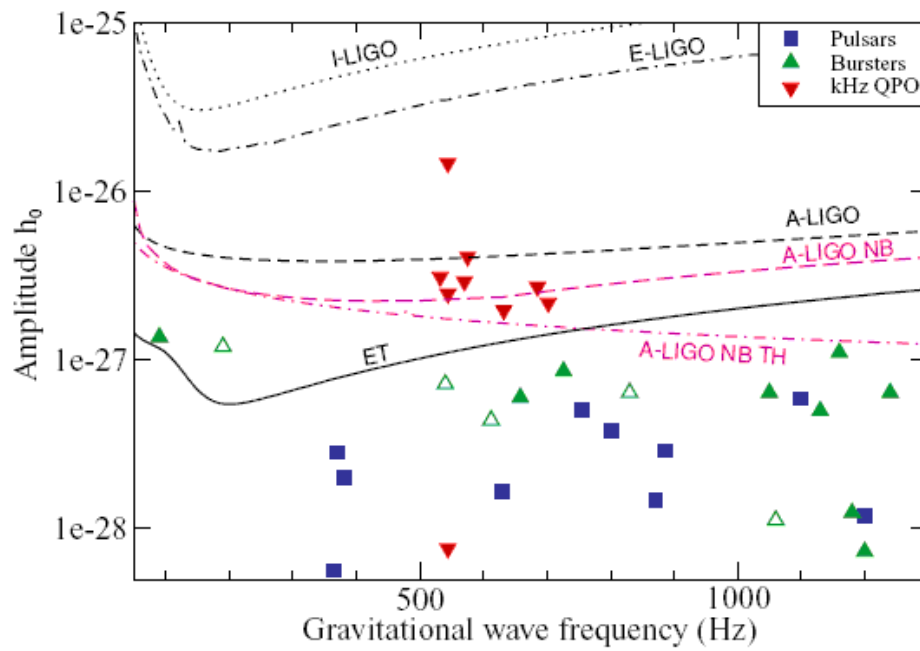


**Figure 1.16:** Expected gravitational wave strain for known LMXBs, for a coherent, *multi-template* search over a 2 year observation. The noise curves are identical to Figure 1.15, but the signal amplitudes have been scaled down (see text for explanation). Symbols and lines are as for Figure 1.15 (from Watts et al. 2008a).

***r*-mode instability**

All rotating stars are unstable to gravitational radiation emission via the Chandrasekhar-Friedmann-Schutz instability (Chandrasekhar 1970; Friedman & Schutz 1978; Papaloizou & Pringle 1978). This instability saturates by non-linear transfer of energy to damped modes (Arras et al. 2003), during which the resulting gravitational wave strain is  $h \approx 5.7 \times 10^{-22}(\nu/1 \text{ kHz})^{1/2}$  (Owen et al. 1998). The exact frequency of the gravitational wave emission depends on the viscosity and is  $\approx (4/3)\nu_*$ , where  $\nu_*$  is the spin frequency (Owen et al. 1998). The instability time-scale is comparable to the viscous damping time-scale when the neutron star period satisfies  $P \lesssim 2.3(T/10^7 \text{ K})^{1/3} \text{ ms}$  (Andersson et al. 1999), making it likely that the instability is present in recycled millisecond pulsars. It is thought that LMXBs follow a limit cycle in which a neutron star is spun up via accretion until it reaches the *r*-mode instability threshold. It is heated frictionally while the instability grows, and the star spins down via gravitational radiation. Once  $P$  falls below the instability threshold, the instability shuts off, and the star is allowed to spin up again as it cools (Levin 1999). The duration of the *r*-mode instability phase was estimated by Levin (1999) to be short ( $\sim 10^{-6} \text{ yr}$ ), making it unlikely that LMXB *r*-modes can be detected.

However, Heyl (2002) noted that the duty cycle also depends on the non-linear coupling between *r*-modes. If the neutron star core contains exotic particles (e.g. hyperons), the frequency threshold at which the instability halts rises sharply, allowing the star to emit gravitational waves in the steady state (Nayyar & Owen 2006). Numerical simulations of the nonlinear saturation state of the *r*-mode instability performed by Bondarescu et al. (2007) showed that the length of the duty cycle and the shape of the *r*-mode instability curve on the  $\nu_*$ - $T$  plane depends on the density of the star and the slippage factor between the crust and core. Their models show that the *r*-mode instability limits the spin frequencies of LMXBs to  $\sim 800 \text{ Hz}$ , and that one in  $10^3$  LMXBs are detectable with Advanced LIGO. More recent simulations show that a very young, rapidly rotating neutron star within 1 Mpc of Earth may be detectable for years after its formation (Bondarescu et al. 2009).

Figure 1.17 shows the maximum expected gravitational wave strains for known LMXBs assuming the *r*-mode scenario, and a coherent, single-template search across a 2 year observation. The markers denote known AMSP, Type-I burst sources, and kHz QPO sources as per Figure 1.15 (Watts et al. 2008a). The predicted gravitational wave amplitudes for *r*-modes are a factor of  $\sim 3$

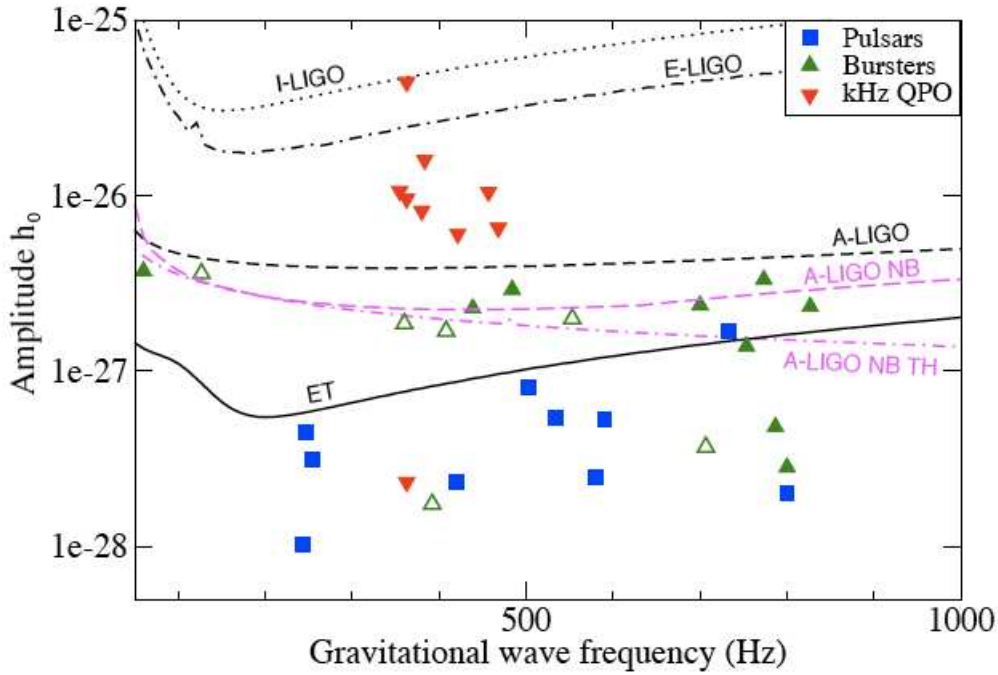


**Figure 1.17:** Maximum expected gravitational wave strain for known LMXBs assuming the presence of r-modes, and a coherent, single-template search across a 2 year observation. Symbols and curves are as for Figure 1.15 (from Watts et al. 2008a).

larger than those for the mountain scenario in Figure 1.15. One of the kHz QPO sources is now well above the theoretical sensitivity threshold of enhanced LIGO. However, as with the mountain scenario, a multi-template search would be less sensitive.

## 1.6 Searches for continuous gravitational waves

There are two types of continuous-wave searches. Coherent searches, which track the gravitational wave phase continuously over the entire observation time, normally span a narrow band and are useful for sources with known signal parameters. The phase of the signal must be tracked over the entire observation time to within  $\pi/4$  of a phase cycle to ensure the signal is not lost (Jaranowski et al. 1998). Semi-coherent searches only track the phase coherently over short segments which are later summed. These searches are optimised to cover a wider range of parameter space.

The detector output can be expressed in the form (Jaranowski et al. 1998)

$$x(t) = n(t) + h(t) \quad (1.6)$$

where  $n(t)$  is the detector noise, assumed to be an additive, stationary, Gaussian, zero-mean, continuous random process, and  $h(t)$  is the gravitational wave signal. With all search methods, the aim is to extract  $h(t)$  over a certain observation time  $T_{\text{obs}}$  while accurately tracking the evolution of the gravitational wave phase assuming a parameterised model. The signal can be written in terms of the detector's response functions according to:

$$h(t) = F_+(t)h_+(t) + F_\times(t)h_\times(t), \quad (1.7)$$

where  $h_+(t), h_\times(t)$  are the two independent gravitational wave polarizations, and  $F_+(t), F_\times(t)$  are the beam-pattern functions in the proper reference frame of the detector (Jaranowski & Krolak 1994). The beam-pattern functions are periodic, with a period of one sidereal day, and are functions of the right ascension  $\alpha$  and declination  $\delta$  of the source as well as the polarization angle  $\psi$ . These three angles describe the orientation of the source with respect to the celestial sphere reference frame.

Each set of parameters describing the phase and amplitude of a signal is called a search template. The data is usually analysed in the form of Short Fourier Transforms (SFTs), constructed from  $\sim 30$ -minute chunks of the detector output. The 30-minute window is chosen to minimize Doppler modulations due to the Earth's rotational and orbital motion, as well as the intrinsic spin-down of the source. A typical full-scale search over a year's worth of data covers approximately  $10^{10}$  templates, and  $10^4$  SFTs. The exact number of templates depends on the nature of the search. The signals emitted by accreting and non-accreting neutron stars must also be modelled separately, as accreting neutron stars in a binary system have their frequencies modulated by their orbital period and accretion-related spin wandering.

### 1.6.1 Coherent searches

In coherent searches, the signal-to-noise ratio increases as the square root of the observation time. They are computationally intensive as the number of required search templates has a strong dependence on the coherent observation time. Hence, the length of the time series that is analysed (the integration time) is typically limited to a few weeks of data. The most common coherent search uses the  $\mathcal{F}$ -statistic (Jaranowski et al. 1998), is defined as

$$\mathcal{F} = \ln \Lambda|_{\mathcal{A}^\mu = \hat{\mathcal{A}}^\mu}. \quad (1.8)$$

In (1.8),  $\mathcal{A}^\mu$  are the amplitude parameters of the signal (the wave strain  $h_0$ , the inclination angle  $\iota$ ,  $\psi$ , and the initial wave phase  $\phi_0$ ),  $\hat{\mathcal{A}}^\mu$  are the maximum likelihood estimators of the amplitude parameters, and

$$\ln \Lambda = (x|h) - \frac{1}{2}(h|h) \quad (1.9)$$

is the likelihood function. The inner product  $(\cdot|\cdot)$  of two variables  $x$  and  $y$  is defined as:

$$(x|y) = 4\Re \int_0^\infty \frac{\tilde{x}(\nu)\tilde{y}^*(\nu)}{S_n(\nu)} d\nu, \quad (1.10)$$

where  $\tilde{\cdot}$  denotes the Fourier transform, the asterisk denotes the complex conjugate,  $\Re$  denotes the real part of a complex number, and  $S_n(\nu)$  is the single-sided power spectral density of the detector noise.

In the absence of a signal, the quantity  $2\mathcal{F}$  has a  $\chi^2$  distribution with 4 degrees of freedom. With a signal present, it has a noncentral  $\chi^2$  distribution with 4 degrees of freedom, and a noncentrality parameter  $\lambda = \sqrt{(h|h)}$  (known as the ‘‘optimal signal to noise ratio’’). Figure 1.18 shows the probability density functions (PDFs) for  $2\mathcal{F}$  for S1 data from the GEO (top left panel) and LIGO detectors (clockwise from top right: L1, H1, and H2) (Abbott et al. 2004). The data contain injected continuous-wave signals with  $h_0$  ranging between  $2.7 \times 10^{-22}$  and  $1.9 \times 10^{-21}$ . The shaded area represents the integral of the PDFs between the measured value of  $2\mathcal{F}$  and  $\infty$ , and the lines represent best-fit  $\chi^2$  distributions with 4 degrees of freedom. The circles represent the PDF of  $2\mathcal{F}$  obtained from Monte Carlo simulations.

Using the  $\mathcal{F}$ -statistic, the minimum signal amplitude detectable in Gaussian stationary noise is

$$\langle h_0 \rangle = 11.4 \sqrt{S_n(\nu)/T_{\text{obs}}}, \quad (1.11)$$

where  $T_{\text{obs}}$  is the observation time, and we assume a false alarm rate of 1%, a false dismissal rate of 10%, and a perfectly-matched template. The signal is averaged over sky position, inclination angle, and polarization angle. The statistical factor of 11.4 increases roughly as the fourth root of the number of search templates.

## 1.6.2 Semi-coherent searches

Due to the computational cost of coherent searches, they are expensive to implement over a large range of parameters and an observation time of longer than several days. As many strong gravitational wave sources are likely still

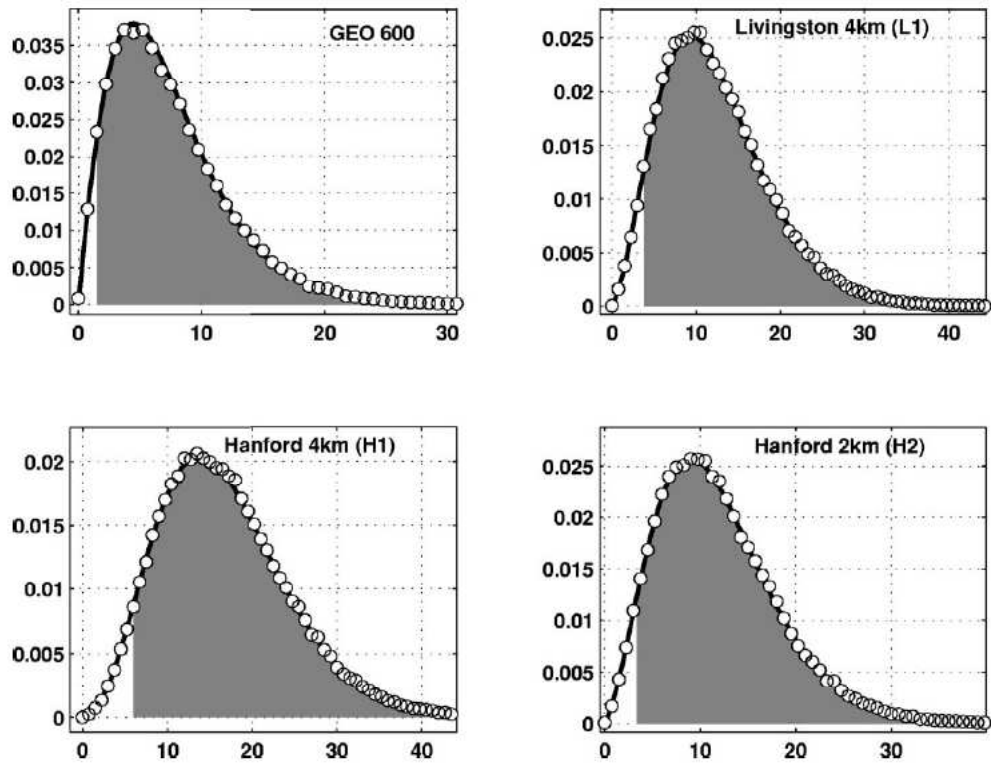


**Figure 1.18:** Probability density functions (PDFs) for  $2\mathcal{F}$  for simulated continuous-wave signals injected into S1 data from the GEO (top left panel) and LIGO detectors (clockwise from top right: L1, H1, and H2). The shaded area represents the integral of the PDFs between the measured value of  $2\mathcal{F}$  and  $\infty$ , the lines represent best-fit  $\chi^2$  distributions with 4 degrees of freedom, and the circles represent the PDF of  $2\mathcal{F}$  obtained from Monte Carlo simulations (from Abbott et al. 2004).

undetected in electromagnetic bands, it is important to carry out broad-band, semi-coherent searches. These searches are carried out over the frequency domain, on Fourier transforms of short data segments. There is a trade-off as they are computationally cheaper but less sensitive. A large part of this thesis focuses on the development and implementation of a semi-coherent cross-correlation search method targeting young, isolated neutron stars (see Chapters 3 and 4). Young neutron stars are ideal targets for semi-coherent searches as their spin frequency evolves relatively quickly. The astrophysical phase model introduced in Chapter 3 provides an even greater saving on the number of parameters.

The three most commonly used semi-coherent search methods within the LSC are the StackSlide (Brady & Creighton 2000), Hough (Krishnan et al. 2004; Abbott et al. 2005a), and PowerFlux (Dergachev 2005). All three methods were employed in a blind, all-sky search spanning frequencies 50–1000 Hz, and frequency derivatives  $-1 \times 10^{-8}$ – $0 \text{ Hz s}^{-1}$ , using data from LIGO’s fourth science run (S4). An upper limit of  $4.28 \times 10^{-24}$  was placed for the gravitational wave strain across the whole sky near 140 Hz (Abbott et al. 2008a).

The sensitivity of semi-coherent searches is given by

$$h_0 \propto \frac{\mathcal{S}^{1/2}}{N^{1/4}} \sqrt{\frac{S_n(\nu)}{T_{\text{coh}}}}, \quad (1.12)$$

where  $N$  is the number of coherently analysed data segments of length  $T_{\text{coh}}$  being summed, and  $\mathcal{S} = \text{erfc}^{-1}(2f_\alpha) + \text{erfc}^{-1}(2f_\beta)$ , where  $f_\alpha$  is the false alarm rate, and  $f_\beta$  is the false dismissal rate. The proportionality constant depends on the individual search algorithm.

### StackSlide

The StackSlide method forms the basis of the other semi-coherent methods. The idea is that any number of SFTs can be stacked, or summed, to increase their signal-to-noise ratio. However, because the frequency of the signal drifts by a certain amount between SFTs (due to spin-down or Doppler modulation), one must ‘slide’ the frequency bins in each SFT to account for the drift. For a given template, the “StackSlide power” is defined to be  $P_{\text{SS}} = (1/N_{\text{SFT}}) \sum_{i=0}^{N_{\text{SFT}}-1} \rho_i$ , where  $\rho_i$  is the normalized signal power for a given template in each SFT, the index  $i$  denotes individual SFTs, and  $N_{\text{SFT}}$  is the total number of SFTs. For a targeted search with a 1% false alarm rate and a 10% false dismissal rate, the minimum signal amplitude detectable is

$\langle h_0 \rangle = 7.7 N_{\text{SFT}}^{-1/4} \sqrt{S_n(\nu)/T_{\text{coh}}}$  (Abbott et al. 2008a). As with (1.11), the signal is averaged over sky position, inclination angle, and polarization angle.

### Hough

In the Hough transform method, it is not the power that is summed. Instead, one computes a weighted sum of binary counts. If the power in a frequency bin exceeds a given threshold, the binary count increases by one. The detection statistic for the weighted Hough method is the ‘‘Hough number count’’  $n_{\text{H}} = \sum_{i=0}^{N_{\text{SFT}}-1} w_i n_i$ , where  $n_i$  is the binary count for SFT  $i$ . The Hough weights for a signal with frequency  $\nu$  are defined as  $w_i \propto [S_n(\nu)]^{-1} [(F_+^i)^2 + (F_\times^i)^2]$ , where  $F_+^i$  and  $F_\times^i$  are the beam-pattern functions evaluated at the midpoint of SFT  $i$ . As the number counts are weighted according to  $F_+$  and  $F_\times$ , SFTs from multiple interferometers can be summed. The advantage of this method is that it is robust when there are transient spectral disturbances (e.g. seismic noise) in the individual SFTs, because, at most, the disturbance adds one to  $n_{\text{H}}$  whereas it might have a large effect on the SFT power  $\rho_i$ . The minimum averaged signal amplitude detectable with the Hough method is  $\langle h_0 \rangle = 8.92 N_{\text{SFT}}^{-1/4} \sqrt{S_n(\nu)/T_{\text{coh}}}$  (Krishnan et al. 2004).

### PowerFlux

The PowerFlux method is similar to StackSlide in the sense that it extracts an average signal power for a given template from a set of SFTs. However, in order to maximize the signal-to-noise ratio, the power is weighted based on the detector noise and beam-pattern functions. The detection statistic for this method, the ‘‘PowerFlux signal estimator’’ is defined as

$$R = \frac{2}{T_{\text{coh}}} \left( \sum_{i=0}^{N_{\text{SFT}}-1} W_i \right)^{-1} \left[ \sum_{i=0}^{N_{\text{SFT}}-1} W_i P_i / (F_\psi^i)^2 \right], \quad (1.13)$$

where  $P_i$  is the power for SFT  $i$  and a given search template. The PowerFlux weights are  $W_i = [(F_\psi^i)^2]^2 / S_n(\nu)^2$  for a signal with frequency  $\nu$ , and assume a source direction and polarization angle. The polarization basis can be chosen such that a linearly polarized signal has an amplitude of either ( $A_+ = 0, A_\times = h_0^{\text{lin}}$ ) or ( $A_+ = h_0^{\text{lin}}, A_\times = 0$ ), and a circularly polarized signal has  $A_+ = A_\times = h_0^{\text{circ}}$ . The PowerFlux weights are calculated using four linear polarization projections  $[(F_\psi^i)^2 = (F_+^i)^2]$  and one circular polarization projection  $[(F_\psi^i)^2 = (F_+^i)^2 + (F_\times^i)^2]$ . The PowerFlux method is the most sensitive of the three,

except in frequency bands with transient spectral noise, where the Hough method performs better.

Searches for binary systems are more expensive as one must search over additional parameters (i.e. the system’s orbital parameters), and take into account phase wandering due to variations in the accretion rate. A variation of the cross-correlation method can be applied to binary systems, and was used to search for the LMXB Sco X-1 in S4 data (Abbott et al. 2007e). Several search methods are in development which are designed specifically for binary systems, e.g. the sideband (or frequency comb) method (Messenger & Woan 2007), the TwoSpect method (Goetz & Riles 2009; Abbott et al. 2009e), and the quadratic search method (Abbott et al. 2009e).

### Sideband

Once the periodic signal from a pulsar in a binary system has been corrected for the Earth’s rotation and orbit, the power falls into a number of frequency modulated sidebands, resembling a comb, centred on the signal frequency. The spacing of the comb’s “teeth” (each sideband) is  $1/P_{\text{orb}}$ , where  $P_{\text{orb}}$  is the orbital period of the binary, and the number of resolvable sidebands is proportional to  $\nu a \sin i/c$ , where  $\nu$  is the emitted gravitational wave frequency, and  $a \sin i/c$  is the projection of the orbital semi-major axis along the observer’s line of sight. By incoherently summing the  $\mathcal{F}$ -statistic at each sideband, the minimum detectable signal amplitude scales as  $\nu^{1/4} T_{\text{obs}}^{1/2}$ , where  $T_{\text{obs}}$  is the observation time. The sideband method is designed to be the first stage of a search pipeline, in which successful candidates are followed up by a fully coherent search. Although the method is relatively less sensitive than other semi-coherent methods, it removes the need to track the unknown orbital phase (Messenger & Woan 2007).

### TwoSpect

The TwoSpect method exploits the periodic orbital modulation of binary signals by computing two successive Fourier transforms of the detector output. The first stage uses SFTs, which are corrected for Earth’s rotational and orbital motion. The SFTs are weighted according to noise and beam-pattern functions in the same way as the PowerFlux method, and the mean power from each frequency bin is subtracted. A second power spectrum is then taken

of frequency bin. The resulting frequency versus frequency plot can then be matched against signal templates. The optimal TwoSpect statistic is defined as

$$R = \frac{\sum_{n=0}^{N_{\text{pix}}-1} \epsilon_n (x_n - \langle s_n \rangle)}{\sum_{n=0}^{N_{\text{pix}}-1} \epsilon_n^2}, \quad (1.14)$$

where  $n$  is the pixel index of the frequency-frequency plot,  $N_{\text{pix}}$  is the total number of pixels, and  $\epsilon_n$ ,  $x_n$  and  $\langle s_n \rangle$  are the weight, power, and expectation value of the noise in the  $n$ -th pixel. TwoSpect is a hierarchical method; it filters the best candidates and passes them on to a more detailed search (Goetz & Riles 2009; Abbott et al. 2009e).

### Quadratic search

The quadratic search aims to reduce the number of orbital search parameters by modelling the gravitational wave phase empirically using the phase model  $\Phi(t) = 2\pi(\phi_0 + \nu_0 t + \alpha t^2/2 + \beta t^3/6)$ , where  $\phi_0$  and  $\nu_0$  are the phase and frequency at the start of the observation, and  $\alpha$  and  $\beta$  are two empirical parameters. The search templates therefore include  $\alpha$  and  $\beta$  instead of the five additional parameters required to describe a binary orbit. As the signal changes with time, for a given choice of  $\alpha$  and  $\beta$ , the model can only track the phase coherently for a short time (e.g.  $\sim 500$  s for  $P_{\text{orb}} \sim 4000$  s). The final detection statistic is the weighted sum of signal powers calculated for each coherent segment (Abbott et al. 2009e).

### 1.6.3 Current astrophysical limits from non-detection of continuous gravitational waves

Since LIGO began collecting data in 2002, numerous searches for gravitational waves from neutron stars have been completed, both targeted and all-sky, over a wide range of spin-down parameters. Although the searches have not yet yielded any detections, the upper limits placed by the non-detections provide important insight into the structure of neutron stars. We now summarise recent noteworthy results from the LIGO *continuous waves* group. Findings from the other search groups are mentioned in Section 1.5.2.

A breakthrough result was obtained during the search targeting the Crab pulsar (Abbott et al. 2008b, 2009d). Nine months of S5 data were analysed using spin-down parameters based closely on radio observations. The Crab has a spin frequency of 29.78 Hz and a frequency derivative of  $\approx -3.7 \times 10^{-10}$  Hz  $\text{s}^{-1}$ . The search was run across a narrow frequency band,  $\pm 6 \times 10^{-3}$  Hz, centred

on twice the spin frequency, and across a frequency derivative band of  $\pm 1.5 \times 10^{-13} \text{ Hz s}^{-1}$ . Upper limits on the wave strain of  $h_0 < 3.9 \times 10^{-25}$  and on the ellipticity of  $\epsilon < 2.3 \times 10^{-4}$  were placed. This was the first time that a gravitational wave search provided upper limits on  $\epsilon$  more stringent than those inferred indirectly by assuming that all of the pulsar's observed spin-down power is radiated gravitationally.

Since then, this limit has been superseded by a joint LIGO-Virgo search of 116 known pulsars (Abbott et al. 2009g) using a Bayesian parameter estimation method (Dupuis & Woan 2005). The new limits on the Crab are  $h_0 < 2 \times 10^{-25}$  and  $\epsilon < 1.2 \times 10^{-4}$ . The power radiated via gravitational waves is hence limited to  $< 2\%$  of the total spin-down power. Although the upper limits do not constrain the composition of the Crab, they do place a limit on the internal magnetic field of  $< 10^{16} \text{ G}$  and rule out certain exotic equations of state. Across the sample of 116 pulsars, the best (lowest) upper limits on  $h$  and  $\epsilon$  placed by the same search are  $h_0 < 2.3 \times 10^{-26}$  for PSR J1603–7202, which has a gravitational wave frequency of 135 Hz (near the detector's most sensitive band) and  $\epsilon < 7.0 \times 10^{-8}$  for PSR J2124–3358, which has a gravitational wave frequency of 406 Hz and a distance of 0.2 kpc (10 times closer than the Crab). The upper limit on the gravitational wave strain from PSR J2124–3358 is  $h_0 < 4.8 \times 10^{-26}$ , only 9.4 times larger than its electromagnetic spin-down limit.

Two blind, all-sky search for unknown pulsars were carried out on S5 data. The first used the PowerFlux method on eight months of S5 data (Abbott et al. 2009a). The search was run across a wide frequency band (50–1100 Hz), and a frequency derivative band of  $-5 \times 10^{-9}$ – $0 \text{ Hz s}^{-1}$ . Averaging over inclination and polarization angles yields an upper limit of  $h_0 < 1 \times 10^{-24}$  at the sensitivity 'sweet spot', near 150 Hz. Figure 1.19 shows the upper limits on the wave strain placed across the entire search frequency band for the best-case (lower curves) and worst-case (upper curves) pulsar orientations. The red, green and blue curves indicate the equatorial, intermediate, and polar sky declination bands respectively. Between  $5 \times 10^3$  (at 50 Hz) and  $2.4 \times 10^6$  (at 1100 Hz) sky points were searched. These limits imply that the galactic population of neutron stars satisfies one or more of the following conditions: either their ellipticities are all  $\lesssim 10^{-6}$ , their birth rate is  $< 1/30 \text{ yr}^{-1}$ , or their typical spin frequency is  $\lesssim 150 \text{ Hz}$ . The first conclusion is drawn from equation (1.5). The second comes from Blandford's argument, which relates the maximum gravitational wave amplitude emitted by galactic sources to their birthrate (Knispel & Allen 2008). The third follows because slow pulsars are unlikely to be detected, as

LIGO's sensitivity falls off sharply at frequencies  $\lesssim 150$  Hz.

The second all-sky search was carried out as part of the Einstein@Home distributed computing project<sup>16</sup> (Abbott et al. 2009c). The search analysed 66 days of S5 data, using a frequency band  $50 - 1000$  Hz and a frequency derivative band  $-\nu/\tau < \dot{\nu} < 0.1\nu/\tau$ , where  $\tau$  is the characteristic age. Below 400 Hz, the authors used  $\tau = 10^3$  yr, and above 400 Hz, they used  $\tau = 8 \times 10^3$  yr. In the 125–225 Hz band, an upper limit was placed on the gravitational wave strain of  $h_0 < 3 \times 10^{-24}$ .

Another promising search has recently been conducted targeting the central compact object in the supernova remnant Cas A (Wette et al. 2008). The neutron star in Cas A is  $\sim 300$  years old and is the youngest known neutron star. Its spin period is unknown; it was detected in 1999 by the Chandra X-ray Observatory as a steady, unpulsed point source (Tananbaum 1999). The coherent search computed the  $\mathcal{F}$ -statistic for 12 days of S5 data, searching over a frequency band of 100–300 Hz, and over the ranges  $-\nu/\tau \leq \dot{\nu} \leq -\nu/6\tau$ , and  $2\dot{\nu}^2/\nu \leq \ddot{\nu} \leq 7\dot{\nu}^2/\nu$ , where  $\dot{\nu}$  and  $\ddot{\nu}$  are the first and second frequency derivatives, and  $\tau \approx 300$  yr. Preliminary results indicate that the electromagnetic spin-down limit for this object will be beaten, with estimated upper limits on the wave strain of approximately  $8 \times 10^{-25}$  near  $\sim 150$  Hz, and on the corresponding ellipticity of  $1 \times 10^{-4}$  (Owen 2009).

These results are tabulated in Table 1.6.3, which lists the data sets, targets, and key results of recent searches for continuous gravitational waves (separated into searches from known radio pulsars, all-sky searches, and targeted searches). For each search, we list the resulting 95% confidence upper limits in gravitational wave strain and ellipticity<sup>17</sup>.

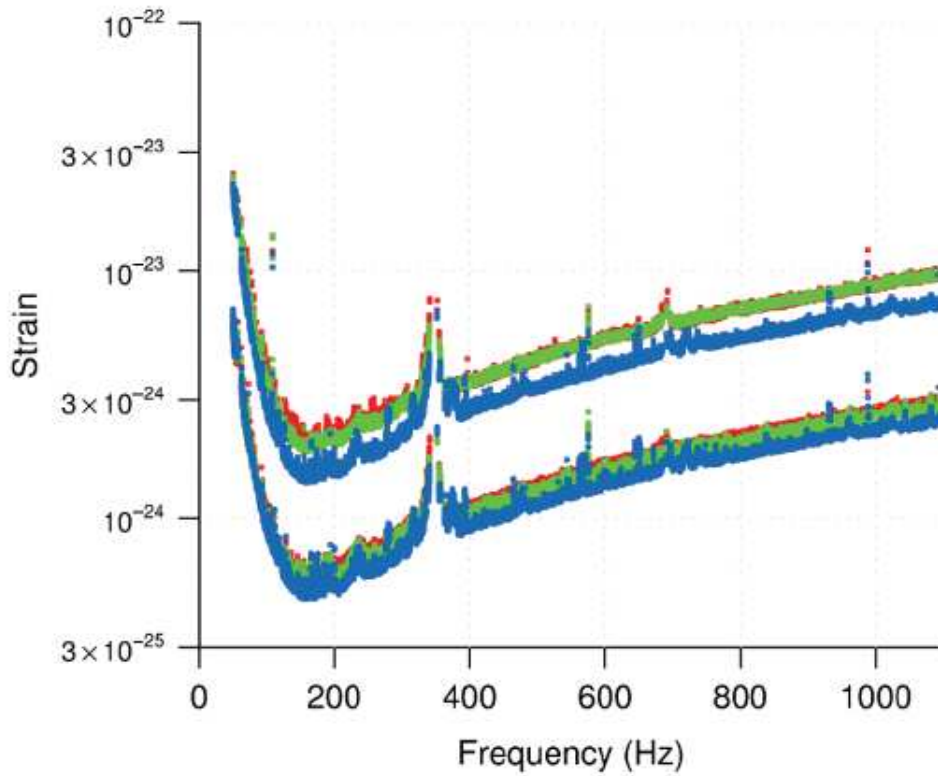
## 1.7 Thesis outline

Table 1.1 in Section 1.2 explains how the aim of this thesis is to exploit radio, X-ray, and gravitational wave observations of neutron stars to measure the ellipticity, magnetic field strength and geometry, and spin evolution of these objects. The thesis is structured as follows.

Chapter 2 presents studies of X-ray timing data from the AMSP XTE J1814–338. Data acquired by the Rossi X-ray Timing Explorer (RXTE) satellite show that the spin period and pulse amplitude of the pulsar are modulated

<sup>16</sup><http://www.einsteinathome.org>

<sup>17</sup>A 95% confidence upper limit is the value above which there is a 95% probability that a detection would have been made



**Figure 1.19:** Gravitational wave strain upper limits from an all-sky PowerFlux S5 search across the frequency band 50–1100 Hz, and the frequency derivative band  $-5 \times 10^{-9}$ – $0 \text{ Hz s}^{-1}$ . The red, green and blue curves indicate the equatorial, intermediate, and polar declination bands respectively. The lower curves denote the best-case pulsar orientations, and vice versa (from Abbott et al. 2009a).

Experiment/data set	Target object	$h_0^{95\%}$	$\epsilon^{95\%}$
LIGO S2 <sup>a</sup>	known radio pulsars	$\lesssim 10^{-24}$	$\lesssim 10^{-5}$
LIGO S3/S4 & GEO <sup>b</sup>	known radio pulsars	$2.6 \times 10^{-25}$	$\lesssim 10^{-6}$
LIGO S5 <sup>c</sup>	known radio pulsars	$2.3 \times 10^{-26}$	$7.0 \times 10^{-8}$
EXPLORER <sup>d</sup>	all-sky	$10^{-22}$	...
LIGO S2 <sup>e</sup>	all-sky	$4.43 \times 10^{-23}$	...
LIGO S2 <sup>f</sup>	all-sky	$6.6 \times 10^{-23}$	...
LIGO S4 <sup>g</sup>	all-sky	$4.28 \times 10^{-24}$	...
LIGO S5 <sup>h</sup>	all-sky	$1.0 \times 10^{-24}$	...
LIGO S5 <sup>i</sup>	all-sky	$3.0 \times 10^{-24}$	...
LIGO/GEO S1 <sup>j</sup>	PSR J1939+2134	$1.4 \times 10^{-22}$	$2.9 \times 10^{-4}$
LIGO S2 <sup>k</sup>	Sco X-1	$1.7 \times 10^{-22}$	$4 \times 10^{-4}$
LIGO S4 <sup>*l</sup>	Sco X-1	$8.5 \times 10^{-24}$	$2.3 \times 10^{-5}$
LIGO S5 <sup>m</sup>	Crab (PSR B0531+21)	$3.9 \times 10^{-24}$	$2.3 \times 10^{-4}$
LIGO S5 & VIRGO <sup>n</sup>	Crab (PSR B0531+21)	$2.0 \times 10^{-25}$	$1.2 \times 10^{-4}$
LIGO S5 <sup>o</sup>	Cas A	$8 \times 10^{-25}$	$1.1 \times 10^{-4}$

<sup>a</sup>Abbott et al. (2005b)<sup>b</sup>Abbott et al. (2007f)<sup>c</sup>Abbott et al. (2009g)<sup>d</sup>Astone et al. (2005)<sup>e</sup>Abbott et al. (2005a)<sup>f</sup>Abbott et al. (2007e)<sup>g</sup>Abbott et al. (2008a)<sup>h</sup>Abbott et al. (2009a)<sup>i</sup>Abbott et al. (2009c)<sup>j</sup>Abbott et al. (2004)<sup>k</sup>Abbott et al. (2007f)<sup>l</sup>Abbott et al. (2007e)<sup>m</sup>Abbott et al. (2008b, 2009d)<sup>n</sup>Abbott et al. (2009g)<sup>o</sup>Wette et al. (2008); Owen (2009)

**Table 1.3:** 95% confidence upper limits in gravitational wave strain ( $h_0^{95\%}$ ) and ellipticity ( $\epsilon^{95\%}$ ) set by recent searches for gravitational waves from neutron stars [after Watts et al. (2008a)].

at a  $\sim 12.2$  day period. This modulation may be consistent with the pulsar precessing due to an accretion-induced deformation. A sufficiently large deformation would result in the pulsar being a strong gravitational wave emitter. We perform simulations based on a simple precession model in an attempt to reproduce the observed timing data. Although we find no suitable model to confirm or rule out the precession, we calculate an upper limit on the ellipticity of the pulsar of  $\epsilon \lesssim 10^{-8}$ , limiting the strength of its gravitational wave emission.

Chapters 3 and 4 detail the design and implementation of a cross-correlation search for continuous gravitational waves. In Chapter 3, we discuss the feasibility of a search targeted at the supernova remnant SN 1987A. We estimate the astrophysical properties that a neutron star born in SN 1987A needs to have in order to be detectable by the search. There are two ways of searching for a neutron star with this method. The first is a straightforward search over a range of frequencies and frequency derivatives. The second takes advantage of the fact that the gravitational wave phase can be modelled non-perturbatively in terms of the magnetic field strength, ellipticity, and electromagnetic braking index of the neutron star. A two-week search run on a 1000-node computing cluster will be sensitive to on a putative neutron star in SN 1987A with  $B \lesssim 2 \times 10^{13}$  G and  $\epsilon \gtrsim 1 \times 10^{-4}$ . The development and implementation of the search code are described in Chapter 4, and the results of code verification tests are presented. The sensitivity of the code to a range of injected signals is estimated. The code is currently undergoing the internal LSC review process, which is nearing completion. The actual search will be run after the deadline for submitting this thesis.

Finally, we turn our attention to polarized radio emission from pulsars. We introduce Stokes tomography as a new method which can be used to interpret polarization data, in conjunction with the pulse profile and PA swing. In Chapter 5, we develop the method, including relativistic aberration effects, and present an atlas of look-up tables of Stokes phase portraits for a range of magnetic configurations, orientations and emission altitudes. The features of Stokes phase portraits for 24 slowly-rotating pulsars are discussed, which challenge the widely held belief that radio polarization originates from low magnetospheric altitudes. We perform detailed modelling of data from two pulsars, PSR J0826+1627 and PSR J0304+1932, and present best-fit estimates for their orientation and magnetic geometry. Chapter 6 builds on the method described in Chapter 5, introducing the effects of interpulse emission, and applies Stokes tomography to MSPs. As noted in Section 1.3.2, the complexity

of MSP pulse profiles and PA swings makes them difficult to model with the RVM, which assumes a purely dipolar field. However, an overview of Stokes phase portraits from 16 MSPs shows that they can be fit reasonably well with a current-modified, swept-back dipole. Using the current-modified dipole, we model two MSPs in detail, PSR J1939+2134 and PSR 0437–4715, with limited success. Our findings indicate that these objects may have even more complex field geometries, such as a force-free or vacuum-like field.

We conclude in Chapter 7. We summarize the results presented in this thesis, and discuss the future potential of each project. In particular, we demonstrate how Stokes tomography can be applied to more sophisticated magnetic fields, presenting examples of Stokes phase portraits for a vacuum field, and for a dipole distorted by the formation of a magnetic mountain.



# 2 Does the accreting millisecond pulsar XTE J1814–338 precess?

## 2.1 Introduction

Accreting millisecond pulsars (AMSPs) are a subset of neutron stars in low-mass X-ray binaries (LMXBs) that exhibit persistent X-ray pulsations with periods below 10 ms. In the standard recycling scenario, AMSPs are the evolutionary link between LMXBs and nonaccreting, radio millisecond pulsars (Alpar et al. 1982; Radhakrishnan & Srinivasan 1982). Thirteen AMSPs have been discovered at the time of writing (Wijnands 2004; Morgan et al. 2005; Galloway 2007; Krimm et al. 2007; Altamirano et al. 2009; Markwardt et al. 2009; Altamirano et al. 2010).

Most AMSPs are X-ray transients. Once every few years, they emerge from quiescence and become detectable during an outburst lasting several weeks. The outburst is attributed to enhanced accretion [e.g. Lasota (2001)], funnelled onto a small number of hotspots on the star. Little is known about the shape, position, or number of these hotspots (Romanova et al. 2004b; Kulkarni & Romanova 2005), but they do give rise to detectable X-ray pulsations, from which the spin period and orbital parameters can be determined. During an outburst, surface thermonuclear burning also causes type I X-ray bursts, which last a few minutes and occur on average once every few days. Type I X-ray bursts have been observed in five AMSPs to date: Aql X-1 (Koyama et al. 1981), SAX J1808.4–3658, XTE J1814–338 (Wijnands 2006), HETE J1900.1–2455 (Vanderspek et al. 2005), and IGR J17511–3057 (Bozzo et al. 2009). In the burst tails, a small component of the X-ray flux ( $\sim 15\%$  for XTE J1814–338) oscillates at the spin frequency.

AMSPs are expected to be relatively powerful gravitational wave sources (Watts et al. 2008a). The fastest, IGR J00291+5934 (Eckert et al. 2004), spins at  $\Omega_*/2\pi = 599$  Hz, well below the theoretical breakup frequency for most nuclear equations of state ( $\sim 1.5$  kHz) (Cook et al. 1994; Bildsten 1998).

Similarly, the fastest radio millisecond pulsar, PSR J1748–2446ad (Hessels et al. 2006), and the fastest nonpulsating LMXB, 4U 1608–52 (Hartman et al. 2003), spin at frequencies of 716 Hz and 619 Hz respectively. The gap below the breakup frequency is explained if the star is deformed by one part in  $\sim 10^8$ , such that gravitational radiation balances the accretion torque at hectohertz frequencies (Bildsten 1998). Several physical mechanisms can produce the requisite deformation: magnetic mountains (Payne & Melatos 2004; Melatos & Payne 2005; Payne & Melatos 2006; Vigelius & Melatos 2008), thermocompositional mountains caused by electron capture gradients (Ushomirsky et al. 2000), toroidal internal magnetic fields (Cutler 2002), and r-modes (Andersson 1998; Owen et al. 1998; Nayyar & Owen 2006). AMSPs are therefore promising targets for ground-based, long-baseline interferometers like the Laser Interferometer Gravitational-Wave Observatory (LIGO). An AMSP at a distance of 1 kpc, spinning at 0.4 kHz with ellipticity  $\epsilon = 10^{-8}$ , generates a wave strain  $h \sim 10^{-27}$ . By comparison, initial LIGO’s sensitivity threshold in the 0.1–0.4 kHz band is  $\sim 10^{-26}$  during the S4 run (Abbott et al. 2007f). Advanced LIGO will get down to  $h \sim 10^{-27}$  in the same band, and narrowband tunability will increase its sensitivity to AMSPs further, as  $\Omega_*$  is known a priori from X-ray timing.

An AMSP with ellipticity  $\epsilon \sim 10^{-8}$  is expected to precess with a period of hours to days. Magnetic mountains, for example, are built around the magnetic axis, which is misaligned in general with the rotation axis in objects which pulsate (Payne & Melatos 2006). More generally, a mass quadrupole of any provenance should be kicked out of alignment continuously by stochastic accretion torques (Jones & Andersson 2002). Hence AMSPs are promising observational candidates for observing short-period precession. Until now, however, precession has been difficult to detect in neutron stars. Only one source, the radio pulsar PSR B1828–11, precesses unambiguously, with period  $P_p = 250$  d (Stairs et al. 2000). Oscillatory trends in pulse arrival times, with periods of several days, have also been reported tentatively in a few other objects (Melatos 2000; Hobbs et al. 2006; Payne & Melatos 2006), but the physical cause is unclear.

Free precession consists of a fast wobble about the angular momentum vector  $\mathbf{J}$ , at approximately the pulsar spin period  $P_* = 2\pi/\Omega_*$  and a slow retrograde rotation about the symmetry axis, with period  $P_p = 2\pi/\Omega_p$ , which modulates the pulse shape and arrival times (Zimmermann & Szedenits 1979; Alpar & Pines 1985; Jones & Andersson 2001, 2002; Link 2003). The precession frequency  $\Omega_p$  depends on the ellipticity,  $\epsilon$ , and the tilt angle  $\theta$  (between the

symmetry axis and  $\mathbf{J}$ ), with

$$\epsilon \cos \theta \approx \Omega_p / \Omega_*. \quad (2.1)$$

The amplitude ratio of the gravitational wave signal at the spin frequency and its second harmonic (Zimmermann & Szedenits 1979; Jaranowski et al. 1998), and in the  $+$  and  $\times$  polarizations, provides *independent* information on  $\epsilon$ ,  $\theta$ , the orientation of  $\mathbf{J}$ , and the emission pattern on the surface of the star. Narrowband tunability facilitates extraction of this information.

In this chapter, we compute theoretically the X-ray signal from a precessing pulsar for a range of orientations and compare three quantities from each pulse profile to the data: the mean flux of the profile, the zero-to-peak pulse amplitude, and the pulse-phase residuals. We search for the signature of precession in X-ray timing data from one particular AMSP, XTE J1814–338. An analogous search was carried out by Akgün et al. (2006) for the radio pulsar PSR B1828-11, who modelled the period residuals and pulse shapes analytically taking into account precession effects (biaxial and triaxial) as well as the contribution from the magnetic spin-down torque. The authors performed searches over a range of beam locations, degrees of triaxiality, tilt angles and angle-dependent spin-down torques, finding a wide range of parameters which match the data. Thus, they were unable to constrain the shape of the star but did find that the angle-dependent spin-down torque contributes to the period residuals. Their method differs from ours in that, instead of fitting the shape of the residuals and comparing for each set of parameters, they determined the validity of a configuration by calculating Bayesian probability distribution functions for the parameters under certain constraints.

The chapter is structured as follows. Section 2.2 describes the precession model and its implementation. Sections 2.3 and 2.4 characterize the predicted X-ray signal for a biaxial, precessing pulsar with one and two hotspots respectively, specifically the relative precession phases between the flux, pulse amplitude, and pulse-phase. Section 2.5 repeats the predictions for a triaxial, precessing pulsar. Section 2.6 describes the data reduction and timing analysis of XTE J1814–338. We compare the measurements with the theory in Section 2.7 and derive upper limits on  $\epsilon$ ,  $\theta$ , and the associated gravitational wave strain in Section 2.8. The limit on  $\theta$  constrains the relative strength of the driving and damping forces in the system.

## 2.2 Precession model

### 2.2.1 Equations of motion

Three Euler angles  $(\theta, \phi, \psi)$  describe the rotation of a rigid body with body axes  $(\mathbf{e}_1, \mathbf{e}_2, \mathbf{e}_3)$  relative to the Cartesian triad  $(\mathbf{i}, \mathbf{j}, \mathbf{k})$  of an inertial observer. We define  $(\theta, \phi, \psi)$  according to the Landau & Lifshitz (1969) convention. Consider, first, the special case of a biaxial, freely precessing neutron star. Let  $\mathbf{e}_3$  be the symmetry axis and take  $\mathbf{k}$  to lie along the total angular momentum  $\mathbf{J}$ , as depicted in Figure 2.1. The angle between  $\mathbf{e}_3$  and  $\mathbf{J}$  is  $\theta$ . The total angular velocity of the precessing system,  $\boldsymbol{\Omega}$ , comprises two components:  $\boldsymbol{\Omega}$  rotates about  $\mathbf{J}$  at a constant angle  $\hat{\theta}$ , with frequency  $\dot{\phi}$ , and  $\mathbf{e}_1$  and  $\mathbf{e}_2$  rotate about  $\mathbf{e}_3$ , with frequency  $\Omega_p = \dot{\psi}$ . The rate of precession is controlled by the ellipticity of the star,  $\epsilon$ , and  $\theta$ , i.e.  $\Omega_p = \epsilon\Omega \cos(\theta + \hat{\theta})$ . Note that  $\mathbf{J}$ ,  $\boldsymbol{\Omega}$ , and  $\mathbf{e}_3$  are coplanar, as indicated by the shading in Figure 2.1. For small angles, one has  $\hat{\theta} \approx (\Delta I_d/I_1) \sin \theta \cos \theta$ , where  $I_1, I_2$  and  $I_3$  denote the star's principal moments of inertia, and  $\Delta I_d$  is defined through  $I_1 = I_2 = I_0 - \Delta I_d/3$  and  $I_3 = I_0 + 2\Delta I_d/3$ .  $\Delta I_d$  is positive for an oblate star, negative for a prolate star, and is related to the ellipticity via  $\epsilon = \Delta I_d/I_0$ .

In terms of the above notation, the six equations of motion are

$$\dot{\theta} = \Omega_1 \cos \psi - \Omega_2 \sin \psi, \quad (2.2)$$

$$\dot{\phi} = (\Omega_1 \sin \psi + \Omega_2 \cos \psi) / \sin \theta, \quad (2.3)$$

$$\dot{\psi} = \Omega_3 - \cos \theta (\Omega_1 \sin \psi + \Omega_2 \cos \psi) / \sin \theta, \quad (2.4)$$

$$I_1 \dot{\Omega}_1 = (I_2 - I_3) \Omega_2 \Omega_3, \quad (2.5)$$

$$I_2 \dot{\Omega}_2 = (I_3 - I_1) \Omega_1 \Omega_3, \quad (2.6)$$

$$I_3 \dot{\Omega}_3 = (I_1 - I_2) \Omega_1 \Omega_2. \quad (2.7)$$

The time origin is arbitrary, so initially we can set  $\psi(0) = 0$  without loss of generality. The angular velocity can be decomposed into  $\boldsymbol{\Omega} = \dot{\phi}\mathbf{k} + \dot{\psi}\mathbf{e}_3$ . This gives  $\dot{\psi} = -\epsilon\dot{\phi}I_0/I_3$ . In biaxial precession,  $\theta$  is constant. Solving (2.2)–(2.7) with  $\dot{\theta} = 0$  and  $\psi(0) = 0$  yields the following expressions, which we use to initialise the angular velocity:

$$\Omega_1(0) = 0, \quad (2.8)$$

$$\Omega_2(0) = \Omega_c \sin \theta, \quad (2.9)$$

$$\Omega_3(0) = \Omega_c (\cos \theta - \epsilon I_0/I_3). \quad (2.10)$$

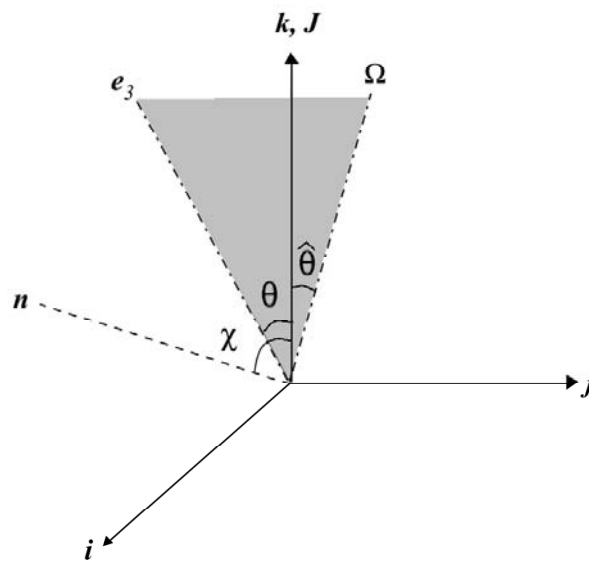


**Figure 2.1:** Geometry of precession. Drawn are the inertial frame axes  $i, j, k$ ; the symmetry axis,  $e_3$ , which makes an angle  $\theta$  with the total angular momentum vector,  $J$ ; the angular velocity vector,  $\Omega$ , which makes an angle  $\hat{\theta}$  with  $J$ ; and the line-of-sight vector  $n$ , which makes an angle  $\chi$  with  $J$ . The dashed line indicates that  $n$  lies in the plane containing  $i$  and  $k$ . The dashed-dotted lines indicate that  $e_3$  and  $\Omega$  are coplanar. The shaded plane containing  $e_3, \Omega$ , and  $J$  rotates about  $J$  with angular frequency  $\dot{\phi}$ .

Without loss of generality, we fix the line-of-sight vector,  $\mathbf{n}$ , to lie in the  $\mathbf{i-k}$  plane, making an angle  $\chi$  with  $\mathbf{J}$  and intersecting the stellar surface intensity map at latitude  $\theta_B$  and phase  $\phi_B$ . The angles  $(\theta_B, \phi_B)$  are defined with respect to the moving body frame, as opposed to the Euler angles, which are defined with respect to the inertial frame. We then compute the observed intensity  $I$  as a function of time from a specific surface intensity map  $F(\theta_B, \phi_B)$ , i.e.  $I = F(\theta_B, \phi_B)$ . Note that Jones & Andersson (2001) assumed  $0 \leq \chi \leq \pi/2$  but did not investigate the dependence of  $I$  on  $\chi$ . In this chapter, we show that the  $\chi$  dependence is significant.

The above initialization gives four searchable parameters:  $\theta$ , the initial azimuth  $\phi(0)$ , the inclination angle  $\chi$ , and the latitude  $\alpha$  of the hotspot(s), defined in Section 2.2.2.

### 2.2.2 Synthetic pulse profiles

Studies of the harmonic ratio and modulation amplitude of type I burst oscillations from six LMXBs point to the existence of a single, hemispheric hotspot (Muno et al. 2002; Payne & Melatos 2006). We thus perform simulations for one and two hotspots, corresponding to

$$F(\theta_B, \phi_B) = \sin(\theta_B + \alpha) \sin(\phi_B) + \text{DC} \quad (2.11)$$

and

$$F(\theta_B, \phi_B) = \sin(\theta_B + \alpha) \sin^2(\phi_B) + \text{DC} \quad (2.12)$$

respectively, where DC represents a constant offset, and  $\alpha$  is the latitude of the hotspot's centre, defined to be zero at the equator and  $\pm 90^\circ$  at the poles. For  $\alpha = 0$ , this corresponds to a surface intensity map containing a bright spot on the  $\mathbf{e}_1$ - $\mathbf{e}_3$  plane, centred on the equator at body coordinates  $(\theta_B, \phi_B) = (90^\circ, 90^\circ)$ , and a dark or bright spot diametrically opposite at body coordinates  $(90^\circ, 270^\circ)$  as per Figure 2.2. For  $\alpha \neq 0$ , the body coordinates in (2.11) and (2.12) are rotated by  $\alpha$  in the  $\mathbf{e}_1$ - $\mathbf{e}_3$  plane.

The light curves are generated by evaluating the intensity of the point on the surface map which is intercepted by the line-of-sight at each time step. These synthesised light curves are analysed in exactly the same way as the observational data. The profile of each pulse in the time series is fitted with a first and second harmonic, i.e.  $a + b \sin(2\pi\gamma + c) + d \sin(4\pi\gamma + e)$ , where  $a$  is the mean flux,  $\gamma$  denotes the pulse phase ( $0 \leq \gamma \leq 1$ ),  $b$  and  $d$  are amplitudes, and  $c$  and  $e$  are phase offsets. The fractional root-mean-square

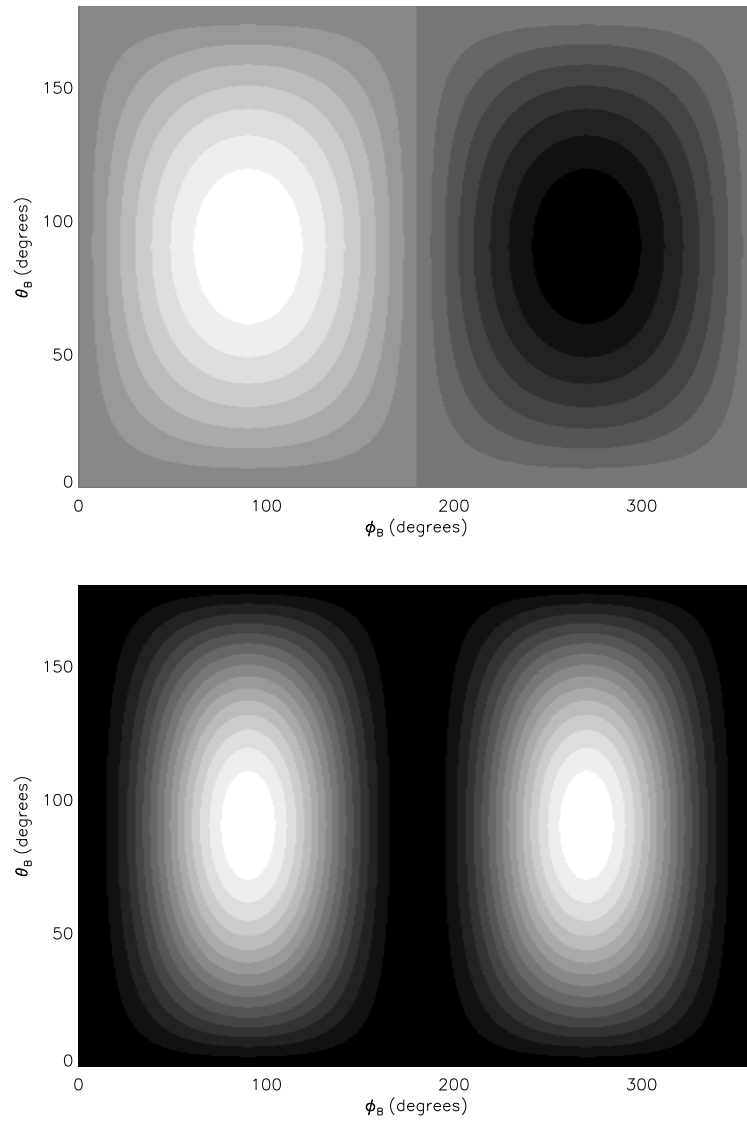


**Figure 2.2:** Top: Surface intensity map of the single hotspot configuration (equation 2.11). Bottom: Surface intensity map of the double hotspot configuration (equation 2.12).

(RMS) amplitudes of the first and second harmonic are  $b/\sqrt{2}a$  and  $d/\sqrt{2}a$  respectively. We define two reference pulse phases in each profile as the phases which maximise the first and second harmonic components. The pulse-phase residuals are the differences between the predicted and observed maxima, i.e.  $\gamma_0 = 1/4 - c/2\pi$  and  $\gamma_1 = 1/8 - e/4\pi$ . In Section 2.6.5, we show that the second harmonic does not contribute to the overall candidate precession signal at a level that can be detected in the X-ray timing data presently available for XTE J1814–338. The quantities  $d/\sqrt{2}a$  and  $\gamma_1$  are therefore neglected in the following analysis.

We fold the time series  $a$ ,  $b/\sqrt{2}a$  and  $\gamma_0$  at the theoretical precession period. These three quantities are modulated at the precession frequency due to the motion of the hotspot(s) relative to the observer (see Figure 2.3 for an example of the output). The average trend in each quantity is fitted with a sinusoid, viz.  $A_n + B_n \sin(2\pi\Gamma + C_n)$ , where  $\Gamma$  is the precession phase, not to be confused with the pulse phase, and  $n$  refers to mean flux, fractional RMS or pulse-phase residuals. This yields three main quantities of observational interest: the relative precession phase of  $a$  and  $b/\sqrt{2}a$  (denoted by  $\Delta\Gamma_{\text{flux-rms}} = |C_{\text{flux}} - C_{\text{rms}}|$ ), the relative precession phase  $\gamma_0$  and  $b/\sqrt{2}a$  (denoted by  $\Delta\Gamma_{\text{phase-rms}} = |C_{\text{phase}} - C_{\text{rms}}|$ ), and the zero-to-peak amplitude of the pulse-phase residuals ( $B_{\text{phase}}$ ). Our simulations run for (on average) three precession periods.

## 2.3 Biaxial star: Single hotspot

In most configurations involving a single hotspot, the precession phases of  $b/\sqrt{2}a$  and  $\gamma_0$  differ by  $\Delta\Gamma_{\text{phase-rms}} \approx \pi/2$ . The precession phases of  $b/\sqrt{2}a$  and  $a$  are either in phase or antiphase, i.e.  $\Delta\Gamma_{\text{flux-rms}} = 0$  or  $\pi$ .  $B_{\text{phase}}$  increases with the tilt angle  $\theta$ .

The effect of varying the four searchable parameters is now discussed in detail.

### 2.3.1 Tilt angle, $\theta$

We consider small tilt angles ( $\theta \leq 10^\circ$ ), as in PSR 1828–11 [ $\theta < 3^\circ$ ; Stairs et al. (2000); Link (2003)] and other astrophysical bodies. We verify that the precession period increases with  $\theta$  according to (2.1). We also find that  $B_{\text{phase}}$  increases linearly with  $\theta$  in the small tilt angle regime  $\theta \leq 10^\circ$ , ranging from 0.003 at  $\theta = 1^\circ$  to 0.028 at  $\theta = 10^\circ$ . There is also a dependence of  $B_{\text{phase}}$  on  $\alpha$  (see bottom panel of Figure 2.5). Jones & Andersson (2001) predicted

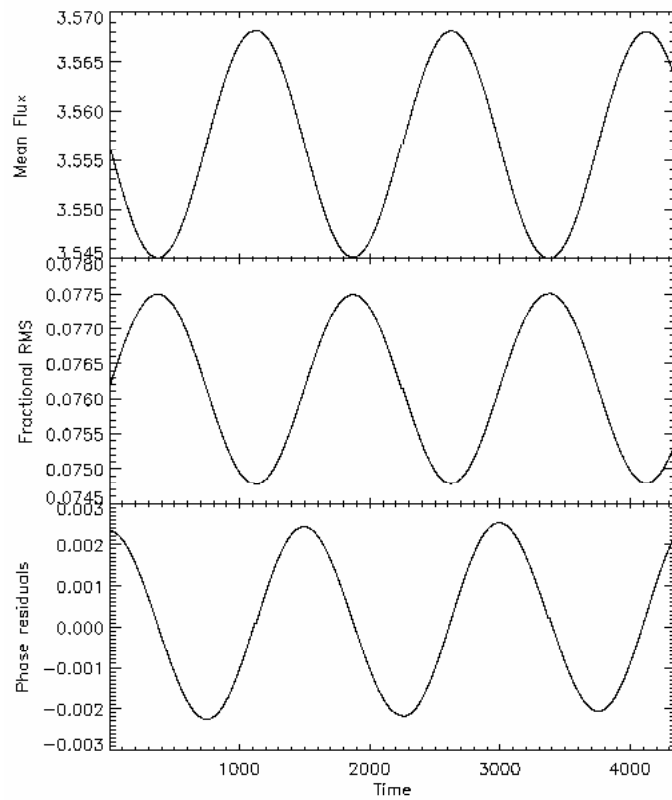


**Figure 2.3:** Sample simulation output for a biaxial star with a single hotspot. Top: mean flux,  $a$ . Center: fractional RMS,  $b/\sqrt{2}a$ . Bottom: pulse-phase residuals,  $\gamma_0$ . The precession period is 1500 time units.

analytically, for a radio pulsar with a directed beam rather than a hotspot, that the pulse-phase residuals vary sinusoidally on the precession time-scale with amplitude  $B_{\text{phase}} \propto \theta / \tan(\pi/2 - \alpha')$ , where  $\alpha'$  in their case is the latitude of the beam. This formula agrees with our results.

Varying  $\theta$  does not affect  $\Delta\Gamma_{\text{flux-rms}}$  or  $\Delta\Gamma_{\text{phase-rms}}$ .  $\Delta\Gamma_{\text{flux-rms}}$  undergoes a phase shift of  $\pi$  around  $\chi = 90^\circ$  which is explained below. Contour maps of  $\Delta\Gamma_{\text{flux-rms}}$ ,  $\Delta\Gamma_{\text{phase-rms}}$  and  $B_{\text{phase}}$  as functions of  $\chi$  and  $\theta$  are plotted in Figure 2.4.

### 2.3.2 Hotspot latitude, $\alpha$ , and inclination, $\chi$

Figure 2.5 displays contour maps of  $\Delta\Gamma_{\text{phase-rms}}$ ,  $\Delta\Gamma_{\text{flux-rms}}$ , and  $B_{\text{phase}}$  as function of  $\chi$  and  $\alpha$  for  $\theta = 1^\circ$ . In the range  $-15^\circ < \alpha < 15^\circ$ ,  $\Gamma_{\text{RMS}}$  undergoes a  $\pi$  phase reversal between certain values of  $\chi$ , which shows up in  $\Delta\Gamma_{\text{phase-rms}}$  and  $\Delta\Gamma_{\text{flux-rms}}$ . As  $\chi$  is increased, a strong second harmonic gradually appears in  $\Gamma_{\text{RMS}}$  over an interval of  $\approx 10^\circ$ . As  $\chi$  increases further, the harmonic disappears and  $\Gamma_{\text{RMS}}$  is shifted by  $\pi$ . The value of  $\chi$  at which this happens depends on  $\alpha$  (see top and middle panels of Figure 2.5). For example, at  $\alpha = -10^\circ$ , the harmonic appears for  $56^\circ < \chi < 64^\circ$ .

The value of  $\Delta\Gamma_{\text{flux-rms}}$  also depends on which hemisphere (north or south) the hotspot is in, relative to  $\mathbf{n}$ . If both are in the same hemisphere, then  $\Delta\Gamma_{\text{flux-rms}} \approx \pi$ . If they are in different hemispheres, then  $\Delta\Gamma_{\text{flux-rms}} \approx 0$ . This change occurs because the mean flux profile ‘flips’. For example, if  $\chi = 30^\circ$ , the fractional RMS is the same whether the hotspot is in the north or south. However, if the hotspot is in the north (south),  $\mathbf{n}$  starts off closer to (further from) the hotspot, and the flux dims (brightens) as the star precesses. The phase shifts of  $\Gamma_{\text{RMS}}$  and the mean flux are explained geometrically in more detail in Section 2.3.4.

$B_{\text{phase}}$  is larger when the hotspot is close to the poles than when the hotspot is near the equator, but hardly varies with  $\chi$ . When  $\chi = 0$ , the observer does not see any evidence of precession at all in the pulse-phase residuals, as  $\mathbf{e}_3$  remains equidistant from  $\mathbf{n}$  at all times.

### 2.3.3 Initial longitude, $\phi(0)$

$\phi(0)$  determines the initial latitude where  $\mathbf{n}$  intersects the surface. When  $\mathbf{n}$  is within  $1^\circ$  of  $\mathbf{J}$ , i.e.  $\chi < 1^\circ$  or  $\chi > 179^\circ$ , as one varies  $\phi(0)$  from 0 to  $2\pi$ ,  $\Delta\Gamma_{\text{phase-rms}}$  oscillates sinusoidally around  $\pi/2$ ,  $\Delta\Gamma_{\text{flux-rms}}$  oscillates sinusoidally

around 0 or  $\pi$  (depending on the hemisphere of the hotspot), and  $B_{\text{phase}}$  peaks at  $\phi(0) = \pi$  or  $2\pi$ . At these extremes,  $\mathbf{n}$  traverses a very small area on the star's surface during each spin period, i.e.  $B_{\text{rms}}, B_{\text{phase}} \ll 1$ . Hence any variation due to  $\phi(0)$ , insignificant for other values of  $\chi$ , now dominates.

### 2.3.4 Geometry of the phase shifts

In this section, we explain geometrically why the relative precession phase of maximum rotation-averaged intensity abruptly changes whenever the line of sight crosses the equator, causing  $\Delta\Gamma_{\text{flux-rms}}$  to jump by  $\pi$  rad. To understand this counterintuitive effect, consider Figure 2.6, which shows the coplanar vectors  $\mathbf{J}$ ,  $\mathbf{e}_3$  (which makes an angle  $\theta$  with  $\mathbf{J}$ ), and  $\boldsymbol{\Omega}$  (which makes an angle  $\hat{\theta}$  with  $\mathbf{J}$ ). In reality,  $\hat{\theta}$  is small, but we enlarge it artificially for illustrative purposes. For  $\alpha = 0$ , the hotspot is at the equator (relative to  $\mathbf{e}_3$ ), and the surface intensity changes from brighter to darker than average at the dot-dashed line. Figure 2.6(a) is a snapshot taken of the pulsar at the start of a precession cycle, while Figure 2.6(b) is taken half a precession cycle later, after a time  $\pi/\dot{\psi}$  elapses. Both snapshots are taken at the same arbitrary pulse-phase, when  $\mathbf{e}_3$  and  $\boldsymbol{\Omega}$  line up as shown.

Now consider two observers,  $\chi_1$  just north of the equator and  $\chi_2$  just south of the equator. The dashed lines show the loci of points where the lines-of-sight intersect the surface during one spin (not precession) period. The lines are tilted with respect to the horizontal at angle  $\hat{\theta}$ , perpendicular to  $\boldsymbol{\Omega}$ , because the pulsar rotates instantaneously about  $\boldsymbol{\Omega}$  during one spin period. At the start of the precession cycle [panel (a)], observer  $\chi_1$  traces a path which passes through more of the dark hemisphere than the bright, while  $\chi_2$  traces a path through more of the bright hemisphere. Half a precession cycle later [panel (b)], the opposite happens. This means that the mean flux seen by  $\chi_1$  increases from minimum to maximum from (a) to (b), whereas the mean flux seen by  $\chi_2$  decreases from maximum to minimum. This ‘flip’ causes the  $\pi$  phase shift in  $\Delta\Gamma_{\text{flux-rms}}$ .

The phase reversal in  $\Gamma_{\text{RMS}}$  at certain inclination angles when the hotspot is in the range  $-15^\circ < \alpha < 15^\circ$  can also be understood with the help of Figure 2.6. For  $\alpha = 0$ , the line dividing the bright and dark hemispheres is at the same position in (a) and (b). Hence, the pulse amplitude  $b$  and times-of-arrivals (TOAs) seen by either observer  $\chi_1$  or  $\chi_2$  is the same at epoch (a) and epoch (b), even though the mean flux  $a$  changes from epoch (a) to epoch (b). As we are measuring  $b/\sqrt{2}a$ , the phase reversal in the mean flux causes

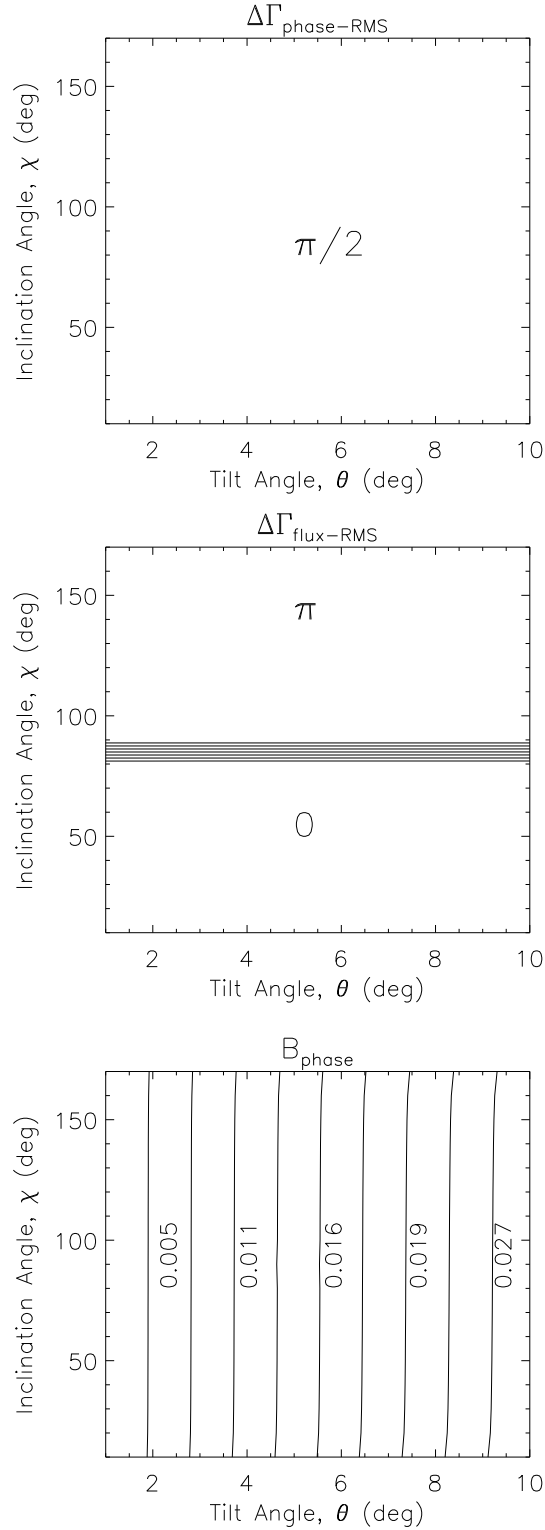


**Figure 2.4:** Relative precession phase of the RMS and pulse-phase residuals,  $\Delta\Gamma_{\text{phase-rms}}$  (top), RMS and mean flux,  $\Delta\Gamma_{\text{flux-rms}}$  (middle), and amplitude of the folded pulse-phase residuals,  $B_{\text{phase}}$  (bottom), versus tilt angle  $\theta$  and inclination angle  $\chi$ , both measured in degrees for a bi-axial pulsar with one hotspot. Parameters:  $\phi_{(0)} = 0^\circ$ ,  $\alpha = 45^\circ$  for  $1^\circ \leq \theta \leq 10^\circ$ , and  $5^\circ \leq \chi \leq 175^\circ$ .

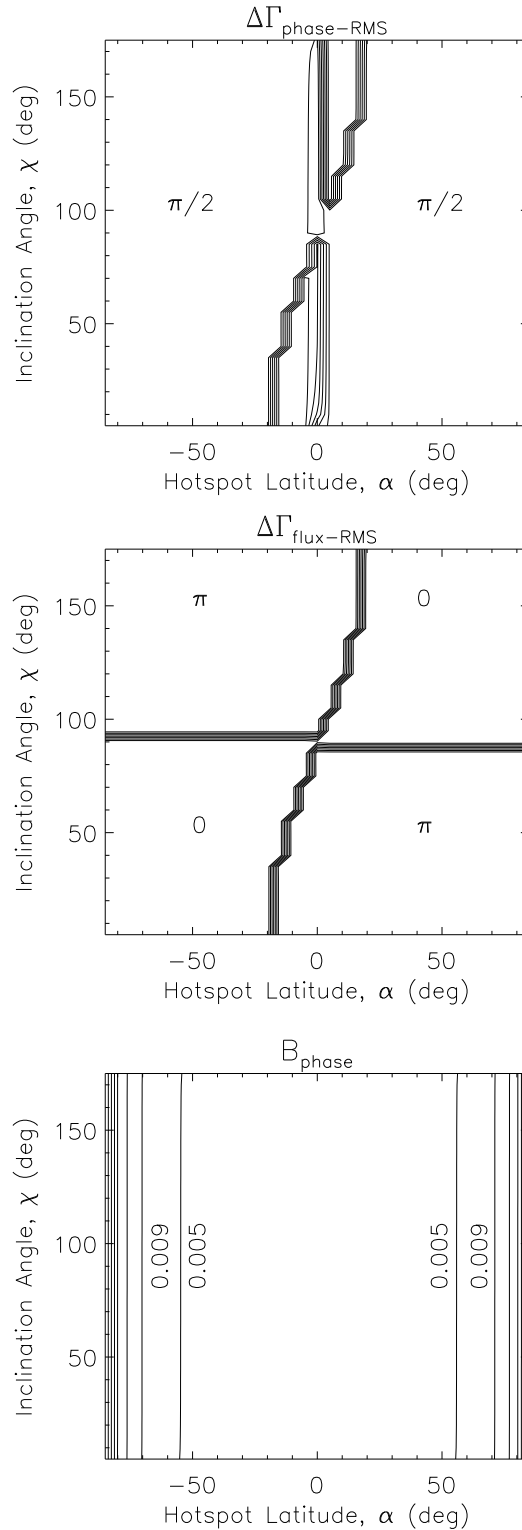


**Figure 2.5:** Relative precession phase of the RMS and pulse-phase residuals,  $\Delta\Gamma_{\text{phase-rms}}$  (top), RMS and mean flux,  $\Delta\Gamma_{\text{flux-rms}}$  (middle), and amplitude of the folded pulse-phase residuals,  $B_{\text{phase}}$  (bottom), versus inclination angle  $\chi$  and hotspot latitude  $\alpha$ , both measured in degrees for a biaxial pulsar with one hotspot. Parameters:  $\theta = 1^\circ$ ,  $\phi_{(0)} = 0$ ,  $5^\circ \leq \alpha \leq 175^\circ$ , and  $5^\circ \leq \chi \leq 175^\circ$ .

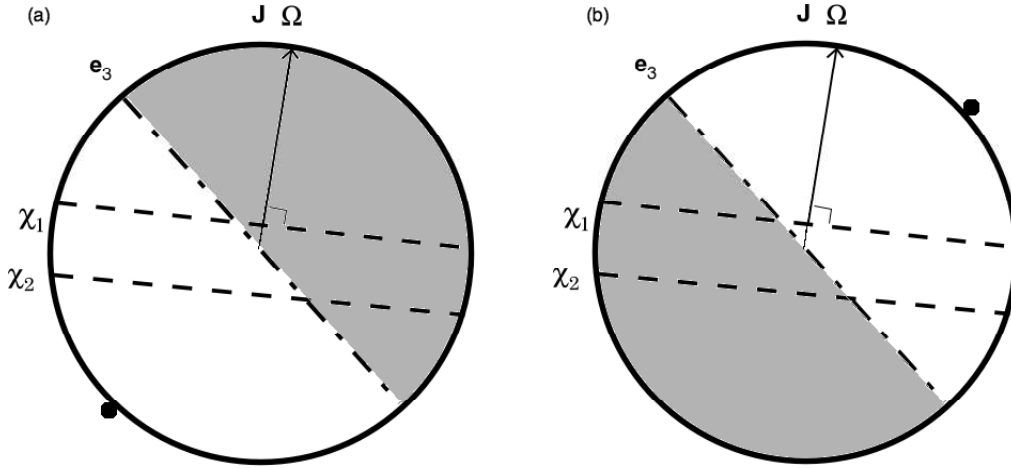


**Figure 2.6:** Schematic illustrating the rotation of one hotspot, from (a) the start of one precession cycle, to (b) midway through the precession cycle. The bright and dark hemispheres are marked.  $\chi_1$  is the position of an observer just north of the equator ( $\chi < 90^\circ$ ).  $\chi_2$  is the position of an observer just south of the equator ( $\chi > 90^\circ$ ). The dashed lines indicate the points on the surface that the observers see each spin period. These lines are perpendicular to  $\Omega$  and hence tilted by the angle  $\hat{\theta}$  (artificially enhanced for clarity) with respect to the horizontal. The hotspot centres are indicated by the black dots.

a phase reversal in  $\Gamma_{\text{RMS}}$  at  $\chi = 90^\circ$ . This effect occurs at larger (smaller)  $\chi$  for  $\alpha > 0^\circ$  ( $\alpha < 0^\circ$ ), and does not occur when  $\alpha > 15^\circ$ . This is because, as the hotspot moves away from  $\alpha = 0^\circ$ , the pulse amplitudes  $b$  seen by  $\chi_1$  and  $\chi_2$  become increasingly different at epochs (a) and (b), so the effect of  $a$  on the fractional RMS is reduced.

We also observe a strong harmonic component in the phase residuals at  $\alpha = 0^\circ$  as the pulse TOAs are identical in epochs (a) and (b).

## 2.4 Biaxial star: Two hotspots

To simulate two diametrically opposed hotspots, the intensity map is changed to equation (2.12). The pulse profiles now contain an increased harmonic component in certain configurations. The parameter study in Section 2.3 is repeated.

### 2.4.1 Tilt angle, $\theta$

Figure 2.7 shows contour maps of the three quantities as a function of  $\theta$  and  $\chi$  for hotspots at  $45^\circ$  and  $225^\circ$ . As with one hotspot, only  $B_{\text{phase}}$  is affected by changing  $\theta$ ; it ranges from 0.002 to 0.075 (see bottom panel of Figure 2.7).

$dB_{\text{phase}}/d\theta$  is smaller in the range  $45^\circ \lesssim \chi \lesssim 135^\circ$ .

### 2.4.2 Hotspot latitude, $\alpha$ and inclination, $\chi$

The positions of the hotspots relative to  $\mathbf{n}$  affect  $\Delta\Gamma_{\text{phase-rms}}$  and  $\Delta\Gamma_{\text{flux-rms}}$ . Figure 2.8 shows contour maps of the two quantities and  $B_{\text{phase}}$  as functions of  $\chi$  and  $\alpha$  for  $\theta = 1^\circ$ . We find  $\Delta\Gamma_{\text{phase-rms}} \approx \pi/2$  in the regions where  $\chi$  is north of a hotspot in the northern hemisphere, or south of one in the southern hemisphere, i.e. if  $\alpha = 45^\circ, 225^\circ$  and  $\chi < 45^\circ$  or  $\chi > 135^\circ$ . Elsewhere, we find  $\Delta\Gamma_{\text{phase-rms}} \approx 3\pi/2$ . As for one hotspot, the fractional RMS reverses phase when  $\mathbf{n}$  lies within  $\sim 5^\circ$  of the hotspots, causing a second harmonic component to develop in the fractional RMS.

As  $\chi$  approaches the equator, the harmonic component in the pulse profiles increases and peaks at  $\chi = 90^\circ$ . The horizontal band across the contour map at  $\chi = 90^\circ$  is caused by the pulse-phase residuals shifting by  $\pi$  (see top panel of Figure 2.8). At  $\alpha = 0^\circ$ , the two hotspots are within  $\theta$  of  $\mathbf{n}$ . For small  $\theta$ , the observer sees the fractional RMS, mean flux and pulse-phase residuals rise and fall twice as the star precesses about  $\mathbf{e}_3$  (at rate  $\dot{\psi}$ ). This halves the apparent precession period.

$\Delta\Gamma_{\text{flux-rms}}$  varies from 0 to  $\pi$  in a similar fashion. The fractional RMS and mean flux are generally out of phase when  $\mathbf{n}$  is north of a hotspot in the northern hemisphere, south of a hotspot in the southern hemisphere, and vice versa. However, the fractional RMS and mean flux undergo phase shifts at different points  $(\chi, \alpha)$ . The fractional RMS ‘flips’ at the points indicated by the diamond pattern in the top panel of Figure 2.8, whereas the mean flux ‘flips’ for  $65^\circ \lesssim \chi \lesssim 115^\circ$ , indicated by the horizontal band in the middle panel of Figure 2.8. The origin of these phase shifts is explained geometrically in Section 2.4.4.

$B_{\text{phase}}$  is largest when both  $\chi$  and  $\alpha$  are close to the poles.

### 2.4.3 Initial longitude, $\phi(0)$

Longitudinal dependences are weak. For example,  $\Delta\Gamma_{\text{phase-rms}}$  varies by  $< 0.02\%$  as  $\phi(0)$  goes from  $0^\circ$  to  $330^\circ$  for  $\chi = 70^\circ$ , as is shown in Figure 2.9. Near  $\chi = 90^\circ$ ,  $\Delta\Gamma_{\text{phase-rms}}$  and  $\Delta\Gamma_{\text{flux-rms}}$  vary more strongly with  $\phi(0)$  due to phase shifts in the pulse-phase residuals and fractional RMS at various configurations. However, these shifts do not translate into true changes in the observed pulse profile, because the second harmonic component, which we do

not consider, dominates in this region and behaves differently. The mean flux profile is not affected.  $\Delta\Gamma_{\text{flux-rms}}$  cycles between  $\approx 0.9$  and  $2\pi$  as  $\phi(0)$  varies from 0 to  $2\pi$  rad, while  $\Delta\Gamma_{\text{phase-rms}}$  cycles between  $\pi/2$  and  $3\pi/2$ .

#### 2.4.4 Geometry of the phase shifts

Figure 2.10 shows a pulsar with two hotspots at (a) the beginning and (b) midway through a precession cycle. The hotspots are located at approximately  $45^\circ, 225^\circ$  to match Figures 2.7 and 2.9. The shaded band indicates the region of the surface which is darker than average; the darkest points lie along the dot-dashed line. The band changes orientation from (a) to (b) as the star precesses rigidly about  $\mathbf{e}_3$  (after a time  $\pi/\dot{\psi}$  elapses).

To explain the flip in the fractional RMS at  $\chi = 45^\circ$  (or equivalently  $135^\circ$ ), we compare the observers at  $\chi_1$  (north of  $45^\circ$ ) and  $\chi_2$  (south of  $45^\circ$ ). In (a) and (b),  $\chi_1$  traces similar paths close to the darkest and brightest regions respectively, leading to similar pulse amplitudes. However, the mean flux is lower in (a) than in (b), so the fractional RMS is a maximum at (a) and a minimum at (b). Similarly,  $\chi_2$  traces a path with a greater pulse amplitude in (a) than in (b), but because these are normalised by the mean flux, which is greater at (a) than at (b), the fractional RMS is a minimum at (a) and a maximum at (b).

In order to explain the flip in mean flux between  $65^\circ < \chi < 115^\circ$ , we compare  $\chi_2$  (south of  $65^\circ$ ) and  $\chi_3$  (south of  $115^\circ$ ). In Figure 2.10(a), both  $\chi_2$  and  $\chi_3$  trace paths of similar brightness over one spin period. However in Figure 2.10(b),  $\chi_2$  traces a path in the darker band, whereas  $\chi_3$  traces a path closer to the bright centre of the hotspot. This confirms that the mean flux profiles seen by  $\chi_2$  and  $\chi_3$  are  $\pi$  out of phase, as our simulations show.

## 2.5 Triaxial star

A triaxial star is described by two separate ellipticity parameters,  $\epsilon_1$  and  $\epsilon_2$ , defined by  $\epsilon_1 = [2(I_3 - I_1)/I_1]^{1/2}$  and  $\epsilon_2 = [2(I_3 - I_2)/I_2]^{1/2}$  (Zimmermann & Szedenits 1979). We pick  $I_1$  to have a reference value of  $I_0 = 0.4M_\star R_\star^2$  and investigate the effect of varying  $\epsilon_2/\epsilon_1$  from 0.3 to 0.7. Within this range, we find that there are no changes in the behaviour of  $\Delta\Gamma_{\text{phase-rms}}$ ,  $\Delta\Gamma_{\text{flux-rms}}$  or  $B_{\text{phase}}$ . The only effect is to change the spin period, i.e.  $P_{0.3} \approx 1.0022P_{0.5}$ ,  $P_{0.7} \approx 0.9994P_{0.5}$  where  $P_{0.3}$  is the spin period for  $\epsilon_2/\epsilon_1 = 0.3$  and so on.

The motion is discussed in detail by Landau & Lifshitz (1969). When  $J^2$  is

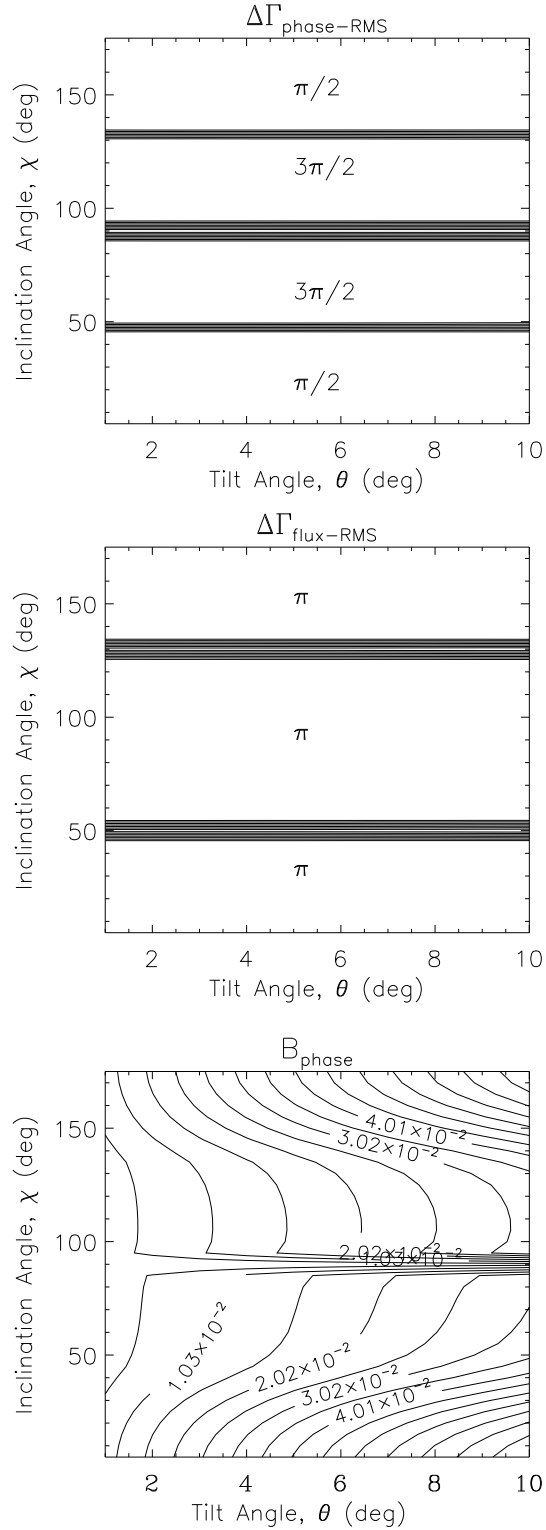


**Figure 2.7:** Relative precession phase of the RMS and pulse-phase residuals,  $\Delta\Gamma_{\text{phase-rms}}$  (top), RMS and mean flux,  $\Delta\Gamma_{\text{flux-rms}}$  (middle), and amplitude of the folded pulse-phase residuals,  $B_{\text{phase}}$  (bottom), versus inclination angle  $\chi$  and tilt angle  $\theta$ , both measured in degrees, for a biaxial pulsar with two hotspots. Parameters:  $\phi(0) = 0$ ,  $\alpha = 45^\circ$ ,  $1^\circ \leq \theta \leq 10^\circ$  and  $5^\circ \leq \chi \leq 175^\circ$ .

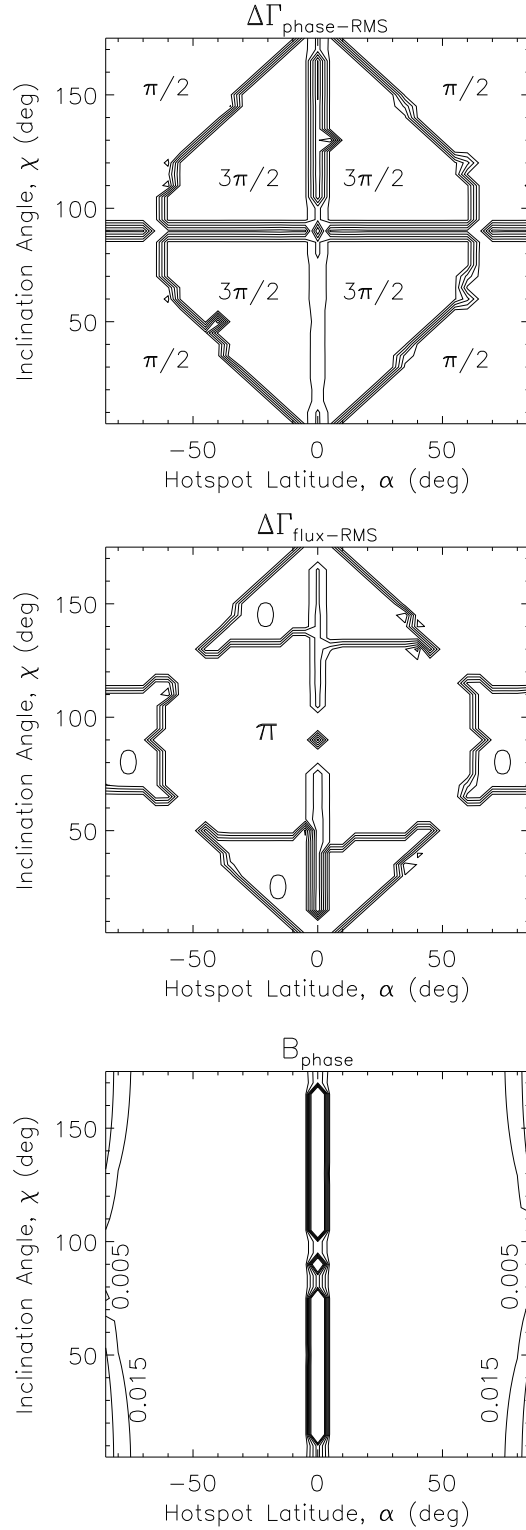


**Figure 2.8:** Relative precession phase of the RMS and pulse-phase residuals,  $\Delta\Gamma_{\text{phase-rms}}$  (top), RMS and mean flux,  $\Delta\Gamma_{\text{flux-rms}}$  (middle), and amplitude of the folded pulse-phase residuals,  $B_{\text{phase}}$  (bottom), versus inclination angle  $\chi$  and hotspot latitude  $\alpha$ , both measured in degrees, for a biaxial pulsar with two hotspots. Parameters:  $\theta = 1^\circ$ ,  $\phi(0) = 0$ ,  $5^\circ \leq \alpha \leq 175^\circ$  and  $5^\circ \leq \chi \leq 175^\circ$ .

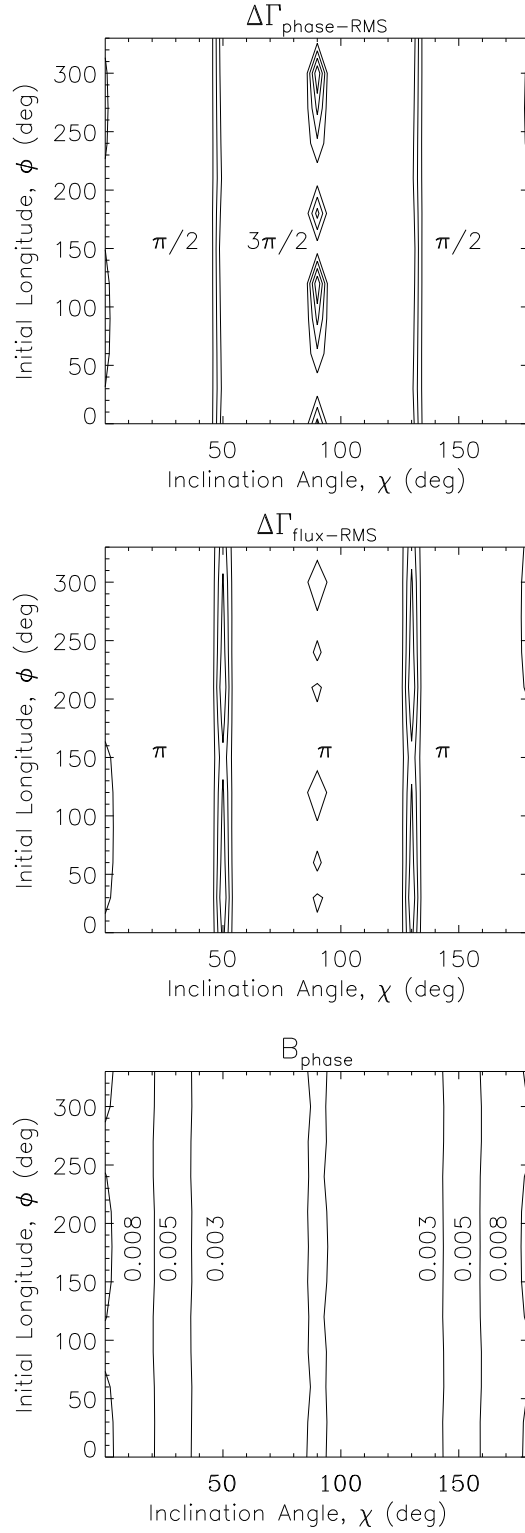


**Figure 2.9:** Relative precession phase of the RMS and pulse-phase residuals,  $\Delta\Gamma_{\text{phase-rms}}$  (top), RMS and mean flux,  $\Delta\Gamma_{\text{flux-rms}}$  (middle), and amplitude of the folded pulse-phase residuals,  $B_{\text{phase}}$  (bottom), versus inclination angle  $\chi$  and initial phase  $\phi(0)$ , both measured in degrees, for a biaxial pulsar with two hotspots. Parameters:  $\theta = 1^\circ$ ,  $\alpha = 45^\circ$ ,  $0^\circ \leq \phi \leq 330^\circ$  and  $0.1^\circ \leq \chi \leq 179.9^\circ$ .

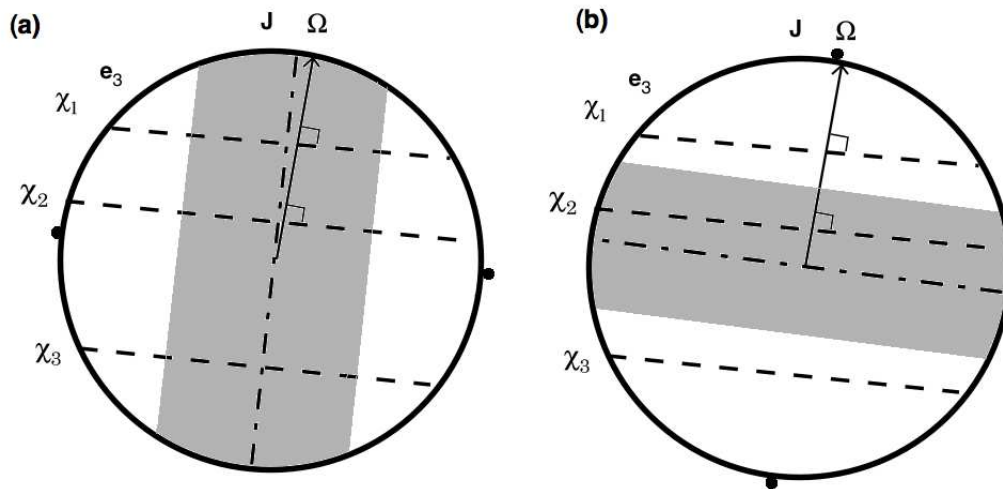


**Figure 2.10:** Schematic illustrating the rotation of two hotspots, from (a) the start of one precession cycle, to (b) midway through the precession cycle. The shaded band indicates the region on the surface that is darker than average, for  $\alpha \approx 45^\circ$ .  $\chi_1$  is the position of an observer just north of a hotspot ( $\chi < 45^\circ$ ),  $\chi_2$  is the position of an observer south of a hotspot ( $\chi > 65^\circ$ ).  $\chi_3$  is the position of an observer south of  $115^\circ$ , where the mean flux profile is seen to flip. The dashed lines indicate the points on the surface that the observers see each spin period. These lines are perpendicular to  $\Omega$  and hence tilted by the angle  $\hat{\theta}$  (artificially enhanced for clarity) with respect to the horizontal. The hotspot centres are indicated by the black dots.

only slightly larger than  $2EI_1$ , where  $E$  is the total energy, the  $\mathbf{e}_1$  axis rotates around  $\mathbf{J}$  in an ellipse whose size increases as  $J$  increases. As  $J^2$  approaches  $2EI_3$ ,  $\mathbf{e}_3$  rotates around  $\mathbf{J}$  in an ellipse. Hence  $\theta$  is not constant: its mean,  $\langle\theta\rangle$ , increases with  $J$ .

We consider small  $\theta$  in astrophysical problems, where  $\theta$  now denotes the tilt angle at the start of the simulation. The angular velocity vector  $\boldsymbol{\Omega}$  rotates periodically around the body axes, with period  $T \sim 2\pi/(\epsilon\Omega)$  (the exact value is given by a complete elliptic integral of the first kind). However,  $\boldsymbol{\Omega}$  does not return to its original position with respect to the *inertial* axes after one cycle. For a biaxial body, the spin frequency is simply  $\dot{\phi}$ . For a triaxial body, we have  $\phi(t) = \phi_1(t) + \phi_2(t)$ , where  $\phi_1(t)$  has period  $T$  and  $\phi_2(t)$  has period  $T'$  [incommensurable with  $T$ ; (Landau & Lifshitz 1969; Zimmermann & Szedenits 1979)].

We repeat the parameter searches in Sections 2.3 and 2.4 and find similar results for one and two hotspots. In some configurations, the precession phase profiles of  $\Delta\Gamma_{\text{phase-rms}}$ ,  $\Delta\Gamma_{\text{flux-rms}}$  and  $B_{\text{phase}}$  become non sinusoidal or contain strong harmonics. For consistency, we fit these profiles with the same format as before (see Section 2.2.2), recovering a modulation similar to Figures 2.7–2.9.

The only noticeable difference is in the case of two hotspots. At  $\chi = 90^\circ$ , between  $\alpha \approx \pm 30^\circ$  to  $\pm 50^\circ$ ,  $\Delta\Gamma_{\text{flux-rms}}$  increases from 3.14 to 3.19. There is also increased variation with  $\phi(0)$  ( $< 5\%$  for  $\Delta\Gamma_{\text{phase-rms}}$  and  $< 7.5\%$  for  $\Delta\Gamma_{\text{flux-rms}}$ ).

## 2.6 X-ray timing analysis

In Sections 2.3–2.5, we show that precession modulates the mean intensity and arrival times of pulses from one or two hotspots. In this section, we search for such modulation in X-ray timing observations of AMSPs made over recent years by the Rossi X-ray Timing Explorer (RXTE). We consider three sources observed by RXTE: SAX J1808.4–3658, XTE J1814–338, and HETE J1900.1–2455. HETE 1900.1–2455 is unsuitable as it displays peculiar behaviour, including persistent X-ray emission and intermittent pulsations even during periods of low accretion (Galloway et al. 2007). SAX J1808.4–3658 is also not ideal as the fractional RMS of the first harmonic changed erratically over the last four outbursts, and a previous analysis of the pulse-phase residuals did not reveal any periodicities consistent with precession (Hartman et al. 2008). The most promising candidate is XTE J1814–338, whose data cover a

66-day outburst in which modulations in the mean flux, RMS, and pulse-phase residuals are visible by eye (see below).

### 2.6.1 XTE J1814–338

XTE J1814–338 is the fifth AMSP to be discovered, with a spin frequency of 314.4 Hz (Markwardt & Swank 2003). Between MJD 52796 and 52834, the object experienced an outburst during which 27 thermonuclear (type I) X-ray bursts were observed. This is the longest interval over which pulsations have been detected consistently. The data from this outburst were analysed previously, but with different emphases. Watts et al. (2005) and Watts & Strohmayer (2006) reported on the variability and energy dependence of these bursts, finding that the burst fractional amplitude (defined in the above papers) is constant during a burst and decreases with increasing photon energy. Papitto et al. (2007) presented a timing analysis and refined orbital parameters previously published. They noted the modulation in the pulse-phase residuals and attributed it to movement of the accretion hotspot as the accretion rate varies.

### 2.6.2 Observations

The source was observed by the RXTE Proportional Counter Array [RXTE PCA; Jahoda et al. (1996)], which consists of five proportional counter units (PCUs). During the course of an observation, different numbers of PCUs are turned on at different epochs, even within one data set. In order to accurately determine the background rate for each data set, the contribution from each PCU at all times must be tracked and accounted for. Data were collected in Event Mode over 64 energy channels (2–60 keV) with 125  $\mu$ s time resolution. The data comprise 91 internally contiguous blocks lasting from 2 to 30 ks and span a total of 66 days. The X-ray flux was measured by fitting a phenomenological model consisting of blackbody and power-law components, each attenuated by neutral absorption, to spectra extracted from Standard-2 mode data in the range 2.5–25 keV. The Standard-2 mode has 129 energy channels and 16 s timing resolution.

### 2.6.3 Timing analysis

The data is processed using LHEASOFT<sup>1</sup> version 5.3 (2003 November 17). We correct the photon times of arrival (TOAs) to the solar system barycentre. The X-ray flux is background subtracted using the RXTE/PCA Mission-Long Bright Source background model<sup>2</sup>. A separate response matrix is calculated for each observation to account for drift in the PCA gains. We remove all type I bursts from the data, subtracting all photons from 15 seconds before to 200 seconds after the burst peak; all the bursts have rise times of 1–8 s and last from 100–200 s (Watts et al. 2005).

The X-ray flux is plotted versus time in Figure 2.11. It rises over the first five days from  $3.5 \times 10^{-10}$  to  $4.4 \times 10^{-10}$  erg cm<sup>-2</sup> s<sup>-1</sup>. It remains between  $4.4 \times 10^{-10}$  and  $5.1 \times 10^{-10}$  erg cm<sup>-2</sup> s<sup>-1</sup> for the next 30 days, exhibiting strong modulations. It then drops sharply over the next two days and falls below the sensitivity threshold ( $0.2 \times 10^{-10}$  erg cm<sup>-2</sup> s<sup>-1</sup>) on MJD 52834. We analyse the first 37 days of data only (between the dashed vertical lines in Figure 2.11).

The published orbital parameters at the time of writing (Markwardt et al. 2003; Chung et al. 2006) are incomplete: neither reference quoted the epoch of mean phase ( $t_{90}$ ). To extract this quantity, we select a long barycentre-corrected data span (observation ID 80418-01-03-00, lasting 30.024 ks) and correct for the satellite orbit using a trial  $t_{90}$  value. Any error in the trial  $t_{90}$  value, or any other orbital parameter, can be extracted by comparing the actual and expected TOAs. The TOA residuals obey equation (3) in Deeter et al. (1981).

The fifth term on the right-hand side of the latter equation shows that the residuals in  $t_{90}$  produce a sinusoidal variation in the TOAs, which we attempt to minimize. We also calculate corrections to the spin period by subtracting a linear trend from the TOAs, and the spin period derivatives by subtracting a quadratic trend [third term in Deeter et al. (1981)]. We do not attempt to correct for other effects as these three terms dominate. The revised orbital parameters are quoted in Table 2.1.

### 2.6.4 Pulse folding

We fold the light curves for each contiguous observing segment at the measured spin period for that segment, taking into account the first-order spin frequency derivative.

<sup>1</sup><http://heasarc.gsfc.nasa.gov/lheasoft>

<sup>2</sup>[http://heasarc.gsfc.nasa.gov/docs/xte/pca\\_news.html](http://heasarc.gsfc.nasa.gov/docs/xte/pca_news.html)

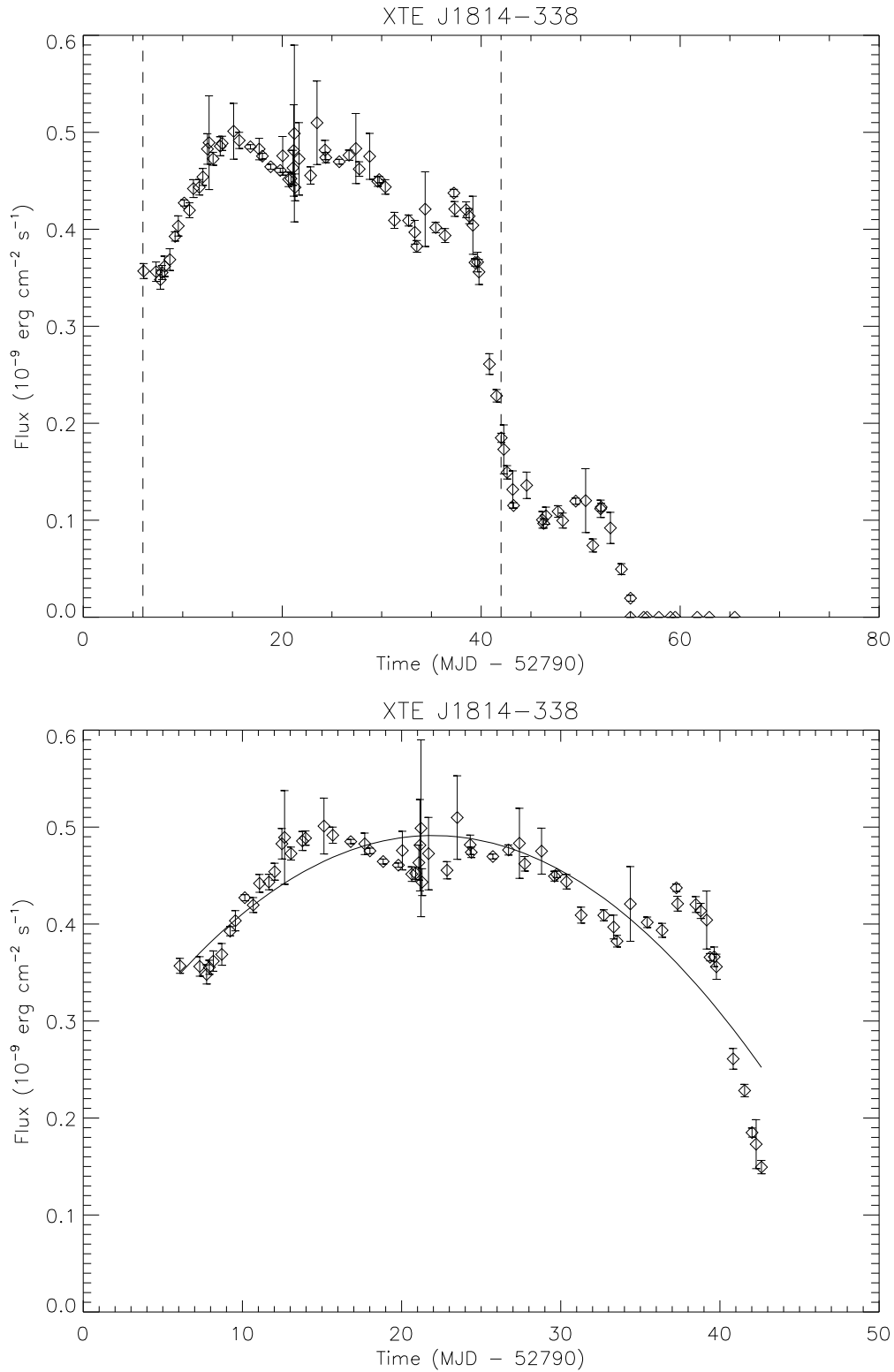


**Figure 2.11:** Total flux of XTE J1814–338 (in units of  $10^{-9} \text{ erg/cm}^2/\text{s}$ ) versus time (Modified Julian Date). Top: The entire 66 day outburst starting at MJD 52796. Bottom: The first 37 days. The flux is measured with the RXTE PCA in the energy band 2.5–25 keV. It is plotted with  $1\text{-}\sigma$  error bars. Overplotted is a quadratic polynomial which is later subtracted in order to extract the amplitude and period of the  $\sim 12$ -day modulation (the ‘bumps’ in the graph).

Barycentric spin period (s)	0.003181105669954(4)
Spin frequency derivative ( $\text{Hz s}^{-1}$ )	$-7.2(3) \times 10^{-14}$
Projected semimajor axis (lt s)	0.390626(2) <sup>a</sup>
Epoch of $\pi/2$ mean phase (MJD)	52808.8975258(4)
Orbital period (s)	15388.7238(2) <sup>a</sup>

**Table 2.1:** Orbital parameters for XTE J1814–338.

<sup>a</sup>Chung et al. (2006)

The folded pulse profiles are then fitted with a sinusoid comprising first and second harmonic components, as with the simulations above, viz.  $a + b\sin(2\pi\gamma + c) + d\sin(4\pi\gamma + e)$ , where  $0 \leq \gamma \leq 1$  denotes the pulse-phase. Fitting is done using the Levenberg-Marquardt nonlinear least-squares algorithm. Again, from the fitted parameters, we measure the fractional RMS of the first and second harmonic ( $b/\sqrt{2}a$  and  $d/\sqrt{2}a$  respectively) as well as the pulse-phase residuals of the first and second harmonic ( $\gamma_0 = 0.25 - c/2\pi$  and  $\gamma_1 = 0.125 - d/4\pi$  respectively).

Uncertainties in the fitted parameters are determined using the constant  $\chi^2$  boundary method (Press et al. 1986); i.e.  $b, c, d$  and  $e$  are iterated separately until  $\chi^2$  increases by unity relative to its minimum. We find that the constant  $\chi^2$  uncertainties are  $\approx 1.5$  times the raw standard deviation from the least-squares fit,  $\sigma_{\text{fit}}$ . Henceforth, to simplify the extensive analysis, we use  $1.5\sigma_{\text{fit}}$  to qualify the uncertainties.

### 2.6.5 First harmonic

In order to clarify whether to include the second harmonic of the observed pulse profile in any further analysis, we take the fitted parameters of the first harmonic to be the ‘true’ parameters and investigate the contribution of the second harmonic to the total signal. In the first 37 days of data, the first and second harmonic pulse-phase residuals  $\gamma_0$  and  $\gamma_1$  are similar. There is a 1.04% difference in their gradients, and a linear trend between the two can be fitted with a slope of unity lying within the  $4\sigma$  limit. As for the fractional RMS, the first harmonic  $b/\sqrt{2}a$  shows a  $4.19 \times 10^{-4} \text{ day}^{-1}$  increase over the first 37 days, whereas the second harmonic  $d/\sqrt{2}a$  decreases by  $3.94 \times 10^{-4} \text{ day}^{-1}$ .

We calculate the Lomb-Scargle periodogram (Lomb 1976; Press et al. 1986) for  $\gamma_0, \gamma_1, b/\sqrt{2}a$  and  $d/\sqrt{2}a$ . The periodogram is discussed fully in Section 2.6.6. For now, we merely note that a significant ( $> 4.5\sigma$ ) 12.2-day periodic signal is found in  $\gamma_0$  and  $b/\sqrt{2}a$ . In the second harmonic, this signal is present

in  $\gamma_1$  at a  $3.5\sigma$  level, but absent in  $d/\sqrt{2}a$ . In order to test the quality of the data, we fit 12.2-day sine waves to  $b/\sqrt{2}a$  and  $d/\sqrt{2}a$ . The  $3\sigma$  upper limit on the fractional amplitude of the fit in  $d/\sqrt{2}a$  is 7.8%, whereas the best fit fractional amplitude in  $b/\sqrt{2}a$  is 6.9%. We cannot therefore rule out the possibility that there is a hidden signal in the second harmonic fractional RMS.

For this reason, and since the first harmonic component of the fractional RMS dominates ( $b/\sqrt{2}a \approx 0.103$ ,  $d/\sqrt{2}a \approx 0.029$ ), we exclude the second harmonic fractional RMS from further consideration. We can also exclude  $\gamma_1$  as it offers no additional information about the candidate precession signal. Nonetheless, in another object with a cleaner signal, or with better data, the pulse-phase residuals can yield extra information in principle, e.g. about the detailed form of the surface intensity map (Hartman et al. 2008).

Hartman et al. (2008) discussed how ‘red noise’ (long-time-scale correlations) affect each harmonic’s fractional RMS and pulse-phase residuals, causing them to vary independently. The authors use a common phase residual which is a weighted combination of  $\gamma_0$  and  $\gamma_1$ , to minimise the intrinsic variation. We do not employ this technique as the same modulation appears in  $\gamma_0$  and  $\gamma_1$ , and it is not detectable in the second harmonic fractional RMS.

### 2.6.6 Searching for precession

The three remaining quantities of interest are the total flux, fractional RMS and pulse-phase residuals of the first harmonic. As any longer period variation can mask shorter periods, a quadratic trend in the flux and a linear trend in the fractional RMS are subtracted, leaving the time series in Figure 2.12. To search for periodicities in these quantities, we construct a Lomb-Scargle periodogram, which calculates the significance of periodicities in unevenly sampled data (Lomb 1976; Press et al. 1986). The periodogram is plotted in Figure 2.13. The peak Lomb power is 18.1 for  $\gamma_0$ , 16.2 for  $b/\sqrt{2}a$ , and 16.4 for  $a$ . These Lomb powers correspond to a significance (the probability of a falsely detected signal) of order  $10^{-6}$  for  $\gamma_0$  and  $10^{-5}$  for the other two quantities. The peak Lomb powers occur at periods  $P_{\text{flux}} = 283 \pm 22$  hours,  $P_{\text{phase}} = 293 \pm 21$  hours, and  $P_{\text{RMS}} = 302 \pm 23$  hours respectively (refer to Figure 2.13). The uncertainties in these periods are obtained in Monte-Carlo fashion by adding quasi-random noise (a Gaussian distribution with the same standard deviation as the original data minus a pure sine wave with the respective periods  $P_{\text{flux}}$ ,  $P_{\text{phase}}$  and  $P_{\text{RMS}}$ ) to noiseless signals with periods  $P_{\text{flux}}$ ,  $P_{\text{phase}}$  and  $P_{\text{RMS}}$ .

The three periods are consistent and imply a mean candidate precession

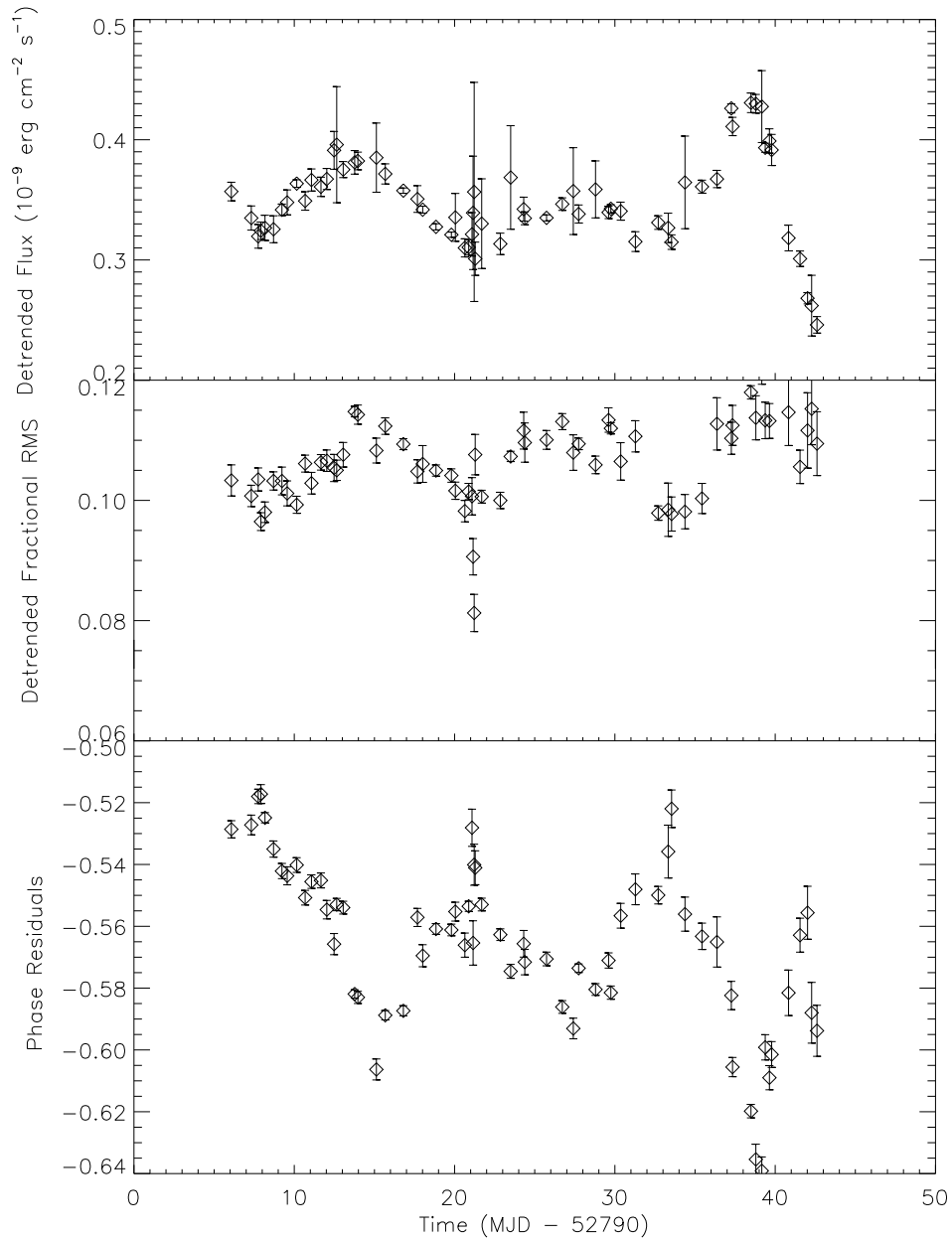


**Figure 2.12:** Top: flux time series (folded on the spin period) after subtracting the long-term quadratic trend in Figure 2.11. Center: fractional RMS of the first harmonic component of the folded pulse profile after folding on the spin period. Bottom: Pulse-phase residuals of first harmonic. All quantities are in the energy band 2.5–25 keV and are plotted with 1- $\sigma$  error bars, derived as explained in Section 2.6.2.

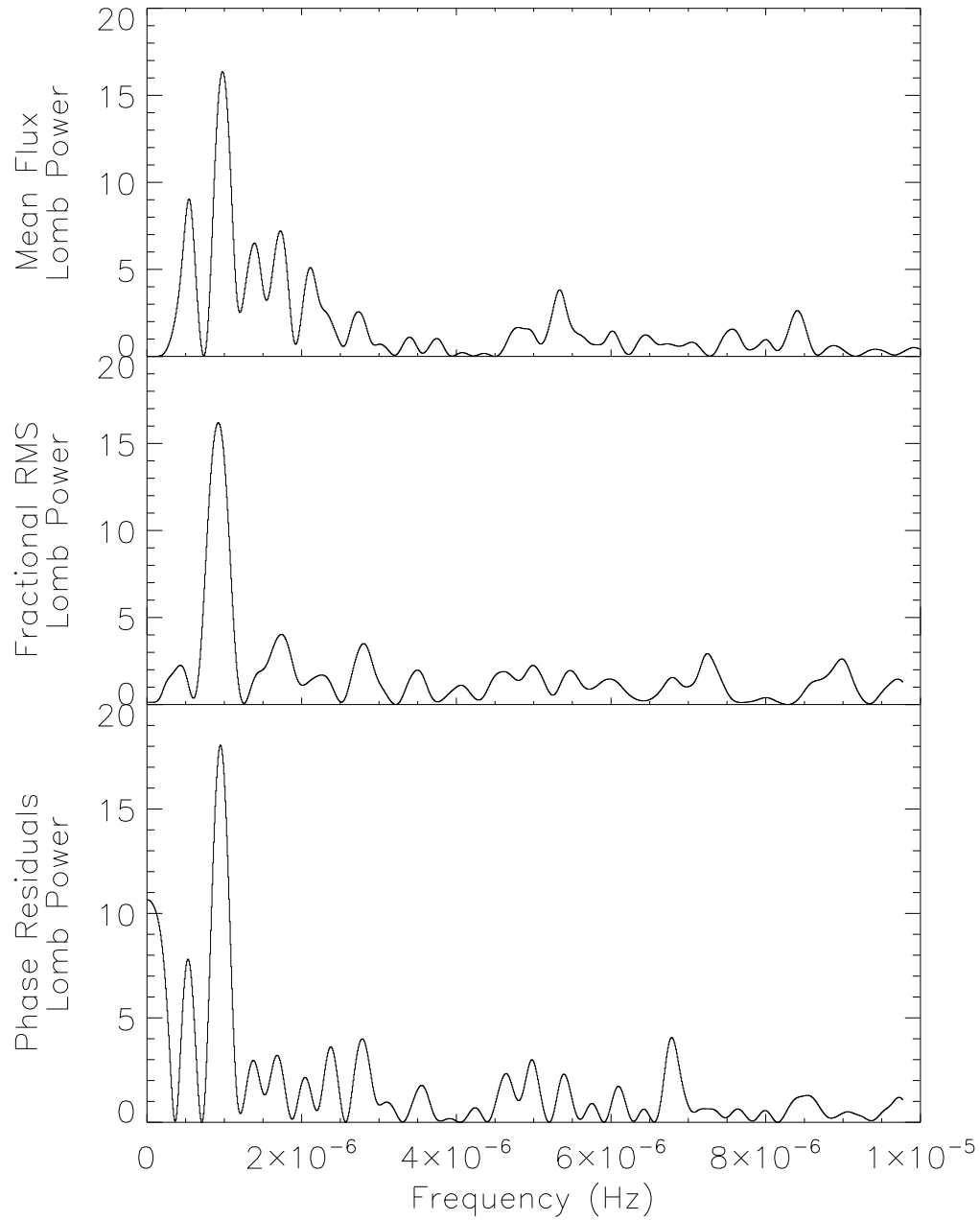


**Figure 2.13:** Lomb periodogram for the following time series. Top: mean flux. Center: fractional RMS. Bottom: pulse-phase residuals. Frequencies are measured in Hz.

$B_{\text{rms}}$	$0.006 \pm 0.003$
$B_{\text{phase}}$	$0.024 \pm 0.003$
$C_{\text{rms}}$	$-2.91 \pm 0.11$
$C_{\text{phase}}$	$0.12 \pm 0.12$
$\Delta\Gamma_{\text{phase-rms}}$	$3.1 \pm 0.2$
$C_{\text{flux}}$	$-2.2 \pm 0.3$
$\Delta\Gamma_{\text{flux-rms}}$	$0.7 \pm 0.3$

**Table 2.2:** Results of fitting the folded mean flux, fractional RMS, and pulse-phase residuals (folding period = 292.59 hours) with the expression  $A + B \sin(2\pi\Gamma + C)$ , where  $\Gamma$  is the precession phase. We list the parameters relevant to the precession model, i.e. the amplitude ( $B_{\text{rms}}$ ) and precession-phase offset ( $C_{\text{rms}}$ ) of the fractional RMS, the amplitude ( $B_{\text{phase}}$ ) and precession-phase offset ( $C_{\text{phase}}$ ) of the pulse-phase residuals, the precession-phase offset of the mean flux ( $C_{\text{flux}}$ ), the relative precession phase of the fractional RMS and pulse-phase residuals ( $\Delta\Gamma_{\text{phase-rms}}$ ), and relative precession phase of the fractional RMS and mean flux ( $\Delta\Gamma_{\text{flux-rms}}$ ). Phases are expressed in radians.

period of  $P_p = 293 \pm 22$  hours.

We now fold the flux, fractional RMS, and pulse-phase residuals at  $P_p$ . The results are shown in Figure 2.14. We describe the resulting folded time series, as with the simulations, with a sinusoid  $B \sin(2\pi\Gamma + C)$  (where  $0 \leq \Gamma \leq 1$  is the precession phase) plus a DC offset. The fitted parameters are listed in Table 2.2. From these parameters, we can construct three quantities which are independent of mean flux and determined only by the orientation of the pulsar: the relative precession phase offset between the flux and the fractional RMS,  $\Delta\Gamma_{\text{flux-rms}}$ , the relative precession phase offset between the pulse-phase residuals and the fractional RMS,  $\Delta\Gamma_{\text{phase-rms}}$ ; and the amplitude of the folded pulse-phase residual profile,  $B_{\text{phase}}$ . The measured values are listed in Table 2.2. Errors are obtained using the constant  $\chi^2$  boundary method described above.

In addition to the quantities in Table 2.2, there is one arbitrary precession phase (corresponding to a choice of time origin) and two arbitrary amplitudes (for the mean flux and RMS), which depend on the unknown (and possibly changing) DC offset flux. The latter offset in general comes from orientation effects and also a DC component in the surface intensity map.

## 2.7 Comparison between data and simulations

The only configuration for which the measured values of  $\Delta\Gamma_{\text{phase-rms}}$ ,  $\Delta\Gamma_{\text{flux-rms}}$  and  $B_{\text{phase}}$  come close to matching the data within experimental errors is a

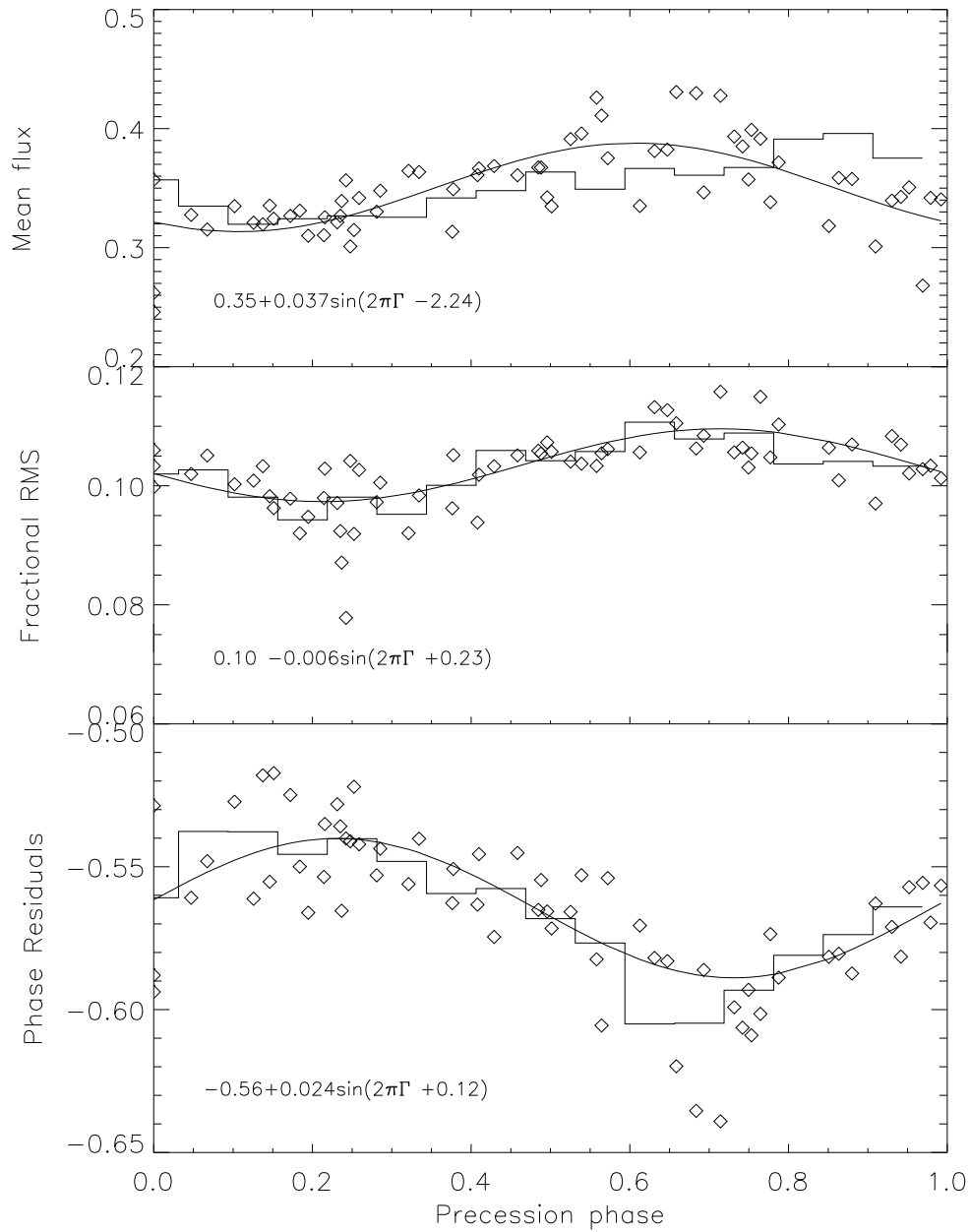


**Figure 2.14:** Slow variation of the pulse characteristics *refolded* on the candidate precession period  $P_p = 293$  hr. Top: mean flux. Center: fractional RMS of the first harmonic. Bottom: pulse-phase residuals of the first harmonic. Measurements are represented by open symbols; the binned profile is represented by the histogram. The fitted sinusoid (with DC offset) is depicted as a solid curve.

biaxial star with one hotspot. This agrees with the single-hemispheric-hotspot model suggested by Muno et al. (2002). For  $\theta = 3^\circ$ ,  $\chi = 179.95^\circ$ ,  $\phi = 210^\circ$ ,  $\alpha < 0^\circ$ , we find  $\Delta\Gamma_{\text{phase-rms}} = 2.6$ ,  $\Delta\Gamma_{\text{flux-rms}} = 1.0$  and  $B_{\text{phase}} = 0.024$ . We plot  $\Gamma_{\text{flux}}$ ,  $\Gamma_{\text{rms}}$ , and  $\gamma_0$ , refolded over the model's precession period, in Figure 2.15. The precession phase in the plots is offset to match the data (cf. Figure 2.14). The exact latitude of the hotspot does not affect these results, as mentioned previously (e.g. if  $\alpha < 0^\circ$ , then we would get the same results for  $\chi = 0.05^\circ$ ). The above model for XTE J1814–338 is unlikely a priori. Given that pulsars are oriented randomly relative to an observer, the likelihood of observing a pulsar with  $\chi < 1^\circ$  or  $\chi > 179^\circ$  is 0.008%. In fact, 95% of the sky area covers the range  $18^\circ \lesssim \chi \lesssim 162^\circ$ . Secondly, for such a small inclination angle,  $\mathbf{n}$  traces a small circle on the pulsar's surface during each rotation, resulting in a smaller ( $< 1\%$ ) fractional RMS than the  $\sim 12\%$  level seen in the data.

For configurations with  $1^\circ < \chi < 179^\circ$ , our simulations fail to match the data. The relative precession phases of the fractional RMS, mean flux and phase residuals do not fall within  $1\sigma$  of the measured values. Hence, if  $\chi$  truly does lie in the above range, two scenarios are possible.

### Scenario 1

If the 293-hr modulation in the data is a real precession signal, our model is incomplete. For example, the intensity map may be more complicated in reality than equations (2.11) or (2.12, perhaps explaining the discrepancy between the simulations and the data in  $\Delta\Gamma_{\text{flux-rms}}$  and  $\Delta\Gamma_{\text{phase-rms}}$ .

Unlike  $\Delta\Gamma_{\text{flux-rms}}$  and  $\Delta\Gamma_{\text{phase-rms}}$ , it is possible to match  $B_{\text{phase}}$  for a relatively broad range of  $\chi$ . For one hotspot, the simulations match ( $0.021 \leq B_{\text{phase}} \leq 0.027$ ) for  $6^\circ \leq \theta \leq 10^\circ$ . For a triaxial star, the match occurs at certain combinations of  $\theta$  and  $\chi$  (see Figure 2.7), with the most probable combination drawn from  $5^\circ \leq \theta \leq 8^\circ$  and  $60^\circ \leq \chi \leq 120^\circ$ . Although this agreement is insufficient as a proof of precession without an intensity map that also reproduces  $\Delta\Gamma_{\text{flux-rms}}$  and  $\Delta\Gamma_{\text{phase-rms}}$ , it does provide some insight as to what the tilt angle would be in such a scenario.

Although we did not include the type I bursts in our analysis, the phase residuals of the burst oscillations are phase-locked with the non-accreting pulse phase residuals and are modulated on the same time-scale over the span of data that we use (Watts et al. 2008b). This supports the precession model since precession of the entire pulsar would move the burst location(s) along with the non-accreting regions. The pulses from both areas would therefore be

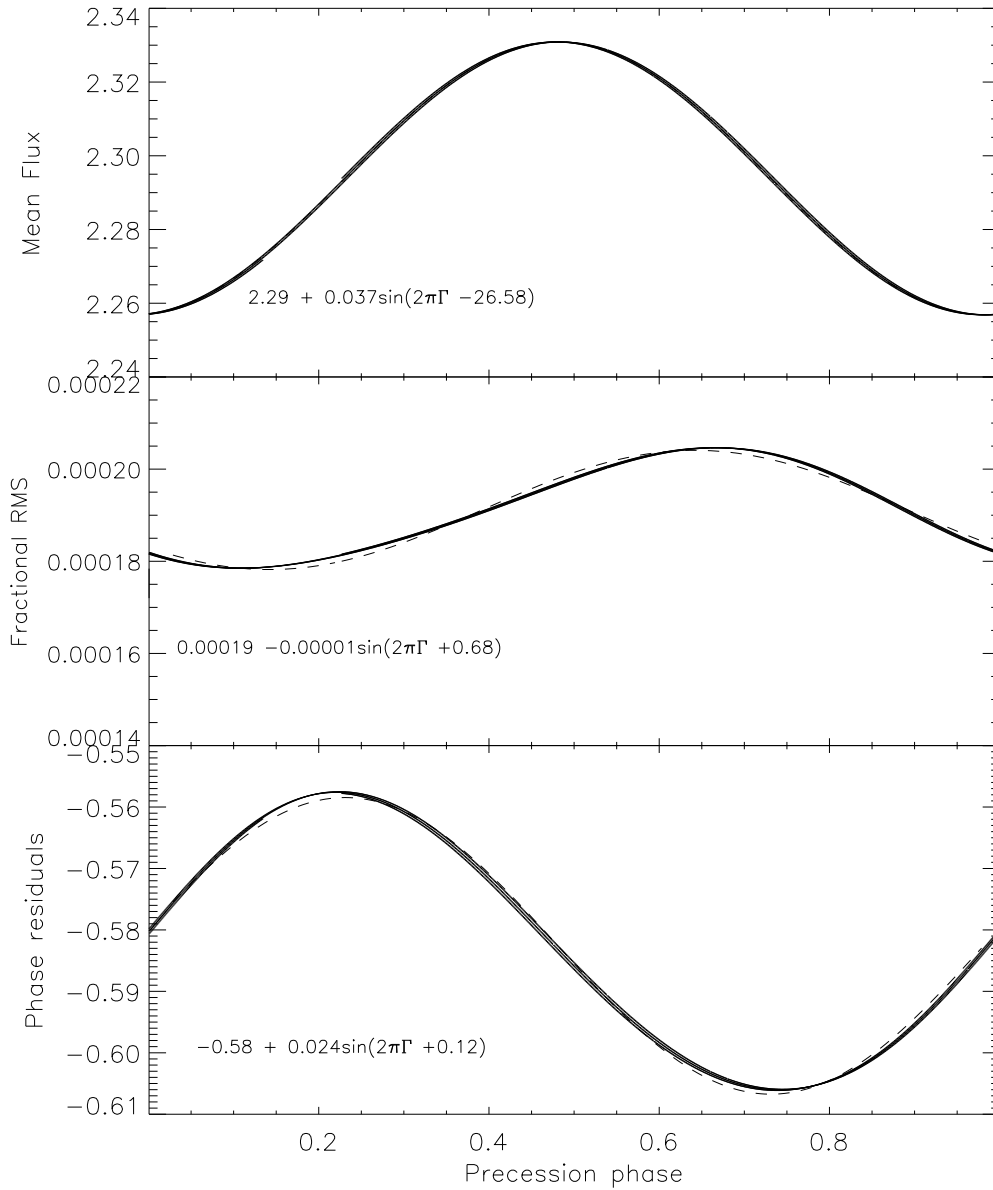


**Figure 2.15:** Refolded simulated time series for the best match configuration ( $\theta = 3^\circ, \chi = 179.95^\circ, \phi = 210^\circ, \alpha = 45^\circ$ ).  $\Delta\Gamma_{\text{flux-rms}} = 1.0$  and  $B_{\text{phase}} = 0.024$  match the data, but  $\Delta\Gamma_{\text{phase-rms}} = 2.6$  lies slightly outside the  $1 - \sigma$  error bar. Top: mean flux. Center: fractional RMS of the first harmonic. Bottom: pulse-phase residuals of the first harmonic. Simulated data are graphed as solid curves. Best-fit sinusoid is graphed as a dashed curve.

modulated in the same way.

Assuming a precession period of 293 hours and a tilt angle of  $6^\circ$ , equation (2.1) implies  $\epsilon \sim 10^{-9}$  for XTE J1814–338. The gravitational wave strain  $h_0$  at Earth from a biaxial rotator is given by

$$h_0 = \frac{16\pi^2 G}{c^4} \frac{\epsilon I_0 \Omega_*^2}{d}, \quad (2.13)$$

where  $G$  is the gravitational constant,  $c$  is the speed of light,  $I_0$  is the star's moment of inertia and  $d$  is the distance to the source. For XTE J1814–338, we have  $d \approx 8 \pm 1.6$  kpc (Strohmayer et al. 2003) and  $Rc^2/GM > 4.2$  (Bhattacharyya et al. 2005), where  $R$  is the star's radius, implying  $10^{-28} \leq h_0 \leq 10^{-27}$ .

## Scenario 2

If the 293-hr modulation is not due to precession [e.g. the hotspot may drift periodically around the star (Papitto et al. 2007), or variations in the accretion rate may induce hotspot motion (Patruno et al. 2009)], then either the precession is heavily damped, making  $\theta$  very small, or  $\epsilon$  itself is smaller than expected.

If it is rigid, the star has a nonzero ellipticity for the reasons listed in Section 2.1. However, in reality the star is elastic and probably contains a superfluid interior. Hence precession is damped via internal dissipation and gravitational radiation (Cutler & Jones 2001). Internal dissipation generally dominates. Based on calculations by Alpar & Saulis (1988), the time-scale for damping the tilt angle Bondi & Gold (1955) is predicted to be between 400 and  $10^4$  precession periods. This effect or a small ellipticity, or some combination of both, lengthens the precession period beyond the  $\sim 37$ -day observation window for  $\epsilon \cos \theta < (P_*/37\text{-d})$ , i.e.  $\epsilon \cos \theta \leq 9.9 \times 10^{-10}$ . This implies  $h_0 \leq 10 \times 10^{-27} \cos(\theta)^{-1}$ .

## 2.8 Conclusion

By analyzing X-ray timing data from the accreting millisecond pulsar XTE J1814–338, we find a 12.2-day periodicity in the mean flux, fractional RMS, and pulse-phase residuals of the first harmonic of the folded pulse. We measure two precession phase offsets relating these three quantities ( $\Delta\Gamma_{\text{phase-rms}} = 3.1 \pm 0.2$  rad and  $\Delta\Gamma_{\text{flux-rms}} = 0.7 \pm 0.3$  rad) as well as the amplitude of the

pulse-phase residuals,  $B_{\text{phase}} = 0.024 \pm 0.003$ .

Simulations of biaxial and triaxial precessing pulsars with one and two hotspots are also performed for a range of inclination angles ( $0^\circ \leq \chi \leq 180^\circ$ ), tilt angles ( $\theta \leq 10^\circ$ ), and hotspot latitudes ( $-85^\circ \leq \alpha \leq 85^\circ$ ).  $B_{\text{phase}}$  is found to depend on the tilt angle, while  $\Delta\Gamma_{\text{phase-rms}}$  and  $\Delta\Gamma_{\text{flux-rms}}$  depend on the relative orientations of the line-of-sight and the hotspot(s). We find no significant dependence on the initial longitude at which the line-of-sight intersects the star except for small ( $< 1^\circ$ ) inclination angles.

Comparing the data with the simulations, we are unable to find a model configuration which matches the measured  $\Delta\Gamma_{\text{phase-rms}}$  or  $\Delta\Gamma_{\text{flux-rms}}$ , unless we choose  $0^\circ \leq \chi \leq 1^\circ$  (or  $179^\circ \leq \chi \leq 180^\circ$ ), an a priori unlikely orientation. However, we are able to match  $B_{\text{phase}}$  for a range of tilt angles  $5^\circ \leq \theta \leq 10^\circ$ , if we are prepared to tolerate a discrepancy of  $50^\circ$  in  $\Delta\Gamma_{\text{phase-rms}}$  and  $55^\circ$  in  $\Delta\Gamma_{\text{flux-rms}}$  between the data and the model. One can therefore draw two possible conclusions: either the star is precessing but our surface intensity map is too simplistic, or the source is not precessing. If we attribute the 12.2-d periodicity to precession, this implies an ellipticity of  $\epsilon \leq 3 \times 10^{-9}$ , a gravitational wave strain  $h_0 \leq 10^{-27}$ , and hence a signal-to-noise ratio of  $10^{-3}$  for initial LIGO and  $10^{-2}$  for advanced LIGO (for a coherent 120-day search). On the other hand, if the precession is damped by internal dissipation ( $\theta$  is small), or the precession period is much longer than the 37-day data span ( $\epsilon$  is small), some other mechanism must cause the observed modulation. In this scenario, we find  $\epsilon \cos \theta \leq 9.9 \times 10^{-10}$  and  $h_0 \leq 10 \times 10^{-27} \cos(\theta)^{-1}$ .

Although we face a negative result for this particular source, this chapter establishes a framework for analyzing modulations in X-ray flux from AMSPs for a range of geometrical configurations and surface intensity maps. We anticipate that the framework will be applied to other AMSPs in the future. Given the values of  $\epsilon$  inferred from the gravitational-wave stalling hypothesis (Bildsten 1998) and the theoretical models, e.g. of magnetic mountains (Payne & Melatos 2006; Vigelius & Melatos 2008), it is clear that long-term X-ray monitoring of AMSPs (over years) is essential for predicting, and then searching for, their gravitational wave signal.

---

Lyne et al. (2010) presented evidence that the periodic modulation seen in PSR B1828–11, thought to be the most concrete evidence of free precession to date, is due instead to timing noise caused by changes in the magnetic geometry of the pulsar magnetosphere. This effect is seen in six pulsars, in which the spin-down rate changes quasi-periodically, and is linked to changes in the pulse shape, pulse mode changing, nulling, and intermittency. [Lyne et al. (2010) appeared after this thesis was submitted.]

# 3 Designing a cross-correlation search for continuous-wave gravitational radiation from a neutron star in the supernova remnant SNR 1987A

## 3.1 Introduction

The Laser Interferometer Gravitational Wave Observatory (LIGO) achieved its design sensitivity during its fifth science run (S5). Analysis of S5 data is progressing well, with new upper limits being placed on the strength of various classes of burst sources (Abbott et al. 2009f), stochastic backgrounds (Giampanis 2008; Abbott et al. 2009b) and continuous-wave sources (Abbott et al. 2009a,c,g). In some cases, the LIGO limits on astrophysical parameters beat those inferred from electromagnetic astronomy, e.g. the maximum ellipticity and internal magnetic field strength of the Crab pulsar (Abbott et al. 2008b, 2009g).

Aspherical, isolated neutron stars constitute one promising class of continuous-wave source candidates (Ostriker & Gunn 1969). The origin of the semi-permanent quadrupole in these objects can be thermoelastic (Melatos 2000; Ushomirsky et al. 2000; Nayyar & Owen 2006; Haskell et al. 2008; Haskell 2008) or hydromagnetic (Bonazzola & Gourgoulhon 1996; Cutler 2002). A coherent search for 78 known radio pulsars was performed on S3 and S4 LIGO and GEO 600 data. Upper limits on the ellipticities of these pulsars were obtained, the smallest being  $\epsilon \leq 7.1 \times 10^{-7}$  for PSR J2124–3358 (Abbott et al. 2007f). More recently, a coherent search for 116 known pulsars was carried out using data from both the LIGO and Virgo detectors, placing an upper limit of  $\epsilon < 7.0 \times 10^{-8}$  for PSR J2124–3358. Young, isolated neutron stars are

arguably the strongest emitters of the class, because their quadrupoles have had less time to relax, e.g. viscoelastically or resistively.

The youngest isolated neutron star accessible to LIGO probably resides in the supernova remnant SNR 1987A. The coincident detection of neutrino bursts from the supernova by detectors all over the world confirmed the core-collapse event, strongly indicating the formation of a neutron star (Aglietta et al. 1987; Hirata et al. 1987; Bionta et al. 1987; Bahcall et al. 1987).<sup>1</sup> Constraints have been placed on the magnetic field strength, spin period, and other birth properties of the putative neutron star (Michel 1994; Ögelman & Alpar 2004); see Section 3.2 for details. However, searches for a pulsar in SNR 1987A have yielded no confirmed sightings; upper limits on its luminosity have been placed in the radio, optical and X-ray bands (Percival et al. 1995; Burrows et al. 2000; Manchester 2007). An unconfirmed detection of a transitory 467.5 Hz optical/infra-red pulsation in SNR 1987A was reported by Middleditch et al. (2000).

The likely existence of a young neutron star in SNR 1987A makes it a good target for gravitational wave searches (Piran & Nakamura 1988; Nakamura 1989). A coherent matched filtering search was carried out in 2003 with the TAMA 300 detector, searching  $1.2 \times 10^3$  hours of data from its first science run over a 1-Hz band centered on 934.9 Hz, assuming a spin-down range of  $(2-3) \times 10^{-10}$  Hz s<sup>-1</sup>. The search yielded an upper limit on the wave strain of  $5 \times 10^{-23}$  (Soida et al. 2003). An earlier matched filtering search was conducted using 10<sup>2</sup> hours of data taken in 1989 by the Garching prototype laser interferometer. The latter search was carried out over 4-Hz bands near 2 kHz and 4 kHz, did not include any spin-down parameters, and yielded an upper limit of  $9 \times 10^{-21}$  on the wave strain (Niebauer et al. 1993).

There are two main types of continuous-wave LIGO searches: coherent and semi-coherent. The former demand phase coherence between the signal and search template over the entire time series. Although sensitive, they are restricted to small observation times and parameter ranges as they are computationally intensive. Semi-coherent searches break the full time series into many small chunks, analyse each chunk coherently, then sum the results incoherently, trading off sensitivity for computational load. Santostasi et al. (2003) discussed the detectability of gravitational waves from SNR 1987A, estimating

---

<sup>1</sup>An unconfirmed correlation was also reported between data taken by the Mont Blanc and Kamioka neutrino detectors and gravitational wave detectors in Maryland and Rome (Amaldi et al. 1989; Galeotti et al. 2008; Dadykin & Ryazhskaya 2009). If confirmed, these observations are consistent with a weak neutrino pulsar operating briefly during the core-collapse event.

that a coherent search based on the Middleditch et al. (2000) spin parameters requires 30 days of integration time and at least  $10^{19}$  search templates covering just the frequency and its first derivative. In reality, the task is even more daunting, because such a young object spins down so rapidly, that five or six higher-order frequency derivatives must be searched in order to accurately track the gravitational wave phase. A Bayesian Markov Chain Monte Carlo method was proposed as an alternative to cover the parameter space efficiently (Umstätter et al. 2004, 2008). As yet, though, SNR 1987A has not been considered a feasible search target, because even Monte Carlo methods are too arduous. In this chapter, we show how to reduce the search space dramatically by assuming an astrophysically motivated phase model.

In this chapter, we discuss how to use a cross-correlation algorithm to search for periodic gravitational waves from a neutron star in SNR 1987A. The search is semi-coherent (Dhurandhar et al. 2008). The signal-to-noise ratio is enhanced by cross-correlating two data sets separated by an adjustable time lag, or two simultaneous data sets from different interferometers, thereby nullifying short-term timing noise (e.g. from rotational glitches). Variants of this method were used in searches for a cosmological stochastic background (Abbott et al. 2007b, 2009b) and for the low-mass X-ray binary Sco X-1 (Abbott et al. 2007e). In Section 3.2, we review the properties of SNR 1987A and its putative neutron star. Section 3.3 briefly describes the cross-correlation algorithm and the data format. We estimate the theoretical sensitivity of the search in Section 3.4. Section 3.5 describes an astrophysical model, which expresses the gravitational wave phase in terms of the initial spin, ellipticity, magnetic field, and electromagnetic braking index of the neutron star. We calculate the semi-coherent phase metric and the number of templates required for the search in the context of the astrophysical phase model. Given the computational resources available to us, we derive upper limits on the gravitational wave strain, ellipticity and magnetic field which can be placed on a neutron star in SNR 1987A with a cross-correlation search. Finally, Section 3.7 summarises the results.

## 3.2 A young neutron star in SNR 1987A

SNR 1987A is the remnant of a Type II core-collapse supernova which occurred in February 1987, 51.4 kpc away in the Large Magellanic Cloud ( $\alpha = 5\text{h } 35\text{m } 28.03\text{s}$ ,  $\delta = -69^\circ 16' 11.79''$ ) (see reviews by Panagia 2008 and in Immler et

al. 2007). Its progenitor was the blue supergiant Sk 1 (Panagia 1987; Gilmozzi et al. 1987; Barkat & Wheeler 1988; Woosley et al. 2002). The colour of the progenitor, as well as the origin of the complex three-ring nebula in the remnant, are still unexplained. Detailed simulations of the evolutionary history of Sk 1, performed by Podsiadlowski et al. (2007), support the theory that two massive stars merged to form an oversized  $20M_{\odot}$  red supergiant  $2 \times 10^5$  years before the supernova, which eventually shrank as its envelope evaporated (e.g. Podsiadlowski & Joss 1989; Podsiadlowski et al. 1990). An alternative theory suggests that Sk 1 was instead a single 18–20  $M_{\odot}$  red supergiant which evolved into a blue supergiant via wind-driven mass loss (e.g. Woosley 1988; Saio et al. 1988; Sugerman et al. 2005).

There is strong evidence for the existence of a neutron star in SNR 1987A. The progenitor mass range required to produce Type II supernovae, 10–25  $M_{\odot}$ , which includes the above evolutionary scenarios, is the same range required to produce neutron star remnants (Woosley et al. 2002; Heger et al. 2003). The secure neutrino detections mentioned in Section 3.1 support this conclusion. Although there have been no confirmed pulsar detections, numerous searches have placed upper limits on the flux and luminosity at radio ( $< 115 \mu\text{Jy}$  at 1390 MHz, Manchester 2007), optical/near-UV ( $< 8 \times 10^{33} \text{ ergs s}^{-1}$ , Graves & et al. 2005), and soft X-ray ( $< 2.3 \times 10^{34} \text{ erg s}^{-1}$ , Burrows et al. 2000) wavelengths. Middleditch et al. (2000) reported finding an optical pulsar in SNR 1987A with a frequency of 467.5 Hz, modulated sinusoidally with a  $\sim 1$ -ks period, consistent with precession for an ellipticity of  $\epsilon \sim 10^{-6}$ . However, the pulsations were reported to have disappeared after 1996 (Middleditch et al. 2000) and were never confirmed independently. It has also been suggested that the neutron star formed from the supernova may have subsequently collapsed to form a black hole (Chevalier 1992). However, this scenario is unlikely as the initial mass of the progenitor was well below the  $\approx 40M_{\odot}$  required to form a black hole (Woosley et al. 2002; Heger et al. 2003).

There are several possible reasons why a pulsar in SNR 1987A has not yet been detected. If its spin period is greater than 0.1 s, it would not be bright enough to be detectable in the optical band (Pacini & Salvati 1987; Manchester 2007). If the radio emission is incoherent or the emission region is patchy, the pulses may have been missed, even if the beam width is as wide as is typical for young pulsars (Manchester 2007). Shternin & Yakovlev (2008) argued that, although the neutron star’s theoretical X-ray luminosity exceeds the observational upper limits by a factor of 20–100, the current upper limits still allow for concealment behind an opaque shell formed by fallback (Woosley

& Weaver 1995). However, simulations by Fryer et al. (1999) suggest that, once fallback ceases, the accreted material cools, leaving no obscuring atmosphere.

Another possible reason why a pulsar has not yet been detected is that its magnetic field is too weak. The weak-field theory is supported by theoretical models, in which the field grows only after the neutron star is formed and can take up to  $10^3$  years to develop (e.g. Blandford & Romani 1988; Reisenegger 2003). A growth model for SNR 1987A was proposed by Michel (1994), in which the magnetic field of a millisecond pulsar intensifies from  $10^{10}$  G at birth to  $\sim 10^{12}$  G after several hundred years (exponential and linear growth were considered, yielding growth times of  $\sim 0.3$ – $0.7$  kyr), before the pulsar has time to spin down significantly. In an alternative model, the neutron star is born with a strong magnetic field, which is amplified during the first few seconds of its life by dynamo action (e.g. Duncan & Thompson 1992; Bonanno et al. 2005). Assuming this model, measurements of the known spin periods of isolated radio pulsars imply a distribution of birth magnetic field strengths between  $10^{12}$  G and  $10^{13}$  G (Arzoumanian et al. 2002; Faucher-Giguère & Kaspi 2006). Several birth scenarios for the pulsar in SNR 1987A were considered by Ögelman & Alpar (2004) in this context, who concluded that the maximum magnetic dipole moment is  $< 1.1 \times 10^{26}$  G cm<sup>3</sup>,  $2.5 \times 10^{28}$  G cm<sup>3</sup>, and  $2.5 \times 10^{30}$  G cm<sup>3</sup> for birth periods of 2 ms, 30 ms, and 0.3 s respectively. However, the dynamo model also accommodates a magnetar in SNR 1987A, with magnetic dipole moment  $> 2.4 \times 10^{34}$  G cm<sup>3</sup>, regardless of the initial spin period (Ögelman & Alpar 2004).

Estimates of the birth spin of the pulsar in SNR 1987A are more uncertain. Simulations of the bounce and post-bounce phases of core collapse were performed by Ott et al. (2006) to determine the correlation between progenitor properties and birth spin. These authors found proto-neutron star spin periods of between 4.7–140 ms, proportional to the progenitor’s spin period. A Monte Carlo population synthesis study using known velocity distributions (Arzoumanian et al. 2002) favoured shorter millisecond periods, but a similar population study by Faucher-Giguère & Kaspi (2006) argued that the birth spin periods could be as high as several hundred milliseconds. Faint, non-pulsed X-ray emission from SNR 1987A was first observed four months after the supernova and decreased steadily in 1989 (Dotani et al. 1987; Inoue et al. 1991), leading to the suggestion that a neutron star could be powering a plerion that is partially obscured by a fragmented supernova envelope. Bandiera et al. (1988) modelled the X-ray spectrum from a nebula containing a central pulsar, with a magnetic field of  $10^{12}$  G and an expansion rate of  $5 \times 10^8$  cm

$s^{-1}$ . The authors found a fit to the SNR 1987A data for a pulsar spin period of 18 ms.

### 3.3 The cross-correlation algorithm

In this section, we briefly summarise the cross-correlation method described in Dhurandhar et al. (2008), a semi-coherent search algorithm designed specifically to search for continuous-wave gravitational radiation. It operates on Short Fourier Transforms (SFTs) of data segments of length  $\Delta T = 30$  min, whose duration is chosen to minimise the Doppler effects due to Earth's rotation. In each SFT, the  $k$ th frequency bin corresponds to the frequency  $\nu_k = k/\Delta T$  for  $0 \leq k \leq N/2$  and  $\nu_k = (k - N)/\Delta T$  for  $N/2 \leq k \leq N - 1$ , where  $N$  is the total number of frequency bins in the SFT.

The output  $x(t)$  of a detector is the sum of the instantaneous noise,  $n(t)$ , and the gravitational wave signal,  $h(t)$ . The noise is assumed to be zero mean, stationary, and Gaussian. Its power is characterised by  $S_n(\nu)$ , the single-sided power spectral density (i.e. the frequency-dependent noise floor) in the following way:

$$\langle \tilde{n}(\nu)^* \tilde{n}(\nu') \rangle = \frac{1}{2} S_n(\nu) \delta(\nu - \nu'), \quad (3.1)$$

where  $*$  denotes complex conjugation. Therefore, in the low signal limit ( $|h(t)| \ll |n(t)|$ ), the power in the  $k$ -th frequency bin of SFT  $I$  can be approximated by

$$\langle |\tilde{x}_{k,I}|^2 \rangle \approx \frac{\Delta T}{2} S_n(\nu_k), \quad (3.2)$$

where we apply the finite time approximation to the delta function in (3.1), i.e.  $\delta_{\Delta T}(\nu) = \sin(\pi\nu\Delta T)/(\pi\nu)$ .

In the cross-correlation algorithm, SFTs are paired according to some criterion (e.g. time lag or interferometer combination) and multiplied to form the raw cross-correlation variable

$$Y_{k,IJ} = \frac{\tilde{x}_{k,I}^* \tilde{x}_{k',J}}{(\Delta T)^2}, \quad (3.3)$$

where  $I$  and  $J$  index the SFTs in the pair. The gravitational wave signal is assumed to be concentrated in a single frequency bin in each SFT (because  $\Delta T \ll \nu/\dot{\nu}$  due to sidereal or intrinsic effects), whose index is denoted by  $k$  or  $k'$ . The frequency bins in the two SFTs are not necessarily the same; they are related by the time lag between the pair and between interferometers, as well as spin-down and Doppler effects. For an isolated source, the instantaneous

frequency at time  $t$  is given by

$$\nu(t) = \hat{\nu}(t) + \hat{\nu}(t) \frac{\mathbf{v} \cdot \mathbf{n}}{c}, \quad (3.4)$$

where  $\hat{\nu}(t)$  is the instantaneous frequency in the rest frame of the source,  $\mathbf{v}$  is the detector velocity relative to the source,  $\mathbf{n}$  is the position vector pointing from the detector to the source, and  $c$  is the speed of light. The instantaneous signal frequencies in SFTs  $I$  and  $J$ ,  $\nu_I$  and  $\nu_J$ , are calculated at the times corresponding to the midpoints of the SFTs,  $T_I$  and  $T_J$ . The frequency bin  $k'$  is therefore shifted from  $k$  by an amount  $\Delta T \delta \nu_{IJ}$ , with  $\delta \nu_{IJ} = \nu_J - \nu_I$  (Dhurandhar et al. 2008). For convenience, we now drop the subscripts  $k, k'$ .

In the low signal limit,  $Y_{IJ}$  is a random, complex variable. The cross-correlation statistic comprises a weighted sum of  $\mathcal{Y}_{IJ}$  over all pairs  $IJ$ .  $\mathcal{Y}_{IJ}$  has variance  $\sigma_{IJ}^2 = S_n^{(I)}(\nu_I) S_n^{(J)}(\nu_J) / (4\Delta T^2)$ , where  $S_n^{(I)}(\nu_I)$  is the power spectral density of SFT  $I$  at frequency  $\nu_I$ , and  $S_n^{(J)}(\nu_J)$  is the power spectral density of SFT  $J$  at frequency  $\nu_J$ .

The parameters describing the amplitude and the phase of the signal are contained within the signal cross-correlation function  $\tilde{G}_{IJ}$ , defined as

$$\begin{aligned} \tilde{G}_{IJ} = & \frac{1}{4} e^{-i\Delta\Phi_{IJ}} e^{-i\pi\Delta T[\nu_I(T_I) - \nu_J(T_J)]} [F_{I+} F_{J+} \mathcal{A}_+^2 + F_{I\times} F_{J\times} \mathcal{A}_\times^2 \\ & - i(F_{I+} F_{J\times} - F_{I\times} F_{J+}) \mathcal{A}_+ \mathcal{A}_\times], \end{aligned} \quad (3.5)$$

with  $\Delta\Phi_{IJ} = \Phi_I(T_I) - \Phi_J(T_J)$ .  $\Phi_I(T_I)$  and  $\nu_I(T_I)$  are the phase and frequency at time  $T_I$ , whereas  $\Phi_J(T_J)$  and  $\nu_J(T_J)$  are evaluated at time  $T_J$ . Note that there is an error in the definition of  $\Delta\Phi_{IJ}$  in Dhurandhar et al. (2008), in which the authors assume  $T_I = T_J$ , and the term  $e^{-i\pi\Delta T[\nu_I(T_I) - \nu_J(T_J)]}$  is left out. We provide a full derivation of  $\tilde{G}_{IJ}$  in Chapter 4. The phase factors are determined by the astrophysical phase model described in Section 3.5.

The terms in square brackets in (3.5) depend on the polarization angle  $\psi$ , and the inclination angle  $\iota$  between  $\mathbf{n}$  and the rotation axis of the pulsar, in the following way:

$$\mathcal{A}_+ = \frac{1 + \cos^2 \iota}{2}, \quad (3.6)$$

$$\mathcal{A}_\times = \cos \iota, \quad (3.7)$$

$$F_+(t; \mathbf{n}, \psi) = a(t; \mathbf{n}) \cos 2\psi + b(t; \mathbf{n}) \sin 2\psi, \quad (3.8)$$

$$F_\times(t; \mathbf{n}, \psi) = b(t; \mathbf{n}) \cos 2\psi - a(t; \mathbf{n}) \sin 2\psi, \quad (3.9)$$

where  $a(t; \mathbf{n})$  and  $b(t; \mathbf{n})$  are the detector response functions for a given sky

position, and are defined in equations (12) and (13) of Jaranowski et al. (1998). The gravitational wave strain tensor is

$$\overleftrightarrow{h}(t) = h_0 \mathcal{A}_+ \cos \Phi(t) \overleftrightarrow{e}_+ + h_0 \mathcal{A}_\times \sin \Phi(t) \overleftrightarrow{e}_\times \quad (3.10)$$

where  $h_0$  is the gravitational wave strain, and  $\overleftrightarrow{e}_{+, \times}$  are the basis tensors for the + and  $\times$  polarizations in the transverse-traceless gauge.

In principle, one should search over the unknowns  $\cos \iota$  and  $\psi$ , but this adds to the already sizeable computational burden. Accordingly, it is customary to average over  $\cos \iota$  and  $\psi$  when computing  $\tilde{\mathcal{G}}_{IJ}$ , with

$$\langle \tilde{\mathcal{G}}_{IJ} \rangle_{\cos \iota, \psi} = \frac{1}{10} \exp^{-i\Delta\Phi_{IJ}} e^{-i\pi\Delta T[\nu_I(T_I) - \nu_J(T_J)]} (a_I a_J + b_I b_J), \quad (3.11)$$

where  $a_{I,J} = a(T_{I,J}; \mathbf{n})$  and  $b_{I,J} = b(T_{I,J}; \mathbf{n})$ . Once the first-pass search is complete, a follow-up search on any promising candidates can then be performed, which searches explicitly over  $\cos \iota$  and  $\psi$ . Preliminary Monte Carlo tests indicate that the detection statistic resulting from (3.11) is approximately 10–15% smaller than if the exact  $\cos \iota$  and  $\psi$  values are used [see Chapter 4 for a detailed comparison].

The cross-correlation detection statistic is a weighted sum of  $Y_{IJ}$  over all pairs, and is given by

$$\rho = \sum_{IJ} (u_{IJ} Y_{IJ} + u_{IJ}^* Y_{IJ}^*), \quad (3.12)$$

where the weights are defined by

$$u_{IJ} = \frac{\tilde{\mathcal{G}}_{IJ}^*}{\sigma_{IJ}^2}. \quad (3.13)$$

For each frequency and sky position that is searched, we obtain *one* real value of  $\rho$ , which is a sum of the Fourier power from all the pairs. Ignoring self-correlations (i.e. no SFT is paired with itself), the mean of  $\rho$  is given by  $\mu_\rho = h_0^2 \sum_{IJ} |u_{IJ}|^2 \sigma_{IJ}^2$ . In the low signal limit, the variance of  $\rho$  is  $\sigma_\rho^2 = 2 \sum_{IJ} |u_{IJ}|^2 \sigma_{IJ}^2$ . In the presence of a strong signal, and if self-correlations are included,  $\mu_\rho$  and  $\sigma_\rho^2$  scale as  $h_0^2$  (Dhurandhar et al. 2008). We provide a detailed derivation of how  $\mu_\rho$  and  $\sigma_\rho$  depend on  $h_0$  in Chapter 4.

## 3.4 Sensitivity

### 3.4.1 Detection threshold

Detection candidates are selected if they exceed a threshold value,  $\rho_{\text{th}}$ . For a given false alarm rate  $\alpha$ , this threshold is given by (Dhurandhar et al. 2008)

$$\rho_{\text{th}} = 2^{1/2} \sigma_\rho \text{erfc}^{-1}(2\alpha/N), \quad (3.14)$$

where  $\text{erfc}$  is the complementary error function, and  $N$  is the number of search templates used. In the presence of a signal, the detection rate for events with  $\rho > \rho_{\text{th}}$  is given by

$$\gamma = \frac{1}{2} \text{erfc} \left( \frac{\rho_{\text{th}} - \mu_\rho}{\sqrt{2} \sigma_\rho} \right). \quad (3.15)$$

As  $\mu_\rho \propto h_0^2$ , one can calculate the lowest gravitational wave strain that is detectable by the search to be (Dhurandhar et al. 2008)

$$h_{\text{th}}(\nu) = \frac{\mathcal{S}^{1/2}}{\sqrt{2} \langle |\tilde{\mathcal{G}}_{IJ}|^2 \rangle^{1/4} N_{\text{pairs}}^{1/4}} \left[ \frac{S_n(\nu)}{\Delta T} \right]^{1/2}. \quad (3.16)$$

In (3.16), we define  $\mathcal{S} = \text{erfc}^{-1}(2\alpha) + \text{erfc}^{-1}(2\beta)$ ,  $\beta$  is the false dismissal rate,  $\langle |\tilde{\mathcal{G}}_{IJ}|^2 \rangle$  is the mean-square of the signal cross-correlation function defined in (3.5),  $N_{\text{pairs}}$  is the number of SFT pairs, and  $S_n(\nu)$  is the single-sided power spectral density of the interferometers (assumed to be identical).

One can estimate  $\langle |\tilde{\mathcal{G}}_{IJ}|^2 \rangle^{1/4}$  theoretically for the special case where  $T_I = T_J$  and  $\tilde{\mathcal{G}}_{IJ}$  is averaged over  $\cos \iota$ ,  $\psi$ , and sidereal time. In this case, the primary contribution to  $\Delta\Phi_{IJ}$  is the term  $[\mathbf{r}(T_I) - \mathbf{r}(T_J)] \cdot \mathbf{n}/c$ , where  $\mathbf{r}(t)$  is the position of the detector at time  $t$  in the frame of the solar system barycentre. Under these assumptions, equation (3.11) can be expressed in terms of the overlap reduction function (Whelan 2006), which depends only on  $\nu$ ,  $\alpha$ , and  $\delta$ . For SNR 1987A, we have  $(\alpha, \delta) = (1.31931 \text{ rad}, -1.20899 \text{ rad})$ , and hence  $\langle |\tilde{\mathcal{G}}_{IJ}|^2 \rangle^{-1/4} = 5.2312$ . Assuming  $\alpha = \beta = 0.1$ ,  $\Delta T = 1800 \text{ s}$ , and  $N_{\text{pairs}} = 10^5$ , equation (3.16) gives

$$h_{\text{th}}(\nu) = 7.48 \times 10^{-3} \left[ \frac{S_n(\nu)}{\text{Hz}^{-1}} \right]^{1/2}. \quad (3.17)$$

Figure 3.1 is a graph of  $h_{\text{th}}$  as a function of  $\nu$ . The values of  $S_n(\nu)$  are based on LIGO's S5 noise characteristics.<sup>2</sup> The S5 run began in November 2005 and accumulated a year's worth of triple coincidence data. For a signal from SNR

<sup>2</sup>Available at [http://www.ligo.caltech.edu/jzweizig/distribution/LSC\\_Data](http://www.ligo.caltech.edu/jzweizig/distribution/LSC_Data)

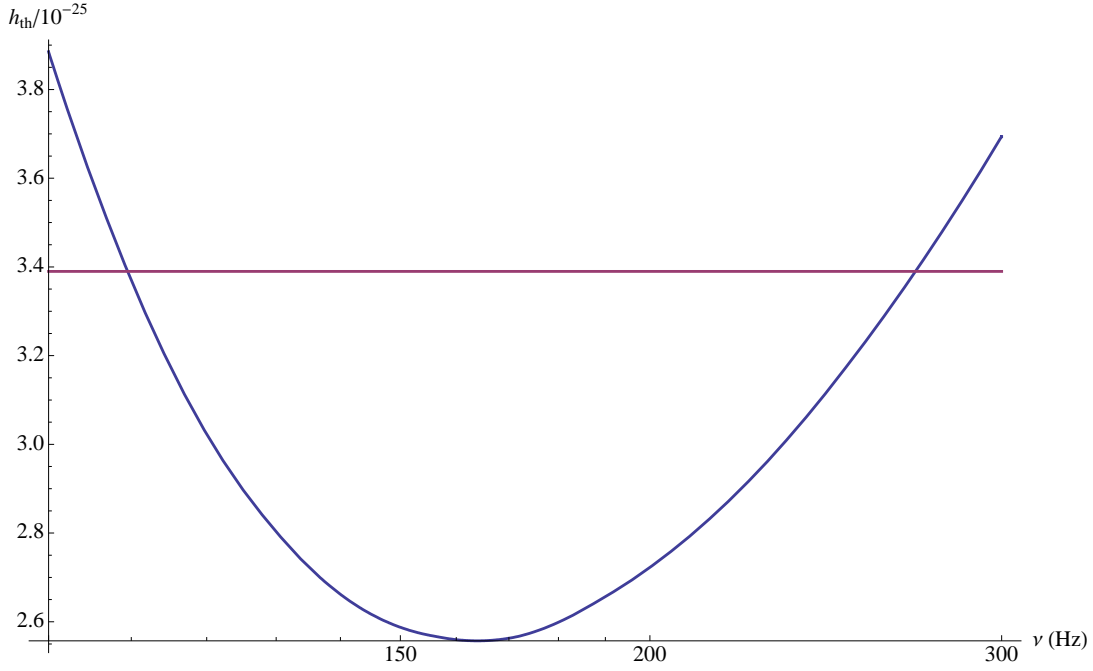


**Figure 3.1:** Theoretical sensitivity of the cross-correlation search for SNR 1987A as a function of gravitational wave frequency (blue curve). The horizontal red line shows the indirect, age-based limit.

1987A to be detectable, we must have  $h_{\text{th}} \leq h_0$ .

### 3.4.2 Minimum ellipticity and indirect, age-based limit

The deformation of a neutron star is parameterised by its ellipticity  $\epsilon$ . The gravitational wave strain at Earth emitted by a biaxial neutron star is

$$h_0 = \frac{4\pi^2 G I \epsilon \nu^2}{c^4 D} \quad (3.18)$$

where  $G$  is Newton's gravitational constant,  $c$  is the speed of light,  $I$  is the moment of inertia,  $D$  is the distance to the source, and  $\nu$  is the gravitational wave frequency, assumed to be twice the spin frequency (Jaranowski et al. 1998).

An upper limit on  $h_0$  can be derived from existing electromagnetic data by assuming all the observed spin down comes from the gravitational wave torque, i.e. the observed frequency derivative  $\dot{\nu}$  satisfies  $\dot{\nu} = -(32\pi^4 G \epsilon^2 I \nu^5)/(5c^5)$  (Wette et al. 2008). Combining this with (3.18) to eliminate  $\epsilon$  gives

$$h_0 \leq \frac{1}{D} \left( \frac{5GI|\dot{\nu}|}{2c^3\nu} \right)^{1/2}. \quad (3.19)$$

Hence, for SNR 1987A to be detectable (i.e.  $h_{\text{th}} \leq h_0$ ), we require

$$h_{\text{th}}(\nu) \leq 1.66 \times 10^{-20} \left( \frac{|\dot{\nu}|}{\nu} \right)^{1/2} \left( \frac{D}{51.4 \text{kpc}} \right)^{-1} \quad (3.20)$$

Unfortunately, without having observed any pulsations from SNR 1987A, it is impossible to determine  $\nu$  or  $|\dot{\nu}|$  a priori. Instead, we note that  $\dot{\nu}$  can be re-expressed in terms of the characteristic age of the source,  $\tau_c = \nu/(4|\dot{\nu}|)$ , assuming that  $\nu$  today is much less than  $\nu$  at birth. The factor 4 arises if one assumes the gravitational radiation dominates electromagnetic spin down, in order to remain consistent with (3.19); in reality, electromagnetic spin down is expected to dominate, with  $\tau_c = \nu/(2|\dot{\nu}|)$ . Equation (3.20) then reduces to

$$h_{\text{th}}(\nu) \leq 3.39 \times 10^{-25} \left( \frac{\tau_c}{19 \text{yr}} \right)^{-1/2} \left( \frac{D}{51.4 \text{kpc}} \right)^{-1}. \quad (3.21)$$

The right-hand side of (3.21) is graphed as a horizontal dashed line in Figure 3.1. The detectability condition (3.21) is then satisfied for spins in the range  $120 \text{ Hz} \lesssim \nu \lesssim 250 \text{ Hz}$ . Note that we have chosen  $\tau_c = 19 \text{ yr}$ , the age of SNR 1987A in 2006 when the S5 search began.

### 3.5 An astrophysical model for the gravitational wave phase

All continuous wave searches to date have used the standard model for the gravitational wave phase, described in terms of a Taylor expansion involving spin frequency derivatives (Jaranowski et al. 1998). For a young object like SNR 1987A, which spins down rapidly, it is not computationally feasible to search over the six or more frequency derivatives typically needed to track the phase accurately. In this section, we present an alternative model for the gravitational wave phase, stated in terms of astrophysical parameters (i.e. the magnetic field strength and the neutron star ellipticity) instead of spin frequency derivatives. It tracks the phase exactly using four parameters.

The phase of a slowly evolving gravitational wave signal,

$$\Phi(t) = \Phi(t_0) + 2\pi \int_{t_0}^t dt \nu(t), \quad (3.22)$$

can be approximated by the Taylor expansion (Jaranowski et al. 1998)

$$\Phi(t) = \Phi(t_0) + 2\pi \sum_{k=0}^s \nu^{(k)} \frac{t^{k+1}}{(k+1)!} + \frac{2\pi \mathbf{n} \cdot \mathbf{r}(t_0)}{c} \sum_{k=0}^s \nu^{(k)} \frac{t^k}{k!} \quad (3.23)$$

where  $\nu^{(k)}$  is the  $k$ -th derivative of the gravitational wave frequency at time  $t_0$ , and  $s$  is the number of spin-down parameters required to achieve a given accuracy. The computational cost of using (3.23) is substantial for rapidly decelerating objects. For a maximum allowable phase error of one cycle, the maximum bin size in the  $k$ -th derivative is  $\nu^{(k)}$  is  $\Delta\nu^{(k)} = (k+1)!/T_{\text{lag}}^{k+1}$ , implying  $N_k \approx \nu^{(k)}/\Delta\nu^{(k)}$  templates in that derivative and  $N_{\text{total}} = \prod_{k=0}^s N_k$  templates overall. We discuss this matter further in Section 3.6.2.

To improve on the above situation, we recognize that  $\dot{\nu}$  for an isolated neutron star is the sum of gravitational-wave and electromagnetic torque contributions:

$$\dot{\nu} = -\frac{32\pi^4 G \epsilon^2 I \nu^5}{5c^5} - \frac{2\pi^3 R_\star^6 B^2 \nu^n}{3\mu_0 I c^3} \left(\frac{\pi R_\star}{c}\right)^{n-3} \quad (3.24)$$

$$= -Q'_1 \nu^5 - Q'_2 \nu^n, \quad (3.25)$$

where  $R_\star$  is the neutron star radius,  $B$  is the polar magnetic field,  $n$  is the electromagnetic braking index (theoretically equal to 3, but could be as low as 1.8; Melatos 1997; Palomba 2005). Assuming that the electromagnetic torque is proportional to a power of  $\nu$ , then  $\nu$  must enter the torque in the combination  $R_\star \nu/c$ , (i.e. the ratio of  $R_\star$  to the characteristic lever arm, the light cylinder distance,  $c/2\pi\nu$ ) on dimensional grounds. In terms of an arbitrary reference frequency,  $\nu_{\text{ref}}$ , we write  $\dot{\nu} = -Q_1 (\nu/\nu_{\text{ref}})^5 - Q_2 (\nu/\nu_{\text{ref}})^n$ , with  $Q_1 = Q'_1 \nu_{\text{ref}}^5$  and  $Q_2 = Q'_2 \nu_{\text{ref}}^n$ . Throughout this chapter, we set  $\nu_{\text{ref}} = 1$  Hz for simplicity.

There may, of course, be other torques acting on a newly born neutron star. For example, nonlinear r-mode instabilities can emit a significant amount of gravitational radiation under certain conditions (Owen et al. 1998). If there is a rapidly rotating pulsar with  $B \leq 10^{11}$  G in SNR 1987A, its instability time scale (27 years) would exceed its age, and the gravitational radiation from the instabilities alone should be detectable by Advanced LIGO (Brink et al. 2004; Bondarescu et al. 2009). However, for the purposes of our search, we assume that the spin down is described by (3.25). An equally serious issue is that  $n$  may change over the 1 yr integration period, although in (3.25), we assume that  $n$  is constant. Young pulsars have  $n < 3$ , and it can be argued that  $n$  approaches 3 over the spin-down time-scale (Melatos 1997). In this search,

we maintain the assumption of constant  $n$ . However, it is possible to extend (3.25) to include time-dependent  $n$  in future searches. We also note that, like the Taylor expansion model, this model does not take into account glitches or timing noise, which may occur in young pulsars. By cross-correlating SFTs up to a year apart, however, the effects of short-term noise are reduced. Again, it is possible to extend (3.25) to include long-term timing noise in the future. We aim to exclude the simplest astrophysical model while recognizing it covers only a small fraction of the total parameter space.

When implementing the search, instead of stepping through a grid of frequency derivatives, we search instead over  $\nu, Q_1, Q_2$ , and  $n$ . This reduces the number of parameters and allows one to track the phase more accurately for a given computational cost, as errors stemming from incorrect choices of  $(\nu, Q_1, Q_2, n)$  grow more slowly with observation time than errors stemming from higher-order frequency derivatives. The improvement is quantified in Section 3.6.2.

### 3.5.1 Historical spin down

We can use the possible spin histories of a source like SNR 1987A with a known age to constrain the invisible values of  $(\nu, Q_1, Q_2, n)$  today and hence the maximum amount of phase evolution to be expected during a LIGO integration. In the simplest situation, where the current spin frequency  $\nu$  is much smaller than the *birth* frequency  $\nu_b$ , the characteristic age  $\tau_c \approx -\nu / [(\langle n \rangle - 1) \dot{\nu}]$  closely approximates the true age irrespective of  $\nu_b$ , where  $\langle n \rangle$  is the mean braking index, averaged over the time since birth. Under these conditions, a source with unknown  $\nu$  and  $\dot{\nu}$  lies on a line of slope  $-\tau_c (\langle n \rangle - 1)$  in the  $\nu$ - $\dot{\nu}$  plane. This is not necessarily true for SNR 1987A, which was only 19 years old at the start of the S5 search. Accordingly, we take a different approach and map out the regions in the  $\nu$ - $\dot{\nu}$  plane which can be reached from  $\nu_b$  by electromagnetic-plus-gravitational-wave spin down and physically sensible choices of  $\epsilon, B$  and  $n$ .

Figure 3.2 shows the range of possible  $\nu$  and  $\dot{\nu}$  values at  $t = 19$  yr obtained by solving (3.25) for  $10^{-6} \leq \epsilon \leq 10^{-3}$ ,  $10^{11.5} \leq B \leq 10^{13}$  G and  $0.1 \text{ kHz} \leq \nu_b \leq 1.2 \text{ kHz}$ . We consider values of  $\nu_b$  spanning the LIGO band, and the values of  $B$  considered cover the expected range for newborn isolated radio pulsars (Arzoumanian et al. 2002; Faucher-Giguère & Kaspi 2006). As for the range of  $\epsilon$ , we choose values which are realistic (e.g. Owen 2005), yet large enough to produce a detectable gravitational wave signal. For reference, we

plot the search sensitivity (black curve in the  $\nu$ - $\dot{\nu}$  plane) obtained from (3.17). According to (3.17), the search is only sensitive to combinations of  $\nu$  and  $\dot{\nu}$  above the black line. The conservative limits set by the characteristic age are plotted as cyan lines. The lines correspond to  $\langle n \rangle = 1.8$  (top),  $\langle n \rangle = 3$  (middle) and  $\langle n \rangle = 5$  (bottom). For a given value of  $\langle n \rangle$ , an object lies on the line for  $\nu \ll \nu_b$ , and below the lines for  $\nu \lesssim \nu_b$ , but never above the line.

The blue, red and purple boxes contain combinations of  $(\nu, \dot{\nu})$  that can be reached for various choices of  $\epsilon$ ,  $B$ ,  $n$ , and  $\nu_b$ . The blue box covers the region in which  $B \leq 10^{11.5}$  G and  $n = 3$ , and the gravitational wave torque ( $Q_1$ ) dominates, i.e.  $\dot{\nu}_{\text{GW}} \gg \dot{\nu}_{\text{EM}}$ , where the subscripts EM and GW denote the electromagnetic and gravitational wave components of the spin down respectively. The red box covers the region in which the electromagnetic torque ( $Q_2$ ) dominates, with  $B = 10^{13}$  G and  $n = 3$ . The purple box also shows a region in which the  $Q_2$  term dominates, where we have chosen  $B = 10^{13}$  G and  $n = 2.3$ . As a rule of thumb,  $\epsilon$  determines the size of the box along the  $\nu$ -axis, and  $\nu_b$  determines the size of the box along the  $\dot{\nu}$ -axis.

Let us first investigate what happens to the blue box when we vary the minimum and maximum ellipticity,  $\epsilon_{\text{min}}$  and  $\epsilon_{\text{max}}$ . The  $Q_1$  term dominates in the region bounded by the blue box. The absolute value of the  $RQ$  slope increases as  $\epsilon_{\text{min}}$  decreases, shrinking the range of  $\dot{\nu}$ . The curve  $PQ$  shifts to the left as  $\epsilon_{\text{max}}$  increases, increasing  $|\dot{\nu}|$ , and hence lowering  $\nu$ .

Let us now see what happens when we vary the minimum and maximum magnetic field,  $B_{\text{min}}$  and  $B_{\text{max}}$ . The absolute value of the  $RS$  slope decreases as  $B_{\text{min}}$  increases, stretching the box sideways as we retreat from the gravitational-wave dominated limit. The blue box is always bounded above by the  $\langle n \rangle = 5$  age line. It shrinks, and flattens as the role of  $Q_1$  diminishes.

We now discuss the purple and red boxes in which  $Q_2$  dominates. The region bounded by the purple box has  $B = 10^{13}$  G, and  $n = 2.3$ , whereas the red box has the same  $B$ , but  $n = 3$ . Reducing  $n$  increases the spin-down rate by a factor of  $(\pi R_\star/c)^{n-3}$ . Hence, for the same  $\epsilon$  and  $B$ , the purple box covers a smaller range of  $\nu$  than the red box. Both are considerably smaller than the blue box for the same range of  $\epsilon$  and  $\nu_b$ . Again, if  $\epsilon_{\text{max}}$  increases, the purple and red boxes expand downwards. In Figure 3.2, we choose to plot the purple box with  $n = 2.3$  because it lies partially within the sensitivity range of the search. Importantly,  $\nu$  and  $\dot{\nu}$  end up outside the search sensitivity range for  $n < 2.3$  or  $B > 10^{13}$  G, restricting the range of astrophysical birth scenarios that our search is sensitive to.

The range of  $\nu$  covered in the  $Q_2$ -dominated limit is sensitive to  $B$ . In Figure

3.3, we show explicitly how varying  $B$  affects  $\nu, \dot{\nu}$ . We plot eight red boxes, for  $10^{11} \text{ G}$  (largest box)  $\leq B \leq 10^{14.5} \text{ G}$  (smallest box), and  $n = 3$ . As  $B$  increases, the red boxes shift to the left. For  $B \geq 5 \times 10^{13} \text{ G}$ , the box falls out of the sensitivity range of the search. Also, the boxes shrink as  $B_{\text{max}}$  increases. This happens because as  $B$  increases,  $\dot{\nu}_{\text{EM}}$  increases. For  $B \gtrsim 10^{14} \text{ G}$ , we find  $\nu \ll \nu_b$  after 19 years, and the boxes end up on the  $\langle n \rangle = 3$  line. All the red boxes are bounded above by the  $\langle n \rangle = 3$  age line.

Figures 3.2 and 3.3 provide constraints on the detectable range of  $\epsilon, B, n$ , over a broad range of  $\nu_b$ . We conclude that, in preparing to select the search templates, it is sensible to consider the parameter range  $10^{-5} \geq \epsilon, B \leq 10^{13} \text{ G}, 2.3 \leq n \leq 5$ . A more detailed breakdown of the detectable and computationally feasible parameter ranges is presented in Section 3.6.2. Note that even though the particular boxes drawn as examples in Figures 3.2 and 3.3 do not cover the entire region between the sensitivity curve and the  $\langle n \rangle = 1.8$  line, one can potentially reach any point in that region with some combination of  $n, \epsilon$  and  $B$ . Also, each  $(\nu, \dot{\nu})$  pair in the figures can be reached by an infinite set of combinations  $(\epsilon, B, n$  and  $\nu_b)$ . However, there are combinations of  $\nu$  and  $\dot{\nu}$  which are allowed in principle by age-based indirect limits but which cannot be reached from  $\nu_b$  with realistic choices of  $\epsilon, B$ , and  $n$ .

## 3.6 Template spacing

The cross-correlation search for SNR 1987A is computationally limited rather than sensitivity limited over much of the parameter space in Figures 3.2 and 3.3. Therefore, the placement of templates is crucial. If the template grid is too coarse, the risk of missing the signal increases; if it is too fine, time is wasted searching redundant templates. In order to compute the optimal spacing, we construct a phase metric (Balasubramanian et al. 1996; Owen 1996) which computes the signal-to-noise ratio as a function of template spacing along each axis of the four-dimensional parameter space  $(\nu, \epsilon, B, n)$ . The coherent phase metric for the conventional Taylor-expansion phase model is widely used in LIGO in both coherent and semi-coherent searches (Brady & Creighton 2000; Prix 2007; Wette et al. 2008), although its semi-coherent form has not been fully investigated. In this section, we derive the semi-coherent phase metric for the astrophysical phase model defined by integrating (3.25). We also estimate the range of detectable spin-down values as well as magnetic field, ellipticity and braking index values given a computationally feasible number of templates.

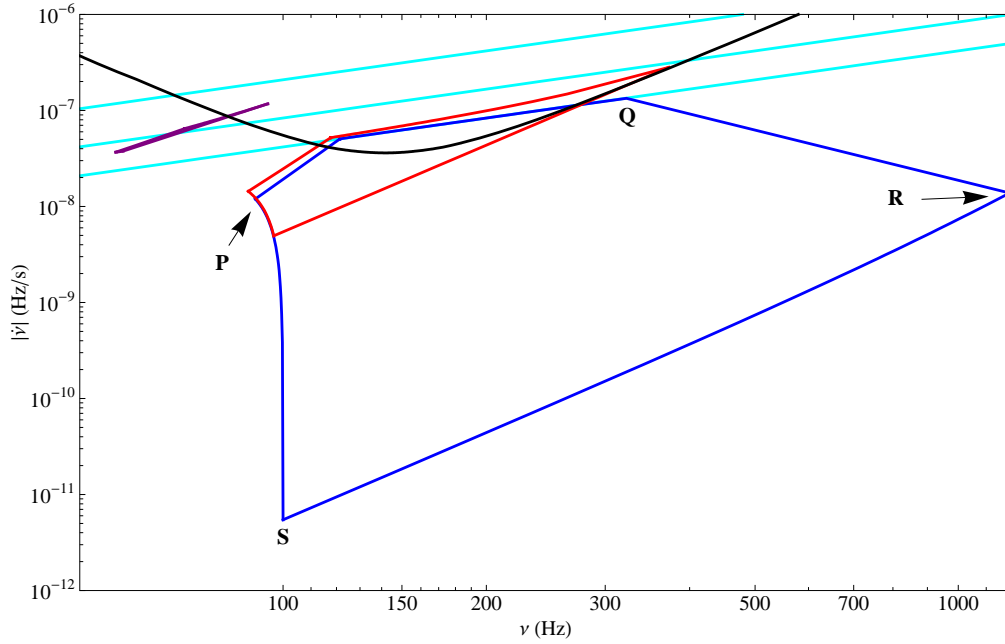


**Figure 3.2:** Final states  $(\nu, \dot{\nu})$  calculated from equation (3.25) on the  $\nu$ - $|\dot{\nu}|$  plane for a range of ellipticities ( $10^{-6} \leq \epsilon \leq 10^{-3}$ ), and birth spin frequencies ( $0.10 \text{ kHz} \leq \nu_b \leq 1.2 \text{ kHz}$ ), and for a 19 yr old pulsar. The blue lines surround the region where the  $Q_1$  term dominates ( $B \leq 10^{11.5} \text{ G}$ , all  $n$ ), the red lines surround the region where the  $Q_2$  term dominates ( $B = 10^{13} \text{ G}$ ,  $n = 3$ ), and the purple lines surround the region where the  $Q_2$  term dominates ( $B = 10^{13} \text{ G}$ ,  $n = 2.3$ ). The black curve shows the theoretical search sensitivity from solving equation (3.17). The  $\nu \ll \nu_b$  age limits are shown in cyan for  $\langle n \rangle = 1.8$  (top),  $\langle n \rangle = 3$  (middle) and  $\langle n \rangle = 5$  (bottom).

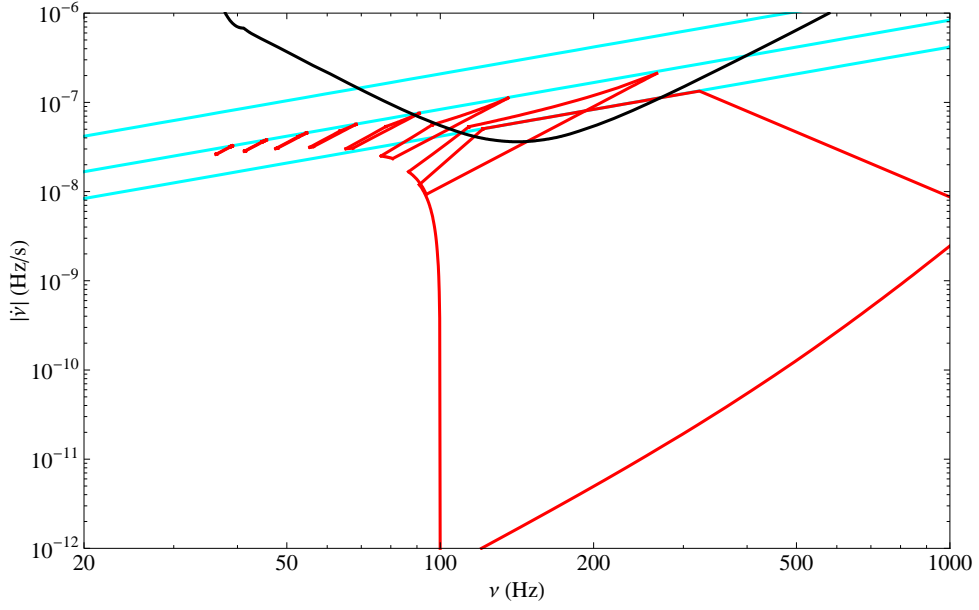


**Figure 3.3:** Final states  $(\nu, \dot{\nu})$  calculated from equation (3.25) on the  $\nu$ - $|\dot{\nu}|$  plane, for a range of magnetic field strengths. The eight red boxes surround regions which have  $n = 3$  and cover the same range of  $\epsilon$  and  $\nu_b$  as Figure 3.2. Their magnetic fields range from  $B = 10^{11}$  G (largest box) to  $B = 10^{14.5}$  G (smallest box).

### 3.6.1 Semi-coherent phase metric

When searching a template grid, it is extremely unlikely that one particular set of parameters will match the true signal exactly. What we have instead is a set of guessed parameters  $\boldsymbol{\theta} + \Delta\boldsymbol{\theta}$ , describing the closest match, which are offset from the true values by a small amount,  $\Delta\boldsymbol{\theta}$ . For a given set of guessed parameters, the power spectrum of a time-coincident SFT pair is

$$\mathcal{P}(\boldsymbol{\theta}, \Delta\boldsymbol{\theta}) = \frac{2\mathcal{A}}{\sqrt{\Delta T}} \left| \int_{T_{\text{start}}}^{T_{\text{start}} + \Delta T} dt e^{i\Delta\Phi(t)} \right|^2, \quad (3.26)$$

where  $\Delta\Phi(t) = \Phi(t, \boldsymbol{\theta} + \Delta\boldsymbol{\theta}) - \Phi(t, \boldsymbol{\theta})$  is the mismatch between the actual and guessed phases,  $T_{\text{start}}$  is the time at the midpoint of the SFT, and  $\mathcal{A}$  is the gravitational wave amplitude.

The mismatch between (3.26) and the power spectrum of the SFT pair if  $\Delta\boldsymbol{\theta} = 0$  is defined to be

$$m(\boldsymbol{\theta}, \Delta\boldsymbol{\theta}) = 1 - \frac{\mathcal{P}(\boldsymbol{\theta}, \Delta\boldsymbol{\theta})}{\mathcal{P}(\boldsymbol{\theta}, 0)} \quad (3.27)$$

and is related to the semi-coherent phase metric  $s_{ij}$  by

$$m(\boldsymbol{\theta}, \Delta\boldsymbol{\theta}) = s_{ij}(\boldsymbol{\theta})\Delta\theta^i\Delta\theta^j, \quad (3.28)$$

where  $1 \leq i, j \leq 4$  label the various search parameters. In order to calculate  $s_{ij}$ , we must first calculate the *coherent* phase metric,  $g_{ij}$ , for an individual SFT pair segment. The components of  $s_{ij}$  are then obtained by averaging  $g_{ij}$  across the entire observation time.

For the cross-correlation search, we have  $\boldsymbol{\theta} = (\nu, Q_1, Q_2, n)$ . Hence, for a given mismatch  $m$ , the minimum (i.e. most conservative) template spacings are given by  $\Delta\nu(\boldsymbol{\theta}) = \sqrt{m/s_{00}(\boldsymbol{\theta})}$ ,  $\Delta Q_1(\boldsymbol{\theta}) = \sqrt{m/s_{11}(\boldsymbol{\theta})}$ ,  $\Delta Q_2(\boldsymbol{\theta}) = \sqrt{m/s_{22}(\boldsymbol{\theta})}$ ,  $\Delta n(\boldsymbol{\theta}) = \sqrt{m/s_{33}(\boldsymbol{\theta})}$ . Note that it may be possible to do better (i.e. expand the spacing) by taking advantage of the covariances between parameters embodied in the metric through (3.28); this issue deserves further study.

The coherent phase metric  $g_{ij}$  is defined to be

$$g_{ij} = \langle \partial_i \Delta\Phi \partial_j \Delta\Phi \rangle - \langle \partial_i \Delta\Phi \rangle \langle \partial_j \Delta\Phi \rangle, \quad (3.29)$$

with  $\langle \dots \rangle = \frac{1}{T_{\text{lag}}} \int_{T_{\text{start}}}^{T_{\text{start}}+T_{\text{lag}}} dt \dots$  and  $\partial_i \Delta\Phi = \partial \Delta\Phi / \partial \Delta\theta^i$  evaluated at  $\Delta\boldsymbol{\theta} = 0$ . Calculating  $g_{ij}$  analytically by integrating (3.25) is non-trivial. However, a good approximation results if we integrate (3.25) *separately* for the gravitational-wave and electromagnetic torques, and combine the answers in quadrature. Details of the calculation are shown in Appendix 3A. In brief, tracking the gravitational-wave and electromagnetic spin down separately yields two “sub-metrics”, one comprising  $\nu$  and  $Q_1$  (gravitational) and the other comprising  $\nu, Q_2$ , and  $n$  (electromagnetic). Diagonal elements of  $s_{ij}$  can be obtained by summing the two sub-metrics.

The semi-coherent metric  $s_{ij}$  is the average of the coherent metric from  $T_{\text{start}} = 0$  to  $T_{\text{start}} = T_{\text{obs}}$ , where  $T_{\text{obs}}$  is the entire observation time spanned by all SFT pairs. It is defined to be

$$s_{ij} = (T_{\text{obs}})^{-1} \int_0^{T_{\text{obs}}} dT_{\text{start}} g_{ij}. \quad (3.30)$$

From Appendix 3B, the diagonal elements of the semi-coherent metric are:

$$s_{00} \approx 10T_{\text{lag}}^2 T_{\text{obs}}^2 \left( \frac{5}{72} K_1^2 \nu^8 Q_1^2 - \frac{1}{36} K_1 K_2 n \nu^{n+3} Q_1 Q_2 + \frac{1}{360} K_2^2 n^2 \nu^{2n-2} Q_2^2 \right), \quad (3.31)$$

$$s_{11} \approx \frac{K_1^2 \nu^{10}}{36} T_{\text{lag}}^2 T_{\text{obs}}^2, \quad (3.32)$$

$$s_{22} \approx \frac{K_2^2 \nu^{2n}}{36} T_{\text{lag}}^2 T_{\text{obs}}^2, \quad (3.33)$$

$$s_{33} \approx \frac{K_2^2 \log(\nu)^2 \nu^{2n} Q_2^2}{36} T_{\text{lag}}^2 T_{\text{obs}}^2, \quad (3.34)$$

with  $K_1 = K_1(\nu, Q_1)$  and  $K_2 = K_2(\nu, Q_2, n)$ . For pure gravitational-wave and electromagnetic spin down, we have  $(K_1, K_2) = (1, 0)$  and  $(0, 1)$  respectively. The full expressions for (3.31)–(3.34) are presented in Appendix 3B. Note that in (3.31)–(3.34), all frequency terms are normalised by  $\nu_{\text{ref}}$ . For clarity, we have set  $\nu_{\text{ref}} = 1$  Hz and do not display it.

In Appendix 3C, we estimate the phase error which accumulates after a time  $T_{\text{lag}}$  from mismatches in  $\nu$ ,  $Q_1$ ,  $Q_2$ , and  $n$ . We find that it scales with  $T_{\text{lag}}$  similarly to (3.31)–(3.34) for  $Q_1$  and  $Q_2$ . For  $\nu$ , the phase error scales instead as  $T_{\text{lag}}$ , and for  $n$ , it scales as  $T_{\text{lag}} \log[1 + (n-1)Q_2 T_{\text{lag}} \nu^{n-1}]$ . In a semi-coherent search, the phase needs to be tracked to within  $\pi/4$  over the interval  $T_{\text{lag}}$ , not  $T_{\text{obs}}$ , unlike in fully coherent searches. Across the entire observation time  $T_{\text{obs}}$ , we require only that the frequency of the signal be tracked to within  $1/\Delta T$ . This adds an overall  $T_{\text{obs}}^2$  dependence to (3.31)–(3.34).

### 3.6.2 Computational cost of the search

The run-time of the search code is proportional to  $N_{\text{pairs}} N_{\text{total}}$ , where  $N_{\text{total}}$  is the total number of templates required to search the parameter space. Trials with  $N_{\text{pairs}} = 10^5$  comprising 1 year’s worth of SFTs (from H1 and L1), and  $T_{\text{lag}} = 1$  hour take  $\sim 1$  s per template on a single, 1-gigaflop computational node. We can therefore search  $\sim 10^9$  templates in a realistic run using  $10^3$  nodes over two weeks.

We now compare the computational cost of the astrophysical phase model (3.25) against the Taylor-expansion model (3.23). The semi-coherent metric for the latter model is not well studied, however recent work has yielded analytic expressions for the metric (Pletsch & Allen 2009; Pletsch 2010). Based on these expressions, we can estimate the number of templates in the following

way.

Firstly, we consider the number of templates required to track the phase coherently over a time  $T_{\text{lag}}$ . For the  $k$ -th frequency derivative in the Taylor expansion model, the corresponding diagonal term of the *coherent* metric scales as  $(g_{ij})_{\text{coh}}^{(k)} \propto T_{\text{lag}}^{2k+2}$  (Whitbeck 2006). The number of templates required to track the  $k$ -th frequency derivative coherently is then  $N_k \propto \sqrt{(g_{ij})_{\text{coh}}^{(k)}} \propto T_{\text{lag}}^{k+1}$ . The total number of templates required for each coherent chunk of length  $T_{\text{lag}}$  is therefore given by  $N_{\text{coh}} = \prod_{k=0}^s N_k$ , i.e.  $N_{\text{coh}} \propto \prod_{k=0}^s T_{\text{lag}}^{k+1}$ , where  $s$  is the number of frequency derivatives required to track the gravitational wave phase (see Section 3.5). Now, assume that over a time  $T_{\text{obs}}$ , we sum a number of chunks incoherently, approximately proportional to  $N_{\text{chunks}} \propto T_{\text{obs}}/T_{\text{lag}}$ .<sup>3</sup> Now, using the semi-coherent metric (Pletsch & Allen 2009; Pletsch 2010), the number of templates required for  $s$  frequency derivatives is proportional to  $\gamma_s N_{\text{coh}}$ , where  $\gamma_s$  is a ‘refinement factor’ which scales as  $N_{\text{chunks}}^{s(s+1)/2}$ . The total number of templates is then approximately

$$N_{\text{total}} \propto N_{\text{chunks}}^{s(s+1)/2} \prod_{k=0}^s T_{\text{lag}}^{k+1} \quad (3.35)$$

$$\propto \left( \frac{T_{\text{obs}}}{T_{\text{lag}}} \right)^{s(s+1)/2} \prod_{k=0}^s T_{\text{lag}}^{k+1}. \quad (3.36)$$

For the range of  $(\nu_b, \epsilon, B, n)$  considered in Section 3.5.1, for  $T_{\text{lag}} = 1$  hr, we must track terms up to and including  $\nu^{(4)}$  in (3.23) in order to keep the phase error overall below  $\pi/4$ . This gives  $N_{\text{total}} \propto T_{\text{obs}}^{10} T_{\text{lag}}^5$ .

Under the astrophysical phase model, we estimate  $N_{\text{total}} = N_\nu N_{Q_1} N_{Q_2} N_n$  from (3.31)–(3.34), where the subscripts denote the number of templates required for each individual parameter, e.g.  $N_\nu \approx \nu/\Delta\nu$ . As (3.31) yields different results for  $N_\nu$  in the gravitational and electromagnetic limits, we bound  $N_\nu$  by taking it to be the sum of squares of the two limits, i.e.  $N_\nu = \left[ N_{\nu, (K_1, K_2)=(1,0)}^2 + N_{\nu, (K_1, K_2)=(0,1)}^2 \right]^{1/2}$ . For a given mismatch  $m$ , we obtain

$$N_{\text{total}} \propto m^{-2} n \nu^{10+3n} \log(\nu) Q_1 Q_2^2 [Q_1^2 + n^2 Q_2^2]^{1/2} T_{\text{lag}}^4 T_{\text{obs}}^4 \quad (3.37)$$

Equation (3.37) is an approximate result, achieved by combining the two sub-metrics used in equations (3.31)–(3.34). It should be regarded as a rule

---

<sup>3</sup>We emphasize that this is only an approximate estimate, as the cross-correlation method sums SFT pairs separated by a time up to and including  $T_{\text{lag}}$ . Strictly speaking,  $N_{\text{chunks}} > T_{\text{obs}}/T_{\text{lag}}$ .

of thumb. If gravitational-wave spin down dominates, we have  $s_{22} = s_{33} = 0$ ,  $\tau_c = (4Q_1\nu^4)^{-1}$ , and hence

$$N_{\text{total}} \propto m^{-1} \nu^2 \tau_c^{-2} T_{\text{lag}}^2 T_{\text{obs}}^2. \quad (3.38)$$

If electromagnetic spin down dominates, we have  $s_{11} = 0$ ,  $\tau_c = [(n-1)Q_2\nu^{n-1}]^{-1}$ , and hence

$$N_{\text{total}} \propto m^{-3/2} n^2 \nu^3 \log(\nu) [(n-1)\tau_c]^{-3} T_{\text{lag}}^3 T_{\text{obs}}^3. \quad (3.39)$$

The required template spacing therefore varies dramatically across the astrophysical parameter range. To illustrate, let us consider  $0.1 \text{ kHz} \leq \nu \leq 1 \text{ kHz}$ ,  $10^{-22} \text{ s}^3 \leq Q_1 \leq 10^{-18} \text{ s}^3$ ,  $10^{-21} \text{ s}^2 \leq Q_2 \leq 10^{-13} \text{ s}^2$ , and  $2.3 \leq n \leq 3.0$ , and hence  $8 \times 10^{-6} \leq \epsilon \leq 8 \times 10^{-4}$ ,  $4 \times 10^9 \text{ G} \leq B \leq 4 \times 10^{13} \text{ G}$ . We assume a mismatch  $m$  of 0.2. The required resolutions in the four search parameters range across

$$2.935 \times 10^{-4} \leq \Delta\nu/\text{Hz} \leq 9.632 \times 10^{-4}, \quad (3.40)$$

$$2.973 \times 10^{-26} \leq \Delta Q_1/\text{s}^3 \leq 3.685 \times 10^{-22}, \quad (3.41)$$

$$3.448 \times 10^{-20} \leq \Delta Q_2/\text{s}^2 \leq 2.120 \times 10^{-16}, \quad (3.42)$$

$$8.674 \times 10^{-8} \leq \Delta n \leq 1.166 \times 10^4 \quad (3.43)$$

in this search volume. The number of templates required for each parameter is its range divided by its bin resolution. If the bin resolution is larger than its range, we require only one template. Equations (3.40)–(3.43) imply a total number of templates between  $2.958 \times 10^5 \leq N_{\text{total}} \leq 4.347 \times 10^{26}$  to cover the entire parameter space. Smaller values of  $\nu$ ,  $Q_1$ ,  $Q_2$  and  $n$  require fewer templates to cover their neighbourhood.

Unfortunately, given the computational restrictions that we face, we cannot search the entire region of astrophysical parameters in Figure 3.2. In the following analysis, we therefore divide each axis in parameter space into (say) ten bins, i.e. a  $10 \times 10 \times 10 \times 10$  hypercubic grid containing  $10^4$  “boxes”, and calculate the localised resolution at the centroid of each box. The grid is spaced logarithmically along  $\epsilon$  and  $B$  to cover  $Q_1$  and  $Q_2$  in a representative fashion. Only those boxes requiring  $N \lesssim 10^9$  are practical to search.

### 3.6.3 Astrophysical upper limits

In this section, we combine the estimates of sensitivity and computational cost in Sections 3.4 and 3.6.2 respectively to identify the ranges of the astrophysical

parameters  $B$  and  $\epsilon$  that can be probed by a realistic search. In the event of a non-detection, upper limits on  $B$  and  $\epsilon$  can be placed.

We solve (3.25) for a range of  $\nu_b$ ,  $\epsilon$ , and  $B$ , and calculate the characteristic wave strain  $h_0$  from (3.18). Figure 3.4 displays contours of  $h_0$  versus  $B$  and  $\epsilon$  for  $n = 3$  at two frequencies corresponding to  $\nu_b = 300$  Hz and  $\nu_b = 1200$  Hz. The cyan shaded areas indicate where  $h_0 \geq h_{\text{th}}$ . The search is sensitive to a larger range of  $\epsilon$  and  $B$  as  $\nu_b$  rises. This occurs because the search sensitivity peaks at  $\nu \approx 150$  Hz. For small  $\nu_b$  and large  $\epsilon$  and  $B$ , the pulsar spins down after  $\tau_c = 19$  yr to give  $\nu < 150$  Hz. In the best case scenario, for  $\nu_b = 1200$  Hz, upper and lower limits on the magnetic field and ellipticity of  $B \leq 1.6 \times 10^{13}$  G and  $\epsilon \geq 2 \times 10^{-4}$  can be achieved.

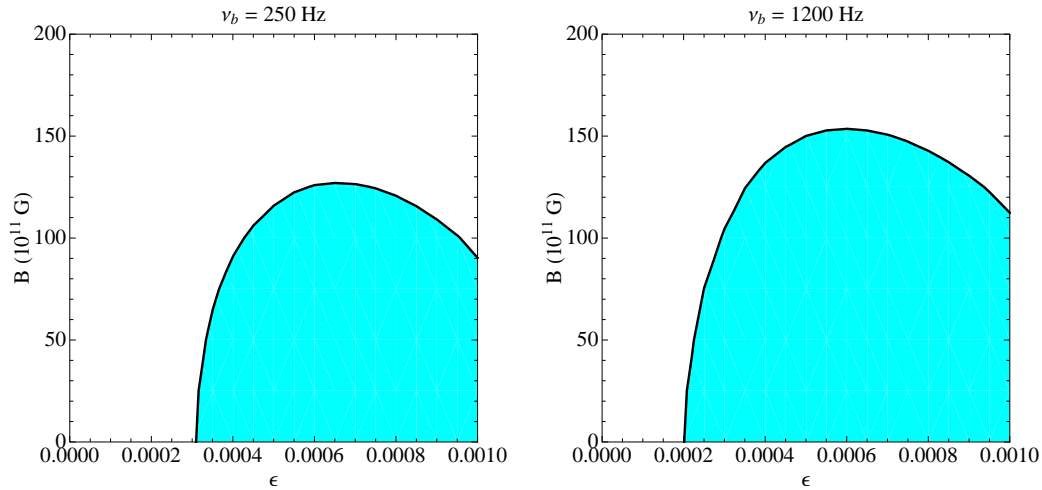


**Figure 3.4:** Contour plots of  $h_0$  as a function of  $\epsilon$  and  $B(10^{11})$  G for SNR 1987A for values of  $\nu_b = 250$  (left panel) and 1200 Hz (right panel). We assume  $n = 3$  and a pulsar age of 19 years, as the S5 run began in 2006. The cyan shaded areas correspond to  $h_0 \geq h_{\text{th}}$ , where  $h_{\text{th}}$  is defined in (3.16).

Unfortunately, the number of search templates required to cover the shaded region in Figure 3.4 is prohibitively large, as discussed in Section 3.6.2. Figure 3.5 is a more comprehensive version of Figure 3.2 that shows both sensitivity and computational cost. Regions in which the search is sensitive (i.e.  $h_0 \geq h_{\text{th}}$ ) for given  $\nu_b$  and  $n$  are shaded in cyan. Overplotted as dark blue dots are the central coordinates of our grid boxes with  $N_{\text{total}} \leq 10^9$ . The panels correspond to a range of *birth* frequencies,  $\nu_b$ , and are grouped in pairs:  $n = 2.335$  (left panel in pair) and  $n = 2.965$  (right panel in pair). The pairs are arranged in order of increasing  $\nu_b$ , starting from  $\nu_b = 145$  Hz (top left) to  $\nu_b = 995$  Hz (bottom right), in intervals of 90 Hz.

The search sensitivity increases with  $\nu_b$  and  $\epsilon$ , and decreases with  $B$ . On the

$\nu_b$ (kHz)	$\epsilon$	$B$ ( $10^{11}$ G)
0.19–0.28	$\gtrsim 3.1 \times 10^{-4}$	$\lesssim 2.0$
0.28–0.55	$\gtrsim 2.5 \times 10^{-4}$	$\lesssim 1.3$
0.55–1.00	$\gtrsim 2.0 \times 10^{-4}$	$\lesssim 0.8$

**Table 3.1:** Table of  $\nu_b$ ,  $\epsilon$ , and  $B$  ranges (approximate) which are detectable by the cross-correlation search for SNR 1987A using LIGO S5 data, for  $2.3 \leq n \leq 3.0$ . The numbers in the table are based on the regions in which the computationally feasible (dark blue dots) and search-sensitive (cyan shaded) regions overlap in Figure 3.5.

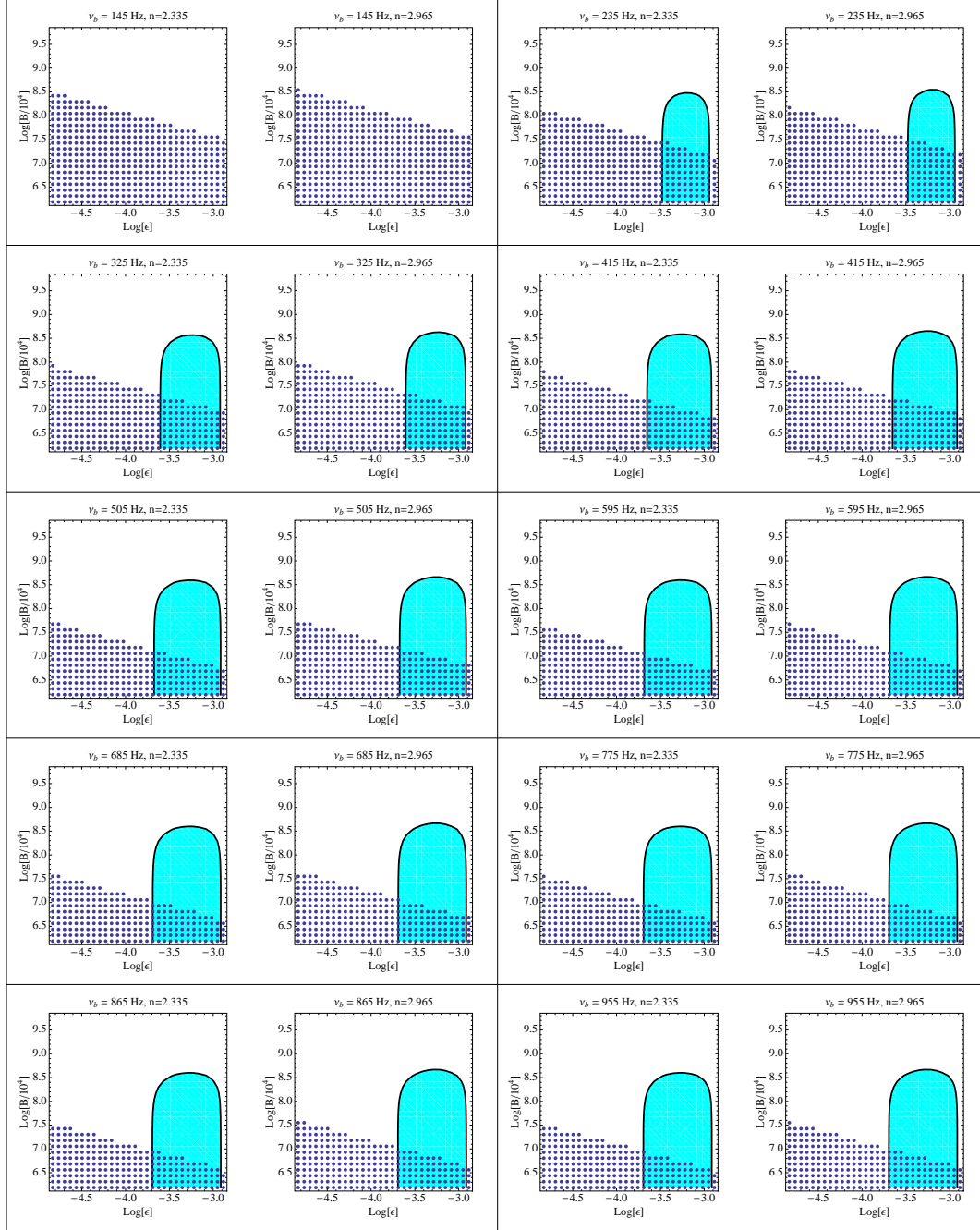
other hand, the computational efficiency of the search decreases with  $\nu_b$  and  $\epsilon$ , and increases with  $B$ . Even so, there is substantial overlap between the regions in which the search is sensitive and the regions which are computationally permissible.

Table 3.1 summarises the approximate range of  $\nu_b$ ,  $\epsilon$ , and  $B$  in which the two regions in Figure 3.5 overlap. If the pulsar in SNR 1987A was born with a frequency between 0.19 kHz and 0.28 kHz, the search is sensitive to  $\epsilon \gtrsim 3.1 \times 10^{-4}$  and  $B \lesssim 2.0 \times 10^{11}$  G. This range narrows as  $\nu_b$  increases; for birth frequencies between 0.55 kHz and 1.00 kHz, the search is sensitive to  $\epsilon \gtrsim 2.0 \times 10^{-4}$  and  $B \lesssim 0.8 \times 10^{11}$  G.

## 3.7 Conclusion

In this chapter, we describe the steps taken to quantify the astrophysical significance of a cross-correlation search for the supernova remnant SNR 1987A in LIGO S5 data.

- We estimate the theoretical sensitivity of the cross-correlation search, and compare it to the conservative, age-based, wave strain estimate. In the frequency band  $110 \text{ Hz} \lesssim \nu \lesssim 270 \text{ Hz}$ , the age-based estimate lies above the detection threshold.
- We introduce an alternative to the Taylor expansion model of the gravitational wave phase based on a set of four astrophysical search parameters  $(\nu, \epsilon, B, n)$ . The new phase model renders a search for a neutron star like SNR 1987A with a high spin-down rate computationally feasible.
- To estimate the optimal template spacing for the search, we calculate the semi-coherent phase metric corresponding to this astrophysical model.



**Figure 3.5:** Log-log contour plots of  $h_0$  as a function of  $\epsilon$  and  $B$  ( $10^4$  G) for a range of birth frequencies,  $\nu_b$ , and braking indices,  $n$ . The frequency of the signal  $\nu$  is obtained by solving (3.25), and integrating over  $\tau_c = 19$  yr. The cyan shaded areas indicate the regions in which  $h_0 \geq h_{\text{th}}$ , where  $h_{\text{th}}$  is defined in (3.16). The panels are arranged in pairs in order of increasing  $\nu_b$ , starting from  $\nu_b = 145$  Hz (top left) to  $\nu_b = 995$  Hz (bottom right), in intervals of 90 Hz. Each pair shows  $n = 2.335$  (left) and  $n = 2.965$  (right). The dark blue dots indicate parameter combinations for which one has  $N_{\text{total}} \leq 10^9$ .

- We place detection limits on  $\epsilon$  and  $B$  for a range of birth spin frequencies,  $0.1 \text{ kHz} \leq \nu_b \leq 1.2 \text{ kHz}$ .

With the required template spacing and current computational capabilities discussed in Section 3.6.2, we will be able to search up to approximately  $10^9$  templates. In the event of a non-detection, the following limits on the pulsar's ellipticity and magnetic field will be placed:  $\epsilon \leq 2 \times 10^{-4}$ ,  $B \geq 1.6 \times 10^{13} \text{ G}$ . The search will be sensitive to electromagnetic braking indices of  $2.3 \leq n \leq 3.0$ . This search is currently scheduled to begin in mid-2010 and will be the first application of the cross-correlation method to a continuous wave search.



# 4 Implementing the Cross-Correlation Search

The three major stages of implementing the LIGO S5 cross-correlation search for SNR 1987A are the following:

- code development within the LAL/LALApps software suite,
- consistency checks of the code (e.g. tests on simulated pure noise and injected signals) to quantify the mean and variance of the detection statistic,
- Monte Carlo tests of the code using injected signals in simulated data, to place empirical upper limits on the search sensitivity.

In this chapter, we detail each of the above three steps. A brief overview of the LAL/LALApps software suite and a description of the search code are presented in Section 4.1. In Section 4.2, the computational efficiency of the code is evaluated, and tests to check the accuracy of the code are described. Finally, the sensitivity of the search code is estimated, for signals with zero spindown, in Section 4.3.

## 4.1 Software development

All gravitational wave data analysis routines used by the Continuous Waves group of the LIGO Scientific Collaboration (LSC) are contained within the LAL/LALApps software repository. LAL (LSC Algorithm Library)<sup>1</sup> contains the core analysis routines used by LALApps (LAL Applications)<sup>2</sup>, which holds search pipelines, utilities, and end-user applications. The code is written in ANSI C99. An introductory installation guide for LAL and LALApps is provided in Appendix 4A for the beginning reader.

---

<sup>1</sup><https://www.lsc-group.phys.uwm.edu/dawsg/projects/lal.html>

<sup>2</sup><https://www.lsc-group.phys.uwm.edu/dawsg/projects/lalapps.html>

The S5 data is divided into Year 1 and Year 2 Short Fourier Transforms (SFTs), collected in 2006 and 2007 respectively, which are both available on the LSC’s computing clusters. For this project, only the Year 1 SFTs are considered. There are 70538 Year 1 SFTs [25105 from the H1 interferometer (IFO), 25321 from H2, and 20112 from L1].

### 4.1.1 Algorithm

The cross-correlation algorithm is implemented in LAL/LALApps in a general-purpose form which can be used outside this particular targeted search. The code is invoked using the command *lalapps\_pulsar\_crosscorr* and takes the command-line options listed in Table A1 as inputs. An example of how to run the code from the command line is provided in Appendix 4B. Aside from the standard LALApps command-line options, there are several additional options. Firstly, the user can choose to search over the gravitational wave frequency and up to two frequency derivatives in the Taylor expansion of the phase model  $(\nu_0, \dot{\nu}, \ddot{\nu})$ , or use the astrophysical model described in Chapter 3 to search over  $\nu_0, Q_1, Q_2, n$ . Secondly, one can choose to target a single sky coordinate, or search within a grid of sky coordinates. Thirdly, the user can choose to run the search using a particular value for the inclination angle between the observer’s line of sight and the pulsar’s rotation axis ( $\cos \iota$ ) and polarization angle of the source ( $\psi$ ) or to average over these variables. Finally, the user can decide to pair up Short Fourier Transforms (SFTs) from only the same interferometer, different interferometers, or a combination of both.

The flow chart in Figure 4.1 summarises the numerical algorithm. First, the command-line options are parsed, and the relevant SFTs are located and read into a time-ordered catalogue. Only the frequency bins corresponding to the user-specified search frequency range are extracted from the SFTs. The general, high-level structure of the code is then: each SFT is paired with another which satisfies the user-specified options (e.g. pairing SFTs from all IFOs, the same IFOs, or different IFOs) and the maximum time lag  $T_{\text{lag}}$  between each pair. For each unique SFT pair, the code loops through each search template and calculates the corresponding normalised cross-correlation statistic,  $\rho$ , for each template.

As shown in Figure 4.1, however, the implementation of the algorithm is not so straightforward. An important issue encountered in the development of the code, which is unique to this search, was the intensive use of CPU virtual memory. As the algorithm requires pairing up an entire year’s worth of SFTs

( $\sim 10^5$  SFTs corresponding to  $\sim 1$  Tb of memory), it is not feasible to load the SFTs and store them all in virtual memory while looping through the search templates. For each SFT, we thus construct a time-ordered linked list which contains only SFTs within a sliding window of length  $T_{\text{lag}}$ , i.e. a first-in-first-out queue. The signal phase, frequency, and detector response functions are calculated for each SFT. Then, SFT pairs are constructed within the sliding window, and the loop over the search templates is performed. For each pair, we calculate and store the quantities  $\mathcal{Y}_\alpha$ ,  $u_\alpha$ ,  $\sigma_\alpha$ ,  $\mathcal{G}_\alpha$ , and  $\rho_\alpha$  which are defined in Chapter 3. To simplify notation, we use the subscript  $\alpha$  to denote the pair indices  $IJ$  used in Chapter 3. As the window slides forward, we delete the SFT at the head of the linked list, add the next SFTs to its tail (as long as they satisfy the user-specified conditions), and repeat the process. Once the loop over all possible pairs is finished, the final value of the detection statistic  $\rho = \sum_\alpha \rho_\alpha$  for a particular search template is calculated. Finally, we output  $\rho$  (normalised by its standard deviation as described in Chapter 3) along with the relevant search parameters used. During the final production run, we will be searching up to  $\sim 10^9$  templates. To minimize the computational expense, it is wise to filter the output so that e.g. only the highest 10% of  $\rho$  values are saved.

## 4.2 Verification

In order to obtain approval from the LSC to run this search, the code and its output were reviewed extensively by an LSC committee (Teviet Creighton, Alberto Vecchio, and Eric Thrane). As part of the review process, several Monte Carlo tests were performed on simulated data to check that the code behaves correctly. In this section, we present the results of these tests.

### 4.2.1 Distribution of $\rho/\sigma_\rho$ when searching over pure noise

A basic consistency check is to run the search on simulated noise with no injected signal. The detector noise  $n(t)$  is typically assumed to be Gaussian with zero mean. Recalling equation (3.12), the detection statistic is  $\rho = \sum_\alpha \rho_\alpha = \sum_\alpha (u_\alpha \mathcal{Y}_\alpha + u_\alpha^* \mathcal{Y}_\alpha^*)$ , where  $u_\alpha$  and  $\mathcal{Y}_\alpha$  are defined in equations (3.3) and (3.13). In the absence of a signal,  $\mathcal{Y}_\alpha$  reduces to the power spectrum of  $n(t)$ .  $\rho_\alpha$  is therefore a product of two independent Gaussian variables with zero mean,  $n_I(t)$  and  $n_J(t)$ , where  $I$  and  $J$  denote the SFTs in the pair. Its distribution is expected to be a modified Bessel function of the second kind

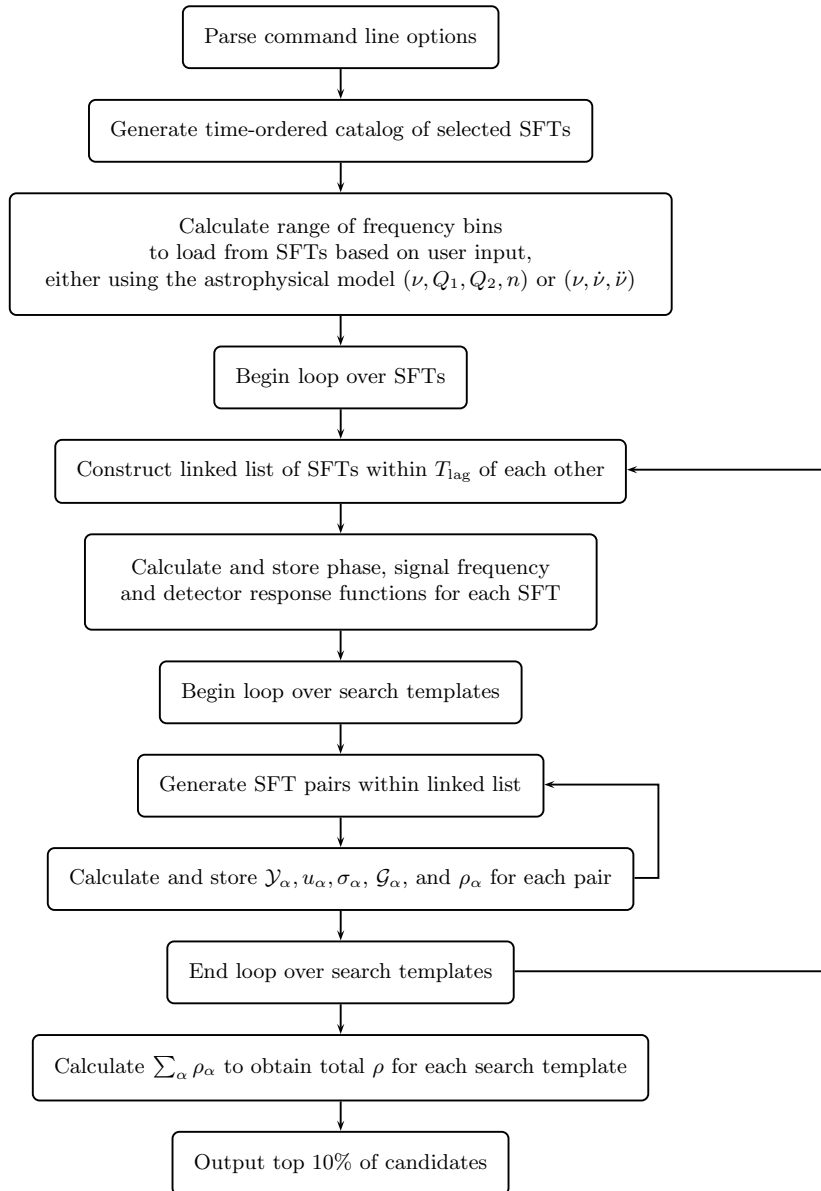


**Figure 4.1:** Flow chart summarising the algorithm used in *lalapps-pulsar-crosscorr*. The variables  $\mathcal{Y}_\alpha$ ,  $u_\alpha$ ,  $\sigma_\alpha$ ,  $\mathcal{G}_\alpha$ , and  $\rho_\alpha$  are defined in equations (3.3), (3.13), (3.5), and (3.12) in Chapter 3, where  $\alpha$  denotes an SFT pair index.

of order zero with zero mean and finite variance (Dhurandhar et al. 2008). Applying the central limit theorem, the sum of a large number of such zero-mean variables (i.e.  $\rho$ ) tends to a Gaussian random variable (Feller 1957). As the number of SFT pairs,  $N_{\text{pairs}}$ , increases, the distribution of  $\rho$  should tend towards a Gaussian with zero mean.

The expected mean  $\mu_\rho$  and variance  $\sigma_\rho^2$  of  $\rho$  in the low signal limit are given by (Dhurandhar et al. 2008)

$$\mu_\rho = h_0^2 \sum_{\alpha} (u_\alpha \mathcal{G}_\alpha + u_\alpha^* \mathcal{G}_\alpha^*), \quad (4.1)$$

$$\sigma_\rho^2 = 2 \sum_{\alpha} |u_\alpha|^2 \sigma_\alpha^2, \quad (4.2)$$

where  $h_0$  is the signal strength (zero for pure noise), and  $u_\alpha$ ,  $\mathcal{G}_\alpha$ , and  $\sigma_\alpha$  are defined in equations (3.13) and (3.5) in Chapter 3. We note that these equations exclude self-correlations (i.e. pairing an SFT with itself), and equation (4.2) assumes  $h(t) \ll n(t)$ . We discuss how to generalise beyond the small-signal limit in Section 4.2.2. The code outputs the normalised cross-correlation statistic,  $\rho/\sigma_\rho$ , whose distribution should have zero mean and a variance of unity for pure noise. We emphasize that the mean and variance of the distribution of  $\rho/\sigma_\rho$ ,  $\mu$  and  $\sigma^2$ , should not be confused with the mean and variance of the pre-normalised  $\rho$  distribution, given by (4.1) and (4.2).

The simulated Gaussian noise is generated using the standard LALApps utility `lalapps_Makefakedata_v4`<sup>3</sup>. This utility creates SFTs using user-specified values of signal strength  $h_0$ , single-sided power spectral density  $[S_n(\nu)]^{1/2}$ , SFT length  $T_{\text{SFT}}$ , total observation time  $T_{\text{obs}}$ , and signal parameters  $\nu$ ,  $\alpha$ ,  $\delta$ ,  $\cos \iota$ , and  $\psi$ . In order to vary  $N_{\text{pairs}}$  for testing purposes, we generate separate sets of 30 minute SFTs for five different values of  $T_{\text{obs}}$  ranging from 1 hour (2 SFTs per IFO) to 1 year (17531 SFTs per IFO) with random signal parameters and  $h_0 = 0$ . The standard analytic approximation of the single-sided power spectral density as a function of the signal frequency is (Damour et al. 2001):

$$S_n(\nu)^{1/2} \approx \alpha_0 \left[ \left( \frac{\alpha_1 \nu}{150 \text{ Hz}} \right)^{-56} + \alpha_2 \left( \frac{\nu}{150 \text{ Hz}} \right)^{-4.52} + \alpha_3 \left( \frac{\nu}{150 \text{ Hz}} \right)^2 + \alpha_4 \right]^{1/2}, \quad (4.3)$$

where  $\alpha_0 = (9 \times 10^{-46})^{1/2} \text{ Hz}^{-1/2}$ ,  $\alpha_1 = 4.49$ ,  $\alpha_2 = 0.16$ ,  $\alpha_3 = 0.32$ , and  $\alpha_4 = 0.52$ . In real LIGO data, variable phenomena like seismic noise make  $S_n(\nu)$  time-dependent on time-scales of hours to days. Simulated noise does

<sup>3</sup>An example of how to run this utility from the command line is provided in Appendix 4B

not suffer from this problem.

For each set of SFTs, we run the search using a frequency band of  $10^{-3}$  Hz, and a frequency resolution of  $10^{-4}$  Hz, corresponding to 100 search templates. We use two values for  $T_{\text{lag}}$ : 0 s and 3600 s. Setting  $T_{\text{lag}} = 0$  correlates only SFTs from different IFOs. This ensures that all pairs (and the resulting  $\rho_\alpha$  values) are completely independent. For  $T_{\text{lag}} = 3600$  s, each SFT is paired with 3 others if we include data from 2 IFOs, and 5 others if we include data from 3 IFOs. In this case, the same SFT ‘contributes’ to more than one  $\rho_\alpha$ . As a result, not all  $\rho_\alpha$  values are completely independent. We investigate the way in which this affects the expected theoretical distribution by comparing the resulting  $\rho$  distributions from both values of  $T_{\text{lag}}$ . The experiment is repeated 1000 times using 100 search templates each time, and the statistics of the resulting  $10^5$   $\rho/\sigma_\rho$  values are compiled.

The mean and standard deviation of the  $\rho/\sigma_\rho$  distribution,  $\mu$  and  $\sigma$ , for five sets of SFT durations are presented in Table 4.1. SFTs are simulated for only 2 IFOs (H1 and L1). The SFTs for each IFO have identical timestamps (i.e. they span identical times). The values of  $\mu$  lie within the 95% confidence limits<sup>4</sup> and deviate from zero by at most 0.0043. The values of  $\sigma$  however, are systematically  $\sim 2\%$  larger than unity and appear to increase with  $T_{\text{obs}}$ . Despite careful checks, the reason for this discrepancy is unclear; it may be due to either a bias in the simulated noise (i.e. the data generated by *lalapps\_Makefakedata\_v4* is not purely Gaussian as expected<sup>5</sup>), or a minor error in the theory or code. We keep this issue in mind as the analysis proceeds, however discrepancies at the  $\lesssim 5\%$  level are not expected to impact the search results significantly.

Figures 4.2(a)–4.2(b) show probability distribution functions (PDFs) of  $\rho/\sigma_\rho$  in histogram form for the trials listed in Table 4.1. From top to bottom, the panels show  $\rho/\sigma_\rho$  for 1 hour, 5 hours, 1 day, 1 month, and 1 year of SFTs respectively for  $T_{\text{lag}} = 0$  s (left panels) and  $T_{\text{lag}} = 3600$  s (right panels). The distributions are denoted by the solid curves. As a comparison, Gaussian distributions with zero mean and unit standard deviation are overplotted as dashed curves.

---

<sup>4</sup>The 95% confidence limits for  $\mu$  are  $\pm 1.96\sigma N^{-1/2} \approx 0.0063$ , where  $N$  is the number of trials ( $10^5$ ).

<sup>5</sup>This is unlikely, as the *lalapps\_Makefakedata\_v4* code has been reviewed and should not contain errors at this level. However, additional consistency checks on the Gaussianity of the simulated data can be run in the future. At the time of writing (August 2010), one existing issue is that this version of the code has been found to simulate data which displays a 1-day periodicity, depending on the inclination and polarization angles of the signal.

$T_{\text{obs}}$	$N_{\text{pairs}}$	$T_{\text{lag}}$ (s)	$\mu$	$\sigma$
1 hour	2	0	-0.001168	1.01652
	6	3600	0.003129	1.01579
5 hours	10	0	-0.002283	1.01691
	21	3600	0.000837	1.02103
1 day	48	0	0.004293	1.01446
	236	3600	0.001872	1.02049
1 month	2920	0	0.003937	1.02211
	7300	3600	0.003599	1.020068
1 year	35040	0	-0.002978	1.02319
	87651	3600	0.000237	1.02643

**Table 4.1:** Mean  $\mu$  and standard deviation  $\sigma$  of  $10^5$  values of  $\rho$  for a search over simulated Gaussian noise using observation times  $T_{\text{obs}} = 1$  hour, 5 hours, 1 day, 1 month, and 1 year. For each value of  $T_{\text{obs}}$ , the number of SFT pairs  $N_{\text{pairs}}$  is listed, along with the maximum SFT pair separation,  $T_{\text{lag}}$ .

The distributions for 1 hour of SFTs are clearly non-Gaussian. For  $T_{\text{lag}} = 0$  s (Figure 4.2(a)), the distribution is symmetric about zero, but more sharply peaked than a Gaussian. For  $T_{\text{lag}} = 3600$  s, the distribution peaks more sharply than a Gaussian and is significantly skewed. As  $T_{\text{obs}}$  increases, the distributions for both  $T_{\text{lag}}$  values gradually approach a Gaussian.

We quantify the Gaussianity of the distributions by plotting their skewness and kurtosis excess. The skewness of a distribution, which measures its reflection asymmetry, is defined as  $\gamma_1 = \mu_3/\mu_2^{3/2}$ , where  $\mu_2$  and  $\mu_3$  are the second and third central moments. For a pure Gaussian,  $\gamma_1$  is zero. The kurtosis measures the degree of peakedness of a distribution and is defined as  $\gamma_2 = \mu_4/\mu_2^2$ , where  $\mu_4$  is the fourth central moment. For a pure Gaussian, one has  $\gamma_2 = 3$ . The kurtosis excess,  $g_2 = \gamma_2 - 3$ , therefore equals zero for a pure Gaussian. Figure 4.3 shows  $\gamma_1$  and  $\gamma_2$  as a function of  $\log(T_{\text{obs}})$  for the  $\rho/\sigma_\rho$  distributions presented in Figures 4.2(a)–4.2(b) using  $T_{\text{lag}} = 3600$  s. Error bars of  $\pm 2s_s$  and  $\pm 2s_k$  are overplotted, where  $2s_s = 2\sqrt{6/N} = 0.015$  is twice the standard error of skewness,  $2s_k = 2\sqrt{24/N} = 0.031$  is twice the standard error of kurtosis, and  $N$  is the total number of trials ( $10^5$ ) (Tabachnick & Fidell 1996). The skewness and kurtosis decrease from  $\gamma_1 = 0.97$ ,  $g_2 = 3.44$  for 1 hour of SFTs to  $\gamma_1 = 0.030$ ,  $g_2 = -0.027$  for 1 year of SFTs.

For  $T_{\text{lag}} = 0$  s, when there is no overlap between SFT pairs and all  $\rho_\alpha$  values are independent, Figure 4.4 shows that the kurtosis also decreases with SFT duration, from  $g_2 = 1.99$  for 1 hour of SFTs to  $g_2 = -0.015$  for 1 year of SFTs. However, the skewness remains roughly centred at zero, fluctuating between  $\gamma_1 = -0.013$  (for 5 hours of SFTs) and  $\gamma_1 = 0.029$  (for 1 hour of SFTs). It is

within the standard errors, except at  $T_{\text{obs}} = 1$  hr.

The shape of the  $\rho$  distribution is therefore significantly affected by  $T_{\text{obs}}$  and, to a lesser extent,  $T_{\text{lag}}$ . However, the overall mean and standard deviation are identical for both choices of  $T_{\text{lag}}$ . As  $T_{\text{obs}}$  (and hence  $N_{\text{pairs}}$ ) increases, the differences in the distributions decrease as they approach Gaussianity. We therefore verify that the search code performs as expected when applied to pure noise.

### 4.2.2 Distribution of $\rho/\sigma_\rho$ as a function of signal strength

The introduction of a gravitational wave signal changes the distribution of  $\rho$  and  $\rho/\sigma_\rho$ . Most notably, the mean and variance increase with the signal strength. In Appendix A of Dhurandhar et al. (2008), the statistics of the  $\rho$  distribution are recalculated, including self-correlations and  $\mathcal{O}(h_0^2)$  terms which are left out in their main analysis. The most general expressions for  $\mu_\rho$  and  $\sigma_\rho^2$  [equations (A2) and (A13) of Dhurandhar et al. (2008)] are given by

$$\mu_\rho = h_0^2 \sum_{\alpha} (u_{\alpha} \tilde{\mathcal{G}}_{\alpha} + u_{\alpha}^* \tilde{\mathcal{G}}_{\alpha}^*), \quad (4.4)$$

$$\begin{aligned} \sigma_\rho^2 = & 2 \sum_{\alpha} |u_{\alpha}|^2 \sigma_{\alpha}^2 + \frac{h_0^2}{\Delta T} \left\{ \sum_{I \neq J} |u_{IJ}|^2 \left( \tilde{\mathcal{G}}_{II} S_n^{(J)} + \tilde{\mathcal{G}}_{JJ} S_n^{(I)} \right) \right\} \\ & + \mathcal{O}(h_0^4), \end{aligned} \quad (4.5)$$

where  $I$  and  $J$  are the SFT indices. Throughout this chapter, and in the actual search, we do not include self-correlations in the search runs. Any terms in (4.4) and (4.5) containing only self-correlations are therefore left out. We provide a full derivation of (4.4) and (4.5) in Appendix 4C.

For the sake of clarity, in this section only, we define three separate notations for  $\sigma_\rho$ , namely  $\sigma_{(0)}$  in the small signal limit  $h(t) \ll n(t)$ ,  $\sigma_{(1)}$  in the range where  $h(t) < n(t)$  but the signal is detectable, and  $\sigma_{(2)}$  in the large signal limit  $h(t) > n(t)$ . This is necessary as the detection statistic behaves differently within each of these three regimes.

We recall that the the code calculates the normalised detection statistic  $\rho/\sigma_{(0)}$ , whose distribution in pure noise is Gaussian with zero mean and unit variance. In the presence of a signal, the mean and variance of  $\rho/\sigma_{(0)}$ ,  $\mu$  and  $\sigma$ ,

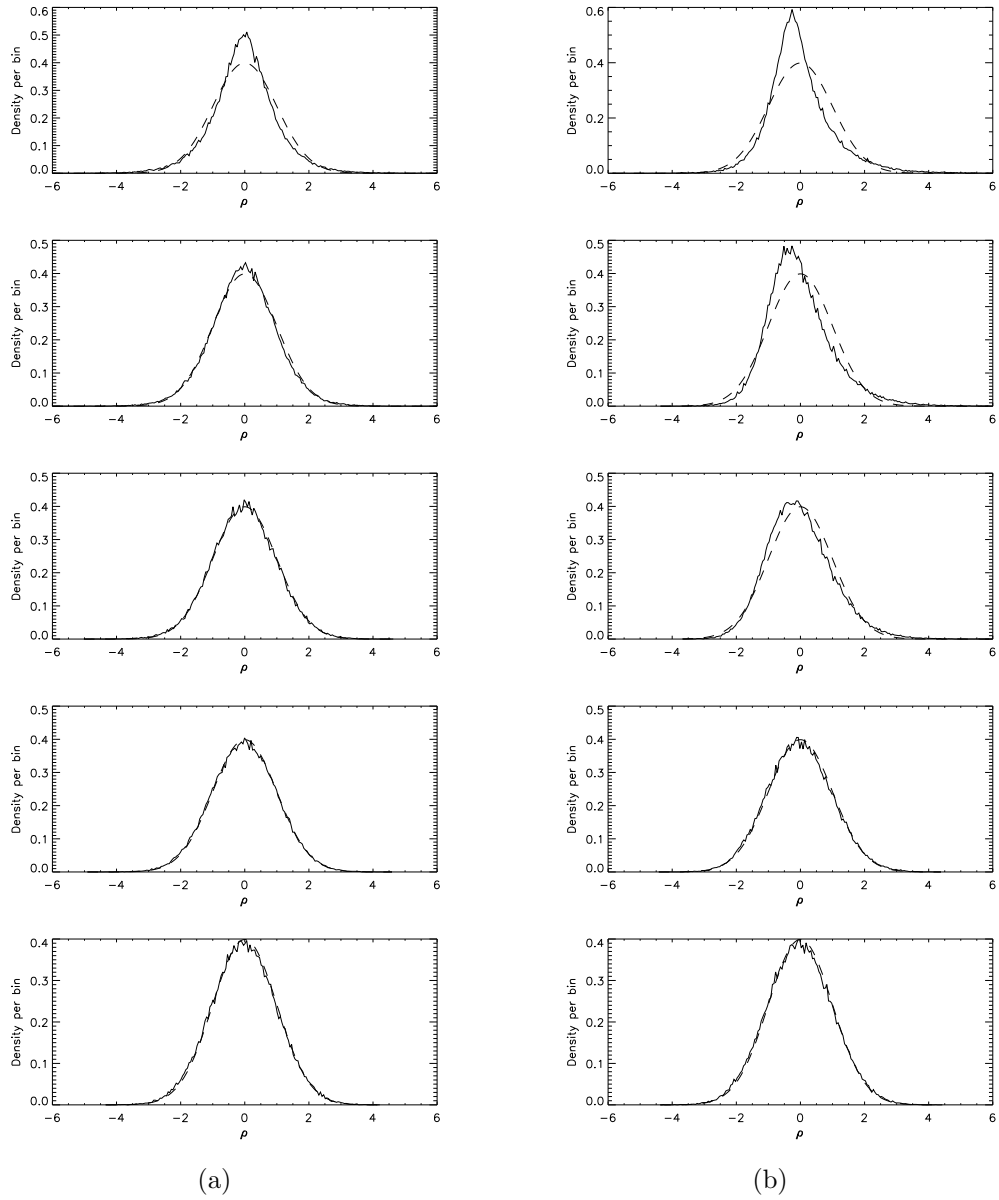


**Figure 4.2:** PDFs of  $\rho$  (solid line) for  $T_{\text{lag}} = 0$  s (left) and  $T_{\text{lag}} = 3600$  s (right) for (top to bottom)  $T_{\text{obs}} = 1$  hour, 5 hours, 1 day, 1 month, and 1 year. For reference, the dashed line shows a Gaussian with  $\mu = 0$  and  $\sigma = 1$ .

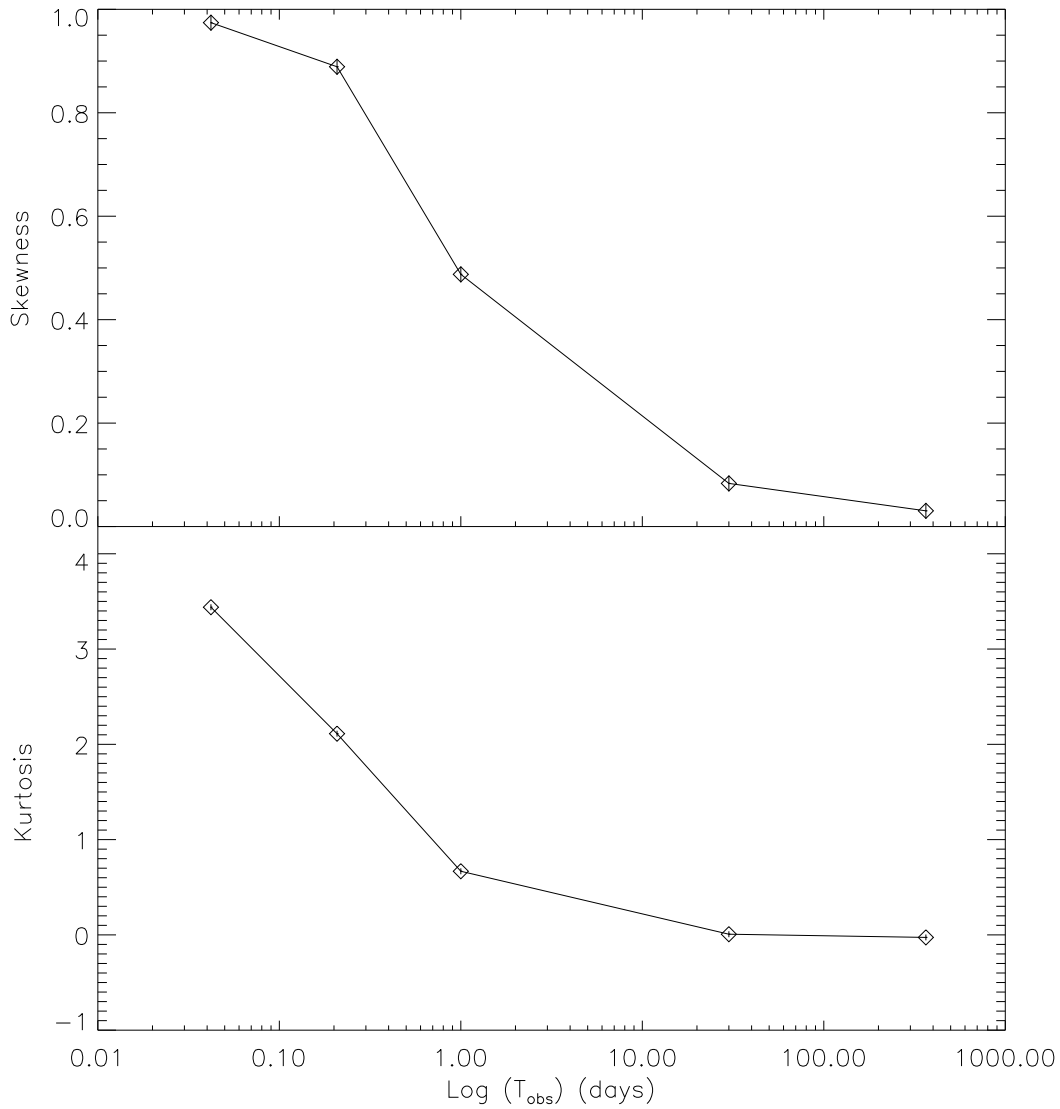


**Figure 4.3:** Skewness,  $\gamma_1$  (top panel), and kurtosis excess,  $\gamma_2 - 3$  (bottom panel), of  $\rho/\sigma_\rho$  as a function of total SFT duration, for  $T_{\text{lag}} = 3600$  s and SFTs containing pure Gaussian noise. The error bars (vertical lines) have peak-to-peak amplitudes of twice the standard error of skewness (top panel) and twice the standard error of kurtosis (bottom panel) (see text for definition).

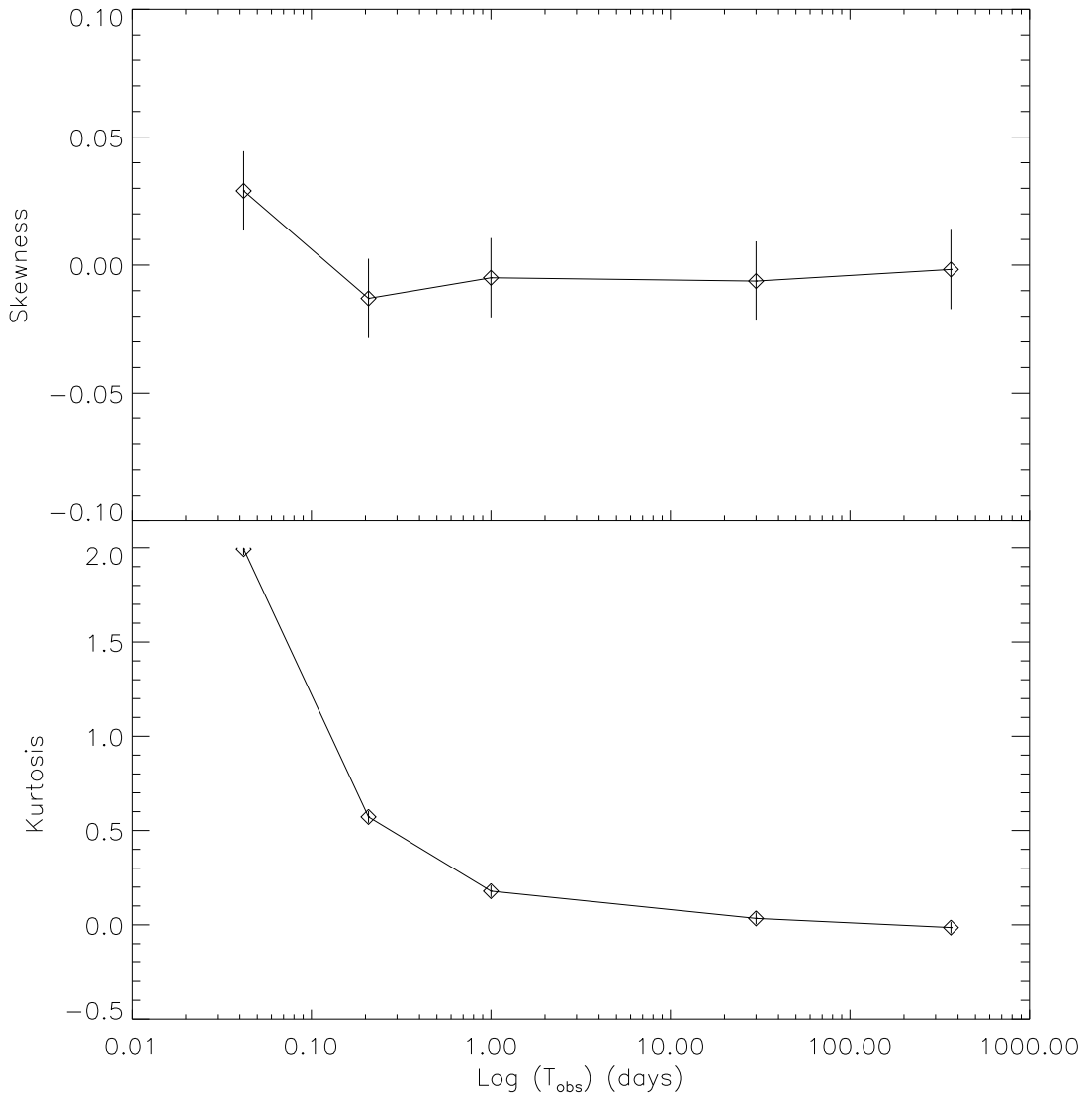


**Figure 4.4:** Skewness,  $\gamma_1$  (top panel), and kurtosis excess,  $\gamma_2 - 3$  (bottom panel), of  $\rho/\sigma_\rho$  as a function of total SFT duration, for  $T_{\text{lag}} = 0$  s and SFTs containing pure Gaussian noise. The error bars (vertical lines) have peak-to-peak amplitudes of twice the standard error of skewness (top panel) and twice the standard error of kurtosis (bottom panel) (see text for definition).

scale similarly to (4.4) and (4.5). They are given by

$$\mu = 2^{1/2} h_0^2 \sum_{\alpha} |u_{\alpha}|, \quad (4.6)$$

$$\sigma^2 = \sum_{I \neq J} |u_{IJ}|^2 \left[ \frac{S_n^I S_n^J}{4\Delta T^2} + \frac{h_0^2}{2\Delta T} \left( \tilde{\mathcal{G}}_{II} S_n^J + \tilde{\mathcal{G}}_{JJ} S_n^I \right) \right] + \mathcal{O}(h_0^4). \quad (4.7)$$

A full derivation is presented in Appendix 4C. In (4.6) and (4.7), we have again ignored self-correlations.

We test (4.6) and (4.7) against numerical results by injecting signals into simulated Gaussian noise with wave strains ranging between  $1 \times 10^{-25} \leq h_0 \leq 5 \times 10^{-22}$  at 150.1 Hz, and no spin down. Again, we use the *lalapps\_Makefakedata\_v4* utility to generate  $10^3$  sets of SFTs for each  $h_0$  value, with random signal parameters  $\alpha, \delta, \cos \iota$ , and  $\psi$ . We choose  $T_{\text{obs}}$  to be 1 year, and run the search using  $T_{\text{lag}} = 3600$  s, and search over a 0.01 Hz band centred on the signal frequency. We also search only the injected  $\alpha, \delta, \cos \iota$ , and  $\psi$  values. For each trial, we analyse only the largest  $\rho/\sigma_{(0)}$  value returned.

The top panel of Figure 4.5 plots  $\langle \rho/\sigma_{(0)} \rangle$ , averaged over the  $10^3$  trials, as a function of  $h_0$ .  $\langle \rho/\sigma_{(0)} \rangle$  increases from  $\approx 0.7$  at  $h_0 = 1 \times 10^{-25}$  to  $\approx 10^7$  at  $5 \times 10^{-22}$ , growing  $\propto h_0^2$  as expected. In the bottom panel of Figure 4.5, we plot the standard deviation of the set of largest  $\rho/\sigma_{(0)}$  values from each trial, as a function of  $h_0$ . We observe the change in behaviour of the standard deviation in the three regimes ( $h(t) \ll n(t)$ ,  $h(t) \lesssim n(t)$ , and  $h(t) > n(t)$ ). For  $h_0 = 1 \times 10^{-25}$ , the signal is too small to be detectable, and  $\sigma_{(0)} = 1$ . At  $h_0 = 1 \times 10^{-24}$ , we have  $\sigma_{(1)} = 44$ , and we are in the second regime where the standard deviation grows approximately as  $h_0$  as predicted by (4.7). In this regime, the effects of the  $\mathcal{O}(h_0^4)$  terms are negligible. However, as  $h_0$  increases further, we enter the third regime in which the signal dominates the noise. Above  $h_0 \approx 10^{-24}$ , the slope of the curve steepens as  $\sigma_{(2)}$  grows approximately as  $h_0^2$ , as the  $\mathcal{O}(h_0^4)$  terms in (4.7) become significant.

In practice, we do not expect the data to contain a signal strong enough to place us in the third regime. We therefore verify that for a realistic signal strength between  $10^{-25} \lesssim h_0 \lesssim 10^{-24}$ , the mean and variance of  $\rho/\sigma_{(0)}$  scale as  $h_0^2$ , as predicted by (4.6) and (4.7).

### 4.2.3 Averaging over $\cos \iota$ and $\psi$

The inclination and polarization angles,  $\iota$  and  $\psi$ , modulate the amplitude of a gravitational wave signal and should strictly be included in the set of search

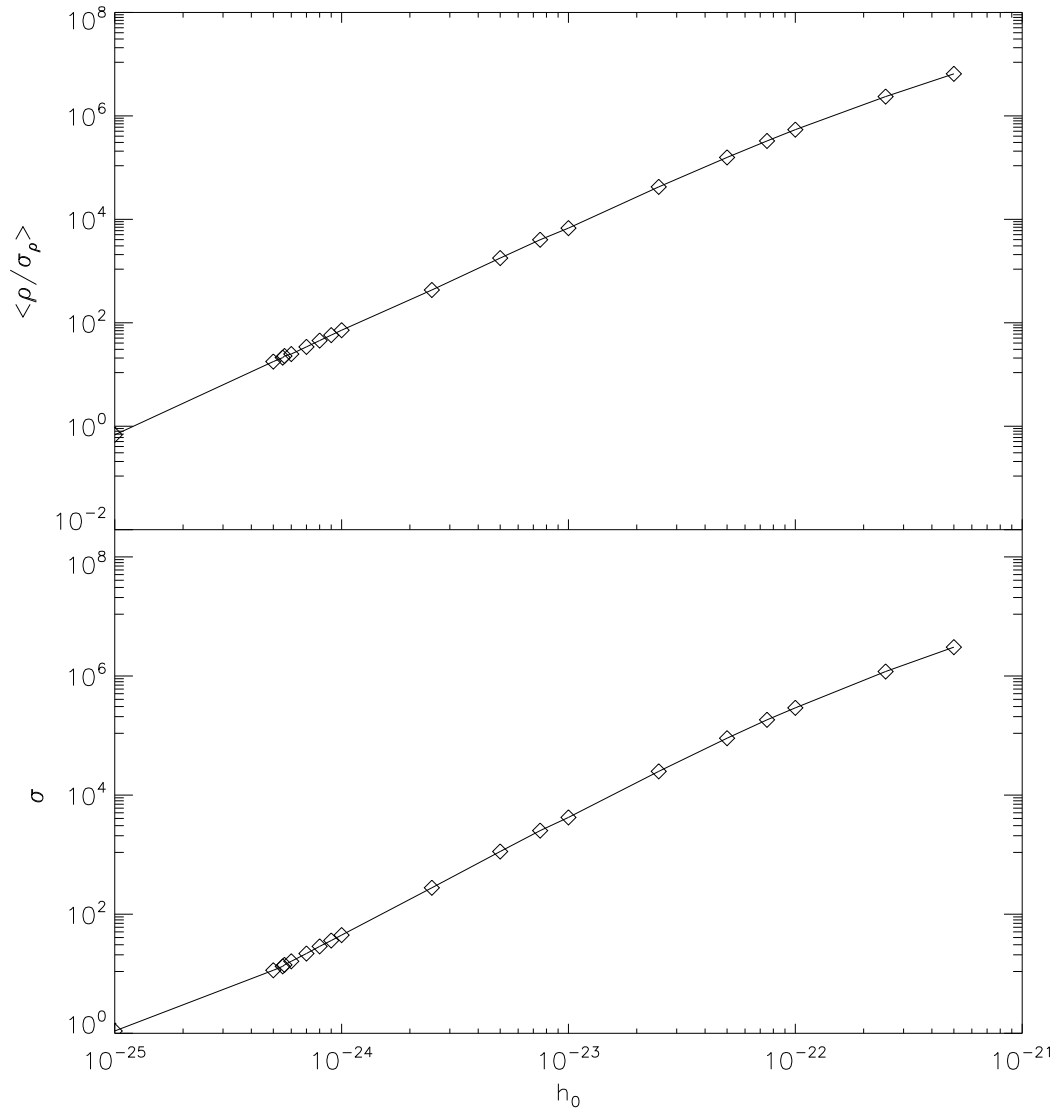


**Figure 4.5:** The mean  $\mu$  (top) and standard deviation  $\sigma$  (bottom) of the normalized detection statistic  $\langle \rho / \sigma_{(0)} \rangle$  as a function of injected gravitational wave strain  $h_0$ , plotted in log-log axes. The injected signals have random parameters  $\alpha, \delta, \cos \iota$ , and  $\psi$ , and a fixed frequency of 150.1 Hz with zero spin down.

parameters. However, for the sake of computational economy, one can choose instead to average over  $\cos \iota$  and  $\psi$  in a first-pass search. In the event of a candidate, follow-up searches can include these parameters as the number of templates is narrowed down.

When averaging over  $\cos \iota$  and  $\psi$ , the signal cross-correlation function  $\tilde{\mathcal{G}}_{IJ}$  is calculated using the handy formula (3.11), which is derived from averaging the beam pattern functions and signal amplitudes in (3.5). For the sake of clarity, we explain the derivation here in detail. We restate equation (3.5), viz.

$$\begin{aligned} \tilde{\mathcal{G}}_{IJ} = & \frac{1}{4} e^{-i\Delta\Phi_{IJ}} e^{-i\pi\Delta T[\nu_I(T_I) - \nu_J(T_J)]} [F_{I+}F_{J+}\mathcal{A}_+^2 + F_{I\times}F_{J\times}\mathcal{A}_\times^2 \\ & - i(F_{I+}F_{J\times} - F_{I\times}F_{J+})\mathcal{A}_+\mathcal{A}_\times], \end{aligned} \quad (4.8)$$

In (4.8), we define  $\Delta\Phi_{IJ} = \Phi_I(T_I) - \Phi_J(T_J)$ , where  $\Phi_I(T_I)$  and  $\Phi_J(T_J)$  are the signal phases at the times of the midpoints of SFTs  $I$  and  $J$  respectively.  $\nu_I(T_I)$  and  $\nu_J(T_J)$  are the signal frequencies of SFTs  $I$  and  $J$  at times  $T_I$  and  $T_J$ , and  $\Delta T$  is the SFT length. The origin of the second exponential factor, which does not appear in Dhurandhar et al. (2008), is described below.  $F_{I+}, F_{J+}$  and  $F_{I\times}, F_{J\times}$  are the beam detector functions for SFTs  $I$  and  $J$ , at times  $T_I$  and  $T_J$ , respectively, and  $\mathcal{A}_+, \mathcal{A}_\times$  describe the inclination of the source with respect to the observer.  $F_{+,\times}$  and  $\mathcal{A}_{+,\times}$  are defined in equations (3.6)–(3.9), which we now restate as

$$\mathcal{A}_+ = \frac{1 + \cos^2 \iota}{2}, \quad (4.9)$$

$$\mathcal{A}_\times = \cos \iota, \quad (4.10)$$

$$F_+(t; \mathbf{n}, \psi) = a(t; \mathbf{n}) \cos 2\psi + b(t; \mathbf{n}) \sin 2\psi, \quad (4.11)$$

$$F_\times(t; \mathbf{n}, \psi) = b(t; \mathbf{n}) \cos 2\psi - b(t; \mathbf{n}) \sin 2\psi. \quad (4.12)$$

In (4.11) and (4.12),  $\mathbf{n}$  is the position vector pointing from the detector to the source, and  $a(t; \mathbf{n})$  and  $b(t; \mathbf{n})$  are the detector response functions at time  $t$  for a given sky position. They are calculated in LALAPPs using the GetNewAM-Coeffs function.

Averaging is performed according to the definition in Jaranowski et al. (1998):

$$\langle \dots \rangle_{\psi, \cos \iota} = \frac{1}{2\pi} \int_0^{2\pi} d\psi \times \frac{1}{2} \int_{-1}^1 d \cos \iota, \quad (4.13)$$

yielding (Dhurandhar et al. 2008)

$$\langle F_{I+}F_{J+} \rangle_\psi = \langle F_{I\times}F_{J\times} \rangle_\psi = \frac{1}{2}(a_I a_J + b_I b_J), \quad (4.14)$$

$$\langle F_{I\times}F_{J+} \rangle_\psi = \langle F_{J\times}F_{I+} \rangle_\psi = 0, \quad (4.15)$$

$$\langle \mathcal{A}_+^2 \rangle_{\cos \iota} = \frac{7}{15}, \quad (4.16)$$

$$\langle \mathcal{A}_\times^2 \rangle_{\cos \iota} = \frac{1}{3}, \quad (4.17)$$

$$\langle \mathcal{A}_+ \mathcal{A}_\times \rangle_{\cos \iota} = 0, \quad (4.18)$$

where  $a_I$  and  $b_I$  are shorthand for  $a(T_I; \mathbf{n})$  and  $b(T_I; \mathbf{n})$  respectively.

Substituting (4.14)–(4.18) into (4.8) gives (3.11):

$$\langle \tilde{\mathcal{G}}_{IJ} \rangle_{\cos \iota, \psi} = \frac{1}{10} e^{-i\Delta\Phi_{IJ}} e^{-i\pi\Delta T[\nu(T_I) - \nu(T_J)]} (a_I a_J + b_I b_J), \quad (4.19)$$

### Correction to $\tilde{\mathcal{G}}_{IJ}$

While testing the code, a small error in the definition of  $\tilde{\mathcal{G}}_{IJ}$  [equation (3.10) in Dhurandhar et al. (2008)] was found. We now rederive  $\tilde{\mathcal{G}}_{IJ}$  in detail. Firstly, the Fourier transform of the gravitational wave signal  $h(t)$  in SFT  $I$  of length  $\Delta T$  is defined in equation (2.25) of Dhurandhar et al. (2008) as

$$\begin{aligned} \tilde{h}_I(\nu) = & e^{i\pi\nu\Delta T} h_0 \left\{ e^{i\Phi(T_I)} \frac{F_+ \mathcal{A}_+ - iF_\times \mathcal{A}_\times}{2} \delta_{\Delta T}[\nu - \nu_I(T_I)] \right. \\ & \left. + e^{-i\Phi(T_I)} \frac{F_+ \mathcal{A}_+ + iF_\times \mathcal{A}_\times}{2} \delta_{\Delta T}[\nu + \nu_I(T_I)] \right\}, \end{aligned} \quad (4.20)$$

where  $T$  is the time at the midpoint of the SFT,  $\nu$  is the Fourier frequency,  $\Phi(T)$  is the signal phase at time  $T$ , and  $\delta_{\Delta T}(\nu) = \sin(\pi\nu\Delta T)/\pi\nu$  is the finite time approximation to the delta function  $\delta(\nu)$ . As we assume that the signal power is concentrated in a single bin, this approximation is valid because  $\nu - \nu_I(T_I) < 1/\Delta T$  always. For  $\nu > 0$ , only the first term of (4.20) remains, and the cross-correlation of SFTs  $I$  and  $J$  is defined as [equation (3.9) of Dhurandhar et al. (2008)]

$$\tilde{h}_I^*(\nu) \tilde{h}_J(\nu + \delta\nu_{IJ}) = h_0^2 \tilde{\mathcal{G}}_{IJ} \delta_{\Delta T}^2[\nu - \nu_I(T_I)], \quad (4.21)$$

where  $\delta\nu_{IJ} = \nu_J(T_J) - \nu_I(T_I)$ . For  $\nu = \nu_I(T_I)$ , (4.21) reduces to

$$\tilde{\mathcal{G}}_{IJ} = \frac{\tilde{h}_I^*[\nu_I(T_I)] \tilde{h}_J[\nu_J(T_J)]}{h_0^2 (\Delta T)^2}. \quad (4.22)$$

Substituting (4.20) into (4.22) results in (4.8).

In Dhurandhar et al. (2008), the term  $e^{-i\pi\Delta T[\nu_I(T_I)-\nu_J(T_J)]}$  in (4.8) is missing, as the authors assume  $\delta\nu_{IJ} = 0$ , which only holds for self-correlations. The product  $\tilde{h}_I^*[\nu_I(T_I)]\tilde{h}_J[\nu_J(T_J)]$  contains two exponential factors:  $e^{i\pi\Delta T[\nu_J(T_J)-\nu_I(T_I)]}$  and  $e^{i[\Phi_J(T_J)-\Phi_I(T_I)]}$ . If  $\delta\nu_{IJ} = 0$ , the first factor goes to unity, and the second factor enters as the  $\Delta\Phi_{IJ}$  term. However, if  $\delta\nu_{IJ} \neq 0$ , then  $e^{-i\pi\Delta T[\nu_I(T_I)-\nu_J(T_J)]} \neq 1$ , and must be factored into  $\tilde{\mathcal{G}}_{IJ}$ .

### Comparison of $\langle \tilde{\mathcal{G}}_{IJ} \rangle_{\cos \iota, \psi}$ to $\tilde{\mathcal{G}}_{IJ}$

Monte Carlo tests comparing  $\rho/\sigma_\rho$ , calculated separately using  $\langle \tilde{\mathcal{G}}_{IJ} \rangle_{\cos \iota, \psi}$  and  $\tilde{\mathcal{G}}_{IJ}$  respectively, reveal unexpected results, indicating that there may be an error in the code which is as yet unresolved. We run three sets of mock searches, using: 1)  $\tilde{\mathcal{G}}_{IJ}$  and all the exact signal parameters  $(\alpha, \delta, \cos \iota, \psi)$ , 2)  $\langle \tilde{\mathcal{G}}_{IJ} \rangle_{\cos \iota, \psi}$  and the exact signal parameters  $(\alpha, \delta)$ , and 3)  $\tilde{\mathcal{G}}_{IJ}$ , the exact signal parameters  $(\alpha, \delta)$ , and random parameters  $(\cos \iota, \psi)$  which are not equal to the exact signal parameters. We generate 500 sets of simulated data with signal parameters  $(\nu, \alpha, \delta, \cos \iota$  and  $\psi)$  distributed randomly, using *lalapps\_Makefakedata\_v4* as in Section 4.2.1. Signals are injected into 1 year of 30-min SFTs (from H1 and L1) with large amplitudes [ $h_0/\sqrt{S_n(\nu)} = 1 \text{ Hz}^{1/2}$ ]. All three searches (sets 1, 2, and 3) are run on the same SFTs across a frequency band of 0.06 Hz, centred on the injected signal frequency (ranging between 50–1000 Hz).

The three sets of searches produce different detection statistics, which we call  $\rho_{\text{exact}}$  (set 1),  $\rho_{\text{ave}}$  (set 2), and  $\rho_{\text{random}}$  (set 3). For all values of  $T_{\text{lag}}$ , one expects  $\rho_{\text{exact}}$  to be larger than  $\rho_{\text{ave}}$  or  $\rho_{\text{random}}$ , as a search over the exact signal parameters should maximise  $\rho$ . We expect  $\rho_{\text{ave}}$  to be some fraction (e.g.  $\sim 0.9$ ) of  $\rho_{\text{exact}}$ .  $\rho_{\text{random}}$  is expected to be even less, as  $\cos \iota$  and  $\psi$  may be sampled at values which are very far from their true (injected) value. Figures 4.6–4.11 show the results of tests run using pair separations of  $T_{\text{lag}} = 0, 3600,$  and  $7200$  s. In each figure, the left panel shows the distribution of  $\rho_{\text{ave}}/\rho_{\text{exact}}$ , while the right panel shows the distribution of  $\rho_{\text{random}}/\rho_{\text{exact}}$ .

The distributions of  $\rho_{\text{ave}}/\rho_{\text{exact}}$  and  $\rho_{\text{random}}/\rho_{\text{exact}}$  are plotted in two ways: as functions of  $\rho_{\text{exact}}$  (Figures 4.6, 4.8, and 4.10) and of injected signal frequency (Figures 4.7, 4.9, and 4.11). The former show how the distributions depend on signal strength, whereas the latter should highlight any frequency-dependent trends caused by e.g. residual Doppler effects.

We now discuss the figures in detail. For  $T_{\text{lag}} = 0$  s, we find unexpectedly that 93 of 500 trials produce  $\rho_{\text{ave}} > \rho_{\text{exact}}$ , with the largest being  $\rho_{\text{ave}} =$

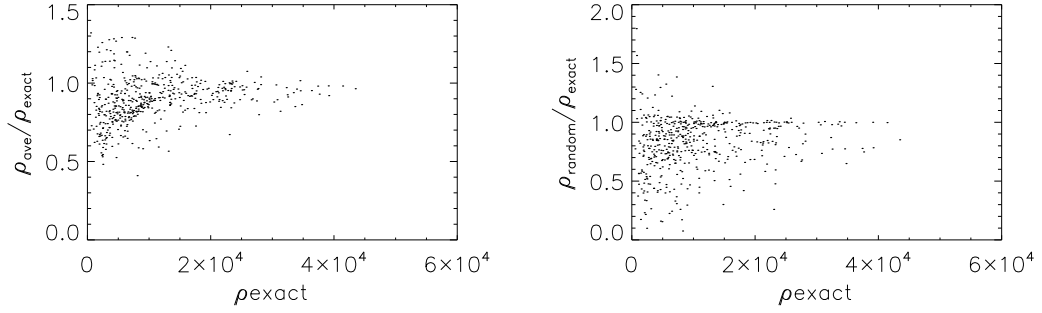


**Figure 4.6:** Distribution of  $\rho_{\text{ave}}/\rho_{\text{exact}}$  (left panel) and  $\rho_{\text{random}}/\rho_{\text{exact}}$  (right panel) as a function of  $\rho_{\text{exact}}$  for  $T_{\text{lag}} = 0$  s. 500 trials are performed, using randomly distributed  $\nu, \alpha, \delta, \cos \iota$ , and  $\psi$  values. Each point on the figure represents one trial.

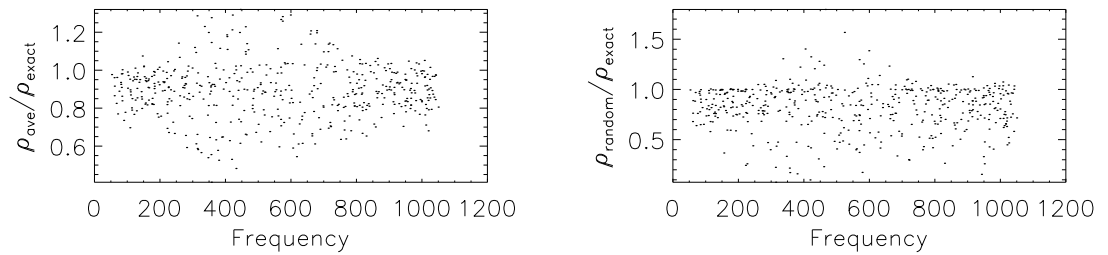


**Figure 4.7:** Distribution of  $\rho_{\text{ave}}/\rho_{\text{exact}}$  (left panel) and  $\rho_{\text{random}}/\rho_{\text{exact}}$  (right panel) as a function of injected signal frequency for  $T_{\text{lag}} = 0$  s. 500 trials are performed, using randomly distributed  $\nu, \alpha, \delta, \cos \iota$ , and  $\psi$  values. Each point on the figure represents one trial.

$1.320 \rho_{\text{exact}}$ . Additionally, 84 of 500 trials produce  $\rho_{\text{random}} > \rho_{\text{exact}}$ , the largest being  $\rho_{\text{random}} = 1.796 \rho_{\text{exact}}$ . On average,  $\langle \rho_{\text{ave}}/\rho_{\text{exact}} \rangle = 0.904$ , and  $\langle \rho_{\text{random}}/\rho_{\text{exact}} \rangle = 0.817$ . Figure 4.6 shows that the two distributions have a wide spread near  $\rho_{\text{exact}} \approx 0$ , and narrow as  $\rho_{\text{exact}}$  increases. The cases in which  $\rho_{\text{exact}}$  exceeds  $\rho_{\text{ave}}$  and  $\rho_{\text{random}}$  occur mostly when  $\rho_{\text{exact}} \lesssim 2 \times 10^4$ , indicating that this effect is more pronounced for weaker signals. Additionally, Figure 4.7 shows that although this effect occurs across all frequencies, the worst cases occur in the frequency band 400 – 600 Hz. The reason for this is unclear. If the discrepancy was caused by residual Doppler effects shifting the signal frequency within each SFT, we would see the effect worsening as the frequency increases <sup>6</sup>.

This puzzling effect decreases as  $T_{\text{lag}}$  is increased. For  $T_{\text{lag}} = 3600$  s, 53 of 500 trials produce  $\rho_{\text{ave}} > \rho_{\text{exact}}$ , the largest being  $\rho_{\text{ave}} = 1.051 \rho_{\text{exact}}$ , while 20 of 500 trials produce  $\rho_{\text{random}} > \rho_{\text{exact}}$ , the largest being  $\rho_{\text{random}} = 1.021 \rho_{\text{exact}}$ . On average,  $\langle \rho_{\text{ave}}/\rho_{\text{exact}} \rangle = 0.893$ , and  $\langle \rho_{\text{random}}/\rho_{\text{exact}} \rangle = 0.825$ . In Figure 4.8, the distribution of  $\rho_{\text{ave}}/\rho_{\text{exact}}$  (left panel) is noticeably less scattered than for  $T_{\text{lag}} = 0$  s. For  $\rho_{\text{exact}} \lesssim 4.8 \times 10^4$ , the lower bound of the distribution, increases from  $\rho_{\text{ave}}/\rho_{\text{exact}} \approx 0.6$ – $0.9$ , whereas above this value, the lower bound of the distribution remains constant at  $\approx 0.9$ . The upper bound of  $\rho_{\text{ave}}/\rho_{\text{exact}}$  also increases from  $8.44 \times 10^3 \leq \rho_{\text{exact}} \lesssim 2.2 \times 10^4$ , after which it decreases. The distribution of  $\rho_{\text{random}}/\rho_{\text{exact}}$  (right panel) has a much wider spread than that of  $\rho_{\text{ave}}/\rho_{\text{exact}}$ , although its upper bound is  $\approx 1.0$  for all values of  $\rho_{\text{exact}}$ . In Figure 4.9, the distributions in the left and right panels also differ. The spread of  $\rho_{\text{ave}}/\rho_{\text{exact}}$  (left panel) widens slightly as the frequency increases, with many cases of  $\rho_{\text{ave}} > \rho_{\text{exact}}$  occurring above  $\sim 600$  Hz. However,  $\rho_{\text{random}}/\rho_{\text{exact}}$  (right panel) is distributed uniformly across the entire frequency band, ranging from  $\sim 0.4$ – $1$ .

When  $T_{\text{lag}}$  is increased further to 7200 s, there are *no* cases where  $\rho_{\text{ave}} > \rho_{\text{exact}}$ . Out of 500 trials, 18 produce  $\rho_{\text{random}} > \rho_{\text{exact}}$ , although the largest ( $\rho_{\text{random}} = 1.005 \rho_{\text{exact}}$ ) is significantly smaller than in the previous cases. On average,  $\langle \rho_{\text{ave}}/\rho_{\text{exact}} \rangle = 0.858$ , and  $\langle \rho_{\text{random}}/\rho_{\text{exact}} \rangle = 0.733$ . Aside from this difference, Figure 4.10 shows distributions of  $\rho_{\text{ave}}/\rho_{\text{exact}}$  (left panel) and  $\rho_{\text{random}}/\rho_{\text{exact}}$  (right panel) which are similar in shape to those of the  $T_{\text{lag}} = 3600$  s case (Figure 4.8). In Figure 4.11, however, we note that the largest values of  $\rho_{\text{ave}}/\rho_{\text{exact}}$  occur between  $\sim 200$ – $600$  Hz, unlike the  $T_{\text{lag}} = 3600$  s case.

---

<sup>6</sup>While testing an early version of the code, it was found that the frequency and phase of the signal were erroneously being calculated at the start and not the midpoint of each SFT, resulting in this frequency-dependence. This error has now been fixed.

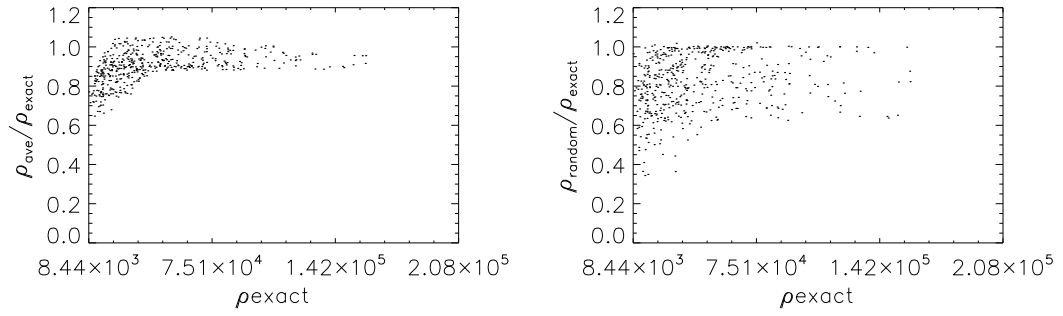


**Figure 4.8:** Distribution of  $\rho_{ave}/\rho_{exact}$  (left panel) and  $\rho_{random}/\rho_{exact}$  (right panel) as a function of  $\rho_{exact}$  for  $T_{lag} = 3600$  s. 500 trials are performed, using randomly distributed  $\nu, \alpha, \delta, \cos \iota,$  and  $\psi$  values. Each point on the figure represents one trial.

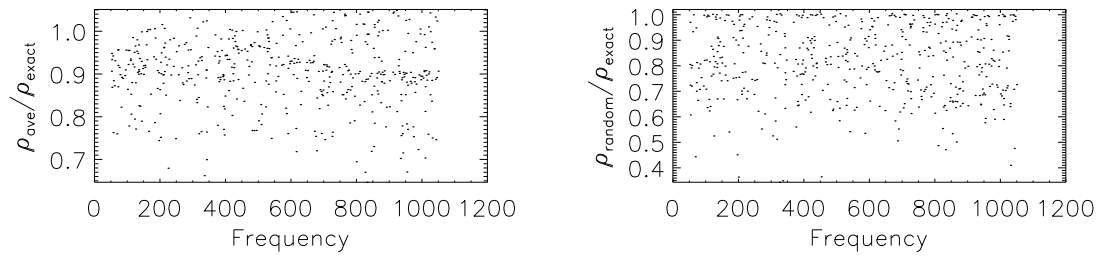


**Figure 4.9:** Distribution of  $\rho_{ave}/\rho_{exact}$  (left panel) and  $\rho_{random}/\rho_{exact}$  (right panel) as a function of injected signal frequency for  $T_{lag} = 3600$  s. 500 trials are performed, using randomly distributed  $\nu, \alpha, \delta, \cos \iota,$  and  $\psi$  values. Each point on the figure represents one trial.

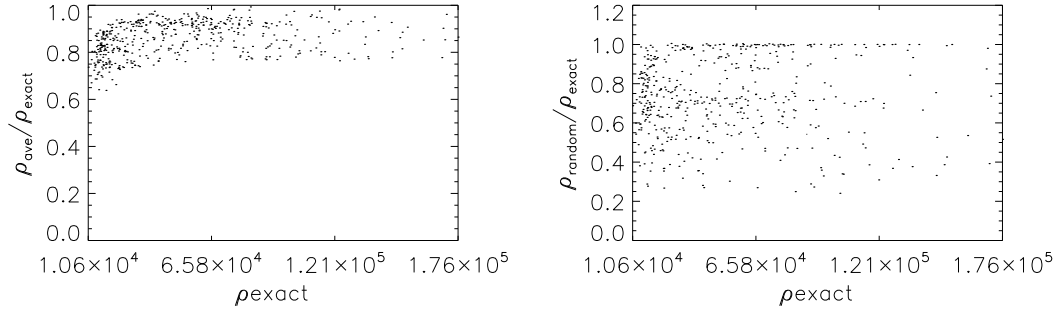


**Figure 4.10:** Distribution of  $\rho_{\text{ave}}/\rho_{\text{exact}}$  (left panel) and  $\rho_{\text{random}}/\rho_{\text{exact}}$  (right panel) as a function of  $\rho_{\text{exact}}$  for  $T_{\text{lag}} = 7200$  s. 500 trials are performed, using randomly distributed  $\nu, \alpha, \delta, \cos \iota,$  and  $\psi$  values. Each point on the figure represents one trial.

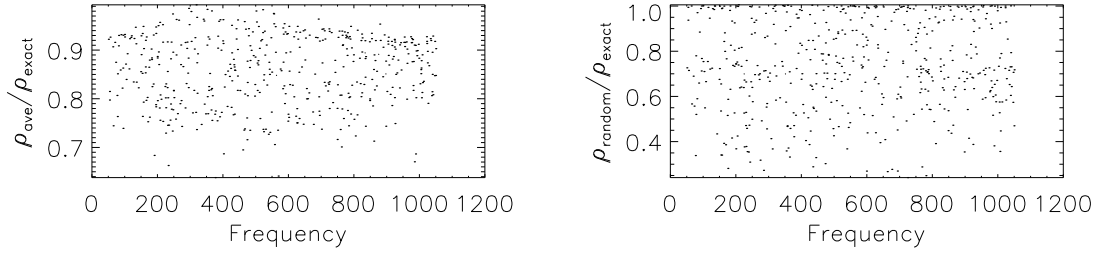


**Figure 4.11:** Distribution of  $\rho_{\text{ave}}/\rho_{\text{exact}}$  (left panel) and  $\rho_{\text{random}}/\rho_{\text{exact}}$  (right panel) as a function of injected signal frequency for  $T_{\text{lag}} = 7200$  s. 500 trials are performed, using randomly distributed  $\nu, \alpha, \delta, \cos \iota,$  and  $\psi$  values. Each point on the figure represents one trial.

In contrast,  $\rho_{\text{random}}/\rho_{\text{exact}}$  is uniformly distributed across the entire frequency band.

The dependence of this effect on  $T_{\text{lag}}$  implies that there may be an error in either the theoretical or numerical calculation of the exponential factors in  $\tilde{\mathcal{G}}_{IJ}$ , as they are the only parameters which change with  $T_{\text{lag}}$ . This remains an open issue which will be resolved in the coming months, after the deadline for submission of this thesis. However, as the excess of  $\rho_{\text{ave}}$  over  $\rho_{\text{exact}}$  is limited to the  $\sim 5\%$  level for  $T_{\text{lag}} \geq 3600$  s, we are able to place upper limits on the sensitivity of the search code to within a 5% accuracy.

### 4.3 Sensitivity estimates

In this section, we present preliminary results of Monte Carlo tests to determine the smallest gravitational wave signal (without spin down) detectable by the search code. A search returns a positive candidate if the resulting detection statistic exceeds a threshold value  $\rho_{\text{th}}$ . In order to place 95% confidence limits on the smallest detectable wave strain, we must find empirically the value of

$h_0$  for which at least 95% of the Monte Carlo trials yield  $\rho \geq \rho_{\text{th}}$ .

We perform tests at three frequencies: 150 Hz, 300 Hz, and 600 Hz. Each test consists of  $10^3$  trials. For each trial, we generate 1 year of 30 minute SFTs using *lalapps\_Makefakedata\_v4*, with signal parameters  $(\alpha, \delta) = (1.31931, -1.20899)$  (the coordinates of SNR 1987A), and random  $\cos \iota$ , and  $\psi$ . We then search for the signal using the exact sky position  $(\alpha, \delta)$ , and averaging over  $\cos \iota$  and  $\psi$ . The power spectral density at a given frequency for each SFT is calculated using equation (4.3).

### 4.3.1 Estimating $\rho_{\text{th}}$

For a given false alarm rate  $\alpha_f$ ,  $\rho_{\text{th}}$  can be estimated empirically from Monte Carlo searches over pure noise in the following way. SFTs containing pure noise are generated, and a search is run over a range of  $\nu, Q_1, Q_2$ , and  $n$ .  $\rho_{\text{th}}$  is then the value of  $\rho$  which yields  $\alpha$  positive detections. In this chapter, we consider  $\alpha_f = 1\%$ , i.e. for  $10^3$  searches over pure noise, we adjust the value of  $\rho_{\text{th}}$  until 10 trials have  $\rho/\sigma_\rho > \rho_{\text{th}}$ .

As shown in Section 4.2.1, for pure noise, the distribution of  $\rho/\sigma_\rho$  is a Gaussian with zero mean and standard deviation  $\approx 1$ . There are two analytic estimates one can perform to validate the results of the Monte Carlo searches. Firstly, equation (3.14) is an analytic expression for  $\rho_{\text{th}}$  for a given false alarm rate and standard deviation,  $\rho_{\text{th}} = \sqrt{2}\sigma\text{erfc}^{-1}(2\alpha_f/N)$ , where  $\alpha_f$  is the false alarm rate, and  $N$  is the number of search templates. For a Gaussian distribution with mean zero and unit standard deviation, this is equivalent to  $\rho_{\text{th}} \approx F^{-1}[1 - (\alpha_f/N)]$ , where  $F^{-1}[x]$  is the inverse cumulative distribution function (CDF) of  $x$ . As  $\rho_{\text{th}}$  increases with the number of search templates, it must be therefore be estimated independently for every search which uses a different  $N$ . Figure 4.12 plots  $\rho_{\text{th}}$  as a function of  $N$ , obtained from solving (3.14).  $\rho_{\text{th}}$  ranges from 3.72 for  $N = 10^2$  to 7.03 for  $N = 10^{10}$ .

We now determine  $\rho_{\text{th}}$  for our Monte Carlo searches. When searching for a signal with no spin down, the signal power is concentrated within one frequency bin. For the sake of computational economy, we therefore limit our search to a 0.1 Hz band, using a frequency resolution of  $10^{-4}$  Hz. Each of the  $10^3$  trials therefore consists of  $N = 10^3$  search templates. For a  $\alpha_f = 0.01$  and  $\sigma = 1$ , the analytic estimates yield  $\rho_{\text{th}} = 4.265$ . For each trial, we choose the largest  $|\rho/\sigma_\rho|$  value returned. We determine  $\rho_{\text{th}}$  empirically by finding the value of  $\rho_{\text{th}}$  which is exceeded by only 10 of the  $|\rho/\sigma_\rho|$  values.

Table 4.2 lists  $\rho_{\text{th}}$  for each of the three trial frequencies. The values of  $\rho_{\text{th}}$

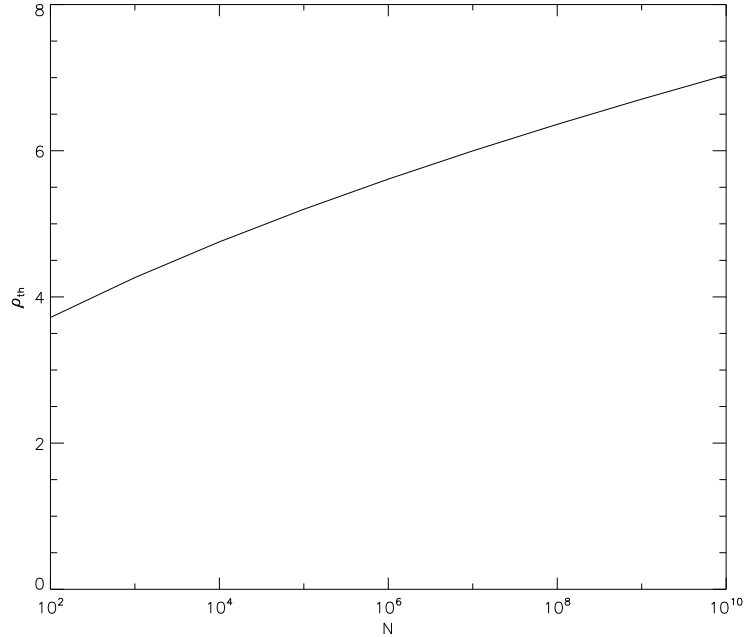


**Figure 4.12:** Analytic estimates for  $\rho_{\text{th}}$ , using (3.14). We assume a false alarm rate  $\alpha_f$  of 0.01, and a standard deviation (in pure noise) of  $\sigma = 1$ , and a total number of search templates between  $10^2 \leq N \leq 10^{10}$ .

Frequency band (Hz)	$\rho_{\text{th}}$
150.0–150.1	4.550
300.0–300.1	4.470
600.0–600.1	4.493

**Table 4.2:**  $\rho_{\text{th}}$  for each 0.1 Hz frequency band (starting at 150 Hz, 300 Hz, and 600 Hz respectively) used in the Monte Carlo searches over pure noise, without spin down.

lie between 4.470–4.550, which are within 5–7% of the second, CDF-based analytic estimate.

### 4.3.2 Sensitivity without spin down

In the case of zero spin down, we inject signals with strains ranging between  $1 \times 10^{-25} \leq h_0 \leq 2 \times 10^{-24}$  into 1 year of SFTs. The mean, normalized detection statistic  $\langle \rho / \sigma_\rho \rangle$  (averaged over  $10^3$  trials) is plotted as a function of  $h_0$  in Figure 4.13. The solid, dotted, and dashed lines denote injected signal frequencies near  $\nu_0 = 150.05$  Hz, 300.05 Hz, and 600.05 Hz respectively. The signal frequencies are injected with a slight mismatch  $\delta\nu = \eta\Delta\nu$ , where  $\eta$  is a random number between 0 and 1, and is different for each trial, and  $\Delta\nu = 10^{-4}$  Hz is the search template spacing in the frequency band, e.g. for

the 150 Hz case, the injected signal frequencies are  $(150.05 + 10^{-4}\eta)$  Hz. This is done to simulate the mismatch between a given set of search templates and a real signal with unknown  $\nu$ . In each trial, we search a 0.1 Hz Band centred on  $\nu_0$ .

As expected, the values of  $\rho/\sigma_\rho$  are largest in the 150 Hz–150.1 Hz band, and the sensitivity decreases with increasing frequency as  $\sqrt{S_n}$  increases. In Figure 4.14, we plot the confidence levels  $C$  (i.e. the fraction of  $\rho/\sigma_\rho$  values, in each set of  $10^3$  trials, which exceed  $\rho_{\text{th}}$ ) as a function of  $h_0$ . For a signal at 150 Hz (solid line),  $C$  increases from 0 at  $h_0 = 1 \times 10^{-25}$  to 1.0 at  $h_0 = 7 \times 10^{-25}$ . For signals at 300 Hz (dotted line) and 600 Hz (dashed line),  $C$  reaches 1.0 at  $h_0 = 9 \times 10^{-25}$  and  $2 \times 10^{-24}$  respectively. Table 4.3 lists the values of  $h_0$  at which the confidence levels are sampled, with the corresponding values of  $C$ . Simple linear interpolation provides an estimate of the value of  $h_0$  which yields  $C = 0.95$ , denoted  $h_0^{95\%}$ : for 150.05 Hz,  $h_0^{95\%} \approx 4.97 \times 10^{-25}$ , for 300.05 Hz,  $h_0^{95\%} \approx 6.92 \times 10^{-25}$ , and for 600.05 Hz,  $h_0^{95\%} \approx 1.41 \times 10^{-24}$ .

Note that the above limits are for a search using  $10^3$  templates. The full search is expected to cover  $\sim 10^9$  templates, corresponding to a larger  $\rho_{\text{th}}$ . Instead of performing Monte Carlo estimates over all  $10^9$  templates, we can estimate  $\rho_{\text{th}}$  analytically from (3.14), giving  $\rho_{\text{th}} = 6.71$ . In Figure 4.15, we plot  $C$  as a function of  $h_0$ , using  $\rho_{\text{th}} = 6.71$ . As expected, the estimates for  $h_0^{95\%}$  are  $\sim 25\%$  larger: for 150.05 Hz,  $h_0^{95\%} \approx 5.90 \times 10^{-25}$ , for 300.05 Hz,  $h_0^{95\%} \approx 8.45 \times 10^{-25}$ , and for 600.05 Hz,  $h_0^{95\%} \approx 1.69 \times 10^{-24}$ . A list of  $h_0$  with the corresponding values of  $C$  is presented in Table 4.4. These estimates will be verified numerically in the future.

### 4.3.3 Sensitivity with spin down

When we include spin down, the search sensitivity can be measured in terms of  $Q_1$  and  $Q_2$ . Hence, instead of injecting signals within a given range of  $h_0$ , we can instead inject signals corresponding to a range of  $Q_1$  and  $Q_2$ . Due to limited computational resources<sup>7</sup>, we are unable to perform sensitivity estimates for values of  $\nu \gtrsim 150$  Hz and  $Q_1 \gtrsim 1 \times 10^{-18}$ . These limits result in detection statistics which fall well below the 95% confidence limit.

We now outline the steps required to complete the sensitivity estimates, which will be performed on the more powerful Atlas cluster in Hannover, Ger-

<sup>7</sup>Each node on the Morgane computing cluster has 2 GB of RAM. In order to generate 1 year of SFTs spanning a 5 Hz band (for  $\nu = 150$  Hz, and  $Q_1 = Q_2 = 10^{-18}$ ), approximately 1.5 GB of RAM is required. Larger  $\nu$ ,  $Q_1$ , and  $Q_2$  values require the SFTs to span a larger frequency band.

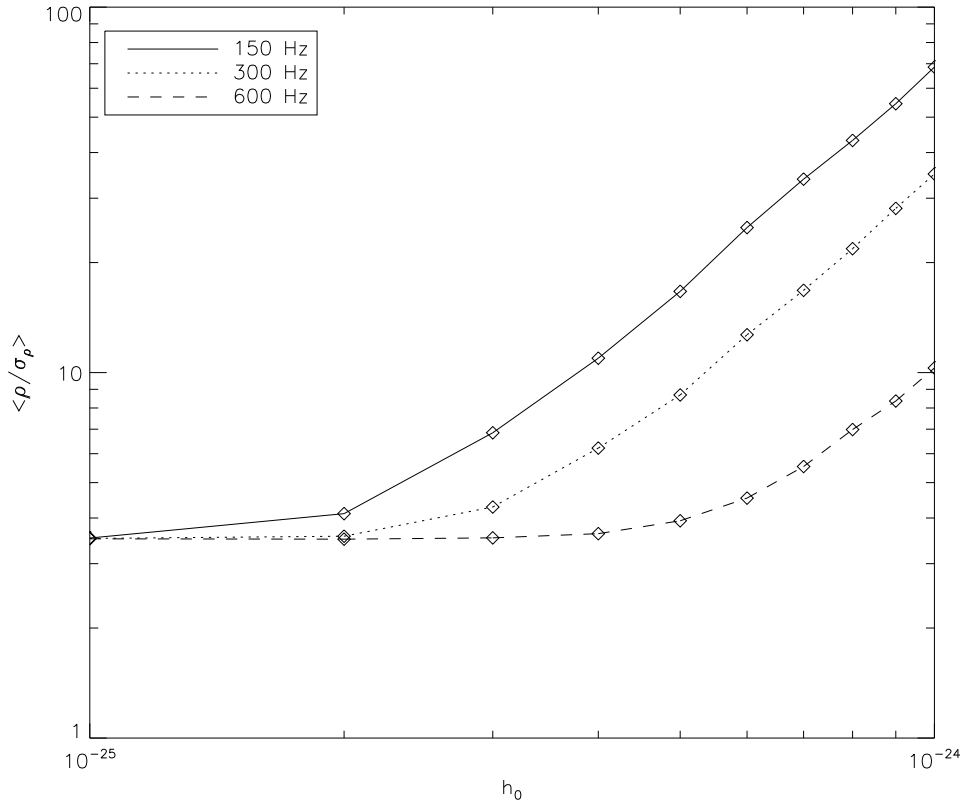


**Figure 4.13:** The mean, normalized detection statistic  $\langle \rho / \sigma_\rho \rangle$  (averaged over  $10^3$  trials) as a function of injected gravitational wave strain  $h_0$ . The injected signals have random parameters  $\cos \iota$ , and  $\psi$ , fixed sky positions  $(\alpha, \delta) = (1.31931 \text{ rad}, -1.20899 \text{ rad})$ , and  $\nu_0$  of  $(150.05 + 10^{-4}\eta) \text{ Hz}$  (solid line),  $(300.05 + 10^{-4}\eta) \text{ Hz}$  (dotted line), and  $(600.05 + 10^{-4}\eta) \text{ Hz}$  (dashed line), where  $\eta$  is a random number between 0 and 1. We  $\rho_{\text{th}}$  corresponding to  $10^3$  search templates per trial. The signals have zero spin down and span 1 year of SFTs.

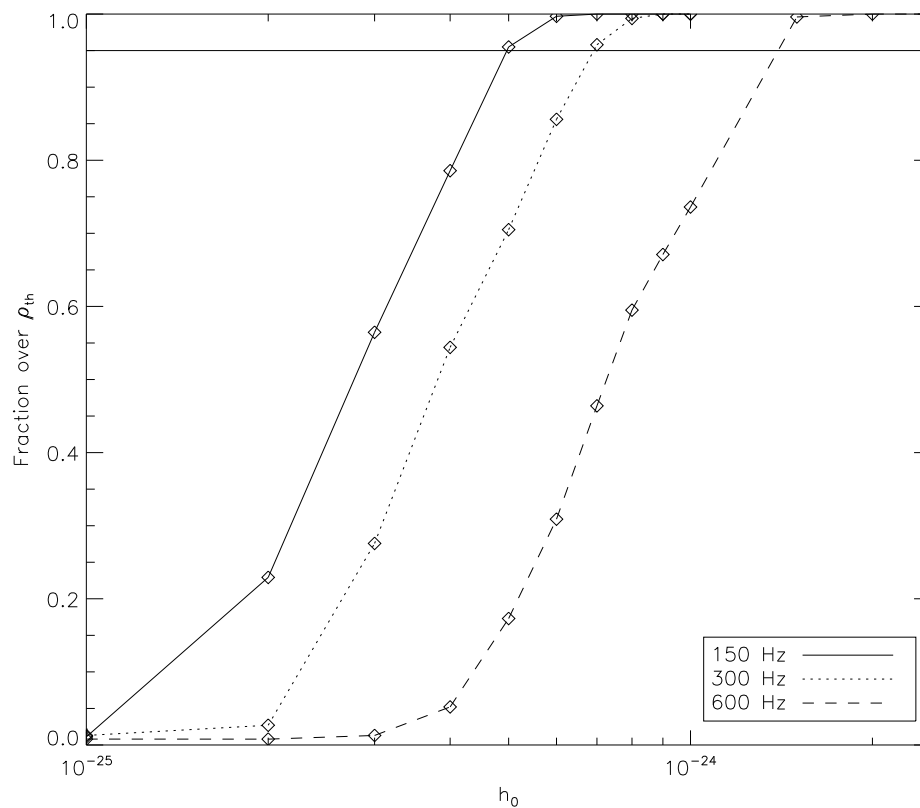


**Figure 4.14:** Confidence levels,  $C$ , as a function of injected gravitational wave strain  $h_0$ . The injected signals have random parameters  $\cos \iota$ , and  $\psi$ , fixed sky positions  $(\alpha, \delta) = (1.31931 \text{ rad}, -1.20899 \text{ rad})$ , and  $\nu_0$  of  $(150.05 + 10^{-4}\eta) \text{ Hz}$  (solid line),  $(300.05 + 10^{-4}\eta) \text{ Hz}$  (dotted line), and  $(600.05 + 10^{-4}\eta) \text{ Hz}$  (dashed line), where  $\eta$  is a random number between 0 and 1. We use  $\rho_{th}$  corresponding to  $10^3$  search templates per trial. The signals have zero spin down and span 1 year of SFTs. The horizontal line shows the 95% confidence level.

$h_0$ ( $10^{-25}$ )	$C$ (150.05 Hz)	$C$ (300.05 Hz)	$C$ (600.05 Hz)
1	0.0111	0.013	0.008
2	0.229	0.027	0.008
3	0.565	0.276	0.013
4	0.786	0.544	0.052
5	0.955	0.704	0.173
6	0.997	0.856	0.309
7	1.0	0.958	0.464
8	1.0	0.994	0.575
9	1.0	1.0	0.671
10	1.0	1.0	0.736
15	1.0	1.0	0.996
20	1.0	1.0	1.0

**Table 4.3:** Table of confidence levels,  $C$ , as a function of  $h_0$  for injected signals at  $(150.05 + 10^{-4}\eta)$  Hz,  $(300.05 + 10^{-4}\eta)$  Hz, and  $(600.05 + 10^{-4}\eta)$  Hz, where  $\eta$  is a random number between 0 and 1. We use  $\rho_{\text{th}}$  corresponding to  $10^3$  search templates per trial. The signals have no spin down and span 1 year of SFTs.

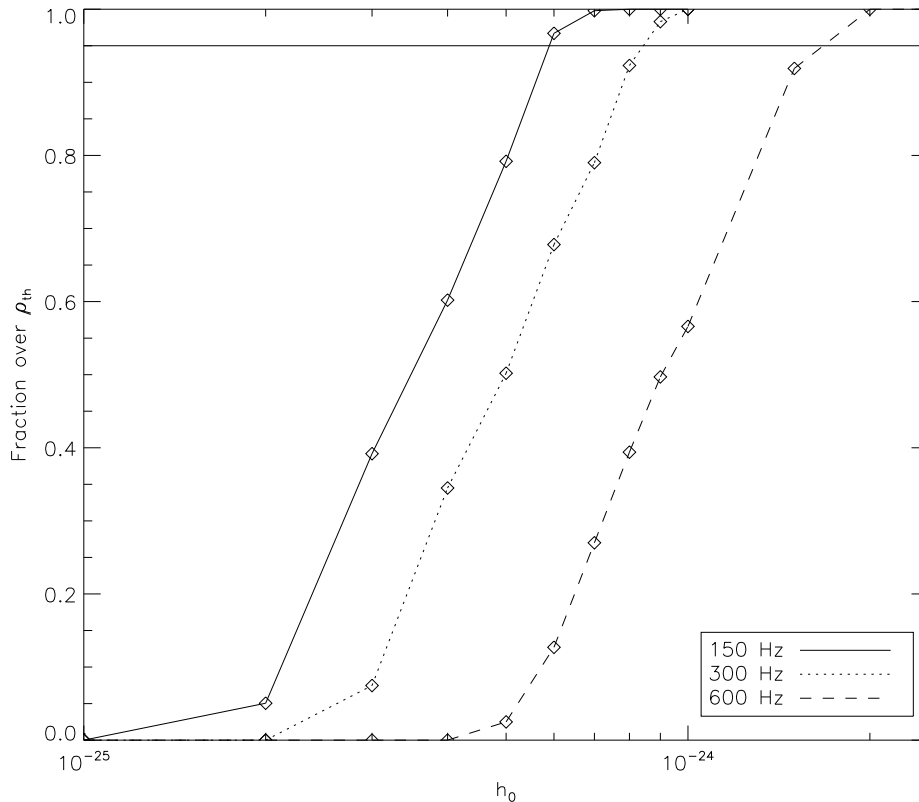


**Figure 4.15:** Confidence levels,  $C$ , as a function of injected gravitational wave strain,  $h_0$ , as in Figure 4.14, but with  $\rho_{\text{th}}$  corresponding to  $10^9$  search templates per trial. The signals have zero spin down and span 1 year of SFT. The horizontal line shows the 95% confidence level.

$h_0$ ( $10^{-25}$ )	$C$ (150.05 Hz)	$C$ (300.05 Hz)	$C$ (600.05 Hz)
1	0.0	0.0	0.0
2	0.051	0.0	0.0
3	0.392	0.075	0.0
4	0.602	0.345	0.0
5	0.792	0.502	0.025
6	0.967	0.678	0.127
7	0.998	0.790	0.270
8	1.0	0.923	0.394
9	1.0	0.983	0.497
10	1.0	1.0	0.566
15	1.0	1.0	0.919
20	1.0	1.0	1.0

**Table 4.4:** Table of confidence levels,  $C$ , as a function of  $h_0$ , as in Table 4.3, but with  $\rho_{\text{th}}$  corresponding to  $10^9$  search templates per trial. The signals have no spin down and span 1 year of SFTs.

many, in the coming months. First, we note that the *lalapps\_Makefakedata\_v4* utility was not written to accommodate the astrophysical phase model. Instead it accepts up to three frequency derivatives. Hence, we take the following steps to generate SFTs using *lalapps\_Makefakedata\_v4*.

1. For given  $\nu$ ,  $Q_1$ ,  $Q_2$ , and  $n$ , we calculate  $\dot{\nu}$ ,  $\ddot{\nu}$ , and  $\dddot{\nu}$ . For simplicity, we assume the electromagnetic braking index  $n = 3$  for all cases.
2. Using equation (3.18), we calculate  $h_0$  from  $\nu$  and  $Q_1$ . In (3.18), we set the distance to the source to be 51.4 kpc, the distance to SNR 1987A.

One restriction is that this method limits the spin-down rate  $\dot{\nu} \lesssim 10^{-7}$  Hz  $\text{s}^{-1}$ . For larger values of  $\dot{\nu}$ , after  $T_{\text{obs}} = 1$  yr, the discrepancy between  $\nu$  set by *lalapps\_Makefakedata\_v4* and  $\nu$  calculated by the astrophysical model becomes larger than  $(1/\Delta T)$  Hz (one SFT frequency bin), and the search code is unable to accurately track the phase of the signal.

## 4.4 Conclusion

In Chapter 3, we discuss the motivation and theoretical framework for the cross-correlation search for a young neutron star in SNR 1987A. In this chapter, we implement the search algorithm. We have added our software to the LAL/LALAPPs software suite used by the LSC. The search code has been under internal LSC review since June 2009.

In order to verify that the code is functioning correctly, we have conducted Monte Carlo tests on simulated Gaussian noise, as well as on simulated signals injected into Gaussian noise. We note the following key results.

- When the search is run on pure noise, the distribution of the detection statistic,  $\rho/\sigma_\rho$ , depends on  $N_{\text{pairs}}$ , the number of pairs included in the search. As  $N_{\text{pairs}}$  increases, the distribution of  $\rho/\sigma_\rho$  approaches a Gaussian with mean zero and unit variance, as expected. We note that the standard deviation of  $\rho/\sigma_\rho$  exceeds unity by  $\approx 2\%$  for all values of  $N_{\text{pairs}}$ . This is not expected to impact the results of the search significantly, although we keep this issue in mind as we proceed with the analysis.
- In the presence of a non-zero signal, the mean of  $\rho/\sigma_\rho$  scales as  $h_0^2$ , as expected. The variance of  $\rho/\sigma_\rho$  also scales as  $h_0^2$ , for  $h_0 < \sqrt{S_n/\text{Hz}}$ . For  $h_0 \gtrsim \sqrt{S_n/\text{Hz}}$ , the variance scales as approximately  $h_0^4$ .
- The software allows the user to search over an exact source inclination angle and polarization angle or average over the two angles. This is done by using either  $\tilde{\mathcal{G}}_{IJ}$  or  $\langle \tilde{\mathcal{G}}_{IJ} \rangle_{\cos\iota, \psi}$  defined in (4.8) and (4.19). Although searching over the exact angles should always yield larger  $\rho/\sigma_\rho$ , when comparing the two methods, we find unexpectedly that in some cases,  $\rho_{\text{ave}}/\rho_{\text{exact}} > 1$ . This effect is worse for small  $T_{\text{lag}}$ , and disappears when  $T_{\text{lag}}$  is increased to 7200 s. It may be indicative of a software error, and will be investigated further.

We also perform preliminary sensitivity estimates, for signals without spin down. We estimate analytically and numerically the quantity  $\rho_{\text{th}}$  for a 0.1 Hz search using  $10^3$  templates, centred on the frequencies 150.05 Hz, 300.05 Hz, and 600.05 Hz. For a 1% false alarm rate, the values of  $\rho_{\text{th}}$  obtained numerically range from 4.470–4.550, and are 5–7% larger than the analytic estimate. Using the numerical results, for a search with  $10^3$  templates, the 95% confidence levels on the wave strain sensitivity are estimated to be  $h_0^{95\%} \approx 4.97 \times 10^{-25}$ ,  $6.92 \times 10^{-25}$ , and  $1.41 \times 10^{-24}$  for 150.05 Hz, 300.05 Hz, and 600.05 Hz respectively. For a search with  $10^9$  templates, we can estimate  $\rho_{\text{th}}$  analytically, yielding 95% confidence levels on the wave strain sensitivity to be  $h_0^{95\%} \approx 5.90 \times 10^{-25}$ ,  $8.45 \times 10^{-25}$ , and  $1.69 \times 10^{-24}$  for 150.05 Hz, 300.05 Hz, and 600.05 Hz respectively. As these results apply to signals with zero spin down, we are unable to directly link the confidence limits to limits on the magnetic field and ellipticity using the astrophysical model discussed in chapter 3. However, as a rough guide, we can apply (3.18) to the results, yielding ellipticity limits of  $1.16 \times 10^{-6}$ ,  $1.02 \times 10^{-7}$ ,

and  $2.04 \times 10^{-7}$  for 150.05 Hz, 300.05 Hz, and 600.05 Hz respectively. We are prevented from making detailed sensitivity estimates for signals with non-zero spin down by computational and time restrictions.

Further work is required before the search begins. It includes:

- resolving the issue of why  $\rho_{\text{ave}}$  exceeds  $\rho_{\text{exact}}$  for small  $T_{\text{lag}}$ ,
- finalizing the exact range of parameters to be searched, using the results from Chapter 3 as a guide, and
- estimating  $\rho_{\text{th}}$  across the entire search template space, and conducting extensive sensitivity estimates based on detector noise instead of simulated Gaussian noise.

The search is expected to begin in mid-late 2010.



# 5 Stokes tomography of radio pulsar magnetospheres. I. Linear polarization

## 5.1 Introduction

Polarimetric studies of pulsar radio emission probe the geometry of the pulsar magnetosphere. Although the phenomenology of the emission is often complex, there are some general trends in the observed pulse shapes and polarization angle (PA) swings that have been explained qualitatively with simple magnetospheric models. In many objects, the data are approximately consistent with *low-altitude* emission from open *dipolar* field lines centred on the magnetic axis (e.g. Rankin 1983; Lyne & Manchester 1988), although in some objects, like the Crab, the emission is thought to emerge as a fan beam from higher altitudes in the outer magnetosphere (e.g. Cheng & Ruderman 1977; Kaspi et al. 2000).

Three lines of evidence favour an approximately dipolar magnetic field in the radio emission region. First, pulses narrow with increasing frequency. According to the radius-to-frequency mapping, the frequency of the radiation is related to the local particle density, which decreases with altitude, as the dipole field lines diverge (Ruderman & Sutherland 1975; Cordes 1978). The width of the pulse profile is commonly used to infer the emission height, with high-frequency pulses originating closer to the surface (e.g. Manchester 1996; von Hoensbroech & Xilouris 1997b; Karastergiou & Johnston 2007; Weltevrede & Johnston 2008)<sup>1</sup>. Second, in many objects, the pulse width  $W$  is inversely related to the spin period  $P$  of the pulsar according to  $W \propto P^{-1/2}$  (Rankin 1993). This relation can be explained geometrically assuming an emission cone tangent to the last open field line of a dipole (e.g. Gangadhara & Gupta 2001).

---

<sup>1</sup>Not all pulsars obey radius-to-frequency mapping; for example in PSR B0525+21 and PSR B0740–28, the emission frequency increases with altitude (von Hoensbroech & Xilouris 1997b).

Under this assumption, the measured pulse widths can also be related to the cone half-opening angle and the angle between the magnetic and rotation axes (Gil et al. 1984). Third, the plane of linear polarization traces out a characteristic S-shaped swing over one pulse period. The swing has been modelled successfully by the rotating vector model assuming a dipole field (or, more generally, an axisymmetric field). The model relates the gradient of the S-shape at the inflection point to the inclination angle of the observer and the angle between the magnetic and rotation axes (Radhakrishnan & Cooke 1969; Lyne & Manchester 1988; Hibschan & Arons 2001). The phase lag between the centroid of the pulse profile and the inflection point has also been used to estimate the emission altitude (Blaskiewicz et al. 1991).

Unfortunately, experience shows that there are limitations in relying only on the pulse profile and PA swing. For example, the three trends mentioned above fail to fix the geometry uniquely. The PA swing looks remarkably similar for many different orientations of the observer and the magnetic axis. Moreover, observations show that many pulsars do not display the clean, S-shaped swing expected from the rotating vector model. Instead, the S-shape is often distorted, suggesting nondipolar configurations (Karastergiou et al. 2005; Johnston et al. 2008b; Han et al. 2009). In particular, many millisecond pulsars have flat PA profiles (Stairs et al. 1999; Ord et al. 2004), highly distorted profiles (e.g. PSR J0437–4715; Navarro et al. 1997) or seemingly random PAs (e.g. giant pulses from PSR J1824–2452A; Knight et al. 2006). Multi-frequency observations show that the PA swing varies with frequency for many pulsars (Johnston et al. 2008a), indicating that the magnetic geometry changes appreciably with altitude. Several mechanisms can distort a dipole field, e.g. a current flowing along the field lines (Hibschan & Arons 2001; Dyks 2008), or rotational sweepback near the light cylinder (Hibschan & Arons 2001; Dyks & Harding 2004; Dyks 2008).

One diagnostic tool which has been used sparingly but holds considerable promise is the *Stokes phase portrait*, that is, the pattern traced out by the four Stokes parameters  $I$ ,  $Q$ ,  $U$  and  $V$  when plotted against each other over one pulse period. PA swings describe how the quantity  $U/Q$  varies with time, but less effort has been devoted to studying how  $Q$  and  $U$  (say) depend on each other. We show here that Stokes phase portraits harbour a great deal of extra information regarding the magnetospheric geometry. The analysis of polarization data on the  $Q$ - $U$  plane is common practice when calculating rotation measure transfer functions for polarized emission from radio galaxies (e.g. Burn 1966; Brentjens & de Bruyn 2005; Haverkorn et al. 2006), and in

optical and UV pulsar data analysis (e.g. Smith et al. 1988; Graham-Smith et al. 1996; Słowikowska et al. 2009).

In this chapter, we calculate theoretically how the Stokes parameters vary with pulse longitude for several magnetic field configurations and beam patterns. We apply the theoretical results to several radio pulsars to determine the observer’s inclination angle,  $i$ , the angle between the magnetic and rotation axes,  $\alpha$ , the emission altitude, and the approximate geometry of the magnetosphere (e.g. the ratio of poloidal to toroidal field). We call this reconstruction technique *Stokes tomography*. In Section 5.2, we define the model and the algorithm used to generate the Stokes phase portraits. Look-up tables of phase portraits, PA swings, and pulse profiles for a pure dipole field at low emission altitudes are presented in Section 5.3. The look-up tables can be compared directly against observational data for any pulsar to determine the emission geometry. In Section 5.4, we present look-up tables for a pure dipole at 10% of the light cylinder radius, where relativistic aberration effects are important. It is shown that many pulsars that are categorised as pure dipoles on the strength of their PA swing possess Stokes phase portraits that are inconsistent with a pure dipole at low emission altitudes. In Section 5.5, look-up tables are presented for a current-modified dipole field with a radially increasing toroidal component, as in standard magnetospheric models (Spitkovsky 2006). We then model two objects in detail, in Sections 5.6 (PSR J0826+2637) and 5.7 (PSR J0304+1932), which have single-peaked and double-peaked pulses respectively. We compare our recovered  $i$ ,  $\alpha$ , and emission altitude with results from more traditional methods. Future applications of Stokes tomography are canvassed briefly in Section 5.8. Additionally, the method can be extended further by generalizing the approach to circularly polarized pulsar radio emission and realistic (e.g. force-free) magnetic fields.

## 5.2 Stokes tomography

### 5.2.1 Radiation field

In the magnetosphere, radiation from highly relativistic particles tied to magnetic field lines is narrowly beamed along the particle velocity vector. The observed emission point  $\mathbf{x}_0(t)$  at any time  $t$  is therefore located where the magnetic vector  $\mathbf{B}[\mathbf{x}_0(t), (t)]$  points along the observer’s line-of-sight vector  $\mathbf{w}$ . The unit tangent vector to the magnetic field at  $\mathbf{x}_0(t)$  is defined as  $\mathbf{t} = \mathbf{B}[\mathbf{x}_0(t), t]/|\mathbf{B}[\mathbf{x}_0(t), t]|$ . For non-relativistic particles, to find the emis-

sion point at time  $t$ , we must therefore solve the equation  $\mathbf{t} = \mathbf{w}$ . In general, however, when considering emission altitudes of  $r \gtrsim 0.1r_{\text{LC}}$ , where  $r_{\text{LC}} = c/\Omega$  is the light cylinder radius, we must account for relativistic aberration. Aberration shifts the emission point and electric field vector by different amounts of order  $r/r_{\text{LC}}$ . The emission point  $\mathbf{x}_0(t)$  at time  $t$  satisfies the equation (Blaskiewicz et al. 1991)

$$\mathbf{w} = \frac{\mathbf{t} + \boldsymbol{\Omega} \times \mathbf{x}_0/c}{|\mathbf{t} + \boldsymbol{\Omega} \times \mathbf{x}_0/c|}, \quad (5.1)$$

where  $\boldsymbol{\Omega}$  is the angular velocity vector. Note that  $\mathbf{B}$  varies with  $t$  intrinsically, as the star rotates in the observer's frame, not just through  $\mathbf{x}_0(t)$ . The normal to the field at  $\mathbf{x}_0$  is defined as  $\mathbf{n} = \boldsymbol{\kappa}/|\boldsymbol{\kappa}|$ , where  $\boldsymbol{\kappa} = (\mathbf{t} \cdot \nabla)\mathbf{t}$  is evaluated at  $\mathbf{x}_0$ . The binormal is defined as  $\mathbf{b} = \mathbf{t} \times \mathbf{n}$ .

The amplitude and direction of the complex electric field vector  $\mathbf{E}$  at the emission point are determined by the radiation physics, which is not understood in detail. A popular assumption is that  $\mathbf{E}$  at time  $t$  points along the instantaneous acceleration vector of the particle,  $\mathbf{a}$ . To first order in  $r/r_{\text{LC}}$ , the acceleration is given by (Dyks 2008)

$$\mathbf{a} = c \frac{\partial \mathbf{t}}{\partial t} + c(\mathbf{v} \cdot \nabla)\mathbf{t} + c\boldsymbol{\Omega} \times \mathbf{t} + \boldsymbol{\Omega} \times (\boldsymbol{\Omega} \times \mathbf{x}_0), \quad (5.2)$$

in terms of the instantaneous velocity vector  $\mathbf{v} = c\mathbf{t} + \boldsymbol{\Omega} \times \mathbf{x}_0$ , assuming no precession ( $\partial\boldsymbol{\Omega}/\partial t = 0$ ). From left to right, the four terms on the right-hand side of (5.2) describe: (i) the change in field aligned velocity  $c\mathbf{t}$  as the magnetic dipole moment (and hence  $\mathbf{t}$ ) rotates infinitesimally in the inertial frame; (ii) the change in field-aligned velocity  $c\mathbf{t}$  as the charge moves infinitesimally along  $\mathbf{v} = c\mathbf{t} + \boldsymbol{\Omega} \times \mathbf{x}_0$  and hence  $\mathbf{t}$  changes; (iii) the change in corotation velocity  $\boldsymbol{\Omega} \times \mathbf{x}_0$  as the charge moves infinitesimally along the field  $\mathbf{t}$ ; and (iv) the change in corotation velocity  $\boldsymbol{\Omega} \times \mathbf{x}_0$  as the charge corotates infinitesimally with the magnetosphere along  $\boldsymbol{\Omega} \times \mathbf{x}_0$  (Dyks 2008; Hibschan & Arons 2001).

The associated Stokes parameters  $(I, Q, U, V)$  describing the polarization state are defined as

$$I = |E_x|^2 + |E_y|^2 \quad (5.3)$$

$$Q = |E_x|^2 - |E_y|^2 \quad (5.4)$$

$$U = 2\text{Re}(E_x E_y^*) \quad (5.5)$$

$$V = 2\text{Im}(E_x E_y^*), \quad (5.6)$$

where  $I$  is the polarized fraction of the total intensity,  $L = (Q^2 + U^2)^{1/2}$  is the

linearly polarized component, and  $V$  is the circularly polarized component. The  $x$ - and  $y$ - components are measured with respect to an orthonormal basis  $(\hat{\mathbf{x}}, \hat{\mathbf{y}})$  which is fixed in the plane of the sky. In this chapter, we choose  $\hat{\mathbf{x}} = \mathbf{\Omega}_p/|\mathbf{\Omega}_p|$  and  $\hat{\mathbf{y}} = \hat{\mathbf{x}} \times \mathbf{w}$ , where  $\mathbf{\Omega}_p = \mathbf{\Omega} - (\mathbf{\Omega} \cdot \mathbf{w})\mathbf{w}$  is the projection of the angular velocity  $\mathbf{\Omega}$  onto the plane of the sky. Then the polarization angle,  $\psi$ , measured counter-clockwise between  $\hat{\mathbf{x}}$  and the linearly polarized part of  $\mathbf{E}$  is given by

$$\psi = \frac{1}{2} \tan^{-1} \frac{U}{Q}. \quad (5.7)$$

### Orientation of $\hat{\mathbf{x}}$ and $\hat{\mathbf{y}}$

In the observational data, the direction of  $\mathbf{\Omega}$  is usually not known. The polarization basis in which the observed Stokes parameters are expressed may therefore differ from the canonical basis. This affects the Stokes phase portraits in the following way.

Consider two polarization bases,  $(\hat{\mathbf{x}}, \hat{\mathbf{y}})$  and  $(\hat{\mathbf{x}}', \hat{\mathbf{y}}')$ , where  $(\hat{\mathbf{x}}', \hat{\mathbf{y}}')$  is rotated clockwise by an angle  $\beta$  with respect to  $(\hat{\mathbf{x}}, \hat{\mathbf{y}})$ . In the canonical (unprimed) basis, the electric field vector transforms as

$$E_x = \cos \beta E'_x + \sin \beta E'_y, \quad (5.8)$$

$$E_y = -\sin \beta E'_x + \cos \beta E'_y, \quad (5.9)$$

and the Stokes parameters transform as

$$I = I' \quad (5.10)$$

$$Q = Q' \cos 2\beta + U' \sin 2\beta \quad (5.11)$$

$$U = -Q' \sin 2\beta + U' \cos 2\beta. \quad (5.12)$$

Hence, in the  $Q$ - $U$  phase portrait, the pattern rotates counter-clockwise through an angle  $2\beta$  with respect to the  $Q'$ - $U'$  phase portrait, but its shape remains invariant. In contrast, in the  $I$ - $Q$  and  $I$ - $U$  phase portraits, both the shape and orientation of the pattern change. When fitting our model to data, in cases where  $\beta$  is unknown, we first work to match the shape of the pattern in the  $Q$ - $U$  data, without worrying about the orientation. Then, armed with a good fit to the  $Q$ - $U$  shape, we rotate the basis to match the orientation as well and deduce  $\beta$ . Finally, knowing  $\beta$ , we match the patterns in the  $I$ - $Q$  and  $I$ - $U$  data. This iterative procedure is explained in more detail in Sections 5.6 and 5.7. Note that the PAs in the two bases are related by  $\psi = \psi' - \beta$ , as

expected.

## 5.2.2 Numerical algorithm

We now describe how to construct  $(I, Q, U, V)$  as functions of pulse longitude (and hence each other) for a prescribed magnetic geometry.

Let us define two reference frames, as depicted in Figure 5.1: the inertial frame in which the observer is at rest, with Cartesian axes  $(\mathbf{e}_x, \mathbf{e}_y, \mathbf{e}_z)$ , and the body frame of the rotating pulsar, with Cartesian axes  $(\mathbf{e}_1, \mathbf{e}_2, \mathbf{e}_3)$ . The line-of-sight vector  $\mathbf{w}$  is chosen to lie in the  $\mathbf{e}_y$ - $\mathbf{e}_z$  plane, making an angle  $i$  with  $\mathbf{e}_z$ . The rotation and magnetic axes are chosen to lie along  $\mathbf{e}_z$  and  $\mathbf{e}_3$  respectively. The orientation of the body axes with respect to the inertial axes is computed as a function of time by solving Euler’s equations of motion for a rigid body; precession can be included in general, although we do not examine it in this chapter.

We define a spherical polar grid  $(r, \theta, \phi)$  in the body frame covering the region  $x_{\min} \leq r/r_{\text{LC}} \leq x_{\max}$ ,  $0 \leq \theta \leq \pi$ ,  $0 \leq \phi \leq 2\pi$ , with  $64 \times 256 \times 64$  grid cells, where the line  $\theta = 0$  lies along  $\mathbf{e}_3$ . In Sections 5.3–5.7 we show that relativistic aberration and an appreciable toroidal field are needed to explain much of the observational data, so most of our analysis is done in the middle to outer magnetosphere, with  $x_{\min} = 0.001$  and  $x_{\max} = 0.38$ . Nonetheless, other choices are possible and easy to implement. Given a magnetic field  $\mathbf{B}(r, \theta, \phi)$ , we compute  $\mathbf{t}$ ,  $\mathbf{n}$ , and  $\mathbf{b}$  at each grid point using second-order central finite differencing and ghost cells at the edges.

In order to calculate  $(I, Q, U, V)$  versus  $t$ , we search the grid at a fixed altitude  $r_0$  to find the emission point satisfying (5.1) (the point  $P$  in Figure 5.1). At  $P$ ,  $(\mathbf{t} + \boldsymbol{\Omega} \times \mathbf{x}_0/c) \cdot \mathbf{w}$  is a maximum; note that the location of  $P$  changes with time in both the body frame and the inertial frame.<sup>2</sup> To fine-tune the location, we interpolate  $\mathbf{t}$  linearly between the four surrounding points and re-compute (5.1) for each interpolated point. In general, there are two points  $\mathbf{x}_0(t)$  satisfying (5.1) on opposite sides of the pulsar, but the observer only sees the one facing him.

We stipulate the shape of the beam pattern  $I(r, \theta, \phi)$  and the degree of linear

---

<sup>2</sup>In general, we must consider  $\pm \mathbf{t}$  in (5.1) to capture emission from particles flowing out from both north and south poles. In this chapter, however, we restrict our attention to emission from one pole only, to avoid cluttering the look-up tables in Sections 5.3 and 5.5. We therefore do not capture “interpulse” emission with our model. The 24 objects studied in Section 5.5.3, and the two objects modelled in detail in Sections 5.6 and 5.7, exhibit either zero or weak interpulse emission in existing data.

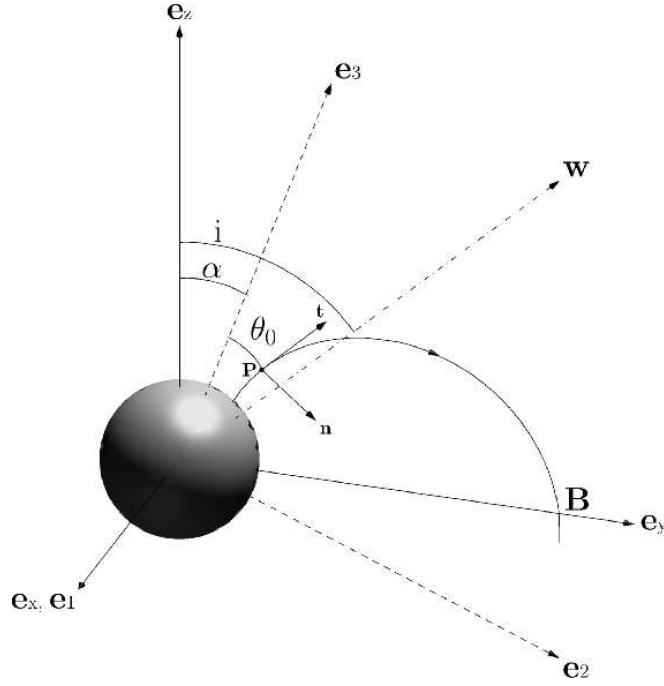


**Figure 5.1:** Orientation of the inertial axes  $\mathbf{e}_x, \mathbf{e}_y, \mathbf{e}_z$  (solid lines) and pulsar body axes  $\mathbf{e}_1, \mathbf{e}_2, \mathbf{e}_3$  (dashed lines) at an instant where  $\mathbf{e}_2$  and  $\mathbf{e}_3$  lie in the  $\mathbf{e}_y$ - $\mathbf{e}_z$  plane. The line of sight vector  $\mathbf{w}$  (dotted line) is defined to always lie in the  $\mathbf{e}_y$ - $\mathbf{e}_z$  plane at an angle  $i$  to  $\mathbf{e}_z$ .  $\mathbf{e}_3$  is tilted with respect to the rotation axis  $\mathbf{e}_z$  by an angle  $\alpha$ . An example of a dipolar field line ( $\mathbf{B}$ ) and its corresponding emission point  $\mathbf{x}_0(t)$  (labelled  $P$ ) are drawn. At  $P$ , the tangent vector is  $\mathbf{t} = \mathbf{w}$  and the normal vector is  $\mathbf{n}$ . The angle between  $\mathbf{t}$  and  $\mathbf{e}_3$  is  $\theta_0$ . The shading on the sphere represents the beam pattern  $I(r, \theta, \phi)$ ;  $I$  is a maximum where the shading is brightest.

polarization  $L(r, \theta, \phi)$ , and assume that  $\mathbf{E}$  is constant and lies along  $\mathbf{a}$ , i.e.

$$\mathbf{E} = La/I. \quad (5.13)$$

In Figure 5.1,  $I(r, \theta, \phi)$  is represented by the shading on the surface of the sphere. It peaks along  $\mathbf{e}_3$  (i.e.  $\theta = 0$ ), i.e. Figure 5.1 depicts a centre-filled beam. Other beam patterns, e.g. a hollow cone, are also considered in Sections 5.3 and 5.5. Note that  $\mathbf{E}$  is purely real in this chapter because we assume  $V = 0$ , i.e. zero circular polarization. Examples of  $I$  and  $L$  are given in Sections 5.2.4 and 5.2.5, drawn either from a phenomenological theory or directly from data.

### 5.2.3 Relativistic aberration

Relativistic aberration acts to shift the pulse centroid relative to the inflection point of the PA swing, such that they are separated in phase by  $\approx$

$4r/r_{\text{LC}}$  radians to leading order (Blaskiewicz et al. 1991; Hibsichman & Arons 2001; Dyks 2008). Hence, aberration introduces an altitude dependence in the case of a pure dipole, which is absent in the non-aberrated case. At large emission altitudes ( $\gtrsim 0.1r_{\text{LC}}$ ), the phase shift can significantly alter the shapes of the Stokes phase portraits. This is investigated further in Section 5.4. Additionally, if the magnetic field sweeps back rotationally, or develops a helical, current-modified component, the emission point at an instant in time varies as a function of altitude. The effects of aberration combined with a current-modified field are investigated in Section 5.5. According to the radius-to-frequency mapping, observing emission from different altitudes is analogous to making observations at several different frequencies.

Equation (5.1) ignores cross-field particle motions (e.g. curvature and gradient drifts) in the outer magnetosphere, where the cyclotron cooling time exceeds the flow time, for the sake of simplicity.

### 5.2.4 Beam pattern

The two most common beam patterns in the literature are the core-and-cone model (Rankin 1983) and the patchy-beam model (Lyne & Manchester 1988). In the core-and-cone model, single-peaked profiles are explained by emission filling the polar flux tube, double-peaked profiles are explained by emission from a hollow cone tangential to the polar flux tube, and triple-peaked profiles are explained by a combination of the two. The patchy-beam model was proposed to explain asymmetric profiles. It suggests that emission comes from randomly distributed locations within an emission beam. In this chapter, for simplicity, we consider two beam shapes based on the Rankin model: (i) a filled core beam (single-peaked pulse profile) and (ii) a hollow cone (double-peaked pulse profile). Both beams are centred on  $\mathbf{e}_3$  and are cylindrically symmetric about it.

The colatitude of the emission point at time  $t$ ,  $\theta_0(t)$ , is obtained from  $\theta_0 = \cos^{-1}[r_0^{-1}\mathbf{x}_0(t) \cdot \mathbf{e}_3]$  and can range over  $0 \leq \theta_0 \leq \pi$ . We model the polarized intensity  $I(t) = I[\theta_0(t)]$  as a gaussian beam,

$$I(\theta_0) = (2\pi\sigma^2)^{-1/2} \exp[-(\theta_0 - \rho)^2/(2\sigma^2)] \quad (5.14)$$

where  $\sigma$  defines the beam width, and  $\rho$  is the half-opening angle of the emission cone. In general,  $\sigma$  and  $\rho$  vary from pulsar to pulsar. However, to generate the look-up tables in Sections 5.3–5.5, we use fixed, representative values:  $\rho = 0^\circ$

and  $\sigma = 10^\circ$  for a filled core, and  $\rho = 25^\circ$  and  $\sigma = 10^\circ$  for a hollow cone. For the sake of simplicity, we assume in what follows that only one pole shines (see footnote above); it is trivial to modify this assumption if necessary.

Equation (5.14) can only be used to model approximately symmetric pulses, e.g. the single-peaked pulse profile of PSR J0826+2637 (Section 5.6). To fit asymmetric profiles, such as that of PSR J0304+1932 (Section 5.7), more complex models, such as a ‘broken cone’ or ‘horseshoe’, are required, in which the intensity varies with longitude  $\phi_0(t)$  as well as  $\theta_0(t)$ . Such asymmetric intensity maps are inspired by the patchy beam model (Lyne & Manchester 1988; Kramer & Johnston 2008).

### Displaced axis of symmetry

Although the magnetic-pole model for pulsar radio emission is commonly used, it is possible that the beam pattern is centred not on the magnetic axis but on another axis that is slightly displaced axis. Fan beams in the outer magnetosphere are an extreme instance of such a geometry (Cheng et al. 2000; Watters et al. 2009), but less dramatic displacements can occur if there are local, quadrupolar surface fields in the vicinity of the magnetic poles.

To illustrate the above effect, we consider an arbitrary example where  $I$  and  $L$  are symmetric about the axis  $\mathbf{e}'_3$  in a reference frame  $(\mathbf{e}'_1, \mathbf{e}'_2, \mathbf{e}'_3)$ , where  $\mathbf{e}'_3$  is tilted with respect to  $\mathbf{e}_3$  by  $10^\circ$ , and where  $\mathbf{e}'_1$  is tilted with respect to  $\mathbf{e}_1$  by  $10^\circ$ . Figure 5.2 compares the original (top panel) and displaced (bottom panel) pulse profiles, PA swings, and Stokes phase portraits for  $(\alpha, i) = (30^\circ, 40^\circ)$ . The displacement causes the pulse phase to lead the PA swing by  $\approx 0.06$  radians. In the bottom panel, the hockey stick in the  $I$ - $Q$  phase portrait broadens slightly, while the shapes in the  $I$ - $U$  and  $Q$ - $U$  planes are tilted and no longer symmetric about  $U = 0$ . Overall, however, tilting the beam by  $\sim 10^\circ$  (the maximum expected from standard polar emission theories, if fan beams are excluded) does not alter the phase portraits greatly. The relative phase shift between the pulse centroid and PA swing inflection is also small compared to other effects such as aberration and/or a toroidal field component. In Sections 5.3–5.5 of this chapter, we therefore assume that the beam and polarization patterns are symmetric about  $\mathbf{e}_3$ , while noting that the Stokes tomography technique can be generalized easily (as in Figure 5.2) to accommodate other possibilities. When modelling individual pulsars in detail, as in Sections 5.6 and 5.7,  $I$  and  $L$  are fitted iteratively and empirically, and asymmetric beam patterns arise naturally.

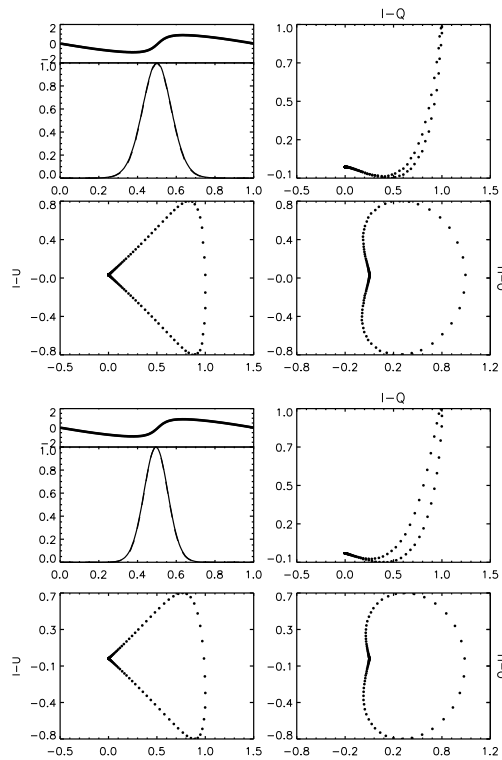


**Figure 5.2:** Theoretical pulse profiles, PA swings, and Stokes phase portraits for a pure dipole and a beam pattern symmetric about  $\mathbf{e}_3$  (top four subpanels), or tilted by  $10^\circ$  with respect to  $\mathbf{e}_3$  and  $\mathbf{e}_1$  (bottom four subpanels), as described in the text. Within each half of the figure, the four subpanels display (clockwise from top left): (a)  $I/I_{\max}$  (bottom) and PA (top; in radians) as functions of pulse longitude, (b)  $I-Q$ , (c)  $Q-U$ , and (d)  $I-U$ . Relativistic aberration is not included in this figure.

### 5.2.5 Linear polarization

The uncertainty surrounding the microscopic emission physics in a pulsar makes it difficult to model its polarization properties, although theoretical progress has been made (e.g. Gil & Snakowski 1990; Melrose 1995; McKinnon & Stinebring 1998; Rankin & Ramachandran 2003; Xu et al. 2000). Much of this work attempts to account for observed orthogonal mode jumps (i.e.  $90^\circ$  jumps in the PA swing). McKinnon & Stinebring (1998) modelled the  $L/I$  distribution statistically, describing  $Q$  as a Gaussian random variable. One physical model assumes that emission comes from inverse Compton scattering, and shows that the fractional linear polarization  $L/I$  varies with  $\theta_0$  (Xu et al. 2000).

In the absence of a unique empirical or theoretical rule for how the fractional linear polarization  $L/I$  varies across the beam, we investigate two simple cases when constructing the look-up tables in Sections 5.3 and 5.5: (i)  $L/I \propto \cos \theta_0$  (generally, but not exclusively, suited to single-peaked profiles), and (ii)  $L/I \propto \sin \theta_0$  (generally, but not exclusively, suited to double component profiles). The proportionality constants are chosen to be unity in Sections 5.3–5.5 for simplicity, but, in reality, approximately 80% of normal pulsars have a pulse-averaged  $L/I \leq 0.3$  (Xilouris et al. 1998).

Although the above models are useful for illustrating the variety of Stokes phase portraits in our look-up tables, they are a rough approximation in any specific object. Model (i) gives  $L/I \sim 1$  for small  $\theta_0$ , higher than the observed fraction in most pulsars. Moreover, in many objects, there is a phase lag between  $I$  and  $L$ , which we ignore. When analysing data from specific objects in detail in Sections 5.6 and 5.7, we extract  $L/I$  from the data itself and feed it into our profile simulator to retrieve  $|E_x|$  and  $|E_y|$ . We do not attempt to model orthogonal mode jumps in this chapter.

### 5.2.6 Summary of algorithm

Figure 5.3(a) summarises, in the form of a flowchart, the steps required to generate the PA swing, pulse profile, and Stokes phase portraits for a pulsar with a given magnetic configuration (as described in Sections 5.2.1–5.2.5 above). Figure 5.3(b) summarises the steps required to match the theoretical PA swing, pulse profile, and Stokes phase portraits from the look-up tables to observational data and thereby infer the pulsar’s orientation and magnetic geometry. For a nondipolar field, the results depend on altitude, so the process must be repeated using several values of  $r$  until a good match is achieved. We

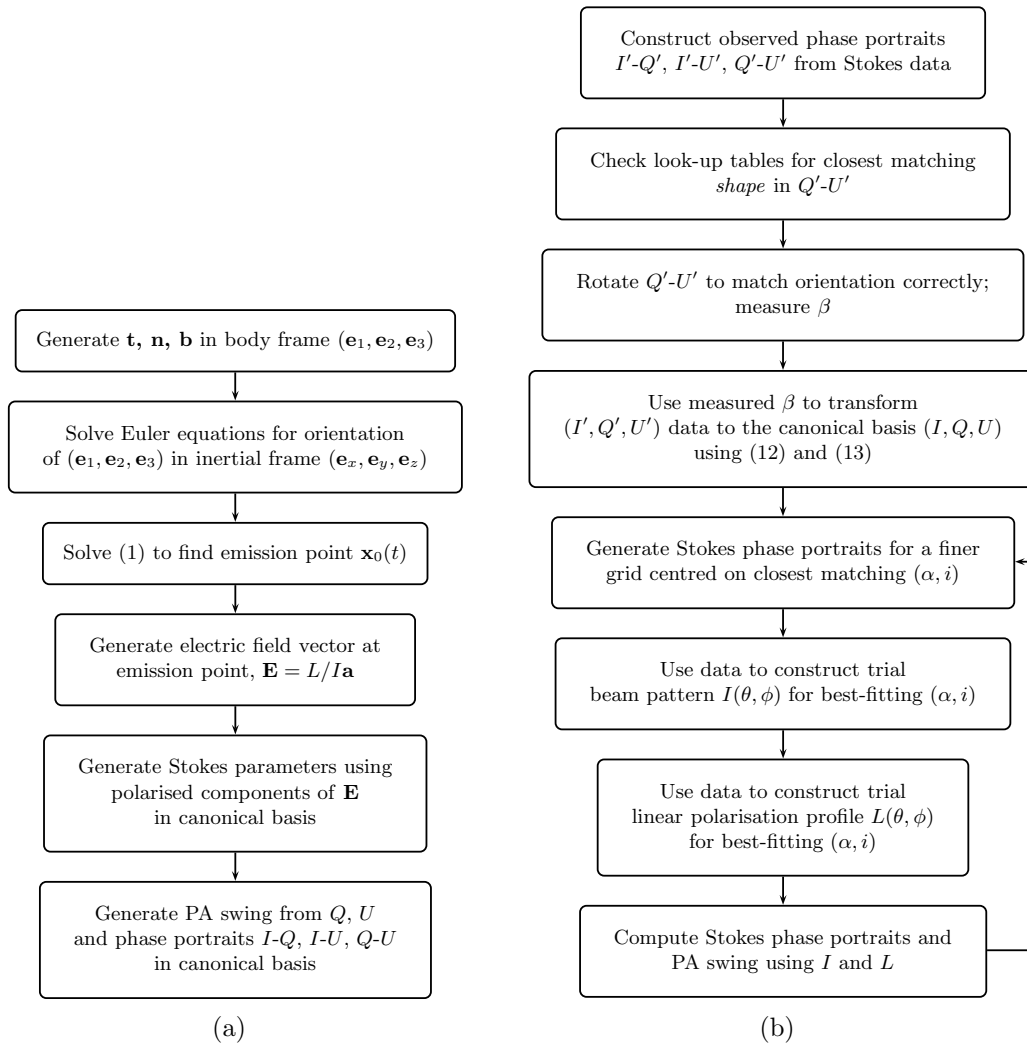


**Figure 5.3:** (a) Recipe to generate look-up tables of Stokes phase portraits, PA swings, and pulse profiles for a given orientation and magnetic geometry. (b) Iterative recipe to extract orientation and magnetic geometry from observational data.

note that in principle, if  $\beta$  is unknown, one can also repeat the process using several values of  $\beta$ . However, throughout this chapter, we find that once an approximate estimate for  $\beta$  is found, it is more useful to explore  $\alpha$  and  $i$  in detail, as varying  $\beta$  only alters the orientation of the  $Q-U$  pattern, and not its shape.

### Fitting technique

Due to the often complex shapes of the Stokes phase portraits, we do not use formal chi-squared fitting techniques in this chapter. When iteratively searching for a fit to the data, we match the patterns by eye. The matches are quantified by comparing the sizes of the shapes from the model and data in the two axes

separately. For example, in Section 5.7, we quantify the match between the data and the model (Figures 5.63 and 5.64) in the  $U$ - $Q$  plane by noting that in the data, the phase portrait is 9% larger in the  $U$  axis, and 8% larger in the  $Q$  axis. Throughout this chapter, the modelled phase portraits are considered a good match to the data when the overall shape of the portraits match, and when the sizes of the shapes differ by less than 10%. Similarly, when modelling multi-component pulse profile shapes empirically, we match the pulse profiles by eye.

A more sophisticated technique, for example, is to apply a bootstrap procedure to obtain confidence intervals for the data, then perform a chi-squared fit. Alternatively, one can impose selection criteria for a ‘good’ fit, stating that each point in the phase portraits in the data and the model should not deviate by more than 10%. In order to do this, however, the modelled Stokes portraits have to be sampled at the same intervals as the data. We will investigate these techniques in the future.

### 5.3 Dipole field at low emission altitudes

In this section, we calculate Stokes phase portraits, PA swings, and pulse profiles for a pulsar with a purely poloidal, dipolar magnetic field at low emission altitudes, where the effects of relativistic aberration are negligible. We generate a two-dimensional look-up table of phase portraits for orientations  $10^\circ \leq i \leq 90^\circ$  and  $10^\circ \leq \alpha \leq 90^\circ$ . For each beam pattern (core emission in Section 5.3.1, conal emission in Section 5.3.2) and polarization pattern ( $L/I = \cos \theta_0, \sin \theta_0$ ), we present three phase portraits ( $I$ - $Q$ ,  $I$ - $U$ ,  $Q$ - $U$ ) for each pair of angles  $(\alpha, i)$ . Finally, in Section 5.4.3, we analyse a selection of full Stokes data obtained from the European Pulsar Network (EPN)<sup>3</sup> online archive (Lorimer et al. 1998) for objects in Gould & Lyne (1998). We show that a dipole field (and hence low-altitude emission) is inconsistent with the observed phase portraits of many superficially dipole-like pulsars, e.g. objects which obey the pulse-width-period relation or exhibit clean, S-shaped PA swings.

---

<sup>3</sup>Available at: <http://www.mpifr-bonn.mpg.de/pulsar/data/>

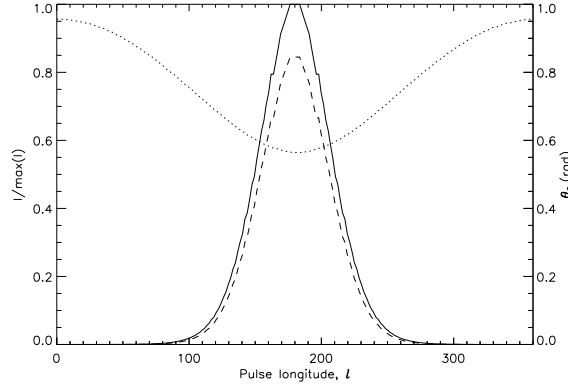


**Figure 5.4:** Dipole field at a low emission altitude  $r \ll r_{LC}$ . Example of a pulse profile for a filled core beam with linear polarization  $L = I \cos \theta_0$  and  $(\alpha, i) = (70^\circ, 20^\circ)$ . Solid, dashed and dotted curves represent the total polarized intensity  $I$ , degree of linear polarization  $L$ , and emission point colatitude  $\theta_0$ . Pulse longitude  $l$  is measured in units of degrees.

### 5.3.1 Filled core emission

$$L = I \cos \theta_0$$

Examples of the  $I$  (solid curve) and  $L$  (dashed curves) profiles for  $(\alpha, i) = (70^\circ, 20^\circ)$  are shown in Figure 5.4.  $I$  is normalised by its peak value. The pulse is single-peaked and maximally polarized at the peak. The dotted curve shows how the magnetic colatitude  $\theta_0(t)$  of the emission point varies across one pulse period. We note the following trends. (i) The pulse profile narrows with increasing  $i$  and  $\alpha$  as the emission point moves further from the magnetic pole. The full-width half-maximum (FWHM) decreases from  $\approx 0.5$  phase units at  $(\alpha, i) = (10^\circ, 10^\circ)$  to  $\approx 0.15$  at  $(\alpha, i) = (90^\circ, 90^\circ)$ . (ii) For  $\alpha = i$ , where  $\theta_0 = 0^\circ$  at the pulse peak, we have  $L(t) = I(t)$ .  $L(t)$  decreases as  $|\alpha - i|$  increases, e.g. we find  $L(t) \approx 0.6I(t)$  at  $(\alpha, i) = (10^\circ, 90^\circ)$ . The maximum value of  $L/I$  can be calculated in terms of  $\alpha$  and  $i$  by solving equation (5.15) below for  $\cos \theta_0$ .

In Figure 5.5, we plot the path traced by  $\mathbf{x}_0(t)$  in the body frame across one pulse period for three cases: (A)  $(\alpha, i) = (20^\circ, 10^\circ)$ , (B)  $(20^\circ, 20^\circ)$ , and (C)  $(20^\circ, 30^\circ)$ . For a dipole field, the emission colatitude  $\theta_0$  is related to  $\alpha$  and  $i$  as follows:

$$\cos(i - \alpha) = \frac{3 \cos^2 \theta_0 - 1}{(1 + 3 \cos^2 \theta_0)^{1/2}}. \quad (5.15)$$

The path changes from an undulation at  $\alpha < i$  (curve C in Figure 5.5) to an ellipse at  $\alpha > i$  (curve A). The difference in geometry is largely responsible for the difference in polarization properties observed for  $\alpha < i$  and  $\alpha > i$ .

The Stokes phase portraits for a filled core with  $L/I = \cos \theta_0$  are drawn in Figures 5.7–5.9. In each figure, the panels are organised in order of increasing

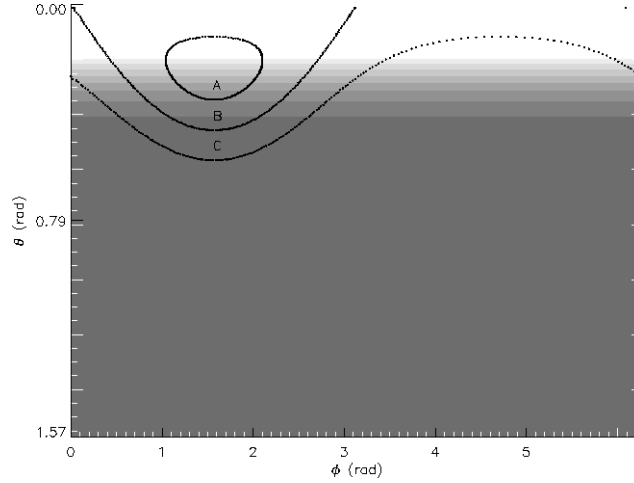


**Figure 5.5:** Examples of the path traced by the emission point  $\hat{\mathbf{x}}_0(t)$  in the body frame (curves), overplotted on the intensity map for a filled core beam (greyscale). The beam is brightest at  $\theta = 0$  (corresponding to the  $\mathbf{e}_3$  axis). Curves A:  $(\alpha, i) = (20^\circ, 10^\circ)$ , B:  $(\alpha, i) = (20^\circ, 20^\circ)$ , and C:  $(\alpha, i) = (20^\circ, 30^\circ)$ .

$i$  (left–right) and  $\alpha$  (top–bottom) in landscape mode. The panels range over  $10^\circ \leq i \leq 90^\circ$  and  $10^\circ \leq \alpha \leq 90^\circ$  and are separated by intervals of  $10^\circ$ . In Figures 5.7 and 5.8,  $I$  is plotted on the horizontal axis (normalised by its peak value), and  $Q$  and  $U$  are plotted on the vertical axis. In Figure 5.9,  $Q$  is plotted on the horizontal axis and  $U$  is plotted on the vertical axis. The same layout is used in all the look-up tables presented in this chapter.

In the  $I$ - $Q$  plane (Figure 5.7), we note the following behaviour. (i) For  $\alpha \leq 30^\circ$  and  $i \geq 50^\circ$ , the pulse traces out an approximately straight line segment which evolves into a slender hockey-stick shape as  $\alpha$  increases and  $i$  decreases. In the body frame, for  $\alpha > i$  (below the diagonal in Figure 5.7),  $\hat{\mathbf{x}}_0(t)$  traces out an ellipse in the quadrant  $0 \leq \theta \leq \pi/2, 0 \leq \phi \leq \pi$  (see Figure 5.5). As  $|\alpha - i|$  increases, the ellipse moves further from  $\theta = 0^\circ$  (and hence away from the beam peak). This reduces the curvature of the hockey stick. For  $\alpha < i$  (above the diagonal in Figure 5.7),  $\hat{\mathbf{x}}_0(t)$  traces out a sinusoidal curve across  $0 \leq \phi \leq 2\pi$ . Again, the curve moves away from  $\theta = 0^\circ$  as  $|\alpha - i|$  increases, reducing the curvature of the hockey stick. The left horn of the hockey stick shortens as  $\hat{\mathbf{x}}_0(t)$  moves away from  $\theta = 0^\circ$ . (ii) For  $\alpha = i$ , the pattern is a straight line with  $dQ/dI < 0$ . In the body frame,  $\hat{\mathbf{x}}_0(t)$  traces out a circle that crosses  $\theta = 0^\circ$  symmetrically. (iii) The shapes are slightly larger in the panels adjacent to the  $\alpha = i$  diagonal (i.e.  $-0.2 < Q < 1.2$  for  $|\alpha - i| \leq 10^\circ$ ) and decrease to e.g.  $0 < Q < 0.6$  at  $(\alpha, i) = (10^\circ, 90^\circ)$  at the corner of Figure 5.7.

In the  $I$ - $U$  plane (Figure 5.8), we note the following behaviour. (i) The pattern is symmetric about  $U = 0$  and traces a sideways balloon shape for most angles, with the pointy tip at  $(U, I) = (0, 0)$ . (ii) For  $\alpha \leq 50^\circ$  and  $i \leq 30^\circ$ , the pattern twists into a figure-eight. This twist occurs when the path traced by  $\hat{\mathbf{x}}_0(t)$  in the body frame elongates from a circle to an oval. (iii) For  $\alpha = i$ , the phase portrait is roughly oval, with major and minor axes along the  $I$ - and  $U$ -axes respectively. It narrows with increasing  $\alpha = i$ . (iv) The patterns are broadest adjacent to the  $\alpha = i$  diagonal (e.g.  $-1 < U < 1$  for  $|\alpha - i| < 10^\circ$ ) and narrow by up to 90% as  $|\alpha - i|$  increases to the corners of Figure 5.8.

In the  $Q$ - $U$  plane (Figure 5.9), we see a mix of ovals, balloons and heart shapes with the following properties. (i) For  $\alpha < i$ , above the diagonal, the shapes broaden with increasing  $\alpha$ , while the reverse is true for  $\alpha > i$ , below the diagonal. (ii) On the diagonal, the ovals narrow with increasing  $\alpha = i$ . (iii) In some cases, e.g.  $(\alpha, i) = (50^\circ, 40^\circ)$ , a cusp forms at the start and end points of the pulse, where  $(U, Q) = (0, 0)$ . This cusp twists into a secondary oval for  $10^\circ \leq \alpha \leq 50^\circ$  and  $i \leq 20^\circ$ . As in the  $I$ - $U$  plane, this secondary loop forms when the pattern traced by  $\hat{\mathbf{x}}_0(t)$  elongates from a circle to an oval. The size of the loop is proportional to the ellipticity of the oval. (iv) As in Figure 5.8, the patterns in the phase portrait are broadest for  $|\alpha - i| < 10^\circ$  directly adjacent to the  $\alpha = i$  diagonal, and narrow as  $|\alpha - i|$  increases.

In Figure 5.10, we plot the PA swings corresponding to each panel in Figures 5.7–5.9. We plot only the parts of the swing that are illuminated by the pulse, i.e. when  $|L| \geq 10^{-2}$ . The threshold is arbitrary and should be adjusted for instrumental resolution when modelling actual data. We note the following behaviour. (i) The PA swings are identical to those predicted by the rotating vector model, as expected for a dipole magnetic field, with the S-shape steepening as  $\alpha$  and  $i$  increase. (ii) Above the  $\alpha = i$  diagonal, we find  $d(\text{PA})/dl > 0$ , where  $l$  is the pulse longitude, whereas the opposite is true below the diagonal. This is consistent with the rotating vector model's prediction that  $d(\text{PA})/dl = \sin \alpha / \sin(i - \alpha)$  at the inflection point. (iii) Along and below the  $\alpha = i$  diagonal, there is phase wrapping in some swings, e.g. clearly visible for  $i = 10^\circ$ .

One limitation of the rotating vector model is that it is difficult to distinguish between orientations with similar  $|d(\text{PA})/dl|$ . This occurs, for example, at two orientations with equal  $\alpha$  and  $i - \alpha$ . For a pure dipole at  $r \ll r_{\text{LC}}$ , the Stokes phase portraits face a similar problem for  $\alpha \gtrsim 40^\circ$ . Comparing  $(\alpha, i) = (50^\circ, 40^\circ)$  and  $(50^\circ, 60^\circ)$ , the hockey sticks in the  $I$ - $Q$  plane are look

alike. The balloons and heart shapes in the  $I-U$  and  $Q-U$  planes are slightly different, although the differences are close to  $I = 0$  and may be hidden if the real data is noisy. However, for  $\alpha \lesssim 30^\circ$ , the Stokes phase portraits clearly discriminate between different orientations with equal  $i - \alpha$ , in a way that the PA swing does not. For example, let us compare the orientations  $(\alpha, i) = (30^\circ, 20^\circ)$  and  $(30^\circ, 40^\circ)$  in Figure 5.6. In the  $I-Q$  plane, the hockey stick at  $(\alpha, i) = (30^\circ, 20^\circ)$  is more curved than at  $(\alpha, i) = (30^\circ, 40^\circ)$ . In the  $I-U$  plane, there is a distinct figure-eight instead of a balloon, whereas in the  $Q-U$  plane, there are two interlocking ovals instead of a heart shape. In this case, the Stokes phase portraits provide an obvious way to differentiate between the two orientations. We note that in Sections 5.4 and 5.5, the differences in the phase portraits for orientations with equal  $|i - \alpha|$  are even more marked. Hence the Stokes phase portraits are useful supplements to the PA swing in many instances.

The Stokes phase portraits produced by  $L = I \cos \theta_0$  are extremely similar to those produced by a model with  $L \propto I$ . For the sake of brevity, we do not investigate the latter model here.

### $L = I \sin \theta_0$

Examples of the  $I$  (solid curve) and  $L$  (dashed curve) profiles for  $(\alpha, i) = (30^\circ, 30^\circ)$  are shown in Figure 5.11.  $I$  is normalised by its peak value. The magnetic colatitude  $\theta_0(t)$  of the emission point (dotted curve) is also shown. The following trends are observed. (i) Along the  $\alpha = i$  diagonal, where  $\theta_0$  goes to zero at the centre of the pulse, the  $\sin \theta_0$  dependence results in a double-peaked  $L$  profile. Away from the diagonal,  $L/I$  increases, reaching 0.8 at  $(\alpha, i) = (90^\circ, 10^\circ)$ . (ii) Away from the diagonal,  $L$  follows  $I$ , as in Section 5.3.1, resulting in similar phase portraits.

The Stokes phase portraits for a filled core with  $L/I = \sin \theta_0$  are drawn in Figures 5.12–5.14. Comparing the Stokes phase portraits and PA swings to those of Section 5.3.1, we note the following differences. (i) In the  $I-Q$  phase portrait (Figure 5.12), along the  $\alpha = i$  diagonal, instead of a straight line, we see a ‘flipped’ hockey stick which slopes in the opposite direction to the hockey sticks for  $\alpha \neq i$ . (ii) In the  $I-U$  phase portrait (Figure 5.13), along the  $\alpha = i$  diagonal, there are broad balloon shapes instead of narrow ovals, and they extend leftwards from  $I = 1$  as opposed to rightwards from  $I = 0$ . (iii) In the  $Q-U$  plane (Figure 5.14), instead of ovals, the diagonal now contains heart shapes with an extremely pronounced cusp, narrowing with increasing

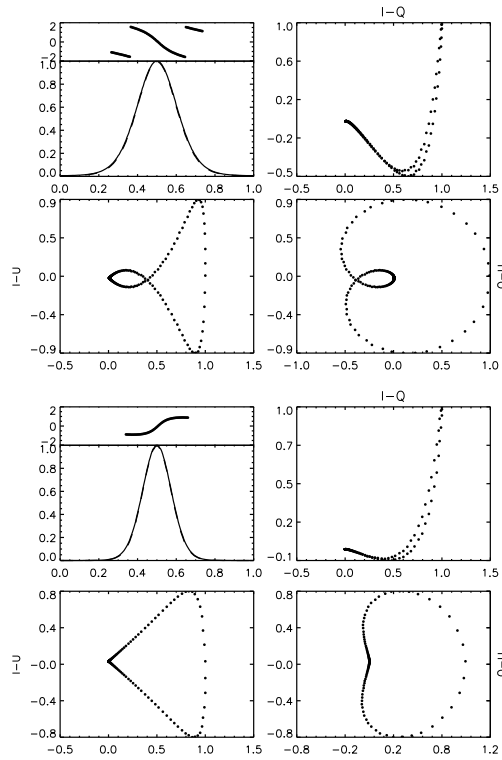


**Figure 5.6:** Two orientations with equal PA-swing gradients ( $|d(\text{PA})/dl|$ ) at the inflection point, but different Stokes phase portraits. Top four panels:  $(\alpha, i) = (30^\circ, 20^\circ)$ , bottom four panels:  $(\alpha, i) = (20^\circ, 30^\circ)$ . Within each half of the figure, the four subpanels display (clockwise from top left): (a)  $I/I_{\text{max}}$  (bottom) and PA (top; in radians) as functions of pulse longitude, (b)  $I-Q$ , (c)  $Q-U$ , and (d)  $I-U$ .

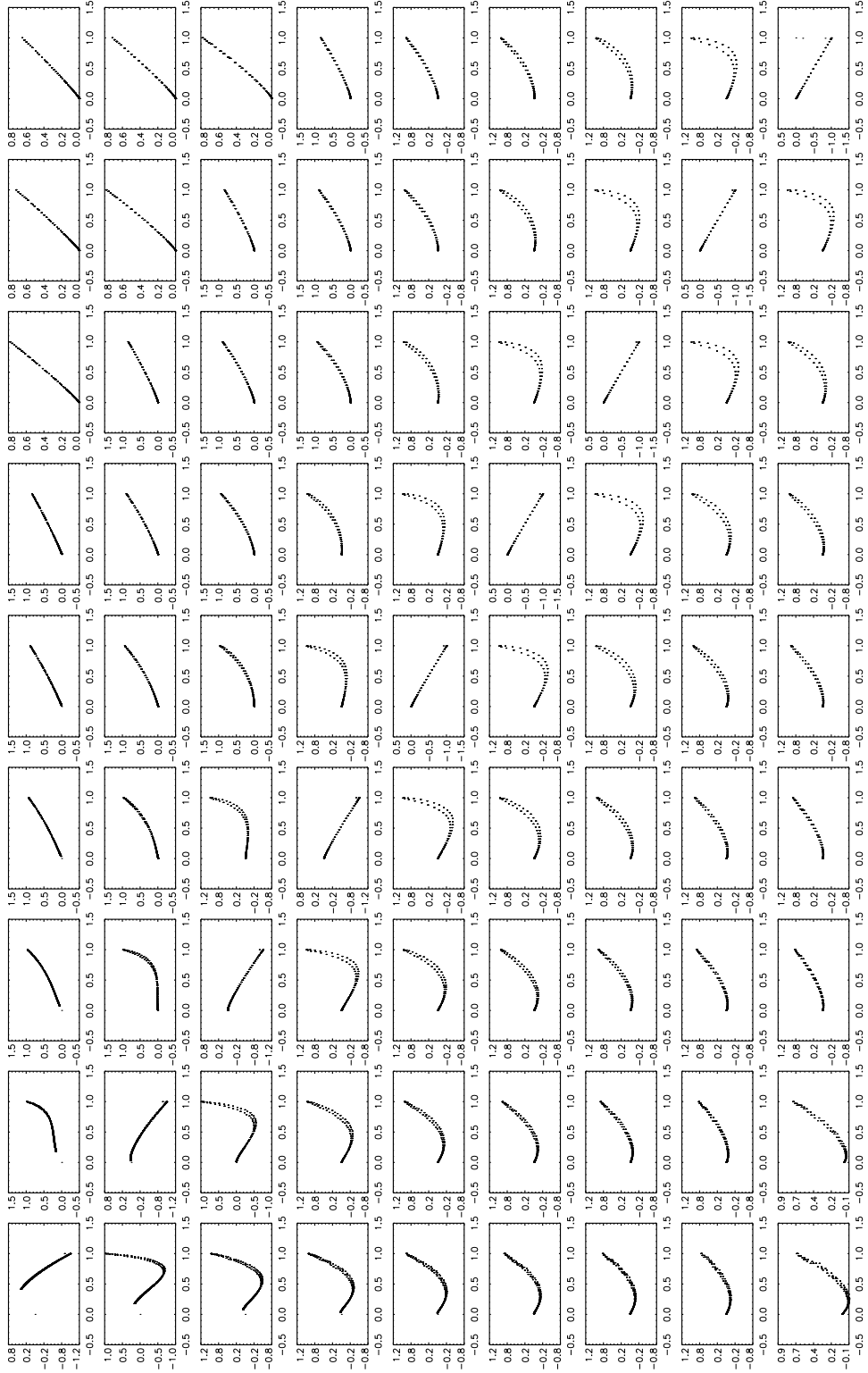


**Figure 5.7:** Dipole field at a low emission altitude  $r \ll r_{\text{LC}}$ . Look-up table of Stokes phase portraits in the  $I$ - $Q$  plane for a filled core beam with degree of linear polarization  $L = I \cos \theta_0$ , where  $\theta_0$  is the emission point colatitude. The panels are organised in landscape mode, in order of increasing  $10^\circ \leq i \leq 90^\circ$  (left–right) and  $10^\circ \leq \alpha \leq 90^\circ$  (top–bottom) in intervals of  $10^\circ$ .  $I$  is plotted on the horizontal axis and normalised by its peak value.  $Q$  is plotted on the vertical axis.

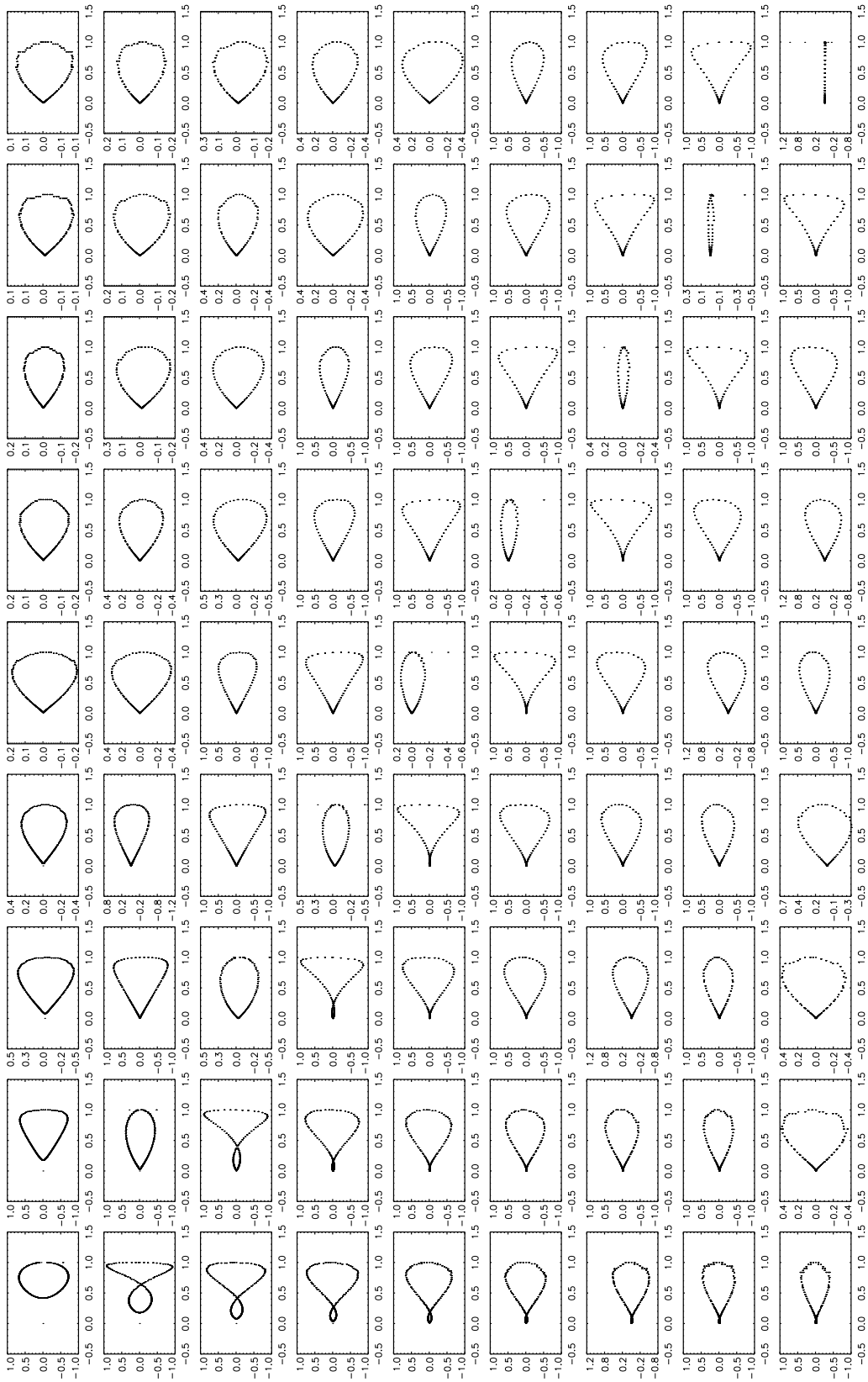


**Figure 5.8:** Dipole field at  $r \ll r_{LC}$ . Layout as for Figure 5.7, but for  $I$ - $U$  ( $I$  on the horizontal axis).

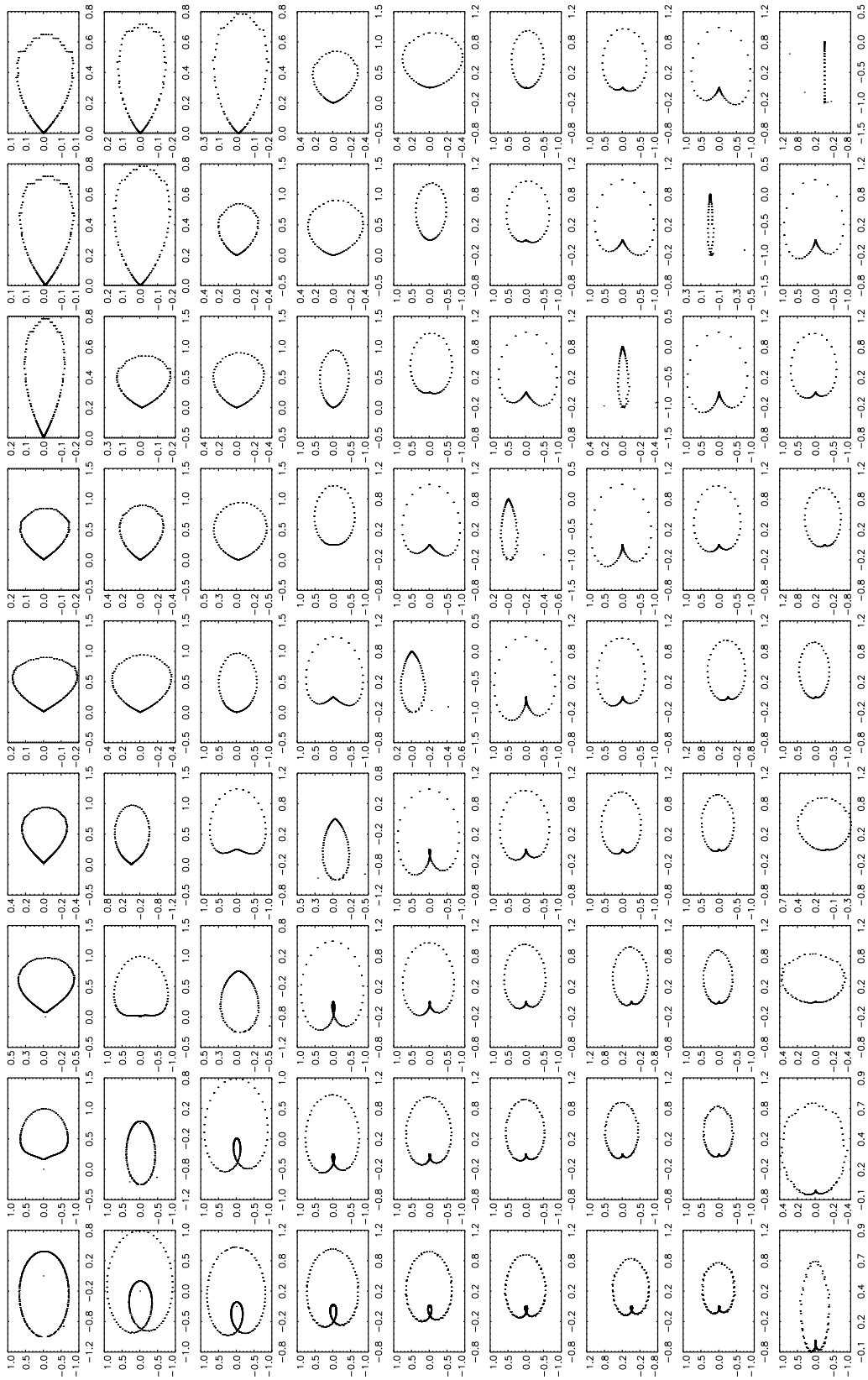


**Figure 5.9:** Dipole field at  $r \ll r_{LC}$ . Layout as for Figure 5.7, but for  $Q$ - $U$  ( $Q$  on the horizontal axis).



**Figure 5.10:** Dipole field at  $r \ll r_{LC}$ . Layout as for Figure 5.7, but for position angle (on the vertical axis in landscape orientation, in units of radians) versus pulse longitude (on the horizontal axis, in units of  $2\pi$  radians).

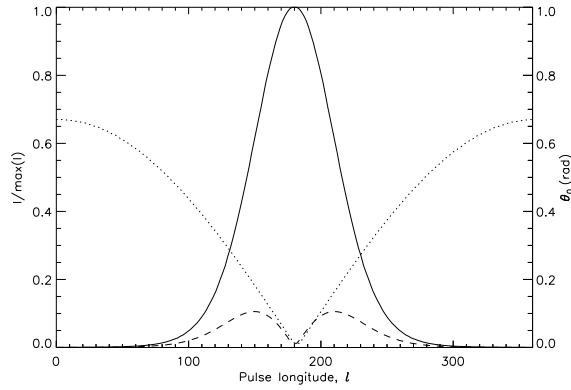


**Figure 5.11:** Dipole field at  $r \ll r_{LC}$ . Example of a pulse profile for a filled core beam with linear polarization  $L = I \sin \theta_0$  and  $(\alpha, i) = (30^\circ, 30^\circ)$ . Solid, dashed and dotted curves represent the total polarized intensity  $I$ , degree of linear polarization  $L$ , and emission point colatitude  $\theta_0$ . Pulse longitude  $l$  is measured in units of degrees.

$\alpha = i$ . There is no noticeable difference between the PA swings in this model (Figure 5.15) and those of Section 5.3.1. This is another example of how the Stokes phase portraits reveal differences in the beam geometry and polarization pattern which are not apparent from the PA swings.

In summary, a filled core beam produces single-peaked pulses, resulting in several unique shapes in the Stokes planes. In the  $I$ - $Q$  plane, a hockey stick shape is typically seen. In the  $I$ - $U$  plane, we see a balloon shape which twists into a figure-eight in the range  $\alpha \leq 50^\circ, i \leq 20^\circ$ . In the  $Q$ - $U$  plane, we see heart shapes for all  $i < \alpha$ , and balloons for  $i - \alpha \geq 10^\circ$ .

### 5.3.2 Hollow cone emission

$$L = I \cos \theta_0$$

Examples of the  $I$  (solid curve) and  $L$  (dashed curve) profiles for  $(\alpha, i) = (70^\circ, 20^\circ)$  and  $(70^\circ, 60^\circ)$  are shown in Figure 5.16.  $I$  is normalised by its peak value. The magnetic colatitude  $\theta_0(t)$  of the emission point (dotted curve) is also shown. The following trends are observed. (i) Emission from a hollow cone results in double-peaked pulse profiles in the range  $|i - \alpha| \leq 30^\circ$ , where the path traced by  $\hat{\mathbf{x}}_0(t)$  crosses the edge of the cone twice. (ii) For  $\alpha < 45^\circ$ , the central dip becomes shallower as  $i$  increases. The reverse is true for  $\alpha > 45^\circ$ . (iii) We find  $L/I \approx 1$  for  $\alpha = i$ , decreasing to  $\approx 0.6$  at  $(\alpha, i) = (10^\circ, 90^\circ)$ . The pulses are generally  $\approx 50\%$  broader than in Section 5.3.1, even though  $\sigma$  is the same in both instances.

The Stokes phase portraits for a hollow cone with  $L/I = \cos \theta_0$  are drawn in

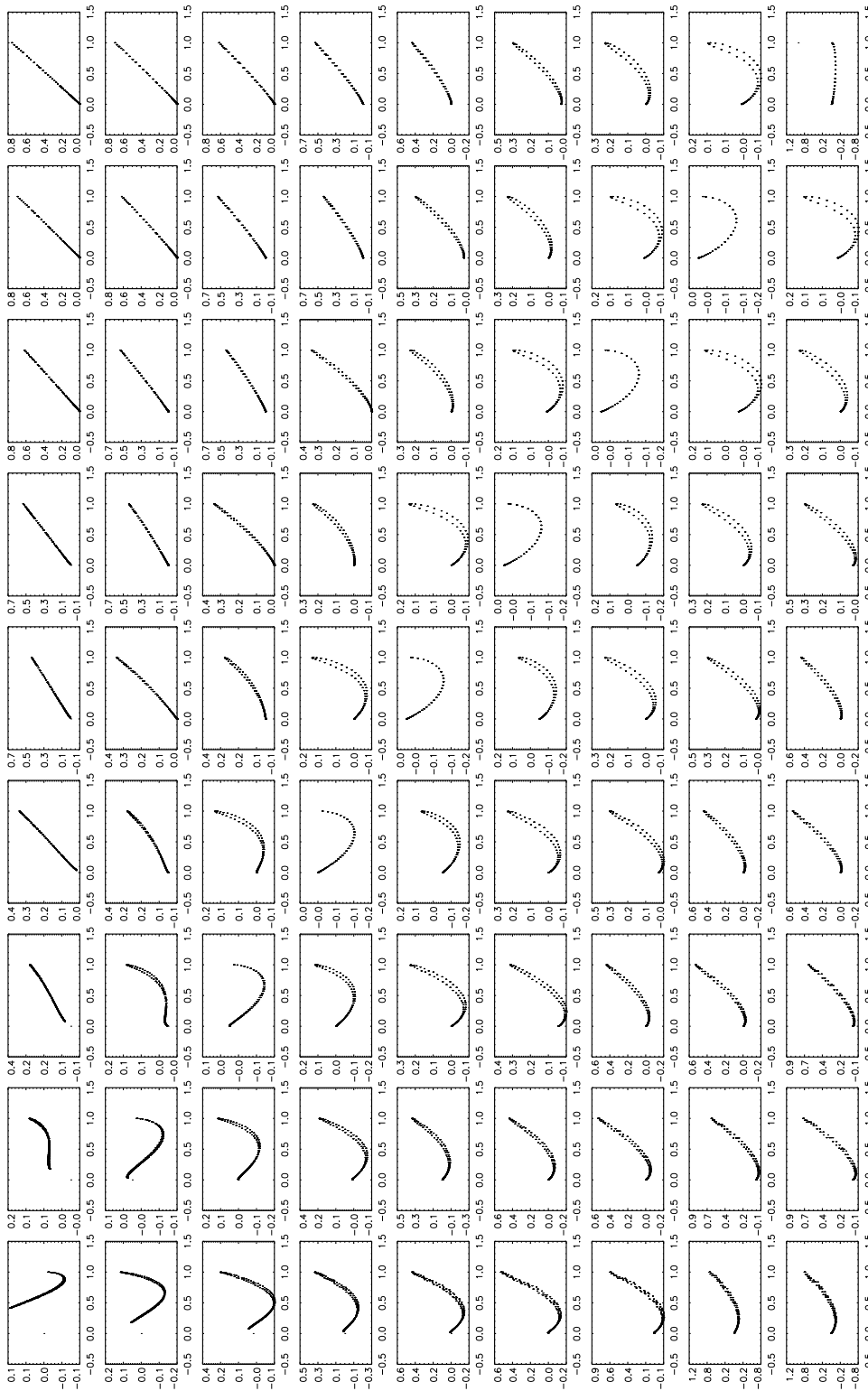


**Figure 5.12:** Dipole field at  $r \ll r_{LC}$ . Look-up table of Stokes phase portraits in the  $I$ - $Q$  plane for a filled core beam with degree of linear polarization  $L = I \sin \theta_0$ , where  $\theta_0$  is the emission point colatitude. The panels are organised in landscape mode, in order of increasing  $10^\circ \leq i \leq 90^\circ$  (left–right) and  $10^\circ \leq \alpha \leq 90^\circ$  (top–bottom) in intervals of  $10^\circ$ .  $I$  is plotted on the horizontal axis and normalised by its peak value.  $Q$  is plotted on the vertical axis.

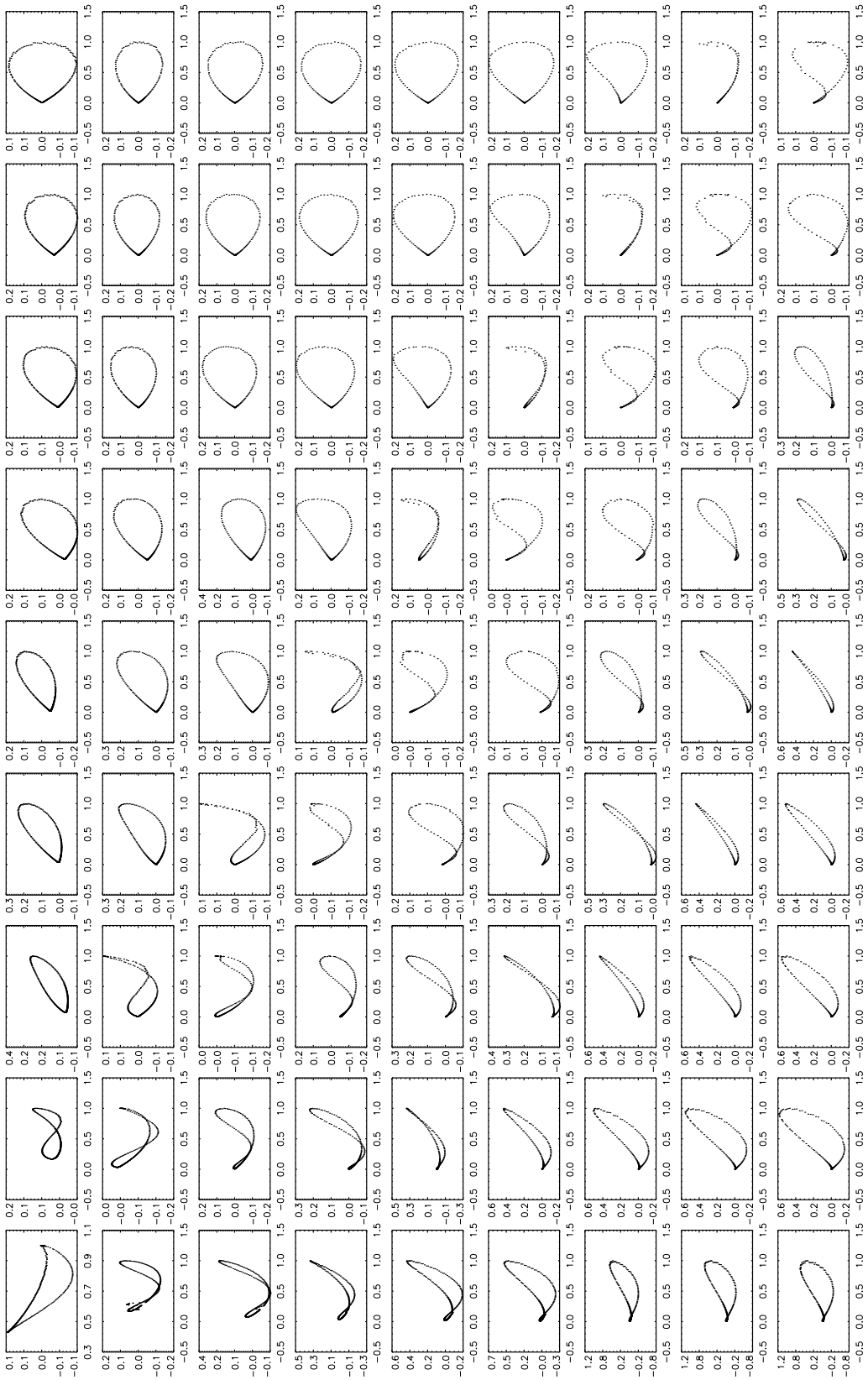


**Figure 5.13:** Dipole field at  $r \ll r_{LC}$ . As for Figure 5.12, but for  $I-U$  ( $I$  on horizontal axis).

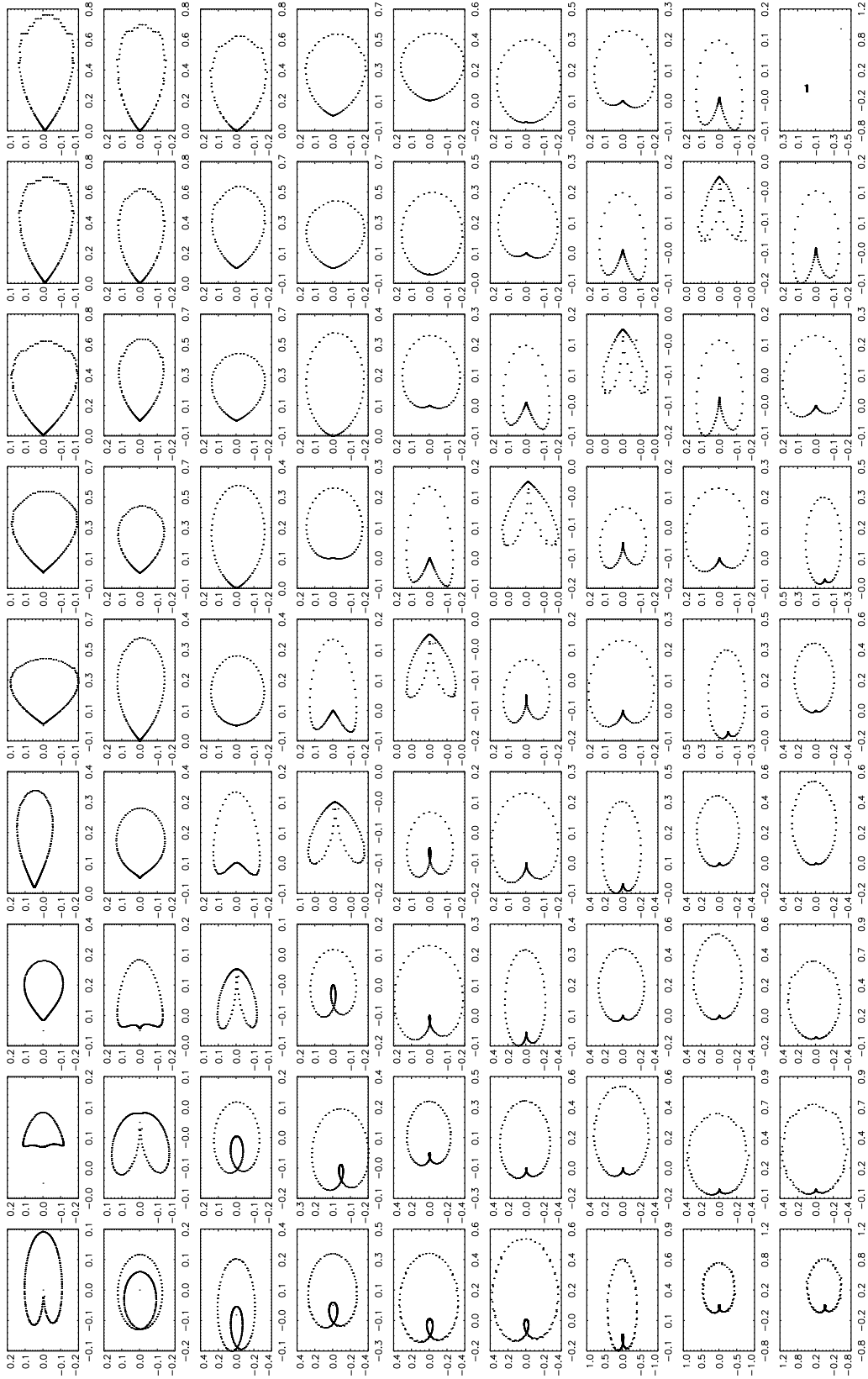


Figure 5.14: Dipole field at  $r \ll r_{LC}$ . As for Figure 5.12, but for  $Q-U$  ( $Q$  on horizontal axis).



**Figure 5.15:** Dipole field at  $r \ll r_{LC}$ . Layout as for Figure 5.17, but for position angle (on the vertical axis in landscape orientation, in units of radians) versus pulse longitude (on the horizontal axis, in units of  $2\pi$  radians).

Figures 5.17–5.19. The paths of  $\hat{\mathbf{x}}_0(t)$  shown in Figure 5.5 still apply but they cross a different beam pattern with a bright band at  $\theta_0 = \rho$ . Hence the Stokes phase portraits look different to the left and right of the  $\alpha = i$  diagonal.

In the  $I$ - $Q$  phase portraits (Figure 5.17), we note the following trends. (i) Where the pulse is double-peaked, the hockey sticks twist into a tilted  $\gamma$  shape. Where the pulse is single-peaked, the patterns are similar to Figure 5.7. (ii) For  $\alpha = i$ , the hockey stick twists into a  $\gamma$ -shape as  $\alpha = i$  increases.

In the  $I$ - $U$  phase portraits (Figure 5.18), we note the following trends. (i) Where the pulse profile is double-peaked, the  $I$ - $U$  portraits feature two interlocking loops forming a triangular shape with twisted corners. Where the pulse is single-peaked, the patterns are similar to those of Figure 5.8. (ii) For  $\alpha = i$ , the pattern evolves from a balloon to a triangular shape with an increasingly deep central cusp as  $\alpha = i$  increases.

Additional twisting in the patterns is also seen in the  $Q$ - $U$  plane (Figure 5.19), although the patterns are still symmetric about  $U = 0$ . (i) For  $\alpha = i$ , the patterns look qualitatively similar to those of Section 5.3.1, although they are  $\sim 90\%$  broader, covering  $-1 \leq U \leq 1$ . (ii) For  $\alpha > i$ , we see heart shapes and nested ovals, whereas for  $\alpha < i$ , we see simpler, convex balloons.

The PA swings (Figure 5.20) are identical to the previous cases, the only difference being that they are visible above a threshold intensity over a greater fraction of the pulse period due to the broader pulse profiles.

### **$L = I \sin \theta_0$**

Examples of the  $I$  (solid curve) and  $L$  (dashed curve) profiles for  $(\alpha, i) = (70^\circ, 20^\circ)$  and  $(70^\circ, 60^\circ)$  are shown in Figure 5.21. We note the following trends. (i)  $L$  follows  $I$  in the same way as Figure 5.16. However,  $L/I$  peaks at  $\approx 0.5$  on the  $\alpha = i$  diagonal. (ii)  $L/I$  increases as  $|\alpha - i|$  increases, reaching  $\approx 0.8$  for  $|\alpha - i| = 80^\circ$ .

The  $I$ - $Q$ ,  $I$ - $U$  and  $Q$ - $U$  phase portraits are shown in Figures 5.22–5.24. The phase portraits are similar to Section 5.3.2, except for orientations that yield double-peaked pulses. Here, the patterns are less twisted. Compared to Section 5.3.2, the lower peak value of  $L/I$  leads to a narrower range of  $U$  and  $Q$ . For example, in the  $Q$ - $U$  plane, along the  $\alpha = i$  diagonal, the heart shape for  $(\alpha, i) = (10^\circ, 10^\circ)$  is approximately 80% smaller than in Figure 5.19 along both the  $U$  and  $Q$  axes. The PA swings (Figure 5.25) are exactly identical to Figure 5.20.

In summary, a hollow cone beam pattern produces Stokes phase portraits

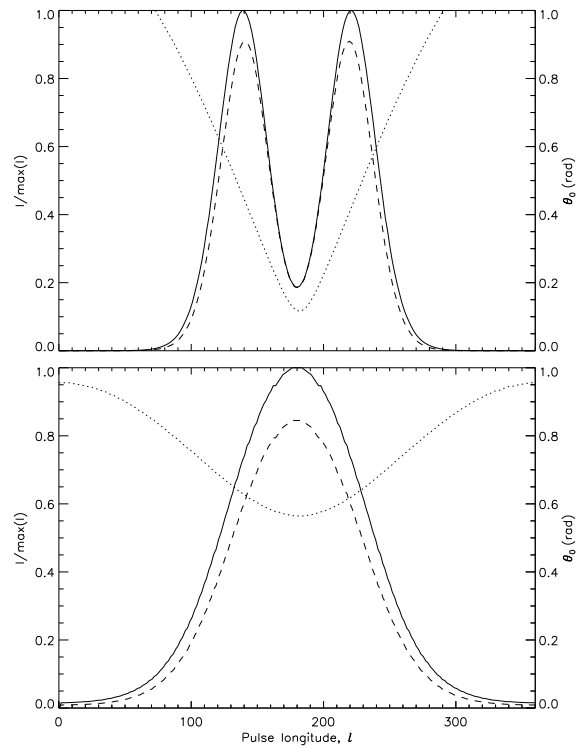


**Figure 5.16:** Dipole field at  $r \ll r_{LC}$ . Examples of pulse profiles for a hollow cone with opening angle  $25^\circ$  and linear polarization  $L = I \cos \theta_0$  for two different orientations  $(\alpha, i)$  (top and bottom panels). Solid, dashed and dotted curves represent the total polarized intensity  $I$ , degree of linear polarization  $L$ , and emission point colatitude  $\theta_0$ . Pulse longitude is measured in units of degrees. Top: double-peaked pulse with  $(\alpha, i) = (70^\circ, 60^\circ)$ ; bottom: single-peaked pulse with  $(\alpha, i) = (70^\circ, 20^\circ)$ .

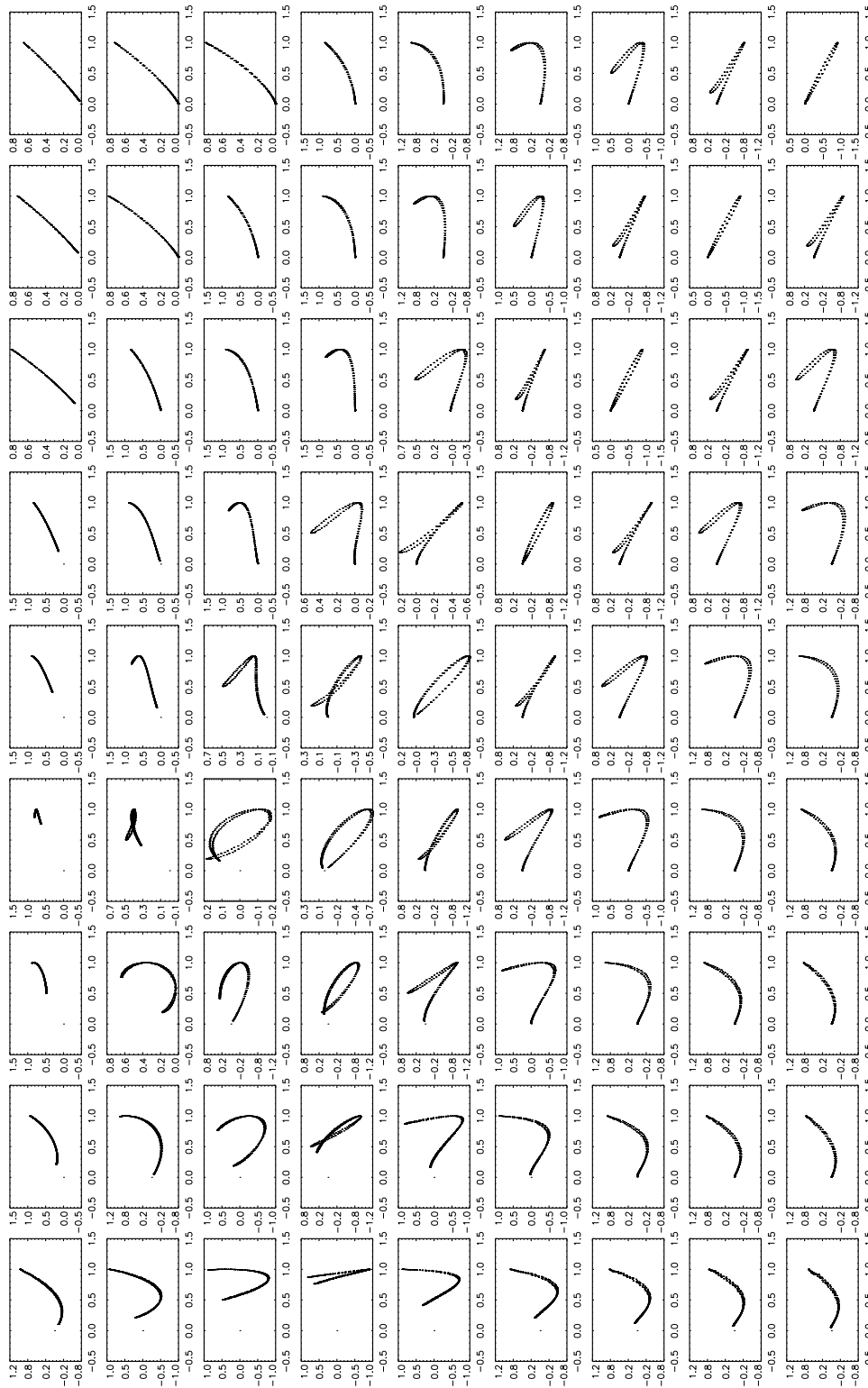


**Figure 5.17:** Dipole field at  $r \ll r_{\text{LC}}$ . Look-up table of Stokes phase portraits in the  $I$ - $Q$  plane for a hollow cone with opening angle  $25^\circ$  with degree of linear polarization  $L = I \cos \theta_0$ , where  $\theta_0$  is the emission point colatitude. The panels are organised in landscape mode, in order of increasing  $10^\circ \leq i \leq 90^\circ$  (left-right) and  $10^\circ \leq \alpha \leq 90^\circ$  (top-bottom) in intervals of  $10^\circ$ .  $I$  is plotted on the horizontal axis and normalised by its peak value.  $Q$  is plotted on the vertical axis.

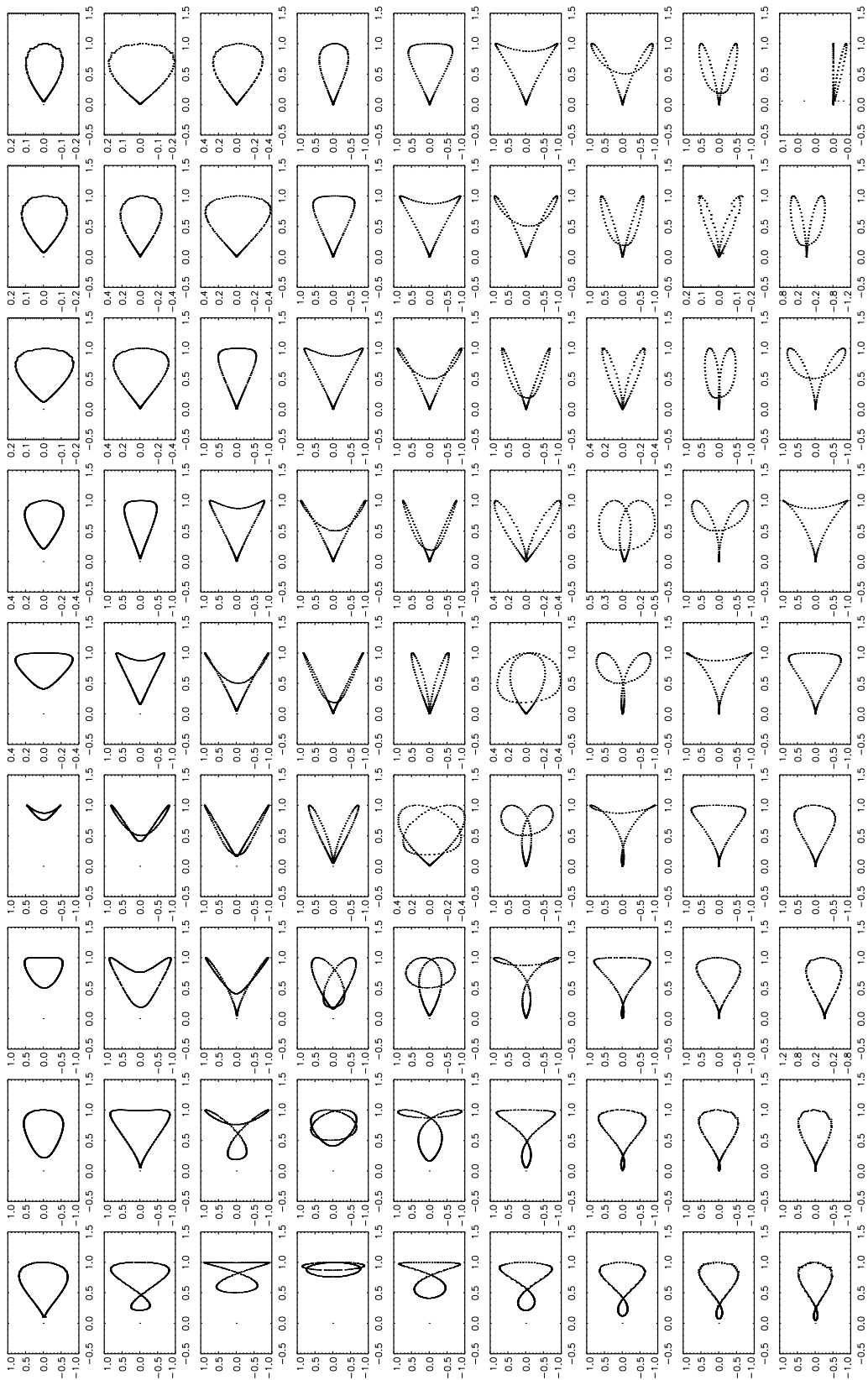


**Figure 5.18:** Dipole field at  $r \ll r_{LC}$ . Layout as for Figure 5.17, but for  $I-U$  ( $I$  on horizontal axis).

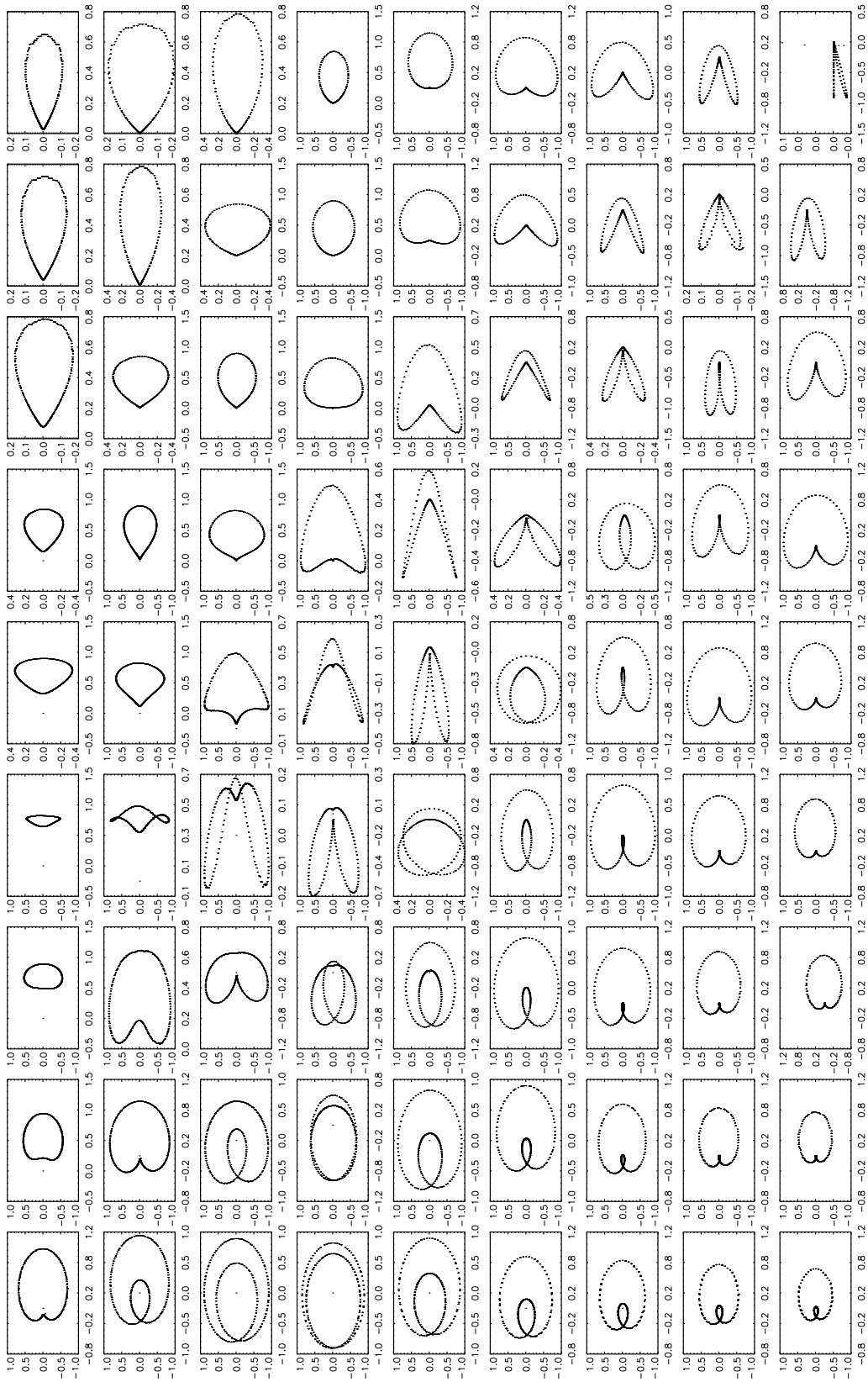
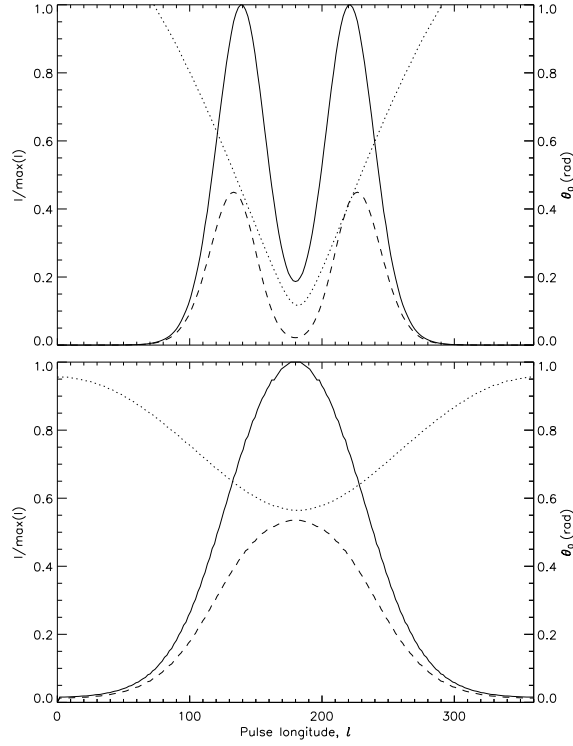


Figure 5.19: Dipole field at  $r \ll r_{LC}$ . Layout as for Figure 5.17, but for  $Q-U$  ( $Q$  on horizontal axis).



**Figure 5.20:** Dipole field at  $r \ll r_{LC}$ . Layout as for Figure 5.17, but for position angle (on the vertical axis in landscape orientation, in units of radians) versus pulse longitude (on the horizontal axis, in units of  $2\pi$  radians).



**Figure 5.21:** As for Figure 5.16, but with linear polarization  $L = I \sin \theta$ .

that differ significantly from those of the filled core beam, when the pulses are double-peaked (for  $|\alpha - i| \leq 30^\circ$ ). In the  $I$ - $Q$  plane, double-peaked pulses trace out a tilted  $\gamma$  shape, whereas single-peaked pulses trace out a hockey stick. In the  $I$ - $U$  plane, double-peaked pulses produce a triangle with twisted corners, whereas single-peaked pulses produce a balloon. In the  $Q$ - $U$  plane, the double-peaked pulses produce a mix of heart shapes and nested ovals, whereas the single-peaked pulses produce heart shapes (for  $\alpha > i$ ) and balloons (for  $\alpha < i$  diagonal).

## 5.4 Dipole field at $r = 0.1r_{LC}$

Relativistic aberration affects the observed Stokes parameters in two ways. Firstly, the change in the emission point due to relativistic beaming [Eq. (5.1)] shifts the pulse centroid and hence  $I(t)$  by  $-r/r_{LC}$  in phase. Beaming also shifts the PA swing in the same direction. Additionally, because the particle's instantaneous acceleration (and hence the observed electric field vector) is tilted away from the magnetic field normal  $\mathbf{n}$  by an amount  $\propto r/r_{LC}$ , the PA swing is phase-shifted by  $3r/r_{LC}$ , resulting in a relative phase shift of  $4r/r_{LC}$  between the PA inflection point and the centroid of the pulse profile. Note that as we are only interested in the relative phase, we ignore time-delay effects,

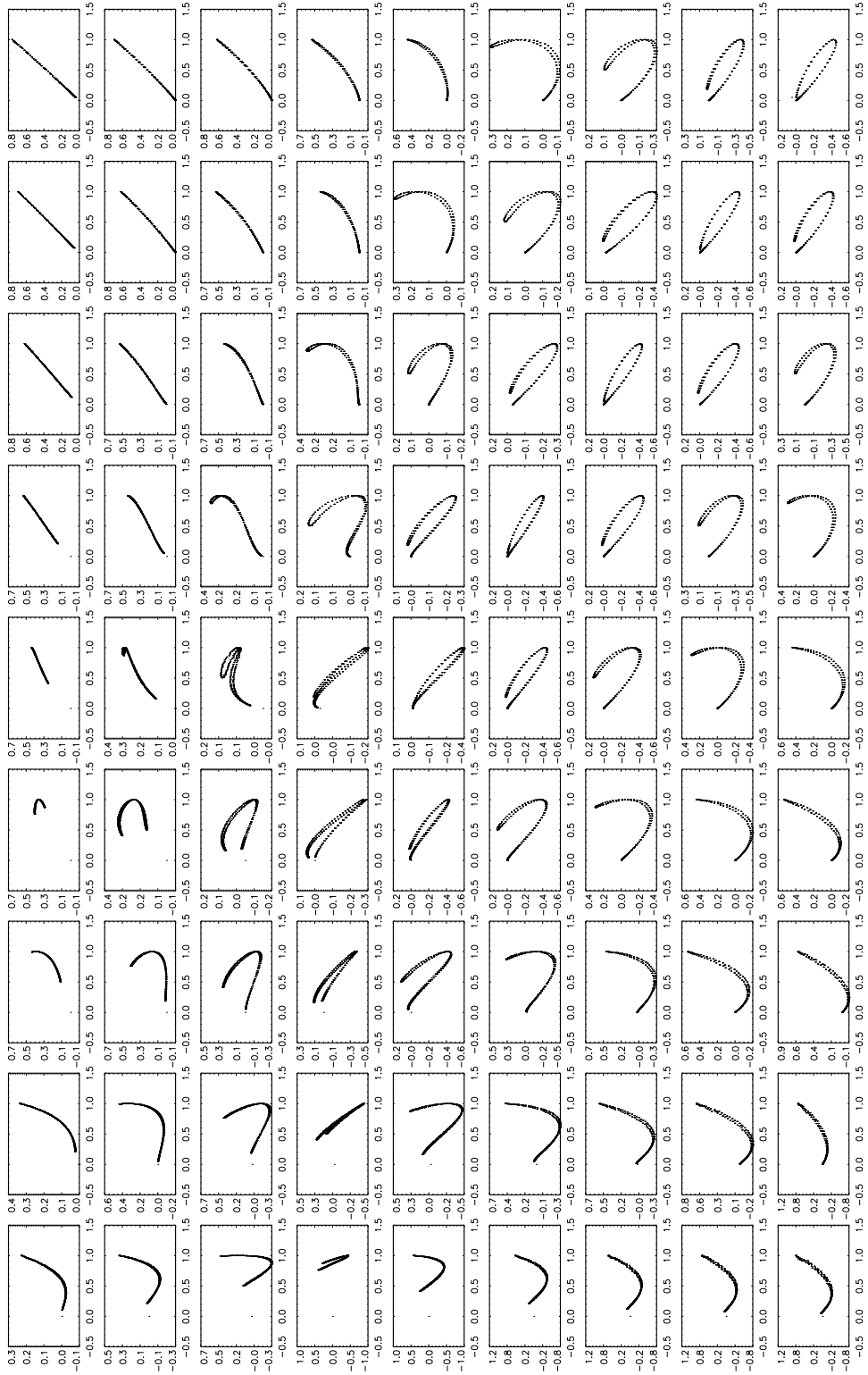


**Figure 5.22:** Dipole field at  $r \ll r_{\text{LC}}$ . Look-up table of Stokes phase portraits in the  $I$ - $Q$  plane for a hollow cone with opening angle  $25^\circ$  with degree of linear polarization  $L = I \sin \theta_0$ , where  $\theta_0$  is the emission point colatitude. The panels are organised in landscape mode, in order of increasing  $10^\circ \leq i \leq 90^\circ$  (left–right) and  $10^\circ \leq \alpha \leq 90^\circ$  (top–bottom) in intervals of  $10^\circ$ .  $I$  is plotted on the horizontal axis and normalised by its peak value.  $Q$  is plotted on the vertical axis.

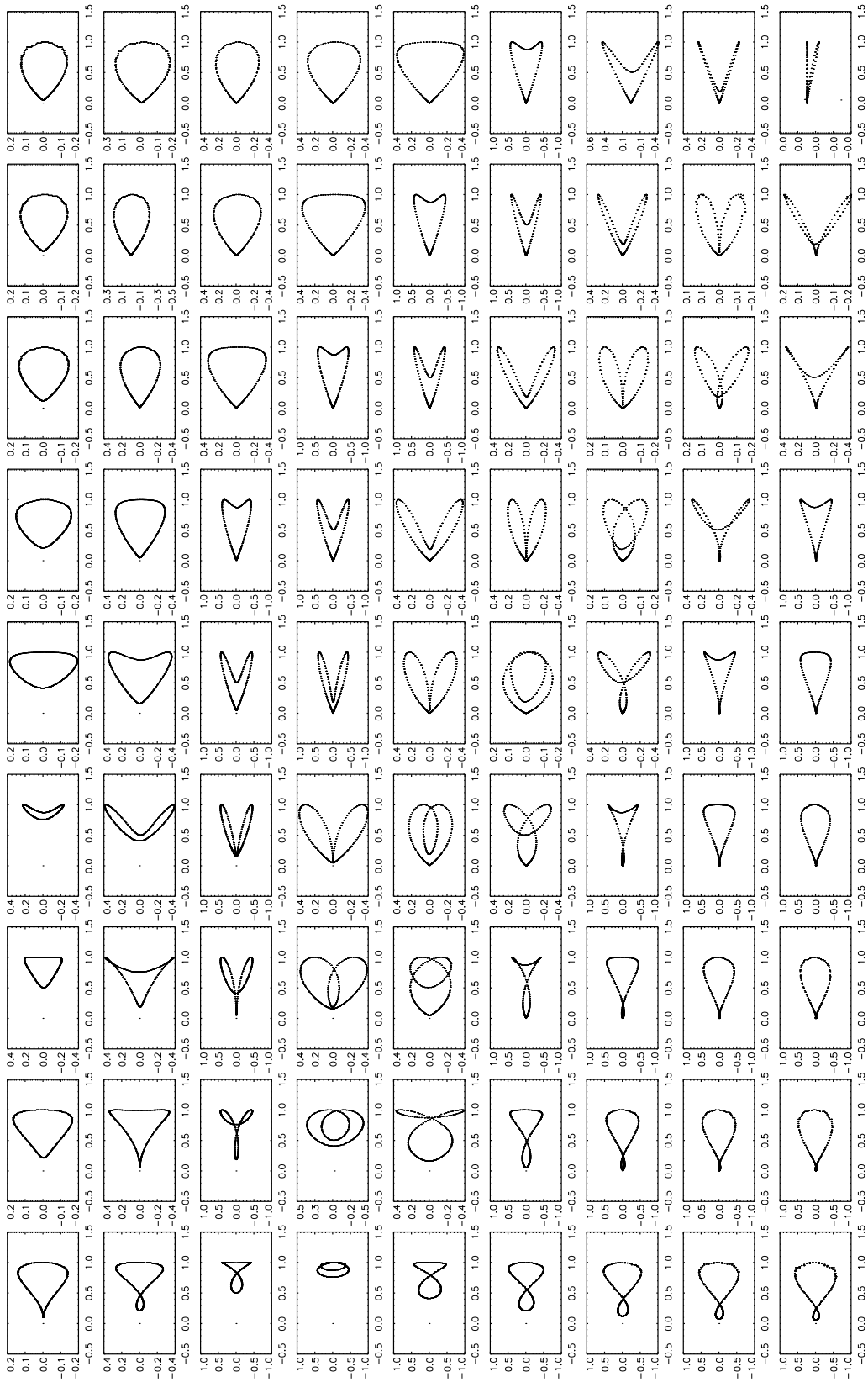
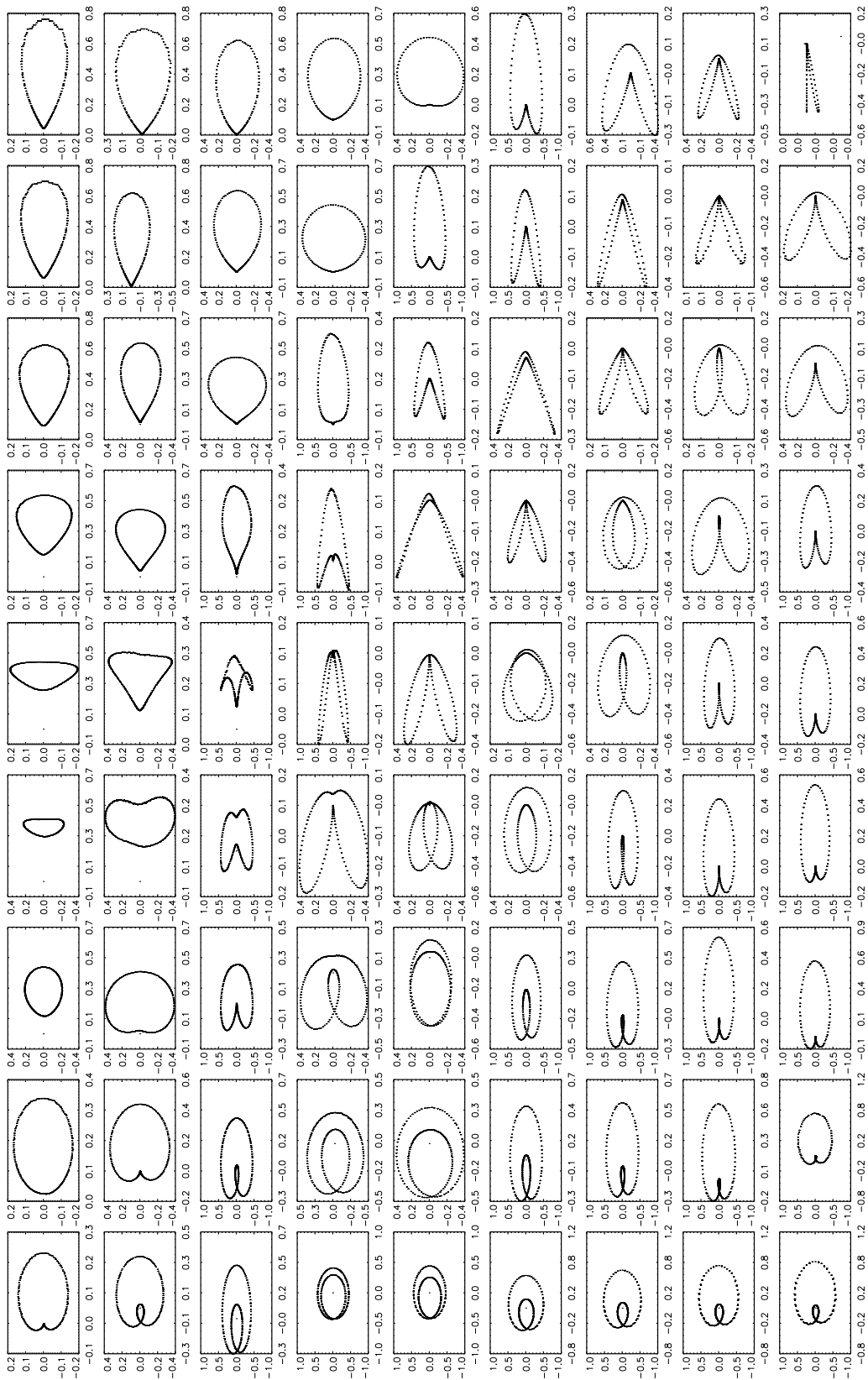
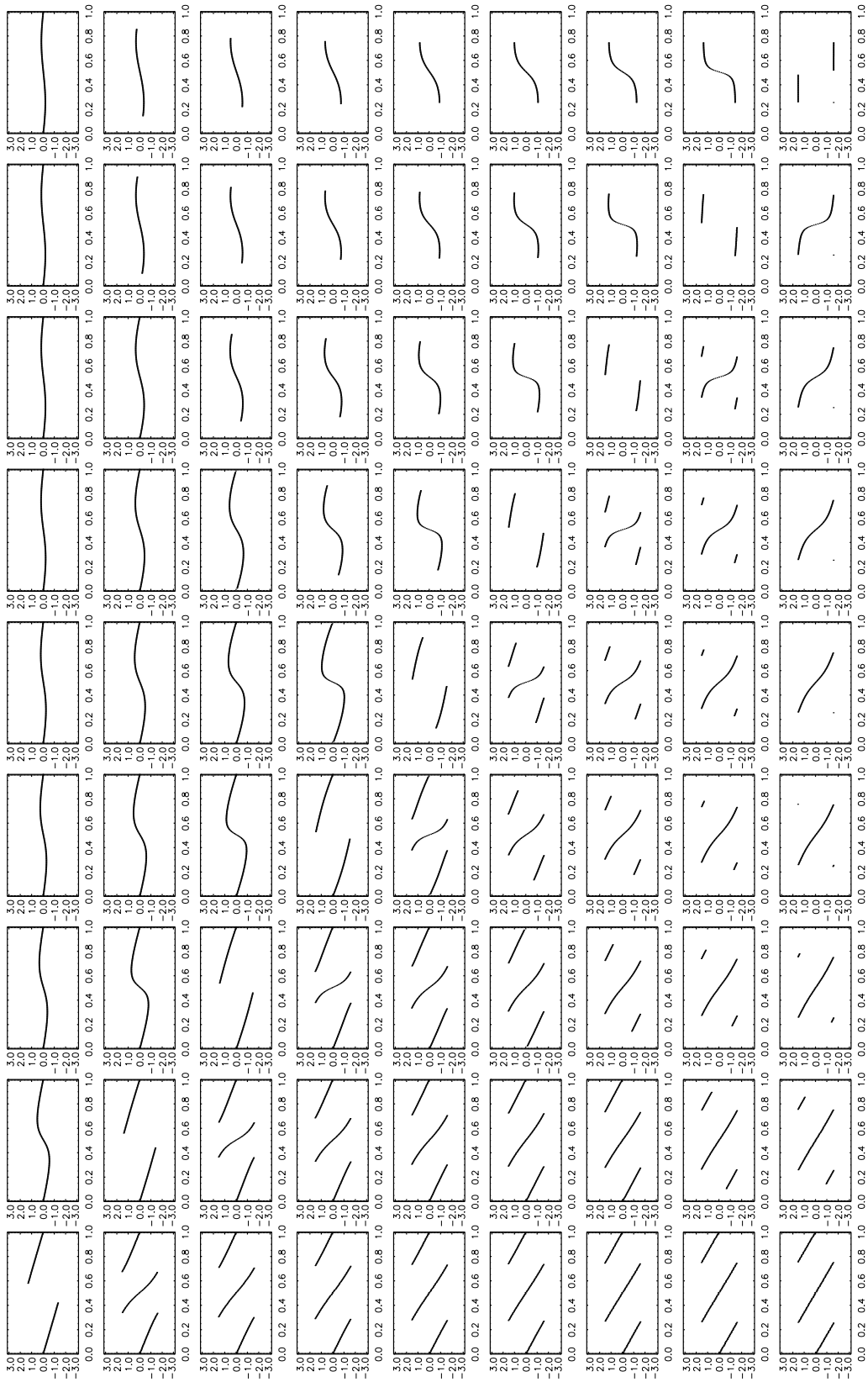


Figure 5.23: Dipole field at  $r \ll r_{LC}$ . Layout as for Figure 5.22, but for  $I-U$  ( $I$  on horizontal axis).



**Figure 5.24:** Dipole field at  $r \ll r_{LC}$ . Layout as for Figure 5.22, but for  $Q-U$  ( $Q$  on horizontal axis).



**Figure 5.25:** Dipole field at  $r \ll r_{LC}$ . Layout as for Figure 5.22, but for position angle (on the vertical axis in landscape orientation, in units of radians) versus pulse longitude (on the horizontal axis, in units of  $2\pi$  radians).

which phase-shift both the pulse profile and the PA swing by an additional  $-r/r_{\text{LC}}$  (Dyks 2008).

In this section, we present look-up tables for a dipole field at an emission altitude  $r = 0.1r_{\text{LC}}$ , where aberration distorts the Stokes phase portraits significantly while leaving the PA swings largely unchanged. We investigate the same beam patterns as in Section 5.3, but for the sake of brevity, we present look-up tables for  $L/I = \cos\theta_0$  only. For each beam pattern (core emission in Section 5.4.1, conal emission in Section 5.4.2) we construct three phase portraits ( $I$ - $Q$ ,  $I$ - $U$  and  $Q$ - $U$ ) for each pair of angles  $(\alpha, i)$  at a fixed emission altitude ( $r = 0.1 r_{\text{LC}}$ ) and tabulate the results in Figures 5.26–5.31.

### 5.4.1 Filled core beam

In this section, we point out the major differences between the Stokes phase portraits for a filled core beam and  $L = I \cos\theta_0$  at  $r = 0.1r_{\text{LC}}$  (Figures 5.26–5.28) and the corresponding non-aberrated situation at  $r \ll r_{\text{LC}}$  (Figures 5.7–5.9).

In the  $I$ - $Q$  plane, the hockey sticks and straight lines in the non-aberrated case (Figure 5.7) broaden into balloons and ovals when aberration becomes important (Figure 5.26). The broadening increases as the panels approach the  $\alpha = i$  diagonal.

In the  $I$ - $U$  plane (Figure 5.27), the symmetry about  $U = 0$  is broken, and the balloons and ovals are tilted. For  $\alpha > i$  (below the diagonal), the balloons tilt upwards (major axis has  $dU/dI > 0$ ), whereas for  $\alpha < i$  (above the diagonal), the ovals tilt downwards (major axis has  $dU/dI < 0$ ). Another difference is that for  $|\alpha - i| = 10^\circ$ , the phase portraits feature figure-eights instead of ovals. Along the  $\alpha = i$  diagonal there is a distorted Z-shape, although we note that the sharp breaks in the pattern are numerical artifacts.

In the  $Q$ - $U$  plane (Figure 5.28), the heart shapes in the  $\alpha > i$  region (below the diagonal) are rotated counter-clockwise. As the panels approach the  $\alpha = i$  diagonal, the top ventricle of the heart shape grows larger than the bottom ventricle. In the  $\alpha < i$  region (above the diagonal), the ovals are rotated clockwise and are tilted downwards (major axis has  $dU/dQ < 0$ ). Along the  $\alpha = i$  diagonal, there are distorted heart shapes instead of ovals.

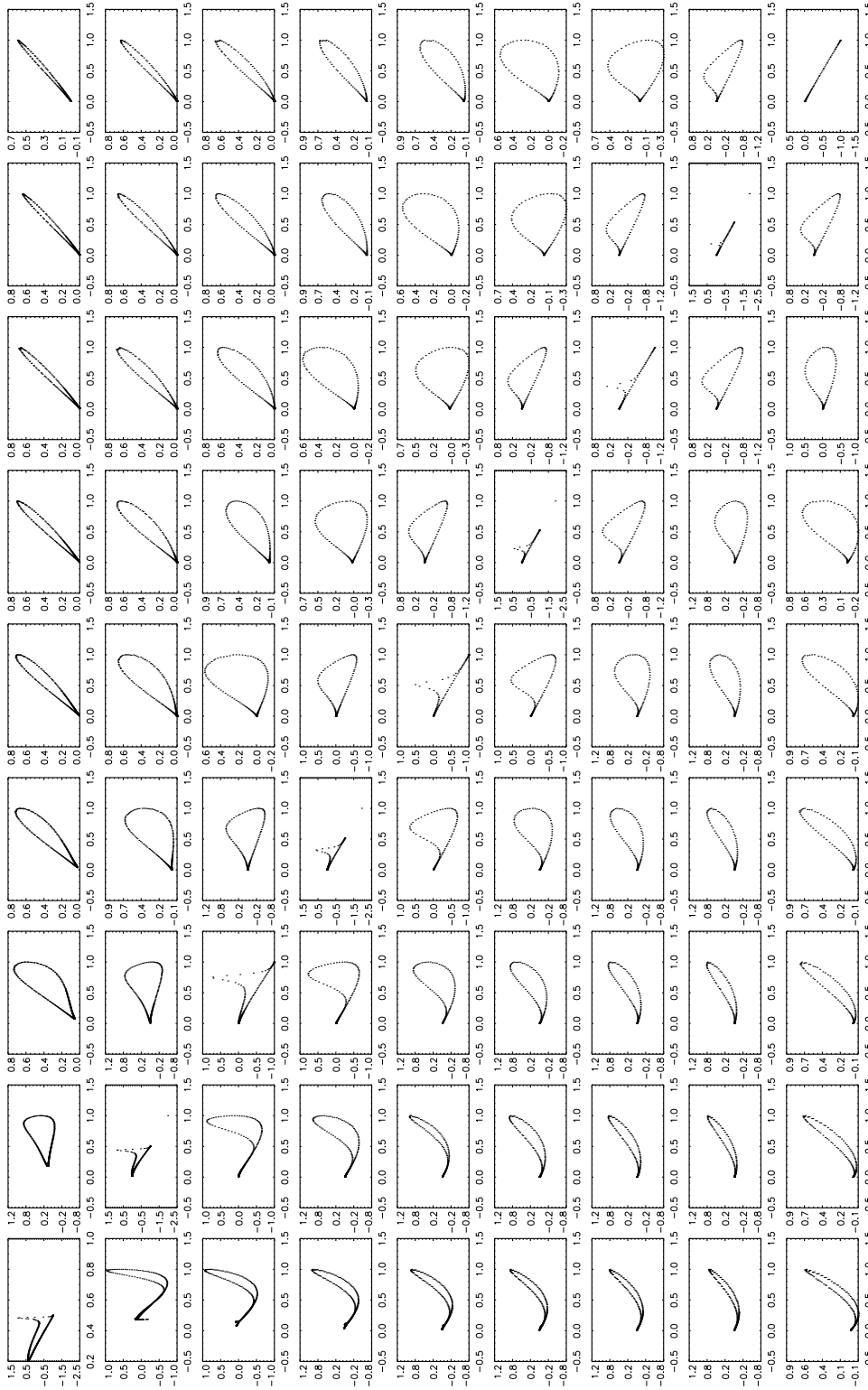


**Figure 5.26:** Dipole field at  $r = 0.1r_{LC}$ . Look-up table of Stokes phase portraits in the  $I$ - $Q$  plane for a filled core beam with degree of linear polarization  $L = I \cos \theta_0$ , where  $\theta_0$  is the emission point colatitude. The panels are organised in landscape mode, in order of increasing  $10^\circ \leq i \leq 90^\circ$  (left–right) and  $10^\circ \leq \alpha \leq 90^\circ$  (top–bottom) in intervals of  $10^\circ$ .  $I$  is plotted on the horizontal axis and normalised by its peak value.  $Q$  is plotted on the vertical axis.

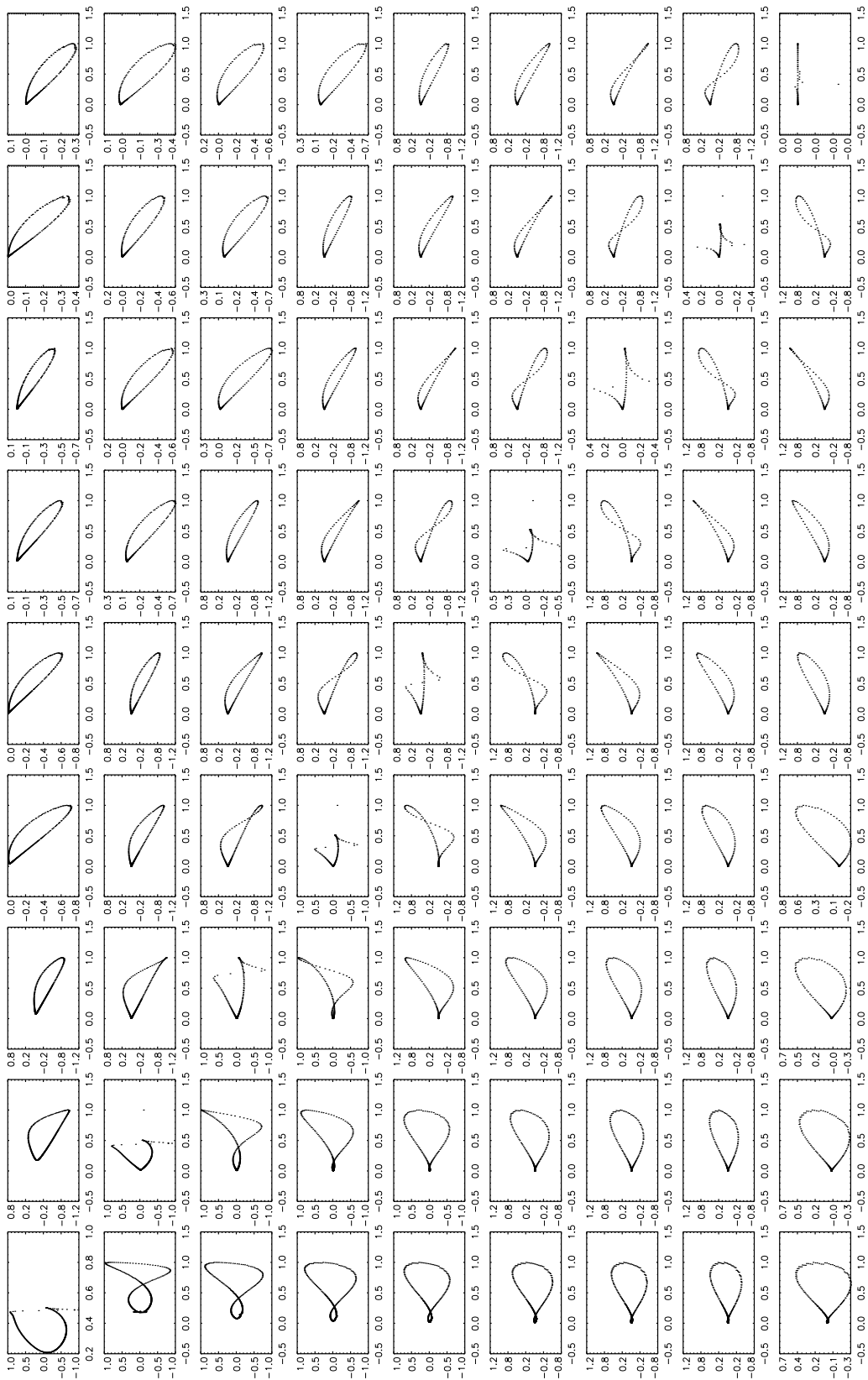


**Figure 5.27:** Dipole field at  $r = 0.1r_{\text{LC}}$ . Layout as for Figure 5.26, but for  $I-U$  ( $I$  on the horizontal axis).

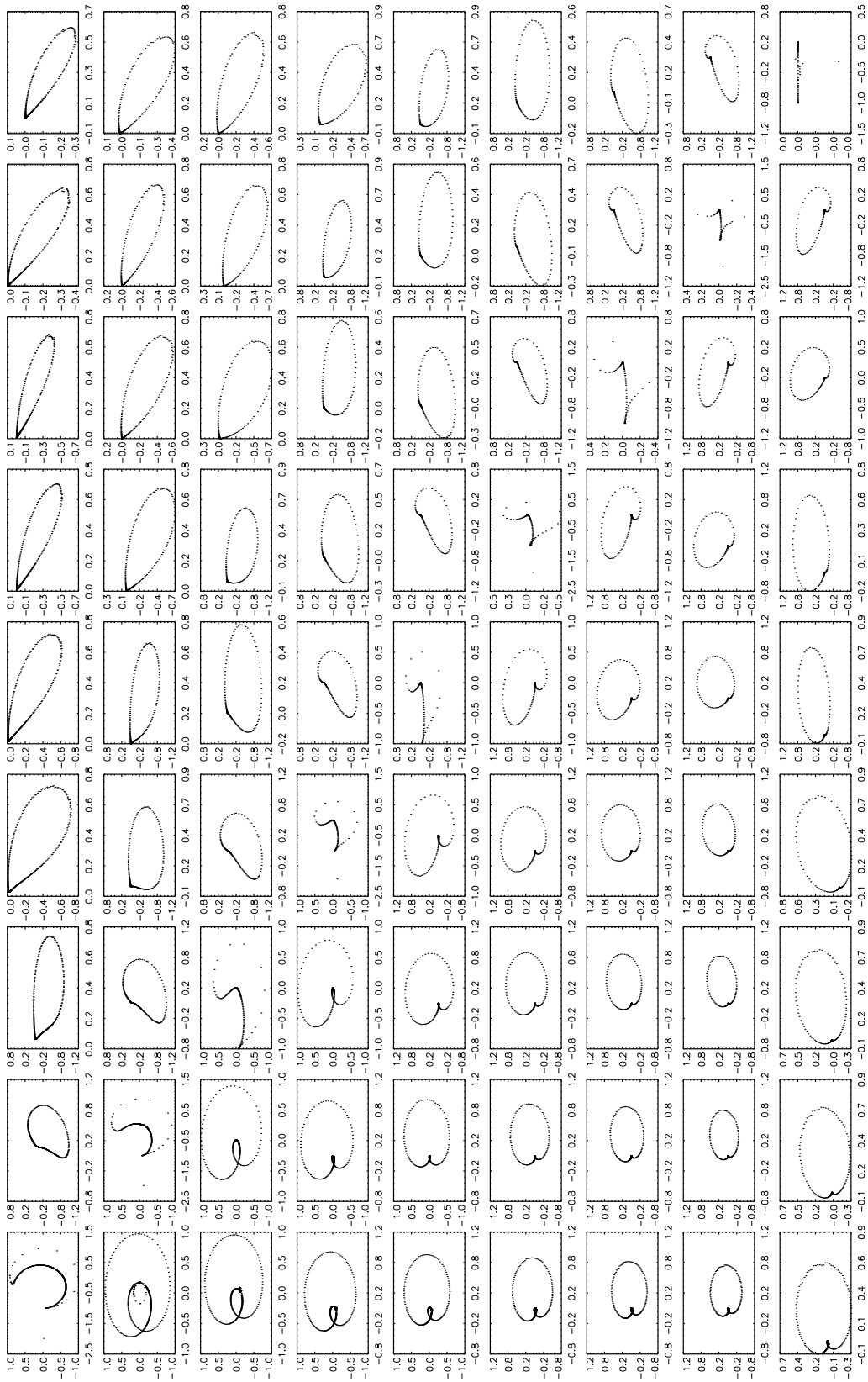


Figure 5.28: Dipole field at  $r = 0.1r_{LC}$ . Layout as for Figure 5.26, but for  $Q-U$  ( $Q$  on the horizontal axis).

### 5.4.2 Hollow cone

We now examine the major differences between the Stokes phase portraits for a hollow cone beam and  $L = I \cos \theta_0$  at  $r = 0.1r_{\text{LC}}$  (Figures 5.29–5.31) and the corresponding non-aberrated case (Figures 5.17–5.19).

Similar to the filled core beam, aberration broadens the shapes in the  $I$ - $Q$  plane (Figures 5.29). At the orientations where the pulse profile is double-peaked, the  $\gamma$ -shapes at  $\alpha \gtrsim 40^\circ$  and  $i \gtrsim 40^\circ$  from Figure 5.17 are replaced by mosquito shapes. For  $\alpha \lesssim 30^\circ$  and  $i \lesssim 30^\circ$ , the  $I$ - $Q$  portraits maintain their general shape but are broader. An exception is  $(\alpha, i) = (20^\circ, 30^\circ)$ , which changes from a C-shape in the non-aberrated case to a figure-eight with aberration.

In the  $I$ - $U$  plane, at the orientations where the pulse profile is double-peaked, the trefoils, triangles, and mosquito shapes retain their general shape. However, they are distorted and asymmetric about  $U = 0$ , as the individual components of the patterns (e.g. the ‘wings’ of the mosquitoes) tilt at different angles and have different widths.

The shapes in the  $Q$ - $U$  plane do change at those orientations where the pulse profile is double-peaked. In the  $\alpha > i$  region (below the diagonal), the interlocking ovals become distorted, asymmetric heart shapes as  $\alpha$  and  $i$  increase. In the  $\alpha < i$  region (above the diagonal), there are figure-eights [e.g.  $(\alpha, i) = (20^\circ, 40^\circ)$ ] which become distorted heart shapes as  $\alpha$  and  $i$  increase. Along the  $\alpha = i$  diagonal, distorted heart shapes evolve into distorted mosquito shapes as  $\alpha$  and  $i$  increase.

### 5.4.3 How common are low emission altitudes?

As our first application of the above theory to observational data, we ask: what proportion of pulsars with superficially dipole-like characteristics (e.g. S-shaped PA swings) are truly consistent with a pure dipole field and low, non-aberrated emission altitude (Section 5.3), when we examine their Stokes phase portraits?

To this end, we select two sets of superficially dipole-like pulsars from the 366 objects presented in Gould & Lyne (1998) and Manchester et al. (1998). Set I contains pulsars that follow closely the  $W \propto P^{-1/2}$  relation (Rankin 1993) and hence are likely *prima facie* to have an approximately dipolar field in the emission region, with or without aberration. They are drawn from near the diagonal line in Figure 9 of Gould & Lyne (1998); as a rule, their pulse width at  $0.1I_{\text{max}}$  (where  $I_{\text{max}}$  is the peak intensity) is less than  $20^\circ$ . Set

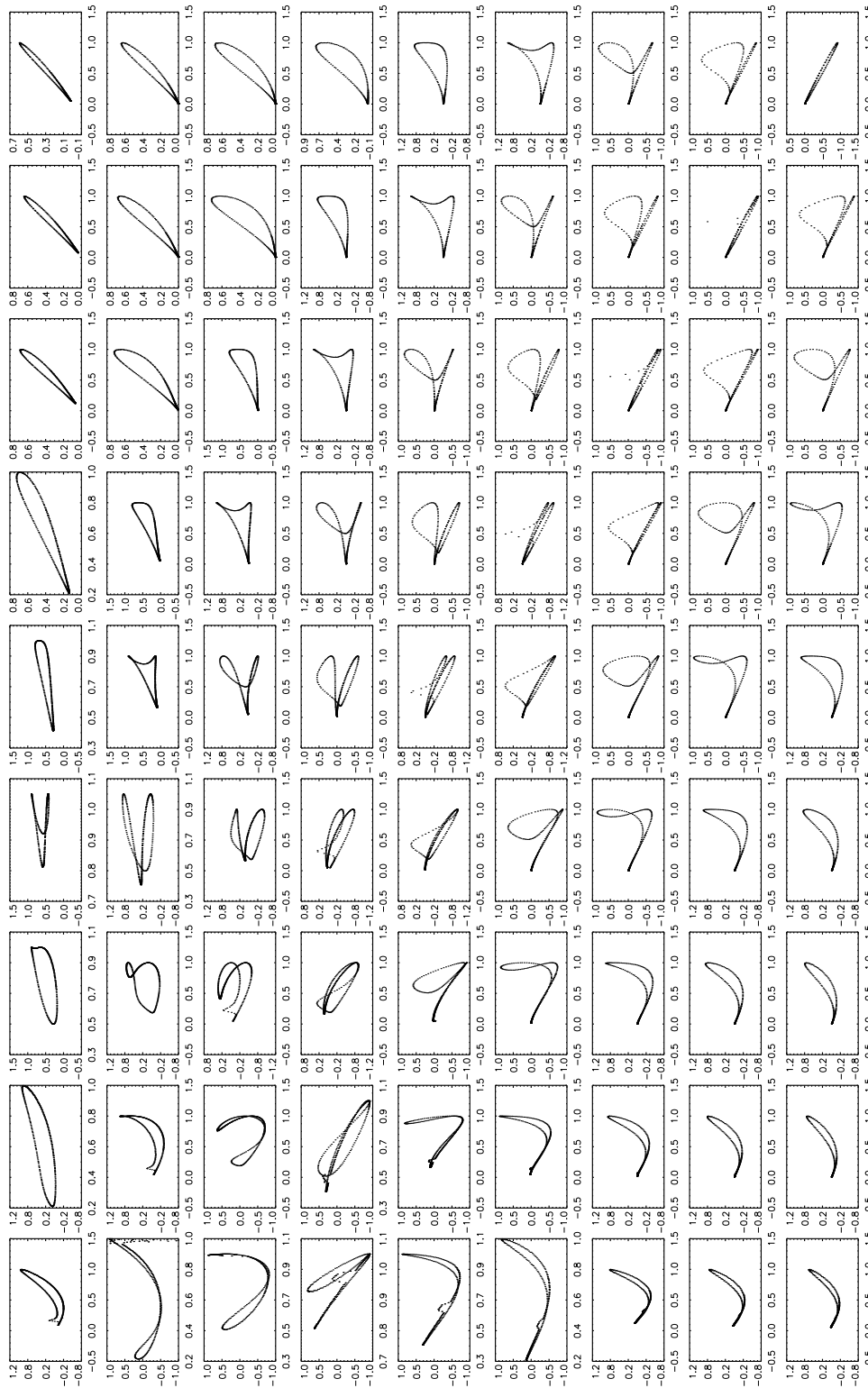


**Figure 5.29:** Dipole field at  $r = 0.1r_{LC}$ . Look-up table of Stokes phase portraits in the  $I$ - $Q$  plane for a hollow cone with opening angle  $25^\circ$  with degree of linear polarization  $L = I \cos \theta_0$ , where  $\theta_0$  is the emission point colatitude. The panels are organised in landscape mode, in order of increasing  $10^\circ \leq i \leq 90^\circ$  (left-right) and  $10^\circ \leq \alpha \leq 90^\circ$  (top-bottom) in intervals of  $10^\circ$ .  $I$  is plotted on the horizontal axis and normalised by its peak value.  $Q$  is plotted on the vertical axis.

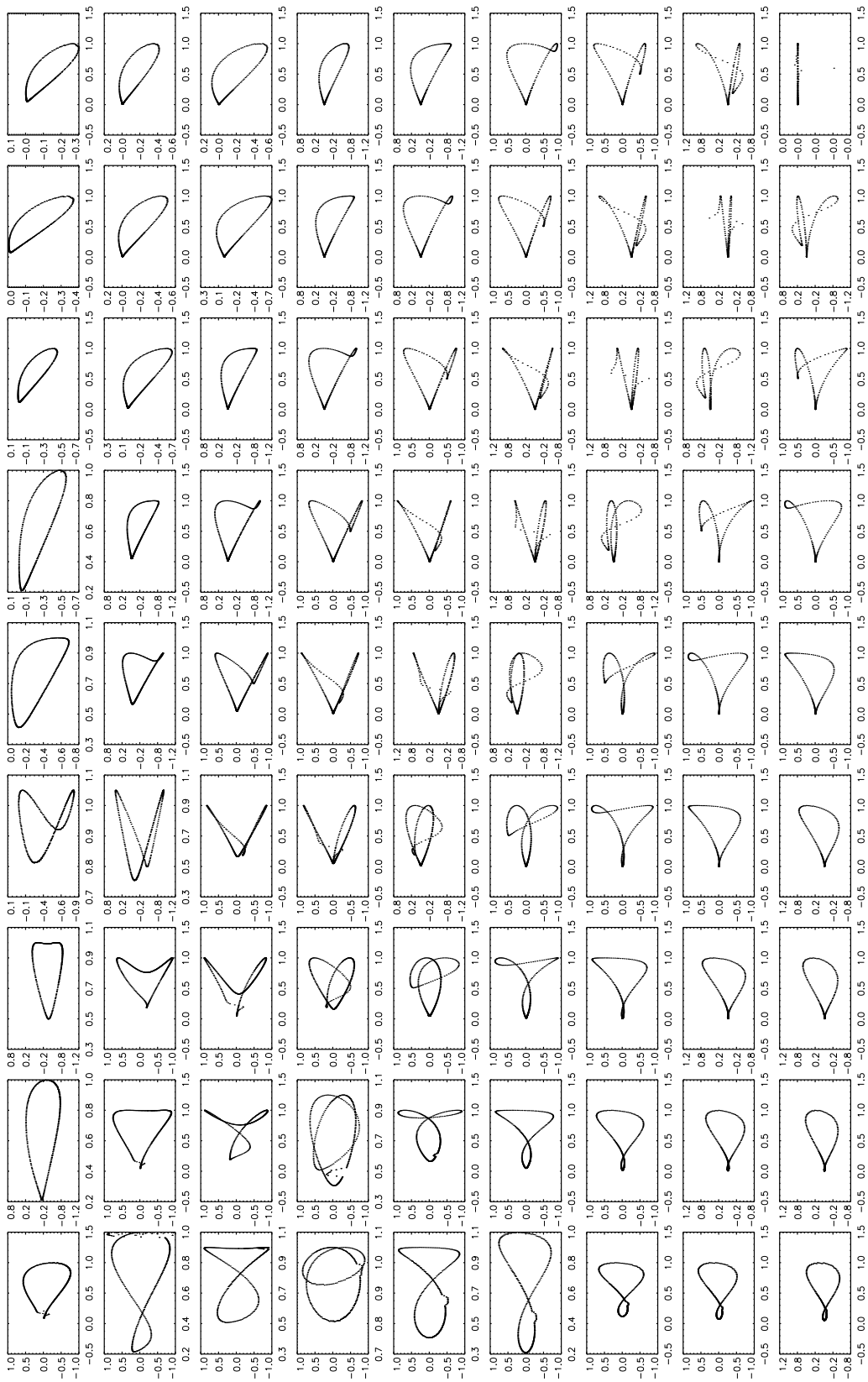


**Figure 5.30:** Dipole field at  $r = 0.1r_{\text{LC}}$ . Layout as for Figure 5.29, but for  $I-U$  ( $I$  on the horizontal axis).

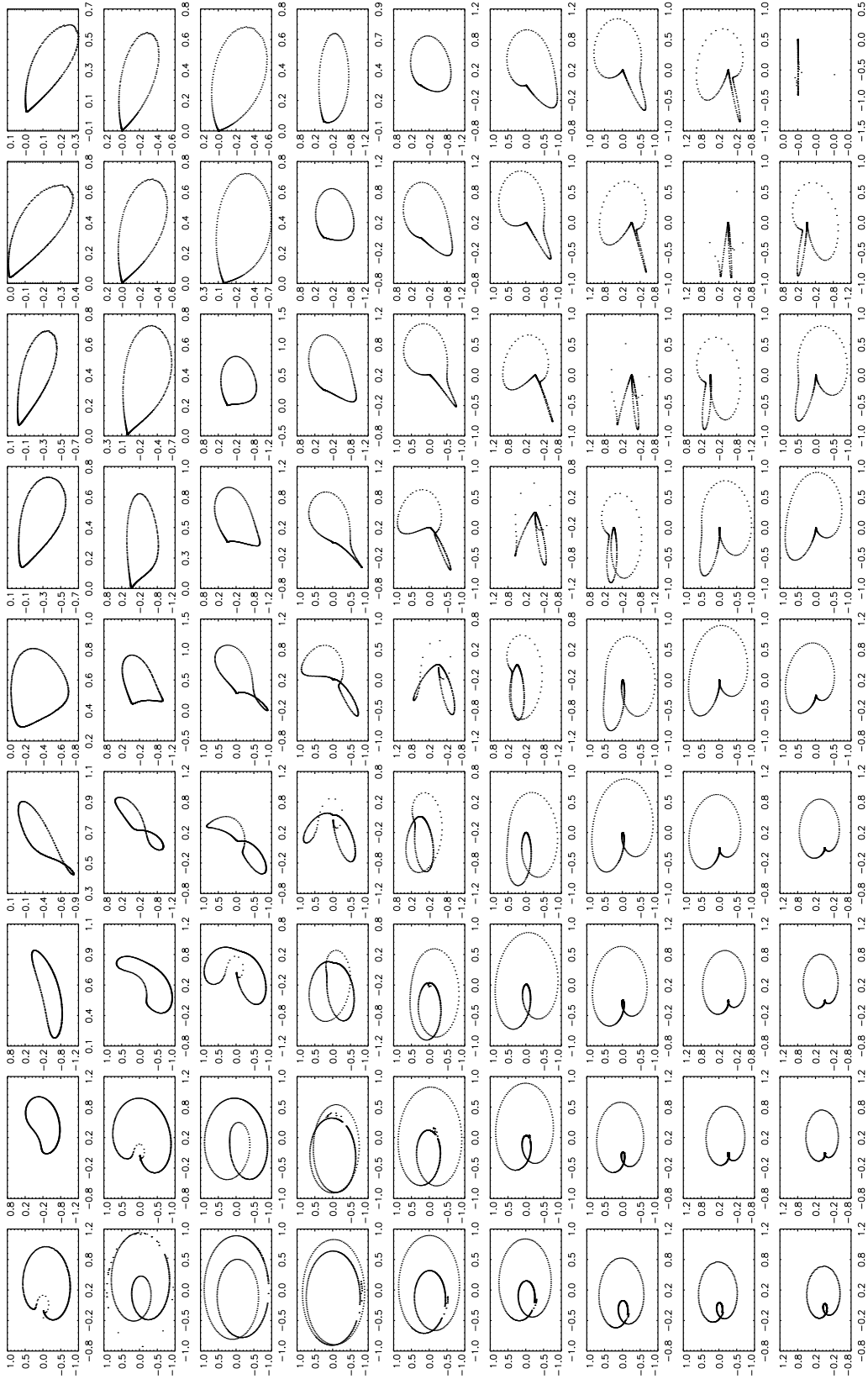


Figure 5.31: Dipole field at  $r = 0.1r_{LC}$ . Layout as for Figure 5.29, but for  $Q-U$  ( $Q$  on the horizontal axis).

II contains pulsars that have a clean, S-shaped PA swing, after allowing for phase wrapping. From the suitable pulsars, we choose 12 at random in each set.

We present the pulse profiles, Stokes phase portraits, and PA swings for Set I at 610 MHz in Figures 5.32 and 5.33. PA data points are only plotted for  $L \geq 0.1L_{\text{max}}$  and  $I \geq 0.1I_{\text{max}}$ . The data are sourced from the EPN online archive (Lorimer et al. 1998). The 12 objects are calibrated separately, so the polarization basis varies from pulsar to pulsar. For the purposes of this section, we do not attempt to determine  $\beta$  for each object; we focus on the *shape* of the  $Q$ - $U$  patterns, not their orientations. From Sections 5.3 and 5.4, we note that one clear fingerprint of low-altitude emission from a pure dipole is the symmetry of the  $Q$ - $U$  pattern about  $U = 0$  (rotated in general by an angle  $2\beta$ ). Hence, in Figures 5.32–5.35, any pattern which is not symmetric about any line cannot originate from a low altitude where aberration is negligible.

Of the 12 objects in Figures 5.32 and 5.33, four have Stokes phase portraits which roughly resemble a dipole at low altitudes: PSR J0628+2415 and PSR J1740–3015 (Figure 5.32, third and fifth rows) match a core beam for large  $i$  and small  $\alpha$  ( $L = I \cos \theta_0$  and  $L = I \sin \theta_0$  give similar answers for these angles). PSR J1823–3106 and J1926+1648 (Figure 5.33, first and fourth rows) match a core beam with  $\alpha \leq i$  and  $L = I \cos \theta_0$ . The other eight pulsars have  $Q$ - $U$  portraits which feature significantly asymmetric shapes. This is reflected in their PA swings, which are not as clean as the other four pulsars. For example, PSR J2046+1540 (Figure 5.33, fifth row) features an asymmetric mosquito in the  $Q$ - $U$  plane. Such a pattern matches a dipole field at  $r = 0.1r_{\text{LC}}$  along  $\alpha = i$  for a hollow cone with  $L = I \cos \theta_0$  (see the look-up table in Figure 5.31), where aberration is important, but cannot be reconciled with emission from low altitudes.

Figures 5.34 and 5.35 display the pulse profiles, Stokes phase portraits, and PA swings for Set II. This set comprises data at multiple frequencies (Gould & Lyne 1998; Manchester et al. 1998), sourced from the EPN online archive. Four of the 12 pulsars in this set feature approximately symmetric mosquito and heart shapes matching a dipole at low emission altitudes. PSR J0528+2200 (Figure 5.34, second row), PSR J2048–1616, and J2346–0609 (Figure 5.35, third and sixth rows) match the  $Q$ - $U$  portraits for a hollow cone with  $\alpha = i \geq 30^\circ$  ( $L = I \cos \theta_0$  and  $L = I \sin \theta_0$  give similar answers for these angles). PSR J2113+4644 (Figure 5.35, fourth row) matches all three phase portraits for a filled core beam for  $0^\circ \leq \alpha - i \leq 10^\circ$  (again,  $L = I \cos \theta_0$  and  $L = I \sin \theta_0$  give similar answers for these angles). In Figure 5.34 and 5.35,

the mosquito and heart shapes of the other eight pulsars are noticeably asymmetric, indicating that the emission originates from higher altitudes, where aberration takes effect.

For a dipole field (or indeed any axisymmetric field), aberration changes the relative phase between the PA swing and pulse profile, but it does not cause the shape of the PA swing to change with emission frequency (unlike the pulse width). In reality, multi-frequency observations show that PA swings do change with frequency (Johnston et al. 2008a). We return to this issue in Section 5.5.3, where we find that the Stokes phase portraits for magnetic geometries with an appreciable toroidal component at  $r \gtrsim 0.1r_{\text{LC}}$  evolve with frequency dramatically and in an informative way.

A key tenet of pulsar radio emission theory holds that core and cone emission mostly comes from low altitudes, where departures from a dipole field are small. Contrary to this view, the results in Figures 5.32-5.35 imply that in a clear majority (> 60%) of objects, the emission originates from high altitudes, where aberration and/or the toroidal field component are significant. Under these circumstances, the values of  $\alpha$  and  $i$  inferred from the PA swing (which still looks respectably S-shaped in many instances) may be wrong. We now turn to explore this important issue in Section 5.5.

## 5.5 Current-modified dipole field

In this section, we examine the pulse profiles, Stokes phase portraits, and PA swings associated with a current-modified magnetic field composed of a dipole with symmetry axis  $\mathbf{e}_3$  plus a toroidal component (cylindrically symmetric about  $\mathbf{e}_3$ ) with magnitude

$$B_\phi = \eta B_p r / r_{\text{LC}}, \quad (5.16)$$

where  $B_p = (B_r^2 + B_\theta^2)^{1/2}$  is the poloidal field strength, and  $\eta$  is a slowly varying factor of order unity. Equation (5.16) is the scaling expected for  $r \lesssim r_{\text{LC}}$  if  $B_\phi$  is generated by a field-aligned Goldreich-Julian current in a plasma-filled magnetosphere (Hibschman & Arons 2001). If  $B_\phi$  is generated by the displacement current, as in a vacuum rotator, it scales as  $r^2$ ; we save this case for future analysis (Deutsch 1955; Melatos 1997).

Since the strength of the toroidal field is of the same order as the aberration, setting  $\eta$  to +1 partially cancels out the effects of aberration. It reduces the relative phase shift between the PA swing and the pulse profile, and results in phase portraits which generally resemble those in Section 5.3 (although

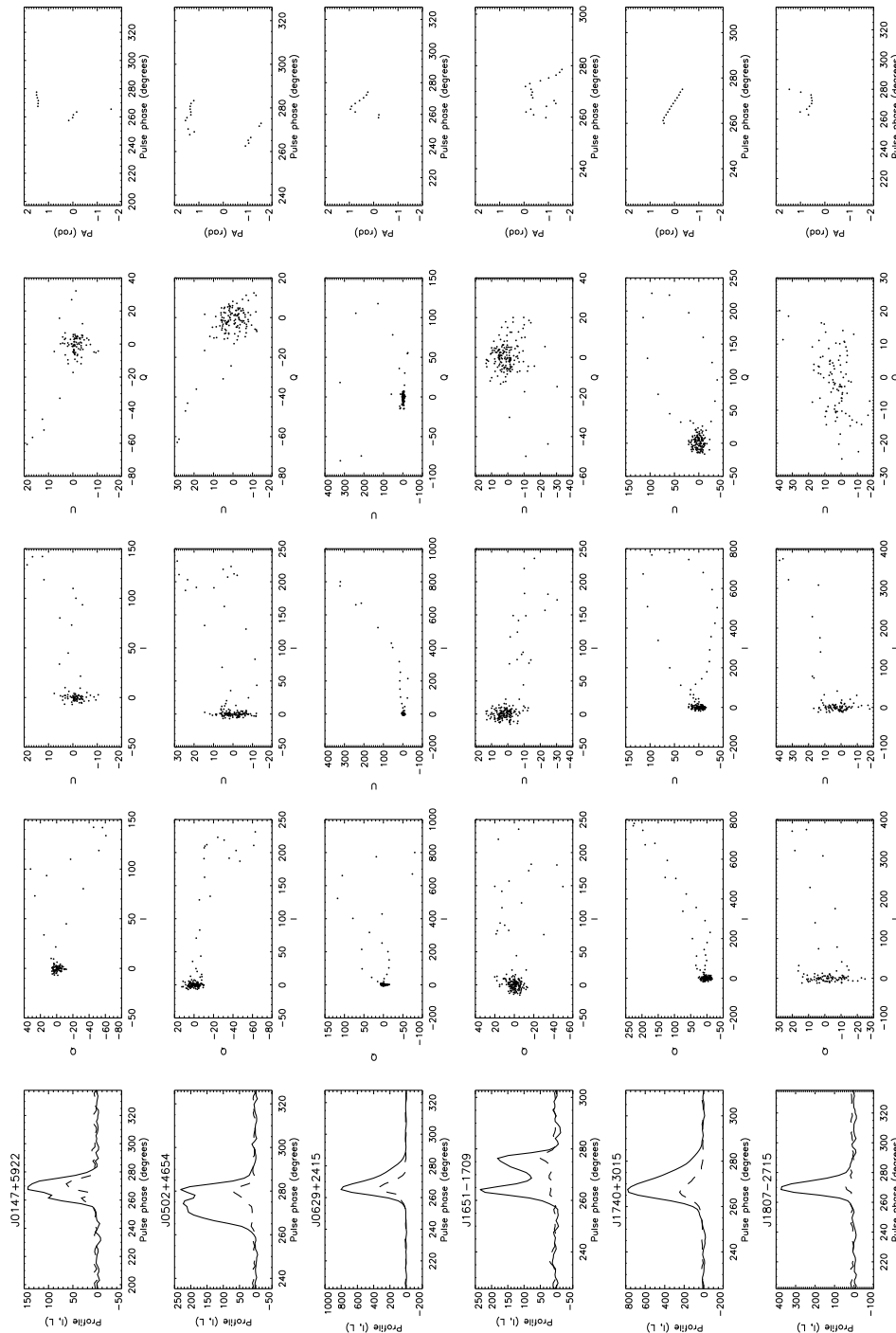


**Figure 5.32:** Pulse profiles, Stokes phase portraits and PA swings for a selection of six superficially dipolar pulsars that closely follow the pulse-width-period relation at 610 MHz (Gould & Lyne 1998). The data for each pulsar occupy a row each in landscape mode. From left to right, the columns show: (1)  $I$  (mJy, solid curve) and  $L$  (mJy, dashed curve), (2) the  $I$ - $Q$  phase portrait, (3) the  $I$ - $U$  phase portrait, (4) the  $Q$ - $U$  phase portrait, and (5) the PA swing (data points with  $L \geq 0.1I_{\max}$  and  $I \geq 0.1I_{\max}$  plotted only). Data are presented courtesy of the EPN online archive.

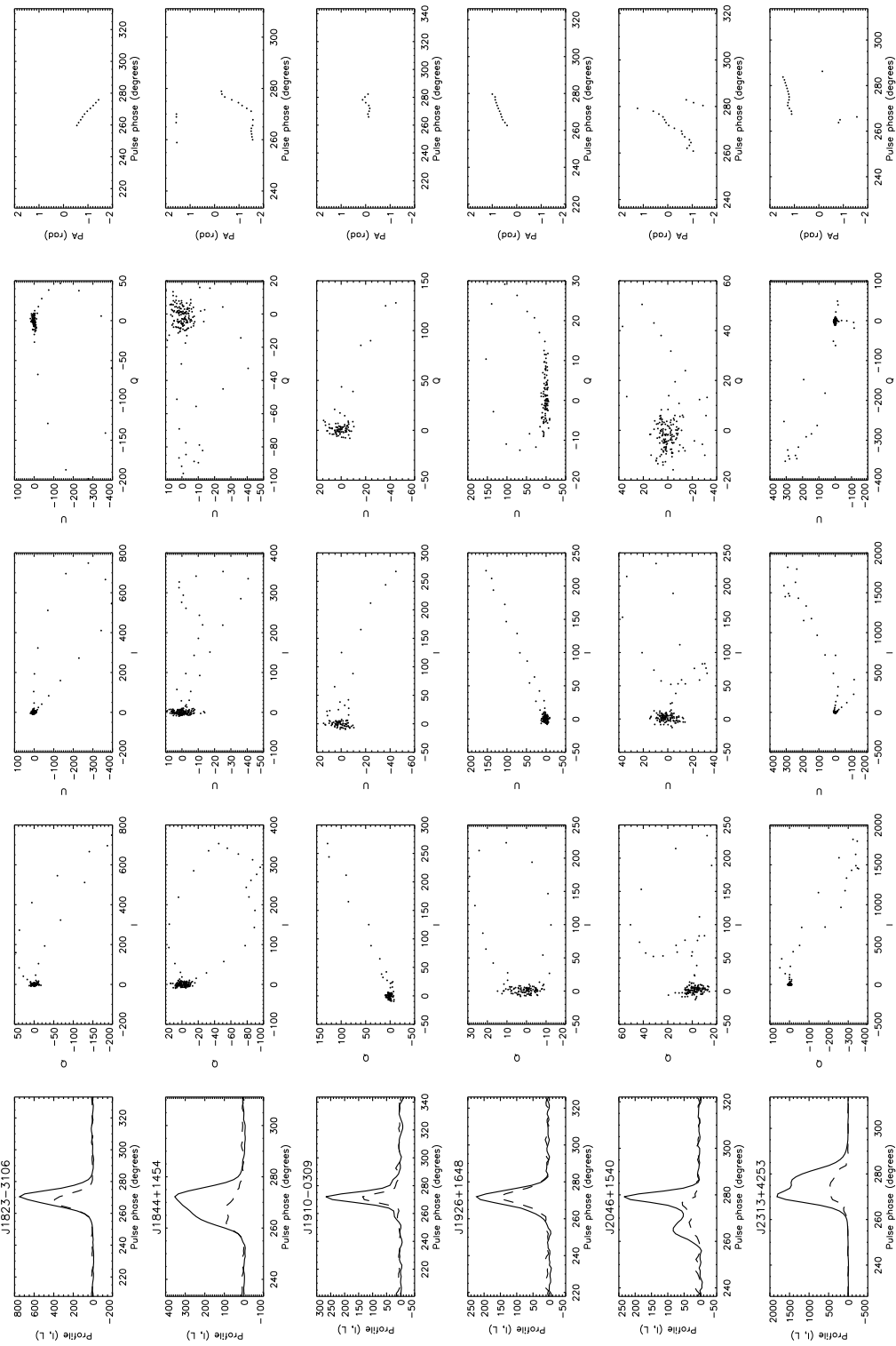


**Figure 5.33:** As for Figure 5.32, for six other objects selected according to the same criterion.

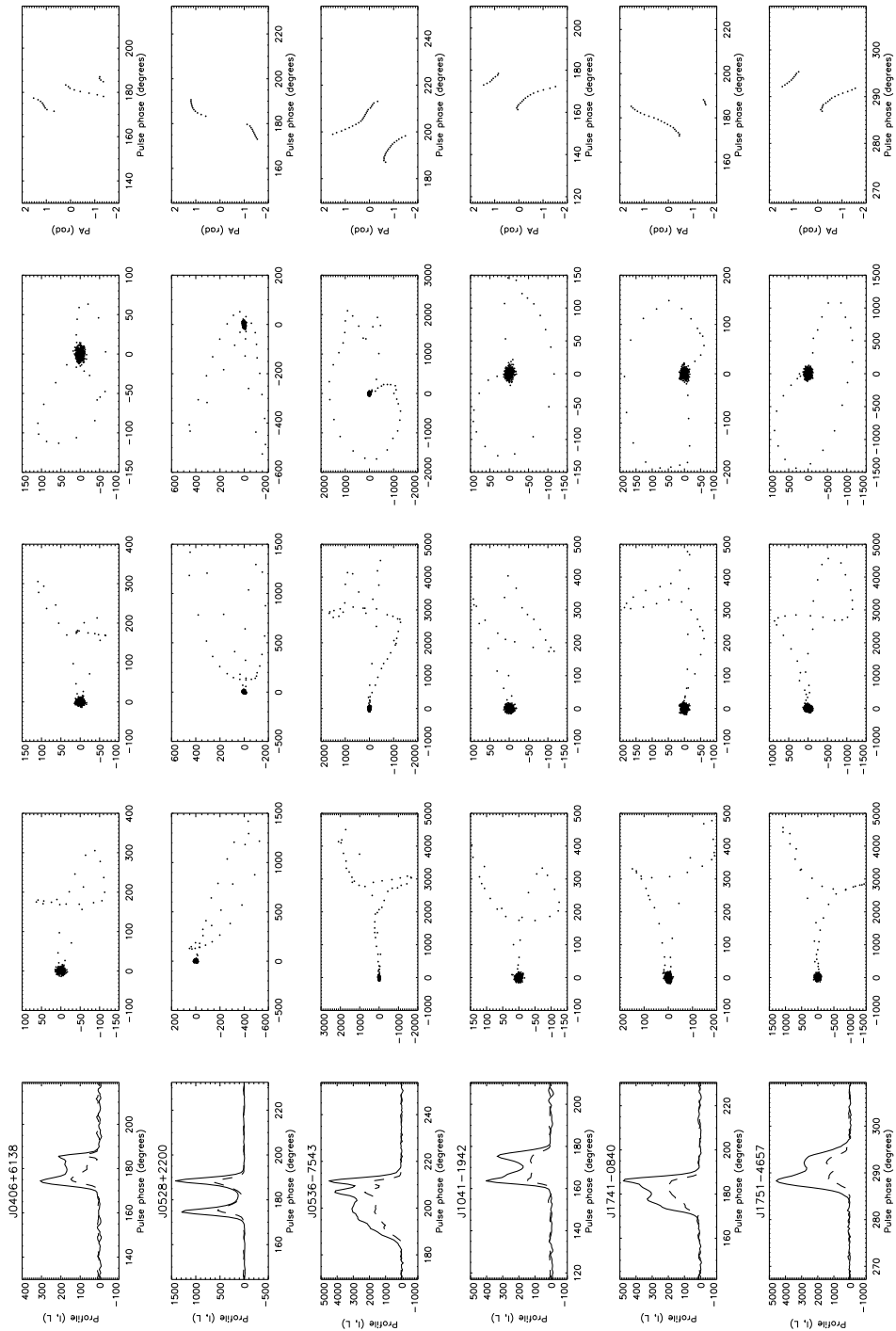


**Figure 5.34:** Pulse profiles, Stokes phase portraits and PA swings for a selection of six superficially dipolar pulsars that exhibit a clean, S-shaped PA swing. All pulsars are observed at 610 MHz (Gould & Lyne 1998), except for PSR J0536–7543 (663 MHz) and PSR J1751–4657 (433 MHz) (Manchester et al. 1998). The data for each pulsar occupy a row each in landscape mode. From left to right, the columns show: (1)  $I$  (mJy, solid curve) and  $L$  (mJy, dashed curve), (2) the  $I$ - $Q$  phase portrait, (3) the  $I$ - $U$  phase portrait, (4) the  $Q$ - $U$  phase portrait, and (5) the PA swing (data points with  $L \geq 0.1L_{\max}$  and  $I \geq 0.1I_{\max}$  plotted only). Data are presented courtesy of the EPN online archive.

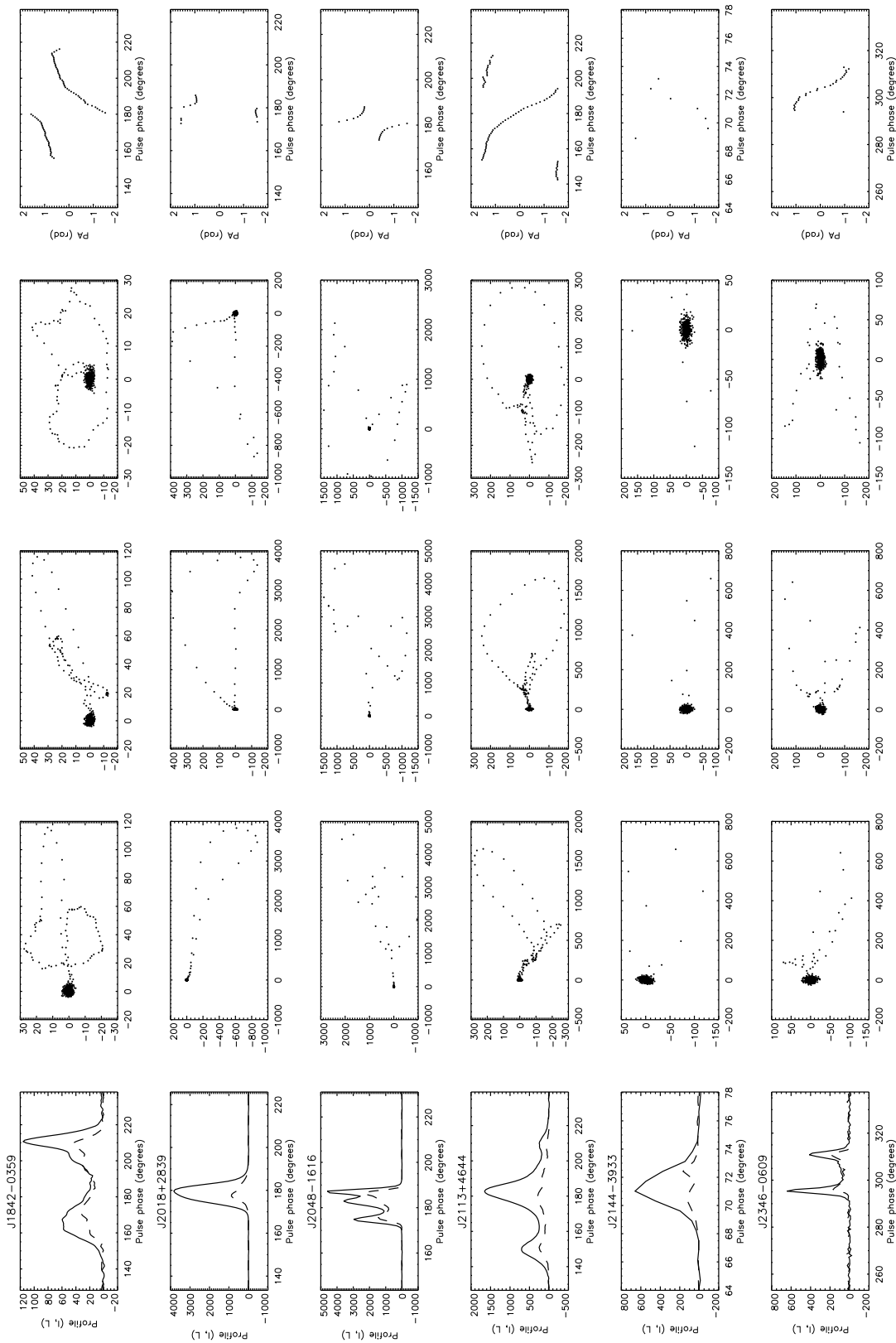


**Figure 5.35:** As for Figure 5.32 for six other objects selected according to the same criterion. All pulsars are observed at 610 MHz (Gould & Lyne 1998), except for PSR J1842-0359 (1.408 GHz) (Gould & Lyne 1998), PSR J2144-3933 (659 MHz) and PSR J2346-0609 (435 MHz) (Manchester et al. 1998).

some mild distortion is still observed as the emission point does change; the cancellation is not perfect). However, if  $\eta$  is set to  $-1$ , the  $B_\phi$  effect reinforces aberration, the phase shift between the PA swing and pulse profile increases, and the distortion of the phase portraits seen in Section 5.4 is enhanced. In order to highlight the  $B_\phi$  effect, we use  $\eta = -1$  throughout this section.

We investigate the same beam and polarization patterns as in Section 5.3. The emission point  $\mathbf{x}_0(t)$  traces out a different locus in the current-modified dipole as compared to the pure dipole, and the locus varies differently with altitude. In Sections 5.5.1 and 5.5.2, we present two-dimensional look-up tables of Stokes phase portraits for orientations  $10^\circ \leq i \leq 90^\circ$  and  $10^\circ \leq \alpha \leq 90^\circ$ . For each beam pattern (core emission in Section 5.5.1, conal emission in Section 5.5.2) and polarization pattern ( $L/I = \cos \theta_0, \sin \theta_0$ ), we construct three phase portraits ( $I$ - $Q$ ,  $I$ - $U$  and  $Q$ - $U$ ) for each pair of angles  $(\alpha, i)$  at a fixed emission altitude ( $r = 0.1 r_{\text{LC}}$ ). In Section 5.5.3, we show some examples of how the phase portraits change with altitude.

### 5.5.1 Filled core emission

$$L = I \cos \theta_0$$

An example of the  $I$  (solid curve) and  $L$  (dashed curve) profiles for a single-peaked pulse with  $(\alpha, i) = (70^\circ, 20^\circ)$  are shown in Figure 5.36.  $I$  is normalised by its peak value. The dotted curve shows how the magnetic colatitude  $\theta_0(t)$  of the emission point varies across one pulse period. We note the following trends. (i) The emission points and pulse profiles are phase-shifted by  $-r/r_{\text{LC}}$  radians due to aberration. (ii) The profiles behave similarly to the pure dipole (Section 5.3.1), narrowing with increasing  $\alpha$  and  $i$ . (iii) For  $|\alpha - i| \leq 10^\circ$ , the profile ‘saturates’ at  $I \approx L \approx 1$  near the pulse peak, because  $\theta_0$  remains near zero for some time. The saturation lasts for  $\approx 0.5$  phase units at  $(\alpha, i) = (10^\circ, 10^\circ)$  and  $\approx 0.13$  phase units at  $(\alpha, i) = (90^\circ, 90^\circ)$ . The squared-off shape of the profile is a numerical artifact caused by the finite grid resolution near  $\theta_0 = 0$ .

Figure 5.37 shows the path traced by  $\hat{\mathbf{x}}_0(t)$  in the body frame across one pulse period for three cases: (A)  $(\alpha, i) = (30^\circ, 10^\circ)$ , (B)  $(30^\circ, 30^\circ)$ , and (C)  $(30^\circ, 50^\circ)$ . As in Figure 5.5, the path changes from an undulation for  $\alpha < i$  (curve C) to an ellipse for  $\alpha > i$  (curve A). The toroidal magnetic field twists the paths, so that they are not reflection symmetric about some longitude, unlike in Figure 5.5. The asymmetry distorts the Stokes phase portraits, but the clear distinction between  $\alpha < i$  and  $\alpha > i$  persists. Note that  $\theta_0$  stagnates near zero in curve B, causing the saturation of the pulse profiles mentioned in

the previous paragraph.

The Stokes phase portraits are drawn in Figures 5.38–5.40. The phase portraits differ from those of the pure dipole in both Sections 5.3 and 5.4. In the  $I$ - $Q$  plane (Figure 5.38), we note the following behaviour. (i) For  $\alpha = i$ , the pulse traces out a balloon shape. The cutoff of the shapes at  $I = 1$  is a numerical artifact due to the saturation of the pulse profile. (ii) For  $\alpha > i$ , we see a tilted balloon shape, whose pointy tip sits at  $(I, Q) = (0, 0)$ . The balloon tilts upwards (major axis has slope  $dQ/dI > 0$ ). For  $i \leq 20^\circ$  and  $\alpha \lesssim 45^\circ$ , the balloon twists into a figure-eight. (iii) For  $\alpha < i$ , we see tilted balloons for  $|\alpha - i| \leq 45^\circ$ , which narrow into tilted ovals as  $i$  increases. The balloons tilt downwards (major axis has  $dQ/dI < 0$ ) for  $i - \alpha \lesssim 25^\circ$  and upwards (major axis has  $dQ/dI > 0$ ) for  $i - \alpha \gtrsim 25^\circ$ .

In the  $I$ - $U$  plane (Figure 5.39), we note the following behaviour. (i) For  $\alpha = i$ , the saturation discussed above results in a vertical ‘wall’ at  $I = 1$ . Away from the wall, for  $\alpha = i$ , we obtain a tilted triangular shape. (ii) For  $\alpha > i$  (below the diagonal in Figure 5.39), the pulse traces out a slender hockey stick, which broadens into a balloon as  $\alpha$  increases. As in Section 5.3.1, the curvature of the hockey stick decreases with increasing  $\alpha$ . (iii) For  $\alpha < i$  (above the diagonal), we obtain balloons for  $i - \alpha \lesssim 10^\circ$ , and narrow ovals for  $i - \alpha \gtrsim 20^\circ$ .

In the  $Q$ - $U$  plane (Figure 5.40), we see a mix of balloons and heart shapes with the following properties. (i) Along the  $\alpha = i$  diagonal, we observe a ‘C’ shape for  $(\alpha, i) = (10^\circ, 10^\circ)$ , which evolves into a distorted heart shape as  $\alpha = i$  increases. (ii) For  $\alpha > i$  (below the diagonal in Figure 5.40), we see heart shapes with a cusp at  $(Q, U) = (0, 0)$ . The cusp becomes less pronounced as  $\alpha$  increases and twists into a secondary oval for  $\alpha \leq 40^\circ$ . (iii) For  $\alpha < i$  (above the diagonal), we see heart shapes for  $|\alpha - i| \leq 10^\circ$ . These shapes evolve into tilted balloons as  $|\alpha - i|$  increases. (iv) As in Figure 5.39, the patterns are broadest for  $|\alpha - i| \leq 10^\circ$  and narrow as  $|\alpha - i|$  increases.

Generally, the heart shapes and balloons in Figure 5.40 are not symmetric about  $U = 0$  or  $Q = 0$  and have a higher degree of rotation than those in Section 5.4. The amount by which the shapes rotate depend on  $|\alpha - i|$ . Geometrically, this happens because  $\theta_0(t)$  increases with  $|\alpha - i|$ . The degree of rotation decreases as  $|\alpha - i|$  increases.

In Figure 5.41, we plot the PA swings corresponding to each panel in Figures 5.38–5.40. We plot only the parts of the swing that are illuminated by the pulse, i.e. when  $L \geq 10^{-2}$ . We note the following behaviour. (i) There are clear distortions in the S-shape for  $|\alpha - i| \leq 10^\circ$ . Along  $\alpha = i$ , where the

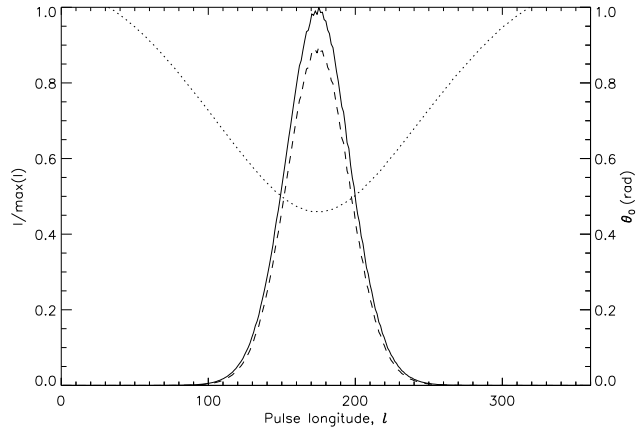


**Figure 5.36:** Current-modified dipole field at  $r = 0.1r_{\text{LC}}$ . Example of a pulse profile for a filled core beam with linear polarization  $L = I \cos \theta_0$  and  $(\alpha, i) = (70^\circ, 30^\circ)$  at  $r = 0.1 r_{\text{LC}}$ . Solid, dashed and dotted curves represent the total polarized intensity  $I$ , degree of linear polarization  $L$ , and emission point colatitude  $\theta_0$ . Pulse longitude  $l$  is measured in units of degrees.

$I \approx 1$  saturation occurs,  $d(PA)/dl$  changes discontinuously. A good example is  $(\alpha, i) = (20^\circ, 20^\circ)$ . The kinks around the discontinuities are numerical artifacts, but the smoothly varying curves leading up to the kinks are real. (ii) For  $|\alpha - i| \geq 20^\circ$ , the shape of the PA swings appear similar to those of Section 5.3. As we have chosen  $\eta = -1$ , the toroidal field enhances the phase shift of the PA swings in Figure 5.41. For example, at  $(\alpha, i) = (40^\circ, 70^\circ)$ , the relative phase shift between the PA swing and the pulse profile is  $\approx 5r/r_{\text{LC}}$ . The phase shift is altitude dependent; we discuss altitudinal variations in Section 5.5.3. The similarity of the PA swings for the pure and current-modified dipoles reinforces the necessity to supplement PA swings with Stokes phase portraits when diagnosing the pulsar magnetosphere.

### $L = I \sin \theta_0$

An example of the  $I$  (solid curve) and  $L$  (dashed curve) profiles for  $(\alpha, i) = (30^\circ, 30^\circ)$  is shown in Figure 5.42. The profiles are similar to those of the pure dipole in Section 5.3.1, displaying the same double-peaked  $L$  profile along the  $\alpha = i$  diagonal. The only difference is caused by the numerical stagnation of  $\theta_0$  near zero for  $|\alpha - i| \leq 10^\circ$ . At these angles, one has  $L \approx 0$  when  $I \approx 1$ .

The Stokes phase portraits for a filled core with  $L/I = \sin \theta_0$  are drawn in Figures 5.43–5.45. Comparing the Stokes phase portraits and PA swings to those in Section 5.5.1, we note the following differences. (i) In the  $I$ - $Q$  phase portrait (Figure 5.43), along the  $\alpha = i$  diagonal, there is an oval shape instead

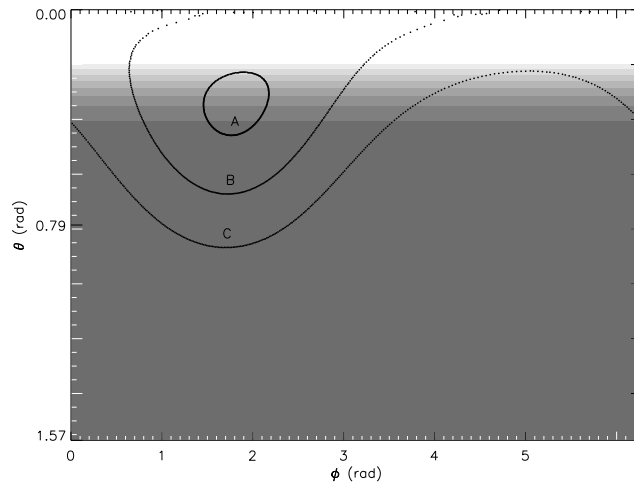


**Figure 5.37:** Current-modified dipole field at  $r = 0.1r_{LC}$ . Examples of the path traced by the emission point  $\hat{\mathbf{x}}_0(t)$  in the body frame (curves), overlaid on the intensity map for a filled core beam (greyscale). The beam is brightest at  $\theta = 0$  (corresponding to the  $\mathbf{e}_3$  axis). Curves A:  $(\alpha, i) = (20^\circ, 10^\circ)$ , B:  $(\alpha, i) = (30^\circ, 30^\circ)$ , and C:  $(\alpha, i) = (30^\circ, 50^\circ)$ .

of a balloon. The panels where  $L/I$  is smaller than in Section 5.5.1 exhibit narrower shapes than their counterparts in Figure 5.38; for example, along the diagonal, the shapes are  $\approx 10$  times narrower than in Figure 5.38. (ii) In the  $I$ - $U$  phase portrait, (Figure 5.44), the  $I = 1$  wall seen in Figure 5.39 for  $|\alpha - i| \leq 10^\circ$  is no longer present. For  $\alpha = i$ , instead of triangles, we see figure-eights. In the adjacent panels, we see tilted ovals and upside-down hockey sticks, which twist into a figure-eight for  $i \leq 20^\circ$ . Again, the shapes along the  $\alpha = i$  diagonal are  $\approx 10$  times narrower than their counterparts in Figure 5.39. (iii) In the  $Q$ - $U$  plane (Figure 5.45), the main difference between Figures 5.40 and 5.45 occurs for  $|\alpha - i| = 10^\circ$ , where the heart shapes are distorted. Along the  $\alpha = i$  diagonal, instead of the C-shape, we see a distorted figure-eight. For  $i - \alpha = 10^\circ$ , one ventricle of the heart shape is elongated. There is no noticeable difference between the PA swings in this model (Figure 5.46) and the model in Section 5.5.1.

In summary, the Stokes phase portraits for a filled core beam are significantly different for pure and current-modified dipoles. Depending on its orientation, the toroidal field can either enhance or diminish the effects of aberration. The hockey stick, balloon, and heart shapes are not symmetric about any axis and are rotated about  $(U, Q) = (0, 0)$ . The PA swings are distorted for  $|\alpha - i| \leq 10^\circ$  but are similar to the pure dipole for other orientations apart the phase shift.

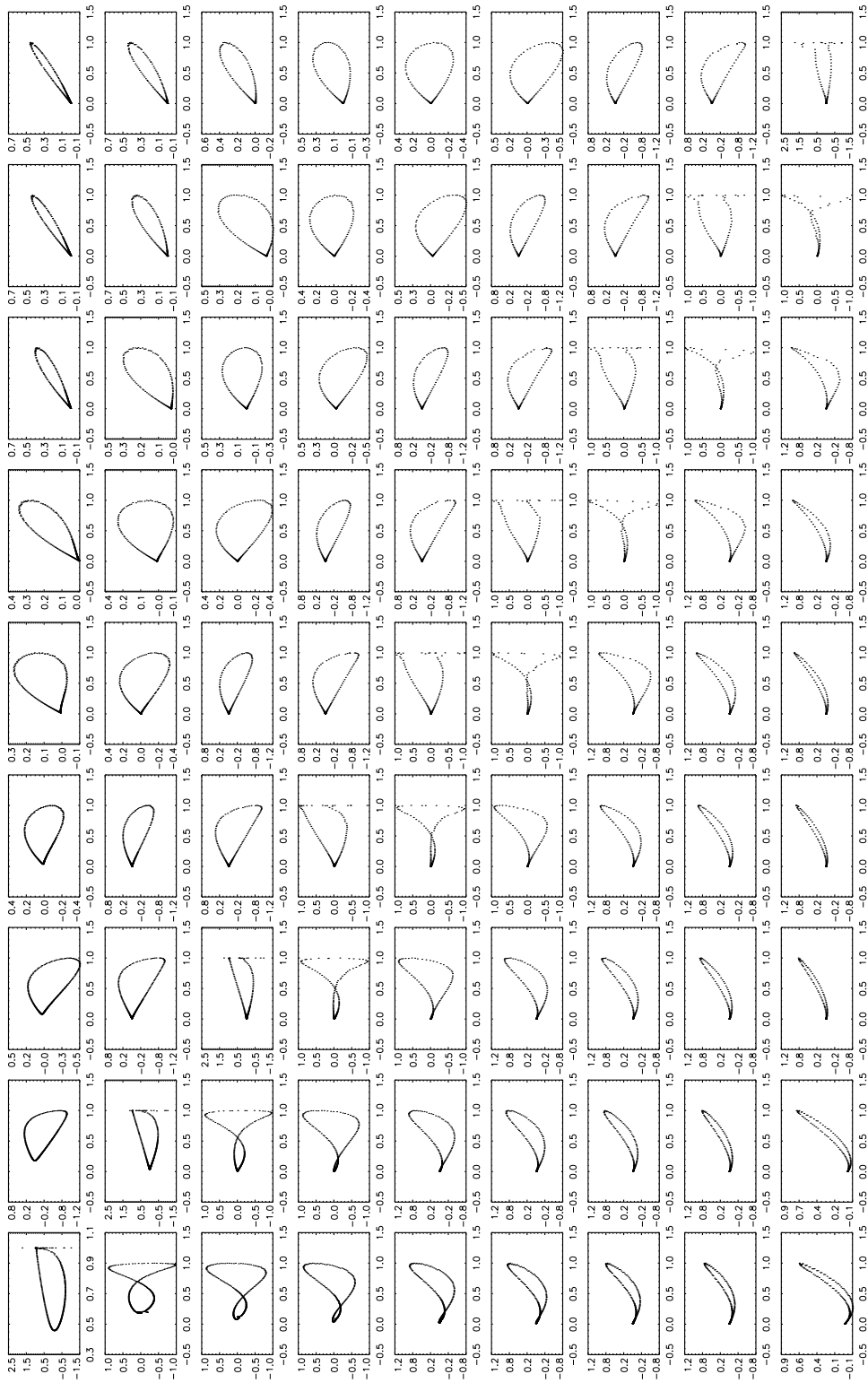


**Figure 5.38:** Current-modified dipole field at  $r = 0.1r_{\text{LC}}$ . Look-up table of Stokes phase portraits in the  $I$ - $Q$  plane for a filled core beam at  $r = 0.1r_{\text{LC}}$  with degree of linear polarization  $L = I \cos \theta_0$ , where  $\theta_0$  is the emission point colatitude. The panels are organised in landscape mode, in order of increasing  $10^\circ \leq i \leq 90^\circ$  (left-right) and  $10^\circ \leq \alpha \leq 90^\circ$  (top-bottom) in intervals of  $10^\circ$ .  $I$  is plotted on the horizontal axis and normalised by its peak value.  $Q$  is plotted on the vertical axis.

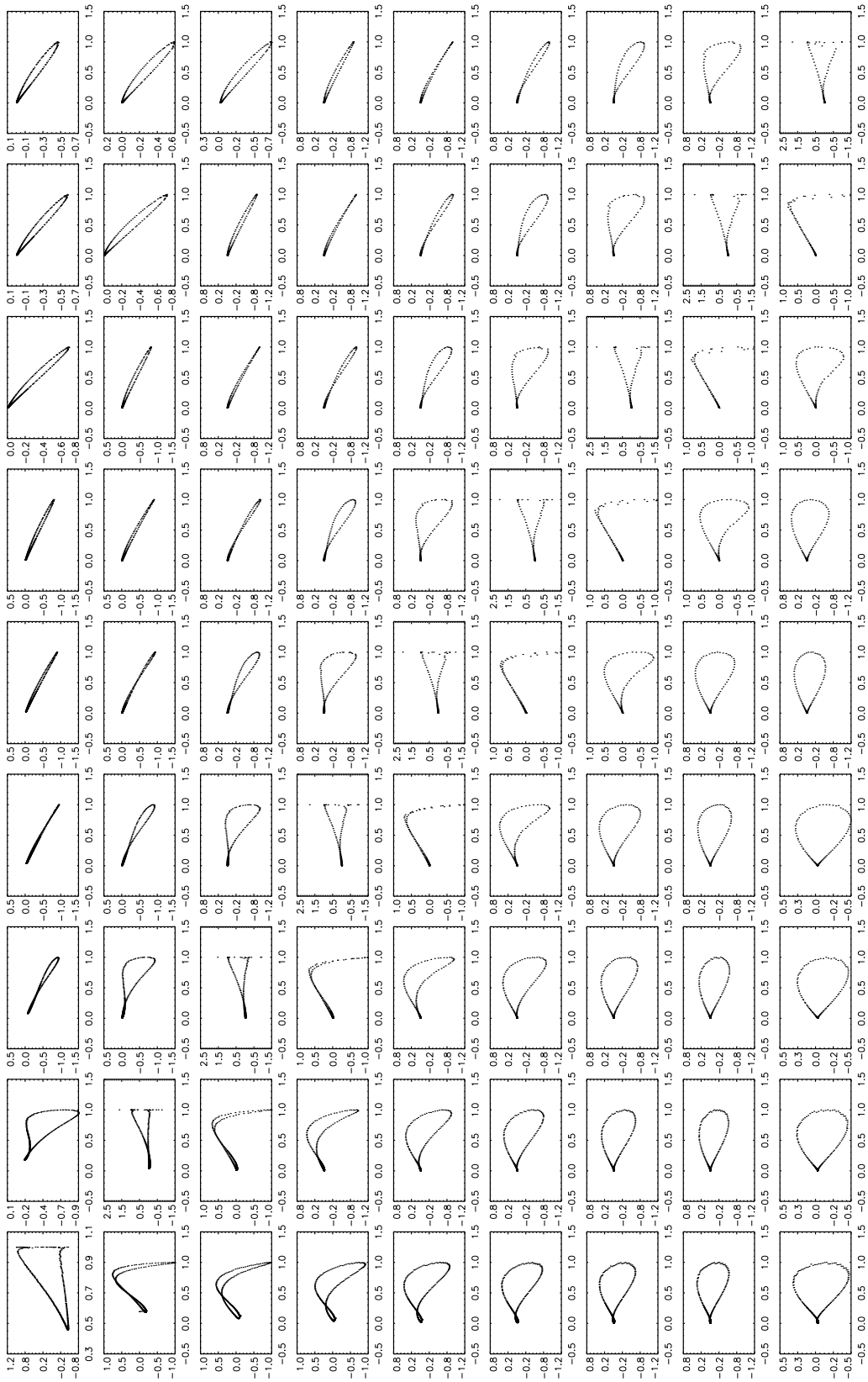


Figure 5.39: As for Figure 5.38, but for  $I$ - $U$  ( $I$  on the horizontal axis).

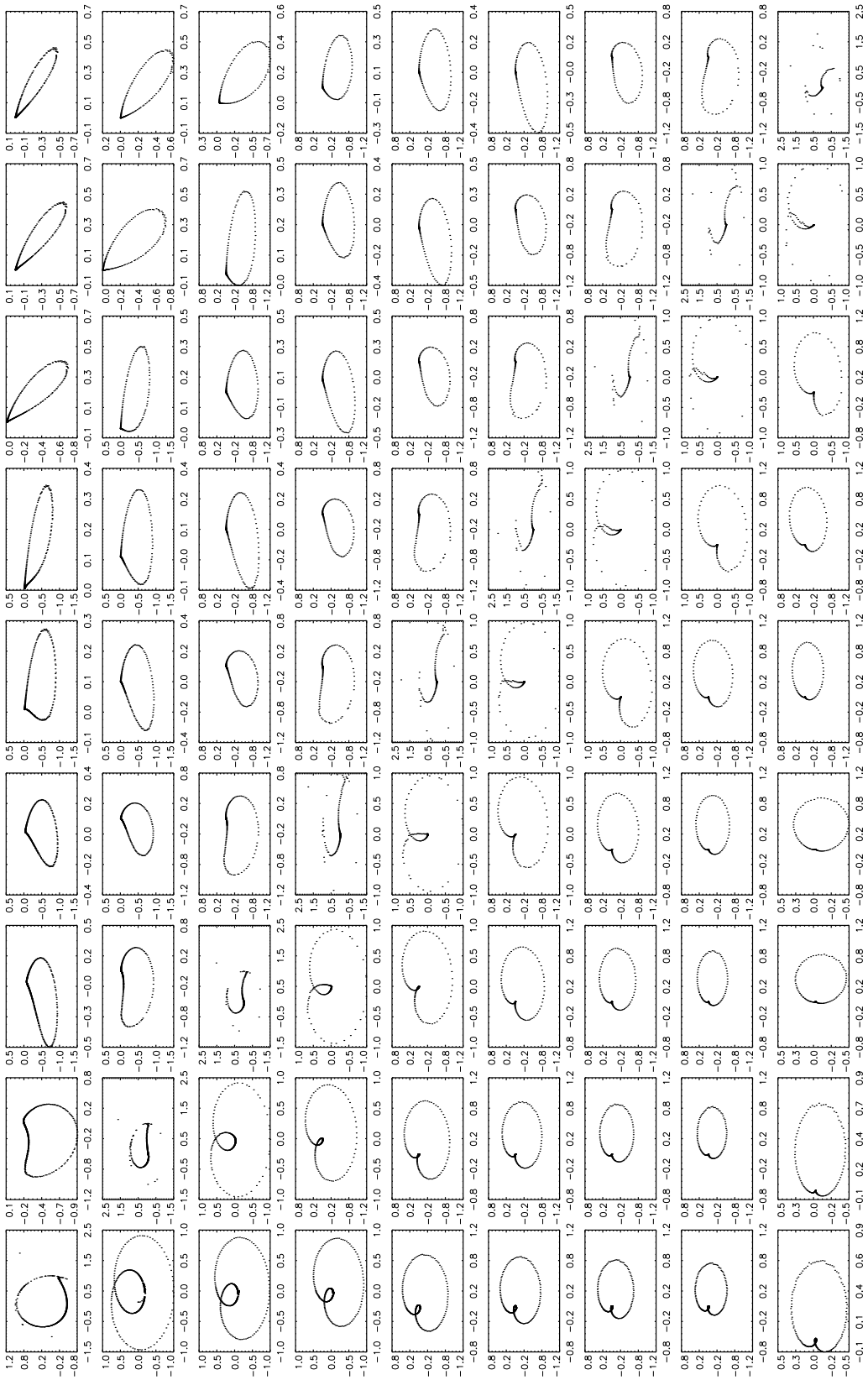
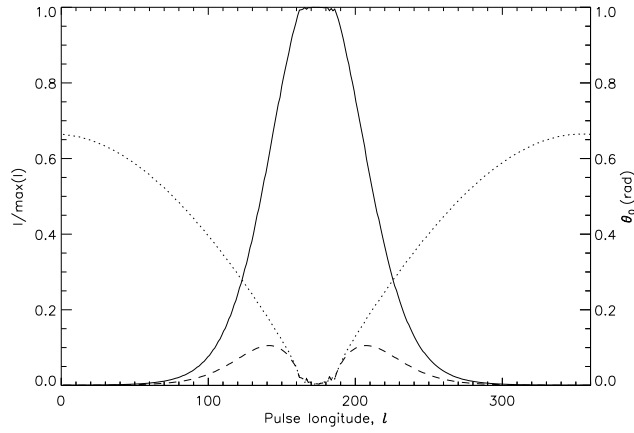


Figure 5.40: As for Figure 5.38, but for  $Q-U$  ( $Q$  on the horizontal axis).



**Figure 5.41:** Current-modified dipole field at  $r = 0.1r_{LC}$ . Layout as for Figure 5.38, but for position angle (on the vertical axis in landscape orientation, in units of radians) versus pulse longitude (on the horizontal axis, in units of  $2\pi$  radians).



**Figure 5.42:** Current-modified dipole field at  $r = 0.1r_{LC}$ . Example of a pulse profile for a filled core beam with linear polarization  $L = I \sin \theta_0$  and  $(\alpha, i) = (30^\circ, 30^\circ)$  at  $r = 0.1 r_{LC}$ . Solid, dashed and dotted curves represent the total polarized intensity  $I$ , degree of linear polarization  $L$ , and emission point colatitude  $\theta_0$ . Pulse longitude  $l$  is measured in units of degrees.

### 5.5.2 Hollow cone emission

$$L = I \cos \theta_0$$

Examples of the  $I$  (solid curve) and  $L$  (dashed curve) profiles for  $(\alpha, i) = (70^\circ, 30^\circ)$  and  $(70^\circ, 60^\circ)$  are shown in Figure 5.47.  $I$  is normalised by its peak value. The magnetic colatitude  $\theta_0(t)$  of the emission point (dotted curve) is also shown. The profiles are double-peaked for  $|\alpha - i| \leq 30^\circ$  and behave similarly to the pure dipole at low altitudes (Section 5.3.2), with the exception of the  $-r/r_{LC}$  phase shift.

The Stokes phase portraits for a hollow cone with  $L/I = \cos \theta_0$  are drawn in Figures 5.48–5.50. In the  $I$ - $Q$  phase portraits (Figure 5.48), we note the following trends. (i) For  $\alpha = i$ , we obtain a tilted balloon at  $(\alpha, i) = (10^\circ, 10^\circ)$ , which evolves into an asymmetric mosquito shape as  $\alpha = i$  increases. (ii) For  $\alpha > i$  (below the diagonal in Figure 5.48), where the pulse is double-peaked, we obtain a mix of figure-eights and distorted mosquito shapes. (iii) For  $\alpha < i$  (above the diagonal), where the pulse is double-peaked, the pulse traces mosquito shapes (for  $\alpha \gtrsim 25^\circ$ ) and a mix of figure-eights and triangular shapes (for  $\alpha \lesssim 25^\circ$ ).

In the  $I$ - $U$  phase portraits (Figure 5.49), we note the following trends. (i) Along the  $\alpha = i$  diagonal, we obtain a tilted crescent at  $(\alpha, i) = (10^\circ, 10^\circ)$  which twists and narrows as  $\alpha = i$  increases. (ii) For  $\alpha > i$  (below the diagonal), where the pulse is double-peaked, we obtain a tilted figure-eight for  $\alpha \leq 30^\circ$ , which twists into a distorted mosquito shape as  $\alpha$  increases. (iii)

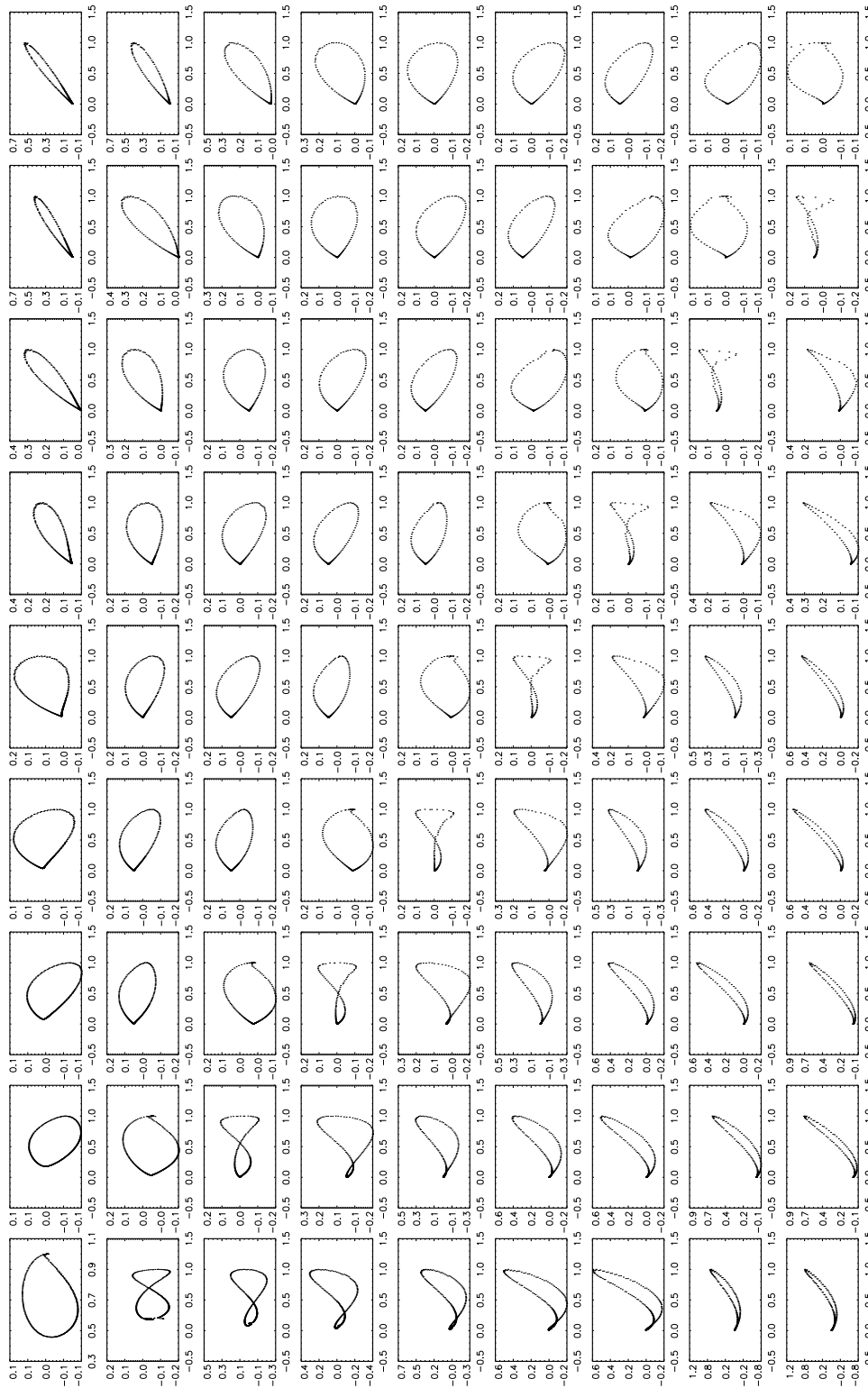


**Figure 5.43:** Current-modified dipole field at  $r = 0.1r_{\text{LC}}$ . Look-up table of Stokes phase portraits in the  $I$ - $Q$  plane for a filled core beam at  $r = 0.1r_{\text{LC}}$  and degree of linear polarization  $L = I \sin \theta_0$ , where  $\theta_0$  is the emission point colatitude. The panels are organised in landscape mode, in order of increasing  $10^\circ \leq i \leq 90^\circ$  (left-right) and  $10^\circ \leq \alpha \leq 90^\circ$  (top-bottom) in intervals of  $10^\circ$ .  $I$  is plotted on the horizontal axis and normalised by its peak value.  $Q$  is plotted on the vertical axis.

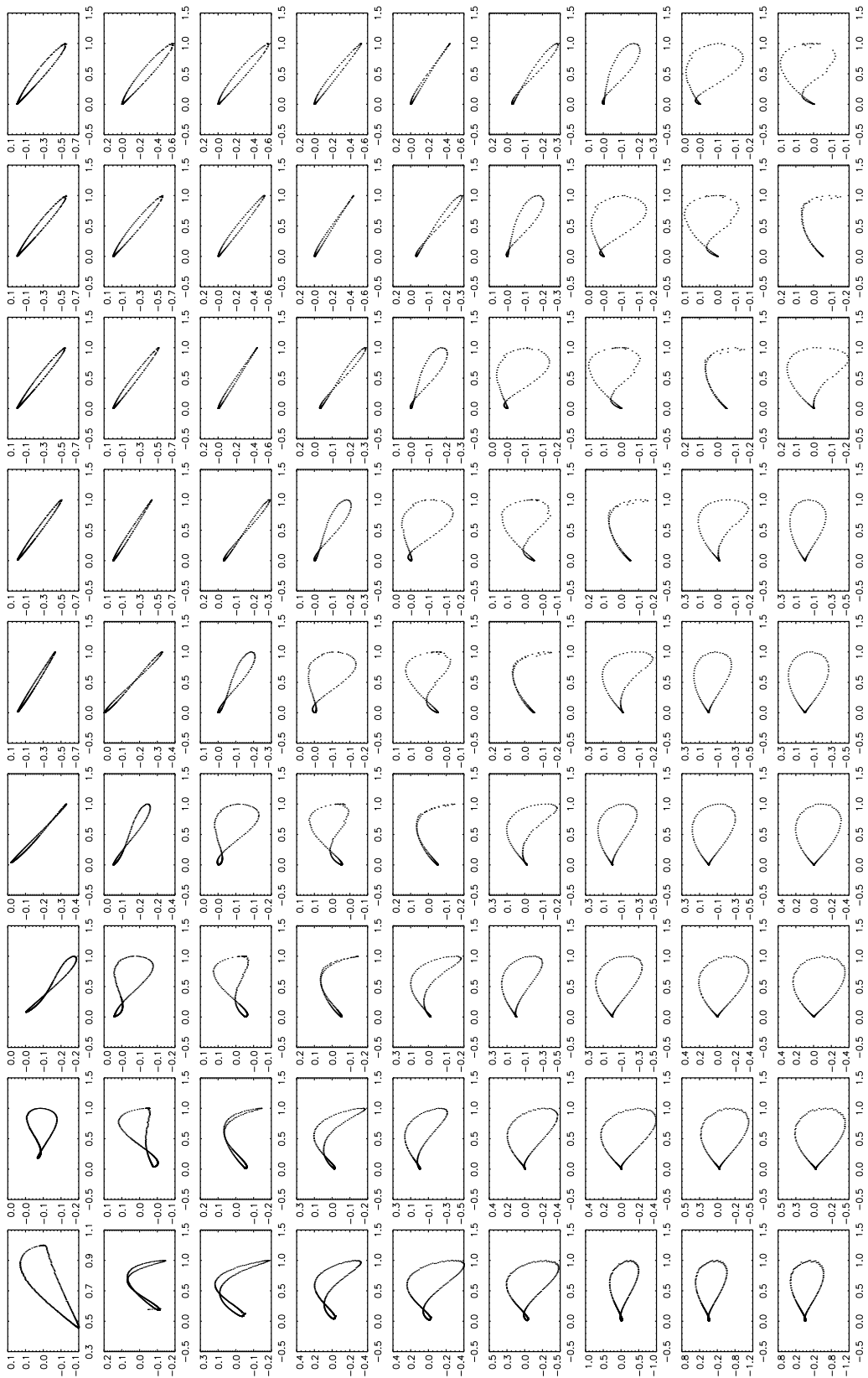


Figure 5.44: As for Figure 5.43, but for  $I-U$  ( $I$  on the horizontal axis).

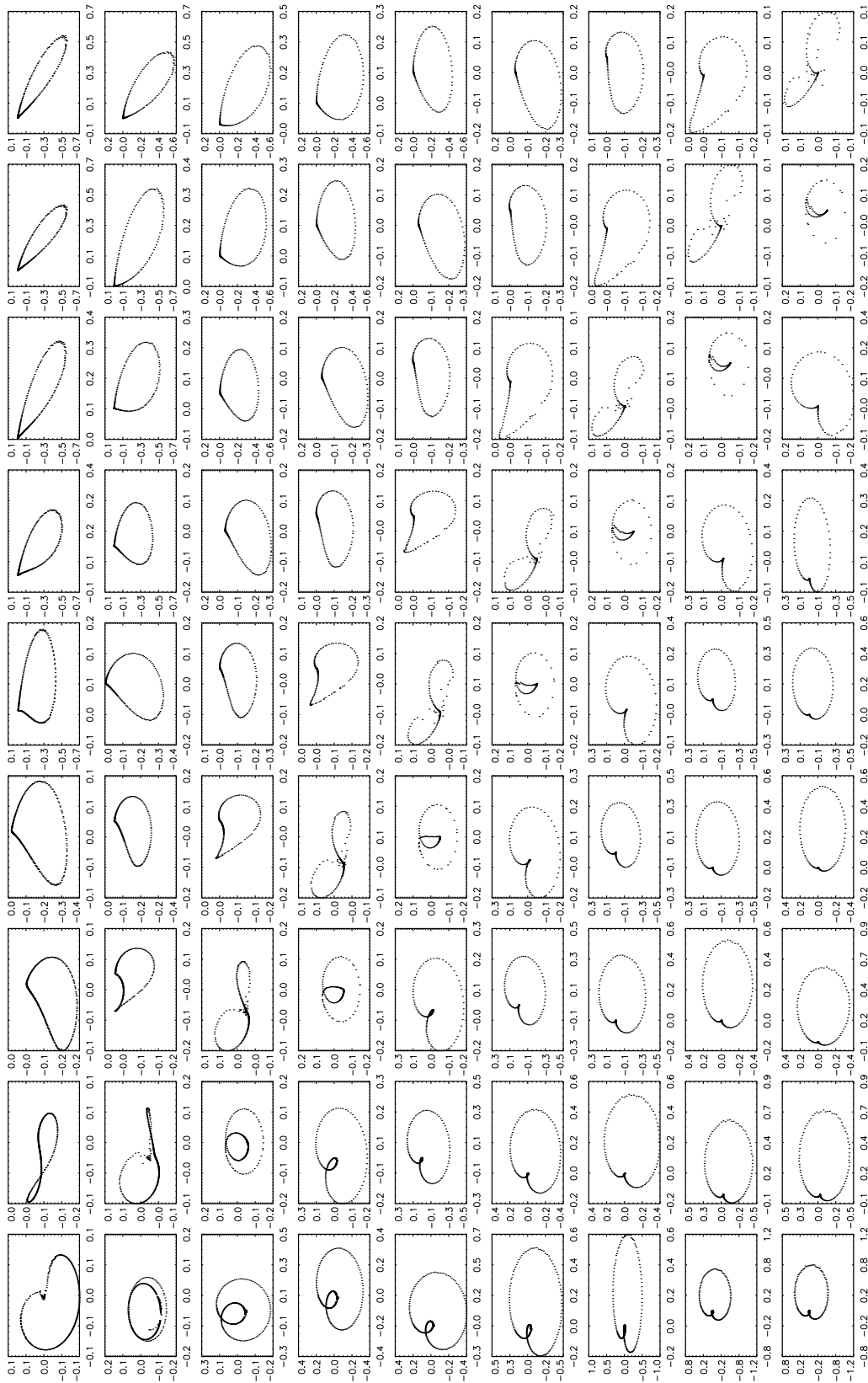


Figure 5.45: As for Figure 5.43, but for  $Q$ - $U$  ( $Q$  on the horizontal axis).



**Figure 5.46:** Current-modified dipole field at  $r = 0.1r_{LC}$ . Layout as for Figure 5.43, but for position angle (on the vertical axis in landscape orientation, in units of radians) versus pulse longitude (on the horizontal axis, in units of  $2\pi$  radians).

For  $\alpha < i$  (above the diagonal), where the pulse is double-peaked, we obtain a tilted figure-eight at  $\alpha = 10$ , which evolves into twisted, interlocking ovals, then a distorted heart shape, as  $\alpha$  increases.

In the  $Q$ - $U$  phase portraits (Figure 5.50), we note the following trends. (i) Along the  $\alpha = i$  diagonal, the pattern evolves from a tilted heart shape to a figure-eight as  $\alpha = i$  increases. (ii) Interestingly, in the panels to the left of the  $\alpha = i$  diagonal, the secondary loop within the heart shape rotates counter-clockwise as  $\alpha$  increases [compare  $(\alpha, i) = (40^\circ, 30^\circ)$ ,  $(60^\circ, 50^\circ)$ , and  $(90^\circ, 90^\circ)$ ]. (iii) For  $\alpha < i$ , where the pulses are double-peaked, a tilted figure-eight pattern emerges. (iv) The phase portraits for orientations which produce single-peaked pulses behave like in Section 5.5.1; i.e. they rotate about  $(U, Q) = (0, 0)$  as  $|\alpha - i|$  increases.

The PA swings (Figure 5.51) are identical to the previous cases for all orientations, the only difference being that they are visible above a threshold intensity over a greater fraction of the pulse period due to the broader pulse profiles.

### **$L = I \sin \theta_0$**

Examples of the  $I$  (solid curve) and  $L$  (dashed curve) profiles for  $(\alpha, i) = (70^\circ, 30^\circ)$  and  $(70^\circ, 60^\circ)$  are shown in Figure 5.52. The profiles are similar to those of Section 5.3.2.

The  $I$ - $Q$ ,  $I$ - $U$ , and  $Q$ - $U$  phase portraits are shown in Figures 5.53–5.55. All three phase portraits are similar to Section 5.5.2, except for orientations that produce double-peaked pulses. Here, the patterns are less twisted. The lower peak value of  $L/I$  as compared to Section 5.5.2 is accompanied by a narrower range of  $U$  and  $Q$ . For example, in the  $Q$ - $U$  plane (Figure 5.55) for  $(\alpha, i) = (10^\circ, 10^\circ)$ , the oval is approximately 80% smaller than its counterpart in Figure 5.50 along both the  $U$  and  $Q$  axes.

The PA swings in Figure 5.56 are identical to Figure 5.51, except in the squared-off valleys where  $\theta_0$  is near zero and we do not plot the curve ( $L < 10^{-2}$ ).

### **5.5.3 Emission altitude**

In this section, we investigate how the emission altitude changes the Stokes phase portraits and PA swings. For the sake of definiteness, we focus on the orientation  $(\alpha, i) = (70^\circ, 30^\circ)$  for a filled core beam with polarization  $L = I \cos \theta_0$ . In Figure 5.57, we present the Stokes phase portraits, PA swing, and

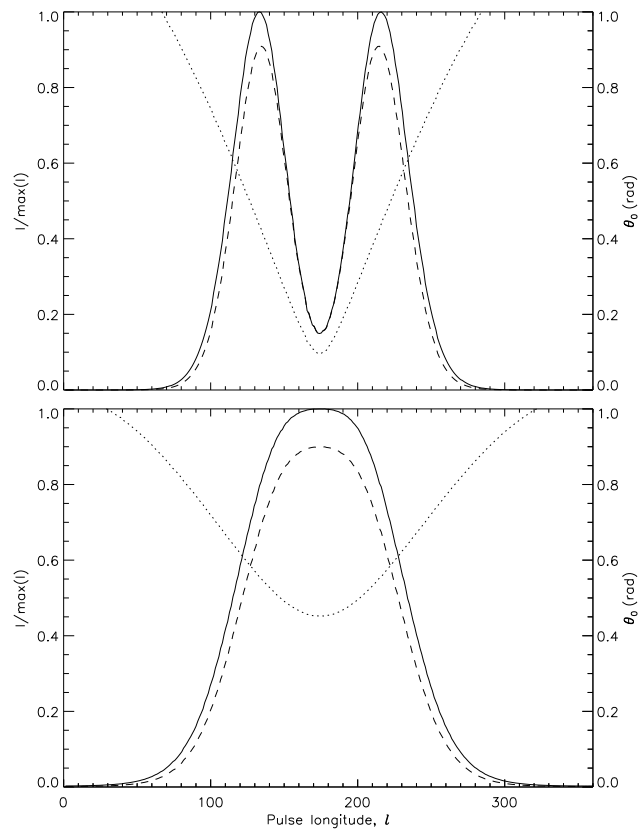


**Figure 5.47:** Current-modified dipole field at  $r = 0.1r_{LC}$ . Examples of pulse profiles for a hollow cone with opening angle  $25^\circ$  and degree of linear polarization  $L = I \cos \theta_0$  at  $r = 0.1r_{LC}$ . Solid, dashed and dotted curves represent the total polarized intensity  $I$ , degree of linear polarization  $L$ , and emission point colatitude  $\theta_0$ . Pulse longitude  $l$  is measured in units of degrees. Top: double-peaked pulse with  $(\alpha, i) = (70^\circ, 60^\circ)$ ; bottom: single-peaked pulse with  $(\alpha, i) = (70^\circ, 30^\circ)$ .

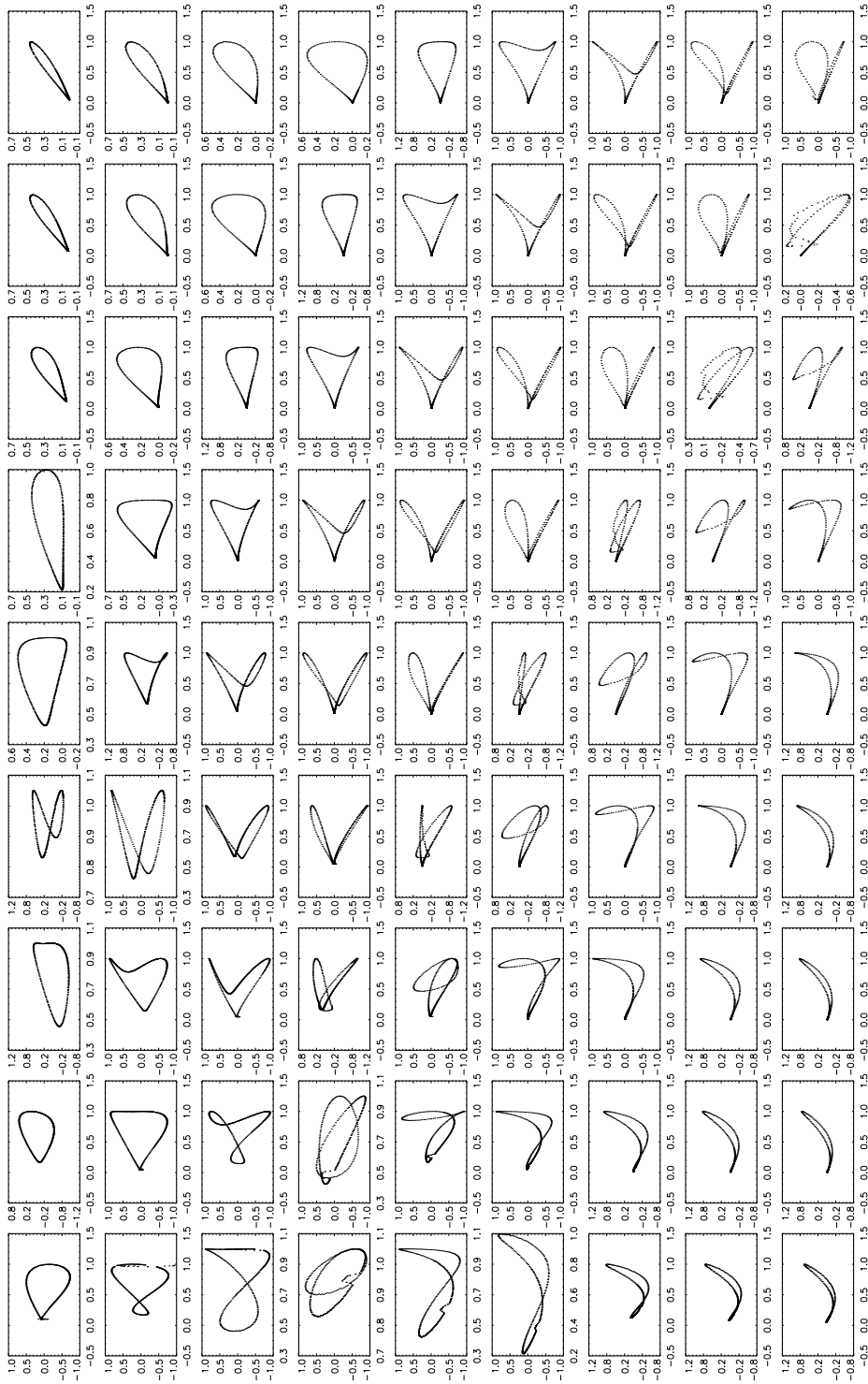


**Figure 5.48:** Current-modified dipole field at  $r = 0.1r_{LC}$ . Look-up table of Stokes phase portraits in the  $I$ - $Q$  plane for a hollow cone with opening angle  $25^\circ$  at  $r = 0.1r_{LC}$  and degree of linear polarization  $L = I \cos \theta_0$ , where  $\theta_0$  is the emission point colatitude. The panels are organised in landscape mode, in order of increasing  $10^\circ \leq i \leq 90^\circ$  (left-right) and  $10^\circ \leq \alpha \leq 90^\circ$  (top-bottom) in intervals of  $10^\circ$ .  $I$  is plotted on the horizontal axis and normalised by its peak value.  $Q$  is plotted on the vertical axis.

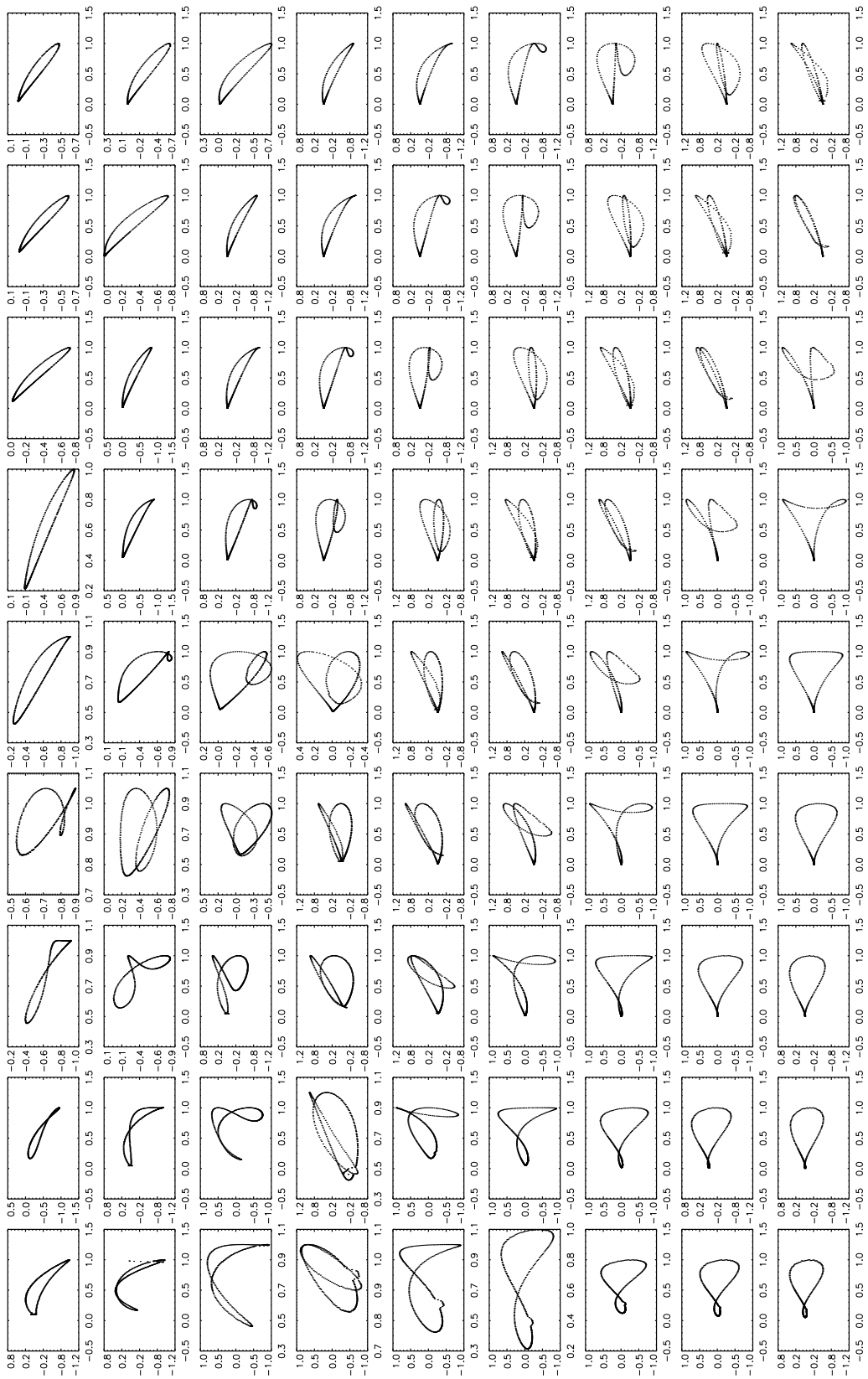


Figure 5.49: As for Figure 5.48, but for  $I-U$  ( $I$  on the horizontal axis).

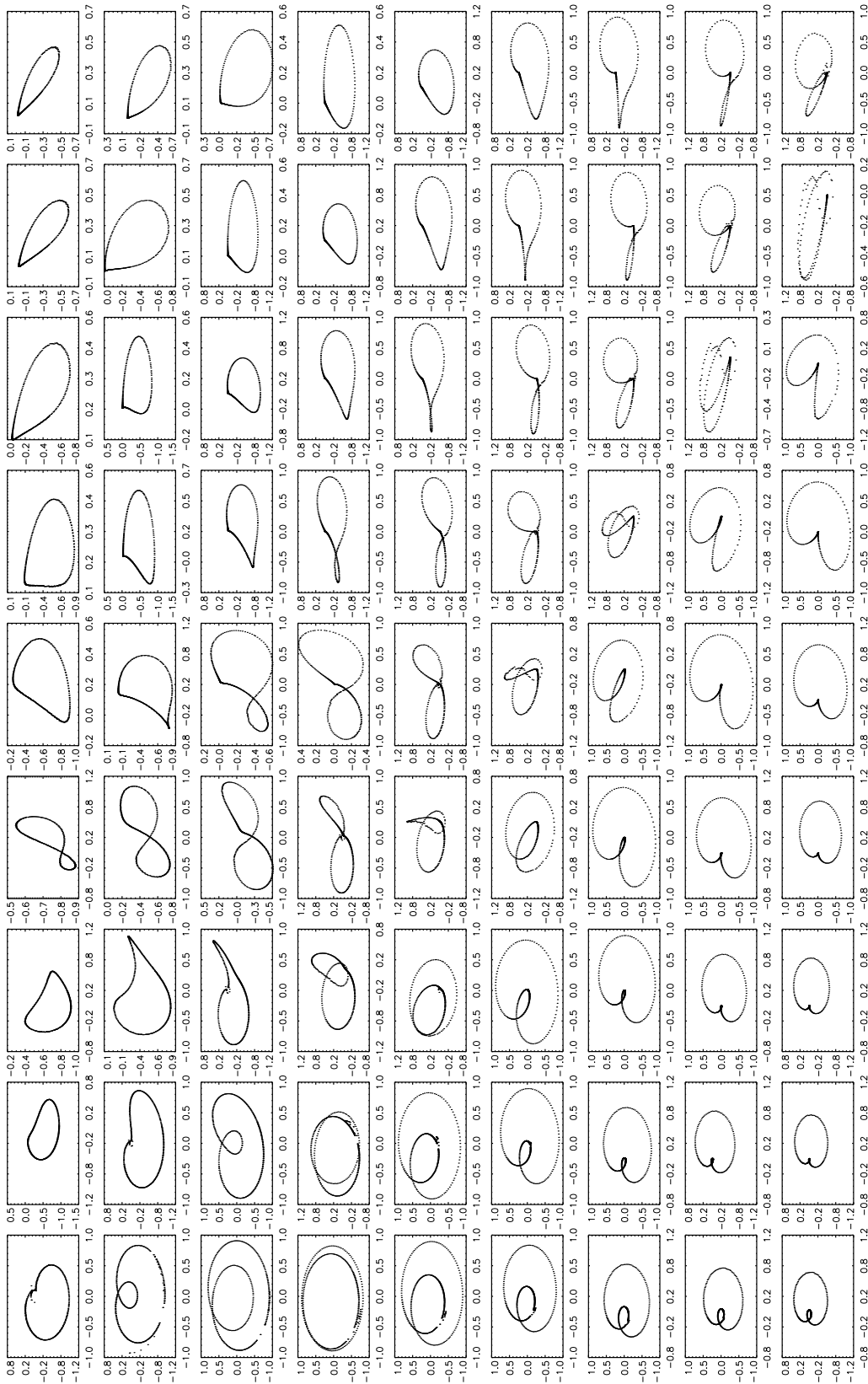
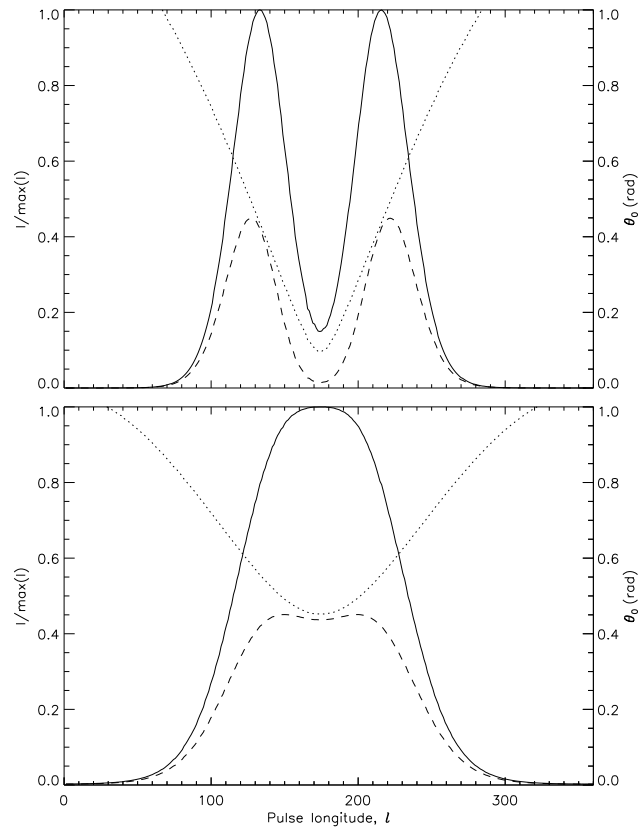


Figure 5.50: As for Figure 5.48, but for  $Q$ - $U$  ( $Q$  on the horizontal axis).



**Figure 5.51:** Current-modified dipole field at  $r = 0.1r_{LC}$ . Layout as for Figure 5.48, but for position angle (on the vertical axis in landscape orientation, in units of radians) versus pulse longitude (on the horizontal axis, in units of  $2\pi$  radians).



**Figure 5.52:** Current-modified dipole field at  $r = 0.1r_{LC}$ . Examples of pulse profiles for a hollow cone with opening angle  $25^\circ$  and degree of linear polarization  $L = I \sin \theta_0$  at  $r = 0.1r_{LC}$ . Solid, dashed and dotted curves represent the total polarized intensity  $I$ , degree of linear polarization  $L$ , and emission point colatitude  $\theta_0$ . Pulse longitude  $l$  is measured in units of degrees. Top: double-peaked pulse with  $(\alpha, i) = (70^\circ, 60^\circ)$ ; bottom: single-peaked pulse with  $(\alpha, i) = (70^\circ, 30^\circ)$ .

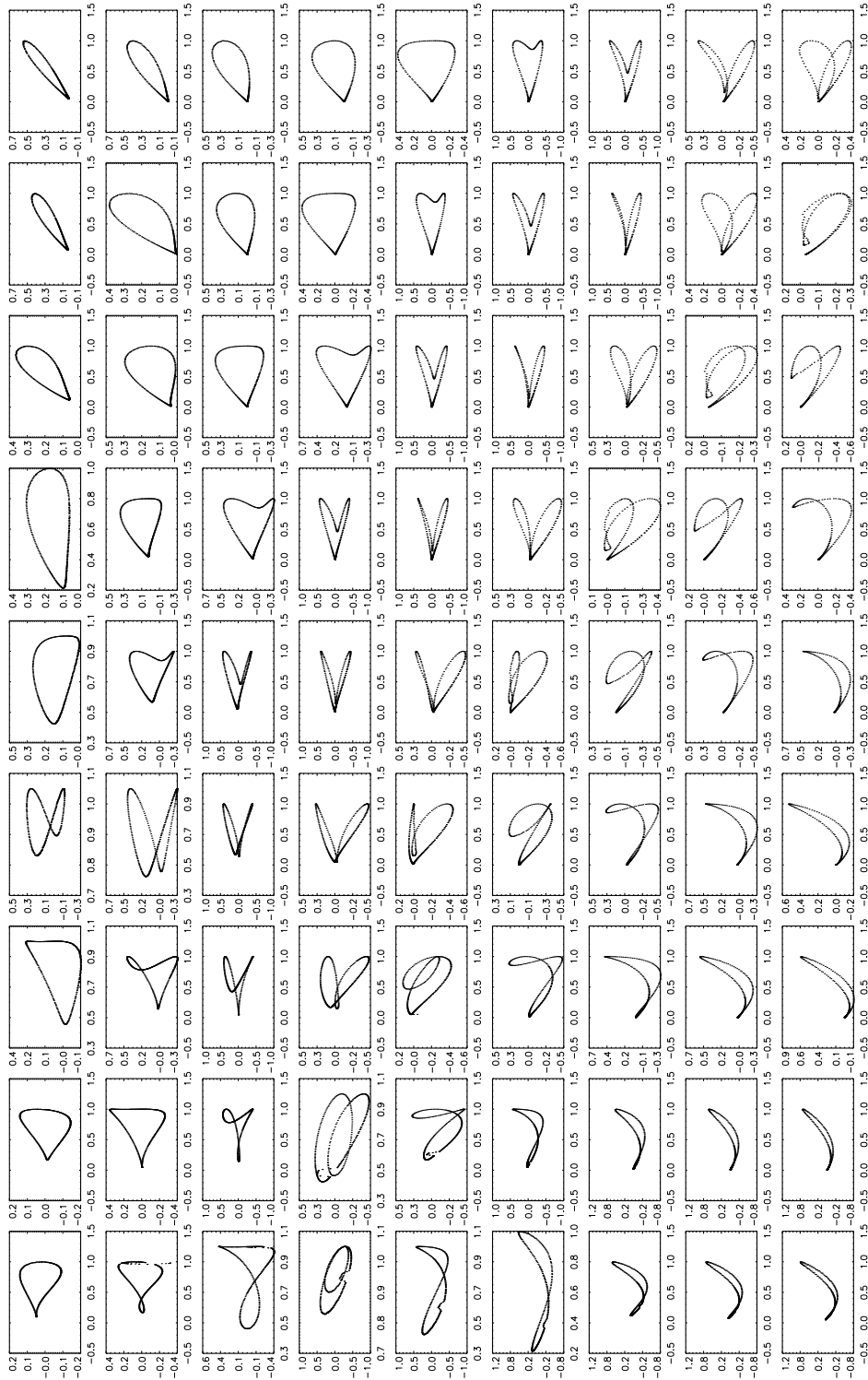


**Figure 5.53:** Current-modified dipole field at  $r = 0.1r_{LC}$ . Look-up table of Stokes phase portraits in the  $I$ - $Q$  plane for a hollow cone with opening angle  $25^\circ$  at  $r = 0.1r_{LC}$  and degree of linear polarization  $L = I \sin \theta_0$ , where  $\theta_0$  is the emission point colatitude. The panels are organised in landscape mode, in order of increasing  $10^\circ \leq i \leq 90^\circ$  (left-right) and  $10^\circ \leq \alpha \leq 90^\circ$  (top-bottom) in intervals of  $10^\circ$ .  $I$  is plotted on the horizontal axis and normalised by its peak value.  $Q$  is plotted on the vertical axis.

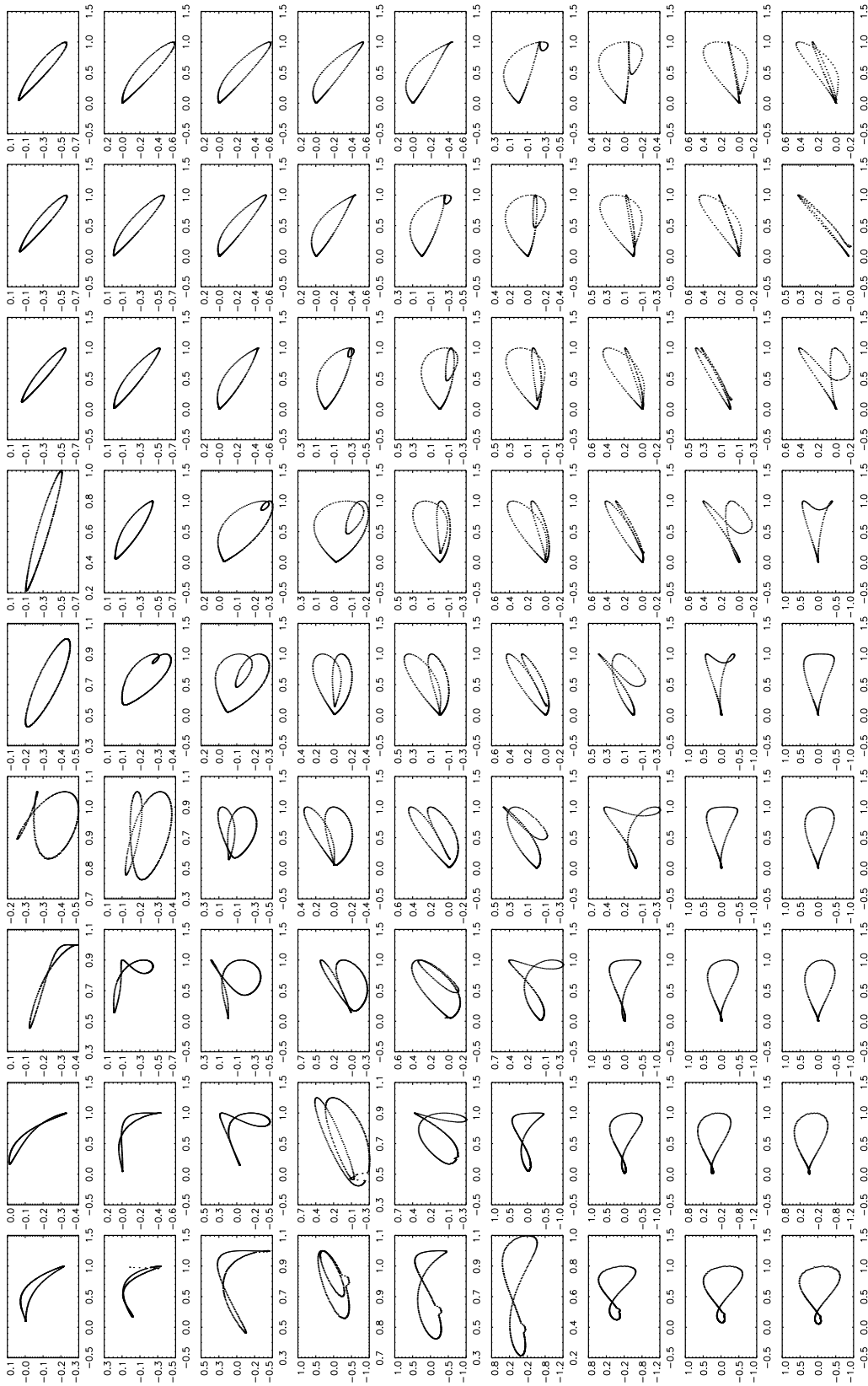


Figure 5.54: As for Figure 5.53, but for  $I$ - $U$  ( $I$  on the horizontal axis).

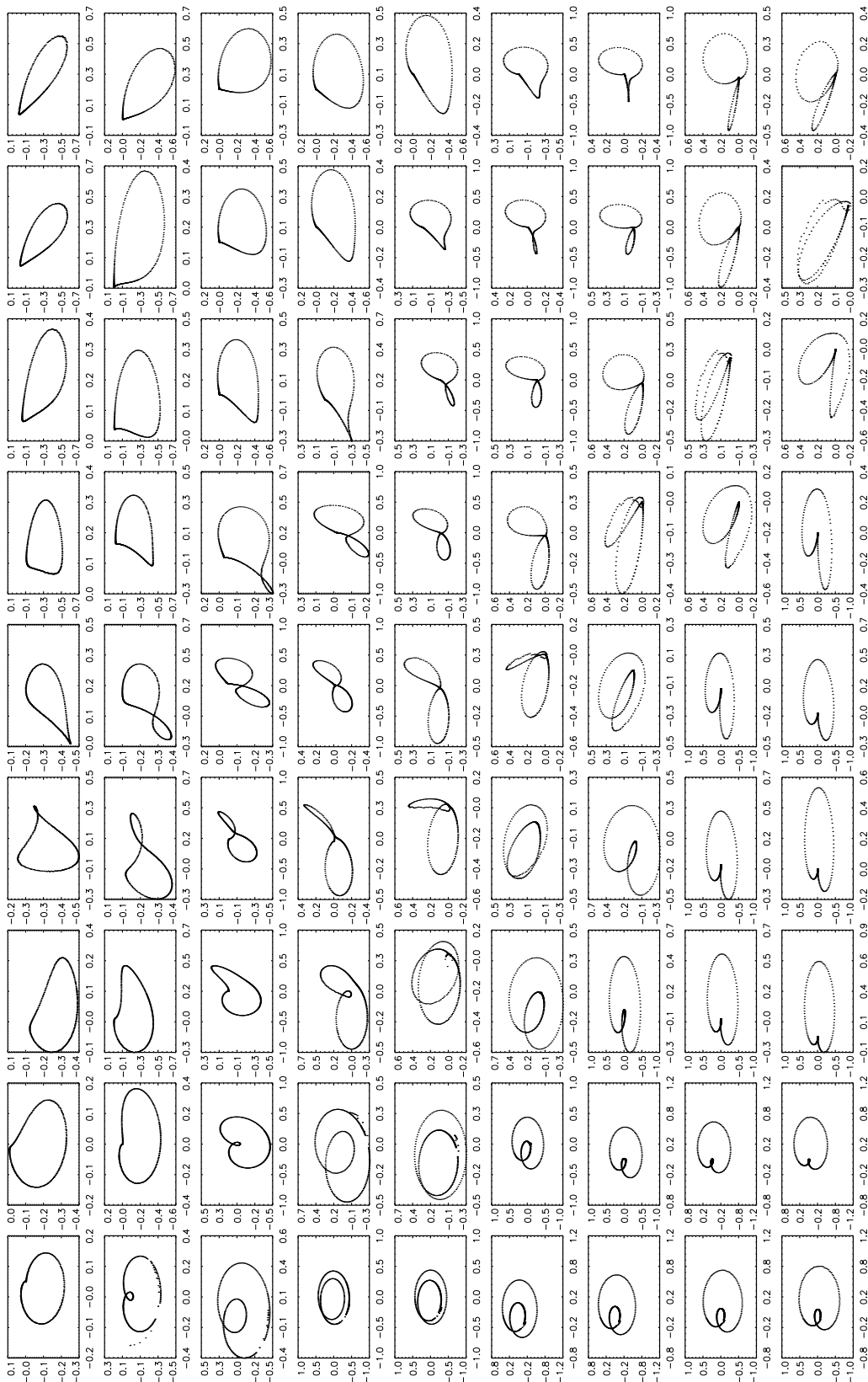
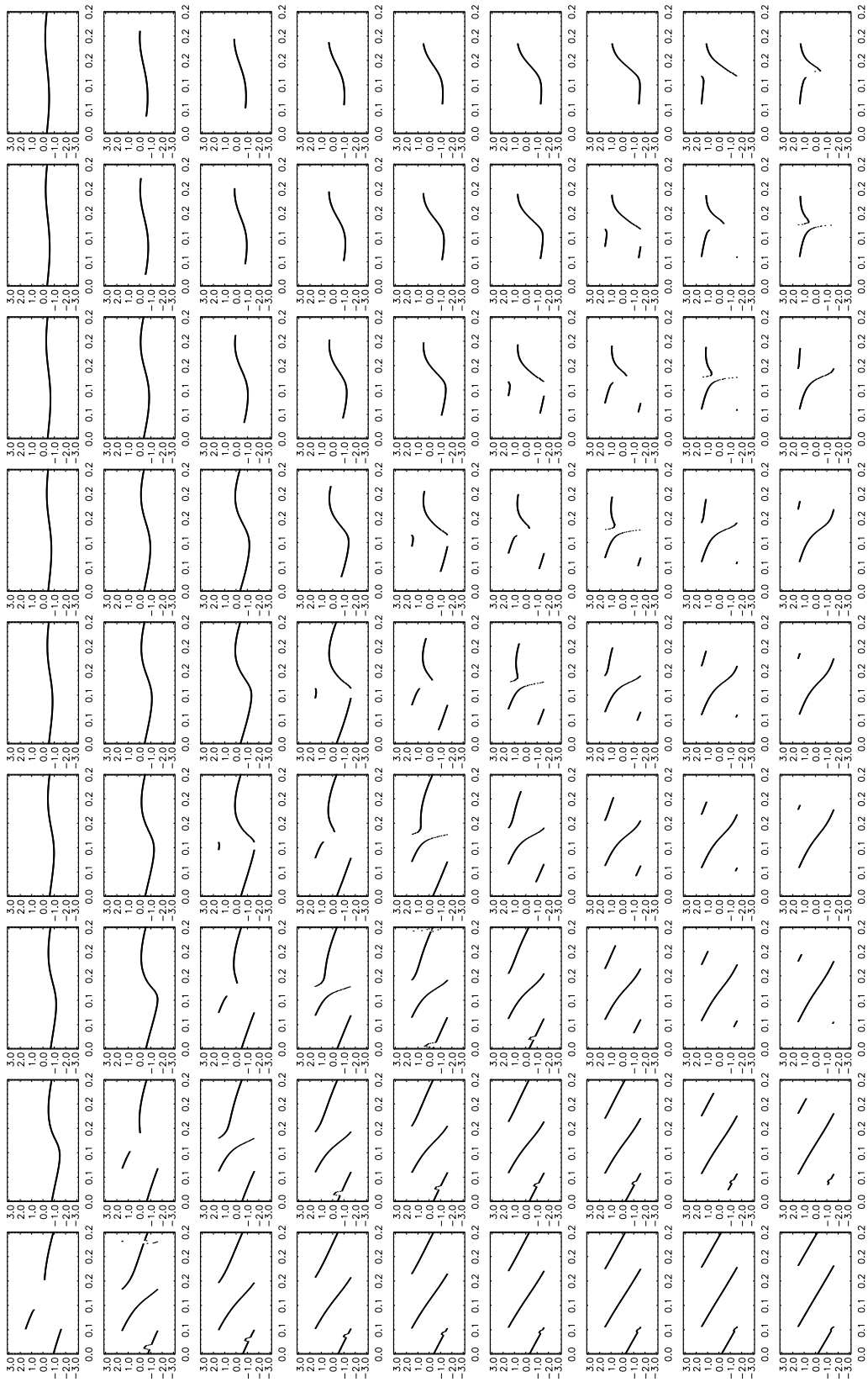


Figure 5.55: As for Figure 5.53, but for  $Q-U$  ( $Q$  on the horizontal axis).



**Figure 5.56:** Current-modified dipole field at  $r = 0.1r_{LC}$ . Layout as for Figure 5.53, but for position angle (on the vertical axis in landscape orientation, in units of radians) versus pulse longitude (on the horizontal axis, in units of  $2\pi$  radians).

locus of  $\hat{\mathbf{x}}_0(t)$  for this orientation at four altitudes ranging from  $r_{\min} = 0.05 r_{\text{LC}}$  to  $r_{\max} = 0.3 r_{\text{LC}}$ . The pure dipole case at  $r \ll r_{\text{LC}}$  is presented at the top of the figure as a comparison.  $I$  is normalised by its peak value.

We begin with an obvious yet fundamental observation: in a current-modified magnetic dipole field, the phase portraits evolve with altitude. The PA swing evolves also but to a lesser degree.

We note the following trends. (i) The peak value of  $L/I$  increases from 0.90 at  $r_{\min}$  to 0.92 at  $r_{\max}$ . (ii) In the  $I$ - $Q$  plane, at  $r = r_{\min}$ , the hockey stick curves upward (major axis has  $dQ/dI > 0$ ) and broadens into a balloon, ranging over  $-0.1 < Q < 0.8$ . As  $r$  increases, the balloon broadens further. At  $r = r_{\max}$ , the balloon ranges over  $-0.4 < Q < 0.7$ . (iii) In the  $I$ - $U$  plane, the balloon narrows and tilts downwards (major axis has  $dU/dI < 0$ ). (iv) In the  $Q$ - $U$  plane, the heart shape rotates clockwise as  $r$  increases, although its size and shape do not alter much. (v) The overall shape of the PA swings does not appear to change significantly as  $r$  increases, but the pulse longitude where the phase wrapping occurs shifts gradually from  $\approx 0.65$  phase units at  $r = r_{\min}$  to  $\approx 0.54$  phase units at  $r = r_{\max}$ .

To explain the trends, we look at the locus of  $\hat{\mathbf{x}}_0(t)$  in the body frame. It traces out an oval which tilts and becomes egg-shaped with increasing  $r$ . The range of  $\theta_0(t)$  remains fairly constant ( $0.4 \text{ rad} \lesssim \theta_0 \lesssim 1.0 \text{ rad}$ ) but  $\phi_0(t)$  shifts from  $1.1 \text{ rad} \lesssim \phi_0 \lesssim 2.2 \text{ rad}$  at  $r = r_{\min}$  to  $0.8 \lesssim \phi_0 \lesssim 1.9$  at  $r = r_{\max}$ . As  $I$  and  $L$  do not depend on  $\phi_0$ , the change in the shapes must be caused by the tilt and asymmetry of the locus. For a large tilt, the path traced from  $l = 0$  to  $l = 0.5$  traverses different values of  $\theta_0$  than the path traced from  $l = 0.5$  to  $l = 1$ , resulting in different ranges of  $|Q|$  and  $|U|$  in the first and second halves of the pulse. This causes the asymmetry about the  $U$ -axis and the broadening and narrowing of the shapes in the  $I$ - $Q$  and  $I$ - $U$  planes.

Figure 5.57 refers to a particular orientation and polarization model, but the trends it depicts are fairly generic. We find that overall, from  $r_{\min}$  to  $r_{\max}$ , the phase portraits change modestly with emission altitude at a fixed  $(\alpha, i)$ . Their sizes, orientation, and detailed substructure (e.g. extra twisting of the secondary loops) change gradually, but there are no cases of the phase portraits changing drastically, for example from a hockey stick to a trefoil. Therefore, when comparing the look-up tables to real data, we do not have to worry about very degenerate matches, i.e. equally good fits for very different combinations of  $(\alpha, i)$  at two or more very different altitudes. We do, however, have to be aware that similar shapes like the hockey stick and banana can interchange as the altitude varies, leading to mild  $(r, \alpha, i)$  degeneracies.

In Sections 5.6 and 5.7, we compute Stokes phase portraits and PA swings for several emission altitudes and compare them to multi-frequency observations of PSR J0826+2637 and PSR J0304+1932.

## 5.6 A detailed single-peaked example: PSR J0826+2637

In this section, we apply the recipe summarised in Figure 5.3(b) to a specific pulsar, PSR J0826+2637. The object has period  $P = 0.531$  s and period derivative  $\dot{P} = 1.724 \times 10^{-15} \text{ s s}^{-1}$  (Taylor et al. 1993). Data for this object, covering frequencies in the range 0.408–1.404 GHz, are obtained from the EPN online archive. The data were originally published in Gould & Lyne (1998). We choose to study this object because it has a clean, single-peaked pulse and simple Stokes phase portraits.

A faint interpulse has been observed in PSR J0826+2637. At 0.408 GHz, the peak interpulse intensity is  $\approx 2\%$  of the main pulse’s peak intensity. At 0.925 GHz, its peak intensity is  $\approx 1\%$  of the main pulse’s intensity. The Stokes phase portraits of the interpulse are noisy (signal-to-noise ratio  $\approx 5$  and 2 for 0.408 GHz and 0.925 GHz respectively). Hence we do not analyse them here. In principle, however, the phase portraits from stronger interpulses provide a useful cross-check on inferences drawn from the main pulse and should be examined concurrently, following the traditional practice with PA swings.

As mentioned in Section 5.2.1, a complication arises from the fact that the published Stokes parameters for this object are not calibrated according to the canonical polarization basis, so  $\beta$  is unknown a priori. Furthermore, the data is calibrated differently at different frequencies. In order to estimate  $\beta$  for each of the data sets,  $Q$  and  $U$  must be transformed according to Equations (5.11) and (5.12). The  $Q$ - $U$  plane in 5.59 features a tilted balloon whose ‘correct’ orientation must be guessed. As a starting point, we assume the simplest case: a pure dipole at  $r \ll r_{\text{LC}}$ . From the pulse profile-PA swing phase delay, the emission radius was previously estimated to be  $(0.006 \pm 0.004)r_{\text{LC}}$ , supporting the above assumption, although the authors note that this estimate is uncertain (Blaskiewicz et al. 1991). If the emission truly originates from a low altitude, then any shape in the  $Q$ - $U$  plane should be symmetric about  $U = 0$ , as seen in Section 5.3. We can therefore determine  $\beta$  empirically at each of the observation frequencies by rotating the  $Q$ - $U$  patterns to put them all in the same basis.

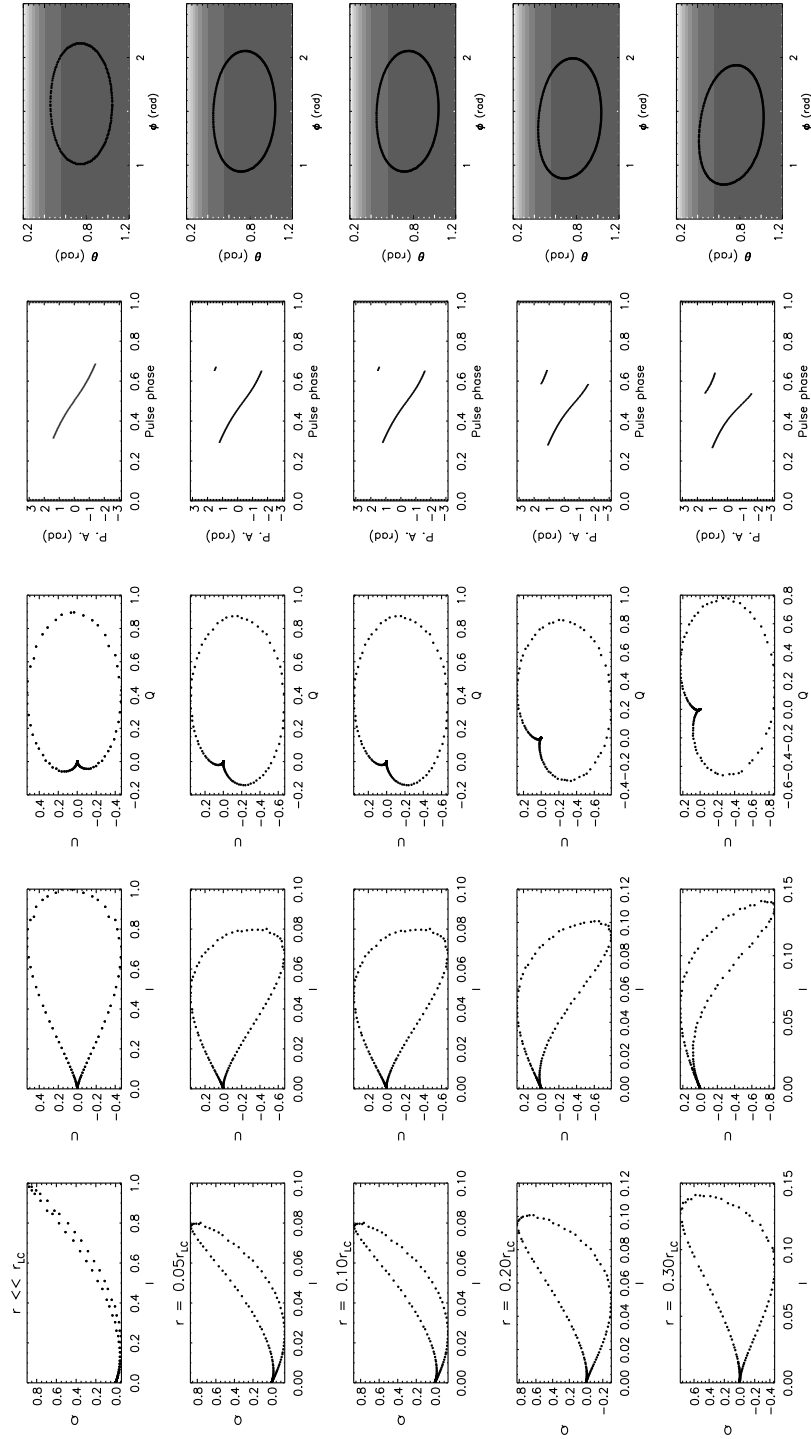


**Figure 5.57:** Stokes phase portraits, PA swings and emission point locus  $\hat{\mathbf{x}}_0(t)$  in the body frame for a filled core beam with polarization  $L = I \cos \theta_0$  and  $(\alpha, i) = (70^\circ, 30^\circ)$ , at five altitudes. In landscape mode, the top row shows a pure dipole at  $r \ll r_{LC}$ . In rows 2–5,  $r$  ranges from  $r = 0.05 r_{LC}$  (second row) to  $r = 0.3 r_{LC}$  (bottom row). From left to right in landscape mode, the columns show: (1) the  $I-Q$  phase portrait, (2) the  $I-U$  phase portrait, (3) the  $Q-U$  phase portrait, (4) the PA swing (data points with  $L \geq 10^{-2}$  plotted only), and (5) the locus of  $\hat{\mathbf{x}}_0(t)$ . The intensity map (greyscale) follows Figure 5.5.

Figure 5.58 shows the pulse profiles, corrected phase portraits, and PA swings for the four observations (0.408, 0.610, 0.925, and 1.404 GHz), arranged in decreasing order in landscape mode. The values of  $\beta$  used in Figure 5.58 are (in order of decreasing observation frequency)  $80^\circ$ ,  $100^\circ$ ,  $55^\circ$ , and  $160^\circ$ . We emphasize that these numbers are based on the fact that any low-altitude pattern in the  $Q$ - $U$  plane should be symmetric about  $U = 0$ . It is possible but unlikely that the intrinsic emission physics  $\mathbf{E} \propto \mathbf{a}$  changes with observation frequency (and hence emission altitude). However, (Blaskiewicz et al. 1991) estimated the same emission altitudes for 0.43 and 1.418 GHz, and this is confirmed by inspecting the  $I$ - $Q$  and  $I$ - $U$  portraits in Figure 5.58. The  $I$ - $Q$  plane features a banana shape which tilts upwards (i.e. whose major axis has  $dQ/dI > 0$ ) and whose shape does not change significantly with frequency after correcting for  $\beta$ . In the  $I$ - $U$  plane, which features a balloon which tilts downwards (in the sense  $dU/dI < 0$ ), the shapes are also similar in all frequencies.

Assuming that all the observations correspond to a narrow range of emission altitudes, we focus on finding an orientation  $(\alpha, i)$  which matches the 0.925 GHz data only in the next sections. The single-peaked pulse profile suggests emission from a filled core beam. We explain in each subsection below the steps taken to find a suitable match, according to the recipe in Figure 5.3(b), by adjusting in turn the magnetic geometry (Section 5.6.1), orientation angles (Section 5.6.2), beam and polarization patterns (Section 5.6.3), and emission altitude (Section 5.6.4).

### 5.6.1 Pure versus current-modified dipole

Upon inspecting the pure dipole look-up tables for  $r \ll r_{\text{LC}}$  in Section 5.3.1, we find that the closest match is for the filled core beam with polarization  $L = I \cos \theta_0$ , for  $(\alpha, i) \approx (40^\circ, 70^\circ)$  in Figures 5.7–5.9. However, the  $I$ - $Q$  plane features a narrow line instead of a banana, and the patterns in  $I$ - $U$  are symmetric about  $U = 0$  instead of tilted. Nevertheless, keeping in mind that  $L$  in the data does not follow  $I$  smoothly, as in the model, we cannot rule out this configuration until we have modelled  $L$  in more detail.

Next, we compare the data to the pure dipole at  $r = 0.1r_{\text{LC}}$ . For a filled core beam with  $L = I \cos \theta_0$  and  $\alpha < i$  (Figures 5.26–5.28), the phase portraits are a better match in the  $I$ - $Q$  and  $I$ - $U$  plane, although the balloon in the  $Q$ - $U$  plane is more tilted than we have assumed in the data.

In the current-modified dipole look-up tables in Section 5.5.1, for the same configuration (Figures 5.38–5.40), we also find some rough matches, but the

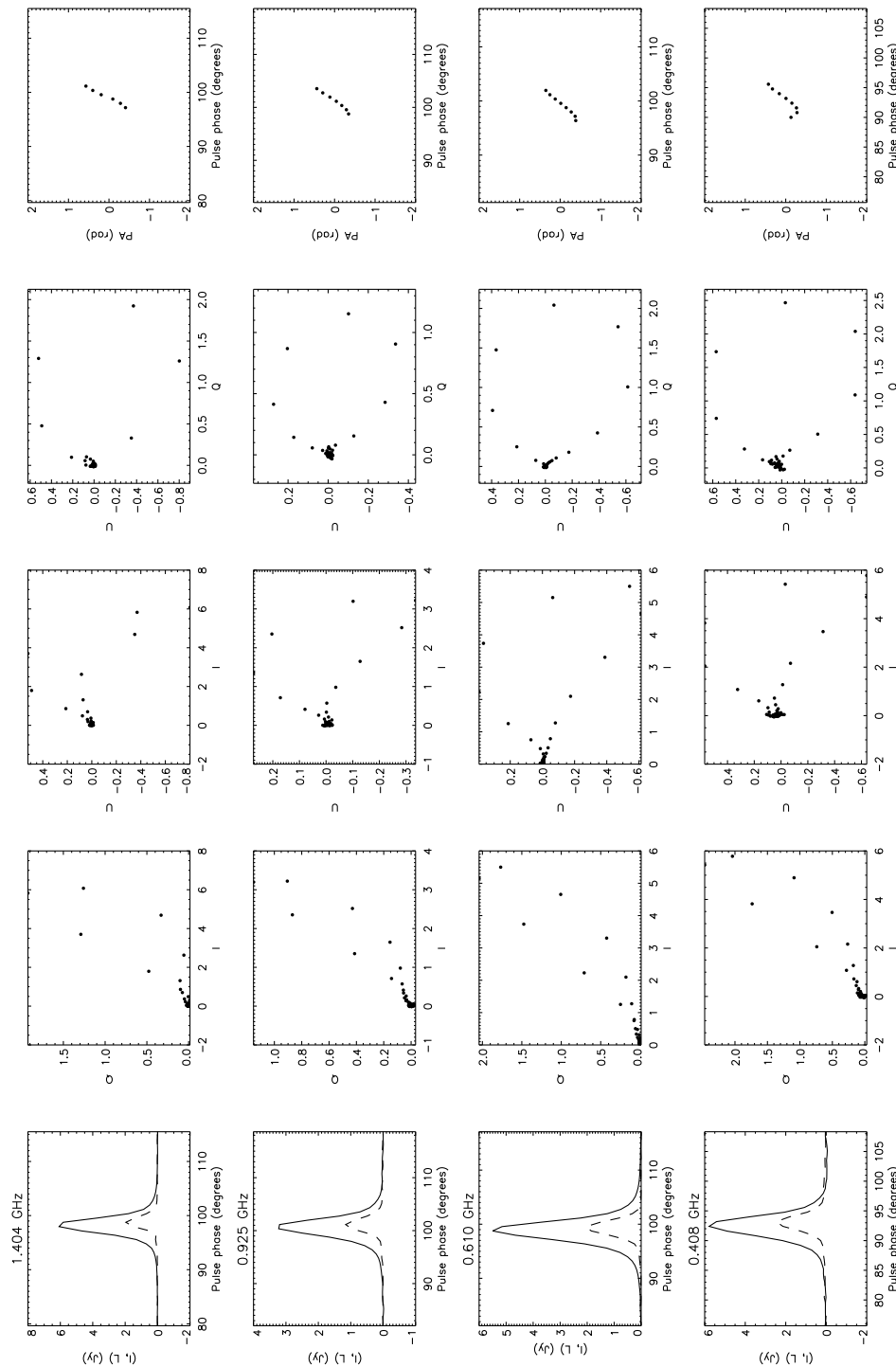


**Figure 5.58:** Multi-frequency pulse profiles, PA swing and Stokes phase portraits for PSR J0826+2637 (Gould & Lyne 1998). In landscape mode, observations at each frequency occupy rows, decreasing from 1.404 GHz (top row) to 0.408 GHz (bottom row). From left to right, the columns show (1)  $I$  (solid curve, in Jy) and  $L$  (dashed curve, in Jy) profiles plotted against time (s), (2)  $I$ - $Q$  phase portrait, (3)  $I$ - $U$  phase portrait, (4)  $Q$ - $U$  phase portrait, and (5) the PA swing (data points with  $L \geq 0.1I_{\max}$  plotted only). Data are presented courtesy of the EPN.

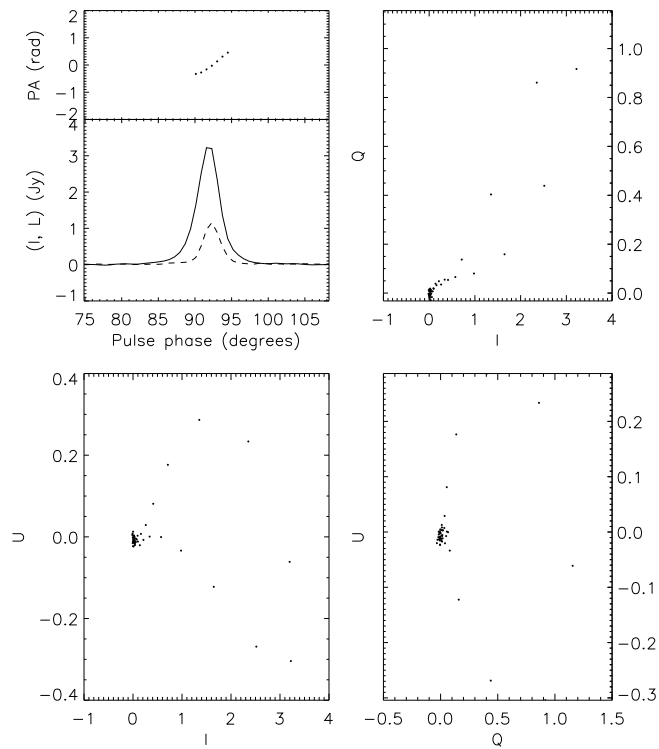


**Figure 5.59:** Polarimetry of PSR J0826+2637 at 0.925 GHz (Gould & Lyne 1998). Clockwise from top left panel: (a)  $I$  (lower subpanel, solid curve, in Jy) and  $L$  (lower subpanel, dashed curve, in Jy) profiles, and PA swing (upper subpanel, dotted curve, in rad) all plotted against time (in s); (b)  $I$ - $Q$  phase portrait; (c)  $I$ - $U$  phase portrait; (d)  $Q$ - $U$  phase portrait. Data are presented courtesy of the EPN.

patterns appear to be more distorted than the data on the whole. For  $(\alpha, i) = (40^\circ, 70^\circ)$ , the  $I$ - $Q$  plane features a broad balloon which is tilted upwards, the  $I$ - $U$  plane features a very narrow balloon which is tilted downwards, and the  $Q$ - $U$  plane features a balloon which is rotated clockwise. This implies that the toroidal magnetic field does *not* contribute to the overall magnetic geometry for this object.

### 5.6.2 Orientation $(\alpha, i)$

In order to refine the orientation of the model, we zoom in on the look-up table in the vicinity of  $(\alpha, i) = (40^\circ, 70^\circ)$  and construct an updated  $7 \times 7$  look-up table in the range  $34^\circ \leq \alpha \leq 46^\circ$ ,  $62^\circ \leq i \leq 74^\circ$ . At this level, we find that the phase portraits resemble each other fairly closely. Hence, we do not attempt to finalise the orientation until we construct better-fitting  $I$  and  $L$  profiles in Section 5.6.3.

We point out that previously measured orientations for PSR J0826+2637, based on the PA swing, lie in the range  $76.9^\circ \leq \alpha \leq 101.0^\circ$ ,  $75.8^\circ \leq i \leq 97.8^\circ$  (Everett & Weisberg 2001, and references therein). *For these angles, neither the pure nor the current-modified dipoles produce phase portraits that agree with the data in Figure 5.59.* This conclusion holds irrespective of  $r$ , i.e. irrespective of the relative importance of the aberration. For example, for a pure dipole with  $(\alpha, i) = (90^\circ, 80^\circ)$ , Figures 5.7–5.9 feature a hockey stick, a triangular shape and a heart shape in  $I$ - $Q$ ,  $I$ - $U$ , and  $Q$ - $U$  respectively. Even a current-modified dipole does not fit well for the angles inferred by previous authors. For example, for  $(\alpha, i) = (90^\circ, 80^\circ)$  in Figures 5.38–5.40, the current-modified dipole predicts a tilted balloon, a triangle, and a heart shape in  $I$ - $Q$ ,  $I$ - $U$ , and  $Q$ - $U$  respectively, inconsistent with the data in Figure 5.58.

### 5.6.3 Beam and polarization patterns

As  $I$  is single-peaked and reasonably symmetric about the pulse centroid (Figure 5.59), the Gaussian beam in equation (5.14), which is symmetric about  $\mathbf{e}_3$ , serves as an adequate first approximation to  $I(\theta, \phi)$ . We set  $\sigma = 3^\circ$ , which generates a pulse width of  $\approx 30^\circ$ , three times the width observed. Unfortunately, the resolution of our numerical grid prevents us from modelling a narrower beam, but this discrepancy does not affect the results, as long as  $L$  is tailored (i.e. stretched in phase) to match  $I$ .

The  $L$  profile is also single-peaked, but it peaks  $\approx 1^\circ$  after the pulse peak.

By inspecting the locus of  $\hat{\mathbf{x}}_0(t)$  in Figure 5.5, we see that a natural way to reproduce the phase lag is to introduce a longitudinal gradient in  $L$ . For orientations close to  $(\alpha, i) = (30^\circ, 70^\circ)$  and at  $r = 0.006r_{\text{LC}}$ , a good match is obtained for the empirical model

$$L/I(\theta_0, \phi_0) = 4 \cos \theta_0 \sin(0.25\phi_0 + 1.86). \quad (5.17)$$

We emphasize that equation (5.17) is the result of an iterative fitting process; it is not unique, nor does it match the data exactly. However, it suffices for the purpose of finding matching Stokes phase portraits.

After constructing a refined  $7 \times 7$  look-up table of phase portraits for (5.17) over the range  $34^\circ \leq \alpha \leq 46^\circ$ ,  $62^\circ \leq i \leq 74^\circ$ , stepping in intervals of  $2^\circ$ , we find that the data are matched most closely for  $(\alpha, i) = (42^\circ, 68^\circ)$ . The results are presented in Figure 5.60. In the top left panel, we plot  $I$  (solid curve) and  $L$  (dashed curve), scaled to units of Jy to match the data, and the PA swing (dotted curve) in units of radians. Stepping clockwise, the next three panels show  $I$ - $Q$ ,  $I$ - $U$ , and  $Q$ - $U$ . There is an ‘uncertainty’ of roughly  $\pm 6^\circ$  in  $\alpha$  and  $i$ , in the sense that models in this range also match the data respectably by eye. Given the multiple idealisations in the model, e.g. in the magnetic geometry, formal chi-squared fits are not attempted. Likewise, we do not expect the ranges of  $U$  and  $Q$  to match exactly, although the model does perform surprisingly well: for  $(\alpha, i) = (36^\circ, 74^\circ)$ , the maximum  $|U|$  and  $|Q|$  values agree with the data to an accuracy of 5% and 8% respectively. The PA swing matches the S-shape in the data. Again, it is impossible to narrow down  $\alpha$  and  $i$  to  $\pm 4^\circ$  using just the PA swing without the Stokes phase portraits.

#### 5.6.4 Emission altitude

We now examine the Stokes phase portraits of PSR J0826+2367 at other emission altitudes. In Figure 5.61, we plot simulated pulse profiles, PA swings, and Stokes phase portraits at four emission altitudes ( $r = 0.006, 0.012, 0.020$  and  $0.025r_{\text{LC}}$ ) for the best-fit orientation  $(\alpha, i) = (42^\circ, 68^\circ)$  found in Section 5.6.3. We retain (5.17) for the polarization map, although  $L(\theta, \phi)$  can certainly change with  $r$  in principle.

We note that although the shapes of the phase portraits match the data qualitatively at  $r = 0.006r_{\text{LC}}$ , the range of  $Q$  and  $U$  differ slightly. The data show that  $Q$  ranges from  $0 \leq Q \leq 1$  and  $U$  ranges from  $-0.3 \leq U \leq 0.3$ . At  $r = 0.012r_{\text{LC}}$ , the ranges seem to match better.  $Q$  ranges from  $0 \leq Q \leq 1.2$ ,

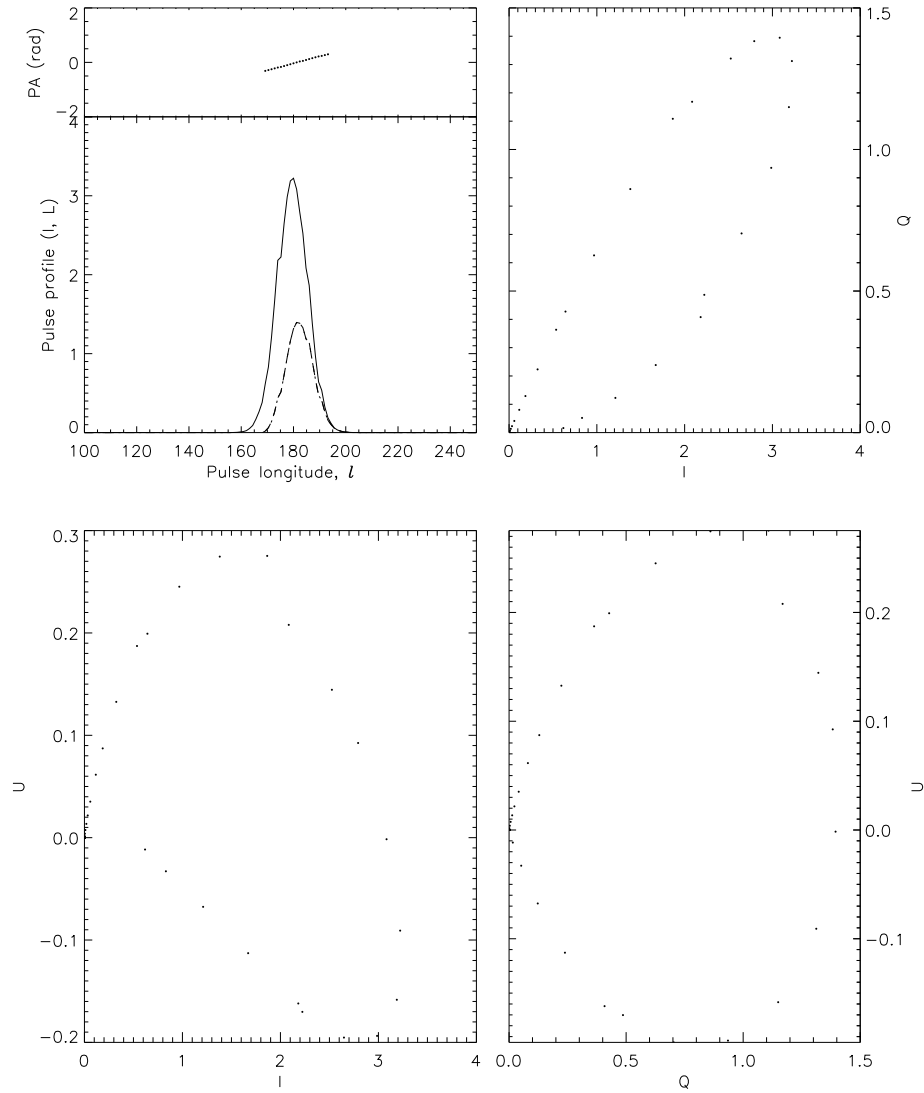


**Figure 5.60:** Pure dipole, low-altitude model for PSR J0826+2637 at  $r = 0.006r_{LC}$ , sharing the pulse profile, Stokes phase portraits and PA swing for filled core beam with polarization pattern given by (5.17) for  $(\alpha, i) = (42^\circ, 68^\circ)$ . Clockwise from top left panel: (a)  $I$  (lower subpanel, solid curve, in Jy) and  $L$  (lower subpanel, dashed curve, in Jy) profiles, and PA swing (upper subpanel, dotted curve, in rad) all plotted against time (in s); (b)  $I$ - $Q$  phase portrait; (c)  $I$ - $U$  phase portrait; (d)  $Q$ - $U$  phase portrait.

and  $U$  ranges from  $-0.3 \leq U \leq 0.2$ . As  $r$  increases from  $0.006r_{\text{LC}}$  to  $0.025r_{\text{LC}}$ , the  $I$ - $Q$  balloon does not change, whereas the  $I$ - $U$  balloon narrows and tilts. The  $Q$ - $U$  balloon rotates clockwise as  $r$  increases. The shape of the PA swing remains invariant.

It is clear from Figure 5.61 that the phase portraits are modestly but noticeable dependent on  $r$  and are therefore a useful diagnostic of the emission altitude in principle. Unfortunately, we lack the information to tie down the radius-to-frequency mapping precisely, because we lack an absolute measurement of  $\beta$  at observation frequency. With the limited information at our disposal, we can only conclude that PSR J0826+2637 is oriented at  $(\alpha, i) = (42 \pm 6^\circ, 68 \pm 6^\circ)$  and that its emission altitude is consistent with a low-altitude origin ( $r \approx 0.01r_{\text{LC}}$ ), because  $B_\phi$  in the emission region is negligible ( $|B_\phi/B_p| \leq 1\%$ ) and aberration is not a major feature in the Stokes phase portraits.

## 5.7 A detailed double-peaked example: PSR J0304+1932

We now consider an object with a more complicated pulse profile, namely PSR J0304+1932, which has  $P = 1.388 \text{ s}$  and  $\dot{P} = 1.296 \times 10^{-15} \text{ s s}^{-1}$  (Taylor et al. 1993). Data from 0.408 GHz to 1.418 GHz were obtained from the EPN online archive [originally published in Gould & Lyne (1998) and Weisberg et al. (1999)]. This object has asymmetric, double-peaked pulse and polarization profiles. There is no interpulse observed in this object.

In analysing the data, we face the same complications as in Section 5.6. The polarization basis for the published Stokes parameters is not defined anywhere, it may be different at different frequencies, and its orientation relative to  $\Omega_p$  is unknown. The previously estimated emission radii for this object are  $(0.003 \pm 0.001)r_{\text{LC}}$  at 0.43 GHz and  $(0.0009 \pm 0.0005)r_{\text{LC}}$  at 1.418 GHz (Blaskiewicz et al. 1991). We therefore repeat the procedure in Section 5.6 and adjust  $\beta$  empirically for each of the observation frequencies so that the shapes in the  $Q$ - $U$  plane are as symmetric as possible about  $U = 0$ .

Figure 5.62 shows the pulse profiles, corrected phase portraits, and PA swings for the four observations (0.610, 0.925, 1.404, and 1.414 GHz), arranged in decreasing order in landscape mode. The Stokes phase portraits for this object are more intricate than those of PSR J0826+2637. The values of  $\beta$  used in Figure 5.62 are (in order of decreasing observation frequency)  $130^\circ, 100^\circ, 120^\circ,$

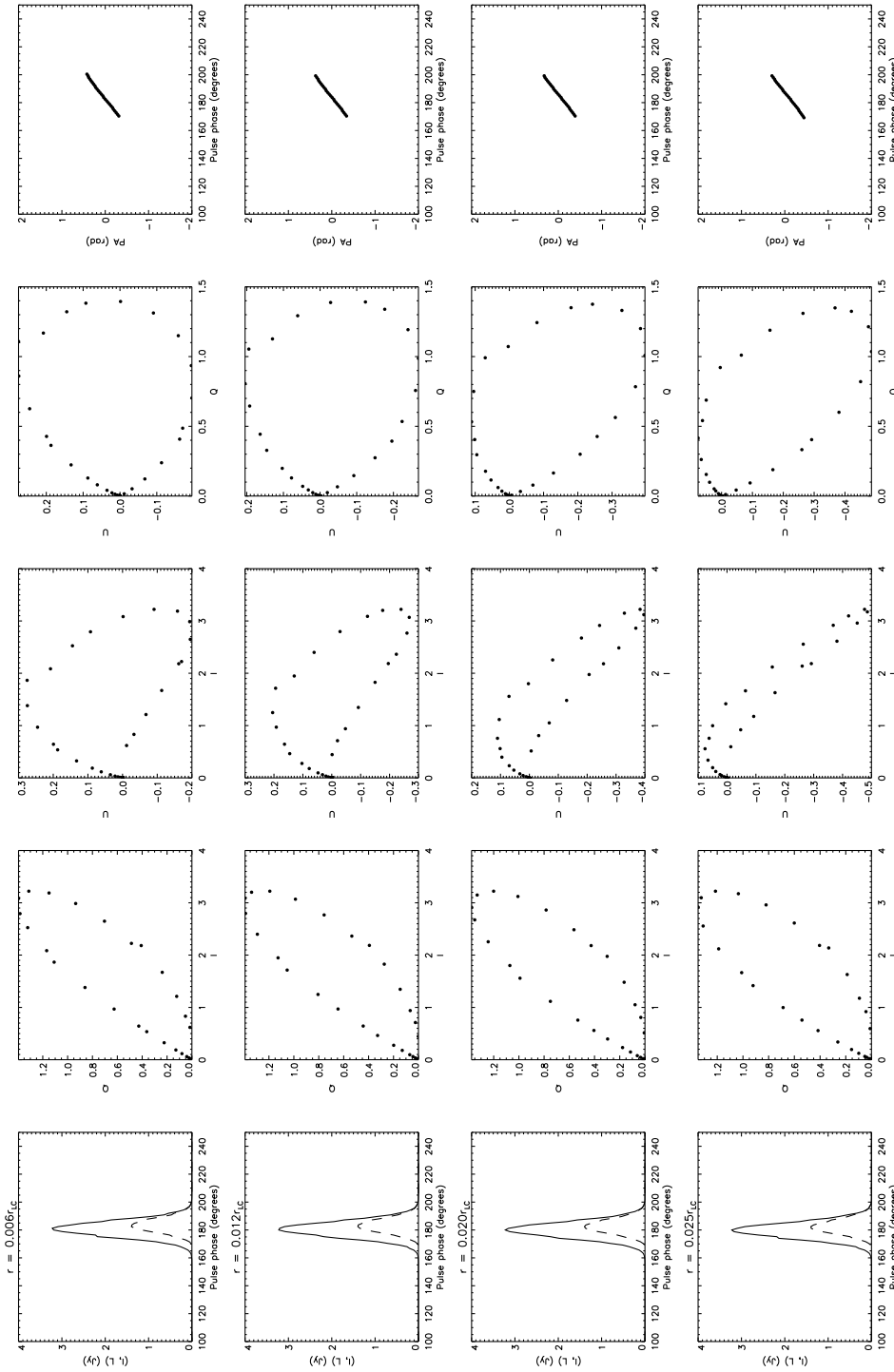


**Figure 5.61:** Simulated pulse profiles, PA swing and Stokes phase portraits for PSR J0826+2637 at four emission altitudes. In landscape mode, plots for each emission altitude occupy rows, increasing from  $r = 0.006r_{LC}$  (top row) to  $r = 0.025r_{LC}$ . From left to right, the columns show (1)  $I$  (solid curve, in Jy) and  $L$  (dashed curve, in Jy) profiles plotted against pulse longitude,  $l$  (in units of  $2\pi$  radians), (2)  $I$ - $Q$  phase portrait, (3)  $I$ - $U$  phase portrait, (4)  $Q$ - $U$  phase portrait and (5) the PA swing (data points with  $L \geq 0.1I_{\max}$  plotted only).

and  $70^\circ$ . One important point is that the heart shape in the  $Q$ - $U$  plane for this object is not symmetric about any line, arguing powerfully against a low emission altitude. The  $I$ - $Q$  plane features a triangular shape which tilts downwards (i.e.  $dQ/dI < 0$ ) and whose shape does not change significantly with frequency. The  $I$ - $U$  plane features a mosquito shape which is also similar at all frequencies.

Initially, we focus on finding an orientation  $(\alpha, i)$  which matches the 1.418 GHz data. Figure 5.63 presents the pulse profile, phase portraits, and PA swing (in rad) at 1.418 GHz. The top left panel shows  $I$  (solid curve, in Jy),  $L$  (dashed curve, in Jy) and the PA swing (dotted curve) where  $L \geq 0.1L_{\max}$ . Stepping clockwise, the next three panels show  $I$ - $Q$ ,  $I$ - $U$  and  $Q$ - $U$ . The double-peaked pulse profile suggests emission from a hollow cone. As in Section 5.6, we explain in the following subsections the steps taken to find a matching orientation, considering the magnetic geometry (Section 5.7.1), orientation angles (Section 5.7.2), beam and polarization patterns (Section 5.7.3), and emission altitude (Section 5.7.4) in turn.

### 5.7.1 Pure versus current-modified dipole

The obvious asymmetry in the  $Q$ - $U$  heart shape rules out a pure dipole at  $r \ll r_{\text{LC}}$  (c.f. Figure 5.19). We therefore compare the data to the look-up tables in Sections 5.4.2 and 5.5.2. The triangle, mosquito and heart shapes in the  $I$ - $Q$ ,  $I$ - $U$  and  $Q$ - $U$  planes respectively resemble the phase portraits approximately for the current-modified dipole at  $(\alpha, i) = (80^\circ, 50^\circ)$  in Figures 5.48-5.50. To a lesser degree, the phase portraits for a pure dipole at  $r = 0.1r_{\text{LC}}$  also bear similarities to the data at the same orientation, although the  $I$ - $U$  plane features a triangular shape instead of a mosquito, and the heart shape in the  $Q$ - $U$  plane is upside-down with respect to the data. Recall that the look-up tables include aberration. Before making a definite statement regarding  $|B_\phi/B_p|$ , however, we model  $I$  and  $L$  in more detail.

### 5.7.2 Orientation $(\alpha, i)$

We now zoom in and construct an updated  $7 \times 7$  look-up table in the range  $74^\circ \leq \alpha \leq 86^\circ$ ,  $44^\circ \leq i \leq 56^\circ$ . As for PSR J0826+2637, the phase portraits at this level resemble each other fairly closely. However, as the asymmetry of the beam and polarization profiles can change the shape of the phase portraits, we do not finalise  $(\alpha, i)$  yet.

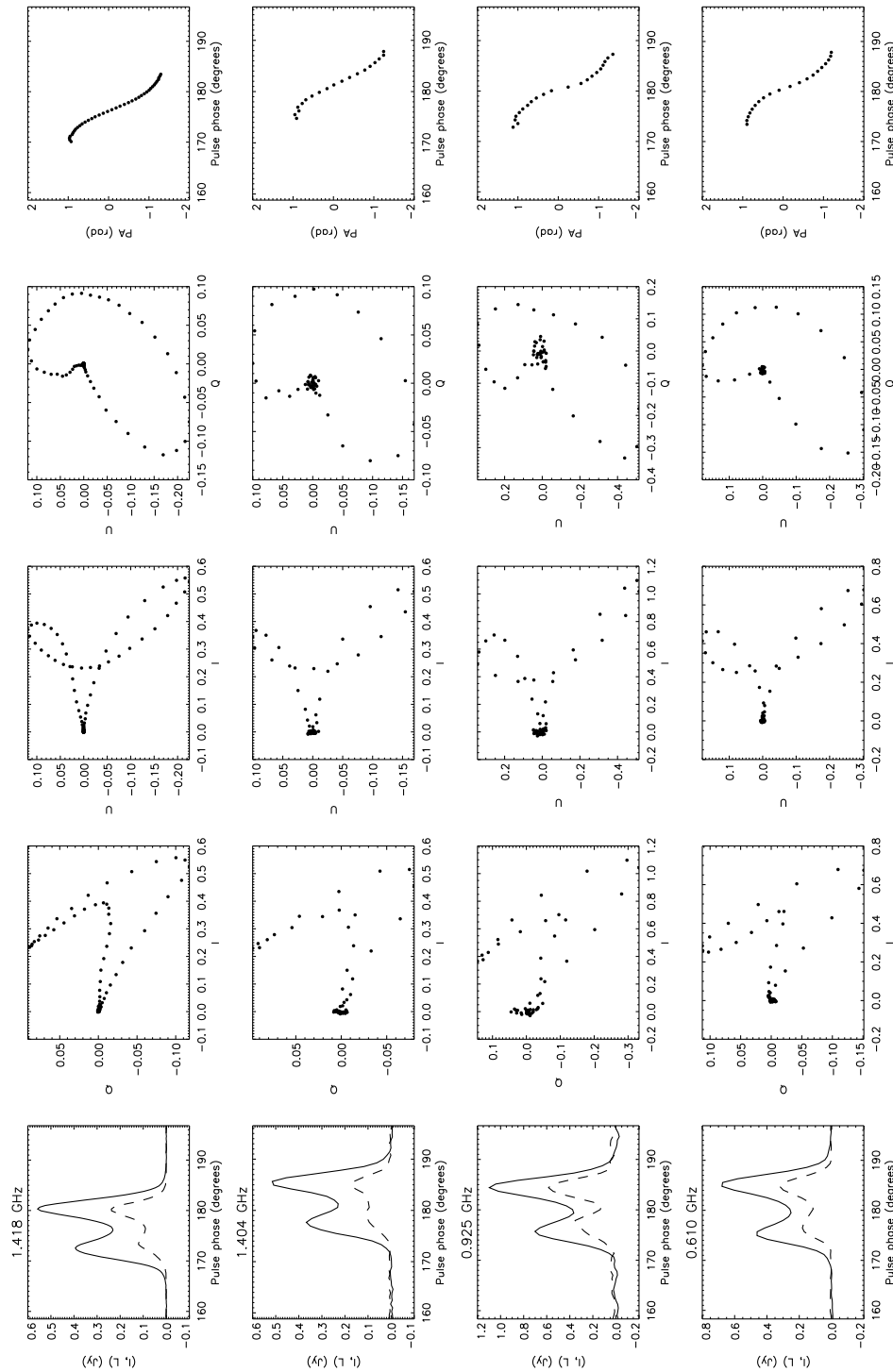


**Figure 5.62:** Multi-frequency pulse profiles, PA swing and Stokes phase portraits for PSR J0304+1932. In landscape mode, observations at each frequency occupy rows, decreasing from 1.418 GHz [top row; Weisberg et al. (1999)] to 1.404–0.610 GHz [second to fourth rows; Gould & Lyne (1998)]. From left to right, in landscape mode, the columns show (1)  $I$  (solid curve, in Jy) and  $L$  (dashed curve, in Jy) profiles plotted against time (in s), (2)  $I$ - $Q$  phase portrait, (3)  $I$ - $U$  phase portrait, (4)  $Q$ - $U$  phase portrait, and (5) the PA swing (data points with  $L \geq 0.1L_{\max}$  plotted only). Data are presented courtesy of the EPN.

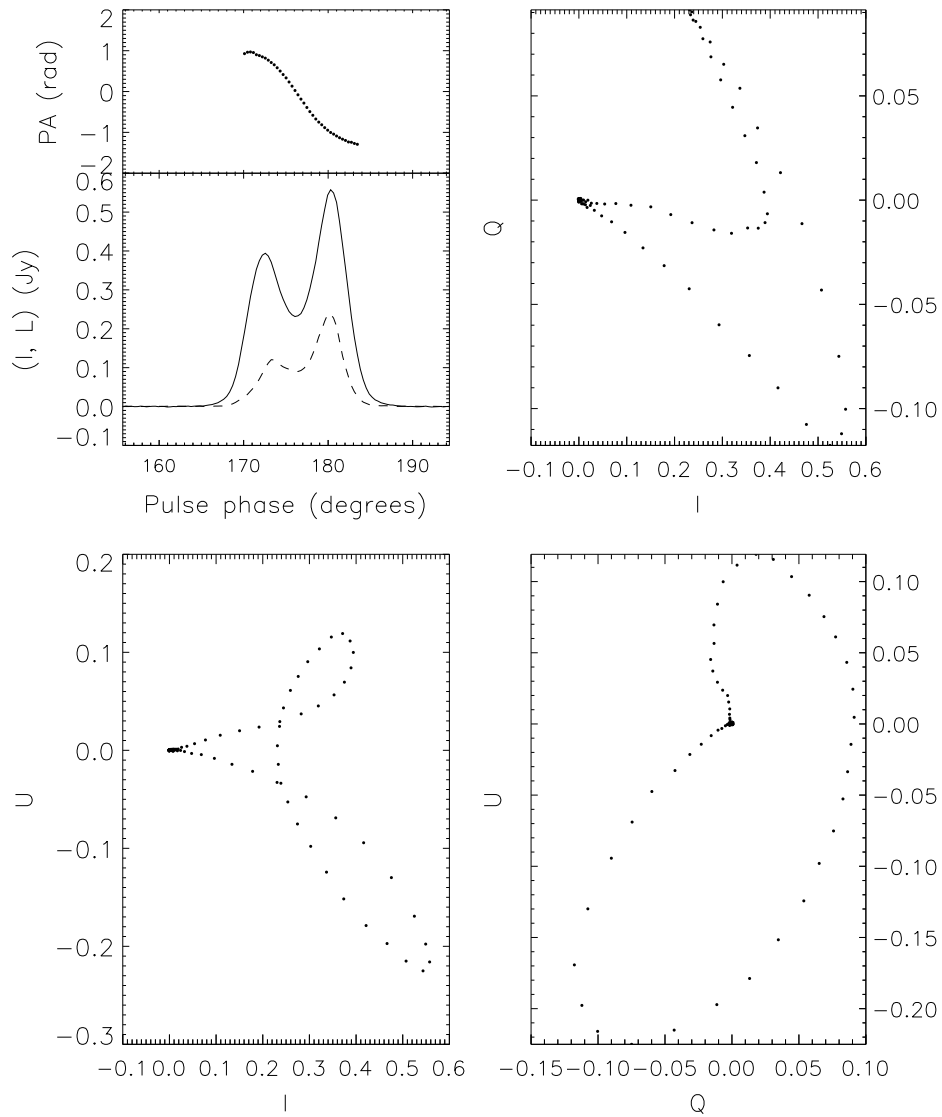


**Figure 5.63:** Polarimetry of PSR J0304+1932 at 1.418 GHz (Weisberg et al. 1999). Clockwise from top left panel: (a)  $I$  (lower subpanel, solid curve, in Jy) and  $L$  (lower subpanel, dashed curve, in Jy) profiles, and PA swing (upper subpanel, dotted curve, in rad) all plotted against time (in s); (b)  $I$ - $Q$  phase portrait; (c)  $I$ - $U$  phase portrait; (d)  $Q$ - $U$  phase portrait. Data are presented courtesy of the EPN.

Previously inferred orientations for PSR J0304+1932, based on the PA swing and assuming a dipole field, lie in the range  $69^\circ \leq \alpha \leq 162^\circ$ ,  $72^\circ \leq i \leq 163^\circ$  (Everett & Weisberg 2001, and references therein). In this range, the pure dipole at  $r \ll r_{\text{LC}}$  certainly does not produce phase portraits that agree with the data in Figure 5.63. For example, in Figures 5.17–5.19, for  $(\alpha, i) = (80^\circ, 80^\circ)$ , we see  $\gamma$ , mosquito and heart shapes (both the latter are symmetric about  $U = 0$ ) in the  $I$ - $Q$ ,  $I$ - $U$ , and  $Q$ - $U$  planes respectively. These patterns are inconsistent with the data. Nor does the current-modified dipole match well within the previously measured range. For example, in Figures 5.48–5.50, for  $(\alpha, i) = (80^\circ, 80^\circ)$ , the phase portraits feature an asymmetric mosquito in the  $I$ - $Q$  plane, two crossed balloons in the  $I$ - $U$  plane, and an asymmetric figure-eight in the  $Q$ - $U$  plane. Again, these shapes are inconsistent with the data.

### 5.7.3 Beam and polarization patterns

We find by trial and error that  $I(\theta_0, \phi_0)$  and  $L(\theta_0, \phi_0)$  must vary with longitude  $\phi_0$  in order to match the data for PSR J0304+1932. Hence, we address this issue before finalising  $(\alpha, i)$ . For the right peak of the pulse to be taller than the left,  $I(\theta_0, \phi_0)$  must be modified from a hollow cone to a ‘horseshoe’, which is brighter at one end. In the data, the pulse width is  $\approx 20^\circ$ , too narrow to be modelled with our software. Instead, we work with a pulse which is  $\approx 4$  times wider. One possible beam pattern which matches the data is

$$I(\theta_0, \phi_0) = (2\pi\sigma^2)^{-1/2} |\sin(0.10\phi_0) + 0.1| \times \exp[-(\theta_0 - \rho)^2/(2\sigma^2)], \quad (5.18)$$

with  $\sigma = 3^\circ$  and  $\rho = 23^\circ$ , together with the polarization pattern

$$L/I = 0.45 \cos \theta_0 |\sin(0.80\phi_0 - 3.12)| \quad (5.19)$$

As for PSR J0826+2637, we emphasize that equations (5.18) and (5.19) are the product of an iterative fitting process; they are not unique, nor do they match the data exactly. Note that  $L \propto \cos \theta_0$  leads to a better fit than  $L \propto \sin \theta_0$  in this particular object, even though  $L \propto \sin \theta_0$  is more commonly associated with double-peaked pulse profiles.

After constructing a refined  $7 \times 7$  look-up table over the range  $74^\circ \leq \alpha \leq 86^\circ$  and  $44^\circ \leq i \leq 56^\circ$ , we find that the data most closely matches the model for  $(\alpha, i) = (76^\circ, 46^\circ)$ , with a ‘by eye’ uncertainty of  $\pm 4^\circ$ . The results are presented

in Figure 5.64. In the top left panel, we plot  $I$  (solid curve) and  $L$  (dashed curve), scaled to units of Jy to match the data, and the PA swing (upper subpanel, dotted curve) in units of radians. Stepping clockwise, the next three panels show  $I$ - $Q$ ,  $I$ - $U$ , and  $Q$ - $U$ .

For  $(\alpha, i) = (76^\circ, 46^\circ)$ , the triangular shape in the  $I$ - $Q$  plane is reproduced reasonably well, although the model shows an extra small loop at  $(I, Q) \approx (0.3, 0.07)$  which is not present in the data but agrees otherwise. In the  $I$ - $U$  plane, the mosquito shape in the model lacks the loop at  $(I, U) \approx (0.35, 0.1)$  seen in the data. The heart shapes in the  $Q$ - $U$  plane match well. The range of  $U$  and  $Q$  values predicted by the model agree with the data to an accuracy of 9% and 8% respectively. The S-shape of the PA swing is reproduced well by the model, and its predicted range also matches the data to within 8%.

#### 5.7.4 Emission altitude

Armed with the best-fit model at 1.418 GHz, we now examine the Stokes phase portraits of PSR J0304+1932 at other frequencies.

In Figure 5.65, we plot simulated pulse profiles, PA swings and Stokes phase portraits at four emission altitudes ( $r = 0.05, 0.1, 0.2$  and  $0.3r_{\text{LC}}$ ) for the best-fit orientation  $(\alpha, i) = (76^\circ, 46^\circ)$  found in Section 5.7.2. We use the same  $I(\theta_0, \phi_0)$  and  $L(\theta_0, \phi_0)$  models at all four altitudes, for the sake of simplicity, although there is evidence in the data that the ratio  $L/I$  changes with altitude.

As the emission altitude increases, the phase portraits become increasingly distorted. The  $I$ - $Q$  phase portrait changes from a broad crescent at  $r = 0.05r_{\text{LC}}$  to an asymmetric mosquito at  $r = 0.3r_{\text{LC}}$ , whereas the  $I$ - $U$  plane changes from a triangular shape to a tilted, narrow hockey stick. The heart shape in the  $Q$ - $U$  plane rotates clockwise, and the ventricles become unequal as the altitude increases. The trends in the model (Figure 5.65) do not really mimic those in the data (Figure 5.62) except in loose terms. This may imply that  $L(\theta_0, \phi_0)$  and  $I(\theta_0, \phi_0)$  change with  $r$ , as suggested by Johnston et al. (2008a), or that the orientation inferred from the phase portraits is wrong, although the reader is reminded that the discrepancies are even greater if the Everett & Weisberg (2001) orientation is used. Without additional information on how the data in Figure 5.62 are calibrated, we can only conclude that at 1.418 GHz, PSR J0304+1932 can be modelled reliably with a current-modified dipole with an orientation  $(\alpha, i) = (76 \pm 4^\circ, 46 \pm 4^\circ)$  at an emission altitude of  $r \approx 0.1r_{\text{LC}}$ .

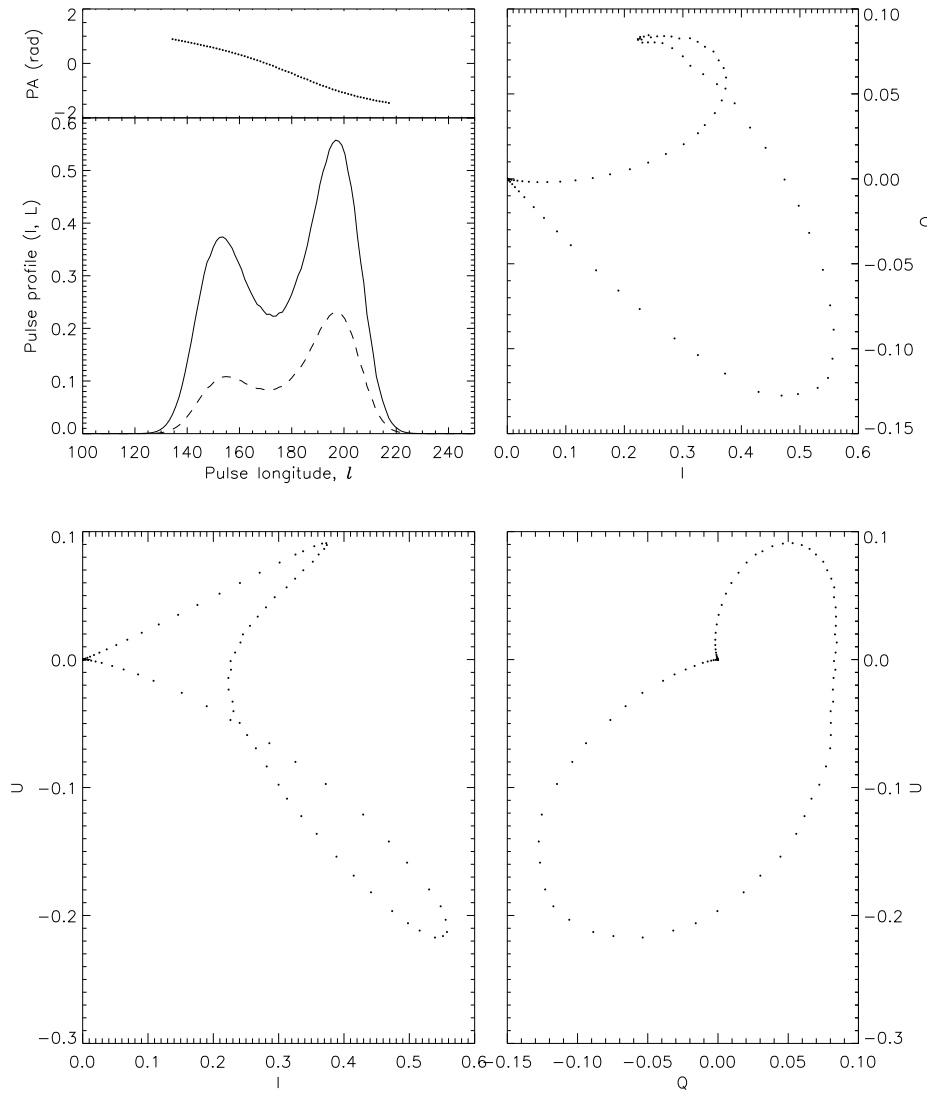


**Figure 5.64:** Current-modified dipole field model for PSR J0304+1932. Pulse profile, Stokes phase portraits and PA swing for a hollow cone given by (5.18) with degree of linear polarization given by the data for  $(\alpha, i) = (76^\circ, 46^\circ)$  at  $r = 0.1r_{LC}$ . Clockwise from top left panel: (a)  $I$  (lower subpanel, solid curve, in Jy) and  $L$  (lower subpanel, dashed curve, in Jy) profiles, and PA swing (upper subpanel, dotted curve, in rad) all plotted against time (in s); (b)  $I$ - $Q$  phase portrait; (c)  $I$ - $U$  phase portrait; (d)  $Q$ - $U$  phase portrait.

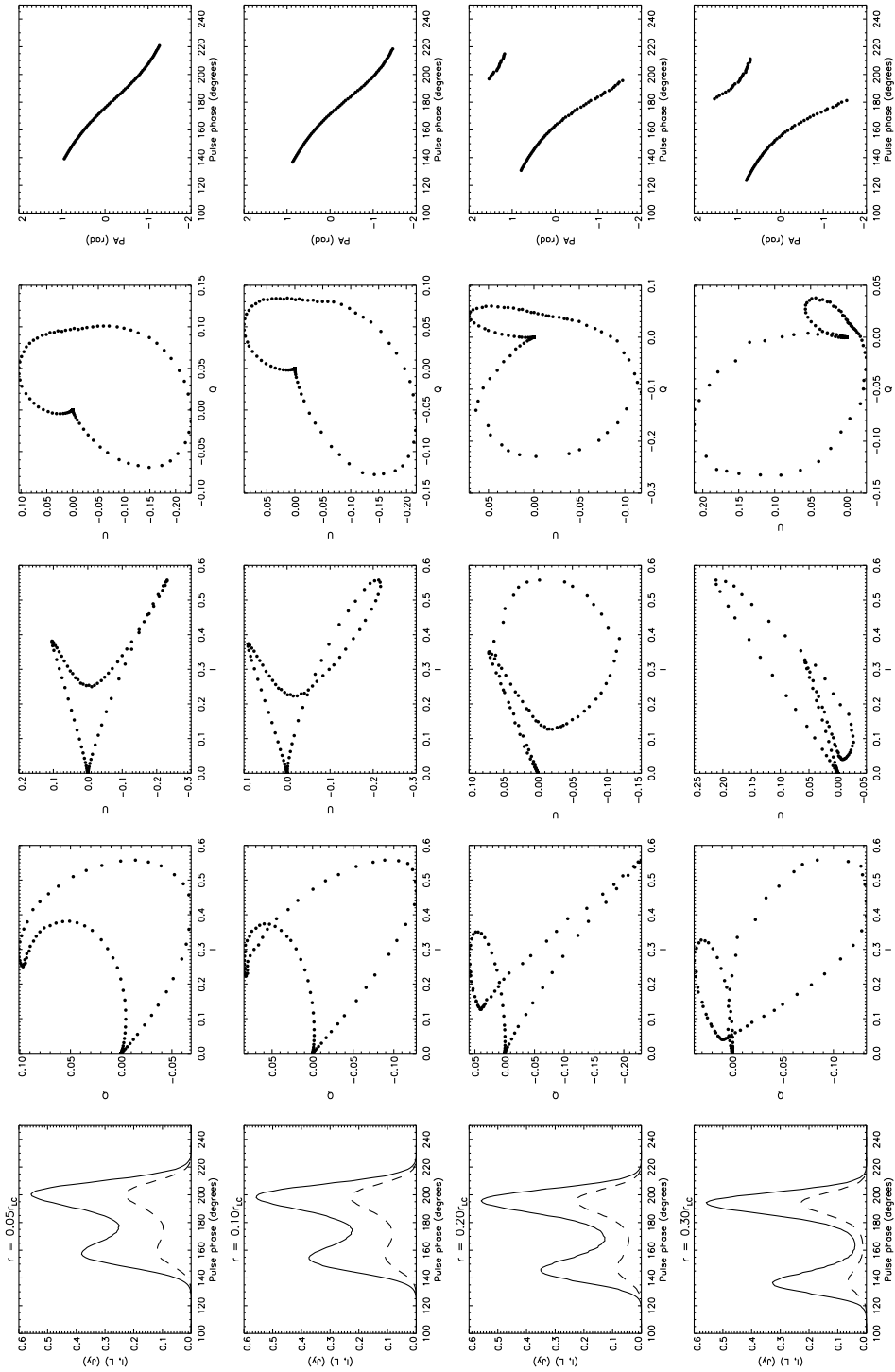


**Figure 5.65:** Simulated pulse profiles, PA swing and Stokes phase portraits for PSR J0304+1932 at three emission altitudes. In landscape mode, plots for each emission altitude occupy rows, increasing from  $r = 0.1r_{LC}$  (top row) to  $r = 0.35r_{LC}$ . From left to right in landscape mode, the columns show (1)  $I$  (solid curve, in Jy) and  $L$  (dashed curve, in Jy) profiles plotted against pulse longitude,  $l$  (in units of  $2\pi$  radians), (2)  $I$ - $Q$  phase portrait, (3)  $I$ - $U$  phase portrait, (4)  $Q$ - $U$  phase portrait and (5) the PA swing (data points with  $L \geq 0.1L_{\max}$  plotted only).

## 5.8 Conclusion

In this chapter, we introduce Stokes phase portraits as an observational probe of a radio pulsar's magnetic geometry, orientation, and emission altitude. Our aim is to supply the reader with a set of easy-to-use tools for analysing pulsar polarization data in a physically instructive way. We present handy look-up tables of pulse and polarization profiles, Stokes phase portraits, and PA swings as functions of magnetic inclination angle  $\alpha$  and line-of-sight inclination angle  $i$ , for a pure and current-modified dipole, emission from a filled core and hollow cone, and two simple models of the degree of linear polarization. For the current-modified dipole, we also investigate how the phase portraits change with emission altitude  $r$ . In all the models, relativistic aberration is incorporated fully to order  $\mathcal{O}(r/r_{LC})$ . To assist the reader, we summarise in Table 5.1 where to find the look-up tables corresponding to each model.

Magnetic geometry	Emission altitude	Beam pattern	$L$ pattern	Figures
Pure dipole	$r \ll r_{\text{LC}}$	Filled core	$I \cos \theta_0$	5.7–5.10
			$I \sin \theta_0$	5.12–5.15
		Hollow cone	$I \cos \theta_0$	5.17–5.20
			$I \sin \theta_0$	5.22–5.25
Pure dipole	$r = 0.1r_{\text{LC}}$	Filled core	$I \cos \theta_0$	5.26–5.28
		Hollow cone	$I \cos \theta_0$	5.29–5.31
Current-modified dipole	$r = 0.1r_{\text{LC}}$	Filled core	$I \cos \theta_0$	5.38–5.41
			$I \sin \theta_0$	5.43–5.46
		Hollow cone	$I \cos \theta_0$	5.48–5.51
			$I \sin \theta_0$	5.53–5.56

**Table 5.1:** Catalog of Stokes phase portraits and PA swing look-up tables in Sections 5.3 and 5.5.

	$L = I \cos \theta_0$	$L = I \sin \theta_0$
Filled core	hockey stick, straight line ( $I$ - $Q$ )	hockey stick ( $I$ - $Q$ )
	balloon, figure-eight ( $I$ - $U$ )	balloon, figure-eight ( $I$ - $U$ )
	balloon, heart ( $Q$ - $U$ )	balloon, heart ( $Q$ - $U$ )
Hollow cone	$\gamma$ shape ( $I$ - $Q$ )	$\gamma$ shape ( $I$ - $Q$ )
	trefoil, mosquito, twisted triangle ( $I$ - $U$ )	trefoil, mosquito, twisted triangle ( $I$ - $U$ )
	balloon, heart, mosquito, interlocking ovals ( $Q$ - $U$ )	balloon, heart, mosquito, interlocking ovals ( $Q$ - $U$ )

**Table 5.2:** Summary of shapes seen in Stokes phase portraits for a pure dipole (Section 5.3). Examples of each shape appear in Figure A1.

	$L = I \cos \theta_0$	$L = I \sin \theta_0$
Filled core	balloon, figure-eight ( $I-Q$ )	balloon, figure-eight ( $I-Q$ )
	hockey stick, banana ( $I-U$ )	balloon, hockey stick, banana ( $I-U$ )
	balloon, heart ( $Q-U$ )	balloon, heart, figure-eight ( $Q-U$ )
Hollow cone	balloon, trefoil, mosquito, twisted triangle ( $I-Q$ )	balloon, mosquito, twisted triangle ( $I-Q$ )
	banana, hockey stick ( $I-U$ )	banana, balloon, hockey stick ( $I-U$ )
	balloon, heart, figure-eight ( $Q-U$ )	balloon, heart, figure-eight ( $Q-U$ )

**Table 5.3:** Summary of shapes seen in Stokes phase portraits for a current-modified dipole (Section 5.5). Examples of each shape appear in Figure A1.

For a pure dipole at low emission altitudes ( $r \ll r_{\text{LC}}$ ), the Stokes phase portraits display relatively simple shapes, summarised in Table 5.2. The shapes are classified according to colloquial descriptors in Appendix 5A. They are symmetric about  $U = 0$ , because the effects of aberration are negligible. The curvature in the shapes is determined by the path traced by  $\hat{\mathbf{x}}_0(t)$ ; for example, as  $|\alpha - i|$  increases, the curvature of the hockey stick in the  $I$ - $Q$  plane decreases. For a filled core, the phase portraits produced by the two polarization models,  $L = I \cos \theta_0$  and  $L = I \sin \theta_0$  are generally similar, except for  $\alpha = i$ , where  $L$  is double-peaked. When the filled core is replaced by a hollow cone, the pulse profiles for  $|\alpha - i| \leq 30^\circ$  become double-peaked, and the phase portraits transform into more complicated shapes.

For a pure dipole at  $r = 0.1r_{\text{LC}}$ , aberration distorts the Stokes phase portraits. The symmetry about  $U = 0$  is broken, causing the shapes in the  $I$ - $U$  and  $Q$ - $U$  planes to tilt and rotate. In the  $I$ - $Q$  plane, the shapes broaden noticeably. A phase shift between the pulse centroid and PA swing inflection point of  $\approx 4r/r_{\text{LC}}$  is also observed (Blaskiewicz et al. 1991; Hibsichman & Arons 2001; Dyks 2008).

For a current-modified dipole at  $r = 0.1r_{\text{LC}}$ , the phase portraits are also asymmetric about  $Q = 0$  and  $U = 0$ . The toroidal field can either partially cancel out or enhance the effects of aberration, depending on its orientation. For  $B_\phi = -B_p r/r_{\text{LC}}$ , the shapes of the phase portraits are summarised in Table 5.3 and in Appendix 5A. For a hollow cone, at those orientations where the pulse is double-peaked, the shapes are more complicated than those of a filled core. The tilt angles of the shapes are roughly proportional to the emission altitude and hence  $B_\phi$ . The heart shapes and balloons seen in the  $Q$ - $U$  plane also rotate about  $(U, Q) = (0, 0)$  as the orientation and/or emission altitude changes.

In Sections 5.6 and 5.7, we apply our look-up tables to multi-frequency observations of two pulsars: PSR J0826+2637 and PSR J0304+1932. We find that previous measurements of  $(\alpha, i)$  from the PA swing do not reproduce the observed phase portraits for either a pure or current-modified magnetic dipole. However, it is possible to obtain good matches to both the PA swing and phase portraits for other choices of  $(\alpha, i)$ . For PSR J0826+2637, the closest match at 0.925 GHz comes from a pure dipole with a filled core beam, with orientation  $(\alpha, i) = (42^\circ, 68^\circ)$  at  $r \approx 0.012r_{\text{LC}}$ . For PSR J0304+1932, the closest match at 1.418 GHz comes from a current-modified dipole with a hollow cone, with orientation  $(\alpha, i) = (76^\circ, 46^\circ)$  at  $r = 0.1r_{\text{LC}}$ . As the multi-frequency data are not usually measured in the canonical polarization basis, we are unable to

extract the radius-to-frequency mapping without additional information.

We close by summarising our main conclusions.

1. Stokes phase portraits contain additional information regarding a pulsar's orientation  $(\alpha, i)$  and magnetic geometry when used in conjunction with PA swings.
2. The observed phase portraits of  $\approx 60\%$  of the 26 pulsars studied in this chapter are asymmetric and hence incompatible with a pure magnetic dipole at low emission altitudes (Section 5.4.3).
3. As a corollary of (ii), the radio emission region in these objects is found to lie at  $r \gtrsim 0.1r_{\text{LC}}$ , where the effects of relativistic aberration and a toroidal field are important. In some cases, one must have  $r \gtrsim 0.2r_{\text{LC}}$ , i.e. the emission comes from the outer magnetosphere (Sections 5.6 and 5.7).
4. The idealised model of a pure or current-modified dipole at  $r \gtrsim 0.1r_{\text{LC}}$  with a filled core beam and  $L = I \cos \theta_0$ , or a hollow cone beam and  $L = I \sin \theta_0$ , manages to account for most gross features in the polarization data from all 26 pulsars studied in this chapter, whether the pulse profiles are single-peaked or double-peaked. Small longitudinal variations in  $I$  and  $L$  are needed to fit certain minor details (e.g. relative peak heights) in the observations.

This chapter is the first in a series. Future papers will examine the Stokes tomography of a force-free rotator, millisecond pulsars, and the circularly polarized component of pulsar radio emission.



# 6 Stokes tomography of radio pulsar magnetospheres. II.

## Millisecond pulsars

The radio polarization characteristics of millisecond pulsars (MSPs) differ significantly from those of non-recycled pulsars. In particular, the position angle (PA) swings of many MSPs deviate from the S-shape predicted by the rotating vector model, even after relativistic aberration is accounted for, indicating that they have non-dipolar magnetic geometries, likely due to a history of accretion. Stokes tomography, introduced by Chung & Melatos (2009), uses phase portraits of the Stokes parameters as a diagnostic tool to infer a pulsar's magnetic geometry and orientation. This chapter applies Stokes tomography to MSPs, generalizing the technique to handle interpulse emission. We present an atlas of look-up tables for the Stokes phase portraits and PA swings of MSPs with current-modified dipole fields, filled core and hollow cone beams, and two empirical linear polarization models. We compare our look-up tables to data from 15 MSPs and find that the Stokes phase portraits for a current-modified dipole approximately match several MSPs whose PA swings are flat or irregular and cannot be reconciled with the standard axisymmetric rotating vector model. PSR J1939+2134 and PSR J0437–4715 are modelled in detail. The data from PSR J1939+2134 at 0.61 GHz can be fitted well with a current-modified dipole at  $(\alpha, i) = (22 \pm 2^\circ, 80 \pm 1^\circ)$  and emission altitude  $0.4 r_{LC}$ . The fit is less accurate for PSR J1939+2134 at 1.414 GHz, and for PSR J0437–4715 at 1.44 GHz, indicating that these objects have a more complicated magnetic field geometry, such as a surface quadrupole, a force-free or vacuum-like field, or a polar magnetic mountain.

## 6.1 Introduction

The two tools used most frequently to characterise the orientation and magnetic geometry of a radio pulsar are its pulse profile and position angle (PA) swing. The rotating vector model (Radhakrishnan & Cooke 1969), which assumes an axisymmetric magnetic field, predicts an S-shaped swing across one pulse period and is traditionally used to determine the inclinations of the magnetic axis of symmetry and the observer’s line of sight to the rotation axis. However, there are limitations when analysing only the PA swing, especially as the magnetosphere is not axisymmetric in general, e.g. the magnetic field includes a current-modified component (Hibschman & Arons 2001).

In Chapter 5, Stokes tomography was introduced as a diagnostic tool to be used alongside more traditional methods of analysis. It exploits the fact that the phase portraits traced out by the four Stokes parameters, when plotted against each other over one pulse period, are unique for any given magnetic geometry and orientation. An atlas of look-up tables, containing Stokes phase portraits and PA swings, was presented in Chapter 5 for a variety of simple models, including pure and current-modified dipole fields, filled core and hollow cone beams, and the associated linear polarization patterns. Stokes tomography was used to successfully model two non-recycled pulsars, PSR J0826+2637 and PSR J0304+1932, and to show that the Stokes phase portraits of 24 nominally “dipolar” pulsars, which obey the period-pulse-width relation and/or exhibit clean S-shaped PA swings, are inconsistent with low-altitude emission from a pure dipole field.

In this chapter, we turn our attention to millisecond pulsars (MSPs). Polarimetric studies of MSP radio emission have uncovered complex behaviour not normally seen in slower pulsars. In particular, the PA swings of many MSPs are neither clean nor S-shaped; instead, they are flat (Stairs et al. 1999; Ord et al. 2004), highly distorted (e.g. PSR J0437–4715; Navarro et al. 1997) or extremely noisy (e.g. giant pulses from PSR J1824–2452A; Knight et al. 2006). Additionally, the PA swing varies dramatically with frequency for many MSPs (Johnston et al. 2008a), indicating that the magnetic geometry changes a lot with altitude, or that the observed pulse profile comprises emission from several different regions and altitudes.

The above trends suggest that MSPs have nondipolar magnetic fields. In a non-recycled pulsar, a dipole field can be distorted by several mechanisms, e.g. a current flowing along the field lines (Hibschman & Arons 2001; Dyks 2008), or rotational sweepback near the light cylinder (Hibschman & Arons 2001; Dyks

& Harding 2004; Dyks 2008). In a recycled pulsar with a history of prolonged accretion, another set of mechanisms comes into play. For example, accreted material channeled onto the magnetic poles distorts the frozen-in magnetic field as it spreads towards the equator (Melatos & Phinney 2001; Payne & Melatos 2004; Vigelius & Melatos 2008). Quadrupolar magnetic fields, proposed to explain the X-ray light curves of Her X-1 (Shakura et al. 1991), can even be comparable to the dipolar component (Long et al. 2008). Multipole fields can also be generated near the inner edge of the partially diamagnetic accretion disk of an X-ray pulsar (Lai et al. 1999). Alternatively, as the pulsar is spun up by accretion, the magnetic pole drifts towards the rotation axis, dragged inward by the motion of superfluid vortices in the pulsar’s core (Srinivasan et al. 1990; Ruderman 1991; Cheng & Dai 1997; Lamb et al. 2009).

In this chapter, we apply Stokes tomography to millisecond pulsar data drawn from the European Pulsar Network’s (EPN) online database. In Section 6.2, we briefly review the fitting recipe for determining the optimal orientation and beam polarization patterns from observed pulse profiles and Stokes phase portraits. We also extend the model in Chapter 5 to treat interpulse emission. We compare our improved look-up tables of Stokes phase portraits and PA swings to observations of 15 MSPs in Section 6.3. We then conduct detailed modelling of PSR J1939+2134, which has a strong interpulse, and PSR J0437–4715, which has a pulse profile with multiple peaks, in Sections 6.4 and 6.5 respectively. Our findings are summarised in Section 6.6.

## 6.2 Stokes tomography

### 6.2.1 Radiation field

For the convenience of the reader, we begin by summarising briefly how to determine the emission point and hence the polarization state of the radiation as a function of pulse longitude, following the recipe laid out in Section 2 of Chapter 5. Our notation and definitions copy Chapter 5.

We define two reference frames, as in Figure 5.1: the inertial frame, in which the observer is at rest, with axes  $(\mathbf{e}_x, \mathbf{e}_y, \mathbf{e}_z)$ , and the body frame of the pulsar. The relative motion between the frames is computed by solving Euler’s equations of motion (including precession in general but not in this chapter). The line-of-sight vector  $\mathbf{w}$  is chosen to lie in the  $\mathbf{e}_y$ - $\mathbf{e}_z$  plane, making an angle  $i$  with  $\mathbf{e}_z$ . The rotation and magnetic axes lie along  $\mathbf{e}_z$  and one of the body frame axes ( $\mathbf{e}_3$ ) respectively, separated by an angle  $\alpha$ . We define a spherical

polar grid  $(r, \theta, \phi)$  in the body frame covering the region  $x_{\min} \leq r/r_{\text{LC}} \leq x_{\max}$ ,  $0 \leq \theta \leq \pi$ ,  $0 \leq \phi \leq 2\pi$ , with  $64 \times 256 \times 128$  grid cells, where the line  $\theta = 0$  lies along  $\mathbf{e}_3$ , and  $r_{\text{LC}} = c/\Omega$  is the light cylinder radius. In this chapter, we take  $x_{\min} = 0.01$  and  $x_{\max} = 0.83$  to accommodate the relatively small magnetospheres (and hence emission altitudes) of MSPs.

Radiation from highly relativistic particles flowing along magnetospheric field lines is narrowly beamed. Hence, without relativistic aberration, the observed emission point  $\mathbf{x}_0(t)$  at any time  $t$  is located where the magnetic vector  $\mathbf{B}[\mathbf{x}_0(t), t]$  points along  $\mathbf{w}$ . When aberration is included, the emission point  $\mathbf{x}_0(t)$  at time  $t$  satisfies the equation (Blaskiewicz et al. 1991; Dyks 2008)

$$\mathbf{w} = \frac{\pm \mathbf{t} + \boldsymbol{\Omega} \times \mathbf{x}_0/c}{|\pm \mathbf{t} + \boldsymbol{\Omega} \times \mathbf{x}_0/c|}, \quad (6.1)$$

where  $\mathbf{t} = \mathbf{B}[\mathbf{x}_0(t), t]/|\mathbf{B}[\mathbf{x}_0(t), t]|$  is the unit tangent vector to the magnetic field at  $\mathbf{x}_0(t)$ , and  $\boldsymbol{\Omega}$  is the angular velocity vector. In Chapter 5, we considered emission from only one pole for simplicity [i.e.  $+\mathbf{t}$  in equation (6.1)], and hence ignored interpulse emission. In this chapter, we include emission from both the north and south poles, requiring both  $\pm \mathbf{t}$  terms to be retained in (6.1). At every instant, we thus have four emission points which satisfy (6.1), two in the hemisphere opposite the observer (which he cannot see), and two facing the observer, which we label  $P_1$  and  $P_2$ . We search the grid at a fixed altitude  $r_0$  to find  $P_1$  and  $P_2$ ; note that the locations of  $P_1$  and  $P_2$  change with time in both the body frame and the inertial frame. The  $\boldsymbol{\Omega} \times \mathbf{x}_0$  term in (6.1) encodes the aberration effect, as in Hibschan & Arons (2001); it is correct to order  $\mathcal{O}(r/r_{\text{LC}})$  and should be replaced by the full relativistic expression when modelling exceptionally good data.

The Stokes parameters  $(I, Q, U, V)$  associated with the complex electric field vector  $\mathbf{E}$  at  $\mathbf{x}_0(t)$ , which describe the polarization state, are defined as

$$I = |E_x|^2 + |E_y|^2 \quad (6.2)$$

$$Q = |E_x|^2 - |E_y|^2 \quad (6.3)$$

$$U = 2\text{Re}(E_x E_y^*) \quad (6.4)$$

$$V = 2\text{Im}(E_x E_y^*), \quad (6.5)$$

where  $I$  is the polarised fraction of the total intensity,  $L = (Q^2 + U^2)^{1/2}$  is the linearly polarised component, and  $V$  is the circularly polarised component. The observed electric field vector  $\mathbf{E}$ , assumed to be in the direction of the

particle acceleration<sup>1</sup>, is the incoherent sum of the electric field vectors at  $P_1$  and  $P_2$ , viz.  $\mathbf{E} = \mathbf{E}_1 + \mathbf{E}_2$ , where the relative phase between  $\mathbf{E}_1$  and  $\mathbf{E}_2$  fluctuates randomly. The observed Stokes parameters therefore reduce to  $I = I_1 + I_2$ ,  $Q = Q_1 + Q_2$ , and  $U = U_1 + U_2$ . In this chapter, we assume that all the emission is linearly polarised for simplicity, i.e.  $V = 0$ . Circular polarization will be examined in a companion paper.

The  $x$ - and  $y$ - components are measured with respect to an orthonormal basis  $(\hat{\mathbf{x}}, \hat{\mathbf{y}})$  which is fixed in the plane of the sky. In this chapter, we choose  $\hat{\mathbf{x}} = \boldsymbol{\Omega}_p / |\boldsymbol{\Omega}_p|$  and  $\hat{\mathbf{y}} = \hat{\mathbf{x}} \times \mathbf{w}$ , where  $\boldsymbol{\Omega}_p = \boldsymbol{\Omega} - (\boldsymbol{\Omega} \cdot \mathbf{w})\mathbf{w}$  is the projection of  $\boldsymbol{\Omega}$  onto the sky. Then the polarization angle,  $\psi$ , between  $\hat{\mathbf{x}}$  and the linearly polarised part of  $\mathbf{E}$  is given by

$$\psi = \frac{1}{2} \tan^{-1} \frac{U}{Q}. \quad (6.6)$$

The observational data obtained from the EPN are not necessarily expressed in the canonical basis  $(\hat{\mathbf{x}}, \hat{\mathbf{y}})$ . However, the  $Q$ - $U$  phase portrait has the same shape in any Cartesian basis; if the basis is rotated by an angle  $\beta$  with respect to  $\hat{\mathbf{x}}$  and  $\hat{\mathbf{y}}$ , the  $Q$ - $U$  phase portrait rotates by an angle  $2\beta$  without being distorted, unlike the  $I$ - $Q$  and  $I$ - $U$  phase portraits, which change shape. Hence, when analysing the data, the first step is to reproduce the shape of the  $Q$ - $U$  phase portrait as closely as possible without worrying about the orientation; infer  $\beta$ ; rotate the  $(I, Q, U, V)$  data into the canonical basis provisionally defined through  $\beta$ ; and then adjust  $\alpha, i$ , and the beam and polarization patterns *iteratively* to reproduce the  $I$ - $Q$  and  $I$ - $U$  portraits. The recipe for doing so is explained in Section 5.2.6 and Figure 5.2.6.

### 6.2.2 Look-up tables of Stokes phase portraits

Figures A2–A17 in Appendix 6A display look-up tables of Stokes phase portraits and PA swings, similar to those in chapter 5, updated to include interpulse emission. The figures are organised into four groups, corresponding to two beam models (filled core and hollow cone) and two polarization models ( $L \propto \cos \theta$ ,  $L \propto \sin \theta$ ; see chapter 5). All the look-up tables are for a current-modified dipole magnetic field, described by equation (5.16).

<sup>1</sup>The instantaneous acceleration is inclined slightly with respect to the normal (or binormal) of  $\mathbf{B}$  at  $\mathbf{x}_0(t)$ , because the emitting charges corotate. For more details, see the discussion around equation (5.2) and equation (A3) in Dyks (2008).

### 6.2.3 Interpulses

An interpulse is a secondary pulse separated from the main pulse by approximately  $180^\circ$  of rotational phase (Manchester & Lyne 1977). It is believed to arise when a pulsar is a nearly orthogonal rotator viewed nearly side-on, shining from both magnetic poles, i.e. with  $\alpha \approx i \approx 90^\circ$ , where ‘ $\approx$ ’ means ‘within roughly one beam width’ in this context (Petrova 2008).

Figure 6.1 compares the Stokes phase portraits, pulse profiles, and PA swings for a pure dipole and current-modified dipole emitting from one and two poles for one illustrative orientation  $(\alpha, i) = (80^\circ, 70^\circ)$ . For clarity, relativistic aberration is *not* included in this example (compare Section 5.2.3 *et seq.*). Clockwise from the top left panel, the figure displays (i) a pure dipole with no interpulse, (ii) a current-modified dipole at  $r = 0.13r_{\text{LC}}$  with no interpulse, (iii) a pure dipole with an interpulse, and (iv) a current-modified dipole at  $r = 0.13r_{\text{LC}}$  with an interpulse. The top two panels in Figure 6.1, which have no interpulse, are the same as in Figures 5–8 and 30–33 in the look-up tables in chapter 5.

Figure 6.2 shows the loci  $\hat{\mathbf{x}}_0(t)$  traced out by  $P_1$  and  $P_2$  over one rotation in the body frame of the pulsar for the various cases in Figure 6.1. The panels are arranged as in Figure 6.1. The bottom panels, in which the interpulse is present, show two paths, one in the north hemisphere, and one in the south. For the current-modified dipole (right panels), the loci are asymmetric, as discussed in chapter 5. For definiteness, we choose a filled-core beam, viz.

$$I(\theta, \phi) = (2\pi\sigma^2)^{-1/2} \left\{ \exp \left[ -\theta^2 / (2\sigma^2) \right] + \exp \left[ -(\theta - \pi)^2 / (2\sigma^2) \right] \right\}, \quad (6.7)$$

which is represented by greyscale shading in Figure 6.2. In (6.7),  $\sigma$  is the width of the beam, chosen arbitrarily to equal  $10^\circ$ . We also choose the linear polarization pattern to be

$$L(\theta, \phi) = I(\theta, \phi) |\cos \theta| \quad (6.8)$$

in Figures 6.1 and 6.2. Other choices (e.g.  $L \propto \sin \theta$ ) are equally valid and have been found empirically in chapter 5 to match the observational data in many objects.

In Figure 6.1, the interpulse traces out a small, secondary loop within the primary pattern in the  $I$ - $Q$ ,  $I$ - $U$  and  $Q$ - $U$  phase portraits. It also changes slightly the range of  $U$  and  $Q$  covered by the main pulse. For example, for

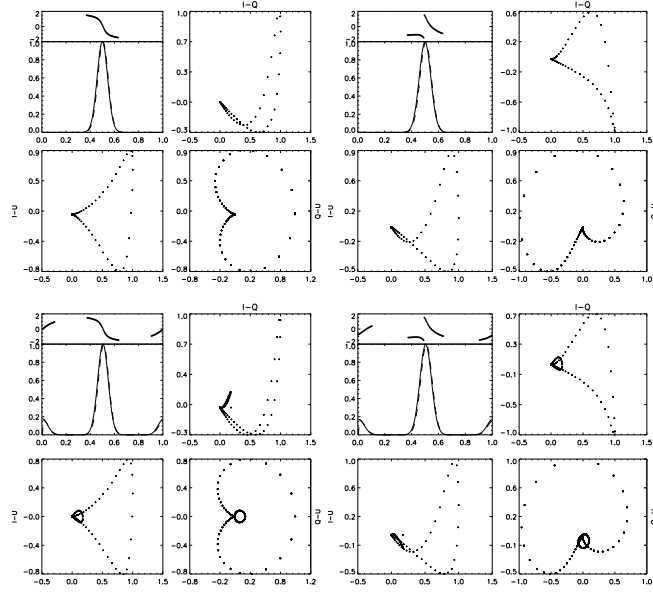


**Figure 6.1:** Stokes tomography of a model pulsar with an interpulse but without relativistic aberration. Top left: dipole field, no interpulse. Top right: current-modified dipole emitting at  $r = 0.13r_{\text{LC}}$ , no interpulse. Bottom left: dipole field with interpulse. Bottom right: current-modified dipole emitting at  $r = 0.13r_{\text{LC}}$  with interpulse. Within each quadrant of the figure, the five subpanels display (clockwise from top left):  $I/I_{\text{max}}$  and PA (in radians) as functions of pulse longitude,  $I-Q$ ,  $Q-U$ , and  $I-U$ . The orientation is  $(\alpha, i) = (80^\circ, 70^\circ)$ . The beam pattern is given by (6.7).

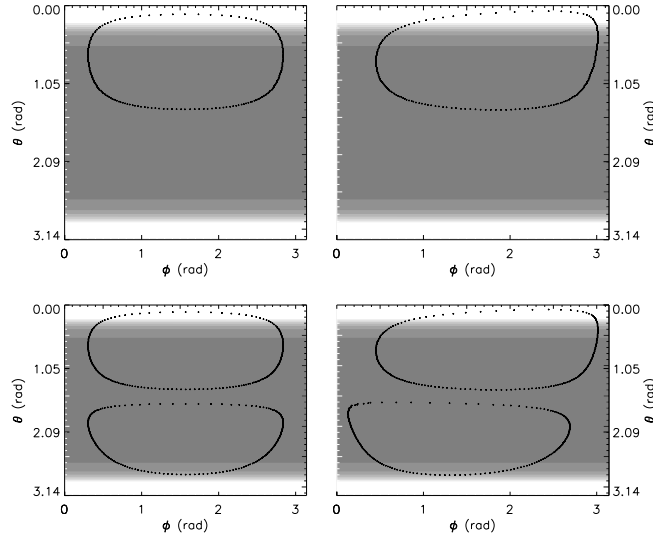


**Figure 6.2:** Locus  $\hat{\mathbf{x}}_0(t)$  traced out by the emission point(s)  $P_1$  and  $P_2$  over one rotation, in the body frame of the model pulsar considered in Figure 6.1. Top left: dipole field, no interpulse. Top right: current-modified dipole emitting at  $r = 0.13r_{\text{LC}}$ , no interpulse. Bottom left: dipole field with interpulse. Bottom right: current-modified dipole emitting at  $r = 0.13r_{\text{LC}}$  with interpulse. The beam pattern  $I(\theta, \phi)$  is represented by greyscale shading (brightness  $\propto I$ ).

the dipole (left panels), the maximum value of  $U$  decreases from 0.9 to 0.8 with the addition of the interpulse. The size of the secondary loop (i.e. the intensity of the interpulse) increases relative to the main pulse as  $\alpha$  approaches  $i$ , as expected. Along  $\alpha = 90^\circ$  and  $i = 90^\circ$ , when the interpulse and the main pulse peak at the same intensity, the primary and secondary patterns overlap in the  $I$ - $Q$ ,  $I$ - $U$  and  $Q$ - $U$  planes, and the phase portraits are indistinguishable from the non-interpulse case. The shapes do not overlap exactly for other orientations, where the main pulse is brighter than the interpulse.

In the  $I$ - $U$  and  $Q$ - $U$  planes, the balloons and heart shapes seen in chapter 5 are also seen when an interpulse is present. For example, for  $\alpha = i = 90^\circ$ , the Stokes parameters trace out two reflection-symmetric patterns with positive and negative  $U$  to form complex, interlocking shapes (see Figures A2–A16 from the atlas of look-up tables in Appendix 6A). As expected, the patterns are more intricate for a hollow cone than for a filled core. For example, the  $Q$ - $U$  portrait at  $(\alpha, i) = (70^\circ, 80^\circ)$  for a filled core contains an asymmetric, tilted heart shape and a small oval, both connected at  $Q = U = 0$  (Figure A4). The same orientation for a hollow cone shows a broader heart shape with two large, secondary ovals (Figure A12).

### 6.2.4 Relativistic aberration

In the observer’s reference frame, charged particles flowing outwards ultra-relativistically along poloidal magnetic field lines also have a small transverse velocity component because they corotate with the star as part of the highly conducting magnetosphere. This displaces  $\mathbf{x}_0(t)$  by a distance of order  $r/r_{\text{LC}}$  compared to its position when aberration is neglected. The electric field vector (parallel to the particle’s acceleration vector) is also displaced, resulting in the well-known delay-radius relation (Blaskiewicz et al. 1991; Hibschan & Arons 2001; Dyks 2008). According to this relation, the centre of the pulse profile leads the steepest point of the PA swing by  $4r/r_{\text{LC}}$ .

We compute  $\mathbf{x}_0(t)$  directly, including aberration, by solving (6.1) numerically. As a cross check, we compare the numerical solution with the analytic approximation given by equation (F2) of Hibschan & Arons (2001), where the tangent field at the aberration-shifted emission point,  $\mathbf{t}$ , can be expressed as the sum of the tangent field at the original, non-aberrated emission point,  $\mathbf{t}_0$ , plus a perturbation  $\mathbf{t}_1 = (\boldsymbol{\Omega} \times \mathbf{x}_0)/c - [(\boldsymbol{\Omega} \times \mathbf{x}_0)/c \cdot \mathbf{t}_0]\mathbf{t}_0$ . As the aberration-induced deflection angle grows linearly with  $r$ , equation (F2) holds most accurately for small  $r$ . At  $r = 0.13r_{\text{LC}}$  and  $0.31r_{\text{LC}}$ , the direct and approximate calculations

of  $\mathbf{t}$  agree to within  $\sim 10\%$  and  $\sim 20\%$  respectively. Note that, although we calculate  $\mathbf{t}$  directly from (6.1), the expression  $\pm\mathbf{t} + \boldsymbol{\Omega} \times \mathbf{x}_0/c$  itself in (6.1) breaks down near the light cylinder, where quadratic relativistic corrections come into play.

Figure 6.3 illustrates how aberration modifies the Stokes phase portraits, pulse profiles, and PA swings for pure dipole and current-modified dipole magnetospheres. For the sake of clarity, we do not include interpulse emission in Figure 6.3, although, in general, interpulse and aberration effects are additive, as one can tell from the look-up tables in Appendix 6A. The emission is placed arbitrarily at an altitude of  $0.1r_{\text{LC}}$  to ensure a reasonably strong effect. We note that aberration introduces an altitude dependence in the case of a pure dipole, which is absent in the non-aberrated case considered in chapter 5.

Aberration acts mainly to shift the relative phases of the pulse centroid and PA swing inflection point. To lowest order in  $r/r_{\text{LC}}$ , the radius-delay relation predicts that the pulse profile is phase shifted by  $\approx -r/r_{\text{LC}}$  radians, whereas the PA swing is phase shifted by  $\approx 3r/r_{\text{LC}}$  radians. Figure 6.3 shows that for  $r = 0.1r_{\text{LC}}$ , the pulse profile is shifted by  $\approx -0.08$  radians, whereas the PA swing is shifted by  $\approx +0.27$  radians. These shifts are enough to dramatically broaden the  $I$ - $Q$  pattern, twist the  $I$ - $U$  pattern, and tilt the  $Q$ - $U$  pattern for the pure dipole (left panels of Figure 6.3). For the current-modified dipole (right panels), the  $I$ - $Q$  pattern narrows, the  $I$ - $U$  patterns twists and rotates, and the  $Q$ - $U$  pattern rotates. Figure 6.4 shows the loci of  $\hat{\mathbf{x}}_0(t)$  traced out by  $P_1$  over one rotation (there is only one set of emission points without an interpulse), with each panel corresponding to the cases in Figure 6.3. The loci of the aberrated emission points (bottom panels) are shifted in  $\phi$  relative to the non-aberrated points (top panels).

In chapter 5, it was shown that, for a pure dipole field without aberration, all phase portraits are reflection symmetric about  $U = 0$ . Aberration breaks this symmetry, causing the shapes in the  $I$ - $U$  and  $Q$ - $U$  plane to tilt (see Section 5.4). Aberration also changes the tilt and the relative sizes of the shapes in the phase portraits, e.g. the ventricles of the hearts in the  $U$ - $Q$  plane.

## 6.3 Miniature population study

We now survey the pulse profiles, Stokes phase portraits, and PA swings for a selection of 16 MSPs from the EPN online database<sup>2</sup> (Lorimer et al. 1998).

<sup>2</sup>Available at: <http://www.mpifr-bonn.mpg.de/pulsar/data/>

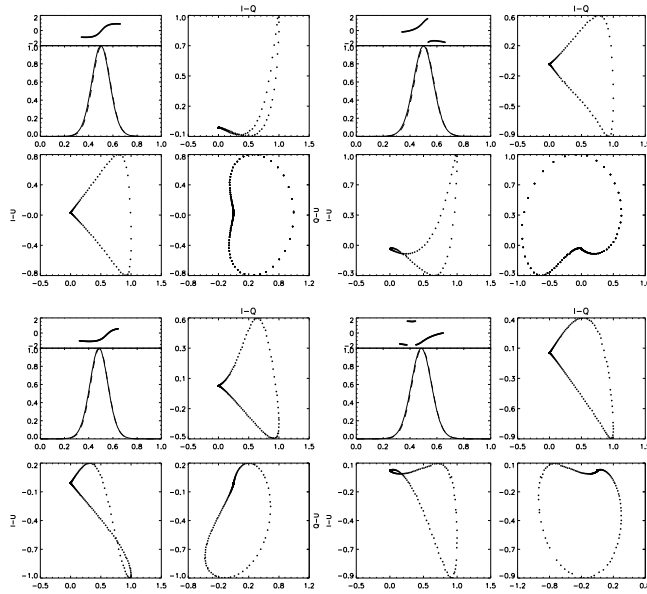


**Figure 6.3:** Stokes tomography for a model pulsar including relativistic aberration but without an interpulse. Top left: dipole field, no aberration. Top right: current-modified dipole emitting at  $r = 0.1r_{\text{LC}}$ , no aberration. Bottom left: dipole field emitting at  $r = 0.1r_{\text{LC}}$  with aberration. Bottom right: current-modified dipole emitting at  $r = 0.1r_{\text{LC}}$  with aberration. Within each quadrant of the figure, the five subpanels displays (clockwise from top left):  $I/I_{\text{max}}$  and PA swing (in radians) as a function of pulse longitude,  $I-Q$ ,  $Q-U$ ,  $I-U$ . The orientation is  $(\alpha, i) = (30^\circ, 40^\circ)$ . The beam pattern is given by (6.7).

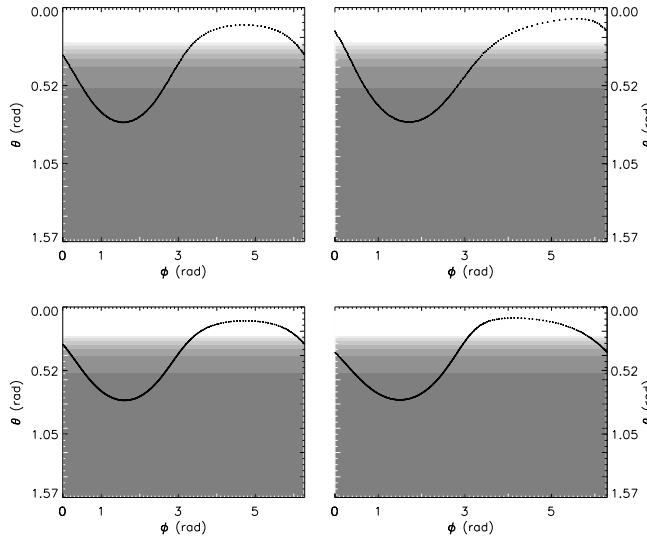


**Figure 6.4:** Locus  $\hat{\mathbf{x}}_0(t)$  traced out by the emission point  $P_1$  across one rotation, in the body frame of the model pulsar considered in Figure 6.3. Top left: dipole field, no aberration. Top right: current-modified dipole emitting at  $r = 0.1r_{\text{LC}}$ , no aberration. Bottom left: dipole field emitting at  $r = 0.1r_{\text{LC}}$  with aberration. Bottom right: current-modified dipole emitting at  $r = 0.1r_{\text{LC}}$  with aberration. The beam pattern  $I(\theta, \phi)$  is represented by greyscale shading (brightness  $\propto I$ ).

These objects are chosen because they have pulse periods  $< 10$  ms, except for PSR J1022+1001, which was included because of its interesting Stokes phase portraits and because its orientation angles  $\alpha$  and  $i$  have been measured with some degree of confidence by previous authors. All objects were observed by Stairs et al. (1999), except for PSR J0437–4715 (Manchester & Johnston 1995). We note that the PA swing  $\psi$  defined in this chapter corresponds to  $-\psi$  in Stairs et al. (1999). Table 6.3 quotes the size of the magnetosphere for each MSP (in units of the stellar radius,  $r_*$ ) and the frequencies where EPN data are available. In the few cases where rotating vector model fits have been attempted in the literature,  $\alpha$  and  $i$  are also quoted, together with the published uncertainties.

### 6.3.1 General trends

In Figures 6.5–6.7, we present the Stokes phase portraits, pulse profiles, and PA swings for the 8 pulsars with the cleanest data. All Stokes parameters are normalized by the peak intensity  $I_{\max}$ . MSPs generally have a lower degree of linear polarization than non-recycled pulsars, so their phase portraits are correspondingly noisier. The PA swing is only drawn at pulse longitudes satisfying  $L \geq 0.1L_{\max}$  and  $I \geq 0.1I_{\max}$ , where  $L_{\max}$  is the peak value of  $L$ . As the absolute orientation of  $\mathbf{\Omega}_p$  (and hence the angle  $\beta$  between the measured and canonical bases) for each set of data is unknown, we start by analysing just the shape of the  $Q$ - $U$  phase portraits, as discussed in Section 6.2.1 and chapter 5.

Many of the pulse and linear polarization profiles are highly asymmetric, suggesting a complex emission pattern. In objects where  $I(t)$  and  $L(t)$  have multiple peaks or interpulse emission, the Stokes phase portraits feature multiple loops, each corresponding to an individual peak. For example, each of the five peaks seen in PSR J0437–4715 at 1.44 GHz (Figure 6.5, top row) corresponds to a distinct sub-pattern in the  $I$ - $Q$  and  $I$ - $U$  planes (see Section 6.5). In the  $Q$ - $U$  plane, the pattern formed is an asymmetric figure-eight over a slightly curved line. PSR J1022+1001 (Figure 6.5, rows 4–6) has an asymmetric, double-peaked pulse profile, which produces an asymmetric heart shape in the  $Q$ - $U$  plane. Also interesting is PSR J1939+2134 (Figure 6.7, rows 4–5), which has a strong interpulse, whose phase portraits narrow with increasing frequency, while those of the main pulse broaden.

The PA swings for the MSPs featured in Figures 6.5–6.7 are less informative. In several cases, where the PA swing is flat or noisy, the phase portraits still

Pulsar	$P$ (ms)	$r_{\text{LC}}/r_{\star}$	Frequency (GHz)	$\alpha$ ( $^{\circ}$ )	$i$ ( $^{\circ}$ )
J0034–0534	1.88	9.09	0.41		
J0218+4232	2.32	11.11	0.41	$8 \pm 11$	—
			0.61	$8 \pm 15$	—
J0437–4715	5.76	27.78	1.44	145	140
			4.6		
J0613–0200	3.06	14.71	0.41		
			0.61		
J1012+5307	5.26	25.64	0.61		
J1022+1001	16.45	83.33	0.41		
			0.61	$140 \pm 16$	$135.1 \pm 4.1$
			1.414	$83 \pm 27$	$75.9 \pm 5.2$
J1643–1224	4.62	22.22	0.61		
J1713+0747	4.57	22.22	0.41		
			0.61		
			1.414		
J1730–2304	8.12	40.00	0.61		
J1744–1134	4.07	19.61	0.61		
J1823–3021A	5.44	26.32	0.61		
J1824–2452	3.05	14.49	0.61	$40.7 \pm 1.7$	$80.7 \pm 3.9$
J1911–1114	3.63	17.54	0.41		
			0.61		
J1939+2134	1.56	7.69	0.61		
			1.414		
J2051–0827	4.51	21.74	0.41		
			0.61		

**Table 6.1:** Pulse periods  $P$  and observation frequencies of 16 millisecond pulsars from the EPN online database with  $P < 10$  ms (except for J1022+1001, which is included because of its interesting Stokes phase portraits). Where a rotating vector model fit has been published previously,  $\alpha$  and  $i$  are quoted with their published uncertainties. The uncertainties for  $\alpha$  and  $i$  for PSR J0437–4715 are not given in the literature. All pulsars were observed by Stairs et al. (1999), except for PSR J0437–4715 (Manchester & Johnston 1995).

trace out a recognisable pattern. For example, in Figure 6.5, the PA swing of PSR J0437–4715 is flat overall but punctuated by several dips, while the PA swing of PSR J1012+5307 is completely flat. Their phase portraits, in contrast, reveal balloons and figure-eights. In Figure 6.6, the PA swings of PSR J1713+0747, PSR J1744–1134 and PSR J1911–1114 are flat, yet their phase portraits are distinguished by straight lines and balloons. The same is true of PSR J1939+2134 in Figure 6.7. This is another instance, to be added to those in chapter 5, where the Stokes phase portraits carry important extra information which is not apparent from the pulse profile and PA swing alone.

### 6.3.2 Magnetic geometry and orientation

The data in Figures 6.5–6.7 are too low in quality to allow detailed fits for the angles  $\alpha$  and  $i$  and the magnetic geometry, except for PSR J1939+2134 and PSR J0437–4715, which we model in detail in Sections 6.4 and 6.5. It is still instructive, however, to compare the observed Stokes phase portraits in Figures 6.5–6.7 with the atlas of look-up tables in Appendix 6A and make some general remarks.

With the exception of PSR J1022+1001, which has an S-shaped PA swing, the PA swings of the five other MSPs are flat or noisy, ruling out a purely dipolar magnetic geometry. Below, we list the MSPs where we have been able to find approximately matching orientations, beam patterns and linear polarization models for a current-modified dipole. The relevant look-up tables are appended in parentheses. In inferring the orientations, we follow some rules of thumb. (i) If there is an interpulse present, we limit the look-up range to  $\alpha \approx i \gtrsim 60^\circ$ . (ii) If there is more than one peak, we model the emission as a hollow cone. (iii) If  $L$  peaks with  $I$ , we assume  $L = I \cos \theta$ , whereas, if  $L$  vanishes at the pulse centroid, we assume  $L = I \sin \theta$ . Away from the  $\alpha = i$  diagonal, both linear polarization patterns yield similar phase portraits.

1. PSR J1012+5307 (0.61 GHz, Figure 6.5, third row): hollow cone,  $L = I \cos \theta$ ,  $(\alpha, i) = (20^\circ, 80^\circ)$  (Figures A10–A13). This object has an interpulse and matches the model if the balloons are rotated by  $\approx 180^\circ$ .
2. PSR J1713+0747 (1.414 GHz, Figure 6.6, third row): filled core beam,  $L = I \sin \theta$ ,  $(\alpha, i) = (10^\circ, 80^\circ)$  (Figures A2–A5). Note, however, that the data makes a straight line in the  $Q$ - $U$  plane, whereas the closest match in the look-up tables is a thin balloon (rotated by  $\approx 180^\circ$ ).

3. J1744–1134 (0.61 GHz, Figure 6.6, fourth row): filled core beam,  $L = I \cos \theta$ ,  $(\alpha, i) = (30^\circ, 70^\circ)$  (Figures A2–A5). The oval shape matches the model if it is rotated by  $\approx 90^\circ$ . We note, however, that this is not a unique match as the oval shape is common.
4. J1824–2452 (0.61 GHz, Figure 6.6, fifth row): hollow cone beam,  $L = I \cos \theta$ ,  $(\alpha, i) = (60^\circ, 60^\circ)$  (Figures A10–A13). The pulse profile has three peaks, suggesting that this object may have a double-peaked interpulse. The data matches the model if the pattern is rotated by  $\approx 180^\circ$ .

Where multi-frequency observations are available, we only analyse the frequency at which the phase portraits are resolved best. We emphasize that the matches are approximate, and that the figures in Appendix 6A show only the phase portraits at one altitude, viz.  $r = 0.1r_{\text{LC}}$ . More detailed modelling of  $I$  and  $L$  as a function of emission altitude and  $(\theta, \phi)$  must be done to obtain more accurate matches, including the possibility that the emission originates from several altitudes (Johnston et al. 2008a).

For PSR J1022+1001 (Figure 6.6, rows 4–6), whose S-shaped PA swing is nominally dipolar, the heart shape in the  $Q$ - $U$  plane roughly matches a pure or current-modified dipole at  $(\alpha, i) \approx (70^\circ, 20^\circ)$  for a hollow cone with either polarization model. However, the observed heart shape differs slightly from the model, and  $L(t)$  is actually triple-peaked, not double-peaked. Further information on  $\beta$  (e.g. at several frequencies) is required in order to accurately determine the orientation and magnetic geometry.

We now test whether the published  $\alpha$  and  $i$  values in Table 6.3, inferred from the rotating vector model, are consistent with the observed Stokes phase portraits. We refer the reader to the look-up tables in Figures A2–A16 in Appendix 6A. For PSR J1022+1001 (Figure 6.5, rows 5–6), the PA swings at 0.61 GHz and 1.414 GHz imply two very different orientations, namely,  $(\alpha, i) = (140^\circ, 135^\circ)$  and  $(83^\circ, 76^\circ)$  respectively (Stairs et al. 1999). Already, this is worrying, as the orientation of a given pulsar should be unique no matter what altitude the emission comes from. Moreover, neither of these orientations yield Stokes phase portraits which match the data, for any beam or linear polarization pattern. One can verify this easily by examining the phase portraits in the vicinity of  $(\alpha, i) = (40^\circ, 50^\circ)$  and  $(80^\circ, 70^\circ)$  in Figures A2–A16 in Appendix 6A. For example, for a hollow cone with  $L = I \sin \theta$ , at  $(80^\circ, 70^\circ)$ , there is an asymmetric balloon with two interlocking ovals in  $Q$ - $U$ , unlike the heart shape in Figure 6.5. For PSR J1824–2452 (Figure 6.6, fifth row), the rotating vector model predicts  $(\alpha, i) = (41^\circ, 81^\circ)$ . For a hollow cone, the look-up

tables in Figure A10–A12 show interlocking ovals in the  $Q$ - $U$  plane, whereas the data reveal an oval joined to a straight line. Significantly, all these discrepancies are in the shape, not the orientation of the  $Q$ - $U$  portrait, which is basis-independent (chapter 5). We comment on J0437–4715 in Section 6.5, where we model it in detail.

### 6.3.3 Emission altitude

We now discuss how the pulse profiles and Stokes phase portraits evolve with frequency for PSR J1022+1001 and PSR J1939+2134, the only EPN MSPs with adequate multi-frequency data.

At 0.41 GHz, PSR J1022+1001 has a double-peaked intensity profile. The first intensity peak is itself double-peaked in terms of its linear polarization, resulting in three  $L$  peaks overall. In the phase portraits, the first intensity peak corresponds to the bottom loop of the figure-eight in the  $I$ - $Q$  plane and the large balloon in the  $I$ - $U$  plane. At 0.61 GHz, the second pulse is stronger than the first. In the  $I$ - $U$  plane, the second pulse corresponds to the long, straight tail emerging from the bottom of the balloon.

At 0.61 GHz, PSR J1939+2134 displays a single-peaked interpulse which peaks at  $\sim 0.6I_{\max}$ . The main pulse is also single-peaked. The two pulses trace out qualitatively similar patterns on the  $I$ - $Q$  and  $I$ - $U$  plane, namely elongated balloons whose major axes are tilted by  $\approx 0^\circ$  and  $\approx 20^\circ$  relative to the  $Q = 0$  and  $U = 0$  axes respectively. At 1.414 GHz, the peak of the interpulse drops to  $\sim 0.4I_{\max}$ , and the main pulse is double-peaked. There is a dramatic difference in  $Q$  for the main pulse: the slope of the major axis of the balloon changes sign, from  $dQ/dI < 0$  (0.61 GHz) to  $dQ/dI > 0$  (1.414 GHz). The balloons of the main pulse also broaden, while those of the interpulse narrow. The second peak of the main pulse appears in the phase portraits as a kink in the balloons in  $I$ - $Q$  and  $I$ - $U$ .

For all the MSPs, the different ways in which individual peaks evolve with frequency imply that  $I$  and  $L$  depend on  $\theta$  and  $\phi$  in a complicated way. The profile components might originate from different emission regions whose magnetic geometries are different functions of  $r$ . As the aberration and toroidal field increase with  $r$ , they also distort the path  $\hat{\mathbf{x}}_0(t)$ , further complicating  $I(t)$  and  $L(t)$ .

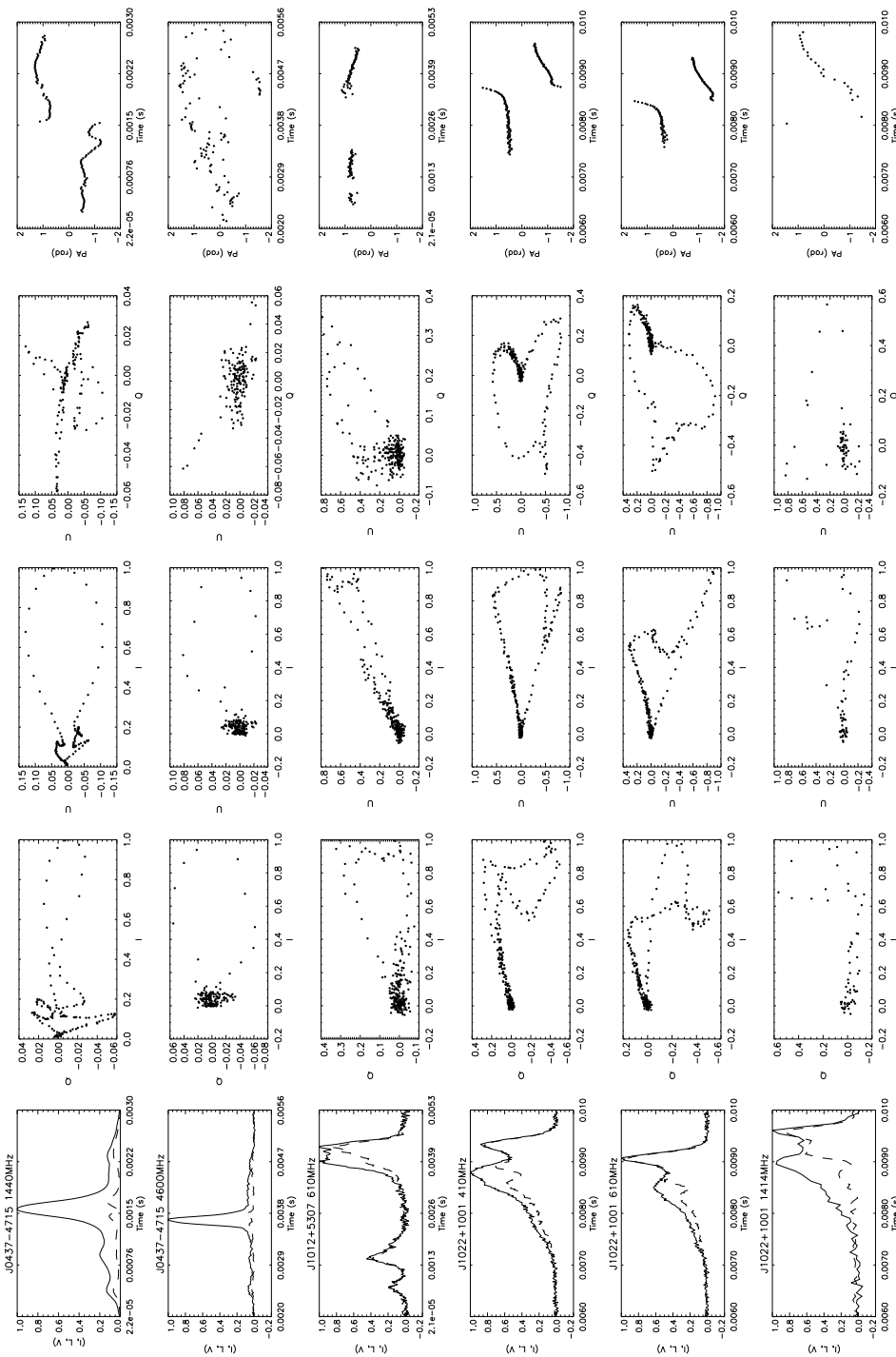


**Figure 6.5:** Pulse profiles, Stokes phase portraits and PA swings for PSR J0437–4715 at 1.44 GHz and 4.6 GHz (Manchester & Johnston 1995), PSR J1012+5307 at 0.61 GHz, and PSR J1022+1001 at 0.41 GHz, 0.61 GHz, and 1.414 GHz (Stairs et al. 1999). The data for each pulsar occupy a row in landscape layout. From left to right, the columns show: (1)  $I/I_{\max}$  (solid curve) and  $L/I_{\max}$  (dashed curve) versus time (in s), (2) the  $I$ - $Q$  phase portrait, (3) the  $I$ - $U$  phase portrait, (4) the  $Q$ - $U$  phase portrait, (5) the PA swing versus time (in s) (data points with  $L \geq 0.1L_{\max}$  and  $I \geq 0.1I_{\max}$  plotted only). Data are presented courtesy of the EPN online archive.

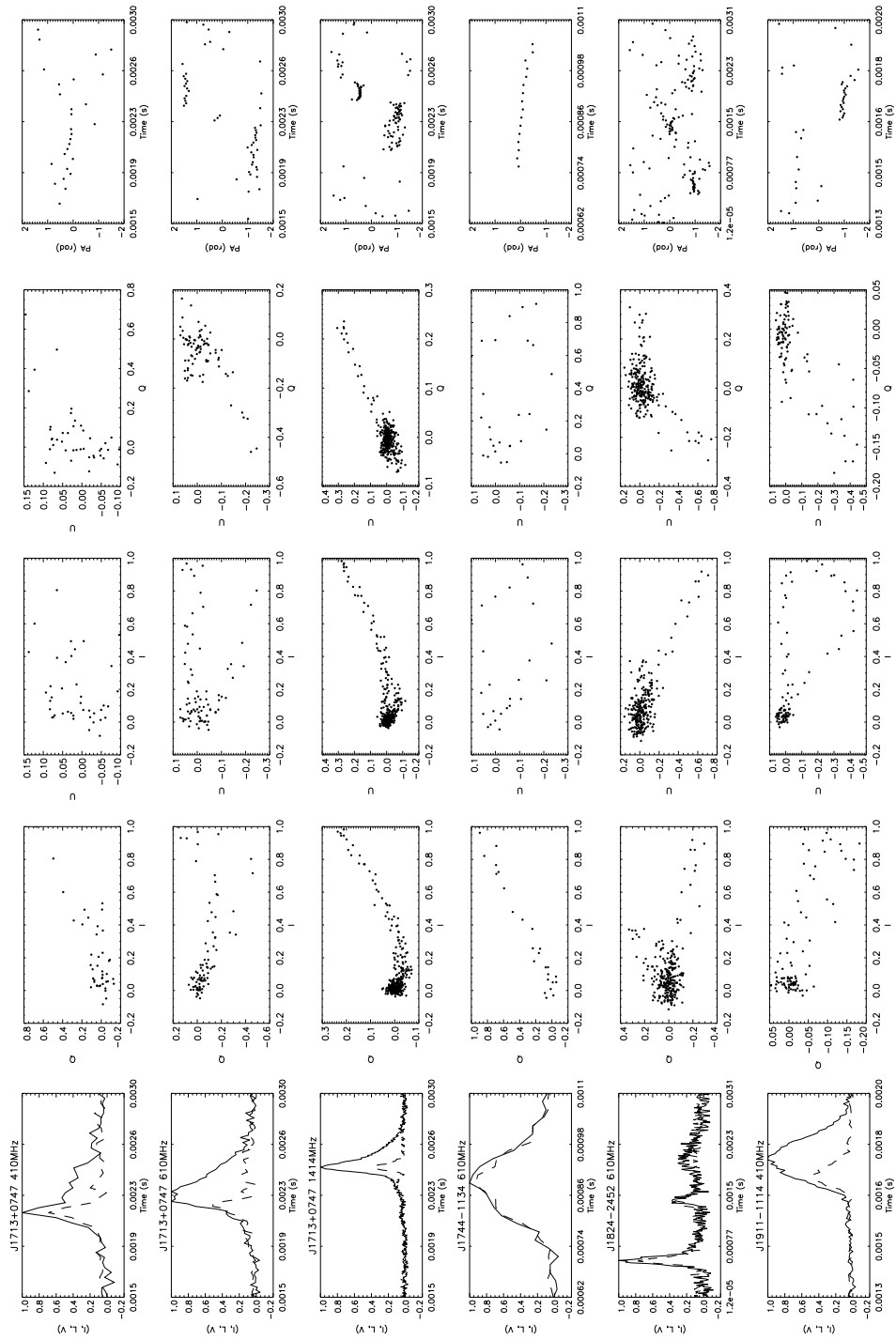


**Figure 6.6:** Pulse profiles, Stokes phase portraits and PA swings for PSR J1713+0747 at 0.41 GHz, 0.61 GHz and 1.41 GHz, PSR J1744–1134 at 0.61 GHz, PSR J1824–2452 at 0.61 GHz, and PSR J1911–1114 at 0.41 GHz (Stairs et al. 1999). The data for each pulsar occupy a row in landscape mode. From left to right, the columns show: (1)  $I/I_{\max}$  (solid curve) and  $L/I_{\max}$  (dashed curve) versus time (in s), (2) the  $I$ - $Q$  phase portrait, (3) the  $I$ - $U$  phase portrait, (4) the  $Q$ - $U$  phase portrait, (5) the PA swing versus time (in s) (data points with  $L \geq 0.1L_{\max}$  and  $I \geq 0.1I_{\max}$  plotted only). Data are presented courtesy of the EPN online archive.

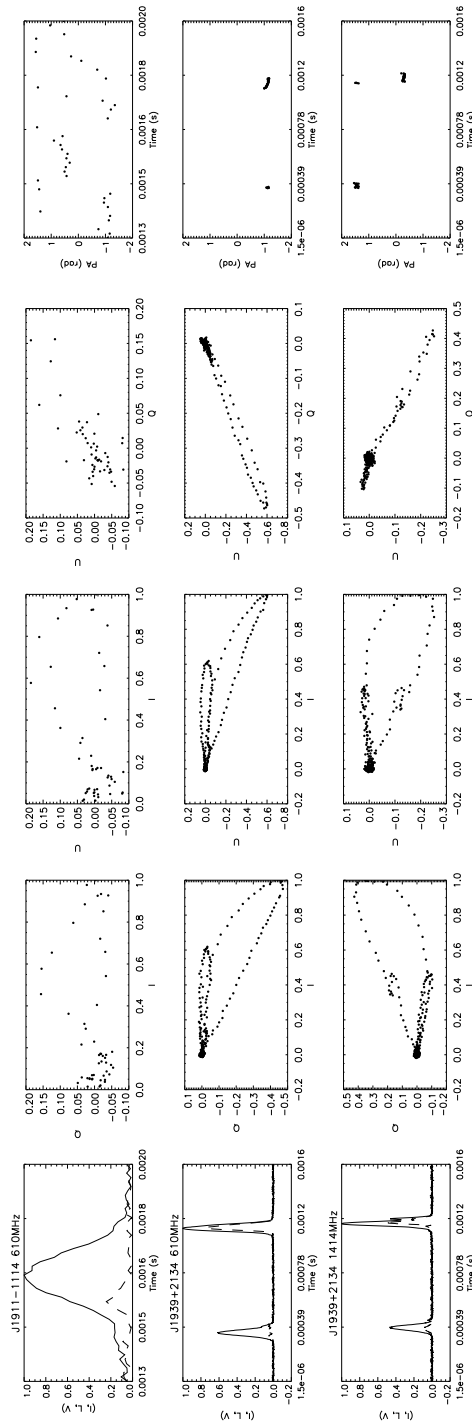


**Figure 6.7:** Pulse profiles, Stokes phase portraits and PA swings for PSR J1911–1114 at 0.61 GHz, and PSR J1939+2134 at 0.61 GHz and 1.414 GHz (Stairs et al. 1999). The data for each pulsar occupy a row in landscape mode. From left to right, the columns show: (1)  $I/I_{\max}$  (solid curve) and  $L/I_{\max}$  (dashed curve) versus time (in s), (2) the  $I$ - $Q$  phase portrait, (3) the  $I$ - $U$  phase portrait, (4) the  $Q$ - $U$  phase portrait, (5) the PA swing versus time (in s) (data points with  $L \geq 0.1L_{\max}$  and  $I \geq 0.1I_{\max}$  plotted only). Data are presented courtesy of the EPN online archive.

## 6.4 A detailed example of interpulse emission: PSR J1939+2134

In this section and the next, we model the pulse and linear polarization profiles of PSR J1939+2134 and PSR J0437–4715 in detail and attempt to determine their orientation from their Stokes phase portraits.

We first apply the iterative recipe from chapter 5 to PSR J1939+2134, which has  $P = 1.558$  ms and  $\dot{P} = 1.051 \times 10^{-19} \text{ s}^{-1}$  (Kaspi et al. 1994), making it the second-fastest known MSP. Data for this object, at 0.61 GHz and 1.414 GHz, are obtained from the EPN online archive. The data were originally published in Stairs et al. (1999). We choose this object because of its strong interpulse emission. As mentioned in chapter 5, the data published in the EPN are not expressed in the canonical polarization basis described in Section 6.2. Additionally, the emission altitude for this object has not been estimated at either frequency due to the flatness of its PA swing. We are therefore obliged to infer  $\beta$  indirectly, from qualitative considerations, in order to bring the data of both frequencies into the canonical basis.

To accomplish this, we make a few general observations, which provide insight into the magnetic geometry and emission pattern. Firstly, we note that the shape of the main pulse changes significantly from an asymmetric single-peaked profile at 0.61 GHz to an asymmetric double-peaked profile at 1.414 GHz. This suggests that the magnetic geometry and possibly the beam pattern change with emission altitude. Both pulse profiles, however, are consistent with hollow cone emission. Secondly, in the main pulse, the linear polarization follows the total intensity closely, suggesting that  $L \propto \cos \theta$  is a reasonable approximation. This is also true to a lesser degree in the interpulse.

The stellar surface of this object lies at  $0.13r_{\text{LC}}$ , placing a lower limit on the emission altitude. If we assume arbitrarily that the data at 0.61 GHz are already in the canonical basis, we find that, at  $(\alpha, i) = (20^\circ, 80^\circ)$ , the models for both pure and current-modified dipoles exhibit tilted balloons in the  $I$ - $U$  and  $Q$ - $U$  planes, similar to the data at  $r \approx 0.4r_{\text{LC}}$ . Unfortunately, without additional information on the absolute orientation of  $\Omega_p$ , we are limited to this assumption.

Figures 6.8 and 6.9 show the pulse profile, PA swing, and Stokes phase portraits of (a) the main pulse and (b) the interpulse at 0.610 GHz and 1.414 GHz respectively. For the 0.610 GHz case, we assume  $\beta = 0$ , whereas for the 1.414 GHz case, we align the narrow balloon shape in the  $Q$ - $U$  plane of Figure

6.9(a) with that of Figure 6.8(a) by assuming  $\beta = 45^\circ$ . In the top left panel of each subfigure, we plot  $I/I_{\max}$  (solid curve),  $L/I_{\max}$  (dashed curve) and the PA swing (dotted curve) wherever  $L \geq 0.1L_{\max}$ . Stepping clockwise, the next three panels show  $I-Q$ ,  $Q-U$  and  $I-U$ .

We now examine the magnetic geometry, beam pattern, orientation, and emission altitude in more depth in Sections 6.4.1–6.4.4. We find that the model with a hollow cone and  $L \propto \cos \theta$  must be generalized by letting  $I$  and  $L$  vary with  $\phi$  in order to fit the data in detail.

### 6.4.1 Magnetic geometry

At 0.61 GHz, the Stokes phase portraits for the main pulse are all narrow balloons. The major axes of the balloons tilt in different directions: we find  $dQ/dI < 0$  in the  $I-Q$  plane,  $dU/dI < 0$  in the  $I-U$  plane, and  $dU/dQ > 0$  in the  $Q-U$  plane. Assuming  $\beta = 0$ , the tilt of the  $Q-U$  phase portrait discounts a pure dipole magnetosphere at a low emission altitude. At larger altitudes where aberration is important, e.g. at  $r = 0.1r_{\text{LC}}$ , the pure and current-modified dipoles produce phase portraits that are similar enough at some orientations to warrant considering both cases.

We now seek a match from the look-up tables for a hollow cone with  $L = I \cos \theta$  (Figures A10–A12), keeping in mind that we are interested in orientations which provide an interpulse ( $\alpha$  or  $i \gtrsim 70^\circ$ ). We find that, at  $(\alpha, i) = (20^\circ, 80^\circ)$ , the phase portraits for  $I-Q$  and  $I-U$  match approximately the balloons in the data, although the sign of  $U$  is reversed (this choice of orientation is justified in Section 6.4.2).

### 6.4.2 Orientation $(\alpha, i)$

Finding the exact orientation is an iterative process, requiring the beam and polarization patterns to be adjusted at each step; see Sections 5.6 and 5.7 for examples. Initially, we seek a match to the data at 0.61 GHz (Figure 6.8). The interpulse is extremely useful in narrowing the range of possible orientations to  $70^\circ \lesssim \alpha, i \lesssim 90^\circ$ . As the interpulse is weaker than the main pulse, we know that  $\alpha$  and  $i$  are less than  $90^\circ$ . From Figures A10–A12, there are two orientations with similar balloons in all three phase portraits, namely  $(\alpha, i) = (20^\circ, 80^\circ)$ . The phase portraits for a pure dipole at  $(\alpha, i) = (20^\circ, 80^\circ)$  are also similar.

Before zooming in to refine the grid around  $(\alpha, i) = (20^\circ, 80^\circ)$ , we experiment with various emission altitudes while tailoring the pattern to fit the data.

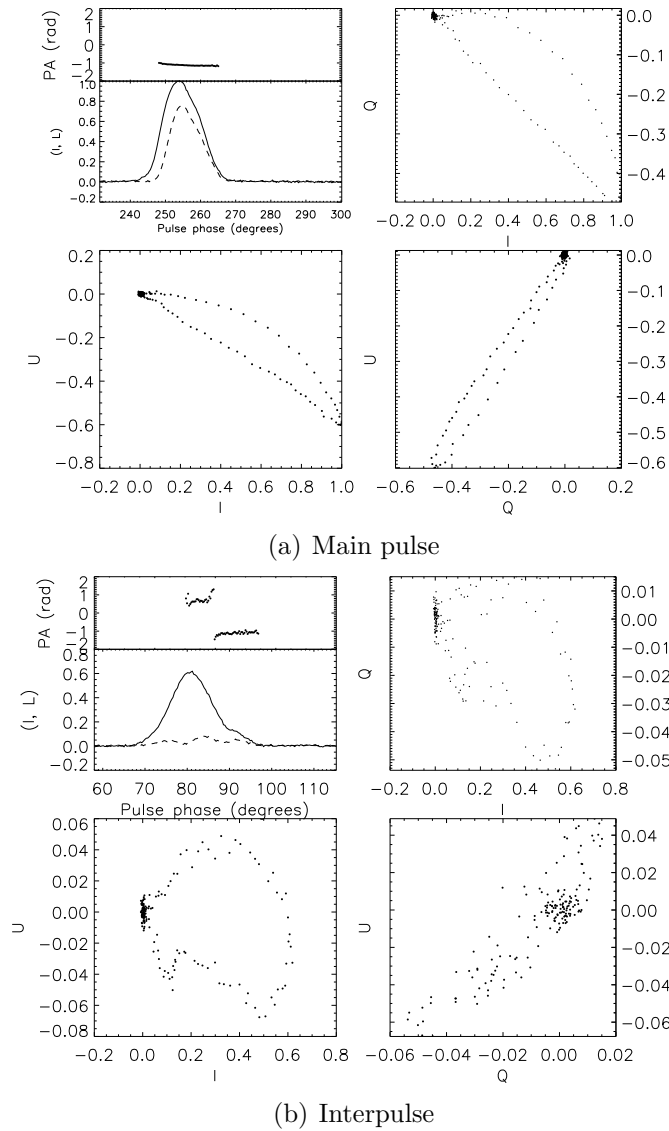


**Figure 6.8:** Polarimetry of (a) the main pulse and (b) the interpulse of PSR J1939+2134 at 0.61 GHz (Stairs et al. 1999). Each subfigure shows (clockwise from top left panel): (i)  $I/I_{\max}$  (lower subpanel, solid curve) and  $L/I_{\max}$  (lower subpanel, dashed curve) profiles and PA swing (upper subpanel, dotted curve, in rad) versus pulse phase (in degrees); (ii)  $I$ - $Q$  phase portrait; (iii)  $Q$ - $U$  phase portrait; (iv)  $I$ - $U$  phase portrait. Data are presented courtesy of the EPN.

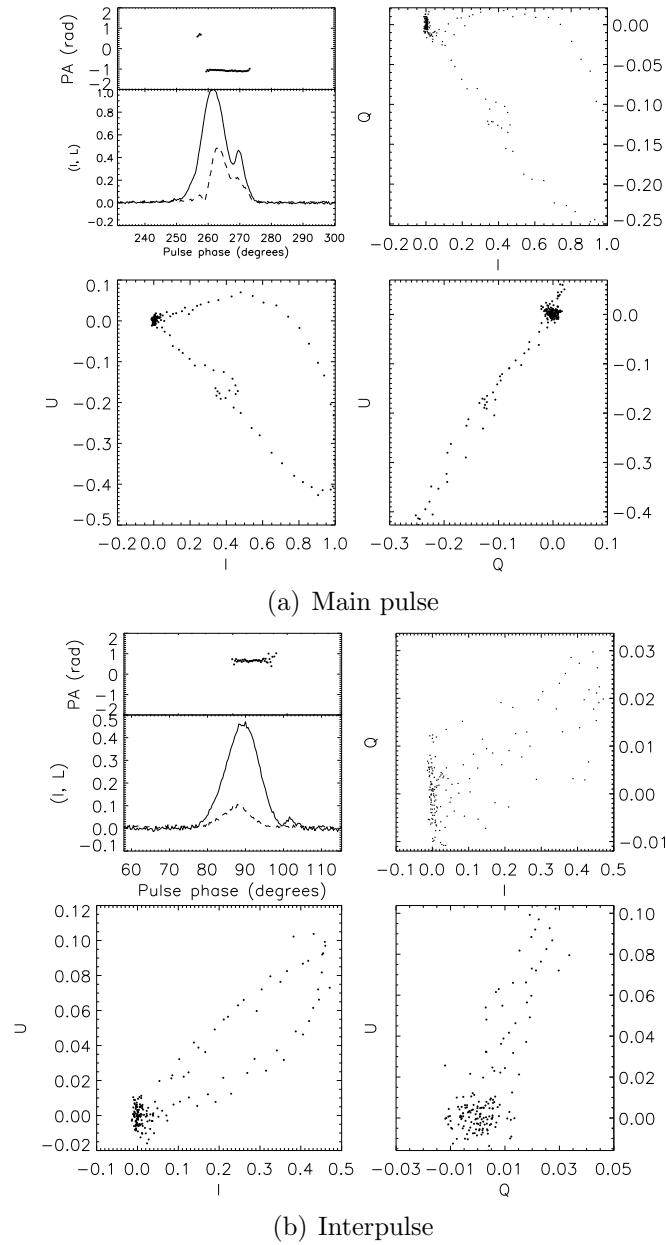


**Figure 6.9:** As for Figure 6.8 but at 1.414 GHz (Stairs et al. 1999). Data are presented courtesy of the EPN.

In Section 6.4.3, we construct beam and linear polarization patterns at the  $0.4r/r_{\text{LC}}$  for the data at 0.61 GHz.

### 6.4.3 Beam and polarization patterns

Both the main pulse and interpulse at 0.61 GHz are single-peaked and skewed to the left. The interpulse peaks at  $\approx 0.6I_{\text{max}}$ . To capture this behaviour, we model the emission region as two hollow cones whose brightness varies longitudinally, i.e. the cones are shaped like horseshoes in cross-section. The best-fit beam pattern is given empirically by

$$I(\theta, \phi) = (2\pi\sigma_1)^{-1/2} [0.8 + |\sin(\phi - 1.05)|] \times \exp[-0.5(\theta - \rho_1)^2/\sigma_1^2] \tag{6.9}$$

$$+ 0.23(2\pi\sigma_2)^{-1/2} [0.4 + |\sin(\phi - 1.65)|] \times \exp[-0.5(\theta - \pi + \rho_2)^2/\sigma_2^2], \tag{6.10}$$

where  $\sigma_1 = 3^\circ$  and  $\sigma_2 = 3.5^\circ$  are the widths of the main pulse and interpulse respectively, and  $\rho_1 = 23^\circ$  and  $\rho_2 = 35^\circ$  are the corresponding opening angles. The modelled pulses are  $\approx 3$  times wider than the data as a result of the resolution of our numerical grid.

Asymmetric emission regions are consistent with the patchy beam model introduced to explain asymmetric pulse profiles (Lyne & Manchester 1988) and with theoretical models of pulsar magnetospheres like the slot gap (Arons 1983). There are several successful precedents for pulse models with horseshoe beams, e.g. the empirical models proposed by Karastergiou & Johnston (2007), and the model for PSR J0304+1932 in Section 5.7.

The linear polarization profiles of the main pulse and interpulse at 0.61 GHz look surprisingly different, naively suggesting a north-south asymmetry. In the main pulse,  $L$  follows the pulse profile closely, lagging the pulse centroid in phase by  $\approx 4.5^\circ$ , peaking at  $\approx 0.8I_{\text{max}}$ . In the interpulse,  $L$  is extremely low, peaking at  $\approx 0.1I_{\text{max}}$ , and appears to be triple-peaked. Despite the apparent difference in the profiles, we are able to reproduce them surprisingly well using the same model, given by

$$L(\theta, \phi) = |\cos \theta \sin(\phi + 0.92)| \tag{6.11}$$

without invoking a north-south asymmetry. As expected, however, (6.11) reproduces the  $L$  profile of the main pulse more accurately than that of the

interpulse. We emphasize that (6.10) and (6.11) are certainly not unique and do not fit the data exactly, but they are adequate for the empirical task at hand.

Adopting (6.10) and (6.11), we generate zoomed-in look-up tables for both pure and current-modified dipoles, in the range  $14^\circ \leq \alpha \leq 24^\circ$ ,  $76^\circ \leq i \leq 84^\circ$ , with a resolution of  $2^\circ$ . We find the closest match is for a current-modified dipole at  $(\alpha, i) = (22^\circ, 80^\circ)$ , with a ‘by eye’ uncertainty of  $\pm 2^\circ$  for  $\alpha$  and  $\pm 1^\circ$  for  $i$  (we use ‘by eye’ in the same sense as in Sections 5.6 and 5.7). This margin would widen if  $I(\theta, \phi)$  and  $L(\theta, \phi)$  were adjusted for each orientation.

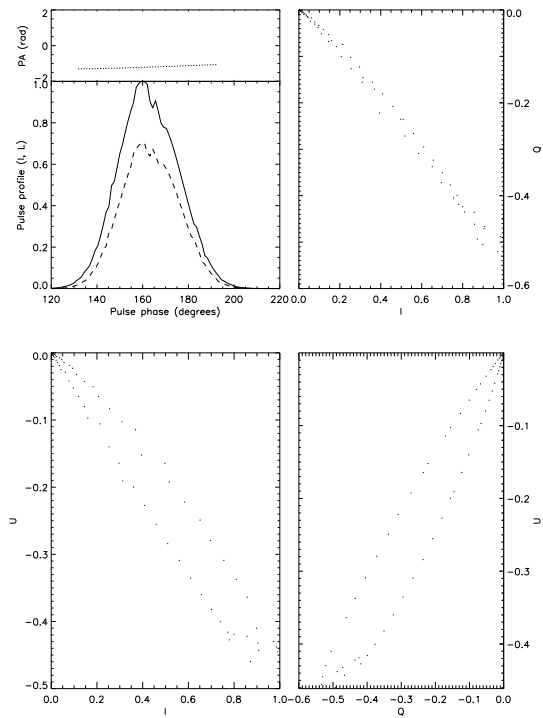
In Figure 6.10, we plot the pulse profile, PA swing and Stokes phase portraits of the model at  $r = 0.4r_{\text{LC}}$  and  $(\alpha, i) = (22^\circ, 80^\circ)$ . The jaggedness of the pulse profiles is the result of our grid resolution. The Stokes phase portraits of the main pulse [Figure 6.10(a)] match the data in Figure 6.8(a) reasonably well. In the data, the  $I$ - $Q$  balloon ranges from  $-0.5 \lesssim Q \lesssim 0$ , whereas in the model it is thinner, but has the same range. The  $I$ - $U$  balloon in the data ranges from  $-0.6 \lesssim U \lesssim 0$ , whereas in the model it ranges from  $-0.45 \lesssim U \lesssim 0$ . The PA swing from the data is flat, but has a slight negative gradient, whereas the model shows a flat swing with a slight positive gradient. For the interpulse, there is poorer agreement in  $L$ . However, the tilted balloon in  $I$ - $Q$  from the data [Figure 6.8(b)] is reproduced well in Figure 6.10(b), including the kink seen at  $(I, Q) \approx (0.2, -0.03)$ . In the  $I$ - $U$  plane, the data shows a tilted balloon, with a strong kink at  $(I, U) \approx (0.2, -0.02)$ . Our model shows a broad hockey stick instead. At a stretch, it can be argued that the balloon with the kink resembles the hockey stick qualitatively<sup>3</sup>, but the main difference is that, in the data,  $U$  covers the range  $-0.07 \lesssim U \lesssim 0.05$ , whereas in the model, we have  $-0.1 \lesssim U \lesssim 0$ . We note that if the upper half of the hockey stick was reflected about  $U = 0$ , we would obtain a more accurate match. In the  $Q$ - $U$  plane, the tilted oval seen in the data is reproduced in the model, but with a different range covered in  $U$ . The modelled PA swing is flat with a negative gradient, and lacks the phase-wrapping seen in the data.

#### 6.4.4 Emission altitude

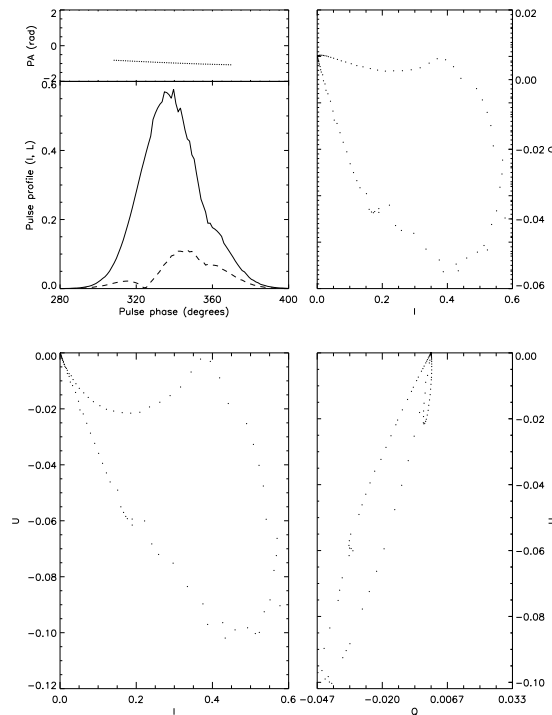
According to the standard radius-to-frequency mapping, the observation frequency scales with emission radius as  $r^{-3/2}$ . If the data at 0.61 GHz correspond to  $r = 0.4r_{\text{LC}}$ , then 1.414 GHz corresponds to  $r = 0.22r_{\text{LC}}$ . Figures 6.11–6.12 show the pulse profiles, PA swing and Stokes phase portraits for both pulses, for

---

<sup>3</sup>It can also be argued that the  $I$ - $U$  data resemble a map of the Australian continent.



(a) Main pulse



(b) Interpulse

**Figure 6.10:** Theoretical polarization model of (a) the main pulse and (b) the interpulse of PSR J1939+2134 for a current-modified dipole emitting at  $r = 0.4r_{LC}$ , with orientation  $(\alpha, i) = (22^\circ, 80^\circ)$ , beam pattern given by (6.10), and linear polarization given by (6.11). Each subfigure shows (clockwise from top left panel): (i)  $I/I_{\max}$  (lower subpanel, solid curve) and  $L/I_{\max}$  (lower subpanel, dashed curve) profiles and PA swing (upper subpanel, dotted curve, in rad) versus pulse phase (in degrees); (ii)  $I-Q$  phase portrait; (iii)  $Q-U$  phase portrait; (iv)  $I-U$  phase portrait.

emission altitudes ranging from  $r = 0.21r_{\text{LC}}$  to  $0.35r_{\text{LC}}$ . The relative strengths of the pulses change with emission altitude. We label them Pulse 1 (Figure 6.11), corresponding to the main pulse in the data, and Pulse 2 (Figure 6.12), corresponding to the interpulse in the data.

The theoretical pulse profile and phase portraits at  $r = 0.22r_{\text{LC}}$  (Figures 6.11–6.12, top row) display some interesting features. First, the main pulse and interpulse have roughly the correct shapes, but swap positions in phase, i.e. the hollow cone which emits the main pulse at  $r = 0.4r_{\text{LC}}$  emits the interpulse at  $r = 0.22r_{\text{LC}}$ , and vice versa. Upon inspection, it is likely that the same is true in the data. The triple-peaked linear polarization profile seen in Figure 6.8(b) is also present in Figure 6.9(a), although the first component in  $L$  is much weaker than the second and third at 1.414 GHz. Additionally, the kinks seen in the  $I$ - $Q$  and  $I$ - $U$  planes of Figure 6.8(b) are seen in Figure 6.9(a). In the data, the interpulse peaks at  $\approx 0.5I_{\text{max}}$ , compared to  $\approx 0.35I_{\text{max}}$  in the model at  $r = 0.28r_{\text{LC}}$ .

Second, the linear polarization profile and phase portraits at  $r = 0.22r_{\text{LC}}$  do not reproduce the data very well. The linear polarization of the main pulse (Pulse 1; Figure 6.11, top row) is  $\approx 50\%$  weaker than observed [Figure 6.9(a)]. Also, in the simulated profile, the third  $L$  peak in the main pulse is comparable to the second peak, while in the data it is weaker. In the simulated  $I$ - $Q$  plane of the main pulse, we see a distorted hockey-stick instead of the expected balloon. In the simulated  $I$ - $U$  plane of the main pulse, there is a reasonable match to the balloon in the data. The kink seen in the data at  $(I, U) \approx (0.4, -0.1)$  is reproduced at  $(I, U) \approx (0.6, -0.25)$  in the model. In the  $Q$ - $U$  plane, the data trace out a straight line with  $dU/dQ > 0$ . Unsurprisingly, the discrepancies in the other two phase portraits lead to a mismatch in  $Q$ - $U$ , where the simulated phase portrait shows a heart shape instead. For the interpulse (Pulse 2; Figure 6.12, top row) the linear polarization is  $\approx 2$  times stronger than observed [Figure 6.9(b)]. The simulated and observed balloons in the  $I$ - $Q$  and  $I$ - $U$  planes are rotated by  $90^\circ$  clockwise with respect to the data, whereas the  $Q$ - $U$  balloon is rotated by  $180^\circ$ .

As the emission altitude increases from  $r = 0.22r_{\text{LC}}$  to  $r = 0.35r_{\text{LC}}$ , the phase portraits of the main pulse (Pulse 1; Figure 6.11) change significantly. In the  $I$ - $Q$  plane, the hockey stick widens into a balloon with a kink at  $(I, Q) \approx (0.4, -0.05)$ , and the shapes rotate clockwise about  $(I, Q) = (0, 0)$ . At  $r = 0.35r_{\text{LC}}$ , the balloon in the  $I$ - $U$  plane starts to resemble the hockey stick seen in Figure 6.10(b). In  $Q$ - $U$ , the heart shape rotates counter-clockwise and narrows into a balloon with a kink at  $(Q, U) = (-0.06, -0.14)$  at  $r = 0.35r_{\text{LC}}$ . We note

that the simulated data for Pulse 1 at  $0.35r_{\text{LC}}$  appears to be a better match to the 1.414 GHz data. In the interpulse (Pulse 2; Figure 6.12), the changes are less marked. The  $I$ - $Q$  balloon narrows and lengthens in  $Q$ , and the  $Q$ - $U$  balloon narrows.

From Figures 6.11–6.12, we draw the following conclusions. (i) Although the simple model given by (6.10) and (6.11) models the 0.61 GHz data reasonably successfully, it fails for the data at 1.414 GHz. However, the observed pulse profiles and Stokes phase portraits suggest that the emission region of the main pulse at 0.61 GHz corresponds to that of the interpulse at 1.414 GHz, and vice versa. Additionally, the emission pattern may change with radius. (ii) The discrepancies between the data and the phase portraits at  $r = 0.22r_{\text{LC}}$  (the altitude predicted by the radius-to-frequency mapping) indicate that the toroidal field may not increase monotonically with  $r$ . We note that the phase portraits at  $r = 0.35r_{\text{LC}}$  provide a better match for the main pulse, which indicates that the emission does not strictly obey radius-to-frequency mapping. However, the phase portraits for the interpulse are still a poor match at this altitude. (iii) It is possible that the data has a different value of  $\beta$  at 1.414 GHz than the one we assume, which would introduce a rotation in the  $Q$ - $U$  plane, and shape changes in the  $I$ - $Q$  and  $I$ - $U$ . The fact that the modelled phase portraits rotate generically with emission altitude suggests that the  $Q$ - $U$  planes of the 0.610 GHz and 1.414 GHz data do not necessarily align.

## **6.5 A detailed multi-peaked example: PSR J0437–4715**

We now repeat the procedure in Sections 5.6, 5.7, and 6.4 for PSR J0437–4715. This object has  $P = 5.758$  ms and  $\dot{P} = 5.729 \times 10^{-20}$  s s $^{-1}$  (Bell et al. 1997). It was chosen because it exhibits five distinct peaks in its pulse profile, clearly visible at 1.44 GHz, and a highly structured PA swing. There is no interpulse observed in this object. Unlike the other objects considered in this chapter and chapter 5, we find that PSR J0437–4715 cannot be modelled by either a pure or a current-modified dipole field, even if a multiple-peaked beam pattern is constructed empirically to fit the  $I(t)$  data exactly. Indeed, the enhanced diagnostic power of the Stokes phase portraits points persuasively to the existence of a strong quadrupole and higher-order multipoles at the radio emission altitude. In this respect, PSR J0437–4715 is an excellent candidate for more detailed Stokes tomography studies in the future. In this section, we re-

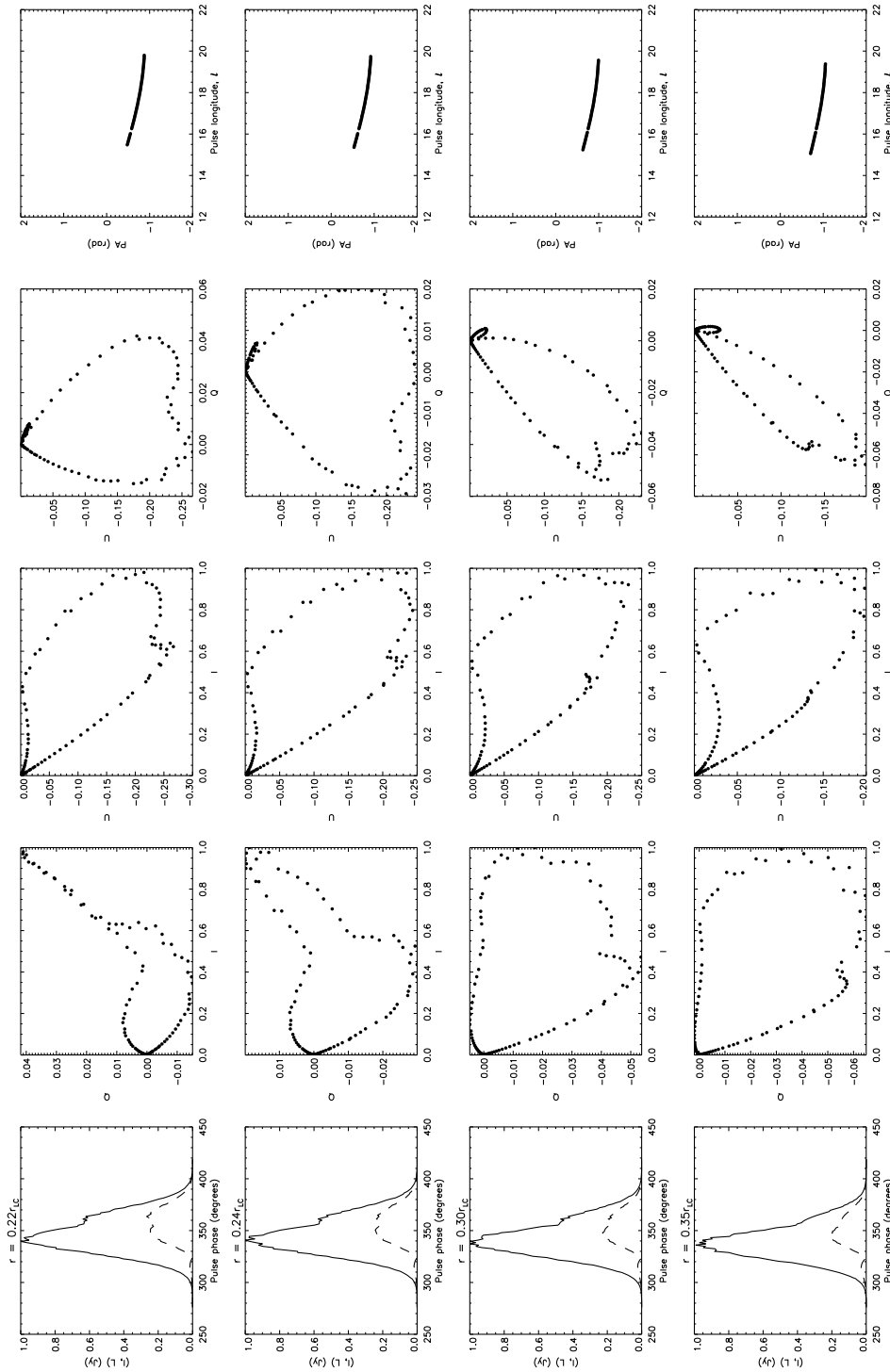


**Figure 6.11:** Theoretical polarization model of Pulse 1 of PSR J1939+2134 as a function of emission altitude, for a current-modified dipole with  $(\alpha, i) = (22^\circ, 80^\circ)$ . In landscape mode, the plots for each emission altitude occupy rows, increasing from  $r = 0.22r_{LC}$  (top row) to  $r = 0.35r_{LC}$  (bottom row). From left to right, the columns show (1)  $I/I_{max}$  (solid curve) and  $L/I_{max}$  (dashed curve) versus pulse phase  $l$  (in units of degrees), (2)  $I$ - $Q$  phase portrait, (3)  $I$ - $U$  phase portrait, (4)  $Q$ - $U$  phase portrait, and (5) the PA swing (in rad; data points with  $L \geq 0.1I_{max}$  plotted only).

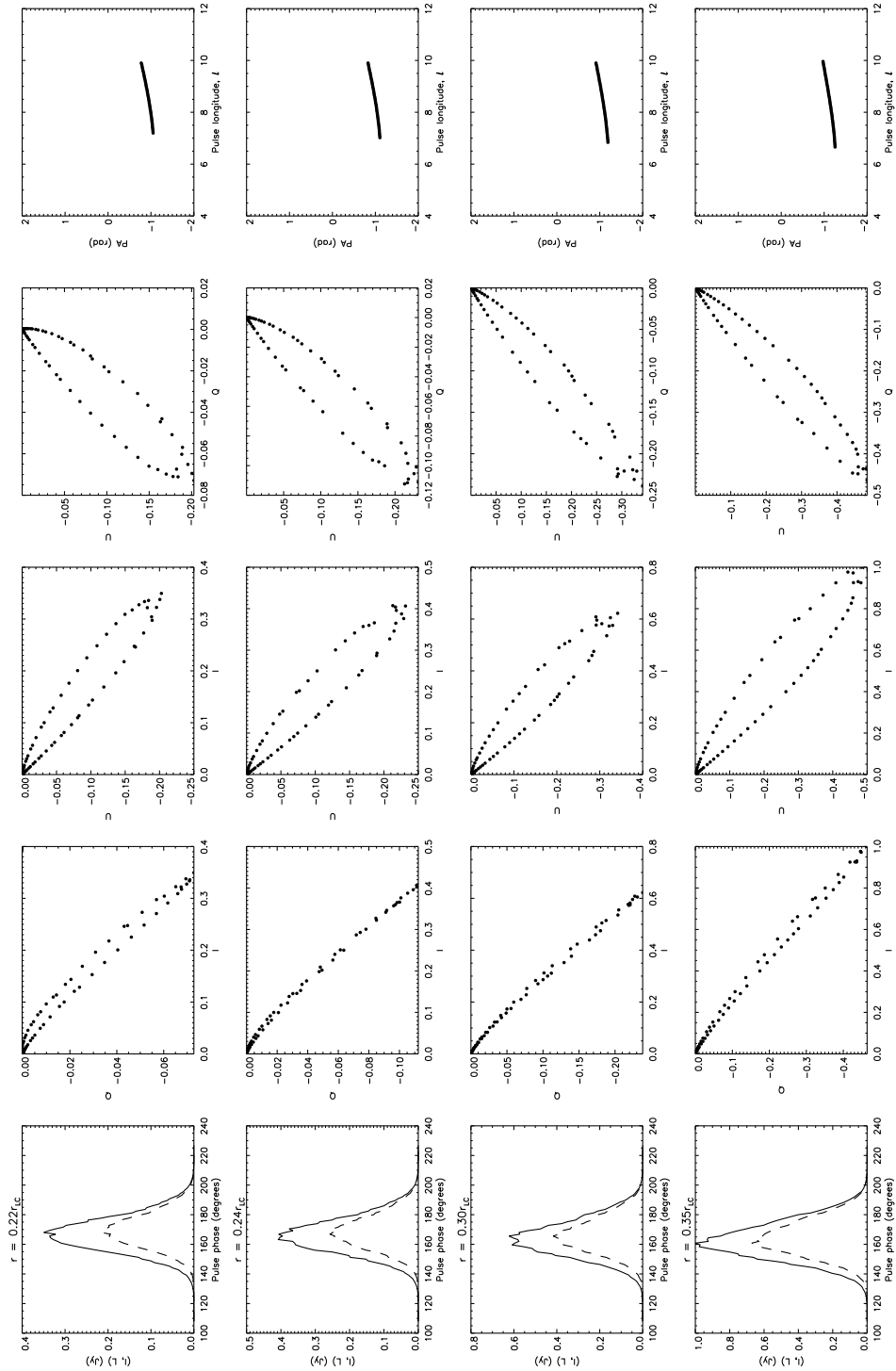
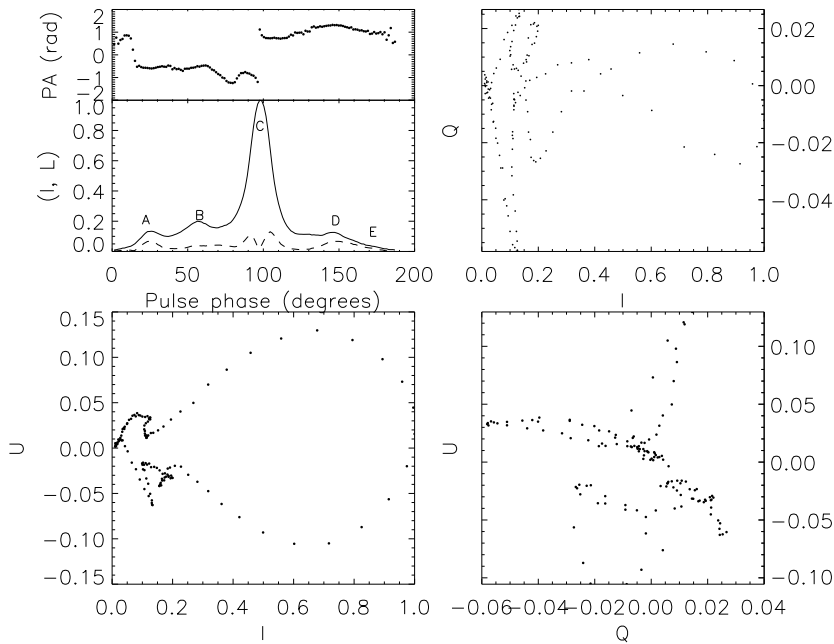


Figure 6.12: As for Figure 6.11 but for Pulse 2 of PSR J1939+2134.



**Figure 6.13:** Polarimetry of PSR J0437–4715 at 1.44 GHz (Manchester & Johnston 1995). Clockwise from top left panel: (a)  $I/I_{\max}$  (lower subpanel, solid curve) and  $L/I_{\max}$  (lower subpanel, dashed curve) profiles, and PA swing (upper subpanel, dotted curve, in rad) all plotted against pulse phase (in degrees); (b)  $I$ - $Q$  phase portrait; (c)  $Q$ - $U$  phase portrait; (d)  $I$ - $U$  phase portrait. Data are presented courtesy of the EPN.

strict ourselves to presenting the argument that the pure and current-modified dipoles categorically fail to match the data for the polarization models that work well for the other objects studied in this chapter and chapter 5.

Data for PSR J0437–4715, at 1.44 GHz and 4.6 GHz, are obtained from the EPN online archive. The data were originally published by Manchester & Johnston (1995). Figure 6.13 presents the pulse profile, phase portraits, and PA swing (in rad) at 1.4 GHz. The top left panel shows  $I/I_{\max}$  (solid curve),  $L/I_{\max}$  (dashed curve) and the PA swing (dotted curve, at longitudes where  $L \geq 0.1L_{\max}$ ). Stepping clockwise, the next three panels show  $I$ - $Q$ ,  $I$ - $U$  and  $Q$ - $U$ .

As with PSR 1939+2134, we assume that the data obtained from the EPN are presented in the canonical polarization basis at one reference frequency, chosen here to be 1.44 GHz. The stellar surface is at  $r = 0.036r_{\text{LC}}$ , providing a lower limit on the emission altitude. The pulse profile has five components, labelled A–E in Figure 6.13, two on either side of the largest peak (C). Each component in the pulse profile corresponds to a distinct sub-pattern in the Stokes phase portraits. In the  $I$ - $Q$  plane, peaks A and B correspond to the two small loops at  $Q > 0$ , peak C is the large figure-eight, and peaks D and E

correspond to the loop at  $Q < 0$ . In the  $I$ - $U$  plane, peaks A and B correspond to the kinks at  $U < 0$ , peak C is the large balloon, and peaks D and E correspond to the kink at  $U > 0$ . The  $U$ - $Q$  plane is complicated, forming a rough X-shape, with one diagonal having  $dU/dQ > 0$  (we call this diagonal 1), and the other having  $dU/dQ < 0$  (diagonal 2). Diagonal 1 corresponds to peak C. In diagonal 2, peaks A and B occupy the  $Q > 0$  region, whereas peaks D and E occupy the  $Q < 0$  region.

The linear polarization within peak C is double-peaked. This kind of structure is common and is best modelled by a filled core beam with  $L = I \sin \theta$ , as demonstrated for several objects in chapter 5. The phase separation of the peaks suggests that A, B, D, and E originate from two hollow cones centred on the same axis (peak C). Peak pairs B/C and C/D are separated by  $\approx 0.7$  rad and  $\approx 0.9$  rad respectively, while A/C and C/E are both separated by  $\approx 1.2$  rad. We confirm a posteriori that  $\alpha$  and  $i$  lie in ranges where interpulse emission does not contribute significantly.

### 6.5.1 Magnetic geometry

In order to determine the magnetic geometry, we search the look-up tables for a good match involving a filled core and a hollow cone beam. We assume  $L = I \sin \theta$  because of the double-peaked  $L$  profile in peak C. The phase portraits for the filled core should match the large patterns corresponding to peak C, while the phase portraits for the hollow cone should match the smaller patterns. We do not expect perfect matches due to the complex beam and polarization patterns. At a minimum, however, we seek an approximate match for the rough figure-eight that forms diagonal 1 in the  $Q$ - $U$  plane, the figure-eight in  $I$ - $Q$  and the balloon in  $I$ - $U$ .

The pure dipole look-up tables at  $r = 0.1r_{LC}$  do not feature figure-eight shapes in the  $I$ - $Q$  plane for any orientation. For  $\alpha < i$ , there are balloons in  $I$ - $U$ , and heart shapes in  $Q$ - $U$ .

For the current-modified dipole (Figures A6–A8), the closest match is at  $(\alpha, i) = (30^\circ, 30^\circ)$  (see Section 6.5.2 for a detailed justification). For a filled core, there are asymmetric figure-eights in the  $Q$ - $U$  and  $I$ - $U$  planes (Figures A6–A8), and a broad oval in  $I$ - $Q$  (Figure A6). The hollow cone phase portraits at this orientation feature asymmetric mosquitoes in  $I$ - $Q$  and  $I$ - $U$  (Figure A14–A15) and an asymmetric heart shape in  $Q$ - $U$  (Figure A16). At this stage, we cannot confidently discount either magnetic configuration, as the Stokes portraits can change when the filled core and hollow cones are combined. This

issue is examined thoroughly in Sections 6.5.3–6.5.4.

## 6.5.2 Orientation

In this section, we justify  $(\alpha, i) = (30^\circ, 30^\circ)$  as the best matching orientation. As PSR J0437–4715 does not have an observed interpulse, we rule out all orientations with  $\alpha \geq 80^\circ, i \geq 80^\circ$ . We also rule out orientations with  $i > \alpha$  because the associated phase portraits look nothing like the data. For example, for a filled core, Figures A6–A8 contain balloons in  $I$ - $Q$ , narrow, tilted balloons and straight lines in  $I$ - $U$ , and ovals in  $U$ - $Q$ . None of these patterns appear in the data in Figure 6.13. The  $Q$ - $U$  discrepancy is especially significant as the shape of the  $Q$ - $U$  portrait is basis-independent.

We reiterate that the complex multiple-peaked beam and polarization patterns complicate the matching process. Some orientations must be tested with beam patterns tailored to fit the data, as described in Section 6.5.3, before being ruled out. For  $(\alpha, i) = (30^\circ, 30^\circ)$ , the appropriate beam pattern is a filled core surrounded by two hollow cones. The resulting phase portraits show distorted, tilted balloons in both  $I$ - $Q$  and  $I$ - $U$ . These shapes resemble roughly the data in Figure 6.13, although there are large discrepancies too, chiefly that the figure-eight in  $I$ - $Q$  is missing, and that  $I$ - $U$  is not symmetric about  $U = 0$ . In Sections 6.5.3 and 6.5.4, we construct detailed beam and linear polarization models in an attempt to improve the fits.

## 6.5.3 Beam pattern

In fitting the complex pulse profile of PSR J0437–4715 at 1.44 GHz, Gangadhara & Thomas (2008) identified 11 Gaussian components. They proposed that the beam pattern comprises five nested cones at different altitudes centred on the filled core, and that the altitudes range from  $0.07r_{\text{LC}}-0.3r_{\text{LC}}$ .

We consider a simpler model and focus on one fixed altitude. We model the pulse profile empirically with a filled core,  $I_1(\theta, \phi)$  (peak C), surrounded by two hollow cones,  $I_2(\theta, \phi)$  (peaks B and D) and  $I_3(\theta, \phi)$  (peaks A and E). The

intensity maps take the *empirical* form

$$I_1(\theta, \phi) = (2\pi\sigma_1^2)^{-1/2} \left\{ \exp \left[ -\theta^2 / (2\sigma_1^2) \right] + \exp \left[ -(\theta - \pi)^2 / (2\sigma_1^2) \right] \right\}, \quad (6.12)$$

$$I_2(\theta, \phi) = \beta_2(\phi)(2\pi\sigma_2^2)^{-1/2} \left\{ \exp \left[ -(\theta - \rho_2)^2 / (2\sigma_2^2) \right] + \exp \left[ -(\theta - \pi + \rho_2)^2 / (2\sigma_2^2) \right] \right\}, \quad (6.13)$$

$$I_3(\theta, \phi) = \beta_3(\phi)(2\pi\sigma_3^2)^{-1/2} \left\{ \exp \left[ -(\theta - \rho_3)^2 / (2\sigma_3^2) \right] + \exp \left[ -(\theta - \pi + \rho_3)^2 / (2\sigma_3^2) \right] \right\}, \quad (6.14)$$

where  $\sigma_1 = 6.5^\circ$ ,  $\sigma_2 = 2.5^\circ$  and  $\sigma_3 = 2^\circ$  are the beam widths of the core and cones,  $\rho_2 = 18^\circ$  and  $\rho_3 = 26^\circ$  are the opening angles of the two cones, and  $\beta_2(\phi)$  and  $\beta_3(\phi)$  are functions describing the longitudinal structure of the two cones, given empirically by

$$\beta_2(\phi) = 0.06|\cos(0.3\phi)|, \quad (6.15)$$

$$\beta_3(\phi) = 0.06|\cos(0.75\phi)|. \quad (6.16)$$

As in Section 6.4, the cones are shaped like horseshoes. Given (6.12)–(6.14), we also find that the linear polarization pattern is fitted empirically by

$$L(\theta, \phi) = (3\theta)^{-1} \sin(\theta - 0.026) - 0.07|\cos(0.75\phi)| \times (2\pi\sigma_2^2)^{-1/2} \exp \left[ -(\theta - \rho_2)^2 / (2\sigma_2^2) \right]. \quad (6.17)$$

We emphasize that equations (6.12)–(6.17) are not unique fits, nor do they produce perfect agreement with the data. In particular, the data show that the B/C peaks are closer to each other than C/D, yet we are unable to reproduce this with a reasonably simple model. Our modelled peaks are equidistant. We also artificially double the width of peak C in order to accommodate the resolution of the numerical grid. The models are sensitive to the pulsar's orientation. Every time we vary  $\alpha$  or  $i$  around  $(30^\circ, 30^\circ)$ , we must adjust the coefficients in (6.12)–(6.17). We find that the closest match to the data, although poor, is achieved at  $(\alpha, i) = (32^\circ, 26^\circ)$ . Due to the poor fit, we do not assign uncertainties to this orientation. The difficulty in achieving a good match may well be telling us that the underlying magnetic geometry is not a current-modified dipole.

### 6.5.4 Decomposed phase portraits

We now demonstrate how the Stokes phase portraits change as we add  $I_2$  and  $I_3$  to the filled core  $I_1$ . Figure 6.14 shows the pulse profile, PA swing, and phase portraits for  $I_1$ ,  $I_1 + I_2$ , and  $I_1 + I_2 + I_3$  respectively at an emission altitude of  $r = 0.1r_{\text{LC}}$ .

For just the filled core (Figure 6.14, top row), corresponding to peak C in the data, there is a figure eight in  $I$ - $Q$ , a upside-down hockey stick in  $I$ - $U$ , and two interlocking ovals in  $Q$ - $U$ . Aside from the obvious dissimilarity with the balloon shape seen in the data in  $I$ - $U$ , the interlocking ovals in  $Q$ - $U$  do not resemble diagonal 1 in the data, irrespective of the orientation. The figure-eight in  $I$ - $Q$  is an approximate match to the data.

For the filled core and one hollow cone (Figure 6.14, middle row), i.e. peaks B, C and D in the data, the conal components broaden the figure eight in  $I$ - $Q$  in the region  $I \lesssim 0.2$  and introduce a kink at  $(I, Q) \approx (0.2, -0.03)$ . In the  $I$ - $U$  plane, kinks are also predicted to occur at  $I \lesssim 0.2$ . The data also contains kinks in this region. In the  $Q$ - $U$  plane, there is another kink near  $(Q, U) \approx (0, 0)$ , though the model is still a poor match to the data.

The addition of the second hollow cone in Figure 6.14 (third row) completes the beam pattern. Still, the overall shapes of the phase portraits do not match the data. The second cone appears as an extra kink in  $I$ - $Q$  and  $I$ - $U$  in the region  $I \lesssim 0.15$ . In  $Q$ - $U$ , the interlocking ovals shift so to form a third, tilted oval in the centre. At a stretch, it might be said that this third oval corresponds to one diagonal of an X-shape while the two interlocking ovals correspond to another. However, we note that if the data are rotated so that the diagonals in the  $Q$ - $U$  plane lines up with the interlocking ovals in the model (i.e.  $\beta \approx 60^\circ$ ), we still obtain poor matches in the  $I$ - $Q$  and  $I$ - $U$  planes. Adjusting the emission altitude does not improve the fit.

For completeness, in Figure 6.15, we present the pulse profile, PA swing, and phase portraits for a filled core with two hollow cones for a pure dipole field at the same orientation and altitude. The phase portraits are a poorer match to the data than the current-modified dipole. The  $I$ - $Q$  plane features a tilted, asymmetric balloon, whereas the  $I$ - $U$  plane features an asymmetric figure-eight. In the  $Q$ - $U$  plane, there is a distorted oval surrounded by a tilted heart shape. Again, the basis-independent  $Q$ - $U$  shape does not resemble the data at all. The kinks seen in the phase portraits of the current-modified dipole also appear in the pure dipole.

We note that, for both the pure and current-modified dipoles, the theoretical

PA swings are smooth and relatively flat and do not contain any of the kinks seen in the data. Attempts to rotate the  $Q$ - $U$  data to yield a better fit, i.e. testing several values of  $\beta$ , are unsuccessful. For example, for  $\beta = 150^\circ$ , in the  $Q$ - $U$  plane, diagonal 1 aligns with the large, interlocking ovals in the model while diagonal 2 aligns with the smaller, third oval. However the  $I$ - $Q$  plane now features a large balloon symmetric about  $Q = 0$ , and the  $I$ - $U$  plane features a broad, tilted balloon, neither of which is a good match to the data.

We conclude that we are unable to fit the Stokes phase portraits for PSR J0437–4715 satisfactorily using a pure or current-modified dipole and the empirical models for the beam and linear polarization patterns which work well in other pulsars, e.g. in chapter 5. There are several possible reasons for this. (i) The beam and polarization patterns might be very different, e.g. two highly asymmetric, nested cones. This would mean that our estimates of  $\alpha$ ,  $i$ ,  $I(t)$  and  $L(t)$  are inaccurate. (ii) If the observed emission does indeed originate from multiple altitudes (Gangadhara & Thomas 2008), we would be unable to reproduce the Stokes phase portraits even if our estimates for  $\alpha$ ,  $i$ ,  $I(t)$  and  $L(t)$  are correct. (iii) The magnetic field in the emission region is neither a pure nor a current-modified dipole.

## 6.6 Conclusion

In this chapter, we generalize the Stokes tomography technique introduced in chapter 5 by adding interpulse emission. In Section 6.3, we present the Stokes phase portraits of 15 MSPs from the EPN online archive. By comparing the data to the generalized look-up tables for a current-modified dipole in Appendix 6A, we are able to infer approximately the geometric orientations for five of the MSPs. This is an improvement on the PA swing and rotating vector model, which yield orientations for only two of the objects — orientations which, it transpires, are inconsistent with the observed Stokes phase portraits. In Section 6.4, we model PSR J1939+2134 in detail, obtaining a match for the data at 0.61 GHz with a current-modified dipole for  $(\alpha, i) = (22 \pm 2^\circ, 80 \pm 1^\circ)$  and  $r = 0.4r_{\text{LC}}$ . However, we are unable to reproduce the data at 1.414 GHz for the same orientation at altitudes in the range  $0.22r_{\text{LC}} \leq r \leq 0.35r_{\text{LC}}$ . In Section 6.5, we repeat the process with PSR J0437–4715. At 1.44 GHz, the closest-matching orientation,  $(\alpha, i) = (32^\circ, 26^\circ)$  with  $r = 0.1r_{\text{LC}}$ , does not reproduce the data satisfactorily.

The results from Sections 6.4 and 6.5 indicate that, while pure or current-

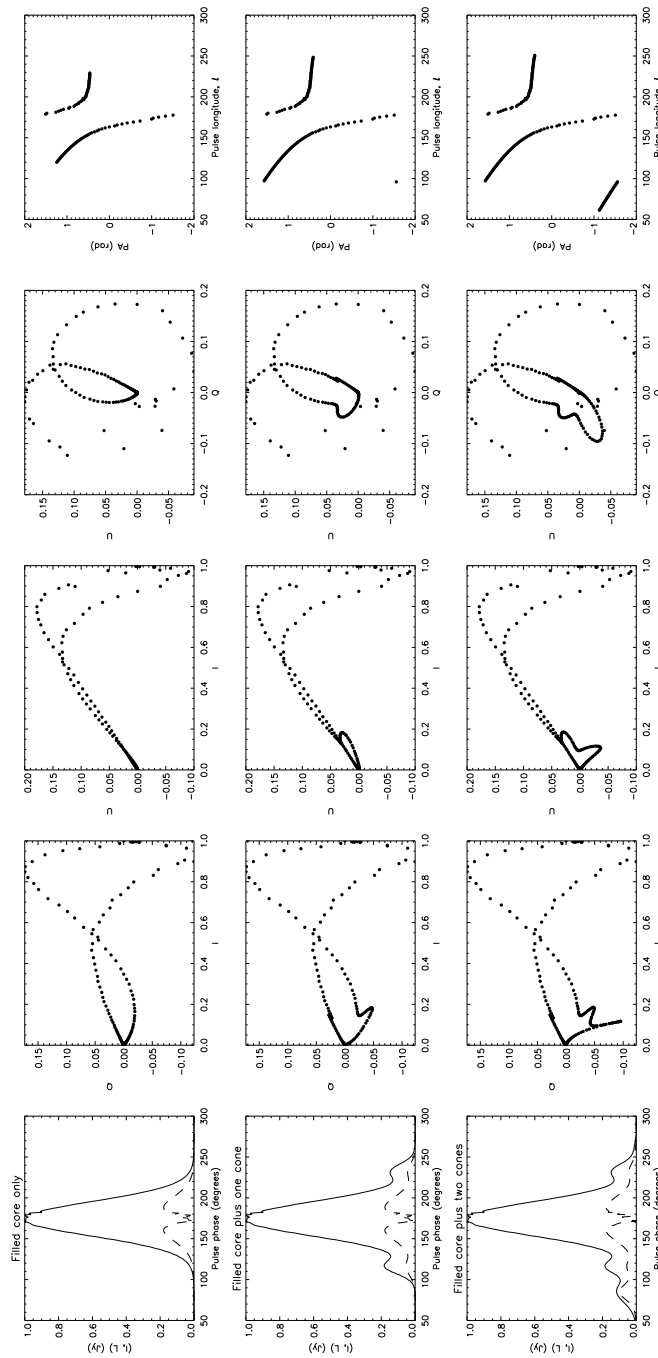


**Figure 6.14:** Bottom-up, component-wise assembly of theoretical polarization models for PSR J0437-4715 for a current-modified dipole emitting at  $r = 0.1r_{\text{LC}}$  with  $(\alpha, i) = (32^\circ, 26^\circ)$ . In landscape orientation, from top to bottom, we plot the following beam patterns: (a) peak C, filled core, equation (6.12); (b) peaks B-D, filled core plus hollow cone, equations (6.12) and (6.13), and (c) peaks A-E, filled core plus two hollow cones, equations (6.12), (6.13) and (6.14). Linear polarization in all three rows is given by (6.17). From left to right, the columns contain (1)  $I/I_{\max}$  (solid curve) and  $L/I_{\max}$  (dashed curve) profiles, plotted against pulse phase (in units of degrees); (2)  $I-Q$  phase portrait; (3)  $I-U$  phase portrait; (4)  $Q-U$  phase portrait, and (5) PA swing (dotted curve, in rad).

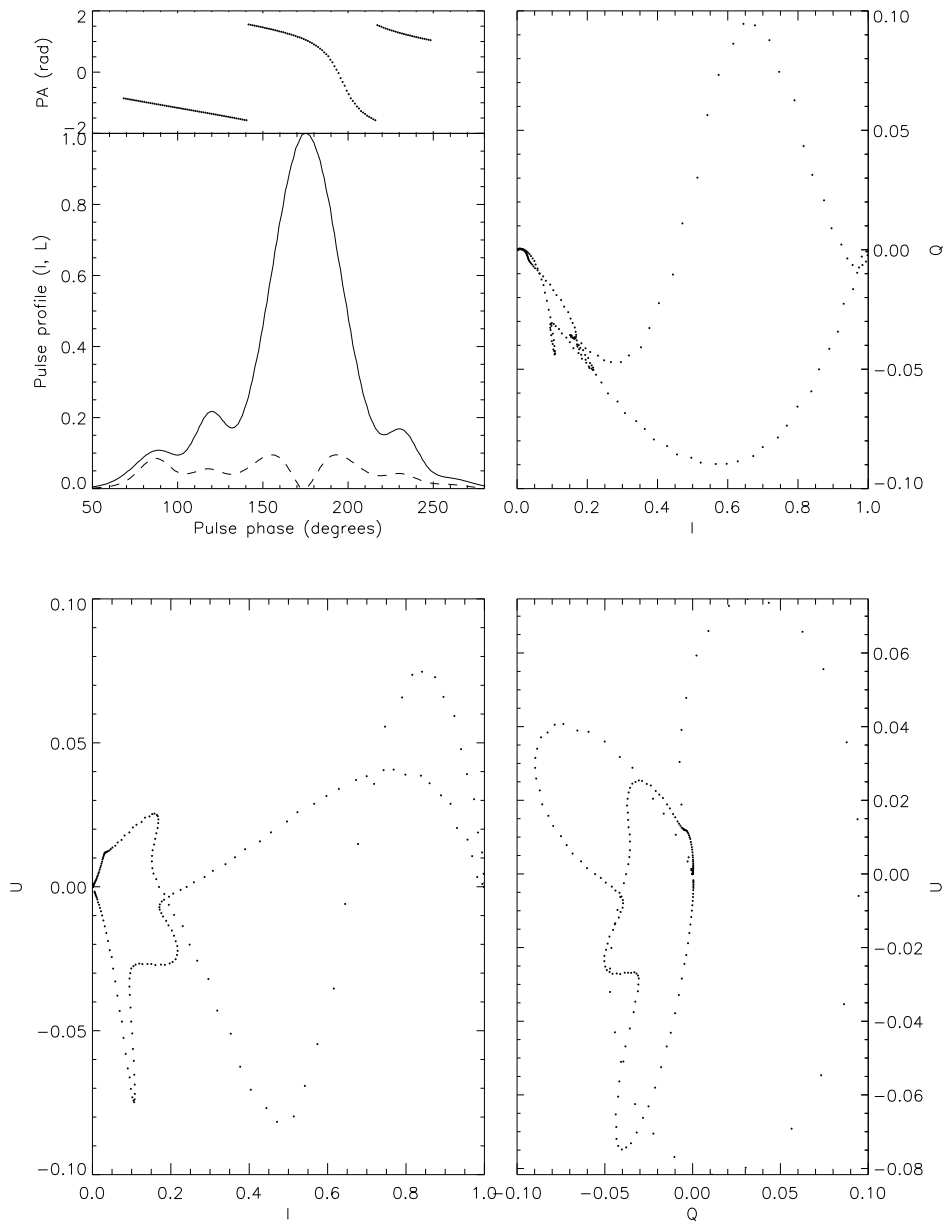


**Figure 6.15:** Theoretical polarization model of PSR J0437–4715 for a pure dipole emitting at  $r = 0.1r_{\text{LC}}$  with  $(\alpha, i) = (32^\circ, 26^\circ)$ , beam pattern given by (6.12), (6.13) and (6.14), and linear polarization given by (6.17). Clockwise from top left panel: (a)  $I/I_{\text{max}}$  (lower subpanel, solid curve) and  $L$  (lower subpanel, dashed curve) profiles, and PA swing (upper subpanel, dotted curve, in rad) all plotted against pulse phase (in units of degrees) (b)  $I$ - $Q$  phase portrait; (c)  $Q$ - $U$  phase portrait; (d)  $I$ - $U$  phase portrait.

modified dipoles are an effective model for non-recycled pulsars (chapter 5), MSPs are likely to have more complicated magnetic geometries. This is not surprising, as the accretion process can significantly distort a pulsar's magnetic field (Lai et al. 1999; Payne & Melatos 2004; Lamb et al. 2009). Alternative magnetic configurations include a surface quadrupole (Lai et al. 1999; Long et al. 2008), a force-free field (Spitkovsky 2006; Bai & Spitkovsky 2009a), a vacuum-like field (Melatos 1997), or a field distorted by the formation of a polar magnetic mountain (Payne & Melatos 2004; Vigelius & Melatos 2008).

We emphasize the utility of the Stokes phase portraits as a diagnostic tool for MSPs, as the degeneracy of the PA swing is especially ambiguous when dealing with non-dipolar fields. Future work will focus on the role played by circular polarization in Stokes tomography, the longitudinal structure of vacuum and force-free magnetospheres, and the polarization signatures of magnetic mountains. These topics will be the subject of companion papers.

# 7 Conclusion

## 7.1 Multimessenger studies of neutron stars

The work presented in this thesis utilizes radio, X-ray, and gravitational wave emission from neutron stars to determine the fundamental properties of these objects, which cannot be directly measured. In Table 1.1 in the introduction, we illustrate how different forms of radiation (electromagnetic or gravitational) can be used to infer the ellipticities, spin histories, orientations, and magnetic field strengths and geometries of neutron stars. This thesis contains three independent projects, each focusing on one emission type or wavelength. (1) From X-ray timing analysis, we place upper limits on the ellipticity of the AMSP XTE J1814–338. (2) We develop and implement a new search method for continuous gravitational waves, which will be used to place limits on the ellipticity and magnetic field strength of the putative neutron star in the supernova remnant SNR 1987A. (3) We introduce the technique of Stokes tomography, which can be used to constrain the magnetic field geometry and orientation of millisecond and slowly-rotating radio pulsars.

In this chapter, we summarise the results of the three projects: X-ray timing (Section 7.2), the cross-correlation search for periodic gravitational waves (Section 7.3), and radio polarimetry (Section 7.4). We also discuss how the results lead on to future work and new directions within the multimessenger theme.

## 7.2 X-ray light curves and precession

In Chapter 2, we analyse 37 days of X-ray timing data from the AMSP XTE J1814–338 in outburst. The data display clear, correlated 12.2-day modulations in the flux and pulse times-of-arrival, which are possibly (although not necessarily) a trait of a freely precessing pulsar. We model a precessing pulsar and compare the simulated flux and phase residuals to the data for a range of magnetic and observer inclination angles, considering surface emission maps

of one and two antipodal, circular hotspots. We find that the observed phase relation between the flux, pulse amplitudes, and phase residuals is only reproducible for an unlikely range of inclination angles ( $< 0.1^\circ$ ). There are two possible interpretations of this result. If the modulations are indeed due to precession, our model inaccurately describes the shape of the hotspot. However, we are still able to place a model-independent upper limit of  $3.0 \times 10^{-9}$  on the ellipticity. If the modulations are *not* due to precession, the upper limit on the ellipticity is then  $\lesssim 9.9 \times 10^{-10}$ .

From these limits, we can infer the following about XTE J1814–338:

- Its ellipticity is not large enough to warrant invoking any exotic equations of state. Ellipticities of order  $10^{-4}$  are thought to be sustainable only by solid strange quark stars, whereas quark-baryon or meson-condensate stars may sustain  $\epsilon \lesssim 10^{-5}$  and conventional neutron stars may sustain  $\epsilon \lesssim 10^{-7}$  (Owen 2005).
- Assuming the pulsar’s magnetic field strength is  $\sim 10^9$  G (Psaltis & Chakrabarty 1999; Rappaport et al. 2004), and that the ellipticity is  $\sim 10^{-9}$ , the gravitational radiation torque is  $\sim 3 \times 10^{-3}$  times smaller than the electromagnetic torque.
- Applying equation (2.4) from Cutler (2002), an ellipticity of  $10^{-9}$  implies an internal toroidal magnetic field of  $10^{12}$  G, consistent with the range expected for LMXBs.

To date, only one outburst has been observed from XTE J1814–338. If the star is precessing, the same modulations would appear in a future outburst. More sophisticated surface intensity maps may reproduce the data more accurately and provide clearer insight into how the accretion flow is channeled onto the surface for this particular source. If, instead, future outbursts lack the modulations, we can rule out precession, and conclude that the modulations observed in 2003 were caused by another transitory mechanism. An additional, independent upper limit on the ellipticity can also be placed by measuring the spin-down in between outbursts. Assuming that the spin-down in quiescence is dominated by gravitational wave emission, the star’s ellipticity can be estimated by applying equations (3.18) and (3.19). For example, SAX J1808.4–3658 spins down at a rate of  $-5.5 \times 10^{-18}$  Hz s $^{-1}$  (Hartman et al. 2009a), implying an ellipticity of  $5.6 \times 10^{-10}$ .

It is likely that the complex accretion flow changes the size and position of the hotspot, as shown by e.g. Long et al. (2008) and Vigelius & Melatos

(2008). One possible extension to this project is the inclusion of a time-dependent hotspot model, to account for such variability. Additionally, it is important to include effects of internal dissipation mechanisms, such as coupling between the crust and core (Jones & Andersson 2001) and superfluid instabilities (Glampedakis et al. 2009), which damp precession.

### 7.3 Gravitational waves and ellipticity

Chapters 3 and 4 describe the design and implementation of a cross-correlation search for continuous gravitational waves. The search was developed in collaboration with LIGO, and will be used to search for a neutron star in the supernova remnant SNR 1987A. In Chapter 3, we estimate the theoretical sensitivity of the search and introduce an astrophysical model to track the gravitational wave phase in terms of the ellipticity and magnetic field strength of a rapidly decelerating, isolated neutron star. We emphasize that in using the astrophysical model, we aim to exclude the simplest astrophysical model while recognizing it covers only a small fraction of the total parameter space. We calculate the semi-coherent phase metric used to determine the optimal spacing of search parameters. For a 2-week search on a 1000-node computing cluster, at LIGO's S5 sensitivity, the search will be sensitive to magnetic field strengths  $B \lesssim 10^{11}$  G and ellipticities  $\epsilon \gtrsim 10^{-4}$ . In Chapter 4, we describe the implementation of the search within the LAL/LALApps software suite used by the LSC. We present results of Monte Carlo testing to verify the output of the code. We confirm that the distribution of the detection statistic matches theoretical predictions for pure Gaussian noise and for an injected signal. Detection thresholds and preliminary sensitivity estimates are obtained for signals without spin down. For a search using  $10^3$  templates, 95% confidence limits on the smallest detectable gravitational wave signal,  $h_0^{95\%}$ , are  $4.97 \times 10^{-25}$ ,  $6.92 \times 10^{-25}$ , and  $1.41 \times 10^{-24}$  at frequencies of 150 Hz, 300 Hz, and 600 Hz respectively. Applying (3.18) to the results, this yields ellipticity limits of  $1.16 \times 10^{-6}$ ,  $1.02 \times 10^{-7}$ , and  $2.04 \times 10^{-7}$  for 150.05 Hz, 300.05 Hz, and 600.05 Hz respectively. We note however, that the ellipticity limits obtained using the astrophysical phase model for a source with spin down will differ. The full search is expected to cover  $\sim 10^9$  templates; yielding values of  $h_0^{95\%}$  which are  $\sim 25\%$  larger. More extensive Monte Carlo tests will be performed in the future to verify these estimates numerically.

Before the full search over S5 data begins, the following steps will be taken.

Firstly, we will clarify why the detection statistic output by Monte Carlo tests run over exact polarization and inclination angles is occasionally smaller than when averaging over the angles. Secondly, we will finalize the parameter space to be explored, taking into consideration the astrophysically interesting range of  $B$  and  $\epsilon$ , as well as the computational limitations discussed in Chapter 3. Thirdly, detailed sensitivity estimates will be performed across the full search template space, using actual detector noise instead of simulated Gaussian noise.

With the advent of Advanced LIGO, it is crucial that the search methods currently in development are tested and running smoothly by 2016. There are exciting prospects for the cross-correlation method beyond the search for SNR 1987A. For example, other young, rapidly-spinning pulsars are likely to be found in clusters such as Westerlund 1, making it an excellent target (Abbott et al. 2009e). The search code will also be extended to incorporate binary systems, allowing objects like Sco X-1 to be targeted. Importantly, we are not limited to targeted searches. With Advanced LIGO's sensitivity, all-sky searches using the cross-correlation method may be able to place constraints on  $\epsilon$  and  $B$  on previously unknown sources. We note that the cross-correlation search, like other semi-coherent searches, is only the first step towards probing a gravitational-wave source. Once a signal is confirmed, we are able to achieve even greater sensitivity by following up using coherent methods such as the  $\mathcal{F}$ -statistic.

The detection of a gravitational wave signal is, of course, the best possible outcome of a search. However, even in the event of a non-detection, upper and lower limits on  $\epsilon$  and  $B$  placed by gravitational wave searches like the cross-correlation search will play a large role in answering the following astrophysical questions, among others:

- Does  $\epsilon$  correlate with its  $B$ , as predicted theoretically (Sierpowska & Bednarek 2001; Arons 2003)?
- What is the internal magnetic field strength implied by  $\epsilon$  (Cutler 2002; Mastrano et al. 2010)?
- Theoretical models predict that free precession either persists or decays depending on  $\epsilon$ , and the orientation of the spin and magnetic axes,  $\mathbf{\Omega}$  and  $\mathbf{B}$  (Melatos 2000). Does  $\epsilon$  correlate with  $\mathbf{\Omega}$ ?
- What does  $\epsilon$  imply about the composition of the pulsar (Owen 2005)?

- The gravitational wave emission mechanism (mountain or  $r$ -modes) can be identified by the ratio of the gravitational wave and spin frequencies (Owen 2009). How much of the pulsar’s energy is radiated via gravitational waves, and how much via electromagnetic radiation?

## 7.4 Radio emission, orientation, and magnetic field structure

Stokes tomography is introduced in Chapters 5 and 6 to supplement traditional methods of analysing the radio pulse shape and PA swing to extract the magnetic geometry of radio pulsars. The shapes traced out by the four Stokes parameters, when plotted against each other over one pulse period in the form of Stokes phase portraits, are unique (or nearly so) for any given magnetic geometry and orientation. An atlas of look-up tables of Stokes phase portraits is presented in Chapters 5 and 6 for a range of simple models, including pure and current-modified dipoles, filled core and hollow cone beams, and the associated linear polarization patterns. We choose a sample of 26 radio pulsars, which obey the pulse-width relation or feature S-shaped PA swings (i.e. signatures of a pure dipole field) and show that for 60% of the sample, the observed emission is incompatible with a pure magnetic dipole at low emission altitudes. We model in detail the phase portraits of two pulsars, PSR J0827+2637 and PSR J0304+1932, with simple models of a pure and current-modified dipole respectively. We also model two millisecond pulsars, PSR J1939+2134 and PSR J0437–4715. The former object is fitted well at 0.61 GHz with a current-modified dipole; at 1.414 GHz, the fit is less accurate. We are unable to model the latter object using a pure or current-modified dipole, indicating that it has a more complicated field geometry.

### 7.4.1 Vacuum dipole field

Stokes tomography is especially important when considering nondipolar magnetic geometries, because the rotating vector model, traditionally used to extract the pulsar’s orientation from the PA swing, assumes a pure dipole. A common theory is that the magnetosphere contains either a force-free or vacuum-like field. In a force-free field [e.g. (Goldreich & Julian 1969; Michel 1973; Blandford 1976)], the magnetospheric plasma is assumed to be dense enough to carry charges and currents, yet tenuous enough such that the parti-

cles have zero inertia. Until recently, this model was too difficult to be solved numerically (Spitkovsky 2006; Kalapotharakos & Contopoulos 2009; Bai & Spitkovsky 2009a,b). Often, the force-free field is approximated by the simpler case of a vacuum dipole field (Deutsch 1955; Melatos 1997). With Stokes tomography, we aim to be able to distinguish between the two models.

To give a taste of what is possible, we consider briefly here a vacuum dipole field in the context of young, highly energetic pulsars, which can emit in multiple wavelengths including radio, X-ray and gamma-ray bands. Since the launch of the Fermi Gamma-ray Space Telescope in 2008, the catalog of gamma-ray pulsars has doubled to over 30 (e.g. Abdo et al. 2009a,b). In cases where both gamma-ray and radio emission are observed, the gamma-ray pulse profiles are typically out of phase with the radio, indicating that different regions emit different wavelengths. This phase offset is observed to increase with the pulsar's age (Thompson 1996; Kaspi et al. 2000). Several theoretical models for  $\gamma$ -ray emission have been proposed, including the polar cap model (Ruderman & Sutherland 1975; Daugherty & Harding 1982, 1996), slot-gap model (Arons & Scharlemann 1979; Arons 1983; Dyks & Rudak 2003; Dyks & Harding 2004), and outer-gap model (Cheng et al. 1986a,b; Romani & Yadigaroglu 1995; Cheng et al. 2000). In the polar cap model, a vacuum gap containing a parallel electric field forms at the stellar surface near the magnetic poles. Electron-positron pair formation fronts form, accelerating electrons at the surface along the field lines. High-energy photons are subsequently produced via curvature radiation. In the slot-gap model, the electric field decreases near the last open magnetic field line. A larger distance is thus required for the electrons to accelerate to the energies required for pair formation, and hence the vacuum, or slot gap, region is thought to be elongated along the last open field line, terminating at a radius of  $\sim 2R_*$ . In the outer-gap model, the vacuum region is located instead in the outer magnetosphere near the light cylinder. Recently, Romani & Watters (2009) developed a method for comparing  $\gamma$ -ray pulse profiles with magnetospheric and emission models, finding that swept-back fields provide better matches to the data than pure dipoles.

The primary diagnostic tool of the magnetospheric geometry provided by gamma-ray emission is the shape of the pulse profile. Several atlases have been constructed matching theoretical pulse shapes to different orientations of pulsar and observer inclination angles assuming a vacuum dipole field (Bai & Spitkovsky 2009c; Watters et al. 2009). Where available, the radio polarization can be analysed concurrently in order to obtain a more complete picture of the pulsar geometry and as a cross-check against specific gamma-ray emission

models. For example, Weltevrede & Wright (2009) analysed both the PA swing and the gamma-ray pulse profile of PSR B1055–52. From the PA swing, the authors used the rotating vector model to determine the magnetic and observer inclination angles. Combining these angles with the shape of the gamma-ray pulse profile, they concluded that only an outer-gap emission model is consistent with the data.

The retarded-time magnetic field generated by a pulsar rotating in a vacuum at a point  $\mathbf{x}$  at time  $t$  is (Cheng et al. 2000; Bai & Spitkovsky 2009c)

$$\mathbf{B}[\mathbf{x}, t] = \frac{\mu_0}{4\pi} \left[ \left( -\frac{\mathbf{m}}{r^3} + \frac{\dot{\mathbf{m}}}{cr^2} + \frac{\ddot{\mathbf{m}}}{c^2r} \right) + \mathbf{xx} \cdot \left( \frac{3\mathbf{m}}{r^5} + \frac{3\dot{\mathbf{m}}}{cr^4} + \frac{\ddot{\mathbf{m}}}{c^2r^3} \right) \right], \quad (7.1)$$

where  $\mathbf{m}$  is the time-varying magnetic moment vector, with  $\dot{\mathbf{m}} = \boldsymbol{\Omega} \times \mathbf{m}$ , and  $\ddot{\mathbf{m}} = \boldsymbol{\Omega} \times (\boldsymbol{\Omega} \times \mathbf{m})$ ,  $\mu_0$  is the permeability of free space,  $c$  is the speed of light, and  $\boldsymbol{\Omega}$  is the angular velocity vector.

Applying the method described in Chapters 5 and 6, we generate Stokes phase portraits for a filled core beam and linear polarization  $L = I \cos \theta$ , where  $L$  is the degree of linear polarization,  $I$  is the total intensity, and  $\theta$  is the colatitude of the emission point. Interpulse emission and relativistic aberration effects are included. In Figure 7.1, we compare the pulse profile, PA swing, and Stokes phase portraits for a vacuum dipole field (bottom four subpanels) to that of a pure dipole (top four panels) at one example orientation  $(\alpha, i) = (70^\circ, 60^\circ)$  at an altitude  $r = 0.1r_{\text{LC}}$ . In both cases, the PA swing appears similar; it is a distorted S-shape which is not symmetric about the pulse centroid. The phase portraits feature the same general shapes (i.e. balloons, figure-eights, and heart shapes in  $I$ - $Q$ ,  $I$ - $U$ , and  $Q$ - $U$  respectively) but there are clear differences. For the vacuum dipole, the  $I$ - $Q$  balloon is narrower, and the shapes in  $I$ - $U$  and  $Q$ - $U$  are much more asymmetric than for the pure dipole. This engenders hope that Stokes tomography may help distinguish between magnetospheric models.

### 7.4.2 Magnetic mountains

Stokes tomography can also be applied to old, recycled pulsars, whose magnetic fields have been distorted by the formation of magnetic mountains. In Section 1.5.3 in the Introduction, we introduce the magnetic mountain model, in which accreted matter accumulates on the surface of the pulsar, then spreads equatorwards, dragging with it the frozen-in magnetic field lines. Payne & Melatos (2004) first modelled an axisymmetric, isothermal mountain and found that

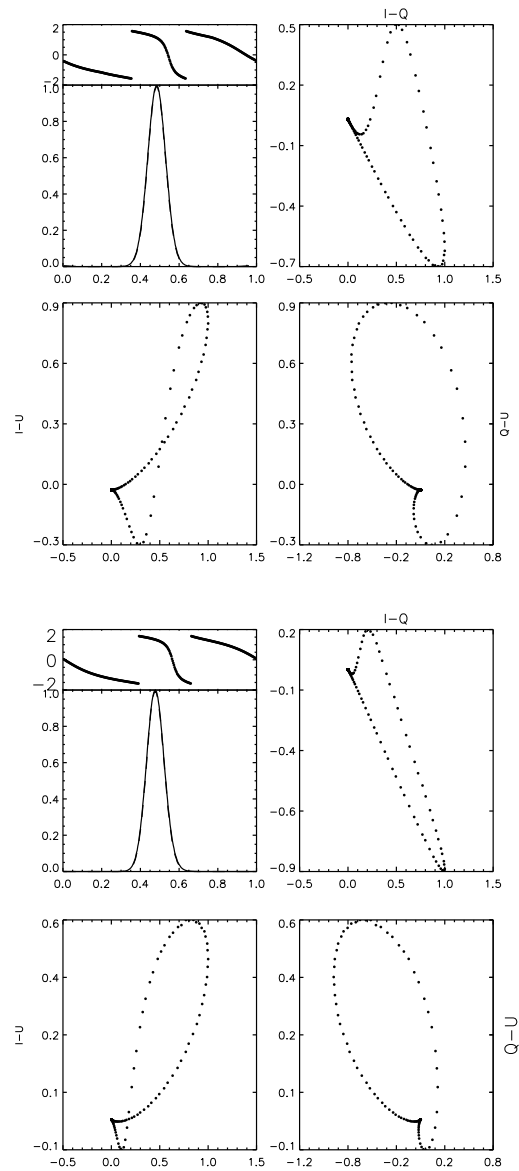


**Figure 7.1:** Stokes tomography of a pure dipole (top four panels) and a vacuum dipole field (bottom four panels), for  $r = 0.1r_{\text{LC}}$ , linear polarization  $L = I \cos \theta$ , and orientation  $(\alpha, i) = (70^\circ, 60^\circ)$ . Within each half of the figure, the four subpanels display (clockwise from top left): (a)  $I/I_{\max}$  (bottom) and PA (top; in radians) as functions of pulse longitude, (b)  $I-Q$ , (c)  $Q-U$ , and (d)  $I-U$ .

the magnetic field is distorted significantly for an accreted mass of  $\gtrsim 10^{-5} M_{\odot}$ . The mountain decays over a timescale of  $10^{7-8}$  yr due to the effects of Ohmic dissipation (Vigelius & Melatos 2009a). It is thus likely that when accretion ceases, and the pulsar begins emitting at radio wavelengths, the magnetic field is still distorted appreciably. Recently, Priymak et al. (2010) extended the model to treat adiabatic mountains, and found that the neutron star equation of state can have a large effect on the structure of the magnetic mountain.

Three-dimensional simulations of magnetic mountain formation and evolution were performed by Vigelius & Melatos (2008) using the general purpose, ideal-MHD solver ZEUS-MP (Hayes et al. 2006). Vigelius & Melatos (2008) found that for a range of accreted masses,  $10^{-9} \leq M_a/M_{\odot} \leq 10^{-3}$ , the mountain is susceptible to a three-dimensional magnetic buoyancy instability. This causes the magnetic field of the pulsar to reconfigure, and settle into a highly distorted, nonaxisymmetric equilibrium. We expect the PA swing and Stokes phase portraits from such distorted fields to deviate greatly from their dipolar forms.

As an illustrative example of how Stokes tomography can be applied to magnetic mountains, we modify our code to accept the array of  $B_r$ ,  $B_{\theta}$ , and  $B_{\phi}$  calculated numerically by Vigelius & Melatos (2008). In order to isolate the effects of the nonaxisymmetric field, we do not include interpulse emission or relativistic aberration. Vigelius & Melatos (2008) use a  $64 \times 128 \times 32$  grid spanning  $r_{\star} \leq r' \leq r_m$ ,  $0 \leq \theta \leq \pi$ , and  $0 \leq \phi \leq 2\pi$ , where  $r_{\star}$  is the stellar radius, and  $r_m$  is the magnetospheric radius. The radial coordinate  $r'$  is stretched logarithmically. This numerical grid is coarser than the one we have used thus far, therefore reducing the resolution of our simulated pulse profiles and Stokes phase portraits. We use the results of Model G from Vigelius & Melatos (2008), in which the accreted mass is  $\approx 1.7 \times 10^{-4} M_{\odot}$ .

Figure 7.2 shows the pulse profile, PA swing, and Stokes phase portraits for Model G, at an orientation of  $(\alpha, i) = (30^{\circ}, 40^{\circ})$ , and an emission altitude of  $r' = 50.94$ , where  $r'$  is normalised by the hydrostatic scale height [see Section 2 of Vigelius & Melatos (2008) for details]. We assume  $L = I \cos \theta$ . The distortion in the PA swing (top left panel) is clear. The pulse profile appears symmetric about its centroid. To compensate for the reduction of the grid resolution, we join the points on the Stokes phase portraits to obtain a clearer picture of their overall structure. Although poorly resolved, the phase portraits are clearly heavily distorted. With further refinement of the ZEUS-MP grid, we will be able to make accurate predictions about the shapes of the PA swing and phase portraits expected from the magnetic mountain model, and compare

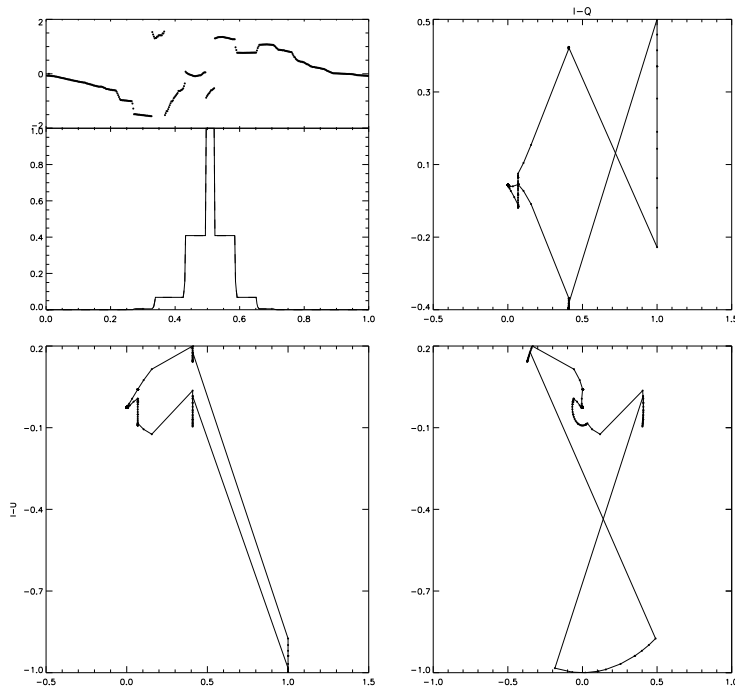


**Figure 7.2:** Stokes tomography of a field distorted by the formation of a magnetic mountain [Model G of Vigelius & Melatos (2008)] at  $r' = 50.94$  (in units of the hydrostatic scale height), for linear polarization  $L = I \cos \theta$ , and orientation  $(\alpha, i) = (30^\circ, 40^\circ)$ . The four subpanels display (clockwise from top left): (a)  $I/I_{\max}$  (bottom) and PA (top; in radians) as functions of pulse longitude, (b)  $I-Q$ , (c)  $Q-U$ , and (d)  $I-U$ .

the results with data from radio millisecond pulsars

We note that the results presented in Figure 7.1 and 7.2 are very preliminary, and require further work. With the help of Stokes tomography, we hope to achieve the following:

- Detailed analysis of the vacuum dipole and force-free fields, focusing on ways to distinguish between the two models.
- Modelling of individual gamma-ray pulsars using radio polarization data, e.g. PSR B1055–52 (Weltevrede & Wright 2009).
- Detailed analysis of the magnetic mountain model, focusing on comparisons to polarization data from millisecond pulsars.
- Inclusion of tangled, multipolar field models.
- Inclusion of circular polarization.

Additionally, the following astrophysical questions will be investigated, among others:

- Which gamma-ray emission models are consistent with the geometries predicted by Stokes tomography?
- Which magnetic mountain models are consistent with the Stokes phase portraits of millisecond pulsars?
- Different neutron star equations of state form different kinds of magnetic mountains (Priymak et al. 2010). Can Stokes tomography help to determine the equation of state through this effect?



# Appendices

## Appendix 3A: Calculation of the coherent metric

$g_{ij}$

This appendix details the calculation of the diagonal terms of the coherent metric,  $g_{ij}$  (3.29). We start by evaluating the frequency  $\nu(t)$  at time  $t$ , by assuming that  $\nu(t)$  is a simple sum of separate, independent contributions from gravitational-wave and electromagnetic spin down:

$$\nu(t) = K_1 \int -Q_1 \nu(t)^5 dt + K_2 \int -Q_2 \nu(t)^n dt \quad (\text{A1})$$

$$= \frac{K_1 \nu}{(1 + 4Q_1 \nu^4 t)^{1/4}} + \frac{K_2 \nu}{[1 + (n-1)Q_2 \nu^{n-1} t]^{1/n-1}}. \quad (\text{A2})$$

Here,  $K_1$  and  $K_2$  are constants which satisfy  $K_1 + K_2 = 1$ , and the search parameters  $\nu, Q_1, Q_2$ , and  $n$  are defined at a reference time  $t_0$ . Recall that  $\nu$  is normalised by  $\nu_{\text{ref}}$ , which we set to 1 Hz and do not write down, for simplicity. The first term in (A2) follows from the first integral in (A1) by assuming  $Q_2 = 0$ . The second term in (A2) follows from the second integral in (A1) by assuming  $Q_1 = 0$ . Needless to say, the exact solution for  $\nu(t)$  follows from solving (3.25) self-consistently for  $Q_1 \neq 0, Q_2 \neq 0$ , but this is too difficult to solve analytically. As the phase metric calculation is useful only in an analytic form, we adopt the approximation in (A1).

The phase at time  $t$  is given by,

$$\Phi(t, \boldsymbol{\theta}) = \int_{t_0}^{t+t_0} dt \nu(t) \quad (\text{A3})$$

$$= \frac{K_1 [1 + 4Q_1 \nu^4 (t + \frac{\mathbf{r} \cdot \mathbf{n}}{c})]^{3/4} - K_1 (1 + 4Q_1 \nu^4 t_0)^{3/4}}{3Q_1 \nu^3} + \frac{K_2 [1 + (n-1)Q_2 \nu^{n-1} (t + \frac{\mathbf{r} \cdot \mathbf{n}}{c})]^{2-n}}{(n-2)Q_2 \nu^{n-2}} - \frac{K_2 [1 + (n-1)Q_2 \nu^{n-1} t_0]^{2-n}}{(n-2)Q_2 \nu^{n-2}}. \quad (\text{A4})$$

We can expand each term in the regimes  $(Q_1\nu^4)^{-1} \gg t$  and  $(Q_2\nu^{n-1})^{-1} \gg t$ , giving

$$\begin{aligned}\Phi(t, \boldsymbol{\theta}) &= K_1\nu \left(t + \frac{\mathbf{r} \cdot \mathbf{n}}{c} - t_0\right) - \frac{K_1}{2}Q_1\nu^5 \left[\left(t + \frac{\mathbf{r} \cdot \mathbf{n}}{c}\right)^2 - t_0^2\right] \\ &\quad + K_2\nu \left(t + \frac{\mathbf{r} \cdot \mathbf{n}}{c} - t_0\right) - \frac{K_2}{2}Q_2\nu^n \left[\left(t + \frac{\mathbf{r} \cdot \mathbf{n}}{c}\right)^2 - t_0^2\right],\end{aligned}\quad (\text{A5})$$

and

$$\begin{aligned}\Phi(t, \boldsymbol{\theta} + \Delta\boldsymbol{\theta}) &= K_1(\nu + \Delta\nu) \left(t + \frac{\mathbf{r} \cdot \mathbf{n}}{c} - t_0\right) \\ &\quad - \frac{K_1}{2}(Q_1 + \Delta Q_1)(\nu + \Delta\nu)^5 \left[\left(t + \frac{\mathbf{r} \cdot \mathbf{n}}{c}\right)^2 - t_0^2\right] \\ &\quad + K_2(\nu + \Delta\nu) \left(t + \frac{\mathbf{r} \cdot \mathbf{n}}{c} - t_0\right) \\ &\quad - \frac{K_2}{2}(Q_2 + \Delta Q_2)(\nu + \Delta\nu)^{n+\Delta n} \left[\left(t + \frac{\mathbf{r} \cdot \mathbf{n}}{c}\right)^2 - t_0^2\right].\end{aligned}\quad (\text{A6})$$

Subtracting (A5) from (A6) gives

$$\begin{aligned}\Delta\Phi(t) &= \Delta\nu(K_2 + K_1) \left(t + \frac{\mathbf{r} \cdot \mathbf{n}}{c} - t_0\right) \\ &\quad - \frac{K_1}{2} \left[\left(t + \frac{\mathbf{r} \cdot \mathbf{n}}{c}\right)^2 - t_0^2\right] [(\nu + \Delta\nu)^5(Q_1 + \Delta Q_1) - \nu^5 Q_1] \\ &\quad - \frac{K_2}{2} \left[\left(t + \frac{\mathbf{r} \cdot \mathbf{n}}{c}\right)^2 - t_0^2\right] [(\nu + \Delta\nu)^{n+\Delta n}(Q_2 + \Delta Q_2) \\ &\quad - \nu^n Q_2]\end{aligned}\quad (\text{A7})$$

We now take the derivative of (A7) with respect to  $\Delta\nu$ ,  $\Delta Q_1$ ,  $\Delta Q_2$ , and  $\Delta n$ . We have

$$\begin{aligned}\partial_{\Delta\nu}\Delta\Phi(t)|_{\Delta\theta=0} &= (K_1 + K_2) \left(t + \frac{\mathbf{r} \cdot \mathbf{n}}{c} - t_0\right) \\ &\quad - \frac{5}{2}\nu^4 Q_1 \left[\left(t + \frac{\mathbf{r} \cdot \mathbf{n}}{c}\right)^2 - t_0^2\right] \\ &\quad - \frac{K_2}{2}n\nu^{n-1} Q_2 \left[\left(t + \frac{\mathbf{r} \cdot \mathbf{n}}{c}\right)^2 - t_0^2\right]\end{aligned}\quad (\text{A8})$$

$$\partial_{\Delta Q_1}\Delta\Phi(t)|_{\Delta\theta=0} = -\frac{K_1}{2}\nu^5 \left[\left(t + \frac{\mathbf{r} \cdot \mathbf{n}}{c}\right)^2 - t_0^2\right]\quad (\text{A9})$$

$$\partial_{\Delta Q_2}\Delta\Phi(t)|_{\Delta\theta=0} = -\frac{K_2}{2}\nu^n \left[\left(t + \frac{\mathbf{r} \cdot \mathbf{n}}{c}\right)^2 - t_0^2\right]\quad (\text{A10})$$

$$\partial_{\Delta n} \Delta \Phi(t)|_{\Delta \theta=0} = -\frac{K_2}{2} \nu^n Q_2 \ln(\nu) \left[ \left( t + \frac{\mathbf{r} \cdot \mathbf{n}}{c} \right)^2 - t_0^2 \right] \quad (\text{A11})$$

We construct  $g_{ij}$  by substituting (A8)–(A11) into (3.29). In this chapter, we only require the diagonal terms of the metric. The relevant terms ( $g_{00}, g_{11}, g_{22}, g_{33}$ ) are

$$\begin{aligned} g_{00} = & T_{\text{lag}}^2 \left( \frac{K_1^2}{12} + \frac{K_1 K_2}{6} + \frac{K_2^2}{12} \right) + T_{\text{lag}}^2 \left( T_{\text{lag}} + 2 \frac{\mathbf{r} \cdot \mathbf{n}}{c} + 2T_{\text{start}} \right) \\ & \left( -\frac{5}{12} K_1^2 \nu^4 Q_1 - \frac{5}{12} K_1 K_2 \nu^4 Q_1 - \frac{1}{12} K_1 K_2 n \nu^{n-1} Q_2 \right. \\ & \left. - \frac{1}{12} K_2^2 n \nu^{n-1} Q_2 \right) + T_{\text{lag}}^2 \left[ 4T_{\text{lag}}^2 + 15 \left( \frac{\mathbf{r} \cdot \mathbf{n}}{c} \right)^2 + 15T_{\text{lag}} T_{\text{start}} + 15T_{\text{start}}^2 \right. \\ & \left. + 15 \frac{\mathbf{r} \cdot \mathbf{n}}{c} (T_{\text{lag}} + 2T_{\text{start}}) \right] \left( \frac{5}{36} K_1^2 \nu^8 Q_1^2 + \frac{1}{18} K_1 K_2 n \nu^{n+3} Q_1 Q_2 \right. \\ & \left. + \frac{1}{180} n^2 \nu^{2n-2} Q_2^2 \right) \end{aligned} \quad (\text{A12})$$

$$\begin{aligned} g_{11} = & \frac{K_1^2 \nu^{10}}{180} \left[ 4T_{\text{lag}}^4 + 15T_{\text{lag}}^2 \left( \frac{\mathbf{r} \cdot \mathbf{n}}{c} \right)^2 + 15T_{\text{lag}}^3 T_{\text{start}} + 15T_{\text{lag}}^2 T_{\text{start}}^2 \right. \\ & \left. + 15T_{\text{lag}}^2 \frac{\mathbf{r} \cdot \mathbf{n}}{c} (T_{\text{lag}} + 2T_{\text{start}}) \right] \end{aligned} \quad (\text{A13})$$

$$\begin{aligned} g_{22} = & \frac{K_2^2 \nu^{2n}}{180} \left[ 4T_{\text{lag}}^4 + 15T_{\text{lag}}^2 \left( \frac{\mathbf{r} \cdot \mathbf{n}}{c} \right)^2 + 15T_{\text{lag}}^3 T_{\text{start}} + 15T_{\text{lag}}^2 T_{\text{start}}^2 \right. \\ & \left. + 15T_{\text{lag}}^2 \frac{\mathbf{r} \cdot \mathbf{n}}{c} (T_{\text{lag}} + 2T_{\text{start}}) \right] \end{aligned} \quad (\text{A14})$$

$$\begin{aligned} g_{33} = & \frac{K_2^2 \log(\nu)^2 \nu^{2n} Q_2^2}{180} \left[ 4T_{\text{lag}}^4 + 15T_{\text{lag}}^2 \left( \frac{\mathbf{r} \cdot \mathbf{n}}{c} \right)^2 + 15T_{\text{lag}}^3 T_{\text{start}} \right. \\ & \left. + 15T_{\text{lag}}^2 T_{\text{start}}^2 + 15T_{\text{lag}}^2 \frac{\mathbf{r} \cdot \mathbf{n}}{c} (T_{\text{lag}} + 2T_{\text{start}}) \right]. \end{aligned} \quad (\text{A15})$$

## Appendix 3B: Semi-coherent metric

In this appendix, we list in full the diagonal terms of the semi-coherent metric presented in (3.31)–(3.34). The relevant terms ( $s_{00}$ ,  $s_{11}$ ,  $s_{22}$ ,  $s_{33}$ ) are

$$\begin{aligned}
s_{00} = & T_{\text{lag}}^2 \left( \frac{1}{12} K_1^2 + \frac{1}{6} K_1 K_2 + \frac{1}{12} K_2^2 \right) \\
& + T_{\text{lag}}^2 \left( T_{\text{lag}} + 2 \frac{\mathbf{r} \cdot \mathbf{n}}{c} + T_{\text{obs}} \right) \left( -\frac{5}{12} \nu^4 Q_1 K_1^2 - \frac{5}{12} K_1 K_2 \nu^4 Q_1 \right. \\
& \left. - \frac{1}{12} K_1 K_2 n \nu^{n-1} Q_2 - \frac{1}{12} K_2^2 n \nu^{n-1} Q_2 \right) \\
& + T_{\text{lag}}^2 \left[ 8T_{\text{lag}}^2 + 30 \left( T_{\text{lag}} \frac{\mathbf{r} \cdot \mathbf{n}}{c} + \frac{\mathbf{r} \cdot \mathbf{n}^2}{c} + \frac{\mathbf{r} \cdot \mathbf{n}}{c} T_{\text{obs}} \right) + 15T_{\text{lag}} T_{\text{obs}} + 10T_{\text{obs}}^2 \right] \\
& \left( \frac{5}{72} K_1^2 \nu^8 Q_1^2 - \frac{1}{36} K_1 K_2 n \nu^{n+3} Q_1 Q_2 + \frac{1}{360} K_2^2 n^2 \nu^{2n-2} Q_2^2 \right) \quad (\text{A16})
\end{aligned}$$

$$\begin{aligned}
s_{11} = & \frac{K_1^2 \nu^{10}}{360} \left[ 8T_{\text{lag}}^4 + 30T_{\text{lag}}^2 \frac{\mathbf{r} \cdot \mathbf{n}^2}{c} + 15T_{\text{lag}}^3 \left( 2 \frac{\mathbf{r} \cdot \mathbf{n}}{c} + T_{\text{obs}} \right) \right. \\
& \left. + 30T_{\text{lag}}^2 T_{\text{obs}} \frac{\mathbf{r} \cdot \mathbf{n}}{c} + 10T_{\text{lag}}^2 T_{\text{obs}}^2 \right] \quad (\text{A17})
\end{aligned}$$

$$\begin{aligned}
s_{22} = & \frac{K_2^2 \nu^{2n}}{360} \left[ 8T_{\text{lag}}^4 + 30T_{\text{lag}}^2 \frac{\mathbf{r} \cdot \mathbf{n}^2}{c} + 15T_{\text{lag}}^3 \left( 2 \frac{\mathbf{r} \cdot \mathbf{n}}{c} + T_{\text{obs}} \right) \right. \\
& \left. + 30T_{\text{lag}}^2 T_{\text{obs}} \frac{\mathbf{r} \cdot \mathbf{n}}{c} + 10T_{\text{lag}}^2 T_{\text{obs}}^2 \right] \quad (\text{A18})
\end{aligned}$$

$$\begin{aligned}
s_{33} = & \frac{K_2^2 \log(\nu)^2 \nu^{2n} Q_2^2}{360} \left[ 8T_{\text{lag}}^4 + 30T_{\text{lag}}^2 \left( \frac{\mathbf{r} \cdot \mathbf{n}}{c} \right)^2 + 15T_{\text{lag}}^3 \left( 2 \frac{\mathbf{r} \cdot \mathbf{n}}{c} + T_{\text{obs}} \right) \right. \\
& \left. + 30T_{\text{lag}}^2 T_{\text{obs}} \frac{\mathbf{r} \cdot \mathbf{n}}{c} + 10T_{\text{lag}}^2 T_{\text{obs}}^2 \right] \quad (\text{A19})
\end{aligned}$$

## Appendix 3C: Analytic accuracy estimates for the astrophysical phase model (3.25)

In this appendix, we motivate (3.31)–(3.34) physically by calculating the phase error in two special cases: (i) pure gravitational-wave spin down, and (ii) pure electromagnetic spin down. In the gravitational wave case, (3.25) reduces to

$$\frac{d\nu}{dt} = -Q_1 \nu^5 \quad (\text{A20})$$

$$\nu(t) = \frac{\nu}{(1 + 4Q_1 \nu^4 t)^{1/4}} \quad (\text{A21})$$

where we take  $\nu_{\text{ref}} = 1$  Hz for simplicity and  $\nu = \nu(t = 0)$ . The gravitational wave phase at  $t = T_{\text{lag}}$  is then

$$\Phi(T_{\text{lag}}) - \Phi(t_0) = \int_{t_0}^{T_{\text{lag}}+t_0} dt \nu(t) \quad (\text{A22})$$

$$= \frac{(1 + 4Q_1\nu^4 T_{\text{lag}})^{3/4} - 1}{3Q_1\nu^3}. \quad (\text{A23})$$

There are two regimes to be considered: (i)  $T_{\text{lag}} \gg (4Q_1\nu^4)^{-1}$ , and (ii)  $T_{\text{lag}} \ll (4Q_1\nu^4)^{-1}$ . In terms of the characteristic age

$$\tau_c(t) = \frac{\nu(t)}{4|\dot{\nu}(t)|}, \quad (\text{A24})$$

the two regimes correspond to (i)  $T_{\text{lag}} \gg \tau_c(t_0)$ , and (ii)  $T_{\text{lag}} \ll \tau_c(t_0)$ . In the case of SNR 1987A, we have  $\tau_c \approx 19$  years (in 2006, when the S5 run began) and  $T_{\text{lag}} \approx 1$  hr, i.e. regime (ii).

Given small errors  $\Delta Q_1$  and  $\Delta\nu$  in  $Q_1$  and  $\nu$ , the phase error that accumulates between the template and the signal after a time  $T_{\text{lag}}$  is

$$\Delta\Phi = \frac{d\Phi}{dQ_1} \Delta Q_1 + \frac{d\Phi}{d\nu} \Delta\nu \quad (\text{A25})$$

$$= -\frac{1}{2}\nu^5 T_{\text{lag}}^2 \Delta Q_1 + T_{\text{lag}} \Delta\nu \quad (\text{A26})$$

Overall, therefore, the number of templates required scales as  $T_{\text{lag}}^3$  regardless of how rapidly the neutron star is spinning down. This scaling matches the conventional Taylor expansion if  $\nu$  and  $\dot{\nu}$  suffice to track the signal ( $N_{\text{total}} \propto T_{\text{lag}}^3$ ) but is much more economical if  $\ddot{\nu}$  is needed ( $N_{\text{total}} \propto T_{\text{lag}}^6$ ), which happens for  $\nu > 1.7 \times 10^{-5} \text{ Hz } (\tau_c/10^2 \text{ yr})^{-2} (T_{\text{lag}}/1 \text{ hour})^{-3}$ . In the SNR 1987A search, we cover frequencies above 0.1 kHz, so  $\ddot{\nu}$  always contributes significantly. Hence the phase model (3.25) is always preferable.

Now suppose the electromagnetic term dominates. Equation (3.25) with  $\nu_{\text{ref}} = 1$  Hz reduces to

$$\frac{d\nu}{dt} = -Q_2\nu^n \quad (\text{A27})$$

$$\nu(t) = \frac{\nu}{[1 + (n-1)Q_2\nu^{n-1}t]^{1/(n-1)}} \quad (\text{A28})$$

and the gravitational wave phase after a time  $T_{\text{lag}}$  is

$$\Phi(T_{\text{lag}}) = \int_{t_0}^{T_{\text{lag}}+t_0} dt \nu(t) \quad (\text{A29})$$

$$= \frac{[1 + (n-1) Q_2 \nu^{n-1} T_{\text{lag}}]^{\frac{2-n}{1-n}} - 1}{(n-2) Q_2 \nu^{n-2}}. \quad (\text{A30})$$

For small errors  $\Delta Q_2$ ,  $\Delta \nu$  and  $\Delta n$  in  $Q_2$ ,  $\nu$  and  $n$ , the phase error between the template at the signal after a time  $T_{\text{lag}}$  is

$$\Delta \Phi = \frac{d\Phi}{dQ_2} \Delta Q_2 + \frac{d\Phi}{d\nu} \Delta \nu + \frac{d\Phi}{dn} \Delta n \quad (\text{A31})$$

$$= - \left( \frac{\nu^n T_{\text{lag}}^2}{2} \right) \Delta Q_2 + T_{\text{lag}} \Delta \nu + T_{\text{lag}} \log [1 + (n-1) Q_2 T_{\text{lag}} \nu^{n-1}] \Delta n \quad (\text{A32})$$

Hence in the electromagnetic limit, the phase error due to  $\Delta \nu$  scales in the same way as in the gravitational wave limit. The phase error due to  $\Delta Q_2$  scales as  $T_{\text{lag}}^2$ , and the phase error due to  $\Delta n$  scales as  $T_{\text{lag}} \log [1 + (n-1) Q_2 T_{\text{lag}} \nu^{n-1}]$ . Overall, the number of templates required scales as  $T_{\text{lag}}^4 \log(T_{\text{lag}})$ . This represents a saving if the second frequency derivative is important which, as shown above, is true for the range of signal frequencies considered in this search.

## Appendix 4A: Installation guideline

These notes are an informal guide to installing LAL & LALapps on UniMelb machines (i686 Linux Ubuntu). I have used my own machine (Guinan) as an example.

The LIGO Data Analysis Software (LAL and LALapps; <http://www.lsc-group.phys.uwm.edu/daswg/projects/lal.html>) requires standard LSC software to be installed prior to installation.

The most complicated aspect of installation is the correct setting of environment variables. Be careful to set all the relevant variables before configuring/installing anything.

### LSC standard software

These packages are available for download and installation at <http://www.lsc-group.phys.uwm.edu/daswg/docs/howto/lscsoft-install.html>. They are:

- pkg-config
- fftw3
- gsl
- libmetaio (we need metaio 8)
- Glue

I have installed them in `/data/gui1/cchung/lscsoft`. Installation notes (taken straight from the above website) are in `/data/gui1/cchung/lscsoft/lscsoft_install`.

There was a problem with installing libmetaio. When running `./configure`, it looks for the MATLAB compiler called 'mex', however on our system, 'mex' is a link to 'pdfetex' (LaTeX compiler) and so this stalled the installation. As a quick fix, I just commented out line 20162 of the `./config` file at `/data/gui1/cchung/tmp/libmetaio-6.1/configure`

```
# $MEX $MEXOPTS $MEXFLAGS -output ax_c_test \\  
ax_c_test.c $MEXLDADD 2> /dev/null 1>&2
```

which calls mex to check for the MEX-file suffix. This seems to work, and shouldn't affect the installation as we are installing libmetaio without Matlab support anyway.

Also, add the following lines to your `.rc` file (note that `.rc` is the configuration file for whichever shell you use. I use zsh, so this would be my `.zshrc` file):

```
LSCSOFT_LOCATION=/data/gui1/cchung/lscsoft # change this as appropriate
export LSCSOFT_LOCATION
LSCSOFT_PREFIX=/data/gui1/cchung/lscsoft
export LSCSOFT_PREFIX
if [ -f ${LSCSOFT_LOCATION}/lscsoft-user-env.sh ] ; then
    . ${LSCSOFT_LOCATION}/lscsoft-user-env.sh
fi
```

#### **m4, automake, autoconf installation**

One extra environment variable which needs to be set now, but is not mentioned in the online notes, is `LAL_DATA_PATH=$LAL_PREFIX/share/lal`. If this is not set, ‘make check’ will fail for LALapps (see below).

Before installing LAL, I had to install a few programs:

- m4 ([http://www.techsw.com/tutorials/operating\\_systems/linux/tools/installing\\_m4\\_macro\\_processor\\_ubuntu\\_linux.php](http://www.techsw.com/tutorials/operating_systems/linux/tools/installing_m4_macro_processor_ubuntu_linux.php)).

Installed in `/data/gui1/cchung/m4`

```
> wget ftp://ftp.gnu.org/gnu/m4/m4-1.4.10.tar.gz
> tar -xvzf m4-1.4.10.tar.gz
> cd m4-1.4.10
> ./configure --prefix=/data/gui1/cchung/m4
> make
> make install
```

- automake (<http://ftp.gnu.org/gnu/automake>) Installed version 1.9 in `/data/gui1/cchung/automake`

```
> tar -xvzf automake-1.9.tar.gz
> cd automake-1.9
> ./configure --prefix=/data/gui1/cchung/automake
> make
> make install
```

- autoconf (<http://ftp.gnu.org/gnu/autoconf>) Installed version 2.61 in `/data/gui1/cchung/autoconf`

```
> tar -xvzf automake-2.61.tar.gz
```

```
> cd autoconf-2.61
> ./configure --prefix=/data/gui1/cchung/autoconf
> make
> make install
```

## Globus gsissh installation

Access to LIGO clusters around the world is handled by the LIGO Data Grid software suite (LDG). To access the clusters with LDG, you need a grid certificate issued by APAC.<sup>1</sup> Since the full LDG 4.7 software doesn't install properly on the Unimelb machines (there is a missing library in Ubuntu which we can't seem to fix), we can just use the failsafe instructions to only install Globus, which will let us ssh into the LSC machines with our grid certificates. Failsafe instructions are here:

<https://www.lsc-group.phys.uwm.edu/lscdatagrid/doc/gsisshUbuntu.html>  
and are also quite straightforward. Note that the current VDT certificate bundle at the time of writing is 47 (not 37 as indicated in the notes).

On guinan, I added the following to my `.zshrc` file

```
export GLOBUS_LOCATION=/data/gui1/cchung/lscsoft/ldg/globus
source /data/gui1/cchung/lscsoft/ldg/globus/etc/globus-user-env.sh
```

which just tells the shell where to find gsissh.

Check that you have `userkey.pem` and `usercert.pem` in your `$HOME/.globus` directory.

Important: if you have a directory called `$HOME/.globus/certificates`, delete it. For some reason, on my machine, this directory contained incorrect information and was confusing gsissh.

Now, gsissh should be working. Test it out with `>gsissh baker` or, if you have an account at a LIGO cluster, `>gsissh <LIGOClusterName>`

## Git installation

Git is available from <http://git-scm.com/>

The direct link to the package is <http://kernel.org/pub/software/scm/git/git-1.6.2.2.tar.gz> To unpack and install:

```
> tar -xvf git-1.6.2.2.tar.gz
```

---

<sup>1</sup><http://wiki.arcs.org.au/bin/view/Main/GridCertificates>

```
> make configure
> ./configure --prefix=$GIT_LOCATION
> make all
> make install
```

where `$GIT_LOCATION=/data/gui1/cchung/lscsoft/git` in my case. Once we have git (and if we have gsissh installed and working), then we can checkout the lalsuite repository which contains Glue, LAL, LALApps and PyLAL. Set (and add to `.rc` file)

```
> GIT_SSH=$GLOBUS_LOCATION/bin/gsissh
> export GIT_SSH
```

Make sure to run these instructions from the same directory where you want your code to live. Instructions are here:

<https://www.lsc-group.phys.uwm.edu/daswg/docs/howto/lalsuite-git.html>  
and are straightforward.

Note that we need to have gsissh and grid certificates working, otherwise checking out with your LIGO username will not work!

## LAL/LALApps installation

LAL is to be installed in `/data/gui1/cchung/lscsoft/opt/lal` (path setting is much easier if it is installed in the same directory as the other packages). In late 2009, the group-specific LAL code was split up into subdirectories, i.e. LALPulsar, LALStochastic, etc. For CW applications, we only need LALPulsar. First, set the following environment variables.

```
LSCSOFT_USER=${LSCSOFT_USER:-<username>}
LAL_PREFIX=${LAL_LOCATION:-"/data/gui1/cchung/lscsoft/opt/lal/"}
LALPULSAR_PREFIX=
${LALPULSAR_LOCATION:-"/data/gui1/cchung/lscsoft/opt/lalpulsar/"}
LALAPPS_PREFIX=
${LALAPPS_LOCATION:-"/data/gui1/cchung/lscsoft/opt/lalapps/"}
```

Git will have put the source code where you told it to. For example, if it's `/data/gui1/cchung/lscsoft/lalsuite`, then set

```
LSCSOFT_SRCDIR= \
${LSCSOFT_SRCDIR:-"/data/gui1/cchung/lscsoft/lalsuite"}
```

Now, start with LAL.

```
> cd ${LSCSOFT_SRCDIR}/lal
> ./00boot
> ./configure --prefix=${LAL_PREFIX} --with-gcc-flags
> make
> make install
```

If you get an error message about configure not being able to find gsl, do

```
> export PKG_CONFIG_PATH= \
    $PKG_CONFIG_PATH:$LSCSOFT_PREFIX/non-lsc/lib/pkgconfig
```

Add the following to your .rc

```
mkdir -p ${LSCSOFT_ROOTDIR}/etc
echo "export LSCSOFT_LOCATION=${LSCSOFT_ROOTDIR}/opt/lscsoft" \
> ${LSCSOFT_ROOTDIR}/etc/lscsoftrc
echo "# setup LAL for development: " \
>> ${LSCSOFT_ROOTDIR}/etc/lscsoftrc
echo "export LAL_LOCATION=${LSCSOFT_LOCATION}/lal" \
>> ${LSCSOFT_ROOTDIR}/etc/lscsoftrc
echo "if [ -f \"$LAL_LOCATION/etc/lal-user-env.sh" ]; then" \
>> ${LSCSOFT_ROOTDIR}/etc/lscsoftrc
echo "    source $LAL_LOCATION/etc/lal-user-env.sh" \
>> ${LSCSOFT_ROOTDIR}/etc/lscsoftrc
echo "fi" >> ${LSCSOFT_ROOTDIR}/etc/lscsoftrc
```

All CW code is now in the LALPulsar directory, which is part of the Git repository. We must install LALPulsar in order to use the CW applications in LALApps.

```
> cd ${LSCSOFT_SRCDIR}/lalpulsar
> ./00boot
> ./configure --prefix=${LALPULSAR_PREFIX} --with-gcc-flags
> make
> make install
```

Add the following to your .rc

```
mkdir -p ${LSCSOFT_ROOTDIR}/etc
echo "# setup LALPULSAR for development: " \
```

```
>> ${LSCSOFT_ROOTDIR}/etc/lscsoftrc
echo "export LALPULSAR_LOCATION=\${LSCSOFT_LOCATION}/lalpulsar" \
>> ${LSCSOFT_ROOTDIR}/etc/lscsoftrc
echo \
"if [ -f "\${LALPULSAR_LOCATION}/etc/lalpulsar-user-env.sh" ]; \
then" >> ${LSCSOFT_ROOTDIR}/etc/lscsoftrc
echo "  source \${LALPULSAR_LOCATION}/etc/lalpulsar-user-env.sh" \
>> ${LSCSOFT_ROOTDIR}/etc/lscsoftrc
echo "fi" >> ${LSCSOFT_ROOTDIR}/etc/lscsoftrc
```

Then, continue with LALApps.

```
> source ${LAL_PREFIX}/etc/lal-user-env.sh
> cd ${LSCSOFT_SRCDIR}/lalapps
> ./00boot
> ./configure --prefix=${LAL_PREFIX} --with-gcc-flags
> make
> make install
```

Add the following to your .rc file

```
echo "# setup LALApps for development:  "
>> ${LSCSOFT_ROOTDIR}/etc/lscsoftrc
echo "export LALAPPS_LOCATION=\${LSCSOFT_LOCATION}/lalapps"
>> ${LSCSOFT_ROOTDIR}/etc/lscsoftrc
echo "if [ -f "\${LALAPPS_LOCATION}/etc/lalapps-user-env.sh" ]; then"
>> ${LSCSOFT_ROOTDIR}/etc/lscsoftrc
echo "  source \${LALAPPS_LOCATION}/etc/lalapps-user-env.sh"
>> ${LSCSOFT_ROOTDIR}/etc/lscsoftrc
echo "fi" >> ${LSCSOFT_ROOTDIR}/etc/lscsoftrc
```

## Appendix 4B: Command line options

We list examples of how to run *lalapps-Makefakedata.v4* and *lalapps-pulsar-crosscorr*. The following command generates 1 year of 30 minute SFTs from the L1 interferometer, covering the frequency range 991.012 Hz–991.815 Hz with zero spindown. The sky position is  $(\alpha, \delta) = (1.16357, -0.0439203)$ , the inclination angle of the source is  $\cos \iota = -0.29359$ , and the polarization angle is  $\psi = 4.75401$ . The power spectral density is  $\sqrt{S_n} = 1.14233 \times 10^{-22} \text{ Hz}^{-1/2}$ ,

and the wave strain is  $h_0 = 1.10061 \times 10^{-21}$ . The reference time and start time of the SFTs are both set to 827884814 (in GPS seconds).

```
lalapps_Makefakedata_v4
--outSFTbname=/scratch/cchung/mcfrequencies/0/sfts
--IF0=L1 --ephemDir=/scratch/cchung/mcfrequencies/0
--ephemYear=05-09 --fmin=991.012 --Band=0.803
--Alpha=1.16357 --Delta=-0.0439203
--h0=1.10061e-21 --cosi=-0.29359 --psi=4.75401 --phi0=0
--Freq=991.413 --noiseSqrtSh=1.14233e-22 --refTime=827884814
--startTime=827884814 --f1dot=0 --duration=31536000
```

The following command runs the cross-correlation search over the frequency range 991.4115–991.4145 Hz.  $Q_1$  and  $Q_2$  are set to zero, and  $T_{\text{lag}}$  is set to 3600 s. The sky position  $(\alpha, \delta) = (1.16357, -0.0439203)$  is used as a search parameter. The averaging over  $\cos \iota$  and  $\psi$  is turned on.

```
lalapps_pulsar_crosscorr
--sftDir '/scratch/cchung/mcfrequencies/0/sfts/*.sft'
--f0 991.4115 --fBand 0.003 --fRes 1e-05 --q1 0 --q1Band 0
--q1Res 1e-25 --q2 0 --q2Band 0 --q2Res 1e-22 --blocksRngMed 51
--ephemDir /scratch/cchung/mcfrequencies/0 --ephemYear 05-09
--averagePsi --averageIota --detChoice 2
--skyRegion '(1.16357, -0.0439203)' --dDelta 0.002
--dAlpha 0.002 --maxlag 3600 --refTime 827884814
--dirnameOut /scratch/cchung/mcfrequencies/0
--filenameOut CrossCorr_ave.dat --useQCoeffs
```

Table A1 lists all the command line options available for *lalapps\_pulsar\_crosscorr*.

Command line option	Description
<code>-autoCorrelate</code>	Include autocorrelations (correlation of an SFT with itself) [FALSE]
<code>-f, -f0</code>	Start search frequency (Hz) [100]
<code>-b, -fBand</code>	Search frequency band (i.e. how far along in frequency to search; Hz) [1]
<code>-fRes</code>	Search frequency resolution (Hz) $[1/\Delta T]$
<code>-f1dot</code>	Start search frequency derivative (Hz s <sup>-1</sup> ) [0.0]
<code>-f1dotBand</code>	Search frequency derivative band (Hz s <sup>-1</sup> ) [0.0]

-r, -fdotRes	Search frequency derivative resolution ( $\text{Hz s}^{-1}$ ) [ $1/\Delta T^2$ ]
-fddot	Start frequency double derivative ( $\text{Hz s}^{-2}$ ) [0.0]
-fddotBand	Search frequency double derivative band ( $\text{Hz s}^{-2}$ ) [0.0]
-fddotRes	Search frequency double derivative resolution ( $\text{Hz s}^{-2}$ ) [ $1/\Delta T^3$ ]
-fRef	Reference frequency $\nu_{\text{ref}}$ , see equation (3.25) (Hz) [1]
-skyRegion	Sky-region polygon (or ‘allsky’). The polygon is bounded by at least 3 pairs of $(\alpha, \delta)$ . A single $(\alpha, \delta)$ pair searches one point. [NULL]
-dAlpha	Sky resolution (right ascension) (rad) [0.0]
-dDelta	Sky resolution (declination) (rad) [0.0]
-Tlag	Maximum time lag for SFT pairs (s) [0.0]
-detChoice	0: Correlate SFTs from same IFOs only; 1: different IFOs only; 2: all IFOs [2]
-refTime	Reference time for signal parameters (SSB) [0.0]
-averagePsi	Average over psi [TRUE]
-averageIota	Average over $\cos \iota$ [TRUE]
-cosi	Inclination angle [0.0]
-psi	Polarisation angle (rad) [0.0]
-q1	Starting $Q_1$ value. $Q_1$ is the gravitational wave torque defined in equation (3.25) [ $1\text{e-}24$ ]
-q1Band	$Q_1$ search band (i.e. how far along in $Q_1$ to search) [0.0]
-q1Res	$Q_1$ search resolution [ $1\text{e-}25$ ]
-q2	Starting $Q_2$ value $Q_2$ is the electromagnetic torque defined in equation (3.25) [ $1\text{e-}20$ ]
-q2Band	$Q_2$ search band (i.e. how far along in $Q_2$ to search) [0.0]
-q2Res	$Q_2$ search resolution [ $1\text{e-}21$ ]
-braking	Pulsar electromagnetic braking index [3]
-brakingBand	Pulsar electromagnetic braking index search band [0.0]
-brakingRes	Pulsar electromagnetic braking index search resolution [0.3]

-useQCoeffs

Use astrophysical spindown model [FALSE]

**Table A1:** All command line options for the cross-correlation search code, *lalapps\_pulsar\_crosscorr*, in LALApps.  $\Delta T$  is the length of each SFT, typically 30 mins. Default values are shown in square brackets.

## Appendix 4C: Derivation of $\mu$ and $\sigma^2$ in the presence of a signal

In this section, we derive the mean,  $\mu$ , and variance,  $\sigma^2$ , of the normalised cross-correlation statistic  $\rho/\sigma_\rho$ . Before doing so, however, we provide the full derivation of the mean and variance,  $\mu_\rho$  and  $\sigma_\rho^2$ , of the raw cross-correlation statistic  $\rho$ , summarised in the Appendix of Dhurandhar et al. (2008) (hereafter DMKW08).

The cross-correlation statistic is defined as  $\rho = \sum_\alpha (\tilde{\mathcal{G}}_\alpha^* \mathcal{Y}_\alpha + \tilde{\mathcal{G}}_\alpha \mathcal{Y}_\alpha^*) / \sigma_\alpha^2$ , with  $\sigma_\alpha^2 = S_n^{(I)}(\nu_k) S_n^{(J)}(\nu_{k'}) / (4\Delta T^2)$ ,  $\mathcal{Y}_\alpha = \tilde{x}_I^* \tilde{x}_J / (\Delta T^2)$ , and  $\alpha = I, J$  is the pair index. More explicitly,

$$\mathcal{Y}_\alpha = \frac{1}{\Delta T^2} (h_I^* + n_I^*) (h_J + n_J) \quad (\text{A33})$$

where  $h_I$  and  $n_I$  denote  $\tilde{h}(\nu_I)$  and  $\tilde{n}(\nu_I)$ , the Fourier transformed signal and noise at the time of the midpoint of SFT  $I$ .

For an ensemble of noise realisations, the mean of  $\rho$  is therefore

$$\begin{aligned} \langle \rho \rangle &= \sum_\alpha \frac{\tilde{\mathcal{G}}_\alpha^*}{\sigma_\alpha^2} \langle \mathcal{Y}_\alpha \rangle + \text{c.c.} \\ &= \sum_\alpha \frac{\tilde{\mathcal{G}}_\alpha^*}{\sigma_\alpha^2 \Delta T^2} \langle h_I^* h_J + h_I^* n_J + h_J n_I^* + n_I^* n_J \rangle + \text{c.c.} \end{aligned} \quad (\text{A34})$$

$$= \sum_\alpha \frac{\tilde{\mathcal{G}}_\alpha^*}{\sigma_\alpha^2 \Delta T^2} \left( \Delta T^2 h_0^2 \tilde{\mathcal{G}}_\alpha + \langle n_I^* n_J \rangle \right) + \text{c.c.}, \quad (\text{A35})$$

where c.c. denotes the complex conjugate of the first term. To get from (A34) to (A35), we use the relations  $h_I^* h_J = h_0^2 \Delta T^2 \tilde{\mathcal{G}}_\alpha$  (equation 3.9 of DMKW08) and  $\langle n_I^* \rangle = \langle n_J \rangle = 0$ . If self-correlations are included ( $I = J$ ), we have  $\langle n_I^* n_J \rangle = \frac{\Delta T}{2} S_n^I \delta_{IJ}$  (equation 2.21 of DMKW08), where  $S_n^I$  denotes the single-

sided power spectral density of SFT  $I$  at frequency  $\nu_I$ . This gives

$$\langle \rho \rangle = \frac{1}{\Delta T} \sum_I \frac{\tilde{\mathcal{G}}_{II}^*}{\sigma_{II}^2} S_n^I + h_0^2 \sum_{\alpha} u_{\alpha} \tilde{\mathcal{G}}_{\alpha} + \text{c.c.} \quad (\text{A36})$$

The variance of  $\rho$  is given by  $\sigma_{\rho}^2 = \langle \rho^2 \rangle - \langle \rho \rangle^2$ . We consider now the  $\langle \rho_{\alpha}^2 \rangle$  term. Let  $\alpha$  denote the pair  $IJ$ , and  $\beta$  denote the pair  $KL$ . We have<sup>2</sup>

$$\langle \rho^2 \rangle = \sum_{\alpha, \beta} \frac{1}{\sigma_{\alpha}^2 \sigma_{\beta}^2} \left\langle \left( \tilde{\mathcal{G}}_{\alpha}^* \mathcal{Y}_{\alpha} + \tilde{\mathcal{G}}_{\alpha} \mathcal{Y}_{\alpha}^* \right) \left( \tilde{\mathcal{G}}_{\beta}^* \mathcal{Y}_{\beta} + \tilde{\mathcal{G}}_{\beta} \mathcal{Y}_{\beta}^* \right) \right\rangle \quad (\text{A37})$$

$$= \sum_{\alpha, \beta} \frac{1}{\sigma_{\alpha}^2 \sigma_{\beta}^2} \left\langle \tilde{\mathcal{G}}_{\alpha}^* \tilde{\mathcal{G}}_{\beta}^* \mathcal{Y}_{\alpha} \mathcal{Y}_{\beta} + \tilde{\mathcal{G}}_{\alpha}^* \tilde{\mathcal{G}}_{\beta} \mathcal{Y}_{\alpha} \mathcal{Y}_{\beta}^* + \text{c.c.} \right\rangle. \quad (\text{A38})$$

Expanding  $\langle \mathcal{Y}_{\alpha} \mathcal{Y}_{\beta} \rangle$  in detail, we have

$$\langle \mathcal{Y}_{\alpha} \mathcal{Y}_{\beta} \rangle = \frac{1}{\Delta T^4} \langle (h_I^* h_J + h_I^* n_J + h_J n_I^* + n_I^* n_J) (h_K^* h_L + h_K^* n_L + h_L n_K^* + n_L n_K^*) \rangle. \quad (\text{A39})$$

Any terms containing odd powers of  $h_0$  vanish because they contain a vanishing  $\langle n \rangle$  or  $\langle n^3 \rangle$  factor (we assume the noise is symmetric).<sup>3</sup> We are therefore left with

$$\begin{aligned} \langle \mathcal{Y}_{\alpha} \mathcal{Y}_{\beta} \rangle &= \frac{1}{\Delta T^4} \langle h_I^* h_J n_K^* n_L + h_K^* h_L n_I^* n_J + h_I^* h_L n_J n_K^* \\ &\quad + h_J h_K^* n_I^* n_L + n_I^* n_J n_K^* n_L \rangle \quad (\text{A40}) \\ &= \frac{1}{\Delta T^4} \left( \frac{\Delta T^3}{2} h_0^2 \tilde{\mathcal{G}}_{IJ} S_n^K \delta_{KL} + \frac{\Delta T^3}{2} h_0^2 \tilde{\mathcal{G}}_{KL} S_n^I \delta_{IJ} \right. \\ &\quad \left. + \frac{\Delta T^3}{2} h_0^2 \tilde{\mathcal{G}}_{IL} S_n^K \delta_{JK} + \frac{\Delta T^3}{2} h_0^2 \tilde{\mathcal{G}}_{JK} S_n^I \delta_{IL} \right. \\ &\quad \left. + \langle n_I^* n_J n_K^* n_L \rangle \right) + \mathcal{O}(h_0^4). \quad (\text{A41}) \end{aligned}$$

In equation (A3) of Dhurandhar et al. (2008), the last term in A41 is written as

$$\langle n_I^* n_J n_K^* n_L \rangle = 2\delta_{I(J\delta_{L)K}} \langle |n_I|^2 \rangle \langle |n_K|^2 \rangle, \quad (\text{A42})$$

where the indices within parentheses are symmetrized over, i.e.  $X_{(IJ)} = (X_{IJ} + X_{JI})/2$ . Using this notation, A41 can be expressed as [equation (A6)

<sup>2</sup>Note that  $\sigma_{IJ} = \sigma_{JI}$ ,  $\tilde{\mathcal{G}}_{IJ} = \tilde{\mathcal{G}}_{JI}^*$ , and  $\mathcal{Y}_{IJ} = \mathcal{Y}_{JI}^*$ .

<sup>3</sup>Additionally, any noise terms containing the product of two conjugates, or two normal terms (e.g.  $\langle n_I n_J \rangle$  or  $\langle n_I^* n_J^* \rangle$ ) are zero. To illustrate, consider the case  $I = J$ , which gives  $\langle n_I n_I \rangle = \langle \text{Re}(n_I)^2 \rangle - \langle \text{Im}(n_I)^2 \rangle + 2i \langle \text{Re}(n_I) \text{Im}(n_I) \rangle$ . For purely random noise, the first two terms cancel each other, and the third term is zero.

of Dhurandhar et al. (2008)]<sup>4</sup>

$$\langle \mathcal{Y}_{IJ} \mathcal{Y}_{KL} \rangle = \frac{1}{\Delta T^2} \delta_{I(J\delta_L)K} S_n^I S_n^K + \frac{h_0^2}{\Delta T} \left[ \tilde{\mathcal{G}}_{I(J\delta_L)K} S_n^K + \delta_{I(J\tilde{\mathcal{G}}_L)K} S_n^I \right]. \quad (\text{A43})$$

Ignoring self-correlations ( $I \neq J, K \neq L$ ), and substituting this into (A38), we have

$$\langle \rho_\alpha^2 \rangle = 2|u_{IJ}|^2 \left[ \frac{S_n^I S_n^J}{4\Delta T^2} + \frac{h_0^2}{2\Delta T} \left( \tilde{\mathcal{G}}_{II} S_n^J + \tilde{\mathcal{G}}_{JJ} S_n^I \right) \right] \quad (\text{A44})$$

For  $I \neq J$ ,  $\langle \rho_\alpha \rangle^2$  is of order  $h_0^4$ , and so the variance of  $\rho$  is just given by (A44) plus  $\mathcal{O}(h_0^4)$  terms. It can be written in the simplified form  $\sigma_\rho^2 = \sigma_{(0)}^2 + h_0^2 \sigma_{(1)}^2$ , where  $\sigma_{(0)}^2$  is the variance in the absence of a signal.

We note that throughout this chapter, we have called the output of the search code  $\rho/\sigma_\rho$ , where  $\sigma_\rho$  is defined in the small signal limit, i.e.  $\sigma_\rho = \sigma_{(0)}$ . We now write this explicitly as

$$\frac{\rho}{\sigma_{(0)}} = \frac{1}{\sqrt{2}} \sum_\alpha \frac{\tilde{\mathcal{G}}_\alpha^* \mathcal{Y}_\alpha + \tilde{\mathcal{G}}_\alpha \mathcal{Y}_\alpha^*}{\sigma_\alpha (\tilde{\mathcal{G}}_\alpha^* \tilde{\mathcal{G}}_\alpha)^{1/2}}. \quad (\text{A45})$$

We now derive the mean and variance of  $\rho/\sigma_0$ . The mean is given by

$$\begin{aligned} \left\langle \frac{\rho}{\sigma_{(0)}} \right\rangle &= \sum_\alpha \left( \frac{\tilde{\mathcal{G}}_\alpha^*}{2\sigma_\alpha^2 \tilde{\mathcal{G}}_\alpha} \right)^{1/2} \langle \mathcal{Y}_\alpha \rangle + \text{c.c.} \\ &= \left[ \sum_\alpha h_0^2 \tilde{\mathcal{G}}_\alpha \left( \frac{\tilde{\mathcal{G}}_\alpha^*}{2\sigma_\alpha^2 \tilde{\mathcal{G}}_\alpha} \right)^{1/2} + \sum_I \frac{1}{2\Delta T} S_n^I \left( \frac{\tilde{\mathcal{G}}_{II}^*}{2\sigma_{II}^2 \tilde{\mathcal{G}}_{II}} \right)^{1/2} \right] + \text{c.c.} \\ &= \sqrt{2} h_0^2 \sum_\alpha |u_\alpha| + \frac{1}{2^{3/2} \Delta T} \sum_I S_n^I |u_{II}| \left( \frac{1}{\tilde{\mathcal{G}}_{II} + \tilde{\mathcal{G}}_{II}^*} \right). \end{aligned} \quad (\text{A46})$$

To calculate the variance of  $\rho/\sigma_{(0)}$ , we first calculate the term  $\langle (\rho/\sigma_{(0)})^2 \rangle$ ,

---

<sup>4</sup>We note that we have been unable to reproduce equation (A6) from Dhurandhar et al. (2008).

given by

$$\begin{aligned} \left\langle \left( \frac{\rho}{\sigma_{(0)}} \right)^2 \right\rangle &= \frac{1}{2} \sum_{\alpha, \beta} \frac{\left( \tilde{\mathcal{G}}_\alpha^* \tilde{\mathcal{G}}_\alpha \tilde{\mathcal{G}}_\beta^* \tilde{\mathcal{G}}_\beta \right)^{-1/2}}{\sigma_\alpha^2 \sigma_\beta^2} \left\langle \left( \tilde{\mathcal{G}}_\alpha^* \mathcal{Y}_\alpha + \tilde{\mathcal{G}}_\alpha \mathcal{Y}_\alpha^* \right) \right. \\ &\quad \left. \times \left( \tilde{\mathcal{G}}_\beta^* \mathcal{Y}_\beta + \tilde{\mathcal{G}}_\beta \mathcal{Y}_\beta^* \right) \right\rangle \end{aligned} \quad (\text{A47})$$

$$\begin{aligned} &= \frac{1}{2} \sum_{\alpha, \beta} \frac{\left( \tilde{\mathcal{G}}_\alpha^* \tilde{\mathcal{G}}_\alpha \tilde{\mathcal{G}}_\beta^* \tilde{\mathcal{G}}_\beta \right)^{-1/2}}{\sigma_\alpha^2 \sigma_\beta^2} \left\langle \tilde{\mathcal{G}}_\alpha^* \tilde{\mathcal{G}}_\beta^* \mathcal{Y}_\alpha \mathcal{Y}_\beta \right. \\ &\quad \left. + \tilde{\mathcal{G}}_\alpha \tilde{\mathcal{G}}_\beta \mathcal{Y}_\alpha \mathcal{Y}_\beta^* + \text{c.c.} \right\rangle \end{aligned} \quad (\text{A48})$$

$$= \frac{1}{2} \sum_{\alpha, \beta} \frac{1}{\sigma_\alpha^2 \sigma_\beta^2} \left( \frac{\tilde{\mathcal{G}}_\alpha^* \tilde{\mathcal{G}}_\beta}{\tilde{\mathcal{G}}_\alpha \tilde{\mathcal{G}}_\beta^*} \right)^{1/2} \langle \mathcal{Y}_\alpha \mathcal{Y}_\beta^* \rangle + \text{c.c.} \quad (\text{A49})$$

Once again, we ignore self-correlations ( $I \neq J, K \neq L$ ), and set  $I = K$  and  $J = L$ . This yields

$$\sigma^2 = \left\langle \left( \frac{\rho}{\sigma_{(0)}} \right)^2 \right\rangle = |u_{IJ}|^2 \left[ \frac{S_n^I S_n^J}{4\Delta T^2} + \frac{h_0^2}{2\Delta T} \left( \tilde{\mathcal{G}}_{II} S_n^J + \tilde{\mathcal{G}}_{JJ} S_n^I \right) \right] + \mathcal{O}(h_0^4). \quad (\text{A50})$$

We note that (A50) has exactly the same form as (A44), but it is a factor of 2 smaller.

## **Appendix 5A: Glossary of phase portrait descriptors**

Figure A1 gathers together, in a handy and easy-to-read table, the colloquial descriptors used to label phase portraits in the text. The parameters for each example are stated in the caption.

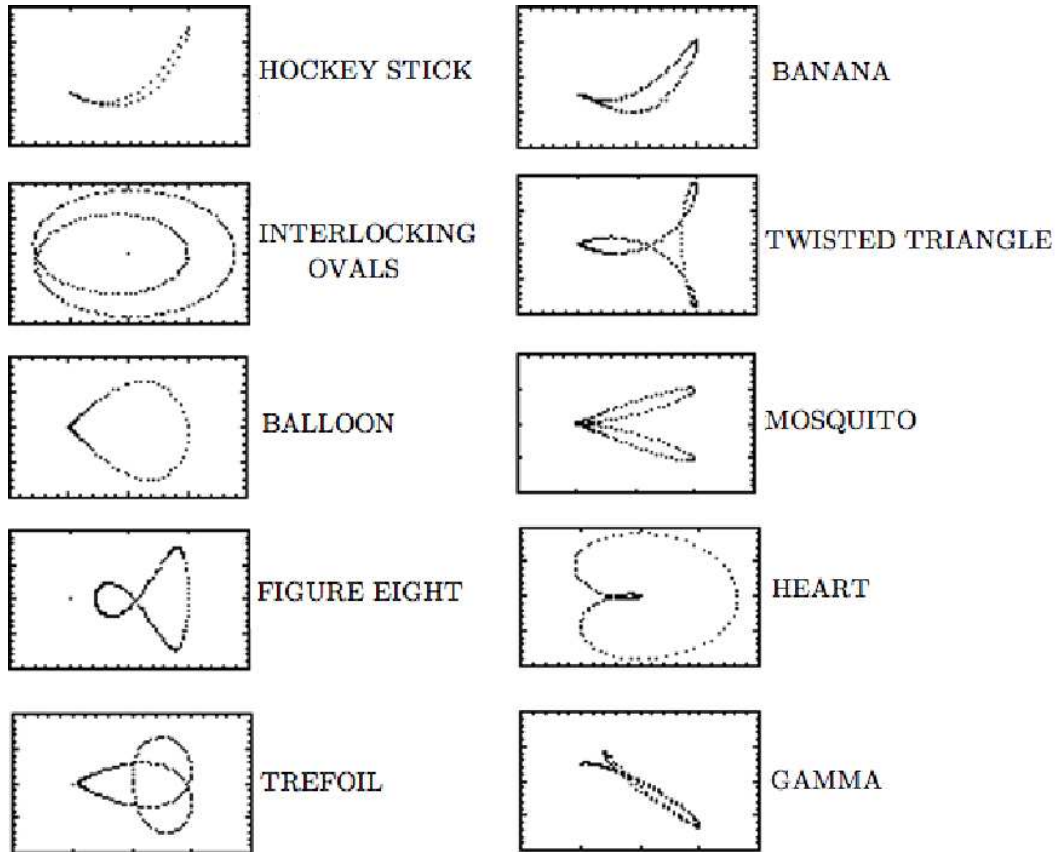


**Figure A1:** Colloquial descriptors of phase portraits encountered in this chapter.

*Left column, top to bottom:* (i)  $I$ - $Q$  for pure dipole, filled core beam,  $(\alpha, i) = (60^\circ, 40^\circ)$ ; (ii)  $U$ - $Q$  for pure dipole, filled core beam,  $(\alpha, i) = (20^\circ, 10^\circ)$ ; (iii)  $I$ - $U$  for pure dipole, filled core beam,  $(\alpha, i) = (30^\circ, 70^\circ)$ ; (iv)  $I$ - $U$  for pure dipole, hollow cone,  $(\alpha, i) = (60^\circ, 10^\circ)$ ; (v)  $I$ - $U$  for pure dipole, hollow cone,  $(\alpha, i) = (50^\circ, 30^\circ)$ . *Right column, top to bottom:* (i)  $I$ - $U$  for current-modified dipole, hollow cone,  $(\alpha, i) = (80^\circ, 20^\circ)$ ; (ii)  $I$ - $U$  for pure dipole, hollow cone,  $(\alpha, i) = (60^\circ, 30^\circ)$ ; (iii)  $I$ - $U$  for pure dipole, hollow cone,  $(\alpha, i) = (50^\circ, 50^\circ)$ ; (iv)  $Q$ - $U$  for pure dipole, hollow cone,  $(\alpha, i) = (70^\circ, 40^\circ)$ ; (v)  $I$ - $Q$  for pure dipole, hollow cone,  $(\alpha, i) = (50^\circ, 40^\circ)$ . All examples share the same polarization pattern  $L/I = \cos \theta_0$ .

---

## Appendix 6A: Atlas of look-up tables of Stokes phase portraits

We present look-up tables for the beam patterns and linear polarization models used in chapter 5, updated to include interpulse and relativistic aberration effects. All figures are for  $r = 0.1r_{LC}$ . Stokes phase portraits and PA swings are shown for a current-modified dipole with

1. a filled core beam with  $L = I \cos \theta$  (Figures A2–A5),
2. a filled core beam with  $L = I \sin \theta$  (Figures A6–A9),
3. a hollow cone with  $L = I \cos \theta$  (Figures A10–A13), and
4. a hollow cone with  $L = I \sin \theta$  (Figures A14–A17).

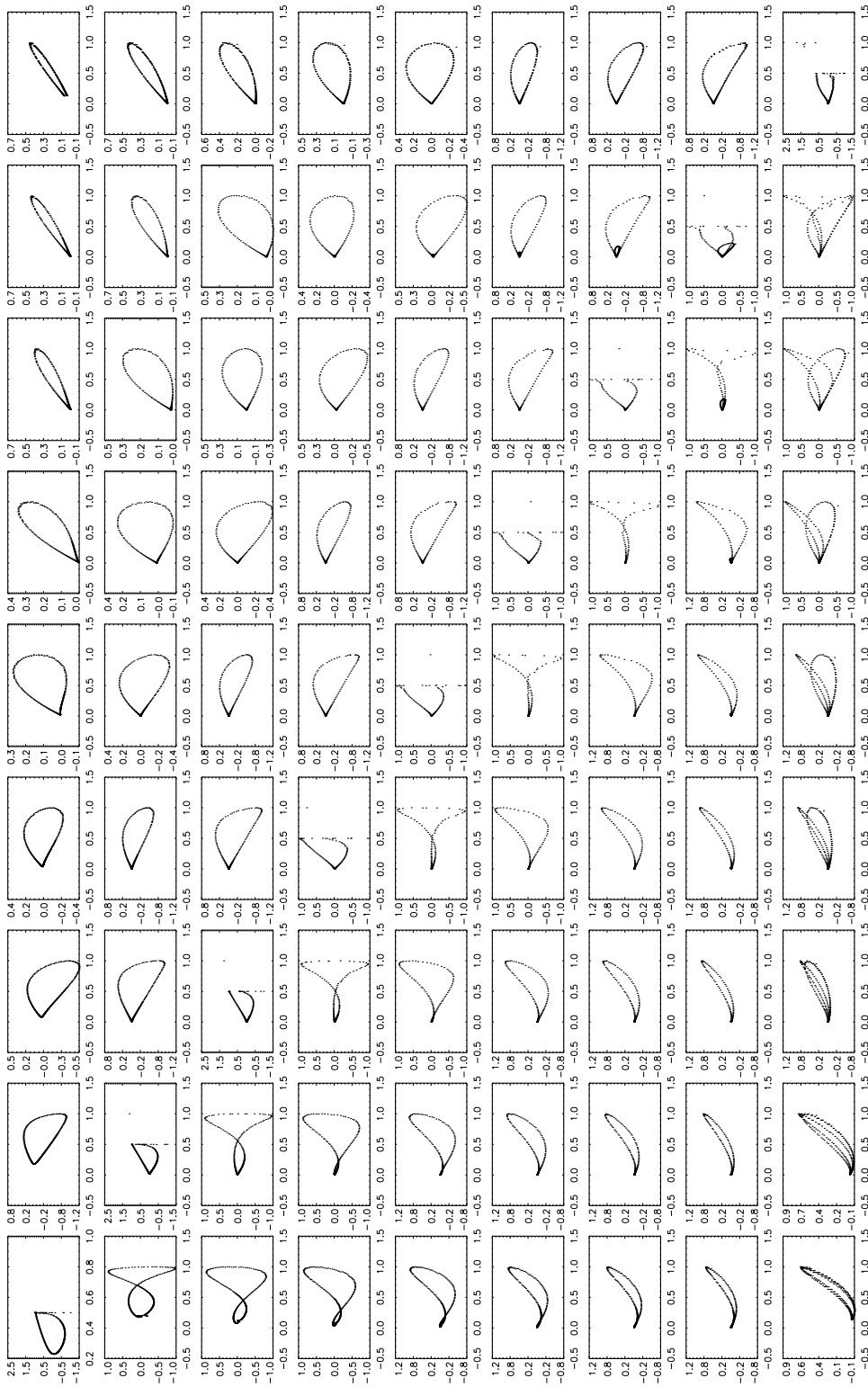


**Figure A2:** Current-modified dipole. Look-up table of Stokes phase portraits in the  $I$ - $Q$  plane for filled core beams with degree of linear polarization  $L = I \cos \theta$ , where  $\theta$  is the emission point colatitude, and  $r = 0.1r_{\text{LC}}$ . The panels are organised in landscape mode, in order of increasing  $10^\circ \leq i \leq 90^\circ$  (left–right) and  $10^\circ \leq \alpha \leq 90^\circ$  (top–bottom) in intervals of  $10^\circ$ .  $I$  is plotted on the horizontal axis and normalised by its peak value.  $Q$  is plotted on the vertical axis.

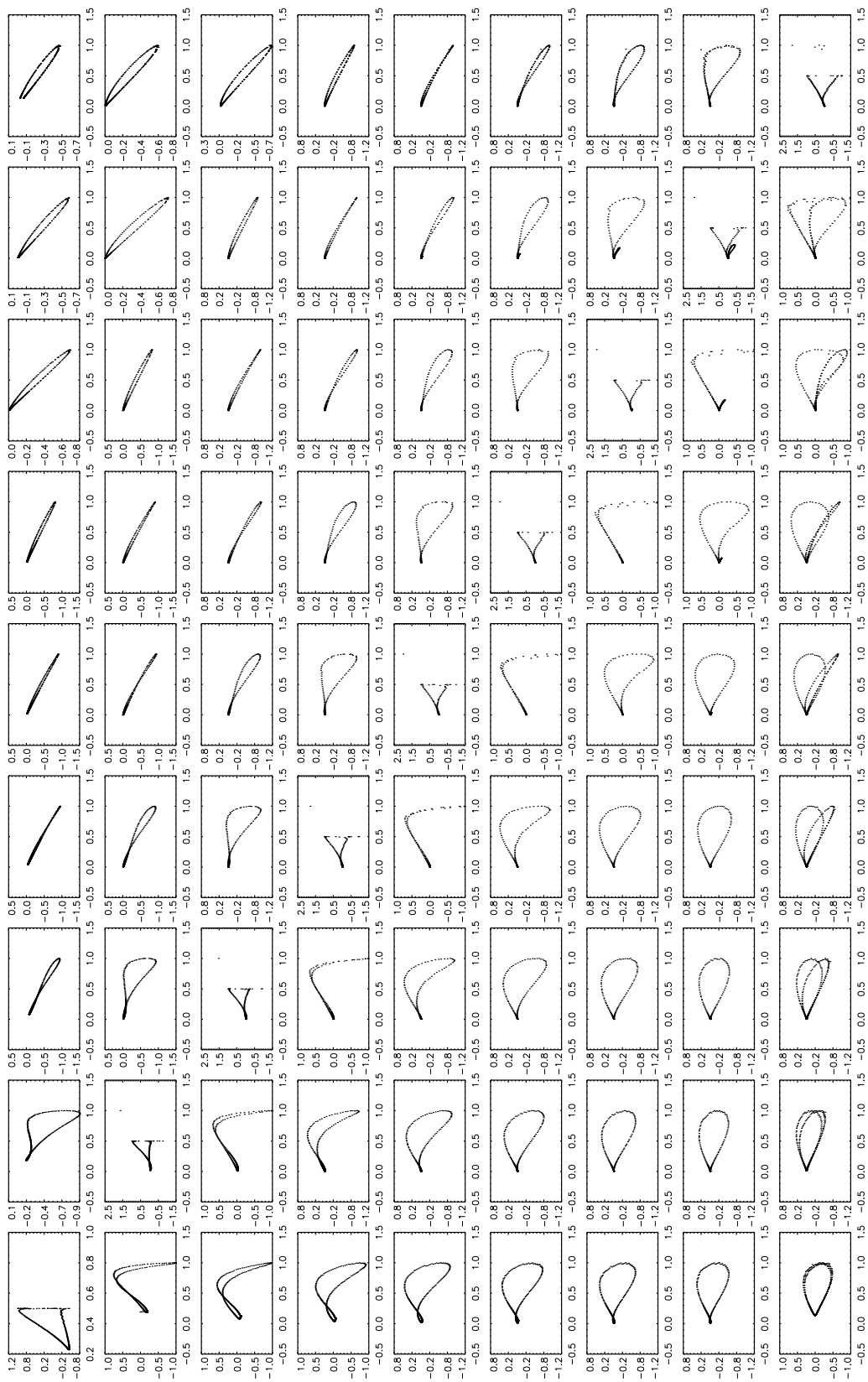


**Figure A3:** Current-modified dipole. Layout as for Figure A2, but for  $I$ - $U$  ( $I$  on the horizontal axis).

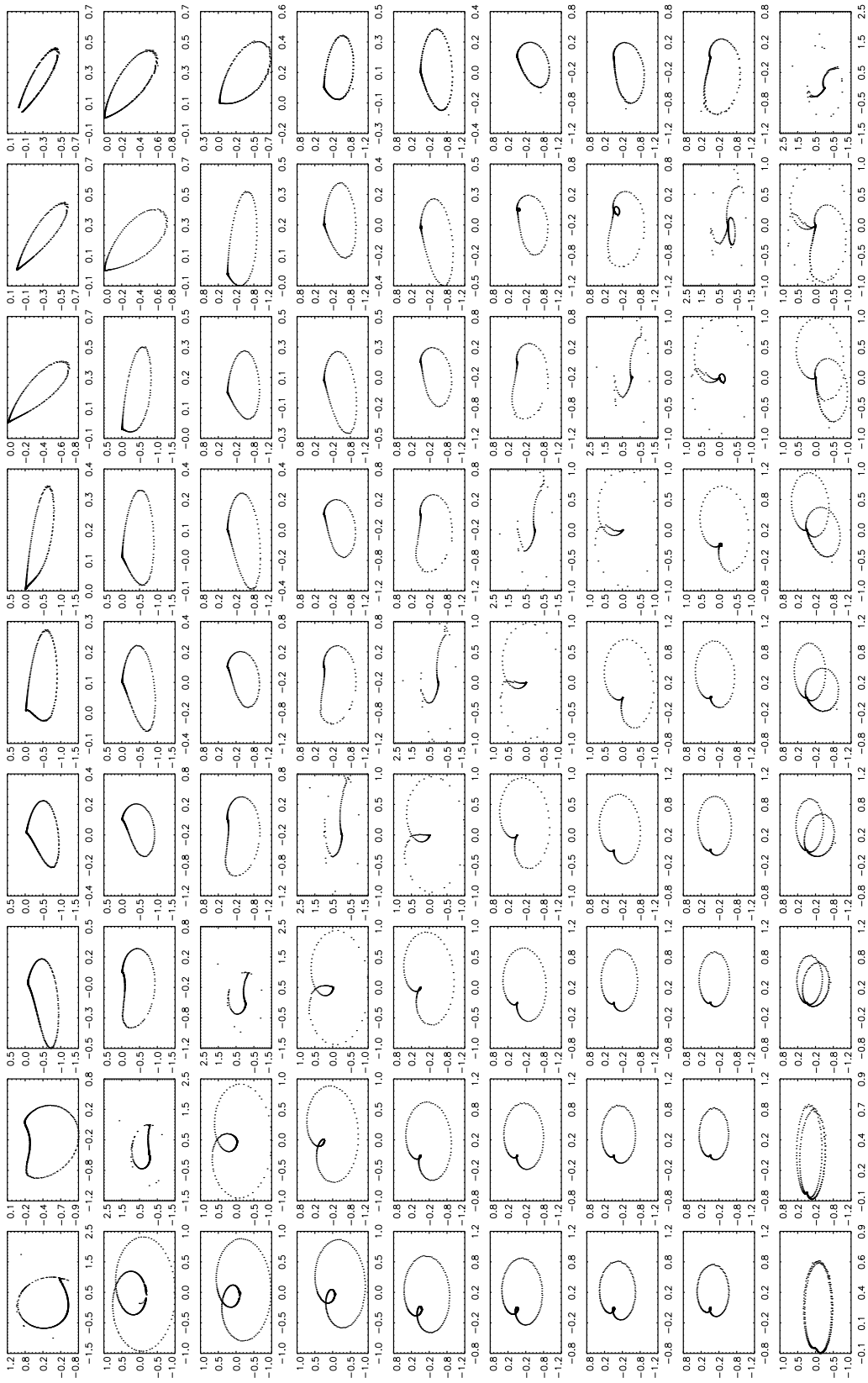


**Figure A4:** Current-modified dipole. Layout as for Figure A2, but for  $Q$ - $U$  ( $Q$  on the horizontal axis).

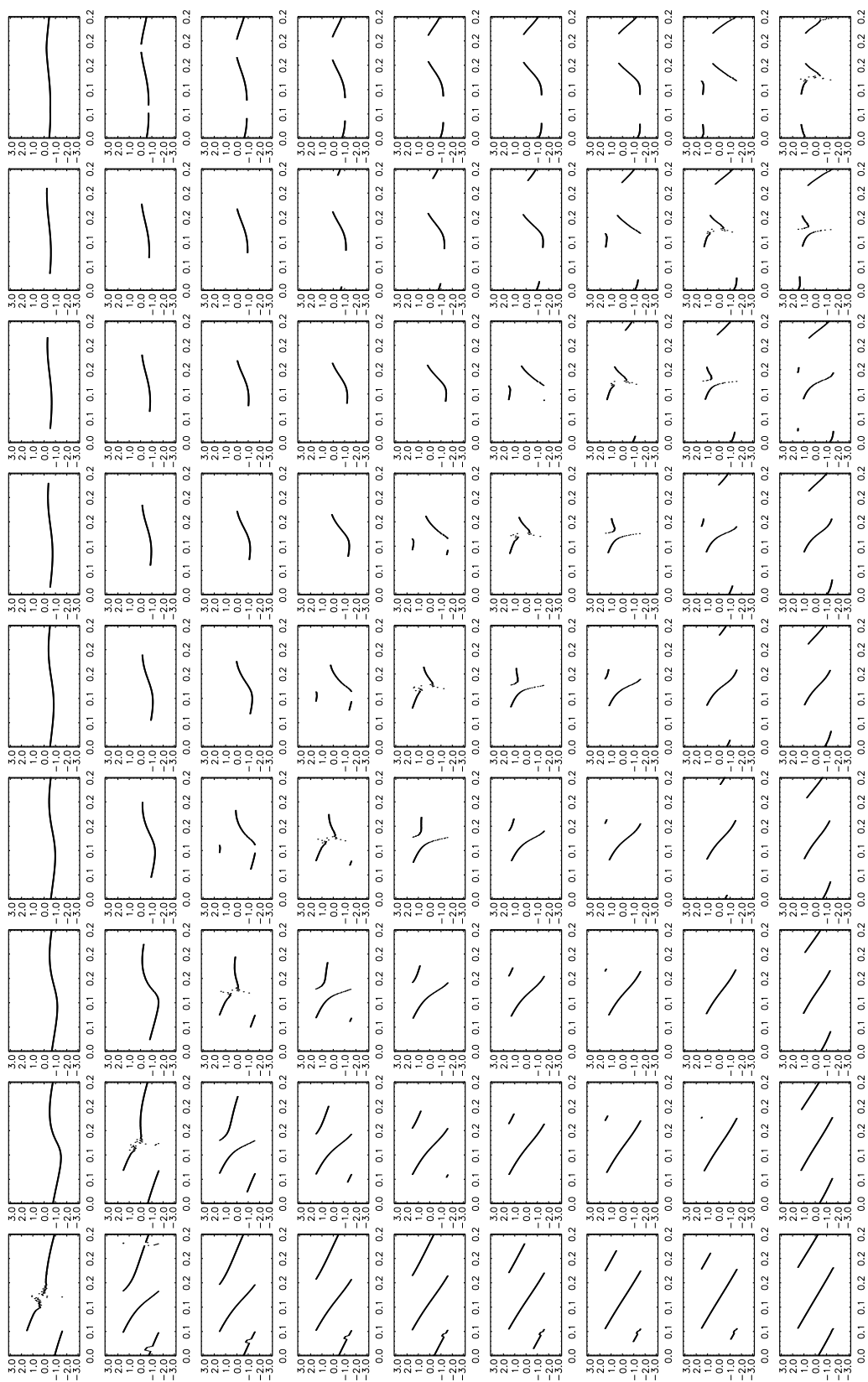


**Figure A5:** Current-modified dipole. Layout as for Figure A2, but for position angle (on the vertical axis in landscape orientation, in units of radians) versus pulse longitude (on the horizontal axis, in units of  $2\pi$  radians).

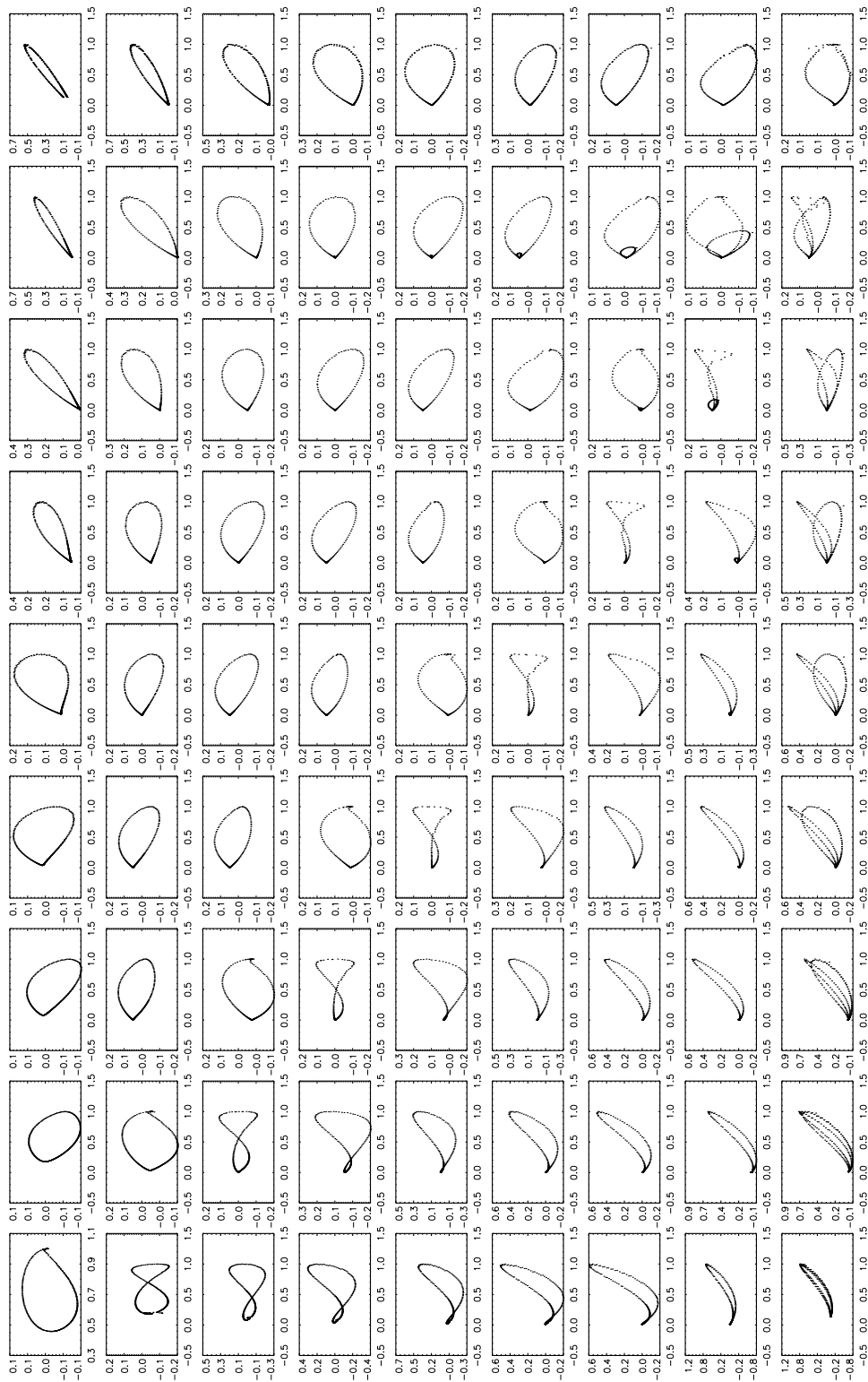


**Figure A6:** Current-modified dipole. Look-up table of Stokes phase portraits in the  $I$ - $Q$  plane for filled core beams with degree of linear polarization  $L = I \sin \theta$ , where  $\theta$  is the emission point colatitude, and  $r = 0.1r_{\text{LC}}$ . The panels are organised in landscape mode, in order of increasing  $10^\circ \leq i \leq 90^\circ$  (left–right) and  $10^\circ \leq \alpha \leq 90^\circ$  (top–bottom) in intervals of  $10^\circ$ .  $I$  is plotted on the horizontal axis and normalised by its peak value.  $Q$  is plotted on the vertical axis.

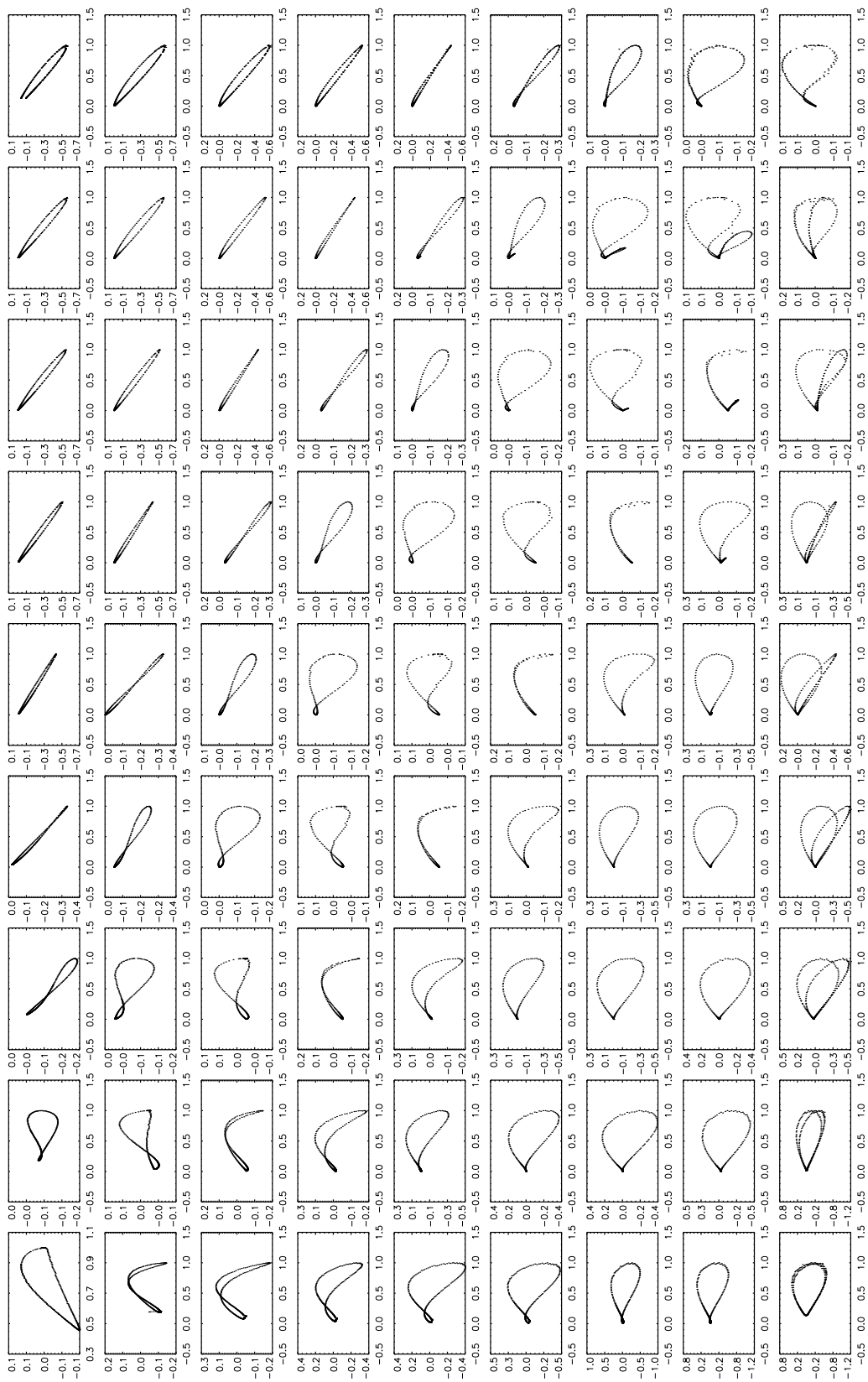


**Figure A7:** Current-modified dipole. Layout as for Figure A6, but for  $I$ - $U$  ( $I$  on the horizontal axis).

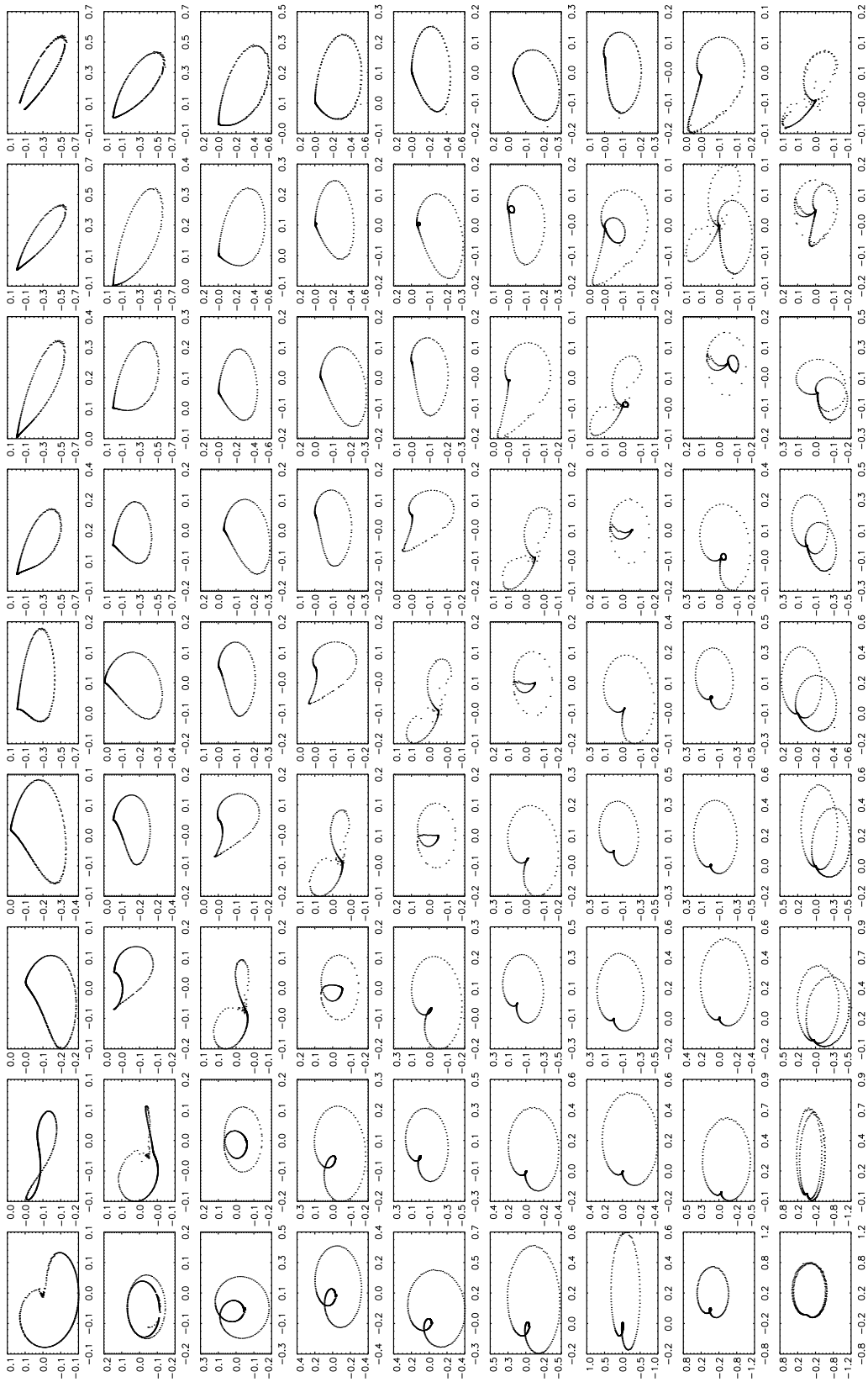


**Figure A8:** Current-modified dipole. Layout as for Figure A6, but for  $Q$ - $U$  ( $Q$  on the horizontal axis).



**Figure A9:** Current-modified dipole. Layout as for Figure A6, but for position angle (on the vertical axis in landscape orientation, in units of radians) versus pulse longitude (on the horizontal axis, in units of  $2\pi$  radians).

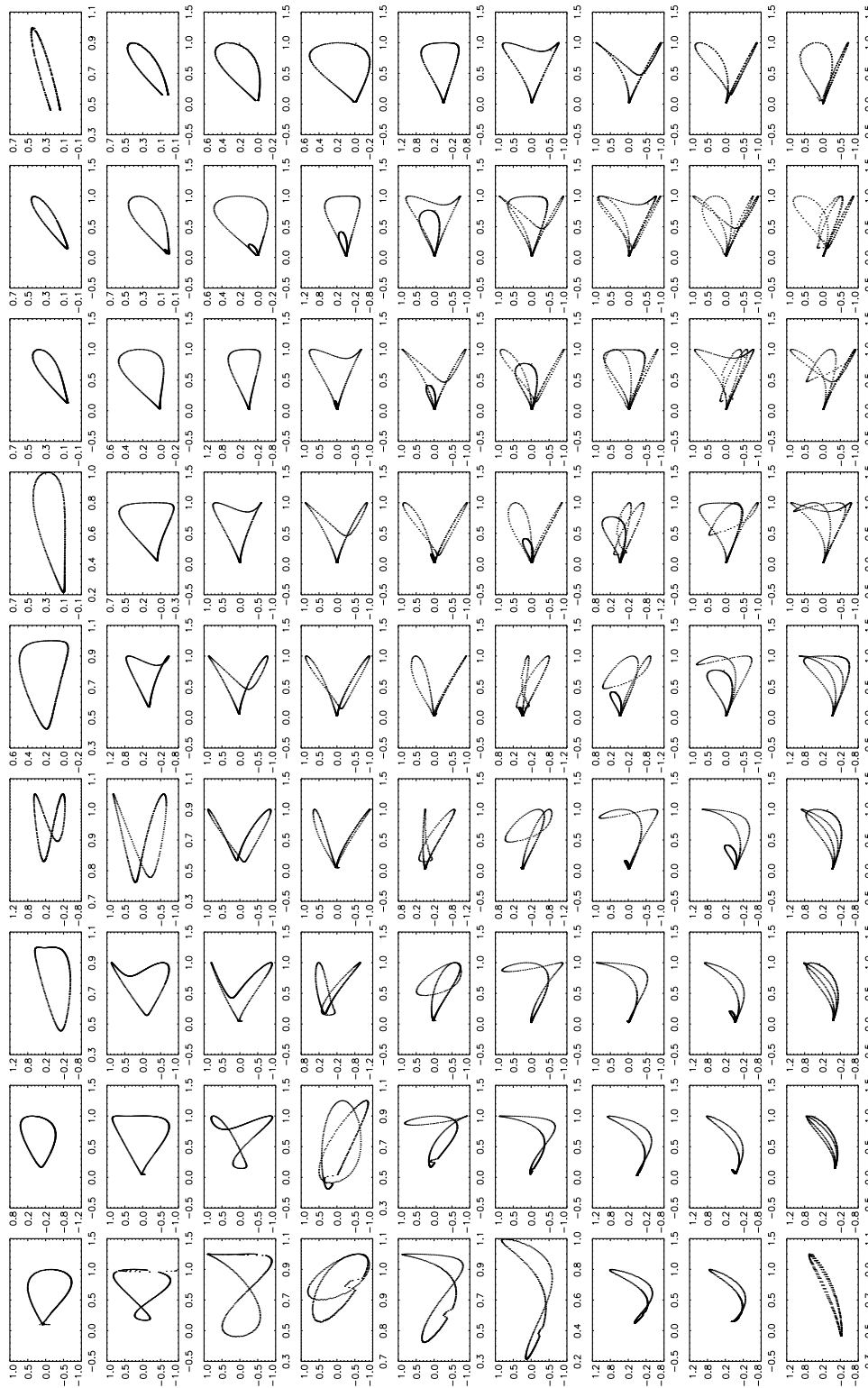


**Figure A10:** Current-modified dipole. Look-up table of Stokes phase portraits in the  $I$ - $Q$  plane for hollow cones with opening angle  $25^\circ$  and degree of linear polarization  $L = I \cos \theta$ , where  $\theta$  is the emission point colatitude, and  $r = 0.1r_{LC}$ . The panels are organised in landscape mode, in order of increasing  $10^\circ \leq i \leq 90^\circ$  (left–right) and  $10^\circ \leq \alpha \leq 90^\circ$  (top–bottom) in intervals of  $10^\circ$ .  $I$  is plotted on the horizontal axis and normalised by its peak value.  $Q$  is plotted on the vertical axis.

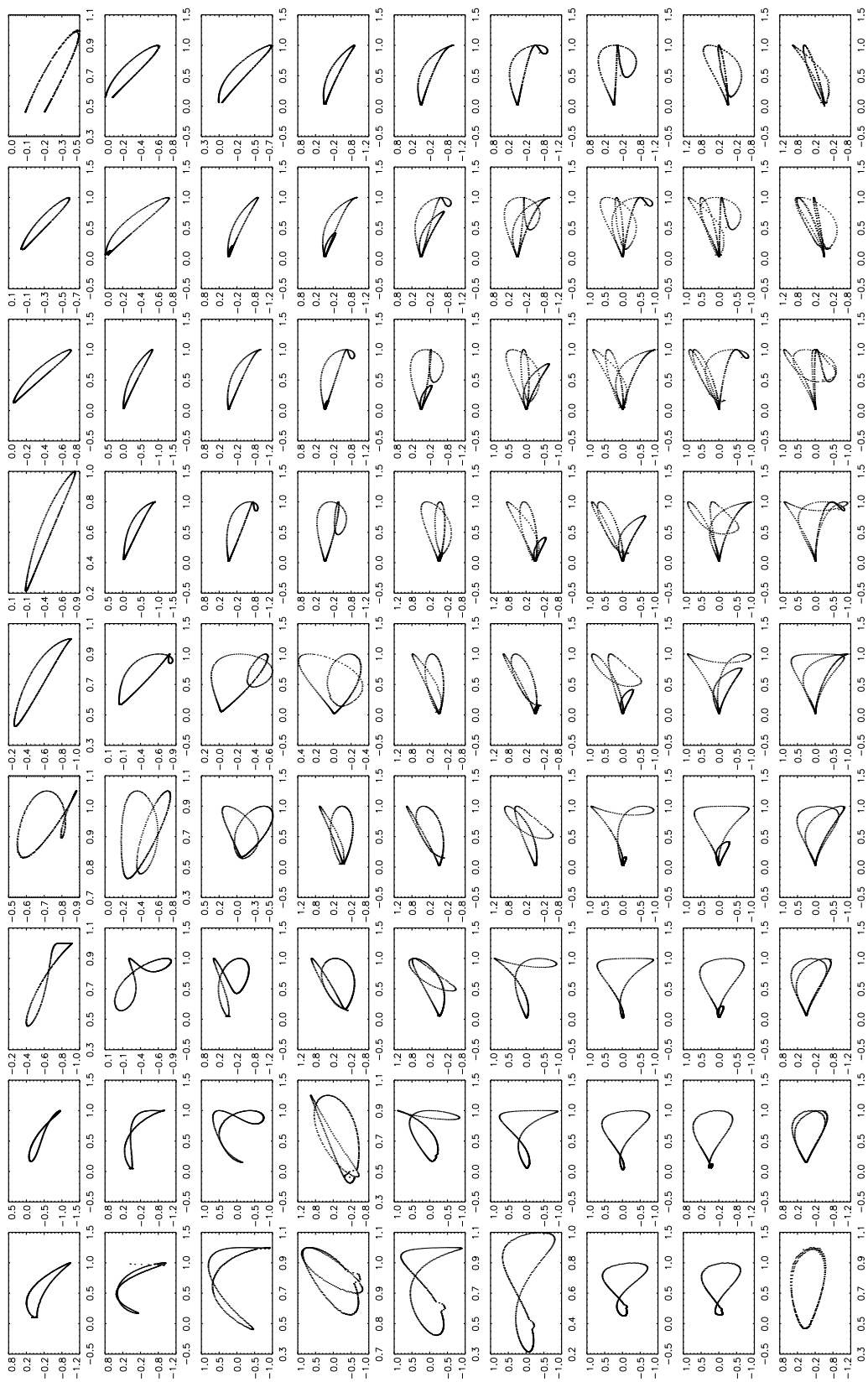


**Figure A11:** Current-modified dipole. Layout as for Figure A10, but for  $I$ - $U$  ( $I$  on the horizontal axis).

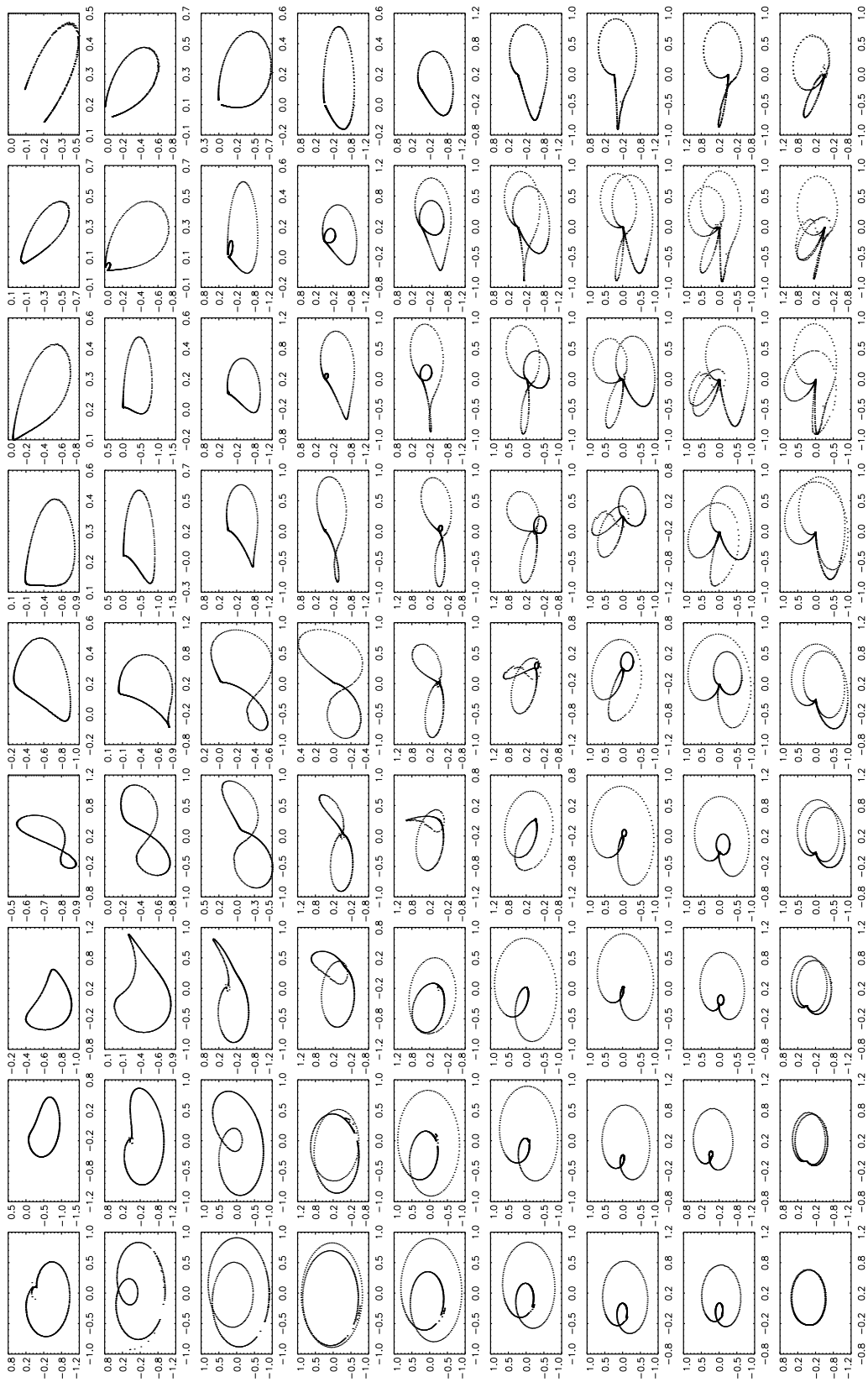


**Figure A12:** Current-modified dipole. Layout as for Figure A10, but for  $Q-U$  ( $Q$  on the horizontal axis).

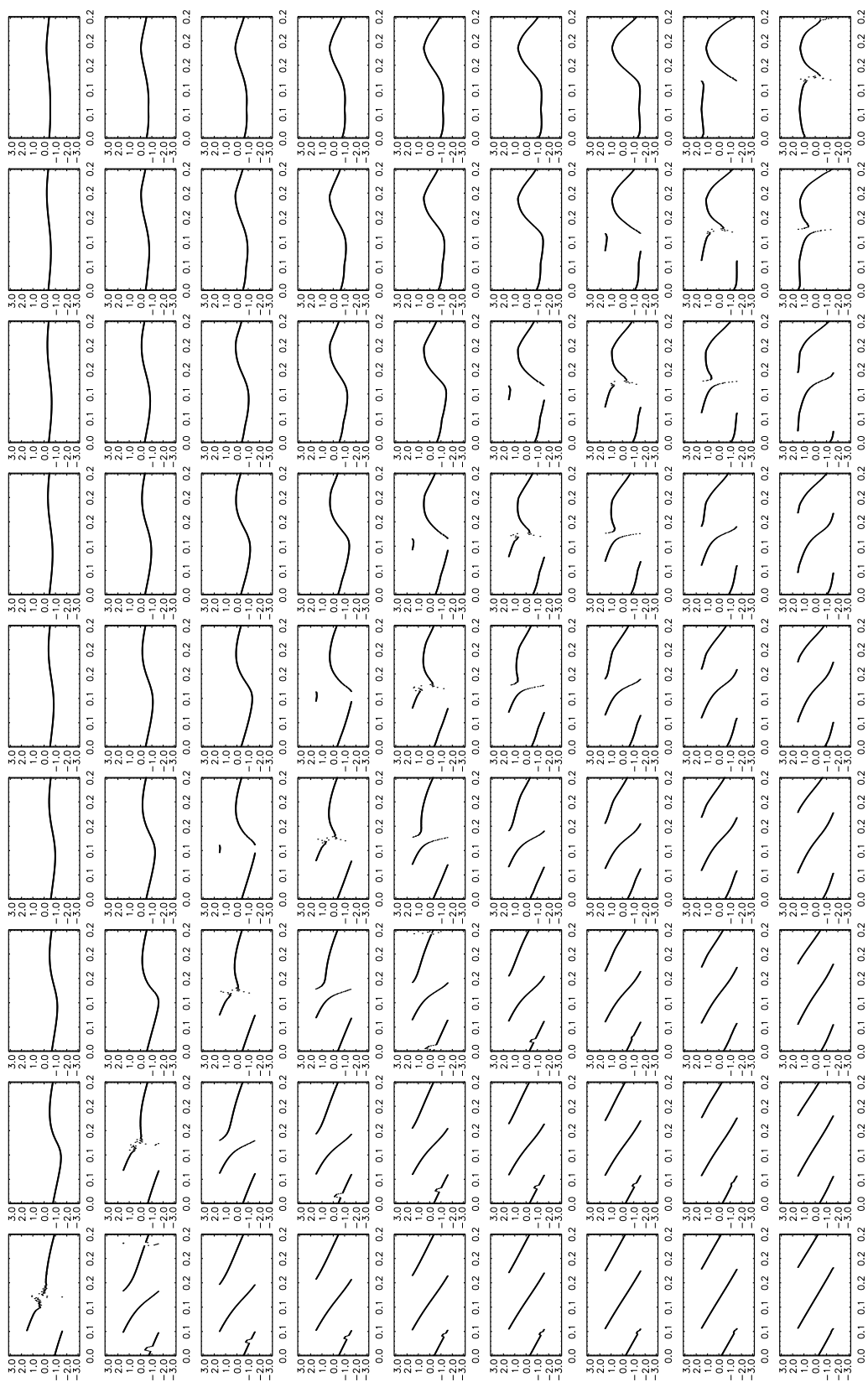


**Figure A13:** Current-modified dipole. Layout as for Figure A10, but for position angle (on the vertical axis in landscape orientation, in units of radians) versus pulse longitude (on the horizontal axis, in units of  $2\pi$  radians).

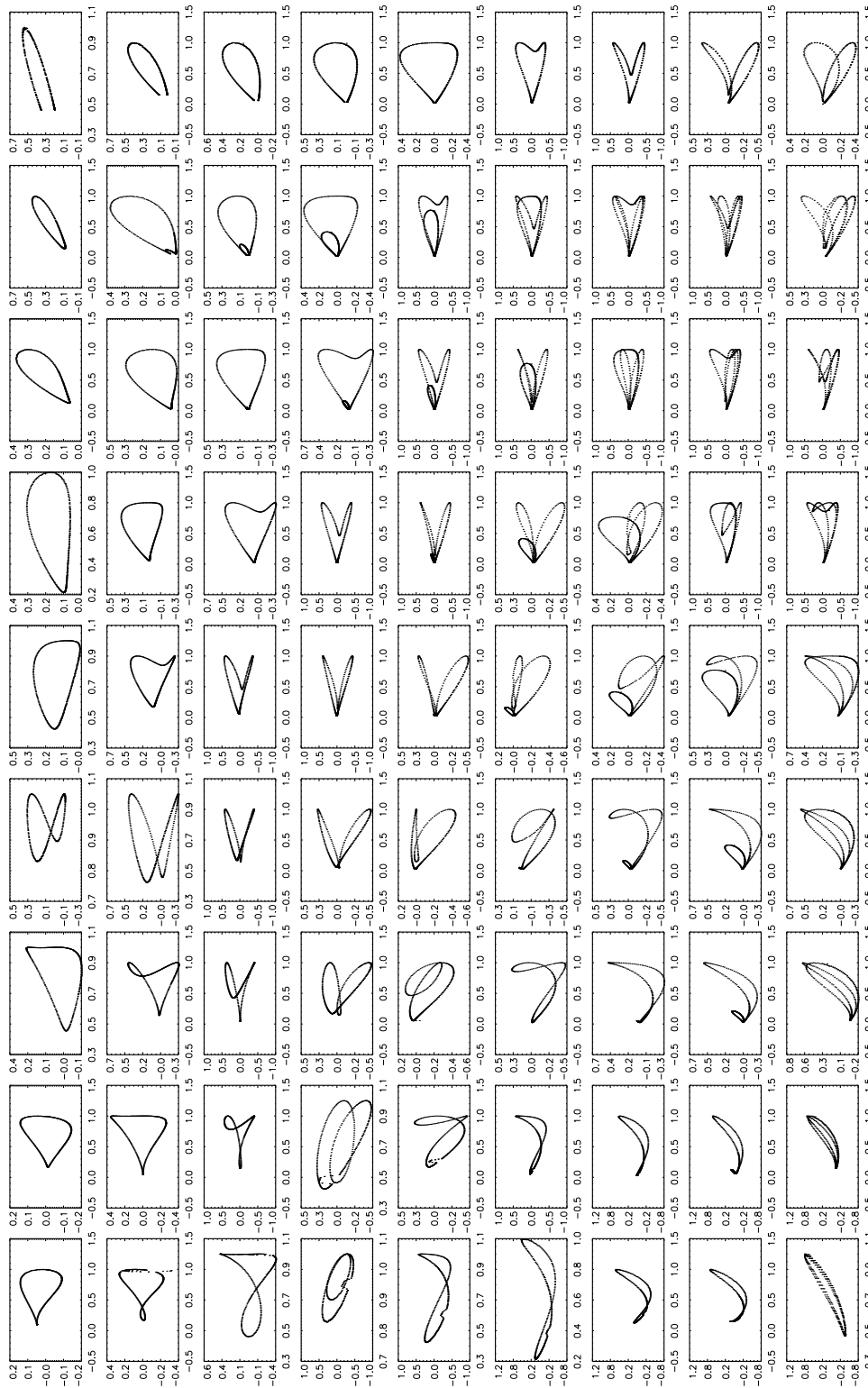


**Figure A14:** Current-modified dipole. Look-up table of Stokes phase portraits in the  $I$ - $Q$  plane for hollow cones with opening angle  $25^\circ$  and degree of linear polarization  $L = I \sin \theta$ , where  $\theta$  is the emission point colatitude, and  $r = 0.1r_{\text{LC}}$ . The panels are organised in landscape mode, in order of increasing  $10^\circ \leq i \leq 90^\circ$  (left–right) and  $10^\circ \leq \alpha \leq 90^\circ$  (top–bottom) in intervals of  $10^\circ$ .  $I$  is plotted on the horizontal axis and normalised by its peak value.  $Q$  is plotted on the vertical axis.

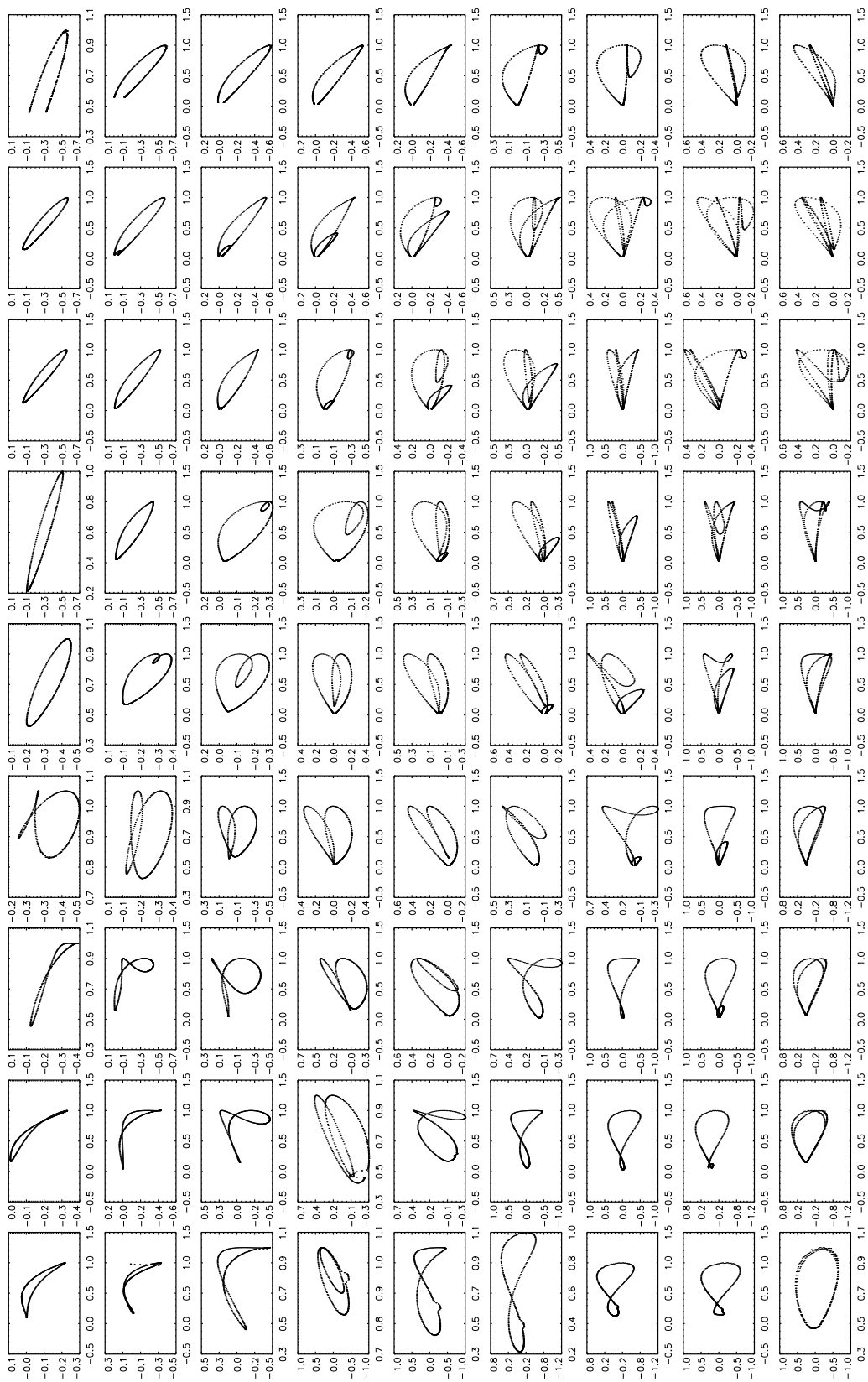


**Figure A15:** Current-modified dipole. Layout as for Figure A14, but for  $I-U$  ( $I$  on the horizontal axis).

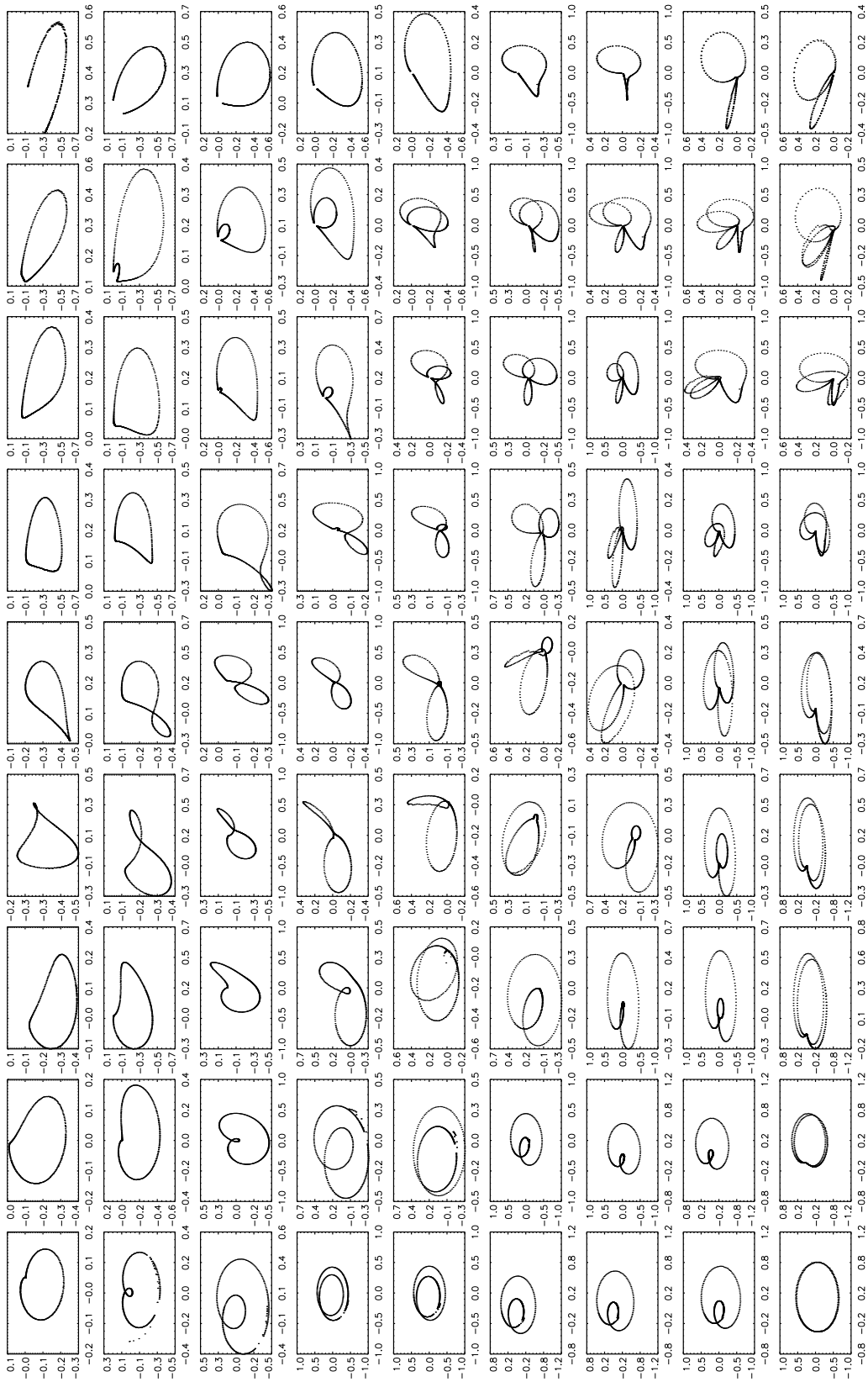


**Figure A16:** Current-modified dipole. Layout as for Figure A14, but for  $Q$ - $U$  ( $Q$  on the horizontal axis).

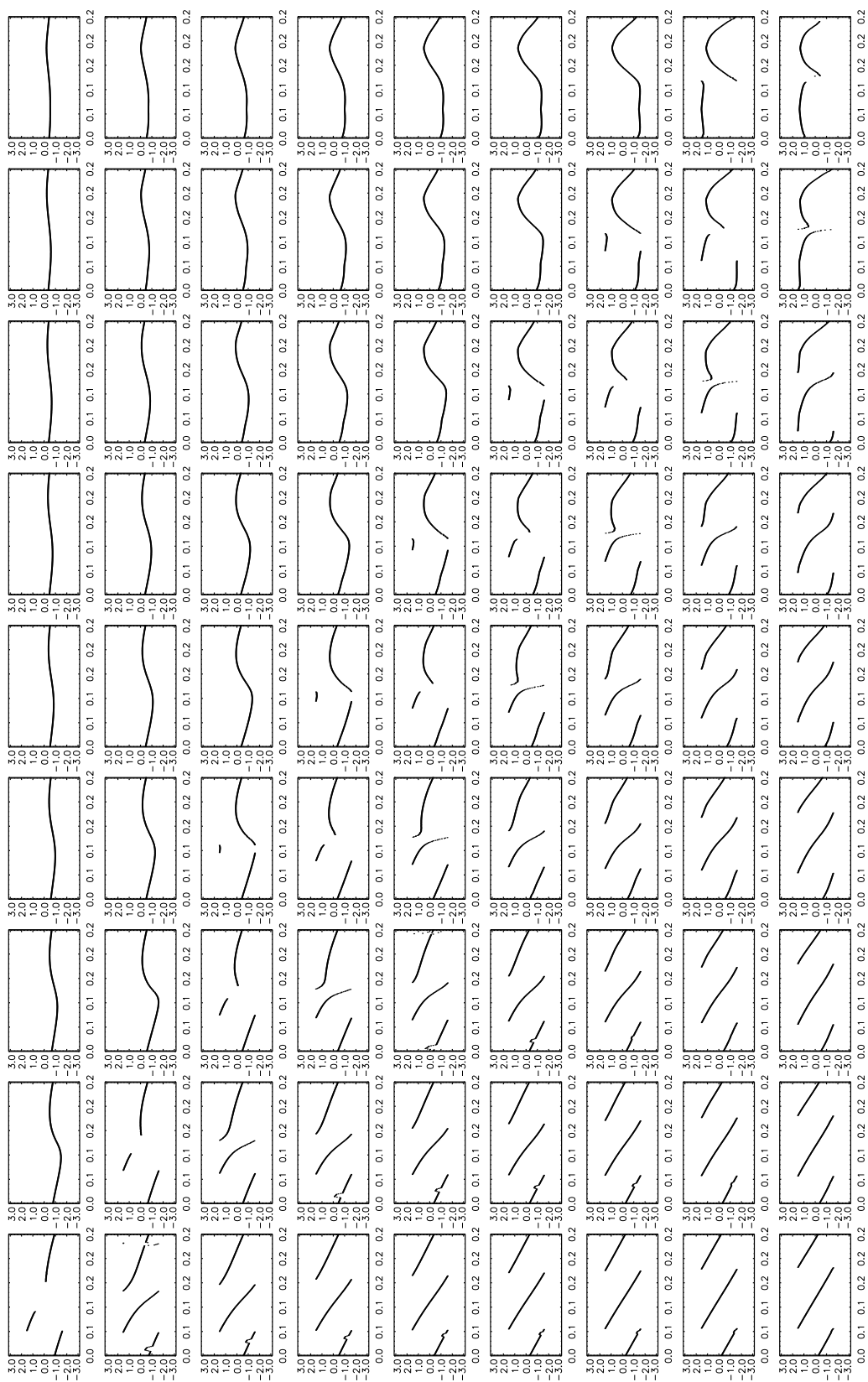


**Figure A17:** Current-modified dipole. Layout as for Figure A14, but for position angle (on the vertical axis in landscape orientation, in units of radians) versus pulse longitude (on the horizontal axis, in units of  $2\pi$  radians).



# Bibliography

- Abbott, B. P. et al. (2004). Setting upper limits on the strength of periodic gravitational waves from PSR J1939+2134 using the first science data from the GEO 600 and LIGO detectors. *Phys. Rev. D*, **69**(8), 082004, arXiv:gr-qc/0308050.
- Abbott, B. P. et al. (2005a). First all-sky upper limits from LIGO on the strength of periodic gravitational waves using the Hough transform. *Phys. Rev. D*, **72**(10), 102004, arXiv:gr-qc/0508065.
- Abbott, B. P. et al. (2005b). Limits on Gravitational-Wave Emission from Selected Pulsars Using LIGO Data. *Physical Review Letters*, **94**(18), 181103, arXiv:gr-qc/0410007.
- Abbott, B. P. et al. (2007a). Advanced LIGO reference design. Online document. <http://www.ligo.caltech.edu/docs/M/M060056-08/M060056-08.pdf>.
- Abbott, B. P. et al. (2007b). First cross-correlation analysis of interferometric and resonant-bar gravitational-wave data for stochastic backgrounds. *Phys. Rev. D*, **76**(2), 022001, arXiv:gr-qc/0703068.
- Abbott, B. P. et al. (2007c). LIGO: the Laser Interferometer Gravitational-Wave Observatory. *Rep. Prog. Phys.*, **72**, 076901.
- Abbott, B. P. et al. (2007d). Searches for periodic gravitational waves from unknown isolated sources and Scorpius X-1: Results from the second LIGO science run. *Phys. Rev. D*, **76**(8), 082001, arXiv:gr-qc/0605028.
- Abbott, B. P. et al. (2007e). Upper limit map of a background of gravitational waves. *Phys. Rev. D*, **76**(8), 082003, arXiv:astro-ph/0703234.
- Abbott, B. P. et al. (2007f). Upper limits on gravitational wave emission from 78 radio pulsars. *Phys. Rev. D*, **76**(4), 042001.
- Abbott, B. P. et al. (2008a). All-sky search for periodic gravitational waves in LIGO S4 data. *Phys. Rev. D*, **77**(2), 022001, 0708.3818.

- Abbott, B. P. et al. (2008b). Beating the Spin-Down Limit on Gravitational Wave Emission from the Crab Pulsar. *ApJL*, **683**, L45–L49, 0805.4758.
- Abbott, B. P. et al. (2008c). Search for Gravitational-Wave Bursts from Soft Gamma Repeaters. *Physical Review Letters*, **101**(21), 211102, 0808.2050.
- Abbott, B. P. et al. (2009a). All-Sky LIGO Search for Periodic Gravitational Waves in the Early Fifth-Science-Run Data. *Physical Review Letters*, **102**(11), 111102, 0810.0283.
- Abbott, B. P. et al. (2009b). An upper limit on the stochastic gravitational-wave background of cosmological origin. *Nature*, **460**, 990–994.
- Abbott, B. P. et al. (2009c). Einstein@Home search for periodic gravitational waves in early S5 LIGO data. *ArXiv e-prints*, 0905.1705.
- Abbott, B. P. et al. (2009d). ERRATUM: "Beating the Spin-Down Limit on Gravitational Wave Emission from the Crab Pulsar" [A HREF="bib\_query\?2008ApJ...683L..45A" ](2008, ApJ, 683, L45);/A]. *ApJL*, **706**, L203–L204.
- Abbott, B. P. et al. (2009e). The lsc-virgo white paper on gravitational wave data analysis (2009-2010 edition). Online document. <https://dcc.ligo.org/public/0004/T0900389/001/main09Public.pdf>.
- Abbott, B. P. et al. (2009f). Search for gravitational-wave bursts in the first year of the fifth LIGO science run. *ArXiv e-prints*, 0905.0020.
- Abbott, B. P. et al. (2009g). Searches for gravitational waves from known pulsars with S5 LIGO data. *ArXiv e-prints*, 0909.3583.
- Abdo, A. A. et al. (2009a). Detection of 16 Gamma-Ray Pulsars Through Blind Frequency Searches Using the Fermi LAT. *Science*, **325**, 840.
- Abdo, A. A. et al. (2009b). Fermi Large Area Telescope Detection of Pulsed  $\gamma$ -rays from the Vela-like Pulsars PSR J1048–5832 and PSR J2229+6114. *ApJ*, **706**, 1331–1340, 0910.2249.
- Acernese, F. et al. (2008). First joint gravitational wave search by the AURIGA EXPLORER NAUTILUS Virgo Collaboration. *Classical and Quantum Gravity*, **25**(20), 205007, 0710.3752.

- Aglietta, M. et al. (1987). On the event observed in the Mont Blanc Underground Neutrino Observatory during the occurrence of supernova 1987a. *Europhysics Letters*, **3**, 1315–1320.
- Akgün, T., Link, B., & Wasserman, I. (2006). Precession of the isolated neutron star PSR B1828-11. *MNRAS*, **365**, 653–672, arXiv:astro-ph/0506606.
- Alford, M. G., Braby, M., & Schmitt, A. (2008). Critical temperature for kaon condensation in color-flavor-locked quark matter. *Journal of Physics G Nuclear Physics*, **35**(2), 025002, 0707.2389.
- Alpar, M. A. & Pines, D. (1985). Gravitational radiation from a solid-crust neutron star. *Nature*, **314**, 334–336.
- Alpar, M. A. & Saulis, J. A. (1988). On the dynamical coupling between the superfluid interior and the crust of a neutron star. *ApJ*, **327**, 723–725.
- Alpar, M. A., Cheng, A. F., Ruderman, M. A., & Shaham, J. (1982). A new class of radio pulsars. *Nature*, **300**, 728–730.
- Altamirano, D., Strohmayer, T. E., Heinke, C. O., Markwardt, C. B., Swank, J. H., Pereira, D., Smith, E., Wijnands, R., Linares, M., Patruno, A., Casella, P., & van der Klis, M. (2009). Discovery of a  $\sim 205$  Hz X-ray pulsar in the globular cluster NGC 6440. *The Astronomer's Telegram*, **2182**, 1.
- Altamirano, D., Wijnands, R., van der Klis, M., Patruno, A., Watts, A., Armas Padilla, M., Cavecchi, Y., Degenaar, N., Kalamkar, M., Kaur, R., Yang, Y. J., Casella, P., Linares, M., Soleri, P., & Rea, N. (2010). Detection of coherent millisecond pulsations at  $\sim 518$  Hz in the LMXB Swift J1749.4-2807 (GRB060602B). *The Astronomer's Telegram*, **2565**, 1.
- Amaldi, E., Bassan, M., Coccia, E., Bonifazi, P., & Castellano, M. G. (1989). Coincidences among the Maryland and Rome gravitational wave detector data and the Mont Blanc and KAMIOKA neutrino detector data in the period of SN1987A. *New York Academy Sciences Annals*, **571**, 561–576.
- Andersson, N. (1998). A New Class of Unstable Modes of Rotating Relativistic Stars. *ApJ*, **502**, 708, arXiv:gr-qc/9706075.
- Andersson, N., Kokkotas, K., & Schutz, B. F. (1999). Gravitational Radiation Limit on the Spin of Young Neutron Stars. *ApJ*, **510**, 846–853, arXiv:astro-ph/9805225.

- Apreda, R., Maggiore, M., Nicolis, A., & Riotto, A. (2002). Gravitational waves from electroweak phase transitions. *Nuclear Physics B*, **631**, 342–368, arXiv:gr-qc/0107033.
- Arons, J. (1983). Pair creation above pulsar polar caps - Geometrical structure and energetics of slot gaps. *ApJ*, **266**, 215–241.
- Arons, J. (1993). Magnetic field topology in pulsars. *ApJ*, **408**, 160–166.
- Arons, J. (1998). General Relativistic Polar Particle Acceleration and Pulsar Death. In N. Shibasaki, editor, *Neutron Stars and Pulsars: Thirty Years after the Discovery*, page 339.
- Arons, J. (2003). Magnetars in the Metagalaxy: An Origin for Ultra-High-Energy Cosmic Rays in the Nearby Universe. *ApJ*, **589**, 871–892, arXiv:astro-ph/0208444.
- Arons, J. & Scharlemann, E. T. (1979). Pair formation above pulsar polar caps - Structure of the low altitude acceleration zone. *ApJ*, **231**, 854–879.
- Arras, P., Flanagan, E. E., Morsink, S. M., Schenk, A. K., Teukolsky, S. A., & Wasserman, I. (2003). Saturation of the r-Mode Instability. *ApJ*, **591**, 1129–1151, arXiv:astro-ph/0202345.
- Arzoumanian, Z., Chernoff, D. F., & Cordes, J. M. (2002). The Velocity Distribution of Isolated Radio Pulsars. *ApJ*, **568**, 289–301, arXiv:astro-ph/0106159.
- Asseo, E. & Khechinashvili, D. (2002). The role of multipolar magnetic fields in pulsar magnetospheres. *MNRAS*, **334**, 743–759, arXiv:astro-ph/0203129.
- Astone, P., Babusci, D., Bassan, M., Borkowski, K. M., Brocco, L., Coccia, E., D'Antonio, S., Fafone, V., Frasca, S., Giordano, G., Jaranowski, P., Królak, A., Marini, A., Minenkov, Y., Modena, I., Modestino, G., Moleti, A., Pai, A., Pallottino, G. V., Palomba, C., Pietka, M., Pizzella, G., Quintieri, L., Ricci, F., Rocchi, A., Ronga, F., Terenzi, R., & Visco, M. (2005). An all-sky search of EXPLORER data. *Classical and Quantum Gravity*, **22**, 1243.
- Baade, W. (1942). The Crab Nebula. *ApJ*, **96**, 188.
- Baade, W. & Zwicky, F. (1934). Remarks on Super-Novae and Cosmic Rays. *Physical Review*, **46**, 76–77.

- Backer, D. C. (1995). Millisecond Pulsar Radiation Properties. *Journal of Astrophysics and Astronomy*, **16**, 165.
- Bahcall, J. N., Dar, A., & Piran, T. (1987). Neutrinos from the recent LMC supernova. *Nature*, **326**, 135–136.
- Bai, X. & Spitkovsky, A. (2009a). Modeling of Gamma-Ray Pulsar Light Curves with Force-Free Magnetic Field. *ArXiv e-prints*, 0910.5741.
- Bai, X. & Spitkovsky, A. (2009b). Modeling Pulsar Gamma-Ray Light Curves Using Realistic Magnetospheric Geometries. *ArXiv e-prints*, 0911.0120.
- Bai, X. & Spitkovsky, A. (2009c). Uncertainties of Modeling Gamma-Ray Pulsar Light Curves with Vacuum Dipole Magnetic Field. *ArXiv e-prints*, 0910.5740.
- Balasubramanian, R., Sathyaprakash, B. S., & Dhurandhar, S. V. (1996). Gravitational waves from coalescing binaries: Detection strategies and Monte Carlo estimation of parameters. *Phys. Rev. D*, **53**, 3033–3055, arXiv:gr-qc/9508011.
- Balberg, S. & Shapiro, S. L. (2000). The Properties of Matter in White Dwarfs and Neutron Stars. *ArXiv Astrophysics e-prints*, arXiv:astro-ph/0004317.
- Bandiera, R., Pacini, F., & Salvati, M. (1988). A synchrotron model for the X-ray emission from supernova 1987A. *Nature*, **332**, 418.
- Barack, L. & Cutler, C. (2007). Using LISA extreme-mass-ratio inspiral sources to test off-Kerr deviations in the geometry of massive black holes. *Phys. Rev. D*, **75**(4), 042003, arXiv:gr-qc/0612029.
- Barkat, Z. & Wheeler, J. C. (1988). Progenitor structure of SN 1987A. *ApJ*, **332**, 247–260.
- Barnard, J. J. & Arons, J. (1986). Wave propagation in pulsar magnetospheres - Refraction of rays in the open flux zone. *ApJ*, **302**, 138–162.
- Belczynski, K. & Taam, R. E. (2008). The Most Massive Progenitors of Neutron Stars: CXO J164710.2-455216. *ApJ*, **685**, 400–405, 0804.4143.
- Bell, J. F., Bailes, M., Manchester, R. N., Lyne, A. G., Camilo, F., & Sandhu, J. S. (1997). Timing Measurements and Their Implications for Four Binary Millisecond Pulsars. *MNRAS*, **286**, 463–469, arXiv:astro-ph/9611081.

- Berti, E., Cardoso, V., & Will, C. M. (2006). Gravitational-wave spectroscopy of massive black holes with the space interferometer LISA. *Phys. Rev. D*, **73**(6), 064030, arXiv:gr-qc/0512160.
- Bhattacharyya, S., Strohmayer, T. E., Miller, M. C., & Markwardt, C. B. (2005). Constraints on Neutron Star Parameters from Burst Oscillation Light Curves of the Accreting Millisecond Pulsar XTE J1814-338. *ApJ*, **619**, 483–491, arXiv:astro-ph/0402534.
- Bildsten, L. (1998). Gravitational Radiation and Rotation of Accreting Neutron Stars. *ApJL*, **501**, L89+, arXiv:astro-ph/9804325.
- Bildsten, L., Chakrabarty, D., Chiu, J., Finger, M. H., Koh, D. T., Nelson, R. W., Prince, T. A., Rubin, B. C., Scott, D. M., Stollberg, M., Vaughan, B. A., Wilson, C. A., & Wilson, R. B. (1997). Observations of Accreting Pulsars. *ApJS*, **113**, 367, arXiv:astro-ph/9707125.
- Bionta, R. M., Blewitt, G., Bratton, C. B., Caspere, D., & Ciocio, A. (1987). Observation of a neutrino burst in coincidence with supernova 1987A in the Large Magellanic Cloud. *Physical Review Letters*, **58**, 1494–1496.
- Bisnovaty-Kogan, G. S. & Komberg, B. V. (1974). Pulsars and close binary systems. *Soviet Astronomy*, **18**, 217.
- Blanchet, L. (2006). Gravitational Radiation from Post-Newtonian Sources and Inspiralling Compact Binaries. *Living Reviews in Relativity*, **9**, 4.
- Blandford, R. D. (1976). Accretion disc electrodynamics - A model for double radio sources. *MNRAS*, **176**, 465–481.
- Blandford, R. D. & Romani, R. W. (1988). On the interpretation of pulsar braking indices. *MNRAS*, **234**, 57P–60P.
- Blaskiewicz, M., Cordes, J. M., & Wasserman, I. (1991). A relativistic model of pulsar polarization. *ApJ*, **370**, 643–669.
- Bonanno, A., Urpin, V., & Belvedere, G. (2005). Protoneutron star dynamos and pulsar magnetism. *A&A*, **440**, 199–205, arXiv:astro-ph/0504328.
- Bonazzola, S. & Gourgoulhon, E. (1996). Gravitational waves from pulsars: emission by the magnetic-field-induced distortion. *A&A*, **312**, 675–690, arXiv:astro-ph/9602107.

- Bondarescu, R., Teukolsky, S. A., & Wasserman, I. (2007). Spin evolution of accreting neutron stars: Nonlinear development of the r-mode instability. *Phys. Rev. D*, **76**(6), 064019, 0704.0799.
- Bondarescu, R., Teukolsky, S. A., & Wasserman, I. (2009). Spinning down newborn neutron stars: Nonlinear development of the r-mode instability. *Phys. Rev. D*, **79**(10), 104003, 0809.3448.
- Bondi, H. & Gold, T. (1955). On the damping of free nutation of the Earth. *MNRAS*, **115**, 41.
- Bondi, H. & Hoyle, F. (1944). On the mechanism of accretion by stars. *MNRAS*, **104**, 273.
- Bozzo, E., Ferrigno, C., Kuulkers, E., Falanga, M., Chenevez, J., Brandt, S., Beckmann, V., Bird, A., Domingo, A., Ebisawa, K., Jonker, P., Kretschmar, P., Markwardt, C., Oosterbroek, T., Paizis, A., Risquez, D., Sanchez-Fernandez, C., Shaw, S., & Wijnands, R. (2009). Swift follow-up of the newly discovered burster millisecond pulsar IGR J17511-3057. *The Astronomer's Telegram*, **2198**, 1.
- Brady, P. R. & Creighton, T. (2000). Searching for periodic sources with LIGO. II. Hierarchical searches. *Phys. Rev. D*, **61**(8), 082001, arXiv:gr-qc/9812014.
- Brentjens, M. A. & de Bruyn, A. G. (2005). Faraday rotation measure synthesis. *A&A*, **441**, 1217–1228, arXiv:astro-ph/0507349.
- Brink, J., Teukolsky, S. A., & Wasserman, I. (2004). Nonlinear coupling network to simulate the development of the r-mode instability in neutron stars. I. Construction. *Phys. Rev. D*, **70**(12), 124017, arXiv:gr-qc/0409048.
- Buonanno, A. & Damour, T. (1999). Effective one-body approach to general relativistic two-body dynamics. *Phys. Rev. D*, **59**(8), 084006, arXiv:gr-qc/9811091.
- Buonanno, A., Maggiore, M., & Ungarelli, C. (1997). Spectrum of relic gravitational waves in string cosmology. *Phys. Rev. D*, **55**, 3330–3336, arXiv:gr-qc/9605072.
- Burderi, L., Di Salvo, T., Stella, L., Fiore, F., Robba, N. R., van der Klis, M., Iaria, R., Mendez, M., Menna, M. T., Campana, S., Gennaro, G., Rebecchi, S., & Burgay, M. (2002). A BeppoSAX Observation of KS 1731-260 in Its

- Quiescent State: Constraints on the Magnetic Field of the Neutron Star. *ApJ*, **574**, 930–936, arXiv:astro-ph/0201175.
- Burderi, L., Riggio, A., di Salvo, T., Papitto, A., Menna, M. T., D’Aì, A., & Iaria, R. (2009). Timing of the 2008 outburst of SAX J1808.4-3658 with XMM-Newton: a stable orbital-period derivative over ten years. *A&A*, **496**, L17–L20, 0902.2128.
- Burn, B. J. (1966). On the depolarization of discrete radio sources by Faraday dispersion. *MNRAS*, **133**, 67.
- Burrows, D. N., Michael, E., Hwang, U., McCray, R., Chevalier, R. A., Petre, R., Garmire, G. P., Holt, S. S., & Nousek, J. A. (2000). The X-Ray Remnant of SN 1987A. *ApJL*, **543**, L149–L152, arXiv:astro-ph/0009265.
- Caldwell, R. R. & Allen, B. (1992). Cosmological constraints on cosmic-string gravitational radiation. *Phys. Rev. D*, **45**, 3447–3468.
- Camenzind, M. (2006). General relativity. Online script. <http://www.lsw.uniheidelberg.de/projects/theory/resource.htm>.
- Cameron, A. G. (1959). Neutron Star Models. *ApJ*, **130**, 884.
- Camilo, F., Lorimer, D. R., Freire, P., Lyne, A. G., & Manchester, R. N. (2000). Observations of 20 Millisecond Pulsars in 47 Tucanae at 20 Centimeters. *ApJ*, **535**, 975–990, arXiv:astro-ph/9911234.
- Capozziello, S. & de Laurentis, M. (2008). Gravitational waves from stellar encounters. *Astroparticle Physics*, **30**, 105–112, 0806.4117.
- Cassam-Chenaï, G., Decourchelle, A., Ballet, J., Sauvageot, J., Dubner, G., & Giacani, E. (2004). XMM-Newton observations of the supernova remnant RX J1713.7-3946 and its central source. *A&A*, **427**, 199–216, arXiv:astro-ph/0407333.
- Chakrabarty, D. & Morgan, E. H. (1998). The two-hour orbit of a binary millisecond X-ray pulsar. *Nature*, **394**, 346–348, arXiv:astro-ph/9804248.
- Chakrabarty, D., Morgan, E. H., Munro, M. P., Galloway, D. K., Wijnands, R., van der Klis, M., & Markwardt, C. B. (2003). Nuclear-powered millisecond pulsars and the maximum spin frequency of neutron stars. *Nature*, **424**, 42–44, arXiv:astro-ph/0307029.

- Chandrasekhar, S. (1931). The Maximum Mass of Ideal White Dwarfs. *ApJ*, **74**, 81.
- Chandrasekhar, S. (1970). Solutions of Two Problems in the Theory of Gravitational Radiation. *Physical Review Letters*, **24**, 611–615.
- Chatterjee, S. & Cordes, J. M. (2004). Smashing the Guitar: An Evolving Neutron Star Bow Shock. *ApJL*, **600**, L51–L54, arXiv:astro-ph/0311340.
- Chen, K. & Ruderman, M. (1993a). Origin and radio pulse properties of millisecond pulsars. *ApJ*, **408**, 179–185.
- Chen, K. & Ruderman, M. (1993b). Pulsar death lines and death valley. *ApJ*, **402**, 264–270.
- Cheng, A. F. & Ruderman, M. A. (1977). A Crab pulsar model - X-ray, optical, and radio emission. *ApJ*, **216**, 865–872.
- Cheng, A. F. & Ruderman, M. A. (1979). A theory of subpulse polarization patterns from radio pulsars. *ApJ*, **229**, 348–360.
- Cheng, K. S. & Dai, Z. G. (1997). On the Bimodal Magnetic Field Distribution of Binary Pulsars. *ApJL*, **476**, L39+.
- Cheng, K. S., Ho, C., & Ruderman, M. (1986a). Energetic radiation from rapidly spinning pulsars. I - Outer magnetosphere gaps. II - VELA and Crab. *ApJ*, **300**, 500–539.
- Cheng, K. S., Ho, C., & Ruderman, M. (1986b). Energetic Radiation from Rapidly Spinning Pulsars. II. VELA and Crab. *ApJ*, **300**, 522.
- Cheng, K. S., Ruderman, M., & Zhang, L. (2000). A Three-dimensional Outer Magnetospheric Gap Model for Gamma-Ray Pulsars: Geometry, Pair Production, Emission Morphologies, and Phase-resolved Spectra. *ApJ*, **537**, 964–976.
- Chevalier, R. A. (1992). And still there is no pulsar. *Nature*, **360**, 628–629.
- Chung, C. T. Y. & Melatos, A. (2009). Stokes tomography of radio pulsar magnetospheres. I. Linear polarisation. *MNRAS*.
- Chung, C. T. Y., Galloway, D. K., & Melatos, A. (2008). Does the accreting millisecond pulsar XTE J1814-338 precess? *MNRAS*, **391**, 254–267, 0808.3820.

- Chung, Y.-y., Chou, Y., Tsai, C., & Chang, H. (2006). Fine Orbital Parameters and Soft Phase Lags of Accretion Powered Millisecond Pulsar XTE J1814-338. In *Bulletin of the American Astronomical Society*, volume 38 of *Bulletin of the American Astronomical Society*, page 81.
- Cocke, W. J., Disney, M. J., & Taylor, D. J. (1969). Discovery of Optical Signals from Pulsar NP 0532. *Nature*, **221**, 525–527.
- Colgate, S. A. & White, R. H. (1966). The Hydrodynamic Behavior of Supernovae Explosions. *ApJ*, **143**, 626.
- Cook, G. B., Shapiro, S. L., & Teukolsky, S. A. (1994). Rapidly rotating neutron stars in general relativity: Realistic equations of state. *ApJ*, **424**, 823–845.
- Cooray, A. (2004). Gravitational-wave background of neutron star-white dwarf binaries. *MNRAS*, **354**, 25–30, arXiv:astro-ph/0406467.
- Cordes, J. M. (1978). Observational limits on the location of pulsar emission regions. *ApJ*, **222**, 1006–1011.
- Cordes, J. M. (1993). The detectability of planetary companions to radio pulsars. In J. A. Phillips, S. E. Thorsett, & S. R. Kulkarni, editor, *Planets Around Pulsars*, volume 36 of *Astronomical Society of the Pacific Conference Series*, pages 43–60.
- Cordes, J. M., Romani, R. W., & Lundgren, S. C. (1993). The Guitar nebula - A bow shock from a slow-spin, high-velocity neutron star. *Nature*, **362**, 133–135.
- Costa, C. A., Aguiar, O. D., Oliveira, Jr., N. F., Gratens, X., de Souza, S. T., & Furtado, S. R. (2008). The Schenberg data acquisition and analysis: results from its first commissioning run. *Classical and Quantum Gravity*, **25**(18), 184002.
- Coward, D. M., Burman, R. R., & Blair, D. G. (2002). Simulating a stochastic background of gravitational waves from neutron star formation at cosmological distances. *MNRAS*, **329**, 411–416.
- Cumming, A. (2008). Magnetic Field Evolution in Accreting Millisecond Pulsars. In R. Wijnands, D. Altamirano, P. Soleri, N. Degenaar, N. Rea, P. Casella, A. Patruno, & M. Linares, editor, *American Institute of Physics*

- Conference Series*, volume 1068 of *American Institute of Physics Conference Series*, pages 152–159.
- Cumming, A., Zweibel, E., & Bildsten, L. (2001). Magnetic Screening in Accreting Neutron Stars. *ApJ*, **557**, 958–966, arXiv:astro-ph/0102178.
- Cutler, C. (2002). Gravitational waves from neutron stars with large toroidal B fields. *Phys. Rev. D*, **66**(8), 084025, arXiv:gr-qc/0206051.
- Cutler, C. & Jones, D. I. (2001). Gravitational wave damping of neutron star wobble. *Phys. Rev. D*, **63**(2), 024002, arXiv:gr-qc/0008021.
- Dadykin, V. L. & Ryazhskaya, O. G. (2009). On one group of experimental results related to the search for neutrino radiation from SN 1987A: Commentary. *Astronomy Letters*, **35**, 384–387.
- Damour, T. & Vilenkin, A. (2001). Gravitational wave bursts from cusps and kinks on cosmic strings. *Phys. Rev. D*, **64**(6), 064008, arXiv:gr-qc/0104026.
- Damour, T. & Vilenkin, A. (2005). Gravitational radiation from cosmic (super)strings: Bursts, stochastic background, and observational windows. *Phys. Rev. D*, **71**(6), 063510, arXiv:hep-th/0410222.
- Damour, T., Iyer, B. R., & Sathyaprakash, B. S. (2001). Comparison of search templates for gravitational waves from binary inspiral. *Phys. Rev. D*, **63**(4), 044023, arXiv:gr-qc/0010009.
- Daugherty, J. K. & Harding, A. K. (1982). Electromagnetic cascades in pulsars. *ApJ*, **252**, 337–347.
- Daugherty, J. K. & Harding, A. K. (1996). Gamma-Ray Pulsars: Emission from Extended Polar CAP Cascades. *ApJ*, **458**, 278, arXiv:astro-ph/9508155.
- Davidson, K. (1973). Accretion at a Magnetic Pole of a Neutron Star. *Nature*, **246**, 1.
- Davies, J. G., Horton, P. W., Lyne, A. G., Rickett, B. J., & Smith, F. G. (1968). Pulsating Radio Source at  $\alpha = 19^h 19^m$ ,  $\delta = +22^{\text{deg}}$ . *Nature*, **217**, 910–912.
- de Freitas Pacheco, J. A. (1998). Do soft gamma repeaters emit gravitational waves? *A&A*, **336**, 397–401, arXiv:astro-ph/9805321.

- Deeter, J. E., Pravdo, S. H., & Boynton, P. E. (1981). Pulse-timing observations of Hercules X-1. *ApJ*, **247**, 1003–1012.
- Degenaar, N., Wijnands, R., Campana, S., Galloway, D., Lewin, W., Homan, J., Chakrabarty, D., Jonker, P., Cackett, E., & Miller, J. (2007). Swift/XRT non-detection of HETE J1900.1-2455. *The Astronomer's Telegram*, **1098**, 1.
- Dergachev, D. (2005). Description of PowerFlux Algorithms and Implementation. LIGO technical document LIGO-T050186, available in <http://admbdsvr.ligo.caltech.edu/dcc/>.
- Deutsch, A. J. (1955). The electromagnetic field of an idealized star in rigid rotation in vacuo. *Annales d'Astrophysique*, **18**, 1.
- Dhurandhar, S., Krishnan, B., Mukhopadhyay, H., & Whelan, J. T. (2008). Cross-correlation search for periodic gravitational waves. *Phys. Rev. D*, **77**(8), 082001, 0712.1578.
- Di Salvo, T. & Burderi, L. (2003). Constraints on the neutron star magnetic field of the two X-ray transients SAX J1808.4-3658 and Aql X-1. *A&A*, **397**, 723–727, arXiv:astro-ph/0210114.
- Di Salvo, T., Méndez, M., van der Klis, M., Ford, E., & Robba, N. R. (2001). Study of the Temporal Behavior of 4U 1728-34 as a Function of Its Position in the Color-Color Diagram. *ApJ*, **546**, 1107–1120, arXiv:astro-ph/0008361.
- di Salvo, T., Burderi, L., Riggio, A., Papitto, A., & Menna, M. T. (2008). Orbital evolution of an accreting millisecond pulsar: witnessing the banquet of a hidden black widow? *MNRAS*, **389**, 1851–1857, 0708.0498.
- Diehl, R., Halloin, H., Kretschmer, K., Lichti, G. G., Schönfelder, V., Strong, A. W., von Kienlin, A., Wang, W., Jean, P., Knödlseher, J., Roques, J.-P., Weidenspointner, G., Schanne, S., Hartmann, D. H., Winkler, C., & Wunderer, C. (2006). Radioactive  $^{26}\text{Al}$  from massive stars in the Galaxy. *Nature*, **439**, 45–47, arXiv:astro-ph/0601015.
- Dimmelmeier, H., Font, J. A., & Müller, E. (2001). Gravitational Waves from Relativistic Rotational Core Collapse. *ApJL*, **560**, L163–L166, arXiv:astro-ph/0103088.

- Dimmelmeier, H., Font, J. A., & Müller, E. (2002). Gravitational waves from relativistic rotational core collapse in axisymmetry. *Classical and Quantum Gravity*, **19**, 1291–1296.
- Dotani, T., Hayashida, K., Inoue, H., Itoh, M., & Koyama, K. (1987). Discovery of an unusual hard X-ray source in the region of supernova 1987A. *Nature*, **330**, 230.
- Duncan, R. C. & Thompson, C. (1992). Formation of very strongly magnetized neutron stars - Implications for gamma-ray bursts. *ApJL*, **392**, L9–L13.
- Dupuis, R. J. & Woan, G. (2005). Bayesian estimation of pulsar parameters from gravitational wave data. *Phys. Rev. D*, **72**(10), 102002, arXiv:gr-qc/0508096.
- Dyks, J. (2008). Altitude-dependent polarization in radio pulsars. *MNRAS*, **391**, 859–868, 0806.0554.
- Dyks, J. & Harding, A. K. (2004). Rotational Sweepback of Magnetic Field Lines in Geometric Models of Pulsar Radio Emission. *ApJ*, **614**, 869–880, arXiv:astro-ph/0402507.
- Dyks, J. & Rudak, B. (2003). Two-Pole Caustic Model for High-Energy Light Curves of Pulsars. *ApJ*, **598**, 1201–1206, arXiv:astro-ph/0303006.
- Dyks, J., Rudak, B., & Demorest, P. (2010). The nature of pulsar radio emission. *MNRAS*, **401**, 1781–1795, 0908.1359.
- Eckert, D., Walter, R., Kretschmar, P., Mas-Hesse, M., Palumbo, G. G. C., Roques, J.-P., Ubertini, P., & Winkler, C. (2004). IGR J00291+5934, a new X-ray transient discovered with INTEGRAL. *The Astronomer's Telegram*, **352**, 1.
- Enoki, M. & Nagashima, M. (2007). The Effect of Orbital Eccentricity on Gravitational Wave Background Radiation from Supermassive Black Hole Binaries. *Progress of Theoretical Physics*, **117**, 241–256, arXiv:astro-ph/0609377.
- Everett, J. E. & Weisberg, J. M. (2001). Emission Beam Geometry of Selected Pulsars Derived from Average Pulse Polarization Data. *ApJ*, **553**, 341–357, arXiv:astro-ph/0009266.
- Fafone, V. (2004). Resonant-mass detectors: status and perspectives. *Classical and Quantum Gravity*, **21**, 377.

- Faucher-Giguère, C.-A. & Kaspi, V. M. (2006). Birth and Evolution of Isolated Radio Pulsars. *ApJ*, **643**, 332–355, arXiv:astro-ph/0512585.
- Feller, W. (1957). *An introduction to probability theory and its applications*. Wiley, New York.
- Fesen, R. A., Hammell, M. C., Morse, J., Chevalier, R. A., Borkowski, K. J., Dopita, M. A., Gerardy, C. L., Lawrence, S. S., Raymond, J. C., & van den Bergh, S. (2006). The Expansion Asymmetry and Age of the Cassiopeia A Supernova Remnant. *ApJ*, **645**, 283–292, arXiv:astro-ph/0603371.
- Friedman, J. L. & Schutz, B. F. (1978). Secular instability of rotating Newtonian stars. *ApJ*, **222**, 281–296.
- Fruchter, A. S., Stinebring, D. R., & Taylor, J. H. (1988). A millisecond pulsar in an eclipsing binary. *Nature*, **333**, 237–239.
- Fryer, C. L., Colgate, S. A., & Pinto, P. A. (1999). Iron Opacity and the Pulsar of SN 1987A. *ApJ*, **511**, 885–895, arXiv:astro-ph/9808309.
- Galeotti, P., Pallottino, G. V., & Pizzella, G. (2008). SN1987A: Revisiting the Data and the Correlation between Neutrino and Gravitational Detectors. *ArXiv e-prints*, 0810.3759.
- Galloway, D. (2007). Pushing the Limit on Neutron Star Spin Rates. In Y. W. Kang, H.-W. Lee, K.-C. Leung, and K.-S. Cheng, editors, *The Seventh Pacific Rim Conference on Stellar Astrophysics*, volume 362 of *Astronomical Society of the Pacific Conference Series*, page 105.
- Galloway, D. (2008). Accreting neutron star spins and the equation of state. In C. Bassa, Z. Wang, A. Cumming, & V. M. Kaspi, editor, *40 Years of Pulsars: Millisecond Pulsars, Magnetars and More*, volume 983 of *American Institute of Physics Conference Series*, pages 510–518.
- Galloway, D. K., Chakrabarty, D., Munro, M. P., & Savov, P. (2001). Discovery of a 270 Hertz X-Ray Burst Oscillation in the X-Ray Dipper 4U 1916-053. *ApJL*, **549**, L85–L88, arXiv:astro-ph/0010072.
- Galloway, D. K., Morgan, E. H., Krauss, M. I., Kaaret, P., & Chakrabarty, D. (2007). Intermittent Pulsations in an Accretion-powered Millisecond Pulsar. *ApJL*, **654**, L73–L76, arXiv:astro-ph/0609693.

- Gangadhara, R. T. & Gupta, Y. (2001). Understanding the Radio Emission Geometry of PSR B0329+54. *ApJ*, **555**, 31–39, arXiv:astro-ph/0103109.
- Gangadhara, R. T. & Thomas, R. M. C. (2008). Millisecond Pulsar Emission Altitude from Relativistic Phase Shift: PSR J0437-4715. In S. S. Hasan, R. T. Gangadhara, & V. Krishan, editor, *Turbulence, Dynamos, Accretion Disks, Pulsars and Collective Plasma Processes*, page 137.
- Gasperini, M. & Veneziano, G. (1993). Pre-big-bang in string cosmology. *Astroparticle Physics*, **1**, 317–339, arXiv:hep-th/9211021.
- Gasperini, M. & Veneziano, G. (2003). The pre-big bang scenario in string cosmology. *Phys. Rep.*, **373**, 1–2, arXiv:hep-th/0207130.
- Ghosh, P. (2007). *Rotation and Accretion Powered Pulsars*. World Scientific Publishing Co.
- Ghosh, P. & Lamb, F. K. (1979). Accretion by rotating magnetic neutron stars. III - Accretion torques and period changes in pulsating X-ray sources. *ApJ*, **234**, 296–316.
- Giampanis, S. (2008). *Search for a high frequency stochastic background of gravitational waves*. Ph.D. thesis, University of Rochester.
- Gil, J. (1985). A model of radio emission from the millisecond pulsar PSR 1937 + 214. *A&A*, **143**, 443–446.
- Gil, J., Gronkowski, P., & Rudnicki, W. (1984). Geometry of the emission region of PSR 0950+08. *A&A*, **132**, 312–316.
- Gil, J. A. & Snakowski, J. K. (1990). Curvature radiation and the core emission of pulsars. *A&A*, **234**, 237–242.
- Gilmozzi, R., Cassatella, A., Clavel, J., Fransson, C., Gonzalez, R., Gry, C., Panagia, N., Talavera, A., & Wamsteker, W. (1987). The progenitor of SN1987A. *Nature*, **328**, 318–320.
- Glampedakis, K., Andersson, N., & Jones, D. I. (2009). Do superfluid instabilities prevent neutron star precession? *MNRAS*, **394**, 1908–1924, 0801.4638.
- Glendenning, N. K. (2001). Phase transitions and crystalline structures in neutron star cores. *Physics Reports*, **342**, 393–447.

- Goetz, E. & Riles, K. (2009). Twospect: an all-sky search for continuous gravitational waves from neutron stars in binary systems. Online document. <https://dcc.ligo.org/public/0002/G0900401/001/binarycwMay2009.pdf>.
- Gold, T. (1968). Rotating Neutron Stars as the Origin of the Pulsating Radio Sources. *Nature*, **218**, 731–732.
- Goldreich, P. & Julian, W. H. (1969). Pulsar Electrodynamics. *ApJ*, **157**, 869.
- Gottardi, L., de Waard, A., Usenko, O., Frossati, G., Podt, M., Flokstra, J., Bassan, M., Fafone, V., Minenkov, Y., & Rocchi, A. (2007). Sensitivity of the spherical gravitational wave detector MiniGRAIL operating at 5K. *Phys. Rev. D*, **76**(10), 102005, 0705.0122.
- Göğüş, E., Alpar, M. A., & Gilfanov, M. (2007). Is the Lack of Pulsations in Low-Mass X-Ray Binaries due to Comptonizing Coronae? *ApJ*, **659**, 580–584, arXiv:astro-ph/0612680.
- Gould, D. M. & Lyne, A. G. (1998). Multifrequency polarimetry of 300 radio pulsars. *MNRAS*, **301**, 235–260.
- Graham-Smith, F., Dolan, J. F., Boyd, P. T., Biggs, J. D., Lyne, A. G., & Percival, J. W. (1996). The ultraviolet polarization of the Crab pulsar. *MNRAS*, **282**, 1354–1358.
- Graves, G. J. M. & et al. (2005). Limits from the Hubble Space Telescope on a Point Source in SN 1987A. *ApJ*, **629**, 944–959, arXiv:astro-ph/0505066.
- Grimm, H., Gilfanov, M., & Sunyaev, R. (2002). The Milky Way in X-rays for an outside observer. Log(N)-Log(S) and luminosity function of X-ray binaries from RXTE/ASM data. *A&A*, **391**, 923–944, arXiv:astro-ph/0109239.
- Grishchuk, L. P. (1974). Amplification of gravitational waves in an isotropic universe. *Soviet Journal of Experimental and Theoretical Physics*, **40**, 409.
- Grishchuk, L. P. (1997). The implications of microwave background anisotropies for laser-interferometer-tested gravitational waves. *Classical and Quantum Gravity*, **14**, 1445–1454, arXiv:gr-qc/9609062.
- Han, J. L., Demorest, P. B., van Straten, W., & Lyne, A. G. (2009). Polarization Observations of 100 Pulsars at 774 MHz by the Green Bank Telescope. *ApJS*, **181**, 557–571, 0901.0962.

- Hankins, T. H. & Rankin, J. M. (2010). Arecibo Multi-Frequency Time-Aligned Pulsar Average-Profile and Polarization Database. *AJ*, **139**, 168–175.
- Harris, W. E. (1996). A Catalog of Parameters for Globular Clusters in the Milky Way. *AJ*, **112**, 1487.
- Harry, G. M., Stevenson, T. R., & Paik, H. J. (1996). Detectability of gravitational wave events by spherical resonant-mass antennas. *Phys. Rev. D*, **54**, 2409–2420, arXiv:gr-qc/9602018.
- Hartman, J. M., Chakrabarty, D., Galloway, D. K., Munro, M. P., Savov, P., Mendez, M., van Straaten, S., & Di Salvo, T. (2003). Discovery of 619 Hz Thermonuclear Burst Oscillations in the Low-Mass X-Ray Binary 4U 1608-52. In *Bulletin of the American Astronomical Society*, volume 35 of *Bulletin of the American Astronomical Society*, page 865.
- Hartman, J. M., Patruno, A., Chakrabarty, D., Kaplan, D. L., Markwardt, C. B., Morgan, E. H., Ray, P. S., van der Klis, M., & Wijnands, R. (2008). The Long-Term Evolution of the Spin, Pulse Shape, and Orbit of the Accretion-powered Millisecond Pulsar SAX J1808.4-3658. *ApJ*, **675**, 1468–1486, 0708.0211.
- Hartman, J. M., Patruno, A., Chakrabarty, D., Markwardt, C. B., Morgan, E. H., van der Klis, M., & Wijnands, R. (2009a). A Decade of Timing an Accretion-powered Millisecond Pulsar: The Continuing Spin Down and Orbital Evolution of SAX J1808.4-3658. *ApJ*, **702**, 1673–1678, 0902.2112.
- Hartman, J. M., Watts, A. L., & Chakrabarty, D. (2009b). The Luminosity and Energy Dependence of Pulse Phase Lags in the Accretion-powered Millisecond Pulsar SAX J1808.4-3658. *ApJ*, **697**, 2102–2107, 0809.3722.
- Hasinger, G. & van der Klis, M. (1989). Two patterns of correlated X-ray timing and spectral behaviour in low-mass X-ray binaries. *A&A*, **225**, 79–96.
- Haskell, B. (2008). Mountains on neutron stars. *Classical and Quantum Gravity*, **25**(11), 114049.
- Haskell, B., Samuelsson, L., Glampedakis, K., & Andersson, N. (2008). Modelling magnetically deformed neutron stars. *MNRAS*, **385**, 531–542, 0705.1780.

- Haverkorn, M., Gaensler, B. M., Brown, J. C., Bizunok, N. S., McClure-Griffiths, N. M., Dickey, J. M., & Green, A. J. (2006). Enhanced Small-Scale Faraday Rotation in the Galactic Spiral Arms. *ApJL*, **637**, L33–L35, arXiv:astro-ph/0512456.
- Hayes, J. C., Norman, M. L., Fiedler, R. A., Bordner, J. O., Li, P. S., Clark, S. E., ud-Doula, A., & Mac Low, M.-M. (2006). Simulating Radiating and Magnetized Flows in Multiple Dimensions with ZEUS-MP. *ApJS*, **165**, 188–228, arXiv:astro-ph/0511545.
- Heger, A., Fryer, C. L., Woosley, S. E., Langer, N., & Hartmann, D. H. (2003). How Massive Single Stars End Their Life. *ApJ*, **591**, 288–300, arXiv:astro-ph/0212469.
- Helfand, D. J., Manchester, R. N., & Taylor, J. H. (1975). Observations of pulsar radio emission. III - Stability of integrated profiles. *ApJ*, **198**, 661–670.
- Hessels, J. W. T., Ransom, S. M., Stairs, I. H., Freire, P. C. C., Kaspi, V. M., & Camilo, F. (2006). A Radio Pulsar Spinning at 716 Hz. *Science*, **311**, 1901–1904, arXiv:astro-ph/0601337.
- Hewish, A. & Okoye, S. E. (1965). Evidence for an Unusual Source of High Radio Brightness Temperature in the Crab Nebula. *Nature*, **207**, 59–60.
- Heyl, J. S. (2002). Low-Mass X-Ray Binaries May Be Important Laser Interferometer Gravitational-Wave Observatory Sources After All. *ApJL*, **574**, L57–L60.
- Hibschman, J. A. & Arons, J. (2001). Polarization Sweeps in Rotation-powered Pulsars. *ApJ*, **546**, 382–393, arXiv:astro-ph/0008117.
- Hirata, K., Kajita, T., Koshiba, M., Nakahata, M., & Oyama, Y. (1987). Observation of a neutrino burst from the supernova SN1987A. *Physical Review Letters*, **58**, 1490–1493.
- Hobbs, G., Lyne, A., & Kramer, M. (2006). Pulsar Timing Noise. *Chinese Journal of Astronomy and Astrophysics Supplement*, **6**, 169–175.
- Hobbs, G., Archibald, A., Arzoumanian, Z., Backer, D., Bailes, M., Bhat, N. D. R., Burgay, M., Burke-Spolaor, S., Champion, D., Cognard, I., Coles, W., Cordes, J., Demorest, P., Desvignes, G., Ferdman, R. D., Finn, L.,

- Freire, P., Gonzalez, M., Hessels, J., Hotan, A., Janssen, G., Jenet, F., Jessner, A., Jordan, C., Kaspi, V., Kramer, M., Kondratiev, V., Lazio, J., Lazaridis, K., Lee, K. J., Levin, Y., Lommen, A., Lorimer, D., Lynch, R., Lyne, A., Manchester, R., McLaughlin, M., Nice, D., Osłowski, S., Pilia, M., Possenti, A., Purver, M., Ransom, S., Reynolds, J., Sanidas, S., Sarkissian, J., Sesana, A., Shannon, R., Siemens, X., Stairs, I., Stappers, B., Stinebring, D., Theureau, G., van Haasteren, R., van Straten, W., Verbiest, J. P. W., Yardley, D. R. B., & You, X. P. (2009). The international pulsar timing array project: using pulsars as a gravitational wave detector. *ArXiv e-prints*, 0911.5206.
- Hobbs, G., Lyne, A. G., & Kramer, M. (2010). An analysis of the timing irregularities for 366 pulsars. *MNRAS*, **402**, 1027–1048, 0912.4537.
- Hohle, M. & Haberl, F. (2009). RX J0720.4-3125 - a precessing X-ray pulsar? In *European Planetary Science Congress 2009, held 14-18 September in Potsdam, Germany*. <http://meetings.copernicus.org/epsc2009>, p.4, page 4.
- Hulse, R. A. & Taylor, J. H. (1975). Discovery of a pulsar in a binary system. *ApJL*, **195**, L51–L53.
- Ibragimov, A. & Poutanen, J. (2009). Accreting millisecond pulsar SAX J1808.4-3658 during its 2002 outburst: evidence for a receding disc. *MNRAS*, **400**, 492–508, 0901.0073.
- Illarionov, A. F. & Sunyaev, R. A. (1975). Why the Number of Galactic X-ray Stars Is so Small? *A&A*, **39**, 185.
- Immler, S., Weiler, K., & McCray, R., editors (2007). *SUPERNOVA 1987A: 20 YEARS AFTER: Supernovae and Gamma-Ray Burste*, volume 937 of *American Institute of Physics Conference Series*.
- Inoue, H., Hayashida, K., Itoh, M., Kondo, H., Mitsuda, K., Takeshima, T., Yoshida, K., & Tanaka, Y. (1991). X-ray observation of SN 1987A from GINGA. *Publ. Astron. Soc. Jpn.*, **43**, 213–223.
- Ivanova, N., Heinke, C. O., & Rasio, F. A. (2008). Formation of Millisecond Pulsars in Globular Clusters. In C. Bassa, Z. Wang, A. Cumming, & V. M. Kaspi, editor, *40 Years of Pulsars: Millisecond Pulsars, Magnetars and More*, volume 983 of *American Institute of Physics Conference Series*, pages 442–447.

- Iyudin, A. F., Aschenbach, V., Burwitz, V., Dennerl, K., Freyberg, M., Haberl, F., & Filipovic, M. (2007). Multiwavelength Appearance of Vela Jr.: Is it up to Expectations? In *ESA Special Publication*, volume 622 of *ESA Special Publication*, page 91.
- Jahoda, K., Swank, J. H., Giles, A. B., Stark, M. J., Strohmayer, T., Zhang, W., & Morgan, E. H. (1996). In-orbit performance and calibration of the Rossi X-ray Timing Explorer (RXTE) Proportional Counter Array (PCA). In O. H. Siegmund and M. A. Gummin, editors, *Proc. SPIE Vol. 2808, p. 59-70, EUV, X-Ray, and Gamma-Ray Instrumentation for Astronomy VII, Oswald H. Siegmund; Mark A. Gummin; Eds.*, volume 2808 of *Presented at the Society of Photo-Optical Instrumentation Engineers (SPIE) Conference*, pages 59–70.
- Janssen, G. H., Stappers, B. W., Kramer, M., Purver, M., Jessner, A., & Cognard, I. (2008). European Pulsar Timing Array. In C. Bassa, Z. Wang, A. Cumming, & V. M. Kaspi, editor, *40 Years of Pulsars: Millisecond Pulsars, Magnetars and More*, volume 983 of *American Institute of Physics Conference Series*, pages 633–635.
- Jaranowski, P. & Krolak, A. (1994). Optimal solution to the inverse problem for the gravitational wave signal of a coalescing compact binary. *Phys. Rev. D*, **49**, 1723–1739.
- Jaranowski, P., Królak, A., & Schutz, B. F. (1998). Data analysis of gravitational-wave signals from spinning neutron stars: The signal and its detection. *Phys. Rev. D*, **58**(6), 063001, arXiv:gr-qc/9804014.
- Johnston, S., Karastergiou, A., Mitra, D., & Gupta, Y. (2008a). Multifrequency integrated profiles of pulsars. *MNRAS*, **388**, 261–274, 0804.3838.
- Johnston, S., Karastergiou, A., Mitra, D., & Gupta, Y. (2008b). Multifrequency integrated profiles of pulsars. *MNRAS*, **388**, 261–274, 0804.3838.
- Jones, D. I. & Andersson, N. (2001). Freely precessing neutron stars: model and observations. *MNRAS*, **324**, 811–824, arXiv:astro-ph/0011063.
- Jones, D. I. & Andersson, N. (2002). Gravitational waves from freely precessing neutron stars. *MNRAS*, **331**, 203–220, arXiv:gr-qc/0106094.
- Kaaret, P., in 't Zand, J. J. M., Heise, J., & Tomsick, J. A. (2002). Discovery of Millisecond Variability in the Neutron Star X-Ray Transient SAX J1750.8-2900. *ApJ*, **575**, 1018–1024, arXiv:astro-ph/0204409.

- Kaaret, P., Morgan, E. H., Vanderspek, R., & Tomsick, J. A. (2006). Discovery of the Millisecond X-Ray Pulsar HETE J1900.1-2455. *ApJ*, **638**, 963–967, arXiv:astro-ph/0510483.
- Kalopotharakos, C. & Contopoulos, I. (2009). Three-dimensional numerical simulations of the pulsar magnetosphere: preliminary results. *A&A*, **496**, 495–502, 0811.2863.
- Kalmus, P., Cannon, K. C., Márka, S., & Owen, B. J. (2009). Stacking gravitational wave signals from soft gamma repeater bursts. *Phys. Rev. D*, **80**(4), 042001, 0904.4906.
- Kamionkowski, M. & Kosowsky, A. (1998). Detectability of inflationary gravitational waves with microwave background polarization. *Phys. Rev. D*, **57**, 685–691, arXiv:astro-ph/9705219.
- Karastergiou, A. & Johnston, S. (2007). An empirical model for the beams of radio pulsars. *MNRAS*, **380**, 1678–1684, 0707.2547.
- Karastergiou, A., Johnston, S., Mitra, D., van Leeuwen, A. G. J., & Edwards, R. T. (2003). —V—: new insight into the circular polarization of radio pulsars. *MNRAS*, **344**, L69–L73, arXiv:astro-ph/0308221.
- Karastergiou, A., Johnston, S., & Manchester, R. N. (2005). Polarization profiles of southern pulsars at 3.1 GHz. *MNRAS*, **359**, 481–492, arXiv:astro-ph/0502337.
- Kaspi, V. M., Taylor, J. H., & Ryba, M. F. (1994). High-precision timing of millisecond pulsars. 3: Long-term monitoring of PSRs B1855+09 and B1937+21. *ApJ*, **428**, 713–728.
- Kaspi, V. M., Lackey, J. R., Mattox, J., Manchester, R. N., Bailes, M., & Pace, R. (2000). High-Energy Gamma-Ray Observations of Two Young, Energetic Radio Pulsars. *ApJ*, **528**, 445–453, arXiv:astro-ph/9906373.
- Keane, E. F. & Kramer, M. (2008). On the birthrates of Galactic neutron stars. *MNRAS*, **391**, 2009–2016, 0810.1512.
- Kijak, J. & Gil, J. (1998). Radio emission regions in pulsars. *MNRAS*, **299**, 855–861.
- Knight, H. S., Bailes, M., Manchester, R. N., & Ord, S. M. (2006). A Study of Giant Pulses from PSR J1824-2452A. *ApJ*, **653**, 580–586, arXiv:astro-ph/0608155.

- Knispel, B. & Allen, B. (2008). Blandford's argument: The strongest continuous gravitational wave signal. *Phys. Rev. D*, **78**(4), 044031, 0804.3075.
- Kocsis, B., Gáspár, M. E., & Márka, S. (2006). Detection Rate Estimates of Gravity Waves Emitted during Parabolic Encounters of Stellar Black Holes in Globular Clusters. *ApJ*, **648**, 411–429, arXiv:astro-ph/0603441.
- Kokkotas, K. & Schmidt, B. (1999). Quasi-Normal Modes of Stars and Black Holes. *Living Reviews in Relativity*, **2**, 2, arXiv:gr-qc/9909058.
- Komesaroff, M. M. (1970). Possible Mechanism for the Pulsar Radio Emission. *Nature*, **225**, 612–614.
- Kosowsky, A., Turner, M. S., & Watkins, R. (1992). Gravitational waves from first-order cosmological phase transitions. *Physical Review Letters*, **69**, 2026–2029.
- Koyama, K., Inoue, H., Makishima, K., Matsuoka, M., Murakami, T., Oda, M., Osgawara, Y., Ohashi, T., Shibazaki, N., Tanaka, Y., Marshall, F. J., Kondo, I. S., Hayakawa, S., Kunieda, H., Makino, F., Masai, K., Nagase, F., Tawara, Y., Miyamoto, S., Tsunemi, H., & Yamashita, K. (1981). Discovery of X-ray bursts from Aquila X-1. *apjl*, **247**, L27–L29.
- Kramer, M. & Johnston, S. (2008). High-precision geometry of a double-pole pulsar. *MNRAS*, **390**, 87–92, 0807.5013.
- Kramer, M., Xilouris, K. M., Lorimer, D. R., Doroshenko, O., Jessner, A., Wielebinski, R., Wolszczan, A., & Camilo, F. (1998). The Characteristics of Millisecond Pulsar Emission. I. Spectra, Pulse Shapes, and the Beaming Fraction. *ApJ*, **501**, 270, arXiv:astro-ph/9801177.
- Kramer, M., Lange, C., Lorimer, D. R., Backer, D. C., Xilouris, K. M., Jessner, A., & Wielebinski, R. (1999). The Characteristics of Millisecond Pulsar Emission. III. From Low to High Frequencies. *ApJ*, **526**, 957–975, arXiv:astro-ph/9906442.
- Krimm, H. A., Markwardt, C. B., Deloye, C. J., Romano, P., Chakrabarty, D., Campana, S., Cummings, J. R., Galloway, D. K., Gehrels, N., Hartman, J. M., Kaaret, P., Morgan, E. H., & Tueller, J. (2007). Discovery of the accretion-powered millisecond pulsar SWIFT J1756.9-2508 with a low-mass companion. *ArXiv e-prints*, **709**, 0709.1693.

- Krishnan, B., Sintes, A. M., Papa, M. A., Schutz, B. F., Frasca, S., & Palomba, C. (2004). Hough transform search for continuous gravitational waves. *Phys. Rev. D*, **70**(8), 082001, arXiv:gr-qc/0407001.
- Kulkarni, A. K. & Romanova, M. M. (2005). Variability Profiles of Millisecond X-Ray Pulsars: Results of Pseudo-Newtonian Three-dimensional Magneto-hydrodynamic Simulations. *ApJ*, **633**, 349–357, arXiv:astro-ph/0507358.
- Kulkarni, S. R. & Hester, J. J. (1988). Discovery of a nebula around PSR1957+20. *Nature*, **335**, 801–803.
- Lai, D., Lovelace, R., & Wasserman, I. (1999). KiloHertz Quasi-Periodic Oscillations, Magnetic Fields and Mass of Neutron Stars in Low-Mass X-Ray Binaries. *ArXiv Astrophysics e-prints*, arXiv:astro-ph/9904111.
- Lamb, F. K., Pethick, C. J., & Pines, D. (1973). A Model for Compact X-Ray Sources: Accretion by Rotating Magnetic Stars. *ApJ*, **184**, 271–290.
- Lamb, F. K., Boutloukos, S., Van Wassenhove, S., Chamberlain, R. T., Lo, K. H., Clare, A., Yu, W., & Miller, M. C. (2009). A Model for the Waveform Behavior of Accreting Millisecond X-Ray Pulsars: Nearly Aligned Magnetic Fields and Moving Emission Regions. *ApJ*, **706**, 417–435, 0808.4159.
- Landau, L. D. & Lifshitz, E. M. (1969). *Mechanics*. Course of Theoretical Physics, Oxford: Pergamon Press, 1969, 2nd ed.
- Lasota, J.-P. (2001). The disc instability model of dwarf novae and low-mass X-ray binary transients. *New Astronomy Review*, **45**, 449–508, arXiv:astro-ph/0102072.
- Lattimer, J. M. & Prakash, M. (2007). Neutron star observations: Prognosis for equation of state constraints. *Physics Reports*, **442**, 109–165, arXiv:astro-ph/0612440.
- Launhardt, R., Zylka, R., & Mezger, P. G. (2002). The nuclear bulge of the Galaxy. III. Large-scale physical characteristics of stars and interstellar matter. *A&A*, **384**, 112–139, arXiv:astro-ph/0201294.
- Laycock, S., Corbet, R. H. D., Coe, M. J., Marshall, F. E., Markwardt, C., & Lochner, J. (2005). Long-Term Behavior of X-Ray Pulsars in the Small Magellanic Cloud. *ApJS*, **161**, 96–117, arXiv:astro-ph/0406420.

- Lenzi, C. H., Magalhães, N. S., Costa, C. A., Marinho, R. M., Araújo, H. A. B., & Aguiar, O. D. (2008). Astrophysics from data analysis of spherical gravitational wave detectors. *General Relativity and Gravitation*, **40**, 183–190, 0710.3330.
- Levin, Y. (1999). Runaway Heating by R-Modes of Neutron Stars in Low-Mass X-Ray Binaries. *ApJ*, **517**, 328–333, arXiv:astro-ph/9810471.
- Lin, D., Remillard, R. A., & Homan, J. (2009). Spectral States of XTE J1701 - 462: Link Between Z and Atoll Sources. *ApJ*, **696**, 1257–1277, 0901.0031.
- Linares, M., van der Klis, M., Altamirano, D., & Markwardt, C. B. (2005). Discovery of KiloHertz Quasi-periodic Oscillations and Shifted Frequency Correlations in the Accreting Millisecond Pulsar XTE J1807-294. *ApJ*, **634**, 1250–1260, arXiv:astro-ph/0509011.
- Link, B. (2003). Precession of Isolated Neutron Stars. In M. Bailes, D. J. Nice, and S. E. Thorsett, editors, *Radio Pulsars*, volume 302 of *Astronomical Society of the Pacific Conference Series*, page 241.
- Lomb, N. R. (1976). Least-squares frequency analysis of unequally spaced data. *Astrophys. Space. Sci.*, **39**, 447–462.
- Long, M., Romanova, M. M., & Lovelace, R. V. E. (2008). Three-dimensional simulations of accretion to stars with complex magnetic fields. *MNRAS*, **386**, 1274–1284, 0802.2308.
- Lorimer, D. R. (2008). Binary and Millisecond Pulsars. *Living Reviews in Relativity*, **11**, 8, 0811.0762.
- Lorimer, D. R., Jessner, A., Seiradakis, J. H., Lyne, A. G., D’Amico, N., Athanasopoulos, A., Xilouris, K. M., Kramer, M., & Wielebinski, R. (1998). A flexible format for exchanging pulsar data. *Astronomy and Astrophysics Supplement Series.*, **128**, 541–544, arXiv:astro-ph/9801097.
- Lorimer, D. R., Camilo, F., Freire, P., Kramer, M., Lyne, A. G., Manchester, R. N., & D’Amico, N. (2003). Millisecond Radio Pulsars in 47 Tucanae. In M. Bailes, D. J. Nice, & S. E. Thorsett, editor, *Radio Pulsars*, volume 302 of *Astronomical Society of the Pacific Conference Series*, page 363.
- Lorimer, D. R., Stairs, I. H., Freire, P. C., Cordes, J. M., Camilo, F., Faulkner, A. J., Lyne, A. G., Nice, D. J., Ransom, S. M., Arzoumanian, Z., Manch-

- ester, R. N., Champion, D. J., van Leeuwen, J., McLaughlin, M. A., Ramanachandran, R., Hessels, J. W., Vlemmings, W., Deshpande, A. A., Bhat, N. D., Chatterjee, S., Han, J. L., Gaensler, B. M., Kasian, L., Deneva, J. S., Reid, B., Lazio, T. J., Kaspi, V. M., Crawford, F., Lommen, A. N., Backer, D. C., Kramer, M., Stappers, B. W., Hobbs, G. B., Possenti, A., D'Amico, N., & Burgay, M. (2006). Arecibo Pulsar Survey Using ALFA. II. The Young, Highly Relativistic Binary Pulsar J1906+0746. *apj*, **640**, 428–434, arXiv:astro-ph/0511523.
- Lutovinov, A. A., Revnivtsev, M. G., Gilfanov, M. R., & Sunyaev, R. A. (2007). Population of HMXB in the Galaxy. In *ESA Special Publication*, volume 622 of *ESA Special Publication*, page 241.
- Lyne, A., Hobbs, G., Kramer, M., Stairs, I., & Stappers, B. (2010). Switched Magnetospheric Regulation of Pulsar Spin-Down. *Science*, **329**, 408–, 1006.5184.
- Lyne, A. G. & Graham-Smith, F. (2006). *Pulsar astronomy*. Pulsar astronomy, 3rd ed., by A.G. Lyne and F. Graham-Smith. Cambridge astrophysics series. Cambridge, UK: Cambridge University Press, 2006 ISBN 0521839548.
- Lyne, A. G. & Manchester, R. N. (1988). The shape of pulsar radio beams. *MNRAS*, **234**, 477–508.
- Maggiore, M. (2000). Gravitational wave experiments and early universe cosmology. *Physics Reports*, **331**, 283–367, arXiv:gr-qc/9909001.
- Makishima, K. (2003). Measuring Magnetic Fields of Neutron Stars. *Progress of Theoretical Physics Supplement*, **151**, 54–63.
- Makishima, K., Mihara, T., Nagase, F., & Tanaka, Y. (1999). Cyclotron Resonance Effects in Two Binary X-Ray Pulsars and the Evolution of Neutron Star Magnetic Fields. *ApJ*, **525**, 978–994.
- Manchester, B. N. (1996). Wide Beams from Young Pulsars (or One Pole for All). In S. Johnston, M. A. Walker, and M. Bailes, editors, *IAU Colloq. 160: Pulsars: Problems and Progress*, volume 105 of *Astronomical Society of the Pacific Conference Series*, page 193.
- Manchester, R. N. (2007). Searching for a Pulsar in SN1987A. In S. Immler, K. Weiler, and R. McCray, editors, *Supernova 1987A: 20 Years After:*

- Supernovae and Gamma-Ray Bursters*, volume 937 of *American Institute of Physics Conference Series*, pages 134–143.
- Manchester, R. N. & Han, J. L. (2004). Polarization Observations of Nine Southern Millisecond Pulsars. *ApJ*, **609**, 354–362, arXiv:astro-ph/0403199.
- Manchester, R. N. & Johnston, S. (1995). Polarization properties of two pulsars. *ApJL*, **441**, L65–L68.
- Manchester, R. N. & Lyne, A. G. (1977). Pulsar interpulses - Two poles or one. *MNRAS*, **181**, 761–767.
- Manchester, R. N., Han, J. L., & Qiao, G. J. (1998). Polarization observations of 66 southern pulsars. *MNRAS*, **295**, 280–298.
- Manchester, R. N., Hobbs, G. B., Teoh, A., & Hobbs, M. (2005). The Australia Telescope National Facility Pulsar Catalogue. *AJ*, **129**, 1993–2006.
- Markwardt, C. B. & Swank, J. H. (2003). XTE J1814-338. *IAU Circ.*, **8144**, 1.
- Markwardt, C. B., Strohmayer, T. E., & Swank, J. H. (2003). Revised Orbit and Burst Oscillations from the Millisecond Pulsar XTE J1814-338. *The Astronomer's Telegram*, **164**, 1.
- Markwardt, C. B., Altamirano, D., Swank, J. H., Strohmayer, T. E., Linares, M., & Pereira, D. (2009). RXTE Detects 245 Hz X-ray Pulsations from IGR J17511-305. *The Astronomer's Telegram*, **2197**, 1.
- Mastrano, A., Resenegger, A., Akgün, T., & Melatos, A. (2010). Gravitational wave emission from a magnetically deformed, non-barotropic star.
- Matsakis, D. N., Taylor, J. H., & Eubanks, T. M. (1997). A statistic for describing pulsar and clock stabilities. *A&A*, **326**, 924–928.
- McKinnon, M. M. & Stinebring, D. R. (1998). A Statistical Model for the Orthogonal Modes of Polarization in Pulsar Radio Emission. *ApJ*, **502**, 883.
- Melatos, A. (1997). Spin-down of an oblique rotator with a current-starved outer magnetosphere. *MNRAS*, **288**, 1049–1059.
- Melatos, A. (2000). Radiative precession of an isolated neutron star. *MNRAS*, **313**, 217–228, arXiv:astro-ph/0004035.

- Melatos, A. & Payne, D. J. B. (2005). Gravitational Radiation from an Accreting Millisecond Pulsar with a Magnetically Confined Mountain. *ApJ*, **623**, 1044–1050, arXiv:astro-ph/0503287.
- Melatos, A. & Phinney, E. S. (2001). Hydromagnetic Structure of a Neutron Star Accreting at Its Polar Caps. *Publications of the Astronomical Society of Australia*, **18**, 421–430.
- Melatos, A., Peralta, C., & Wyithe, J. S. B. (2008). Avalanche Dynamics of Radio Pulsar Glitches. *ApJ*, **672**, 1103–1118, 0710.1021.
- Melrose, D., Miller, A., Karastergiou, A., & Luo, Q. (2006). An empirical model for the polarization of pulsar radio emission. *MNRAS*, **365**, 638–646, arXiv:astro-ph/0510837.
- Melrose, D. B. (1995). The Models for Radio Emission from Pulsars - the Outstanding Issues. *Journal of Astrophysics and Astronomy*, **16**, 137.
- Méndez, M. & van der Klis, M. (1999). Precise Measurements of the Kilohertz Quasi-periodic Oscillations in 4U 1728-34. *ApJL*, **517**, L51–L54, arXiv:astro-ph/9903303.
- Mereghetti, S. (2008). The strongest cosmic magnets: soft gamma-ray repeaters and anomalous X-ray pulsars. *The Astronomy and Astrophysics Review*, **15**, 225–287, 0804.0250.
- Messenger, C. & Woan, G. (2007). A fast search strategy for gravitational waves from low-mass x-ray binaries. *Classical and Quantum Gravity*, **24**, 469, arXiv:gr-qc/0703155.
- Mészáros, P. (1992). High-energy radiation from magnetized neutron stars.
- Michel, F. C. (1973). Rotating Magnetospheres: an Exact 3-D Solution. *ApJL*, **180**, L133.
- Michel, F. C. (1982). Theory of pulsar magnetospheres. *Reviews of Modern Physics*, **54**, 1–66.
- Michel, F. C. (1994). A Fast Pulsar in Supernova 1987A. *MNRAS*, **267**, L4+.
- Middleditch, J., Kristian, J. A., Kunkel, W. E., Hill, K. M., Watson, R. D., Lucinio, R., Imamura, J. N., Steiman-Cameron, T. Y., Shearer, A., Butler, R., Redfern, M., & Danks, A. C. (2000). Rapid photometry of supernova 1987A: a 2.14 ms pulsar? *New Astronomy*, **5**, 243–283.

- Migliari, S., van der Klis, M., & Fender, R. P. (2003). Evidence of a decrease of kHz quasi-periodic oscillation peak separation towards low frequencies in 4U 1728-34 (GX 354-0). *MNRAS*, **345**, L35–L39, arXiv:astro-ph/0309288.
- Minkowski, R. (1942). The Crab Nebula. *ApJ*, **96**, 199.
- Morgan, E., Kaaret, P., & Vanderspek, R. (2005). HETE J1900.1-2455 is a millisecond pulsar. *The Astronomer's Telegram*, **523**, 1.
- Muno, M. P., Özel, F., & Chakrabarty, D. (2002). The Amplitude Evolution and Harmonic Content of Millisecond Oscillations in Thermonuclear X-Ray Bursts. *ApJ*, **581**, 550–561, arXiv:astro-ph/0204501.
- Muno, M. P., Clark, J. S., Crowther, P. A., Dougherty, S. M., de Grijs, R., Law, C., McMillan, S. L. W., Morris, M. R., Negueruela, I., Pooley, D., Portegies Zwart, S., & Yusef-Zadeh, F. (2006). A Neutron Star with a Massive Progenitor in Westerlund 1. *ApJL*, **636**, L41–L44, arXiv:astro-ph/0509408.
- Nakamura, T. (1989). Binary Sub-Millisecond Pulsar and Rotating Core Collapse Model for SN1987A. *Progress of Theoretical Physics*, **81**, 1006–1020.
- Nakamura, T. & Fukugita, M. (1989). Rotating stellar collapse model for supernova SN 1987A. *ApJ*, **337**, 466–469.
- Navarro, J., Manchester, R. N., Sandhu, J. S., Kulkarni, S. R., & Bailes, M. (1997). Mean Pulse Shape and Polarization of PSR J0437-4715. *ApJ*, **486**, 1019.
- Nayyar, M. & Owen, B. J. (2006). R-modes of accreting hyperon stars as persistent sources of gravitational waves. *Phys. Rev. D*, **73**(8), 084001, arXiv:astro-ph/0512041.
- Niebauer, T. M., Rüdiger, A., Schilling, R., Schnupp, L., Winkler, W., & Danzmann, K. (1993). Pulsar search using data compression with the Garching gravitational wave detector. *Phys. Rev. D*, **47**, 3106–3123.
- Ögelman, H. & Alpar, M. A. (2004). Constraints on a Putative Pulsar in SN 1987A. *ApJL*, **603**, L33–L35, arXiv:astro-ph/0402147.
- Oppenheimer, J. R. & Volkoff, G. M. (1939). On Massive Neutron Cores. *Physical Review*, **55**, 374–381.

- Ord, S. M., van Straten, W., Hotan, A. W., & Bailes, M. (2004). Polarimetric profiles of 27 millisecond pulsars. *MNRAS*, **352**, 804–814.
- Ostriker, J. P. & Gunn, J. E. (1969). On the Nature of Pulsars. I. Theory. *ApJ*, **157**, 1395.
- Ott, C. D. (2009). TOPICAL REVIEW: The gravitational-wave signature of core-collapse supernovae. *Classical and Quantum Gravity*, **26**(6), 063001, 0809.0695.
- Ott, C. D., Burrows, A., Livne, E., & Walder, R. (2004). Gravitational Waves from Axisymmetric, Rotating Stellar Core Collapse. *ApJ*, **600**, 834–864, arXiv:astro-ph/0307472.
- Ott, C. D., Burrows, A., Thompson, T. A., Livne, E., & Walder, R. (2006). The Spin Periods and Rotational Profiles of Neutron Stars at Birth. *ApJS*, **164**, 130–155, arXiv:astro-ph/0508462.
- Owen, B. J. (1996). Search templates for gravitational waves from inspiraling binaries: Choice of template spacing. *Phys. Rev. D*, **53**, 6749–6761, arXiv:gr-qc/9511032.
- Owen, B. J. (2005). Maximum Elastic Deformations of Compact Stars with Exotic Equations of State. *Physical Review Letters*, **95**(21), 211101, arXiv:astro-ph/0503399.
- Owen, B. J. (2009). How photon astronomy affects searches for continuous gravitational waves. *Classical and Quantum Gravity*, **26**(20), 204014, 0904.4848.
- Owen, B. J., Lindblom, L., Cutler, C., Schutz, B. F., Vecchio, A., & Andersson, N. (1998). Gravitational waves from hot young rapidly rotating neutron stars. *Phys. Rev. D*, **58**(8), 084020, arXiv:gr-qc/9804044.
- Pacini, F. (1967). Energy Emission from a Neutron Star. *Nature*, **216**, 567–568.
- Pacini, F. & Salpeter, E. E. (1968). Some Models for Pulsed Radio Sources. *Nature*, **218**, 733–734.
- Pacini, F. & Salvati, M. (1987). Optical and X-ray radiation from fast pulsars - Effects of duty cycle and spectral shape. *ApJ*, **321**, 447–449.

- Palomba, C. (2005). Simulation of a population of isolated neutron stars evolving through the emission of gravitational waves. *MNRAS*, **359**, 1150–1164, arXiv:astro-ph/0503046.
- Panagia, N. (1987). Ultraviolet photometry and the energetics of SN 1987A. In I. J. Danziger, editor, *European Southern Observatory Astrophysics Symposia*, volume 26 of *European Southern Observatory Astrophysics Symposia*, pages 55–62.
- Panagia, N. (2008). Supernova 1987A: Twenty Years After. *Chinese Journal of Astronomy and Astrophysics Supplement*, **8**, 155–164.
- Papaloizou, J. & Pringle, J. E. (1978). Non-radial oscillations of rotating stars and their relevance to the short-period oscillations of cataclysmic variables. *MNRAS*, **182**, 423–442.
- Papitto, A., di Salvo, T., Burderi, L., Menna, M. T., Lavagetto, G., & Riggio, A. (2007). Timing of the accreting millisecond pulsar XTE J1814-338. *MNRAS*, **375**, 971–976, arXiv:astro-ph/0611942.
- Patruno, A., Wijnands, R., & van der Klis, M. (2009). An Alternative Interpretation of the Timing Noise in Accreting Millisecond Pulsars. *ApJL*, **698**, L60–L63, 0902.4118.
- Payne, D. J. B. & Melatos, A. (2004). Burial of the polar magnetic field of an accreting neutron star - I. Self-consistent analytic and numerical equilibria. *MNRAS*, **351**, 569–584, arXiv:astro-ph/0403173.
- Payne, D. J. B. & Melatos, A. (2006). Frequency Spectrum of Gravitational Radiation from Global Hydromagnetic Oscillations of a Magnetically Confined Mountain on an Accreting Neutron Star. *ApJ*, **641**, 471–478, arXiv:astro-ph/0510053.
- Payne, D. J. B. & Melatos, A. (2007). Burial of the polar magnetic field of an accreting neutron star - II. Hydromagnetic stability of axisymmetric equilibria. *MNRAS*, **376**, 609–624, arXiv:astro-ph/0703203.
- Peralta, C., Melatos, A., Giacobello, M., & Ooi, A. (2006). Gravitational Radiation from Nonaxisymmetric Spherical Couette Flow in a Neutron Star. *ApJL*, **644**, L53–L56, arXiv:gr-qc/0604123.

- Percival, J. W., Boyd, P. T., Biggs, J. D., Dolan, J. F., Bless, R. C., Elliot, J. L., Nelson, M. J., Robinson, E. L., Taylor, M. J., van Citters, G. W., & Wolinski, K. G. (1995). A Search for a Pulsar in the Remnant of SN 1987A with the Hubble Space Telescope High-Speed Photometer. *ApJ*, **446**, 832.
- Petrova, S. A. (2008). Physics of Interpulse Emission in Radio Pulsars. *ApJ*, **673**, 400–410, 0709.3173.
- Piran, T. & Nakamura, T. (1988). Can Current Detectors Detect Gravitational Radiation from Newborn Pulsars? *Progress of Theoretical Physics*, **80**, 18–21.
- Pletsch, H. (2010). Parameter-space metric of semicoherent searches for continuous gravitational waves. LIGO document LIGO-P1000006-v1, available in <http://dcc.ligo.org>.
- Pletsch, H. J. & Allen, B. (2009). Exploiting Large-Scale Correlations to Detect Continuous Gravitational Waves. *Physical Review Letters*, **103**(18), 181102, 0906.0023.
- Podsiadlowski, P. & Joss, P. C. (1989). An alternative binary model for SN1987A. *Nature*, **338**, 401–403.
- Podsiadlowski, P., Joss, P. C., & Rappaport, S. (1990). A merger model for SN 1987 A. *A&A*, **227**, L9–L12.
- Podsiadlowski, P., Morris, T. S., & Ivanova, N. (2007). The progenitor of SN 1987A. In S. Immler, K. Weiler, and R. McCray, editors, *Supernova 1987A: 20 Years After: Supernovae and Gamma-Ray Bursters*, volume 937 of *American Institute of Physics Conference Series*, pages 125–133.
- Portegies Zwart, S. F. (2007). The gravitational wave signature of young and dense star clusters. *Advances in Space Research*, **39**, 275–279.
- Portegies Zwart, S. F., Makino, J., McMillan, S. L. W., & Hut, P. (2001). How Many Young Star Clusters Exist in the Galactic Center? *ApJL*, **546**, L101–L104, arXiv:astro-ph/0008490.
- Possenti, A., Cerutti, R., Colpi, M., & Mereghetti, S. (2002). Re-examining the X-ray versus spin-down luminosity correlation of rotation powered pulsars. *A&A*, **387**, 993–1002, arXiv:astro-ph/0109452.

- Poutanen, J., Ibragimov, A., & Annala, M. (2009). On the Nature of Pulse Profile Variations and Timing Noise in Accreting Millisecond Pulsars. *ApJL*, **706**, L129–L132, 0910.5868.
- Press, W. H., Flannery, B. P., Teukolsky, S. A., & Vetterling, W. T. (1986). *Numerical Recipes: The Art of Scientific Computing*. Cambridge University Press, Cambridge (UK) and New York, 1st edition.
- Pretorius, F. (2005). Evolution of Binary Black-Hole Spacetimes. *Physical Review Letters*, **95**(12), 121101, arXiv:gr-qc/0507014.
- Pretorius, F. (2007). Binary Black Hole Coalescence. *ArXiv e-prints*, 0710.1338.
- Pringle, J. E. & Rees, M. J. (1972). Accretion Disc Models for Compact X-Ray Sources. *A&A*, **21**, 1.
- Prix, R. (2007). Search for continuous gravitational waves: Metric of the multidetector F-statistic. *Phys. Rev. D*, **75**(2), 023004, arXiv:gr-qc/0606088.
- Priymak, M., Melatos, A., & Payne, D. J. B. (2010). Quadrupole moment of a magnetically confined mountain on an accreting neutron star: effect of the equation of state.
- Psaltis, D. (2004). Accreting Neutron Stars and Black Holes: A Decade of Discoveries. *ArXiv Astrophysics e-prints*.
- Psaltis, D. (2006). Accreting neutron stars and black holes: a decade of discoveries. In W. H. G. Lewin and M. van der Klis, editors, *Compact stellar X-ray sources*, pages 1–38. Cambridge University Press, Cambridge, 2006.
- Psaltis, D. & Chakrabarty, D. (1999). The Disk-Magnetosphere Interaction in the Accretion-powered Millisecond Pulsar SAX J1808.4-3658. *apj*, **521**, 332–340, arXiv:astro-ph/9809335.
- Radhakrishnan, V. & Cooke, D. J. (1969). Magnetic Poles and the Polarization Structure of Pulsar Radiation. *Ann. Phys. (Leipzig)*, **3**, 225.
- Radhakrishnan, V. & Srinivasan, G. (1982). On the origin of the recently discovered ultra-rapid pulsar. *Current Science*, **51**, 1096–1099.
- Rankin, J. M. (1983). Toward an empirical theory of pulsar emission. I Morphological taxonomy. *ApJ*, **274**, 333–368.

- Rankin, J. M. (1990). Toward an empirical theory of pulsar emission. IV - Geometry of the core emission region. *ApJ*, **352**, 247–257.
- Rankin, J. M. (1993). Toward an empirical theory of pulsar emission. VI - The geometry of the conal emission region. *ApJ*, **405**, 285–297.
- Rankin, J. M. & Ramachandran, R. (2003). Toward an Empirical Theory of Pulsar Emission. VIII. Subbeam Circulation and the Polarization-Modal Structure of Conal Beams. *ApJ*, **590**, 411–423, arXiv:astro-ph/0209343.
- Rappaport, S. A., Fregeau, J. M., & Spruit, H. (2004). Accretion onto Fast X-Ray Pulsars. *ApJ*, **606**, 436–443, arXiv:astro-ph/0310224.
- Regimbau, T. & de Freitas Pacheco, J. A. (2001). Cosmic background of gravitational waves from rotating neutron stars. *A&A*, **376**, 381–385, arXiv:astro-ph/0105260.
- Regimbau, T. & de Freitas Pacheco, J. A. (2006a). Gravitational wave background from magnetars. *A&A*, **447**, 1–7, arXiv:astro-ph/0509880.
- Regimbau, T. & de Freitas Pacheco, J. A. (2006b). Stochastic Background from Coalescences of Neutron Star-Neutron Star Binaries. *ApJ*, **642**, 455–461, arXiv:gr-qc/0512008.
- Reisenegger, A. (2003). Origin and evolution of neutron star magnetic fields. *ArXiv Astrophysics e-prints*, arXiv:astro-ph/0307133.
- Revnivtsev, M., Lutovinov, A., Churazov, E., Sazonov, S., Gilfanov, M., Grebenev, S., & Sunyaev, R. (2008). Low-mass X-ray binaries in the bulge of the Milky Way. *A&A*, **491**, 209–217, 0805.0259.
- Romani, R. W. (1990). A unified model of neutron-star magnetic fields. *Nature*, **347**, 741–743.
- Romani, R. W. & Watters, K. P. (2009). Constraining Pulsar Magnetosphere Geometry with Gamma-Ray Light Curves. *ArXiv e-prints*, 0912.3845.
- Romani, R. W. & Yadigaroglu, I. (1995). Gamma-ray pulsars: Emission zones and viewing geometries. *ApJ*, **438**, 314–321, arXiv:astro-ph/9401045.
- Romanova, M. M., Ustyugova, G. V., Koldoba, A. V., & Lovelace, R. V. E. (2004a). Three-dimensional Simulations of Disk Accretion to an Inclined Dipole. II. Hot Spots and Variability. *ApJ*, **610**, 920–932, arXiv:astro-ph/0404496.

- Romanova, M. M., Ustyugova, G. V., Koldoba, A. V., & Lovelace, R. V. E. (2004b). Three-dimensional Simulations of Disk Accretion to an Inclined Dipole. II. Hot Spots and Variability. *ApJ*, **610**, 920–932, arXiv:astro-ph/0404496.
- Ruderman, M. (1991). Neutron star crustal plate tectonics. I - Magnetic dipole evolution in millisecond pulsars and low-mass X-ray binaries. *ApJ*, **366**, 261–269.
- Ruderman, M., Shaham, J., Tavani, M., & Eichler, D. (1989). Late evolution of very low mass X-ray binaries sustained by radiation from their primaries. *ApJ*, **343**, 292–312.
- Ruderman, M. A. & Sutherland, P. G. (1973). Magnetic fields-Possible origin in neutron stars and white dwarfs. *Nature*, **246**, 93.
- Ruderman, M. A. & Sutherland, P. G. (1975). Theory of pulsars - Polar caps, sparks, and coherent microwave radiation. *ApJ*, **196**, 51–72.
- Rutledge, R. E., Bildsten, L., Brown, E. F., Pavlov, G. G., & Zavlin, V. E. (2001). Quiescent Thermal Emission from the Neutron Star in Aquila X-1. *ApJ*, **559**, 1054–1059, arXiv:astro-ph/0105319.
- Ryan, F. D. (1997). Accuracy of estimating the multipole moments of a massive body from the gravitational waves of a binary inspiral. *Phys. Rev. D*, **56**, 1845–1855.
- Saio, H., Nomoto, K., & Kato, M. (1988). Why did the progenitor of SN 1987A undergo the blue-red-blue evolution? *ApJ*, **331**, 388–393.
- Santostasi, G., Johnson, W., & Frank, J. (2003). Detectability of Gravitational Waves from SN 1987A. *ApJ*, **586**, 1191–1198, arXiv:gr-qc/0302050.
- Schneider, R., Ferrari, V., Matarrese, S., & Portegies Zwart, S. F. (2001). Low-frequency gravitational waves from cosmological compact binaries. *MNRAS*, **324**, 797–810, arXiv:astro-ph/0002055.
- Seiradakis, J. H. & Wielebinski, R. (2004). Morphology and characteristics of radio pulsars. *The Astronomy and Astrophysics Review*, **12**, 239–271, arXiv:hep-ph/0410022.
- Seiradakis, J. H., Gil, J. A., Graham, D. A., Jessner, A., Kramer, M., Malofeev, V. M., Sieber, W., & Wielebinski, R. (1995). Pulsar profiles at high

- frequencies. I. The data. *Astronomy and Astrophysics Supplement Series*, **111**, 205.
- Shabanova, T. V., Lyne, A. G., & Urama, J. O. (2001). Evidence for Free Precession in the Pulsar B1642-03. *ApJ*, **552**, 321–325, arXiv:astro-ph/0101282.
- Shakura, N. I., Postnov, K. A., & Prokhorov, M. E. (1991). Presence of a Quadrupole Component of the Magnetic Field Near the Surface of the Neutron Star in HERCULES-X-1. *Soviet Astronomy Letters*, **17**, 339.
- Shitov, Y. P. (1983). Period Dependence of the Spectrum and the Phenomenon of Twisting of the Magnetic Fields of Pulsars. *Soviet Astronomy*, **27**, 314.
- Shitov, Y. P. (1985). Pulsar Radio Polarization and the Magnetic Field Twist Effect. *Soviet Astronomy*, **29**, 33.
- Shternin, P. S. & Yakovlev, D. G. (2008). A young cooling neutron star in the remnant of Supernova 1987A. *Astronomy Letters*, **34**, 675–685.
- Sierpowska, A. & Bednarek, W. (2001). On the evolution of the Galactic pulsar population. In A. Gimenez, V. Reglero, & C. Winkler, editor, *Exploring the Gamma-Ray Universe*, volume 459 of *ESA Special Publication*, pages 215–217.
- Słowikowska, A., Kanbach, G., Kramer, M., & Stefanescu, A. (2009). Optical polarization of the Crab pulsar: precision measurements and comparison to the radio emission. *MNRAS*, **397**, 103–123, 0901.4559.
- Smith, F. G., Jones, D. H. P., Dick, J. S. B., & Pike, C. D. (1988). The optical polarization of the Crab Pulsar. *MNRAS*, **233**, 305–319.
- Solda, K., Ando, M., Kanda, N., Tagoshi, H., Tatsumi, D., Tsubono, K., & the TAMA Collaboration (2003). Search for continuous gravitational waves from the SN1987A remnant using TAMA300 data. *Classical and Quantum Gravity*, **20**, 645.
- Spitkovsky, A. (2006). Time-dependent Force-free Pulsar Magnetospheres: Axisymmetric and Oblique Rotators. *ApJL*, **648**, L51–L54, arXiv:astro-ph/0603147.
- Spitkovsky, A., Levin, Y., & Ushomirsky, G. (2002). Propagation of Thermonuclear Flames on Rapidly Rotating Neutron Stars: Extreme Weather during Type I X-Ray Bursts. *ApJ*, **566**, 1018–1038, arXiv:astro-ph/0108074.

- Srinivasan, G., Bhattacharya, D., Muslimov, A. G., & Tsygan, A. J. (1990). A novel mechanism for the decay of neutron star magnetic fields. *Current Science*, **59**, 31–38.
- Stairs, I. H., Thorsett, S. E., & Camilo, F. (1999). Coherently Dedispersed Polarimetry of Millisecond Pulsars. *ApJS*, **123**, 627–638, arXiv:astro-ph/9810399.
- Stairs, I. H., Lyne, A. G., & Shemar, S. L. (2000). Evidence for free precession in a pulsar. *Nature*, **406**, 484–486.
- Starobinskii, A. A. (1979). Spectrum of relict gravitational radiation and the early state of the universe. *ZhETF Pis ma Redaktsiiu*, **30**, 719–723.
- Stella, L., Campana, S., Colpi, M., Mereghetti, S., & Tavani, M. (1994). Do quiescent soft X-ray transients contain millisecond radio pulsars? *ApJL*, **423**, L47–L50.
- Stella, L., Dall’Osso, S., Israel, G. L., & Vecchio, A. (2005). Gravitational Radiation from Newborn Magnetars in the Virgo Cluster. *ApJL*, **634**, L165–L168, arXiv:astro-ph/0511068.
- Stinebring, D. R. (1982). *Pulsar polarization: Dual-frequency observations and the production of orthogonally polarized radiation*. Ph.D. thesis, Cornell Univ., Ithaca, NY.
- Strohmayer, T. E., Zhang, W., Swank, J. H., Smale, A., Titarchuk, L., Day, C., & Lee, U. (1996). Millisecond X-Ray Variability from an Accreting Neutron Star System. *ApJL*, **469**, L9+.
- Strohmayer, T. E., Markwardt, C. B., Swank, J. H., & in’t Zand, J. (2003). X-Ray Bursts from the Accreting Millisecond Pulsar XTE J1814-338. *ApJL*, **596**, L67–L70, arXiv:astro-ph/0308353.
- Sturrock, P. A. (1971). A Model of Pulsars. *ApJ*, **164**, 529.
- Sugerman, B. E. K., Crofts, A. P. S., Kunkel, W. E., Heathcote, S. R., & Lawrence, S. S. (2005). A New View of the Circumstellar Environment of SN 1987A. *ApJ*, **627**, 888–903, arXiv:astro-ph/0502268.
- Tabachnick, B. & Fidell, L. (1996). *Using multivariate statistics*. New York : Harper & Row, c1989.

- Tananbaum, H. (1999). Cassiopeia A. *IAU Circ.*, **7246**, 1.
- Tauris, T. M. & Konar, S. (2001). Torque decay in the pulsar (P, $\dot{P}$ ) diagram. Effects of crustal ohmic dissipation and alignment. *A&A*, **376**, 543–552, arXiv:astro-ph/0101531.
- Tauris, T. M. & van den Heuvel, E. P. J. (2006). Formation and evolution of compact stellar X-ray sources. In Lewin, W. H. G. & van der Klis, M., editor, *Compact stellar X-ray sources*, pages 623–665. Cambridge University Press.
- Tavani, M. (1992). Pulsar-irradiated stars in dense globular clusters. *A&A*, **261**, 472–474.
- Taylor, J. H., Manchester, R. N., & Lyne, A. G. (1993). Catalog of 558 pulsars. *ApJS*, **88**, 529–568.
- Thompson, C. & Duncan, R. C. (1993). Neutron star dynamos and the origins of pulsar magnetism. *ApJ*, **408**, 194–217.
- Thompson, C. & Duncan, R. C. (1996). The Soft Gamma Repeaters as Very Strongly Magnetized Neutron Stars. II. Quiescent Neutrino, X-Ray, and Alfvén Wave Emission. *ApJ*, **473**, 322.
- Thompson, D. J. (1996). Recent Gamma-Ray Observations. In S. Johnston, M. A. Walker, & M. Bailes, editor, *IAU Colloq. 160: Pulsars: Problems and Progress*, volume 105 of *Astronomical Society of the Pacific Conference Series*, page 307.
- Thorne, K. S. (1987). Gravitational radiation. In S. W. Hawking and W. Israel, editors, *Three hundred years of gravitation*, p. 330 - 458, pages 330–458. Cambridge University Press, Cambridge, 1987.
- Thorne, K. S. & Braginskii, V. B. (1976). Gravitational-wave bursts from the nuclei of distant galaxies and quasars - Proposal for detection using Doppler tracking of interplanetary spacecraft. *ApJL*, **204**, L1–L6.
- Truemper, J., Pietsch, W., Reppin, C., Voges, W., Staubert, R., & Kendziorra, E. (1978). Evidence for strong cyclotron line emission in the hard X-ray spectrum of Hercules X-1. *ApJL*, **219**, L105–L110.
- Umstätter, R., Meyer, R., Dupuis, R. J., Veitch, J., Woan, G., & Christensen, N. (2004). Estimating the parameters of gravitational waves from neutron

- stars using an adaptive MCMC method. *Classical and Quantum Gravity*, **21**, 1655.
- Umstätter, R., Meyer, R., & Christensen, N. (2008). A Bayesian method to set upper limits on the strength of a periodic gravitational wave signal from the remnant of SN1987A: possible applications in LIGO searches. *ArXiv e-prints*, 0808.2225.
- Ushomirsky, G., Cutler, C., & Bildsten, L. (2000). Deformations of accreting neutron star crusts and gravitational wave emission. *MNRAS*, **319**, 902–932, arXiv:astro-ph/0001136.
- van der Klis, M. (2004). A review of rapid X-ray variability in X-ray binaries. *ArXiv Astrophysics e-prints*, arXiv:astro-ph/0410551.
- van der Klis, M., Swank, J. H., Zhang, W., Jahoda, K., Morgan, E. H., Lewin, W. H. G., Vaughan, B., & van Paradijs, J. (1996). Discovery of Submillisecond Quasi-periodic Oscillations in the X-Ray Flux of Scorpius X-1. *ApJL*, **469**, L1+, arXiv:astro-ph/9607047.
- van Eysden, C. A. & Melatos, A. (2008). Gravitational radiation from pulsar glitches. *Classical and Quantum Gravity*, **25**(22), 225020, 0809.4352.
- van Straaten, S., van der Klis, M., & Wijnands, R. (2005). Relations Between Timing Features and Colors in Accreting Millisecond Pulsars. *ApJ*, **619**, 455–482, arXiv:astro-ph/0410505.
- Vanderspek, R., Morgan, E., Crew, G., Graziani, C., & Suzuki, M. (2005). Possible new X-ray burst source detected by HETE. *The Astronomer's Telegram*, **516**, 1.
- Verbunt, F., van den Heuvel, E. P. J., van Paradijs, J., & Rappaport, S. A. (1987). Formation of isolated millisecond pulsars in globular clusters. *Nature*, **329**, 312–314.
- Vigelius, M. & Melatos, A. (2008). Three-dimensional stability of magnetically confined mountains on accreting neutron stars. *ArXiv e-prints*, **802**, 0802.3238.
- Vigelius, M. & Melatos, A. (2009a). Improved estimate of the detectability of gravitational radiation from a magnetically confined mountain on an accreting neutron star. *MNRAS*, **395**, 1972–1984, 0902.4264.

- Vigelius, M. & Melatos, A. (2009b). Resistive relaxation of a magnetically confined mountain on an accreting neutron star. *MNRAS*, **395**, 1985–1998, 0902.4484.
- Vigelius, M. & Melatos, A. (2010). Gravitational-wave spin-down and stalling lower limits on the electrical resistivity of the accreted mountain in a millisecond pulsar.
- von Hoensbroech, A. & Xilouris, K. M. (1997a). Does radius-to-frequency mapping persist close to the pulsar surface? *A&A*, **324**, 981–987.
- von Hoensbroech, A. & Xilouris, K. M. (1997b). Does radius-to-frequency mapping persist close to the pulsar surface? *A&A*, **324**, 981–987.
- von Hoensbroech, A., Lesch, H., & Kunzl, T. (1998). Natural polarization modes in pulsar magnetospheres. *A&A*, **336**, 209–219, arXiv:astro-ph/9804318.
- Wagoner, R. V. (1984). Gravitational radiation from accreting neutron stars. *ApJ*, **278**, 345–348.
- Warszawski, L., Berloff, N. G., & Melatos, A. (2009). Quantum Mechanical Model Of Pulsar Glitches And Gravitational Waves. In *American Astronomical Society Meeting Abstracts*, volume 214 of *American Astronomical Society Meeting Abstracts*, page 605.07.
- Watters, K. P., Romani, R. W., Weltevrede, P., & Johnston, S. (2009). An Atlas for Interpreting  $\gamma$ -Ray Pulsar Light Curves. *ApJ*, **695**, 1289–1301, 0812.3931.
- Watts, A., Krishnan, B., Bildsten, L., & Schutz, B. (2008a). Detecting gravitational wave emission from the known accreting neutron stars. *ArXiv e-prints*, **803**, 0803.4097.
- Watts, A. L. & Strohmayer, T. E. (2006). The energy dependence of burst oscillations from the accreting millisecond pulsar XTE J1814-338. *MNRAS*, **373**, 769–780, arXiv:astro-ph/0607420.
- Watts, A. L., Strohmayer, T. E., & Markwardt, C. B. (2005). Analysis of Variability in the Burst Oscillations of the Accreting Millisecond Pulsar XTE J1814-338. *ApJ*, **634**, 547–564, arXiv:astro-ph/0508148.

- Watts, A. L., Patruno, A., & van der Klis, M. (2008b). Coherence of burst oscillations and accretion-powered pulsations in the accreting millisecond pulsar XTE J1814-338. *ArXiv e-prints*, **805**, 0805.4610.
- Weber, J. (1960). Detection and generation of gravitational waves. *Phys. Rev.*, **117**(1), 306–313.
- Weisberg, J. M., Cordes, J. M., Lundgren, S. C., Dawson, B. R., Despotes, J. T., Morgan, J. J., Weitz, K. A., Zink, E. C., & Backer, D. C. (1999). Arecibo 1418 MHz Polarimetry of 98 Pulsars: Full Stokes Profiles and Morphological Classifications. *ApJS*, **121**, 171–217.
- Weltevrede, P. & Johnston, S. (2008). Profile and polarization characteristics of energetic pulsars. *MNRAS*, **391**, 1210–1226, 0809.2438.
- Weltevrede, P. & Wright, G. (2009). Mapping the magnetosphere of PSR B1055-52. *MNRAS*, **395**, 2117–2126, 0902.2824.
- Wette, K., Owen, B. J., Allen, B., Ashley, M., Betzwieser, J., Christensen, N., Creighton, T. D., Dergachev, V., Gholami, I., Goetz, E., Gustafson, R., Hammer, D., Jones, D. I., Krishnan, B., Landry, M., Machenschalk, B., McClelland, D. E., Mendell, G., Messenger, C. J., Papa, M. A., Patel, P., Pitkin, M., Pletsch, H. J., Prix, R., Riles, K., Sancho de la Jordana, L., Scott, S. M., Sintes, A. M., Trias, M., Whelan, J. T., & Woan, G. (2008). Searching for gravitational waves from Cassiopeia A with LIGO. *Classical and Quantum Gravity*, **25**(23), 235011, 0802.3332.
- Wette, K., Vigelius, M., & Melatos, A. (2010). Sinking of a magnetically confined mountain on an accreting neutron star. *MNRAS*, **402**, 1099–1110, 0910.5064.
- Whelan, J. T. (2006). Comments on Anisotropic Stochastic Background Searches. Online document. <http://www.ligo.caltech.edu/docs/T/T060162-01.pdf>.
- Whitbeck, D. M. (2006). *Observational consequences of gravitational wave emission from spinning compact sources*. Ph.D. thesis, Proquest Dissertations And Theses 2006. Section 0176, Part 0606 84 pages; [Ph.D. dissertation]. United States – Pennsylvania: The Pennsylvania State University; 2006. Publication Number: AAT 3231915. Source: DAI-B 67/08, Feb 2007.

- Wijnands, R. (2004). An observational review of accretion-driven millisecond X-ray pulsars. *Nuclear Physics B Proceedings Supplements*, **132**, 496–505, arXiv:astro-ph/0309347.
- Wijnands, R. (2006). Accretion-Driven Millisecond X-ray Pulsars. In J. A. Lowry, editor, *Trends in Pulsar Research*, page 53.
- Wijnands, R. & van der Klis, M. (1998). A millisecond pulsar in an X-ray binary system. *Nature*, **394**, 344–346.
- Wijnands, R., van der Klis, M., Homan, J., Chakrabarty, D., Markwardt, C. B., & Morgan, E. H. (2003). Quasi-periodic X-ray brightness fluctuations in an accreting millisecond pulsar. *Nature*, **424**, 44–47, arXiv:astro-ph/0307123.
- Woosley, S. & Janka, T. (2005). The physics of core-collapse supernovae. *Nature Physics*, **1**, 147–154, arXiv:astro-ph/0601261.
- Woosley, S. E. (1988). SN 1987A - After the peak. *ApJ*, **330**, 218–253.
- Woosley, S. E. & Weaver, T. A. (1995). The Evolution and Explosion of Massive Stars. II. Explosive Hydrodynamics and Nucleosynthesis. *ApJS*, **101**, 181.
- Woosley, S. E., Heger, A., & Weaver, T. A. (2002). The evolution and explosion of massive stars. *Reviews of Modern Physics*, **74**, 1015–1071.
- Xilouris, K. M., Kramer, M., Jessner, A., von Hoensbroech, A., Lorimer, D., Wiełebinski, R., Wolszczan, A., & Camilo, F. (1998). The Characteristics of Millisecond Pulsar Emission. II. Polarimetry. *ApJ*, **501**, 286, arXiv:astro-ph/9801178.
- Xu, R. X., Liu, J. F., Han, J. L., & Qiao, G. J. (2000). An Inverse Compton Scattering Model of Pulsar Emission. III. Polarization. *ApJ*, **535**, 354–364, arXiv:astro-ph/9911253.
- Yakovlev, D. G. & Pethick, C. J. (2004). Neutron Star Cooling. *ARA&A*, **42**, 169–210, arXiv:astro-ph/0402143.
- Zel'dovich, Y. B. & Novikov, I. D. (1965). Reviews of Topical Problems: Relativistic Astrophysics. I. *Soviet Physics Uspekhi*, **7**, 763–788.
- Zel'Dovich, Y. B. & Shakura, N. I. (1969). X-Ray Emission Accompanying the Accretion of Gas by a Neutron Star. *Soviet Astronomy*, **13**, 175.

Zimmermann, M. & Szedenits, Jr., E. (1979). Gravitational waves from rotating and precessing rigid bodies - Simple models and applications to pulsars. *Phys. Rev. D*, **20**, 351–355.

Zwinger, T. & Mueller, E. (1997). Dynamics and gravitational wave signature of axisymmetric rotational core collapse. *A&A*, **320**, 209–227.